SEISMIC VULNERABILITY AND POUNDING HAZARD OF ASYMMETRIC BUILDINGS WITH TRANSFER SYSTEM: EXPERIMENTAL AND ANALYTICAL MODELING

LI XIN, WANG

B. Sc., M. Sc.

A Thesis Submitted in Partial Fulfillment of the Requirements for the Degree of Doctor of Philosophy

Department of Civil and Structural Engineering

The Hong Kong Polytechnic University

May, 2007

To

My family

CERTIFICATE OF ORIGINALITY

I hereby declare that this thesis is my own work and that, to the best of my knowledge and belief, it reproduces no material previously published or written, nor material that has been accepted for the award of any other degree or diploma, except where due acknowledgement has been made in the text.

__________________________ (Signed)

WANG Lixin (Name of student)

ABSTRACT

Geographically, Hong Kong is not located in a region with frequent attacks from destructive earthquakes, and historically, there is no provision for seismic design of building structures. However, several previous studies and publications suggest that Hong Kong should be regarded as a region with moderate seismic risk. The main objective of the present study is to investigate the seismic vulnerability of existing wind-designed tall buildings in Hong Kong, for which very often transfer systems and asymmetric structural plans are used. It remains a big issue on how such non-seismic-designed high-rise buildings will perform under the strike of earthquakes.

In this study, the seismic vulnerability of an asymmetric 21-story building in Hong Kong with transfer plate is assessed through conducting shaking table tests. A 1:25 scaled model was designed according to the "additional-mass-similarity-law" and fabricated using micro-concrete, steel wires and meshes. The completed model was tested on the MTS seismic shaking table at The Hong Kong Polytechnic University, subjected to compressed waves of five past earthquakes with scaled peak accelerations of 0.05, 0.1, 0.15, 0.2 and 0.3g. The test results reveal that the transfer plate and stories above are most vulnerable and susceptible to severe damages under the attack of earthquakes. An asymmetric rocking motion and failure pattern of the upper structure above the transfer plate are observed for the first time in our tests.

The damages of the model were evaluated quantitatively through various seismic damage indices, including the ductility, inter-story drift ratio, frequency ratio,

final softening, and Park and Ang damage index. A new but simple algorithm was developed to estimate the overall Park and Ang damage index of the whole structure from measured acceleration and displacement data by idealizing one story as one equivalent element. Utilizing the Park and Ang damage index as a benchmark, the other damage indices are correlated explicitly with various damage states (i.e. slight damage, minor damage, moderate damage, severe damage and collapse) for the first time. This correlation provides a practical approach to assess seismic damages rapidly and is expected to be applicable to other similar buildings in Hong Kong.

In addition to direct damages to individual buildings, earthquakes may also induce damages to buildings through seismic pounding of adjacent structures, especially in metropolitan regions such as Hong Kong. In this thesis, seismic torsional pounding is studied from both theoretical and experimental aspects.

Theoretically, seismic pounding is modeled using the nonlinear Hertz contact. Numerical simulations are conducted to study the torsional pounding between two flexible single-story towers as well as between a flexible tower and a neighboring barrier. An analytical solution is also obtained for the latter case. The results show torsional pounding is much more complex than translational pounding. Possible chaotic impacts make torsional pounding more difficult to be predicted.

The more complex torsional pounding between adjacent multi-story buildings is studied through conducting shaking table tests. Two 1:45 steel models were fabricated to simulate two adjacent 21-story buildings with both transfer plates and asymmetric plans. Pounding tests were conducted between the two models as well as between a flexible model and a nearly rigid wall. The observed pounding can be periodic, group periodic (i.e. a group of non-periodic impacts repeating themselves periodically) or chaotic. Energy may be transferred through pounding from the more massive and rigid structure to the lighter and more flexible one, which causes abnormal large responses and damages to the lighter structure. When the separation distance is zero, the two models respond like a new system, which may have a different dynamic characteristic from those of the individual structures. Thus, pounding may induce an unplanned period shift to existing buildings, which makes their seismic responses more unpredictable than a stand-alone-building.

List of Publications

Chau, K.T., Wang, L.X. and Wei, X.X., 2004. Nonlinear Seismic Torsional Poundings between Two Adjacent Structures. *2004 HKSTAM (The Hong Kong Society of Theoretical and Applied Mechanics) Annual Conference*, March 6, 2004, City University of Hong Kong, Hong Kong.

Wang, L.X., Wen, Z.P. and Chau, K.T., 2004. Vibrations of Assymetric Wall-Frame Structures with Varying Mass and Stiffness along the Height. *2004 ANCER Annual Meeting*, July 28-30, 2004, Hawaii, USA (full paper in CD-ROM).

Chau, K.T., Wei, X.X. and Wang, L.X., 2004. Experimental and theoretical simulations of seismic torsional poundings between two adjacent structures. *Proceedings of the 13th World Conference on Earthquake Engineering (13WCEE)*, August 1-6, 2004, Vancouver, Canada, Paper No. 2176, pp. 284 (full paper in CD-ROM).

Wang, L.X., Chau, K.T., Meng, Q.L. and Wei, X.X., 2005. Earthquake-induced Poundings between Two Asymmetric Tall Buildings: The results of shaking table tests. *2005 HKSTAM (The Hong Kong Society of Theoretical and Applied Mechanics) Annual Conference*, March 12, 2005, The Hong Kong Polytechnic University, Hong Kong, pp. 14.

Chau, K.T., Wang, L.X., Wei, X.X. and Meng, Q.L., 2005. Shaking table simulations of torsional poundings between two 20-story asymmetric buildings in Hong Kong. *2005 ANCER Annual Meeting*, November 10-13, 2005, Jeju, Korea (full paper in CD-ROM).

Chau, K.T., Wang, L.X. and Wei, X.X., 2006. Torsional poundings between two adjacent asymmetric structures. *The 4th International Conference on Earthquake Engineering (4ICEE)*, October 12-13, 2006, Taipei, Taiwan, Paper No. 105, pp. 66

(full paper in CD-ROM).

Wang, L.X. and Chau, K.T., 2006. Rocking failure of a multi-storey building model at transfer plate on shaking table. *Proceedings of the 7th National Conference on Earthquake Engineering*, November 16-19, 2006, Guangzhou, China, Vol.2, pp. 1293-1302.

Wang, L.X., Chau, K.T. and Wei, X.X., 2008. Numerical simulations of nonlinear seismic torsional pounding between two single-story structures. *Advances in Structural Engineering* (in press).

Wei, X.X., Wang, L.X. and Chau, K.T., 2008. Nonlinear seismic torsional pounding between an asymmetric tower and a barrier. *Earthquake Spectra* (in press).

Wang, L.X. and Chau, K.T., 2008. Seismic vulnerability of asymmetric tall buildings in Hong Kong, Part I: Shaking table tests. *Journal of Structural Engineering, ASCE* (under review).

Chau, K.T. and Wang, L.X., 2008. Seismic vulnerability of asymmetric tall buildings in Hong Kong, Part II: Damage assessments. *Journal of Structural Engineering, ASCE* (under review).

ACKNOWLEDGEMENTS

First of all, I am deeply indebted to my chief supervisor, Prof. K.T. Chau, for his patient, persistent and beneficial guidance during my whole Ph.D. study period. His open, critical and creative thinking as well as high efficiency all left me deep impressions. I also benefited a lot from his prudent attitude to research. I would like to express my sincere gratitude to Prof. Y. Chen from China Earthquake Administration, chief supervisor of my M.Sc. degree, for his introduction and kind encouragement to my study in Hong Kong. Special thanks also go to my co-supervisor, Prof. Z.P. Wen from Institute of Geophysics, China Earthquake Administration, for his instructive guidance and passionate encouragement to my study.

I am truly grateful to Prof. X.X. Wei for her beneficial discussion and guidance on my research of seismic pounding. Her smart thinking and hardworking also left me a deep impression. Thanks also go to Dr. S.Z. Wu and Dr. R.H.C. Wong for their help and encouragement to me during the study.

The assistances to my experimental work from Dr. Q.L. Meng and Mr. H.B. Zhang are highly appreciated. Without their help, the accomplishment of the experiments will be impossible. Same thanks also go to the technicians in Light Structures & Dynamics Laboratory and Concrete Laboratory at The Hong Kong Polytechnic University, especially Mr. T.T. Wai, M.C. Ng, C.S. Liu, C.F. Cheung, K.H. Wong and W.K. Ho, and also Mr. C.P. Chow, a final-year undergraduate student, for their generous help and collaboration during the experiment procedure. The instructive advice and guidance on manipulation of experimental data from Prof. S. Zhan are also much appreciated.

Appreciation is extended to the financial support to my study and research from The Hong Kong Polytechnic University, which makes the experiments and other related work become possible.

I also would like to thank my colleagues and friends in CSE Department at The Hong Kong Polytechnic University in the past several years, especially to Dr. M.R. Jiao, J.D. Zhao, D. Wu, Y.W. Jiang, G.F. Zhu, F.L. Hua, L. Yu, and Mr. H.Y. Lin, for their warm friendship and generous help to my study and life in Hong Kong.

Last but not least, I am greatly indebted to my family and Ms. X.Y. Li for their persistent support and encouragement throughout the whole study period.

TABLE OF CONTENTS

LIST OF TABLES

LIST OF FIGURES

CHAPTER 1 INTRODUCTION

1.1 Background

Earthquake has been one of the main natural hazards, causing tremendous loss to both human lives and properties in the world. According to the information from the website of USGS (the United States Geological Survey) Earthquake Hazards Program (http://earthquake.usgs.gov/), a catastrophic earthquake of magnitude 8.2 occurred on September 1, 1923 in Kwanto area in Japan, near Tokyo. The earthquake and the subsequent fires and tsunami of up to 11 meters high killed 143,000 persons and ravaged many cities within Kwanto area, including Tokyo and Yokohama. The great 1960 Chile earthquake with a moment magnitude of 9.5 was the largest earthquake recorded since the invention of modern seismographs in the world, and killed more than 2,000 and injured 3,000. The damage in southern Chile was up to $550 million. Huge tsunami was induced, causing 61 deaths and $75 million damage in Hawaii; 138 deaths and $50 million damage in Japan; 32 dead and missing in the Philippines; and $500,000 damage to the west coast of the United States. The 1964 Alaska Earthquake of a moment magnitude of 9.2 and the subsequent tsunami took 125 lives and caused about $311 million of property loss. More recently, on December 26, 2004, an earthquake with a moment magnitude of 9.1 occurred off the west coast of northern Sumatra, Indonesia. The earthquake and the induced tsunami killed more than 157,577 people. All the above data are abridged from the website of USGS (http://earthquake.usgs.gov/).

According to USGS (http://neic.usgs.gov/neis/eqlists/eqstats.html), annually there is 1 earthquake of magnitude 8 or higher, 17 earthquakes of magnitude 7-7.9, 134 earthquakes of magnitude 6-6.9, and 1319 earthquakes of magnitude 5-5.9. Most of those earthquakes occurred along the boundaries between tectonic plates (called inter-plate earthquakes). For example, earthquakes occurring where plate boundaries converge, such as at trenches, contribute more than 90 percent of the world's release of seismic energy (Bolt, 2004).

However, shallow-focus earthquakes may also take place within plates (called intra-plate earthquakes) (Bolt, 2004). The well-known examples were the great earthquakes that struck the New Madrid area of Missouri in 1811 and 1812, which caused heavy damage in the area and were felt as far away as Washington D.C., New England, and Montreal, Canada (Bolt, 2004). A number of disastrous intra-plate earthquakes also occurred in the mainland of China, for example, on July 27, 1976, an earthquake of magnitude 7.5 hit Tangshan, which was not considered as a strong seismic region traditionally. The earthquake caused a death toll of 255,000 and severe damages to structures as illustrated in Figures 1.1(a) and (b).

Historically, China has suffered more seismic damages and human losses than the other regions of the world. As early as 1556, the great Shanxi earthquake occurred in the central part of China and killed more than 830,000 people (Figure 1.1(c)), which was the deadliest earthquake in human history (Chen, 2000). As shown in

Figure 1.1(d), the regions that were heavily damaged covered an area of 280,000 km^2 and crossed several provinces. In the twentieth century, besides the 1976 Tangshan earthquake, the 1920 Gansu earthquake and the 1927 Tsinghai earthquake both killed more than 200,000.

Situated at the south coast of China, Hong Kong is not located in a region with frequent attacks from destructive earthquakes and no serious damage has ever been caused by earthquakes. Therefore, there has been no provision for seismic design of building structures in Hong Kong. However, although the nearest active tectonic plate boundary (i.e., the boundary between the Philippine Sea plate and the Eurasia plate) is about 680 km away from Hong Kong, historic records have indicated that Hong Kong did experience strong earthquake shaking in the last 400 years.

In 1605, an earthquake of magnitude 7.5 happened at Qiongshan, Guangdong Province (now belonging to Hainan Province); in 1874, an earthquake of magnitude 5 3/4 occurred at Dangan Island, only 30 km south of Hong Kong, which is the largest earthquake observed within 100 km of Hong Kong in the past 500 years and caused an earthquake intensity of V-VI in Hong Kong; the biggest earthquake recorded within 300 km of Hong Kong even reached a magnitude of 7.4, which happened in Shantou area in 1918; on Sept. 16, 1994, buildings on the reclamation areas of Hong Kong experienced a strong far field earthquake of magnitude 7.3 occurred in the vicinity of Dongsha Island, about 450 km away from Hong Kong. Thousands of people felt the ground shaking and left their office buildings. This is the strongest earthquake shaking felt by the public in Hong Kong since 1918.

More recently, the public in Hong Kong felt several earthquake shaking within four months in 2006. On September 14, 2006, an earthquake of magnitude 3.7 occurred at Dangan Island. Dangan Island area, situated about 35 km southeast of Hong Kong Observatory, is definitely a potential seismic source region that can generate earthquakes affecting Hong Kong. Actually it is believed that the maximum credible earthquake magnitude at Dangan Island area may be up to 7.5 (Chau et al., 2002). As mentioned above, in 1874 an earthquake of magnitude 5¾ did occur in this region and led to an earthquake intensity of V-VI on the Modified Mercalli Scale in Hong Kong. On December 26, 2006, two earthquakes struck off the southern coast of Taiwan (of magnitudes 7.1 and 6.9 respectively), and thousands of people in Hong Kong felt the ground shaking and left their homes. Another serious consequence of the earthquakes was that several major international undersea optical fibre cables were broken and Internet services of Asia (including Hong Kong) were slowed down. According to CNN (Cable News Network) reports, data transfer in Hong Kong was slowed down up to 50% (http://www.cnn.com/2006/WORLD/asiapcf/12/27/internet.-asia.reut/index.html). Financial transactions, particularly in the currency market, were also affected. Therefore, although the earthquakes did not cause direct human loss or building collapse in Hong Kong, the economy was affected significantly since Hong Kong is one of the world financial centers and its economy depends greatly on international communication. This may be a new type of financial losses to modern society caused by earthquakes.

In recent years, realizing the potential risk or consequences caused by earthquakes, many researches have been carried out to quantify the seismicity level of Hong Kong. Studies conducted by Lee et al. (1996) have concluded that the Hong Kong region has a probability of exceedance of 10% over a return period of 50 years to experience a peak acceleration of 75-115 gal on bedrock. The seismic level of the Hong Kong is rated as seismic intensity VII with a return period of 475 years. This finding is consistent with those indicated on the seismic zoning map (as shown in Figure 1.2) published by China Earthquake Administration (State Seismological Bureau, 1991). In 1998, Wong et al. (1998a, b) completed a comprehensive seismic hazard analysis based on up-to-date earthquake records with more extensive geographical coverage. Similar conclusions have been reached in that Hong Kong is a region of moderate seismic hazard. Recently the new Chinese code for seismic design of buildings (GB 50011-2001, 2001) has classified Hong Kong as an area of seismic intensity VII with a return period of 475 years and a maximum ground shaking of 0.15g may be encountered in Hong Kong at least once in every 475 years. Therefore, based on all the above studies and publications, Hong Kong should be regarded as a region with moderate seismic risk (Chau et al., 1998).

On the other hand, as Hong Kong is now a major financial centre and one of the most densely populated cities in the world, any interruption to critical facilities and business operations may have serious social and economical consequences. This plus the recent earthquake disasters in Kobe, Taiwan, India and Turkey has raised an increasing concern in local researchers, engineers and the public to the possibility of Hong Kong experiencing a strong earthquake shaking.

In fact, a working group on “seismic design of building in Hong Kong” has been established by the Buildings Department of Hong Kong SAR Government in 1998, and will make appropriate recommendation to the government on the possibility of incorporating the seismic design in the Hong Kong codes. At present, a large number of researches need to be carried out to study the seismic vulnerability of existing wind-designed tall buildings in Hong Kong.

1.2 Motivations and Objectives

1.2.1 Seismic vulnerability

As mentioned before, buildings in Hong Kong were designed according to wind code but not seismic code. Actually, it remains a big issue on how non-seismic-designed buildings will perform under the strike of earthquakes worldwide (Balendra et al., 1999), in the view of the fundamental differences between wind and seismic designs (Nordenson, 1989).

The vulnerability of tall buildings is rather uncertain since the existing loss estimation methodology, such as ATC-13 (ATC, 1985) and HAZUS99 (FEMA, 1999), only classify buildings of more than 8 stories as high-rise. This criterion obviously is not applicable in Hong Kong, where most of the newly constructed buildings, whether for residential or commercial uses, are much more than only 8 stories. The fragility curves or damage probability matrices for taller buildings are obviously quite different from those of 8-story buildings, for higher modes will play more important roles in the taller structures than for the lower ones.

An distinct characteristic of buildings in Hong Kong is that transfer systems are widely used for both residential and commercial buildings (as shown in Figure 1.3), to satisfy different functions above and below transfer systems; typically the upper parts are employed for residential purposes while the lower parts used for shopping centers, restaurants or car parks. However, from the aspect of seismic vulnerability, the transfer systems are not recommended according to Chinese code for seismic design of buildings (GB 50011-2001, 2001), as they introduce abrupt changes of stiffness along the heights.

The other notable characteristic of buildings in Hong Kong is that very often asymmetric plan layouts are used for aesthetic or functional needs, or constrained by the shape of the usable land. Figure 1.3 (c) and (d) showed two examples of this kind of buildings. The asymmetric structural plans usually result in eccentricity between the centers of mass and the centers of stiffness, making those structures prone to torsional responses even under unidirectional ground shaking. According to Chinese code for seismic design of buildings (GB 50011-2001, 2001), the asymmetric plan layouts should also be avoided.

Obviously, to study the seismic vulnerability of wind-designed tall buildings in Hong Kong, the above two distinct characteristics should be included and considered. However, none local research has been attempted to include both the two factors in assessing the seismic vulnerability in the past.

Wen et al. (2002) studied the seismic vulnerability of a 21-story reinforced concrete frame-shear wall building in Hong Kong and the combined effects of the soil condition and epicentral distance on the seismic vulnerability were investigated. The equivalent lateral force method was adopted to analyze the seismic responses and forces. And the resulting story shear forces were compared with the story yield shear forces to estimate the ductility, and subsequently the damage states of the building.

One big advantage of this simple method is that the computational effort required is much less than those of nonlinear dynamic analyses. However, it is a rather approximate and simplified method, for by applying the equivalent lateral force method, each story of a building is modeled by only one lateral degree of freedom along the shaking direction. The higher mode effects can only be approximately accounted for whereas the effects of torsional motions were not considered.

Su et al. (2002) assessed seismic performance of transfer structures using various seismic assessment methodologies. A hypothetical 35-story reinforced concrete structure was developed to be studied based on Hong Kong design practice. The structure had a transfer plate of 2.5 m thick at the 6th story level, with the upper structure above the transfer plate supported by coupled shear walls whereas the structure below the transfer plate supported by “mega-columns” (of 2.5 m diameter). The results indicated that the mega-columns supporting the transfer plate and the coupling beams at higher zones (higher than the 18th floor) were the most vulnerable components under earthquake shaking. Again, the model studied was symmetric and torsional vibrations were not significant.

From experimental aspect, Lam et al. (2002) and Li et al. (2006) conducted a shaking table test for a 1:20 scaled model of a typical 42-story building with transfer system in Hong Kong. The results showed that the story above the transfer plate is the weakest story and is prone to severe damages under the shaking of earthquakes. Recommendations are proposed for future seismic provisions, such as reducing any change in stiffness at the transfer zone. However, the building was generally symmetric and torsional response has not been significant.

Therefore, there is a need to study the seismic vulnerability of typical buildings in Hong Kong with both asymmetric plan and transfer system, either theoretically or experimentally. Therefore, the first objective of this study is to study the seismic vulnerability of such buildings through conducting model testing on shaking table. Although it is difficult that the performance of the reduced-scale model can accurately reflect that of the actual building, it is hoped that the model testing can still provide some valuable insights into the seismic vulnerability of this kind of buildings. More specifically, a 1:25 scaled model will be designed and fabricated for a selected 21-story building in Hong Kong, and then tested on the shaking table under the shaking of different earthquake with different peak accelerations. The damages of the model during the tests will be assessed through both visual inspections and various seismic damage indices, including the ductility, inter-story drift ratio, frequency ratio, final softening index, and Park and Ang damage index (Park and Ang, 1985).

A FEM (Finite Element Method) model will be set up using commercial package Sap2000 for the same scaled model before the shaking table tests. The obtained modal properties, dynamic responses and stress concentrations under earthquake excitations from FEM analyses will provide guidance for the shaking table tests. The FEM prediction will also be compared with the experimental results.

1.2.2 Seismic torsional pounding

During real earthquakes, sometimes the seismic vulnerability of a building structure is not only determined by the dynamic characteristics of the structure itself, but also influenced by vibrations of adjacent buildings through pounding. Pounding hazard may be especially severe in metropolitan regions like Hong Kong, where many buildings are very closely distributed due to limited land and separation distances between buildings are insufficient to avoid impacts under earthquake excitations. The second part of the thesis will concentrate on the seismic pounding issue.

Seismic pounding (i.e. earthquake induced collisions between adjacent structures) has been frequently observed in past strong earthquakes, for example, in the 1964 Alaska earthquake (Anagnostopoulos, 1994), the 1968 Tokachi-Oki earthquake (Wakabayashi, 1986), the 1976 Tangshan earthquake (Liu et al., 1993), and the 1999 Chi-Chi earthquake (Naeim et al., 2000).

The 1985 Mexico City earthquake may have the largest number of buildings severely damaged due to pounding effects in the recorded history of earthquake damages (Bertero, 1986). According to the statistic by Rosenblueth and Meli (1986), out of a total of 330 collapsed or severely damaged multi-story buildings in the 1985 Mexico City earthquake, pounding occurred in over 40% of all the cases and led to collapse in 15% cases.

Based on the survey on damages caused by pounding in the San Francisco Bay area during the 1989 Loma Prieta earthquake, Kasai et al. (1992) found more than 200 pounding occurrences involving more than 500 structures; in 21% cases pounding caused major structural damages and in the other 79% cases pounding induced architectural and/or minor structural damages.

A considerable amount of research has been conducted on the modeling of pounding phenomenon between structures, based on either single degree-of-freedom (SDOF) models or multi-degree-of-freedom (MDOF) models. Among them, the pounding model by Davis (1992), which utilizes the nonlinear Hertzian contact to model the impact force, is considered to be more realistic because actual poundings are seldom linear. Chau and Wei (2001) extended the model of Davis (1992) to consider pounding as nonlinear Hertz impact between two SDOF oscillators. Shaking table tests have also been performed by Chau et al. (2003) to verify the nonlinear impact model.

However, as indicated previously, buildings with asymmetric plans, which are common in Hong Kong, will in general undergo torsional vibrations in addition to lateral responses when subjected to earthquake shaking. Torsional responses may result in torsional pounding between adjacent structures, which is much more complicated than unidirectional pounding. Actually pounding induced by torsional response of building has been observed during earthquakes. For example, during the 1985 Mexico City earthquake, torsional poundings were observed between corner buildings (building at the corner of an intersection of two perpendicular roads) and caused severe local damages (Bertero, 1986). The torsional responses of those corner buildings resulted from their asymmetrically distributed stiffness. During the 1989 Loma Prieta earthquake, poundings induced by torsional behaviors of buildings were also observed for corner buildings in San Francisco Marina district as well as the Oakland City Center (Kasai and Maison, 1997). Seismic torsional pounding may even occur in rather symmetric buildings (Leibovich et al., 1996). However, there are relatively few theoretical and experimental research conducted on this topic. Therefore, the second objective of this thesis is to study the torsional pounding phenomena between both simplified theoretical models and complex physical models of actual buildings.

Extending the models by Davis (1992) and Chau and Wei (2001), the torsional pounding between two flexible single-story towers as well as between a flexible tower and a neighboring barrier will be studied using the nonlinear Hertz contact law. Numerical integrations will be used to solve the equations of motion. For the torsional pounding between an asymmetric single-story tower and a rigid barrier, an analytical solution is also obtained and compared with the numerical results. Parametric studies will be conducted to investigate the influences of various parameters, such as the excitation frequency, damping ratio, eccentricity and separation distance.

In addition to the theoretical study on torsional pounding between single-story structures, more complicated seismic poundings between real adjacent multi-story buildings will be studied through conducting shaking table tests. More specifically, two 1:45 scale steel models are fabricated to simulate two real 21-story asymmetric buildings with transfer systems in Hong Kong. Pounding tests are conducted between the two flexible models as well as between one flexible model and one nearly rigid wall on the shaking table. The experimental results will also be compared with the theoretical studies.

1.3 Outline of the Thesis

The seismic vulnerability of buildings in Hong Kong will be investigated through experimental and analytical modeling in this study from the following two aspects: the seismic vulnerability and torsional pounding hazard. Accordingly, the thesis will be organized in two main parts: Chapters 2-6 will concentrate on experimental studies of the seismic vulnerability of a selected 21-story building in Hong Kong; whereas Chapters 7 and 8 will concentrate on the theoretical and experimental studies on seismic torsional poundings between adjacent structures.

More specifically, Chapter 2 focuses on the FEM analyses of a 1:25 scaled model of the selected 21-story asymmetric building with transfer plate in Hong Kong. The modal characteristics of the model as well as the dynamic responses and stress concentrations under earthquake excitations are investigated using FEM. The results will guide the conduct of the shaking table tests.

Chapter 3 introduces the design and fabrication of the physical scaled model for the shaking table tests. The similarity law for structural dynamics, which is the basis of the model design, will be briefly introduced first. The model design is then carried out according to it. Finally the fabrication procedure and instrumentations of various transducers and sensors are described.

Chapter 4 describes the procedure of the shaking table tests by applying various earthquakes of various peak accelerations. Modal test is conducted after each set of tests to monitor the change of natural frequencies of the model due to potential damages. The dynamic responses of the model during various earthquake inputs are investigated. The crack patterns induced are examined through visual inspection.

Chapter 5 focuses on quantitative evaluations of damages of the model using various seismic damage indices, including the ductility, inter-story drift ratio, frequency ratio, final softening, and Park and Ang damage index. Using the estimated Park and Ang damage index as a benchmark, the correlations between other damage indices with various damage states (i.e. slight damage, minor damage, moderate damage, severe damage and collapse) are finally established.

Chapter 6 summarizes the model testing described in Chapters 3-5, then makes some comparisons between the experimental results and the finite element analysis results described in Chapter 2, and finally compares the structural features between the model and the actual building, including beams, columns and walls. Discussions and recommendations are made on the future model testing.

Chapter 7 concentrates on the theoretical studies on torsional pounding between adjacent structures. First, literature reviews on pounding hazard, pounding modeling and mitigation are given. Then, the torsional pounding between two flexible single-story towers will be numerically simulated using the nonlinear Hertz contact law. Finally, an analytical solution is obtained for the torsional pounding between a tower and a rigid barrier, and the results are compared with the numerical simulations.

Chapter 8 introduces the experimental studies on seismic pounding between real multi-story buildings. Two scaled steel models are designed and fabricated to model two adjacent 21-story asymmetric buildings with transfer systems in Hong Kong. Pounding tests are conducted between the two flexible models as well as between one flexible model and one nearly rigid wall on the shaking table. The phase diagrams, maximum dynamic responses and maximum impact forces are investigated. The experimental results will also be compared with the theoretical studies.

Chapter 9 summarizes the main conclusions of the whole thesis and indicates the implications of the results. The limitations of the present study are also discussed and recommendations are made for further studies.

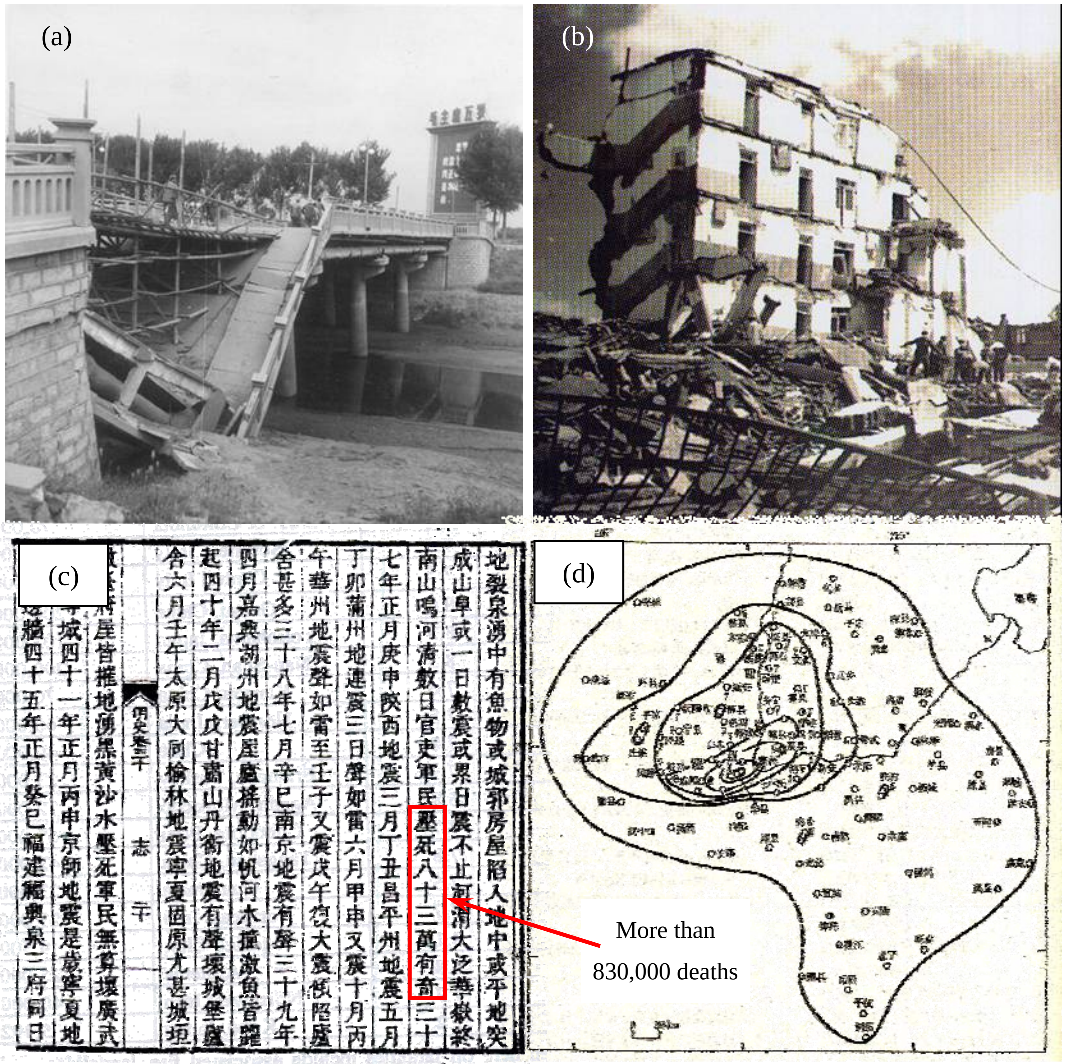

Figure 1.1 Damages caused by past major earthquakes in China: (a), (b) structures damaged during the 1976 Tangshan earthquake (Qi and Jiang, 1999); (c) historical record of the 1556 Shanxi earthquake which killed more than 830,000 people (Chen, 2000); (d) the influence zone of the 1556 Shanxi earthquake (State Seismological Bureau, 1995).

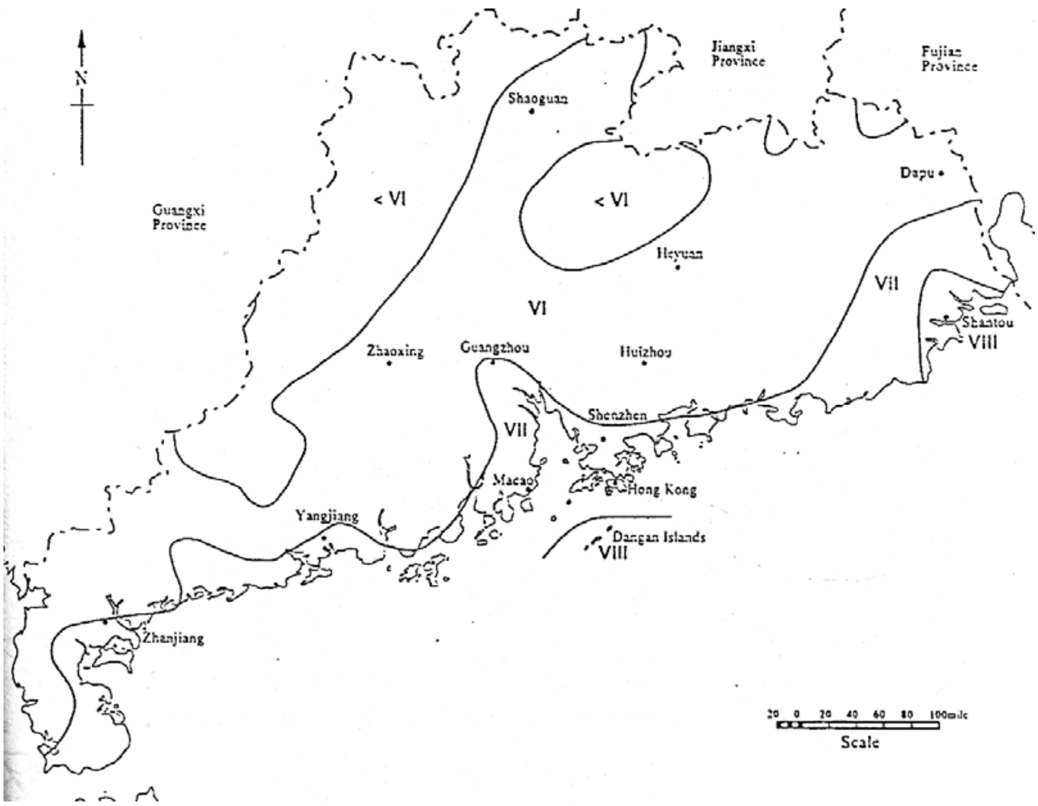

Figure 1.2 Seismic intensity zonation of Guangdong Province, China (after State Seismological Bureau, 1991).

Figure 1.3 Photographs showing several typical high-rise buildings in Hong Kong with transfer systems: (a) Sorrento Tower (residential); (b) May House; (c) Conrad International Hotel; (d) Four Seasons Place. The latter three buildings are for commercial uses. Note that asymmetric plans are used for the latter two structures.

PART A

SEISMIC VULNERABILITY USING SHAKING TABLE TESTS

CHAPTER 2 DYNAMIC CHARACTERISTICS OF BUILDING MODEL FROM FINITE ELEMENT ANALYSES

2.1 Introduction

As mentioned in Chapter 1, previous studies and investigations have suggested that Hong Kong should be regarded as a region with moderate seismic risk (Chau et al., 1998). In recent years, local researchers, engineers and the general public have begun to concern the possibility of a strong earthquake attack in the vicinity of Hong Kong. For example, it has been believed that the maximum credible earthquake magnitude at Dangan Island area, which is only 30 km south of Hong Kong, may be up to 7.5 (Chau et al., 2002). On the other hand, due to historical reasons, most Hong Kong buildings are constructed according to wind code with no seismic provision. It remains an unsettled issue on how these buildings will perform under the strike of earthquakes (Balendra et al., 1999), in view of the fundamental differences between wind and seismic designs (Nordenson, 1989).

Moreover, the vulnerability of tall buildings is rather uncertain since the existing loss estimation methodologies, such as ATC-13 (ATC, 1985) and HAZUS99 (FEMA, 1999), only classify buildings of more than 8 stories as high-rise. Obviously, such classification is not applicable for the case of Hong Kong, where most of newly constructed buildings are more than 30 stories. The seismic vulnerability for taller buildings is obviously different from that of 8-story buildings, for higher modes will play more important roles for taller structures.

To make things more complicated, transfer system and asymmetric structural plan are commonly used in high-rise buildings in Hong Kong as descried in Chapter 1. Transfer system normally introduces abrupt changes to stiffness along the building height, whereas asymmetric plan makes the center of stiffness offset from the center of mass and normally induces torsional responses under earthquake shaking. To assess the seismic vulnerability for such irregular structures, proper and accurate methods are needed.

At present, the widely-used methodologies for seismic assessment include the equivalent static force method, the modal response spectrum method, and the linear or nonlinear time history method (Saatcioglu and Humar, 2003). Among them, the dynamic time history analysis method is normally considered as the most accurate approach. Actually as Tso and Meng (1982) concluded, that for eccentrically set-back buildings dynamic analysis may be the only reliable procedure for estimating the torsional loading on these buildings.

In this study, the seismic vulnerability of a 21-story asymmetric building with transfer plate in Hong Kong is considered through a model test on shaking table. To guide our model design, a FEM (Finite Element Method) analysis of the model is conducted using the commercial package SAP2000. In particular, dynamic time history analyses will be conducted to study the model's responses and vulnerability under earthquake excitations. Through the FEM analyses, modal characteristics of the model as well as dynamic stress concentration of the model are also obtained. This information provides us the guidance to determine the locations of strain gauges, accelerometers and displacement transducers in our shaking table tests.

In this chapter, the building selected for investigation will be described first. Then a FEM model will be set up for a scaled model of the building. The modal characteristics are obtained through FEM analysis. Finally dynamic responses of the model as well as stress concentration in the model under earthquake excitation will be obtained through time history analysis.

2.2 Building Selected for Investigation

As indicated in Chapter 1, the two most distinct characteristics of high-rise buildings in Hong Kong are the use of transfer systems and the use of asymmetric structural plans. Therefore, this study attempts to investigate the seismic vulnerability of such kind of tall buildings. Thus, a structure with these features was selected among over 100,000 buildings in Hong Kong.

After extensive field investigations, a 21-story reinforced concrete frame-shear wall building situated in Wanchai on Hong Kong Island was selected. The building is called the Empire Hotel, which has a plan of “L-shape” as well as a transfer plate between the lower and upper floors. As shown in Figure 2.1(a), the building locates in one of the most crowded areas in Hong Kong densely filled with high-rise buildings and skyscrapers. The detailed structural design diagrams of the building are obtained from the Buildings Department of the Hong Kong Government.

One of the most noticeable characteristics of the Empire Hotel (referred to as EH hereafter) building is its L-shaped plan, as shown by the small sketch in Figure 2.1(a). From the photographs in Figures 2.1(b) and (c), it can be noticed that the two sides of the building have different numbers of guest rooms (i.e. different dimensions). This unsymmetrical structural form is conducing to torsional responses when subjected to earthquake excitations.

Another distinct feature of the EH building is the employment of a transfer plate of 1.5 m thick at the 2^{nd} floor (see the small sketch in Figure 2.2). This kind of transfer system is commonly used in Hong Kong. In this thesis, the story number is defined in the following way: the $n-1^{th}$ floor plus the space between n^{th} floor and $n-1^{th}$ floor is defined as the n^{th} story. For example, the ground floor (G/F) plus the space between 1/F and G/F is called the 1^{st} story. From the plan views shown in Figures 2.2(a) and (b), it is clearly seen that the building has totally different structural forms below and above the transfer plate. In particular, the first two stories below the transfer plate mainly consist of columns, core walls and limited shear walls (see Figure 2.2(a)), whereas the typical floors above the transfer plate consist of shear walls and core walls (see Figure 2.2(b)).

As shown in Figure 2.2(a), the columns in the first two stories below the transfer plate include 16 circular columns of either 1.0 m or 1.2 m in diameters and 4 rectangular ones (of 1.2×0.8 m, 1.5×0.685 m and 1.5×0.55 m in dimensions), and core walls of mostly 300 mm thick. In Figure 2.2(b), the shear walls of the typical stories are normally of 200 mm thick. The slab thicknesses of the first and second floors are 150 mm and 200 mm respectively whereas the typical floor has a slab thickness of 125 mm. The concrete of grade C30 (corresponding to a cubic compressive strength of 30 MPa) is used.

The structural forms adopted in the upper and lower stories are determined by their various functional requirements. In the present hotel building, the first two stories serve as the reception lobby, bar and restaurant, where large clearance and open spaces are needed, so column-beam system is adopted. The typical stories are for guest rooms, so shear walls are adopted to provide resistance to vertical and lateral loads for the upper part of the structure.

The story heights and floor areas of each story are listed in Table 2.1. The building has a total height of 69.65 m and the upper typical story has a height of 3 m. Larger story heights are designated for the first two stories, the third story and the roof story. The first two stories are for lobby mezzanine, whereas the third story serves as a business center and the roof story consists of a swimming pool and a health club.

Geographically, the EH building is situated in a reclamation area. A soil layer of about 50 m thick is found beneath the ground surface. The soil profile mainly consists of fill material, marine deposit and completely decomposed granite and the details can be referred to Section 3.3.1. The soil profile has an equivalent shear wave speed of 237 m/s and belongs to Site Classification II according to “Chinese Code for Seismic

Design of Buildings" (GB50011-2001, 2001). However, only the super structure above the ground level is considered in this study and the complication due to soil-pile-structure interaction is not considered. Potential soil-pile and soil-pile-structure interactions have been discussed by Koo et al. (2003), Chau and Yang (2002) and many others, but they are out of the scope of the present study.

2.3 FEM Analyses

In this study, a 1:25 scaled physical model of the EH building will be fabricated and tested on the shaking table to investigate the seismic vulnerability of typical buildings in Hong Kong The length scale of 1:25 is determined primarily by the headroom clearance of our laboratory and the load capacity of the MTS shaking table at the Hong Kong Polytechnic University (see Chapter 3 for further details). To design our physical model test, FEM analysis of the 1:25 scaled model is conducted first. The results of FEM analysis provide the dynamic characteristics of the model as well as the locations of stress concentration in the model when it is subjected to seismic excitation. This information provides us the guidance to determine the locations of strain gauges, accelerometers and displacement transducers.

However, it should be borne in mind that FEM analysis is for idealized model (such as line element concept for beam and column and rigid floor assumption). The results of FEM may not necessarily reflect the true behavior of the model, and special care must be taken in interpreting the results. Nevertheless, FEM analysis should provide insightful information for the design of the monitoring system in our shaking table tests.

2.3.1 Model set-up

The FEM model set-up is based on the detail drawings of the building obtained from the Buildings Department of the Hong Kong SAR Government. All dimensions are scaled down according to the 1:25 length scale (i.e. the length scale $\lambda_l = 1/25$). The micro-concrete with a Young's modulus of 7.09 GPa is used. Note that the micro-concrete is a concrete mix with a reduced aggregate size (Noor, 1991) and is obtained by mixing cement, sand and water in our shaking table tests. The detailed design for the micro-concrete is given in Chapter 3.

The commercial computer package, SAP2000 v.8.1.2, is used in the FEM analysis in the present study. Nonlinear dynamic response of the model is highly sensitive to the choice of the constitutive model used in modeling the damage process of the micro-concrete, but reliable constitutive model is not available for the material. Therefore, only elastic analysis will be conducted.

Figure 2.3 shows various views of the building model used in SAP 2000. It is clearly seen that the first two stories have different structural scheming from the upper typical stories. In the FEM model, frame elements are used to model beams and columns, and shell elements are used to model walls and floor slabs. Rigid diaphragm action is assumed for all the floor slabs (i.e. the slabs are considered to be rigid in their own planes). However, as will be seen in later Chapter 4, this assumption may not be appropriate for the present structure. The nodes at the ground level are all assumed to be fixed, as no soil interaction is considered here.

2.3.2 Modal characteristics

First, modal analysis is conducted to determine the modal characteristics of the model. As additional mass (of 4.43 ton weight totally) is added to the scaled model to better fulfill the similarity law (see Chapter 3 for details), the model with additional mass is considered in the FEM analysis. For comparison purpose, a model with no additional mass is also analyzed using FEM.

The spatial distribution of the additional mass is given in Chapter 3. In the real physical model, the additional mass is in the form of cast-iron plates inserted into each story, whereas in the FEM model the additional mass is modeled through the increase of the densities of the floor slabs. Note that the stiffness of the structure will not change by this adjusted density.

For comparison, the natural periods and frequencies of the first six modes of the model and the model with additional mass are given in Table 2.2. As can be seen, the natural frequencies reduce when the additional mass is added. This is expected because the added mass increases the total weight but does not change the stiffness of the model (recall that $\omega = \sqrt{k/m}$ for single degree of freedom oscillator, where ω

is the circular frequency, k is the stiffness and m is the mass of the oscillator). The first six natural frequencies of the model with additional mass are all below 20 Hz and are within the working frequency range of the MTS shaking table (1-50 Hz) used in the present study.

The corresponding three-dimensional mode shapes of the first six modes for the model with additional mass are shown in Figure 2.4. From the diagrams, it can be seen that the first three modes roughly correspond to the first modes in the x, y and θ (torsional) directions respectively. It should be emphasized that there are not pure modes because the two translational vibrations are all coupled with the torsional motions. The latter three modes represent the higher modes with very distinct vertically variations of responses.

Figure 2.5 shows the normalized mode shapes of the first six modes at Corner II of the model (i.e. the translational displacements of Corner II at different floors). Note that all displacements have been normalized with respect to the maximum displacement of each mode. As can be seen, the maximum responses of all the six modes occur at the roof, but for the latter three modes the middle-level (6/F-9/F) responses of the model are also not negligible. Moreover, it is clearly seen that there are sudden changes in the mode shapes at 2/F for the latter three modes. This is probably due to the abrupt change of stiffness across the transfer plate.

To further investigate the stiffness changes, the statically lateral stiffness of each story is also estimated using FEM analysis. For the n^{th} story, its lateral stiffness is estimated through the following approach: (i) first all degrees of freedom of all vertical elements of the story are fixed at the bottom (i.e. above the $n-1^{\text{th}}$ floor slab); (ii) a horizontal force F_n is then applied at the center of mass of the n^{th} floor slab; (iii) the lateral stiffness of the n^{th} story can be estimated as $k_n = F_n / \delta_n$ (where δ_n is the resulting horizontal displacement of the center of mass of the n^{th} floor slab).

The results of estimated lateral stiffness of different stories are listed in Table 2.3. Also shown are the ratios of lateral stiffness of different stories with respect to the stiffness of the typical stories (4^{th}-20^{th}). Note that the first two stories (consisting of frames and core walls) have a smaller lateral stiffness than the above typical stories (consisting of shear walls and core walls). The top (or 21^{st}) story has the same structural form as the typical stories and its smaller stiffness is due to its higher story height (see Table 2.1).

According to "Chinese Code for Seismic Design of Buildings" (GB50011-2001, 2001), if the lateral stiffness of one story is less than 70% of the stiffness of the story above it, the building should be considered to be vertically irregular and special measures should be adopted for the weak story. It is clear that the transfer plate system induces severe vertically irregular to the present building. More importantly, this kind of structural irregularity is not favorable in seismic design of buildings. Therefore, the study of the seismic performance of such building is of paramount importance for regions of moderate seismicity with no seismic provisions in building regulation, like Hong Kong.

2.3.3 Time history analyses

2.3.3.1 Input earthquake wave

For the dynamic time history analysis, real earthquake records have been employed. In particular, the 1995 Kobe earthquake (with a moment magnitude of 6.9 and a peak acceleration of 0.821g) is selected as the input. The earthquake record is first compressed using a time scale of $\lambda_t = \sqrt{\lambda_l} = 0.2$ according to the requirement of the similarity law (refer to Chapter 3 for details). Figure 2.6(a) shows the time history of Kobe earthquake after time compression, where the peak acceleration has been scaled down to 0.1g. The earthquake excitation will be input along the *x* direction as shown in Figure 2.3. The Fourier spectrum of the earthquake wave after time compression is shown in Figure 2.6(b), from which it is found that the predominant frequency is about 7.243 Hz. The frequency range corresponding to 70% peak of the Fourier amplitude is 4.870-14.299 Hz. Referring to Table 2.2, it can be seen that the predominant frequency range of the selected earthquake is close to the first six natural frequencies of the model, thus relatively large responses and subsequent damages may be expected. Therefore, the 1995 Kobe earthquake is a reasonable choice for the proposed model. Actually, as will be described in Chapter 3, the same earthquake record will also be selected as one of the inputs in our shaking table tests.

2.3.3.2 Dynamic responses

The compressed Kobe earthquake wave with a 0.1g peak acceleration shown in Figure 2.6(a) was used in our FEM time history analysis. Figure 2.7 shows the acceleration and displacement time histories in the direction of excitation (i.e. the x direction) at Corner II (see Figure 2.5 for definition) at the roof (21/F) and the transfer plate level (2/F) respectively. The peak acceleration responses at 21/F and 2/F are 0.262g and 0.105g respectively. That is, the response of the part below the transfer plate is at about the same level with the ground acceleration, whereas the response is amplified significantly at the roof (about 262% of the input level). As shown in Figure 2.7(b), the peak displacement at the roof reaches 2.936 mm, which is more than 14 times of that at the transfer plate of 0.208 mm.

To further investigate potential story damage, the inter-story drift ratios (IDR) are calculated for each story as a function of time. The inter-story drift at the n^{th} story is defined as the displacement at the n^{th} floor subtracting that at the n-1^{th} floor, and the inter-story drift ratio equals to the inter-story drift divided by the story height.

A maximum IDR value is selected for each story over the entire time history, and the results at the four corners (I-IV) along the x and y directions are plotted in Figure 2.8 respectively. As can be seen, due to rigid floor slabs assumed in our FEM analysis, Corners I and II have the same IDR values along the x direction at every floor, whereas Corners III and IV have different IDR values since the translational responses appear to couple with the torsional responses. In particular, Corners III and IV have different distances to the center of rotation. Similarly along the y direction, Corners I and IV as well as Corners II and III have the same IDR values respectively. Results of FEM analysis suggests that the maximum inter-story drift ratios along the x direction occur at 17/F-18/F and the parts below the transfer plate (2/F) have relatively small IDR values.

The maximum inter-story drift ratios along the *y* direction show more complicated patterns. Since only unidirectional (i.e. the *x* direction) earthquake input is used in this study, the structural vibrations along the *y* direction are totally induced by the torsional responses, resulting in much smaller IDR values than those along the *x* direction. For this case, the IDR values at Corners I and IV for upper stories are more uniform than those along the *x* directions. The maximum IDR values along the *y* direction occur at 4/F for Corners I and IV, and at 15/F for Corners II and III. The IDR curves at Corners II and III along the *y* direction contain more drastic changes than that along the *x* direction. A lower IDR value occurs at the 3rd story for Corners II and III. Note, however, that those IDR values plotted in Figure 2.8 do not necessarily occur at the same time (since a maximum value has been picked over the entire time history).

To investigate the rotational responses, the maximum absolute rotation angles at every floor are plotted along the building height in Figure 2.9. The rotation is given in the unit of degree and is computed from the difference of translational displacements at two selected corners divided by the distance between them, as shown by the equations in the figure. Since the floor slabs are assumed rigid, the rotations calculated using four different methods are all the same (see Figure 2.9). From those curves, the maximum rotation occurs at the roof, suggesting that the first rotational mode dominates. However, the curve is not a completely straight line, probably due to the higher mode responses.

2.3.3.3 Stress concentration

Besides the maximum responses, the maximum forces and stress in structural elements are also investigated. The results will help to decide the locations of strain gauges used in our shaking table tests to be described in Chapters 3 and 4. Figure 2.10 shows the maximum shear forces and bending moments at columns and beams when the model is subjected to the input of 0.1g Kobe earthquake. The maximum values occur at columns below the transfer plate as indicated in the figure.

Figure 2.11 shows the maximum normal and shear stress values of wall elements during the input time history. The maximum stresses appear at the bottom of walls just above the transfer plate. Moreover, the maximum stresses concentrate at those walls situated at two diagonal corners of the building (Corners I and III in the figure). This suggests that there may be diagonal rocking of the whole structure. Actually, this phenomenon has been observed and validated in our shaking table tests later and the details can be referred in Chapter 4.

To show the exact locations of the maximum bending stresses and bending moments, sketches for the first three stories are given in Figures 2.12-2.14. The distribution of those maximum stresses will be used as a reference on deciding where to install strain gauges in our shaking table tests later. Note that the strain gauges will not be placed totally according to the FEM results due to the possible uncertainty in FEM analyses. As described in Chapter 3, by taking the FEM results as reference, the 32-channel strain gauges (as sketched by the black or gray filled rectangles on the surfaces of walls or columns shown in Figures 2.12-2.14) will be distributed as evenly as possible within the whole building plan.

Table 2.1 The story heights and floor areas of different stories of the EH building.

Story	Height (m)	Area (m^2)
1	4.95	796.98
2	3.7	849.7
3	4	622.2
4-20	3	622.2
21	4.5	622.2
Total	69.65	

Table 2.2 Natural periods and frequencies of the first six modes of the model with and without additional mass.

Mode	Without additional mass		With additional mass	
	Period (s)	Frequency (Hz)	Period (s)	Frequency (Hz)
1	0.109	9.174	0.316	3.165
2	0.096	10.417	0.276	3.623
3	0.092	10.870	0.255	3.922
4	0.028	35.714	0.078	12.821
5	0.025	40.000	0.071	14.085
6	0.023	43.478	0.063	15.873

Table 2.3 Lateral stiffness of different stories of the model from FEM analysis.

Story	Stiffness ($\times 10^8$ N/m)	Ratio
1	2.30	0.31
2	2.29	0.31
3	7.60	1.03
4-20	7.39	1.00
21	4.78	0.65

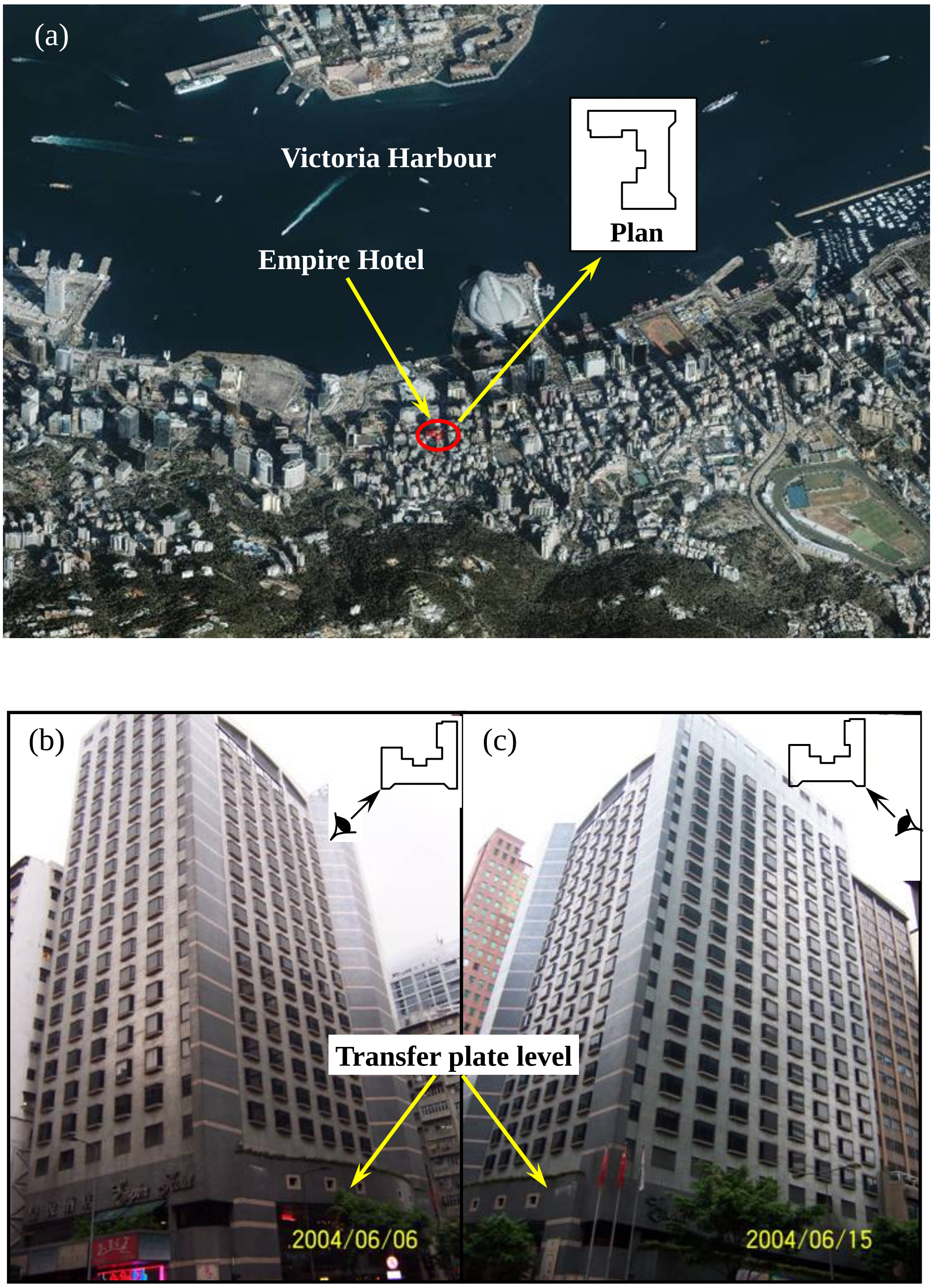

Figure 2.1 Photographs of the 21-story Empire Hotel (EH) building situated on Hong Kong Island: (a) the location map (the attached small sketch showing its story plan); (b) left-side view; (b) right-side view.

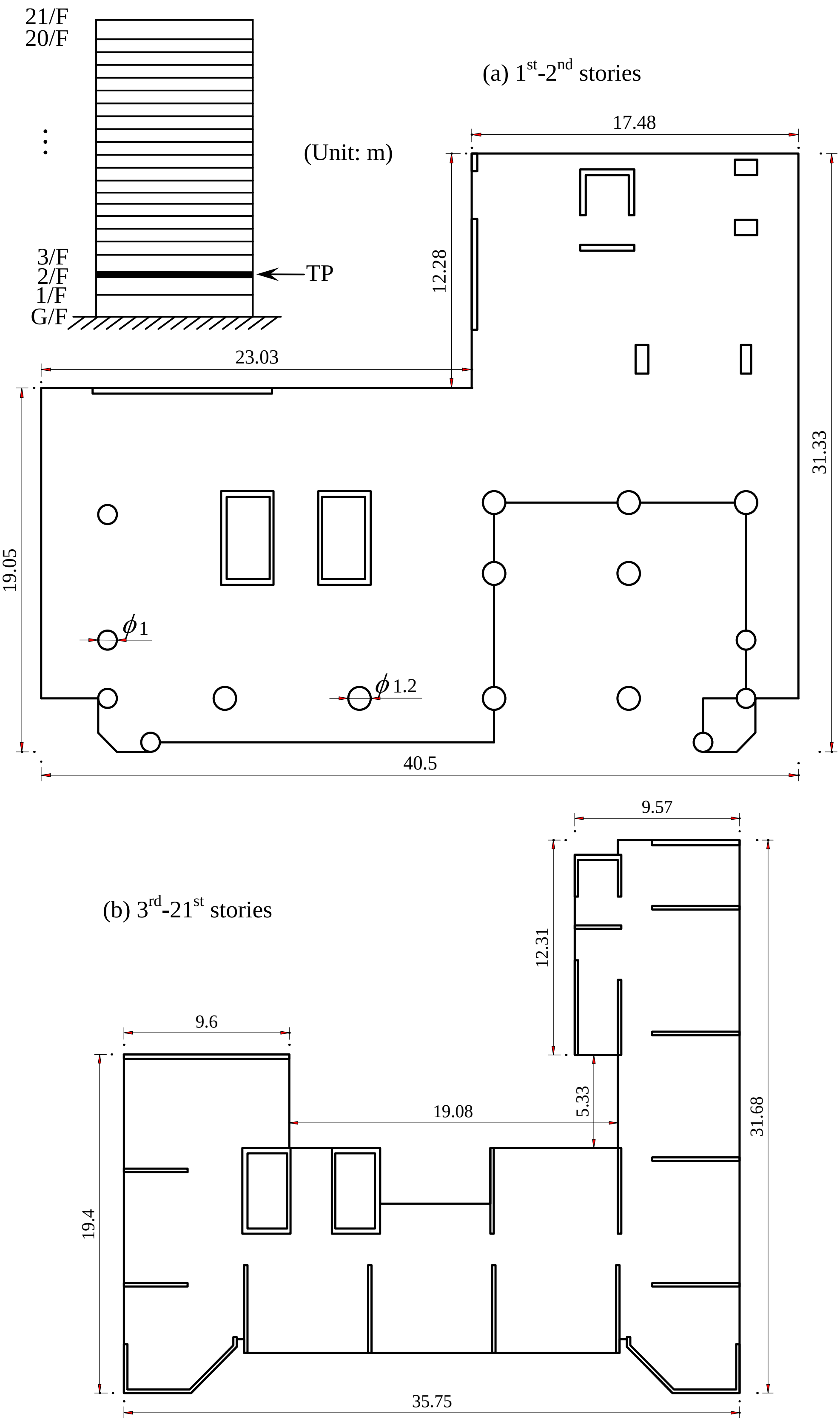

Figure 2.2 Floor plans for (a) 1st-2nd stories; (b) typical (3rd-21st) stories of the EH building. The small sketch attached shows the elevation view of the building, where TP denotes the transfer plate.

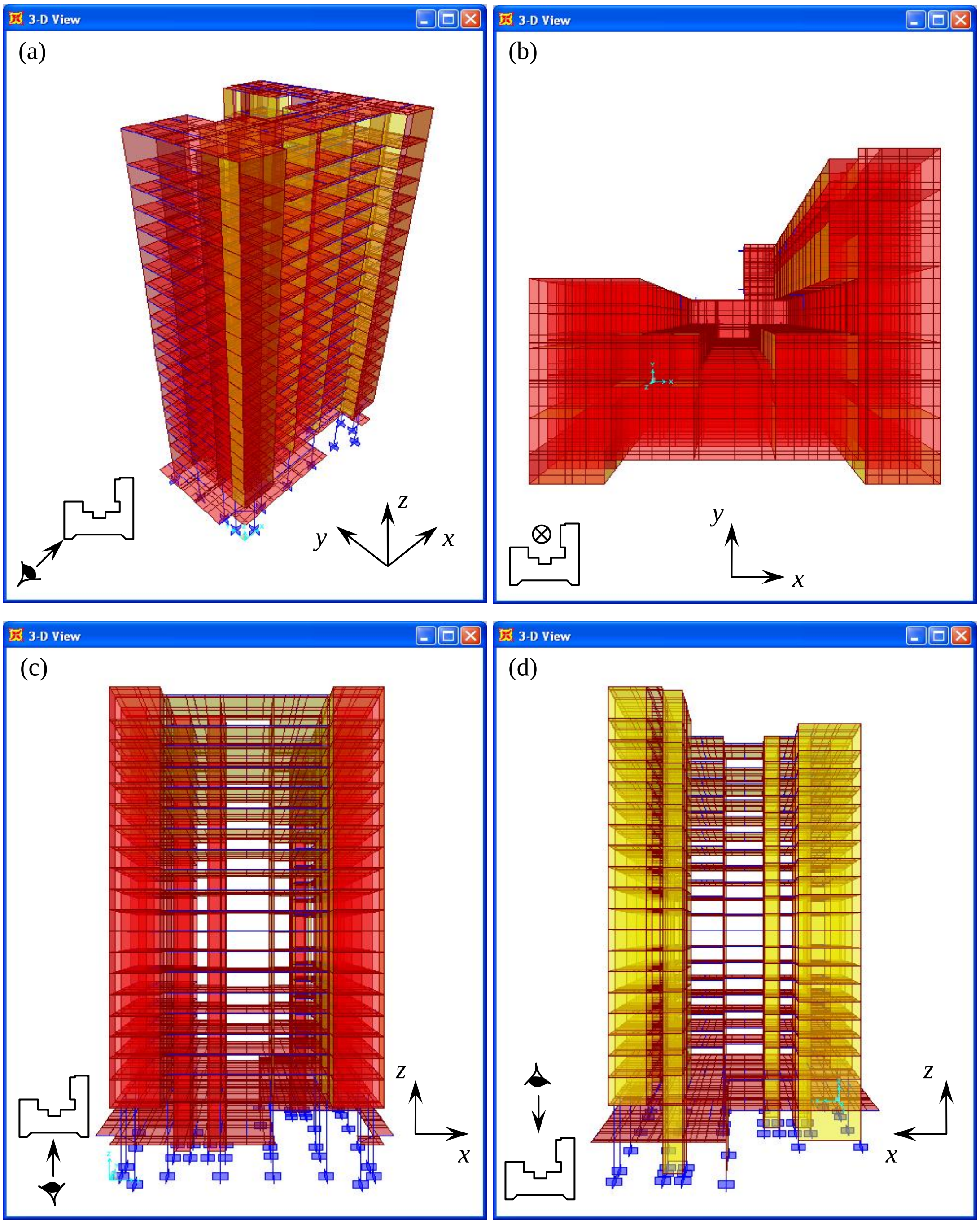

Figure 2.3 The 1:25 FEM model of the EH building used in SAP 2000: (a) 3D perspective view; (b) plan view from the top; (c) front view; (d) back view.

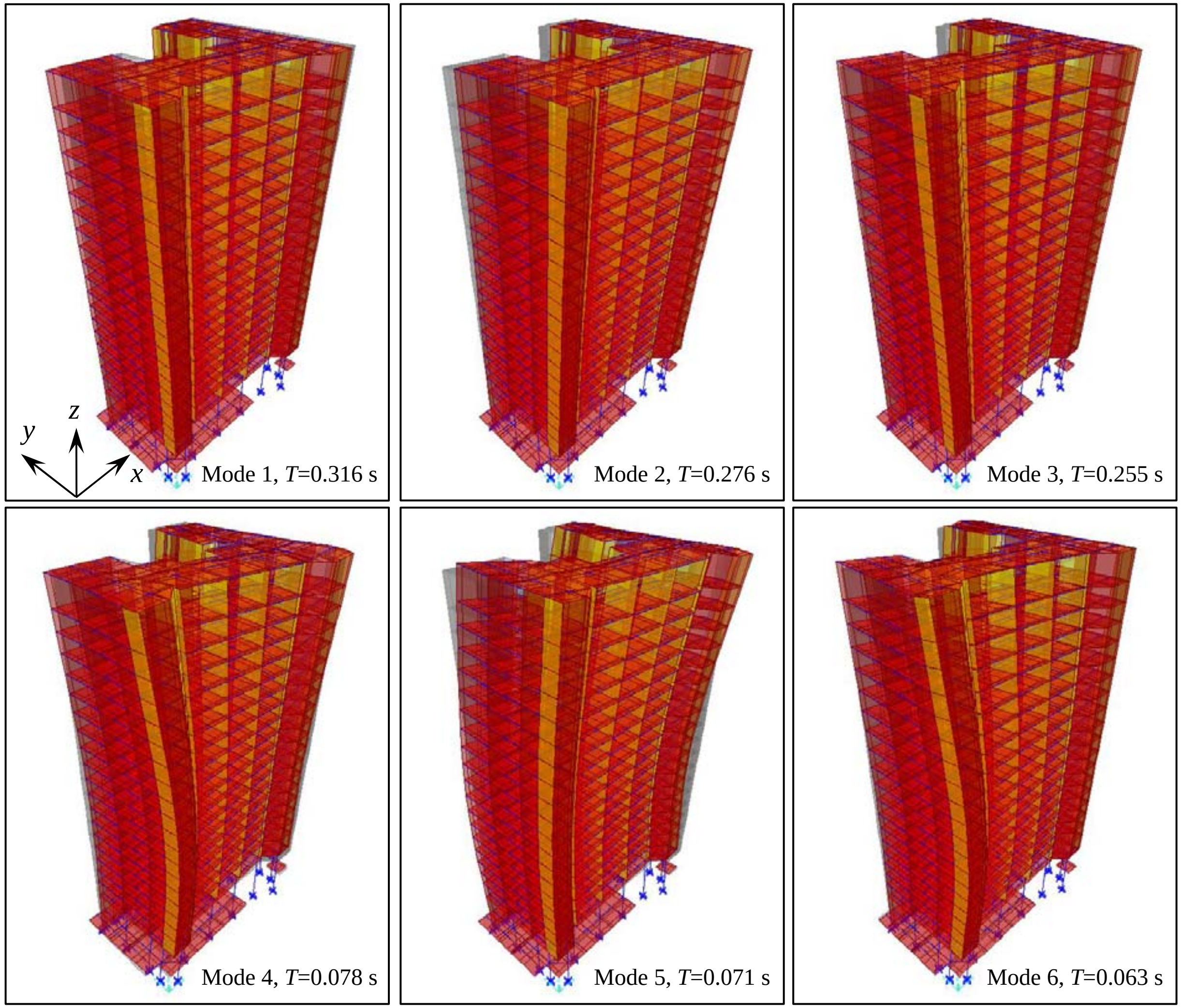

Figure 2.4 The first six mode shapes of the EH model.

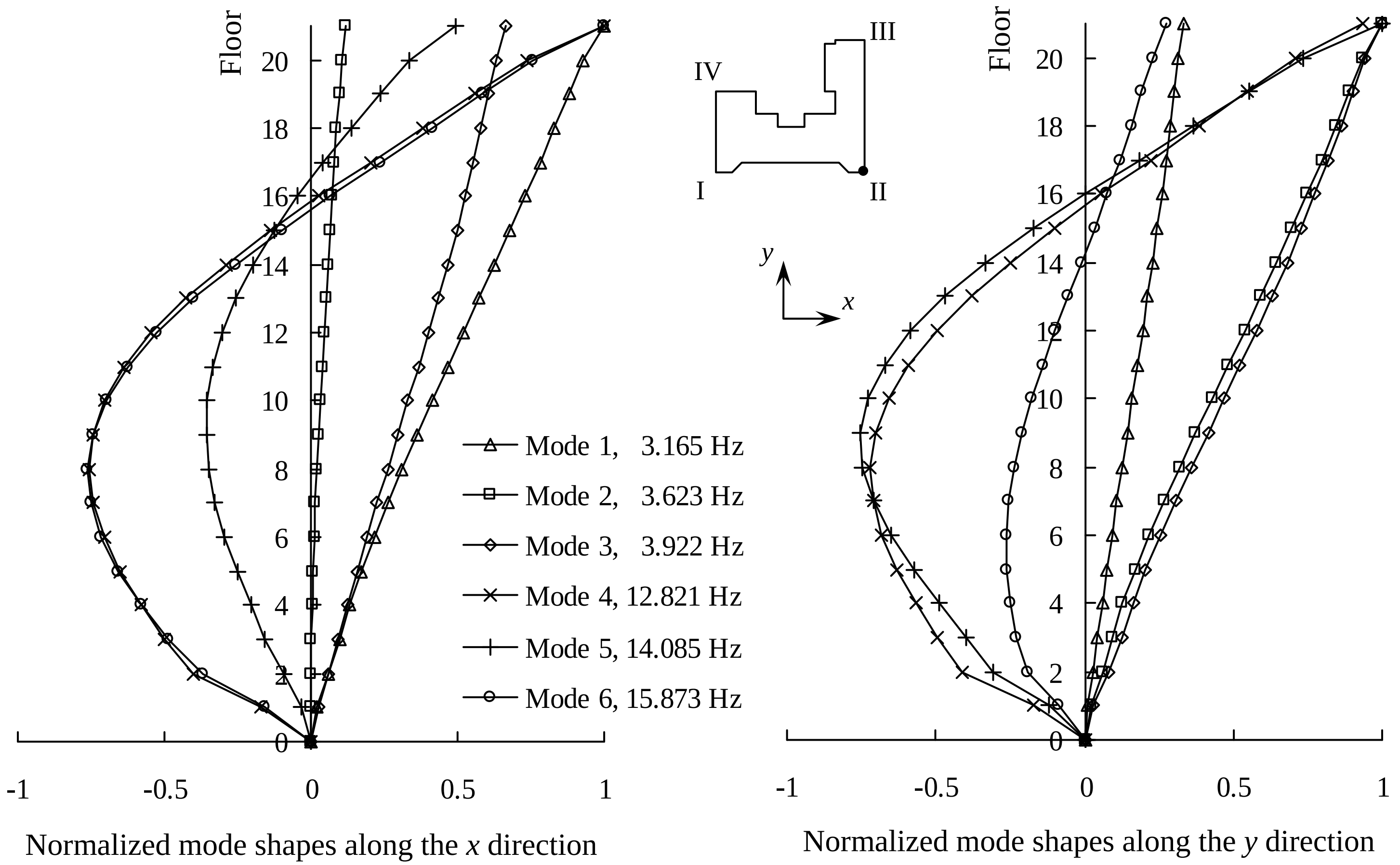

Figure 2.5 Normalized mode shapes of the first six modes at Corner II of the EH model.

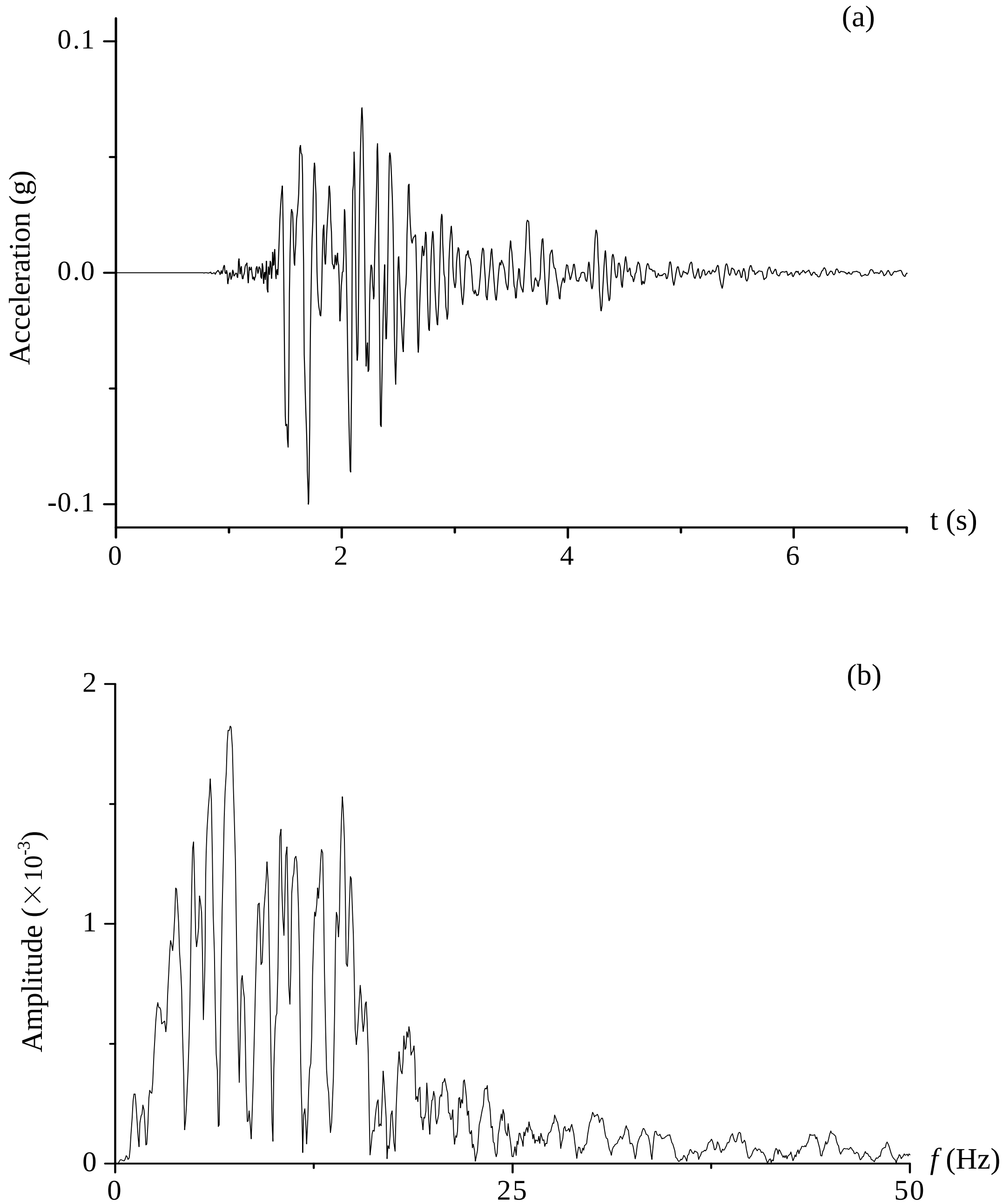

Figure 2.6 (a) The acceleration time history of the 1995 Kobe earthquake and (b) its Fourier spectrum. Note that the duration has been compressed using a factor of 0.2 and the peak acceleration has been scaled to 0.1g.

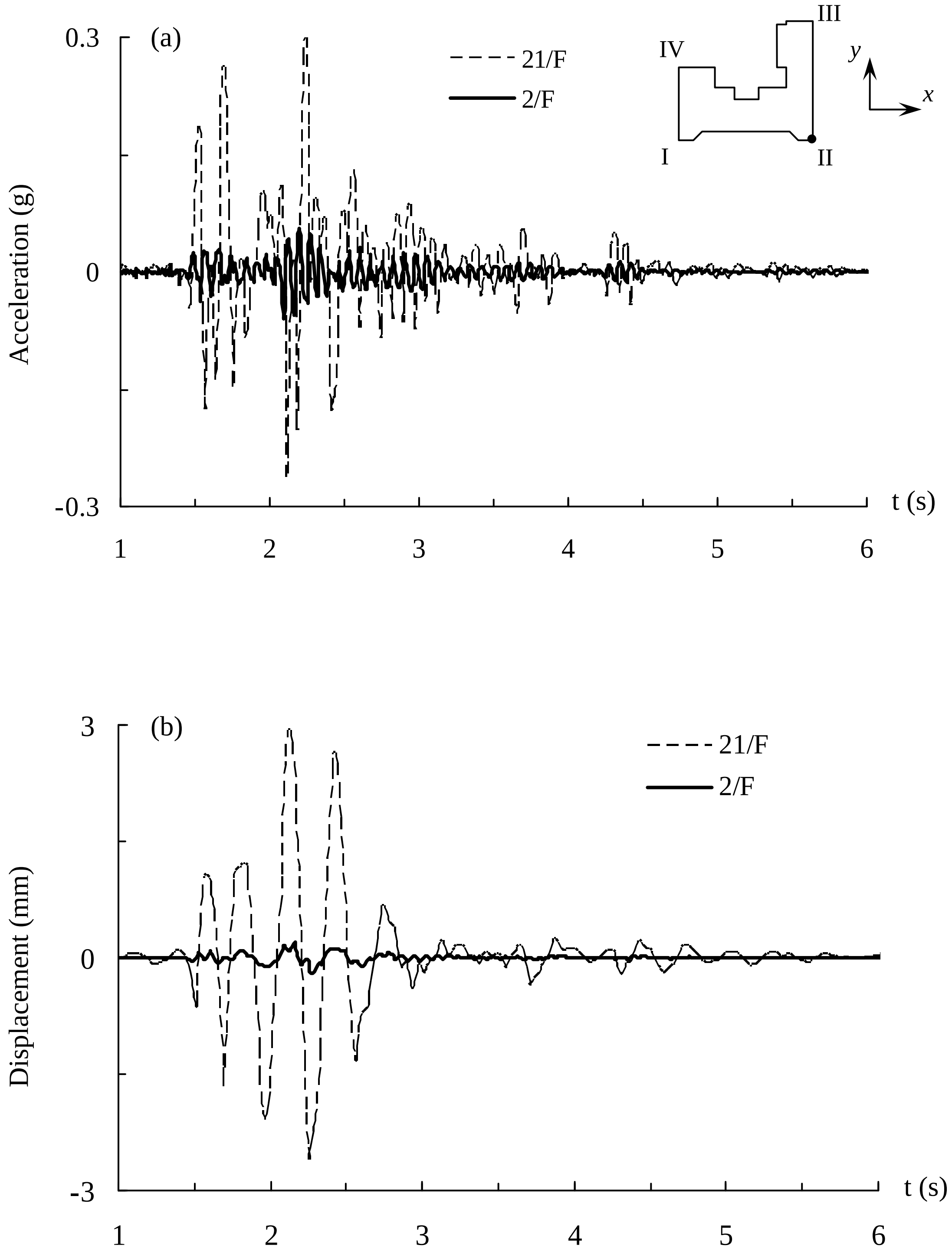

Figure 2.7 The time history of responses in the *x* direction at Corner II at the roof (21/F) and the transfer plate (2/F) respectively: (a) accelerations; (b) displacements. The input is the 0.1g Kobe earthquake wave given in Figure 2.6(a).

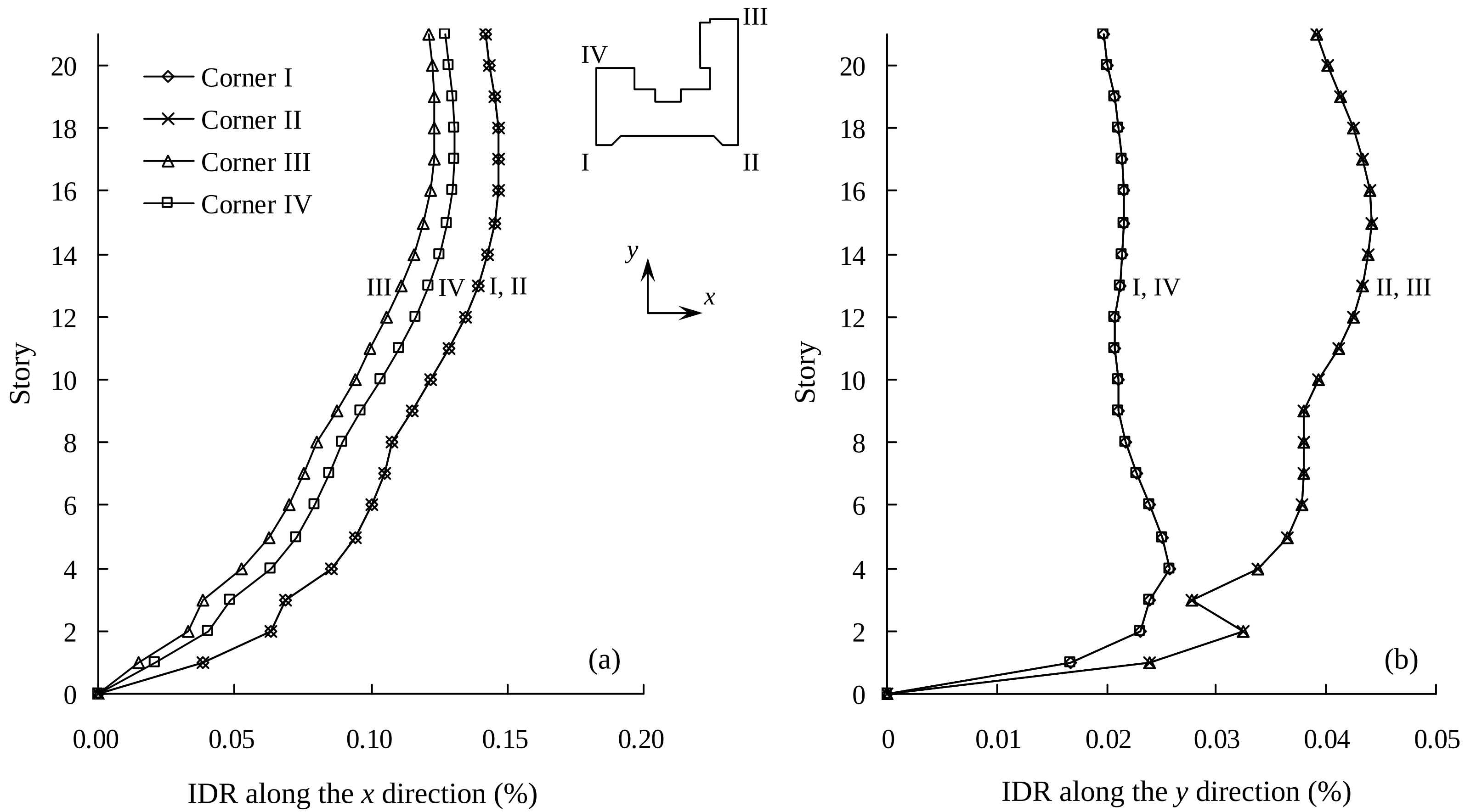

Figure 2.8 The maximum inter-story drift ratios at the four corners along the *x*- and *y*- directions for the 0.1g Kobe earthquake input. The results are from elastic FEM analysis.

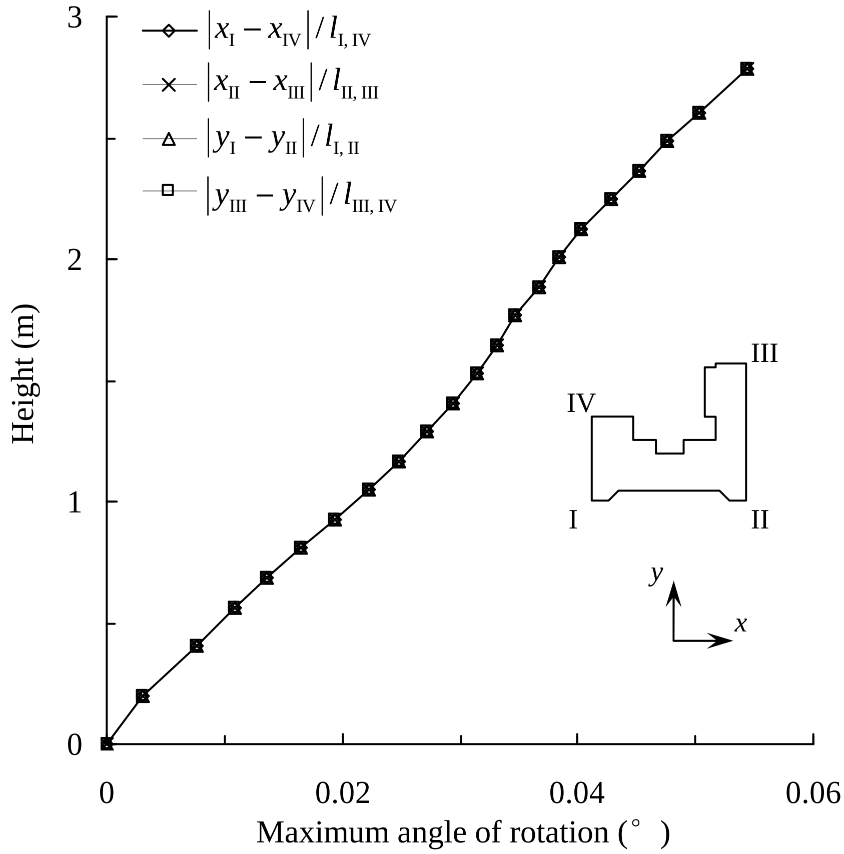

Figure 2.9 The maximum rotation angles calculated from the translational displacements of each pair of corners. In the figure, l denotes the distance between two corners. The input is given in Figure 2.6(a).

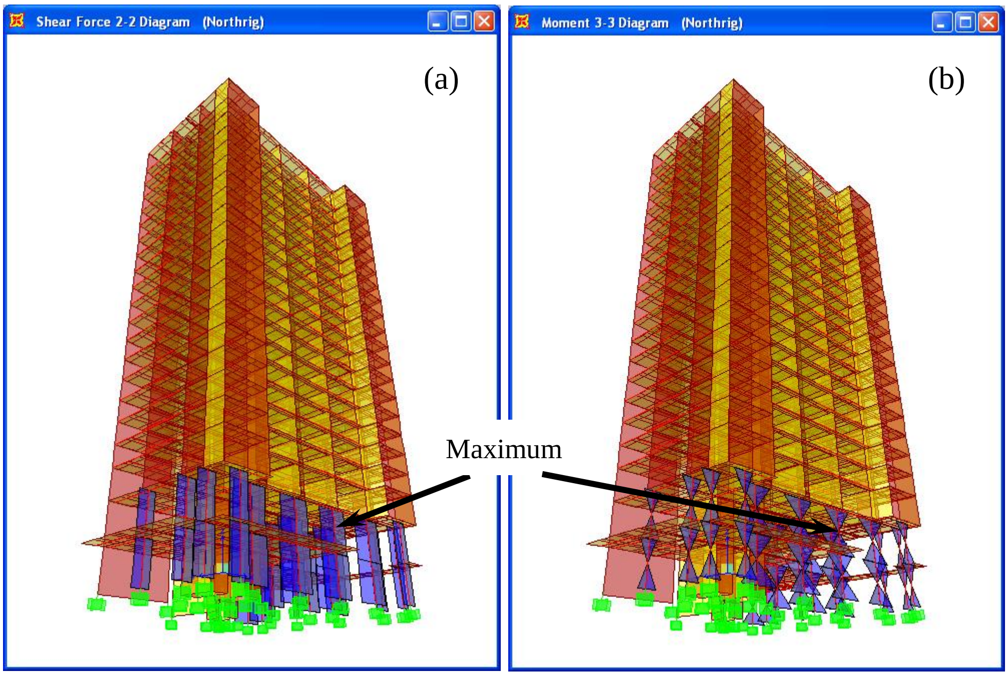

Figure 2.10 The maximum (a) shear forces and (b) bending moments at columns and beams subjected to the 0.1g Kobe earthquake input. The arrows indicate the locations of the maximum shear forces and bending moments. The details can be referred in Figures 2.12 and 2.13 later.

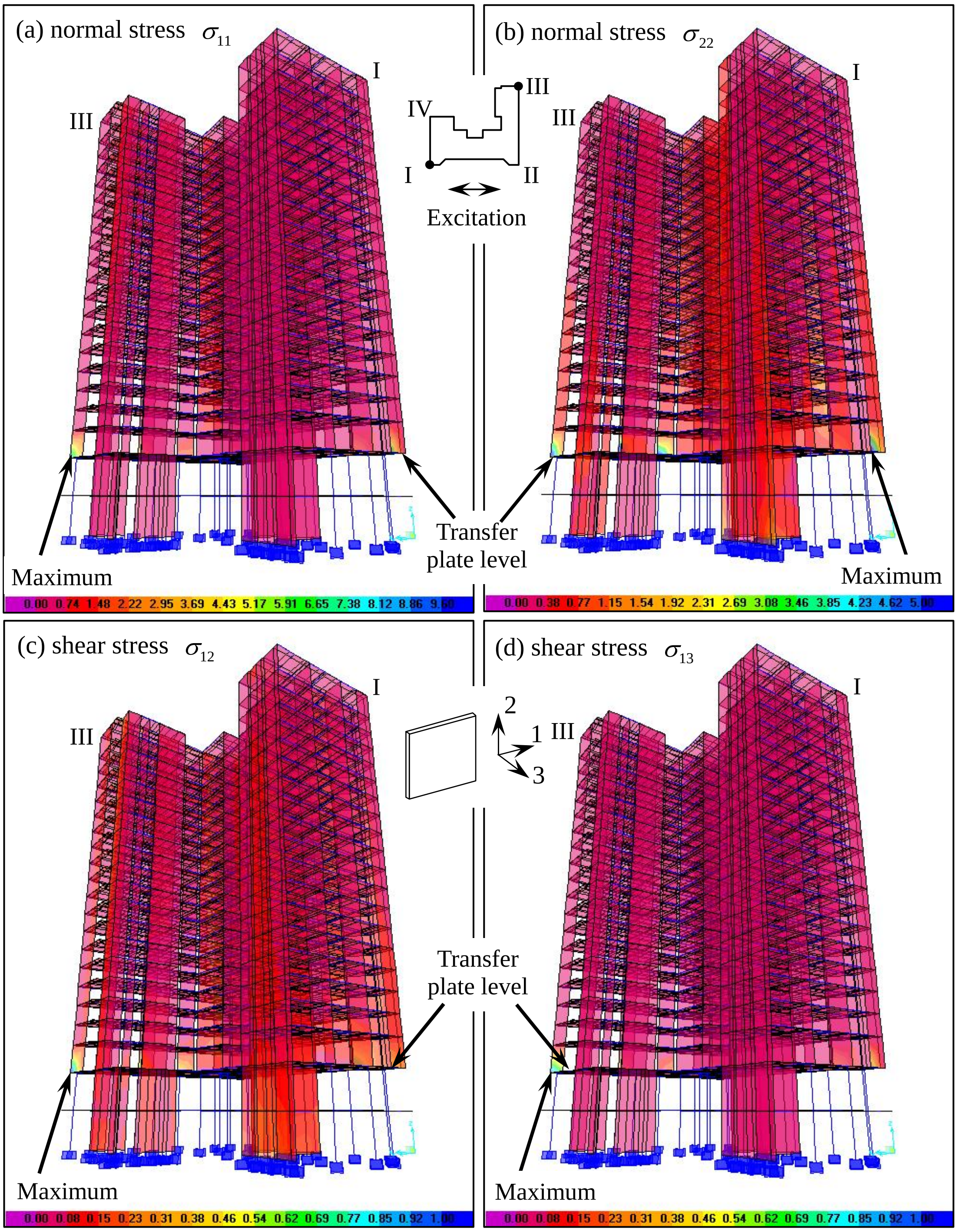

Figure 2.11 The maximum (a) normal stress σ_{11}; (b) normal stress σ_{22}; (c) shear stress σ_{12}; (d) shear stress σ_{13} of wall elements for the 0.1g Kobe earthquake input. It is clearly seen that the maximum stresses concentrate on the two diagonal corners (Corners I and III) just above the transfer plate level. The local coordinate system of wall elements is sketched by the 1, 2, 3 axes in the figure.

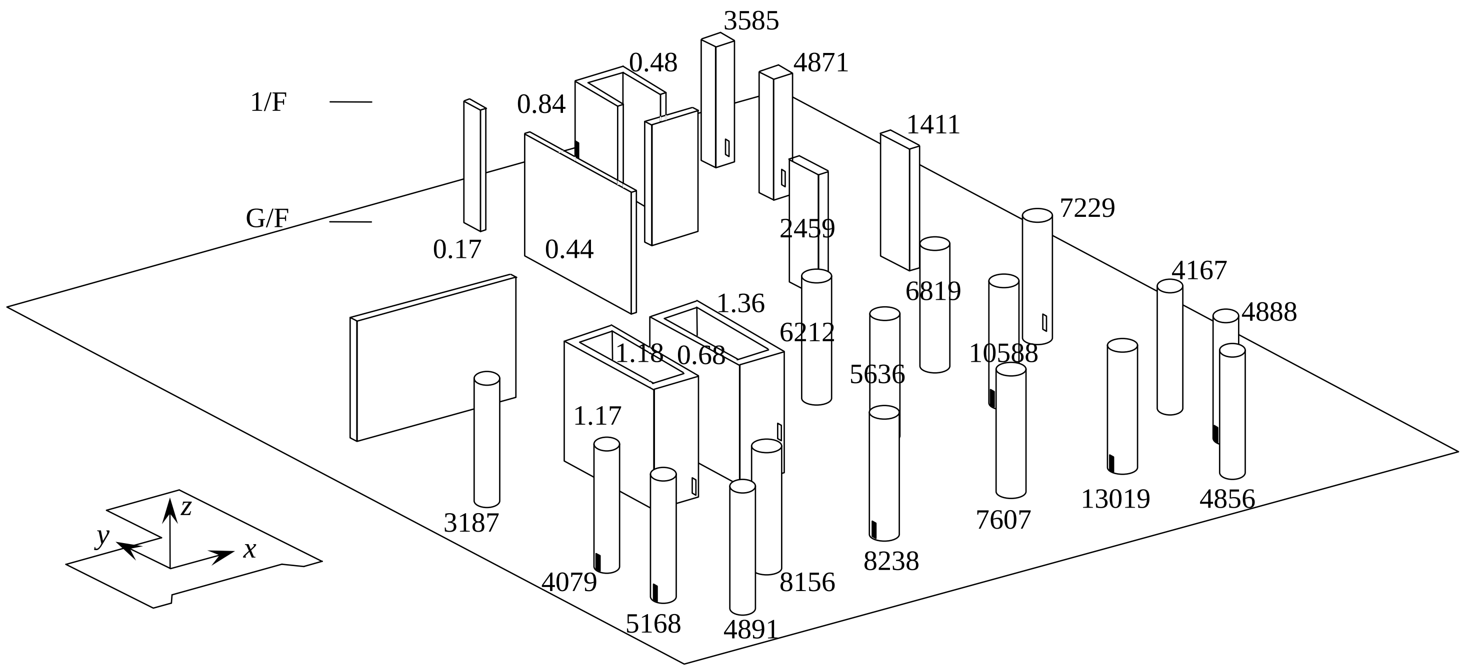

Figure 2.12 The maximum bending stresses (unit: MP) on walls and bending moments (unit: N. mm) at columns between G/F and 1/F for the 0.1g Kobe earthquake input. The filled or not-filled diamonds on the surfaces of walls or columns denote the strain gauges that are installed in our later shaking table tests. The not-filled diamonds represent those strain gauges which are out of sight from this view angle.

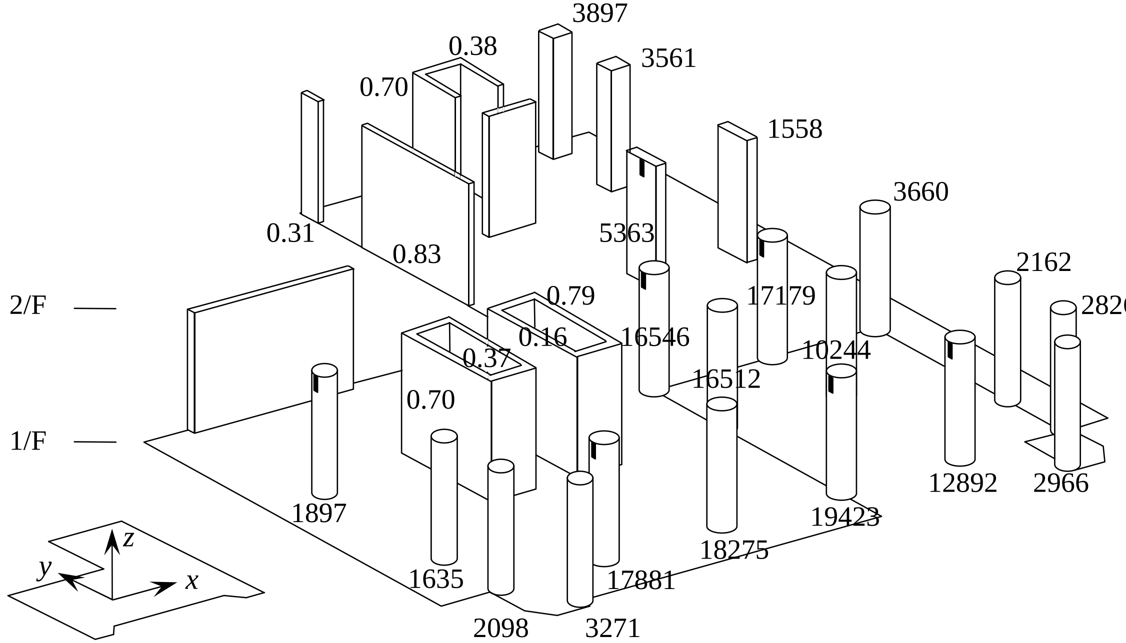

Figure 2.13 The maximum bending stresses (unit: MPa) on walls and bending moments (unit: N.mm) at columns between 1/F and 2/F for the 0.1g Kobe earthquake input. The filled diamonds on the surfaces of walls or columns denote the strain gauges that are installed in our later shaking table tests.

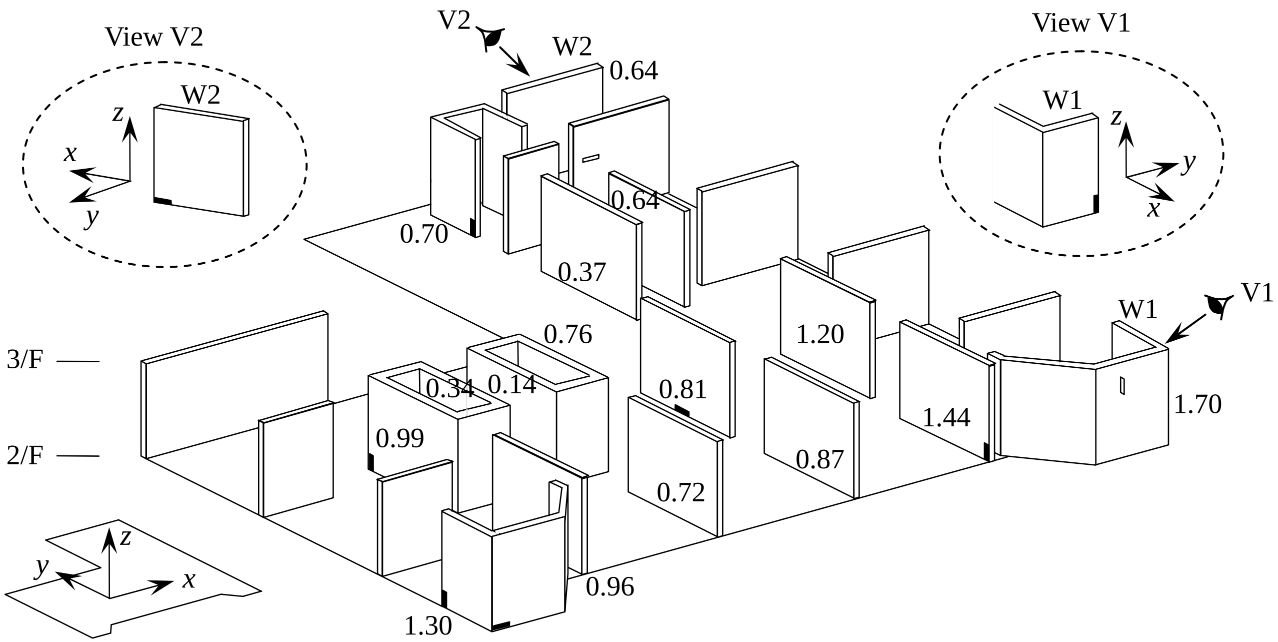

Figure 2.14 The maximum bending stresses (unit: MPa) on walls between 2/F and 3/F for the 0.1g Kobe earthquake input. The filled or not-filled diamonds on the surfaces of walls denote the strain gauges that are installed in our later shaking table tests. The not-filled diamonds represent those strain gauges which are out of sight from this view angle.

CHAPTER 3 SIMILARITY LAW AND MODEL DESIGN

The seismic vulnerability of the building selected in Section 2.2 will be assessed through conducting shaking table tests on a physical scaled model. The shaking table tests and results will be introduced in Chapter 4 and this chapter will concentrate on the design and fabrication of the scaled model. A brief review is first given for previous model tests on shaking tables. Then the similarity law for structural dynamics, which is the basis of model design, will be introduced. The model design will be carried out accordingly. Finally the model fabrication and instrumentations will be discussed and presented.

3.1 Introduction to Model Tests on Shaking Tables

3.1.1 Shaking table tests on structure vulnerability

Shaking table test has been a helpful modern means for studying seismic responses and damages of buildings, especially for those with complex plan layouts or discontinuous elevation configuration. It would be difficult to accurately analyze and predict their seismic responses using theoretical methods. In practice, shaking table tests can also be used to verify theoretical methods and hypotheses, and to test aseismic performance of various kinds of structural systems.

In recent years, several large shaking tables have been developed, providing the probability of large-scale or even full-scale structural model tests, such as the Large High Performance Outdoor Shake Table (LHPOST) in USA and the E-Defense shake table in Japan. The LHPOST, which has a dimension of 7.6 m×12.2 m and a load capacity of 2000 ton, is developed at The University of California, San Diego (http://nees.ucsd.edu/). The E-Defense shake table, developed by National research Institute for Earth science and Disaster prevention in Japan (NIED), is of 20 m×15 m size and 1200 ton load capacity (http://www.bosai.go.jp/hyogo/ehyogo/index.html).

However, in most cases, reduced-scale model tests are preferred, due to limited sizes and loading capacities of most existing shaking tables as well as economic reasons. In order that model test results can reflect actual responses of prototype structures, the similarity law for structural dynamics should normally be abided in model design, which will be explained in Section 3.2.

A number of scaled model tests have been conducted in the world in the past few decades. For example, Bertero et al. (1983) conducted a shaking table test on a 1:5 scaled model of a 7-story reinforced concrete structure; Moehle and Alarcon (1986) tested two scaled models on shaking table to study responses of irregular structures; Hosoya et al. (1995) tested two 1:7 scaled models for a reinforced concrete 11-story frame structure; Filiatrault et al. (1998) conducted a shaking table test to study seismic performance of ductile and nominally ductile reinforced concrete moment resisting frames.

However, the largest number of scaled model tests for real building structures may have been conducted in China. That is because in China there are some specialized requirements from national codes or specifications for special structures. These special structures may include those very tall or complex buildings beyond the code specifications, including Code for Seismic Design of Buildings (GB 50011-2001, 2001) and Technical Specification for Concrete Structures of Tall Building (JGJ 3-2002, 2002), or those adopting very special forms of structures. For these special structures, when there is no similar design experience, model tests are advised to be conducted to examine their seismic responses (Ministry of Construction, 2003, 2006).

Therefore, shaking table tests have been conducted for most of special buildings newly constructed in China. For example, structures tested on the shaking table at the State Key Laboratory for Disaster Reduction in Civil Engineering at Tongji University, Shanghai include the Shanghai TV Tower, the Kaixuanmen high-rise building in Shanghai, the Tianwang Tower in Guangzhou, and the Futong Tower in Haikou (Lu et al., 1999). Recently, a shaking table test has been conducted for the 610 m high New Guangzhou TV Tower at Earthquake Engineering Research & Test Center of Guangzhou University (http://eertc.gzhu.edu.cn/).

To simulate various forms of structures in the world, models tested on shaking table can be made of various materials, including wood, stone, masonry, steel, reinforced concrete and composite materials. Some recently-conducted tests using various materials are briefly reviewed below.

For wooden structures, Seo et al. (1999) tested two 1:4 scaled models for a typical Korean wooden house; Shimizu et al. (2001) tested a full-size two-story wooden frame with braces on shaking table; more recently, Hirano and Ando (2003) conducted a full-scale shaking table test for a two-story Japanese post and beam wooden house.

For stone or masonry structures, Tomazevic and Klemenc (1997) tested two 1:5 scaled models of a typical three-story confined masonry building (masonry walls confined by vertical reinforced-concrete or reinforced-masonry elements along their vertical edges); Kim and Ryu (2003) constructed a full-scale model for a five-story stone pagoda; Cohen et al. (2004) tested two half-scale single-story reinforced masonry buildings with flexible roof diaphragms.

As for steel structures, Yao and Chang (1995) subjected a 1:5 scaled steel gable frame to earthquake ground motions; Akiyama (2000) conducted full-scale shaking table tests on the fundamental structural elements of steel moment frames; Xu and Chen (2004) conducted shaking table tests on a three-story steel shear building.

Beside those materials mentioned above, reinforced concrete (RC) may be the most popular material for building models in shaking table tests. For example, Skjaerbaek et al. (1998) tested three 1:5 scaled RC frame models; Lu et al. (1999) carried out a shaking table test on 1:20 scaled model of a 7-story “U-shaped” RC structure in Shanghai; Lam et al. (2002) conducted a shaking table test on a 1:20 scaled model of a 42-story RC building in Hong Kong; Ma et al. (2003) tested a 1:5 scaled frame RC model on shaking table to study damage to building structures due to underground blast-induced ground motions.

Different from those tests of whole structures mentioned above, some other studies concentrate on seismic performance of individual structural elements on shaking tables, such as beams, columns and walls. For instance, based on US and Japan seismic design respectively, Park et al. (2003) tested three 1:6 scaled models of a reinforced concrete bridge column on shake table for their seismic performance. Lin et al. (2004) and Bairrao et al. (2005) constructed reinforced concrete beams and vibrated them on shaking tables respectively.

3.1.2 Shaking table tests conducted in Hong Kong

As mentioned previously in Chapter 1, since seismic hazard in Hong Kong has traditionally been considered to be low, local building structures have been designed with no seismic provisions. No shaking table test has ever been carried out to study seismic vulnerability of wind-designed buildings in Hong Kong before 2000. In recent years, realizing the potential risk of earthquake shaking, a shaking table test was conducted in 2001 on a 1:20 scaled model of a 42-story building with transfer system in Hong Kong (Lam et al., 2002; Li et al, 2006). The purpose is to understand the seismic resistance of existing high-rise buildings in Hong Kong and provide guidelines for the future seismic provisions.

To be specific, the selected prototype is a 42-story reinforced concrete residential building with a transfer plate of 2.7 m thick at the 4^{th} story level. The typical floors above the transfer plate consist of shear walls and a central core, whereas for the stories below the transfer plate, columns are used to support the upper structure. The authors believed that the selected building can reflect the main features of typical wind-designed buildings in Hong Kong (Lam et al., 2002; Li et al., 2006).

As shown in Figure 3.1, a 1:20 scaled model of the prototype was fabricated using fine wires (typically of 2.5, 6 and 8 mm diameters) and micro-concrete (a mixture of cement, sand and water). The model was subjected to earthquake shakings of various peak accelerations on the shaking table (of 5 m×5 m size and 6 degrees of freedom) at the Institute of Engineering Mechanics (IEM), China Earthquake Administration.

The test results show that the building was moderately damaged after earthquake excitation with peak acceleration of 0.15-0.20g, but was still repairable. According to Chinese Code for Seismic Design of Buildings (GB 50011-2001, 2001), a maximum ground shaking of 0.15g at rock site is expected in Hong Kong at least once in every 475 years. The building was severely damaged and beyond repair after earthquake shaking of peak acceleration at 0.25-0.34g. It was recommended that the structural walls above the transfer plate should be strengthened and any change in stiffness at the transfer zone should be avoided as far as possible (Lam et al., 2002).

3.1.3 Objectives of the present shaking table test

The present shaking table test is distinguished from the test conducted by Lam et al. (2002) in several aspects. First the model studied by Lam et al. (2002) is a residential building whereas the prototype in the present study is a hotel building. Secondly, although transfer system has been used in the building of Lam et al. (2002), their model is essentially symmetric and torsional response is not significant. However, the selected building in this study has both a transfer plate and an asymmetric plan, and it is believed that torsional response will play a more important role in its seismic behavior.

Torsion caused by the non-coincidence of the center of mass and the center of stiffness on the floor plan has been identified as one of the potential causes of damages during earthquakes (Wakabayashi, 1986). Seismic damages caused by torsional responses have been found in a number of past earthquakes, for example, in the 1964 Alaska earthquake in USA, the 1972 Managua earthquake in Nicaragua (Liu, 1993), and the 1978 Miyagiken-Oki earthquake in Japan (Wakabayashi, 1986).

Torsional vibrations induced especially severe damages in the 1985 Mexico City earthquake. Rosenblueth and Meli (1986) reported that 42% of the buildings that suffered collapse or severe damages were on corner sites. The authors argued that the poor performance of those buildings was due to their asymmetric layouts, since most of those corner buildings had wider open facades to the streets than the corresponding facades at the rear. Their centers of stiffness were likely to be eccentric from their centers of mass, and thus significant torsional responses would be resulted.

As indicated in Chapter 1, besides transfer system, asymmetric plan has also been widely adopted in Hong Kong building structures. So it is needed to study seismic vulnerability of tall buildings which have both asymmetric plans and transfer systems. That is the reason why the present building was selected to be studied (refer to Section 2.2).

Another important difference between the present test and that of Lam et al. (2002) may consist in the damage evaluation methods. Lam et al. (2002) only assess damages qualitatively through visual inspection, inter-story drift ratio and reduction of natural frequency; whereas in this study, structural damages will be evaluated quantitatively through various damage indices, including ductility, inter-story drift ratio, variation of natural frequency as well as Park and Ang damage index.

To summarize, the present shaking table test was carried out with the following main objectives:

(1). The selected prototype building is a reinforced concrete frame-shear wall structure with a transfer plate as well as a "L-shaped" plan, which means that torsional vibrations will play a more important role in its seismic responses. Therefore, it will provide a good means and opportunity to investigate effects of both asymmetric plan and transfer system on seismic vulnerability of non-seismic-designed buildings.

(2). In the present model test, the structural damages under the excitations of different earthquakes will be quantitatively evaluated using various seismic damage indices, including ductility, inter-story drift ratio, variation of natural frequency and Park and Ang damage index. A simple algorithm will be developed to estimate Park and Ang damage index from the measured response data. Using Park and Ang index as a benchmark, the correlations between other damage indices with various damage levels (i.e. slight damage, minor damage, moderate damage, severe damage and collapse) will be established.

(3). In this study, the test results will be compared with the predictions from FEM analyses conducted in Chapter 2, with the purpose of verifying the assumptions used in FEM study.

3.2 Similarity Law for Structural Dynamics

As mentioned in previous Section 3.1.1, due to limited sizes of most existing shaking tables and economic reasons, very often reduced-scale models rather than full-scale models are tested on shaking tables to simulate seismic responses of real structures. To assure models can reflect actual responses of prototypes, scaled models should be designed and fabricated according to the similarity law, which puts certain requirements on ratios of various physical parameters between models and prototypes, and will first be introduced.

3.2.1 Similarity law from the Buckingham Pi Theorem

The Buckingham Pi Theorem is the basis of dimensional analyses, which asserts that any complete physical relationship can be expressed in terms of a set of independent dimensionless products composed of the relevant physical parameters

(Baker et al., 1991). Or in more mathematical discussement, the Pi Theorem says,

> "If the equation $F(q_1, q_2, \cdots q_n) = 0$ is complete, the solution has the form $f(\pi_1, \pi_2, \cdots \pi_{n-k}) = 0$, where the π terms are independent products of the parameters q_1, q_2, etc., and are dimensionless in the fundamental dimension." (pp.19, Baker et al., 1991)

The number of π terms in the solution equations is less than the number of parameters (n) by a factor k; usually k equals to the number of fundamental dimensions (such as length, mass and time). A physical phenomenon should be independent of the unit of measurement of the involved parameters. Therefore, two systems are similar only if all the corresponding π terms are equal in the two systems (Buckingham, 1914). For our shaking table tests, the Buckingham Pi Theorem requires that all the corresponding π terms should be equal in the model and the prototype.

To be specific, in linear elastic range, all related parameters involved in shaking table tests can be presented by an equation as (Zhang, 1997):

$$\sigma = f(l, E, \rho, t, x, v, a, g, \omega, \xi) \tag{3.1}$$

where σ is the stress, l is the dimension, E is the elastic modulus, ρ is density, t is time, x, v and a denote the displacement, velocity and acceleration respectively, g is the gravity acceleration, ω is the structural circular natural frequency, and ξ is the damping ratio. Note that the damping ratio was not included in Zhang (1997) and has been included here for completeness. It should be borne in mind that using those parameters in the above equation, only elastic behaviors are considered and inelastic behaviors (such as structural damage) can not be reflected. This is one limitation of the present study.

If l, E, ρ are selected to be the fundamental dimensions, the dimensions of all the other parameters can be expressed by the products of l, E, ρ and the dimensionless π terms can be obtained (Zhang, 1997).

$$\pi_0 = \sigma / E \qquad \pi_4 = t/(lE^{-0.5}\rho^{0.5})$$

$$\pi_5 = x/l \qquad \pi_6 = v/(E^{0.5}\rho^{-0.5})$$

$$\pi_7 = a/(l^{-1}E\rho^{-1}) \qquad \pi_8 = g/(l^{-1}E\rho^{-1})$$

$$\pi_9 = \omega/(l^{-1}E^{0.5}\rho^{-0.5}) \qquad \pi_{10} = \xi \tag{3.2}$$

All these dimensionless π terms should be equal in the prototype and the model according to the Buckingham Pi Theorem. If a parameter A is denoted by A_p in the prototype and is A_m in the model system, the ratio between the model and the prototype for A is denoted by $\lambda_A = A_m / A_p$. To make these π terms given in Equation (3.2) the same in the model and the prototype, the ratios of various parameters should satisfy (Zhang, 1997):

$$\lambda_\sigma = \lambda_E \qquad \lambda_v = \sqrt{\lambda_E / \lambda_\rho}$$

$$\lambda_t = \lambda_l \sqrt{\lambda_\rho / \lambda_E} \qquad \lambda_a = \lambda_E / (\lambda_l \lambda_\rho) = \lambda_g$$

$$\lambda_x = \lambda_l \qquad \lambda_\omega = \sqrt{\lambda_E / \lambda_\rho} / \lambda_l \qquad \lambda_\xi = 1 \tag{3.3}$$

However, it is hard for all the similarity requirements in Equation (3.33) to be satisfied simultaneously in real experiments. The main difficulty consists in that all experiments are conducted on the earth, and thus the gravity acceleration remains the same for both the prototype and the model, that is, $\lambda_a = \lambda_g = 1$. From Equation (3.3), we can easily know that this requirement equals to $\lambda_E = \lambda_l \lambda_\rho$. This means that the three ratios λ_E, λ_l and λ_ρ should not be assigned arbitrarily, which brings much difficulties in the model design. Especially for small scaled models which have a relatively smaller λ_l than λ_E, and thus a rather large value of λ_ρ is needed. That is to say, the material density of the model must be much larger than that of the prototype, which is usually hard to be achieved in real tests.

The usual way to solve this problem is to attach additional masses to the model to increase the equivalent density ratio λ_ρ (Baker, 1991). This method increases the total mass of the model but will not influence the stiffness of the model. From the requirement $\lambda_E = \lambda_l \lambda_\rho$, we can get:

$$\lambda_m = \lambda_\rho \lambda_l^3 = \lambda_E \lambda_l^2 \tag{3.4}$$

where λ_m is the mass ratio between the total mass of the model (m_t) and the mass of the prototype (m_p) (i.e. $\lambda_m = m_t / m_p = \lambda_E \lambda_l^2$). The total mass of model m_t is the summation of the mass of the model itself m_m and the additional mass m_a (i.e. $m_t = m_m + m_a$). Thus, the similarity law can be satisfied through the introduction of additional mass. This is called the additional mass law (Zhang, 1997) (Note: Zhang (1997) called it the “artificial mass law”; here the word “additional” is used since the word “artificial” may be somewhat confusing). From the above formulae, it is easy to know the required additional mass is:

$$m_a = m_t - m_m = \lambda_E \lambda_l^2 m_p - m_m \tag{3.5}$$

Following this method, all the requirements of the similarity law based on Equation (3.3) are summarized and listed in the second column of Table 3.1.

This method can properly scale gravity forces and accelerations, however, several difficulties still exist. For example, attached mass is hard to truly model distributed mass even if the total mass is correct, and centers of mass of components and hence moments may be changed; stress distribution may be affected; attachment can be difficult under severe dynamic load conditions (Baker, 1991). Therefore, enough attention should be paid in adopting this method, for example, the additional mass should be attached firmly on the model and the distribution of additional mass should resemble the actual mass distribution in the prototype as far as possible.

3.2.2 Similarity law from governing equations

The more traditional and usual method of developing similarity law is via the Buckingham Pi Theorem as described above. This method does not require that the complete governing equations of the studied phenomenon are provided, but only requires that the complete set of physical parameters involved in the problem is given. However, if the adopted physical parameters are not complete for the problem studied, the obtained results may be incorrect.

The other possible method of developing similarity law is via the governing equations which describe the dynamic process of the studied problem (Baker et al., 1991). This method avoids the above shortcoming of the Pi Theorem, but it requires that you must know enough about the physics of your problem and be able to write down a complete set of governing equations to describe the physics.

Using this method, the complete governing equations for individual problem must be given, however, to develop the similarity law we do not need to solve them. In this section, we will develop the similarity law for our shaking table tests from the equations of motions directly and the results will be compared with the previous results from the Pi Theorem.

The equations of motions of the model and the prototype under earthquake excitations can be written as:

$$m_m \ddot{x}_m + c_m \dot{x}_m + k_m x_m = -m_m \ddot{x}_{gm} \tag{3.6}$$

$$m_p \ddot{x}_p + c_p \dot{x}_p + k_p x_p = -m_p \ddot{x}_{gp} \tag{3.7}$$

where m, c and k represent the mass, damping and stiffness respectively, the subscripts m and p correspond to the model and the prototype respectively, x is the displacement response, and x_g is the input ground motion. Similar as in Section 3.2.1, only elastic responses are considered here, and the stiffness and damping are taken as constants.

First the following ratios of the corresponding parameters between the model and the prototype are defined.

$$\lambda_m = \frac{m_m}{m_p}, \quad \lambda_t = \frac{t_m}{t_p}, \quad \lambda_l = \frac{l_m}{l_p} = \frac{x_m}{x_p} \tag{3.8}$$

$$\lambda_k = \frac{k_m}{k_p}, \quad \lambda_c = \frac{c_m}{c_p} \tag{3.9}$$

where t is time and l is the length. Take the differentials of displacement once and twice respectively, and we can easily get the ratios of velocity, acceleration and gravity acceleration as.

$$\lambda_v = \frac{\dot{x}_m}{\dot{x}_p} = \frac{\lambda_l}{\lambda_t}, \quad \lambda_a = \frac{\ddot{x}_m}{\ddot{x}_p} = \frac{\lambda_l}{\lambda_t^2}, \quad \lambda_g = \frac{\ddot{x}_{gm}}{\ddot{x}_{gp}} = \lambda_a = \frac{\lambda_l}{\lambda_t^2} \tag{3.10}$$

Then all the parameters of the model can be expressed by that of the prototype plus those ratios defined, such as $m_m = \lambda_m m_p$, $x_m = \lambda_l x_p$, $\ddot{x}_m = \frac{\lambda_l}{\lambda_t^2}\ddot{x}_p$. After that, all of them are substituted into Equation (3.6), and we get:

$$\lambda_m \frac{\lambda_l}{\lambda_t^2} m_p \ddot{x}_p + \lambda_c \frac{\lambda_l}{\lambda_t} c_p \dot{x}_p + \lambda_k \lambda_l k_p x_p = -\lambda_m \frac{\lambda_l}{\lambda_t^2} m_p \ddot{x}_{gp} \tag{3.11}$$

Since the above formula and Equation (3.7) should be valid at the same time, by comparing the two equations, we can easily get the following similarity requirements.

$$\lambda_m \frac{\lambda_l}{\lambda_t^2} = \lambda_c \frac{\lambda_l}{\lambda_t} = \lambda_k \lambda_l \tag{3.12}$$

From the above procedure, it can be easily seen that if and if only the above equation is satisfied, the structural responses of the model and the prototype will be similar, and the model can be used to simulate and further to predict the seismic behavior of the prototype. Therefore, Equation (3.12) is the base of our similarity law.

Using this basic equation, if we select m, l and t as the fundamental parameters as general, the other ratios can all be expressed in terms of them.

$$\lambda_k = \frac{\lambda_m}{\lambda_t^2}, \quad \lambda_c = \frac{\lambda_m}{\lambda_t} \tag{3.13}$$

$$\lambda_\rho = \frac{\lambda_m}{\lambda_l^3}, \quad \lambda_\sigma = \frac{\lambda_k}{\lambda_l} = \frac{\lambda_m}{\lambda_l \lambda_t^2}, \quad \lambda_E = \lambda_\sigma = \frac{\lambda_m}{\lambda_l \lambda_t^2} \tag{3.14}$$

where λ_ρ, λ_σ and λ_E are the ratios of the density, stress and Young's modulus respectively. If we define the circular natural frequency as $\omega = \sqrt{k/m}$ and the damping ratio as $\xi = c/(2m\omega)$, we can further get:

$$\lambda_\omega = \sqrt{\frac{\lambda_k}{\lambda_m}} = \frac{1}{\lambda_t} \tag{3.15}$$

$$\lambda_\xi = \frac{\lambda_c}{\lambda_m \lambda_\omega} = 1 \tag{3.16}$$

In the above analysis, we did not require the gravity ratio $\lambda_g \ (= \lambda_l / \lambda_t^2)$ to be unity. However, as discussed in Section 3.2.1, since all shaking table tests are conducted on the earth and the gravity should be the same for the model and prototype. That is to say, $\lambda_g = \lambda_a = \lambda_l / \lambda_t^2 = 1$, so we have $\lambda_t = 1/\sqrt{\lambda_l}$. Based on this relation, we can rewrite some of the above requirements in new forms, such as:

$$\lambda_E = \lambda_\sigma = \frac{\lambda_m}{\lambda_l^2}, \quad \lambda_v = \sqrt{\lambda_l}, \quad \lambda_\omega = \frac{1}{\sqrt{\lambda_l}} \tag{3.17}$$

From the above equations, we can get a requirement on the mass ratio $\lambda_m = \lambda_E \lambda_l^2$, which is obviously equivalent to $\lambda_E = \lambda_l \lambda_\rho$ obtained in the previous Pi Theorem method in view of the relation $\lambda_m = \lambda_\rho \lambda_l^3$. As mentioned before, this requirement is hard to be satisfied especially for small scaled models and the mass of the model is usually insufficient. To overcome this problem, additional mass (m_a) should be added to increase the total mass of the model. From the relationship $\lambda_m = \lambda_E \lambda_l^2$ and $\lambda_m = (m_m + m_a) / m_p$, the amount of the additional mass needed can be determined as:

$$m_a = \lambda_E \lambda_l^2 m_p - m_m \tag{3.18}$$

where m_m and m_p are the masses of the model and the prototype respectively. Comparing Equation (3.18) with Equation (3.5), we can find that the result here is identical with the additional mass law developed from the Buckingham Pi Theorem.

The requirements of the additional mass law developed from the governing equations were summarized in the third column of Table 3.2, based on the three fundamental parameters m, l and t. In the table, if we change the fundamental parameters to l, E and ρ, and express all others parameters in terms of them, we can easily find that the scale requirements in the third column of Table 3.1 are identical with those in the second column obtained from the Buckingham Pi Theorem, which means that for this case the two methods are equivalent.

In the present study, the additional mass similarity law as listed in the third column of Table 3.1 is adopted and cast-iron plates are used to serve as the additional mass. But due to the limited load capacity of our shaking table as well as the limited spaces within each story of the model to accommodate the additional mass, the actual additional mass achieved is slightly insufficient. The details will be introduced in the following sections.

3.3 Model Design Constrained by Similarity Law

As introduced in Chapter 2, the 21-story Empire Hotel building with a "L-shaped" plan and a transfer plate in Hong Kong was selected for investigation in this study, and its location, photographs and typical floor plan have been shown previously in Chapter 2. The detailed structural design drawings of the building were collected from the Buildings Department of Hong Kong SAR Government. The full details of the design procedure will be introduced in this section.

3.3.1 Model dimensions

The tests are performed on a MTS uniaxial seismic shaking table of size 3m×3m at the Hong Kong Polytechnic University (see Figure 3.15). It is capable of producing a maximum horizontal acceleration of 1g at the maximum load of 10 tons. The maximum velocity and displacement can be up to 0.5 m/s and 10 cm respectively. The actuator is controlled by a 469DU digital seismic table controller, and the working frequency of the table ranges from 1 to 50 Hz. The shaking table can simulate motions with control in displacement, velocity or acceleration (i.e. a three-variable-control). The displacement control is primarily for low frequency range, velocity control for middle frequency range, and acceleration control for high frequency range. The maximum overturning moment that can be restrained by the bearing of the table is 10 ton·m.

As shown in Chapter 2, the total height of the prototype is 69.65 m and its horizontal dimension is 35.75 m×31.675 m. Since the clearance between the shaking table and the crane at the ceiling of our laboratory is fixed (3.3 m), the length scale of the model is constrained. The size of the current shaking table is 3 m×3 m. These factors determined the maximum possible dimension of the model. On the other hand, the length scale should be as large as possible under those constraints to reduce the distortion between the model and the prototype. After considering all these factors, a 1/25 length scale is adopted in the present study (i.e. $\lambda_l = 0.04$).

With this length scale, the model has a height of 2.786 m and a plan dimension of 1.43 m×1.267 m. As shown by the elevation view given in Figure 3.2, typical stories have a height of 120 mm whereas the lower three stories and the roof story are of higher story heights, varying from 160 mm to 208 mm. Those stories need large open spaces for their different functions from typical stories (serving as guest rooms) in the hotel. For example, the first two stories are used as the reception lobby, bar and restaurant, the third story for a business center, and the top story for a swimming pool and a health club. Some typical structural dimensions of both the model and the prototype are listed in Table 3.2.

After the length scale is determined, the geometrical configurations of all structural elements in the model, including beams, columns, walls and slabs, are determined accordingly. As shown in Figure 3.2, the deep beams at the transfer plate have a depth of 60 mm. From the cross-sections at various levels shown in Figures 3.3-3.4, it is clear that the building adopts totally different structural forms below and above the transfer plate. The first two stories below the transfer plate mainly consist of columns and core walls (see Figure 3.3), whereas only shear walls and core walls are used for typical stories above the transfer plate (see Figure 3.4).

3.3.2 Mechanical properties of micro-concrete

The scaled model to be tested in our shaking table tests will be fabricated using micro-concrete, steel wires and steel meshes. Micro-concrete is a concrete mix with a reduced aggregate size and has been widely used in small scale modeling of concrete structures (Noor, 1991). In this study the micro-concrete is mixed using cement, water and sand, similar as in the tests of Lu et al. (1999) and Lam et al. (2002). Compared to concrete, micro-concrete has comparatively smaller elastic modulus (i.e. Young's modulus) but similar density, which provides an obvious advantage in the design and fabrication of reduced-scale models following the additional mass similarity law. According to Equation (3.18), the smaller value of λ_E, the less additional mass m_a will be needed to satisfy the similarity requirement.

First the target elastic modulus of the micro-concrete used in the model fabrication is estimated. According to the descriptions in Chapter 2, the areas of the 1st, 2nd and typical floor (3rd-21st) of the prototype are 810.2, 825.3 and 628.2 m^2 respectively. The elastic modulus of the concrete is $E_p = 30$ GPa. The total mass (m_p) is estimated to be 16285.56 ton by assuming a design load density of 1.2 ton/ m^2. Since the density of micro-concrete is close to that of concrete, we assumed temporarily the density ratio to be unity (i.e. $\lambda_\rho = 1$). Then the mass of the model can be estimated as $m_m = m_p \lambda_l^3 = 1.04$ ton with $\lambda_l = 0.04$.

To estimate the target material strength, let's consider two extreme cases first. The first one is that no additional mass is added and only the micro-concrete is used (i.e. $\lambda_\rho = 1$). Then from the relation $\lambda_E = \lambda_l \lambda_\rho$, we can get $\lambda_E = \lambda_l = 0.04$. This means Young's modulus of the micro-concrete must be $E_m = 1.2$ GPa when $E_p = 30$ GPa, which is a value too small to be achieved for realistic micro-concrete. In another words, the similarity law can not be satisfied if no additional mass is added. The values of other related parameters for this extreme case are listed in the second column of Table 3.3.

The second case considered is the maximum additional mass added within the load capacity of the shaking table. As introduced previously, our shaking table has a load capacity of 10 ton and an overturning moment capacity of 10 ton·m. For a rough estimation, we assume the center of mass of the model situates at the mid-height (i.e. $H/2=$ 1.393 m, where $H=2.786$ m is the total height of the model). Then the maximum dead load on the shaking table should be 10/1.393 = 7.18 ton, considering the overturning moment capacity of 10 ton·m. But since the model is constructed and situated on a reinforced concrete base slab of 200 mm thick (refer to Section 3.4.1), which has a weight of about 2 ton. Minus 2 ton from 7.18 ton, we get the maximum total weight of the model plus the additional mass is 5.18 ton (i.e. $m_m + m_a = 5.18$ ton). Recall $m_m = 1.04$ ton, and we get the maximum amount of the additional mass is $m_a = 4.14$ ton.

Using Equation (3.18), we can get $\lambda_E = \dfrac{m_m + m_a}{m_p \lambda_l^2} = 0.199$ and $E_m = \lambda_E E_p =$ 5.97 GPa. This is the target Young's modulus of the micro-concrete. For comparison, various parameter ratios for this case are also listed in the third column of Table 3.3.

With the above target strength, material tests were carried out to determine the appropriate mix proportion of cement, sand and water for the micro-concrete. Totally, six sets of micro-concrete specimens of six different mix proportions have been fabricated and tested. Each set of specimens consisted of three test cubes of dimension 70.7×70.7×70.7 mm and three cylinders of ϕ100×200 mm (ϕ means diameter here) (see Figure 3.5); the test cubes were used to measure the cube strength whereas the cylinders for obtaining Young's modulus of the micro-concrete. All the specimens were fabricated simultaneously and the moulds were removed after 24 hours, and then the specimens were cured under room temperature for 28 days before testing. Note that during the curing period, the specimens were not immersed in water in order to reflect the actual strength of the model, since the model was also not immersed in water during fabrication.

The results of the cube strength and Young's modulus together with the mixing proportion, density and Young's modulus ratio between the model and the prototype (λ_E), are compiled and listed in Table 3.4. The mixing proportion of cement, sand and water is measured by weight. Note that all of the results are the average values of test results of three specimens in each group. According to Chinese standard for test method of mechanical properties of ordinary concrete (GB/T 50081-2002, 2003), if the difference between the strength of one specimen and the middle value of the group is larger than 15%, the maximum and minimum values will be abandoned and the middle value will be selected to be the strength of the group.

Considering the target Young's modulus ratio discussed above ($\lambda_E = 0.199$), the mixing proportion of specimen set No.4 was selected to be used in the model fabrication, which has a mix proportion of cement, water and sand of 1: 1.65: 7.95 by weight. The strain-stress curves of the three specimens in set No.4 as well as their corresponding Young's modulus values are shown in Figure 3.6. From Table 3.4, the average Young's modulus ratio of this specimen set is $\lambda_E = 0.176$ and this value is slightly smaller than the target value (0.199), which means less additional mass will be needed. According to Equation (3.18), now the required additional mass should be $m_a = \lambda_E \lambda_l^2 m_p - m_m = 3.55$ ton.

Small cast-iron plates will be used to serve as the additional mass in the test. Note that Young's modulus of the actual micro-concrete used in the model fabrication was not exactly the same as the design value, for the quality control was not good enough. So the amount of additional mass needed should be determined according to the strength of the micro-concrete actually used after the model was completed. The details will be discussed in Section 3.4.5.

3.3.3 Reinforcements

The reinforcements of micro-concrete in the model are determined according to the reinforcement ratio of the prototype. In the actual building, walls are reinforced using two layers of steel bars of T20-150, where 20 and 150 denote the bar diameter and the spacing in unit of mm respectively, and T means high yield steel (with a yield strength of $f_y = 410$ MPa); slabs are reinforced with two layers of steel bars of T12-200 or T16-200; beams and columns are reinforced using the same high yield steel with a reinforcement ratio of about 4% and 5% respectively.

The reinforcements in the model are designed in such a way that all structural elements have similar reinforcement ratios as the prototype. The columns in the first two stories are reinforced using 6 or 8 steel bars of 4 mm diameter ($f_y = 302$ MPa) and the stirrups are made of 1.2 mm steel wires ($f_y = 121$ MPa) at 40 mm spacing [see Figure 3.10(a)]. Steel bars of 6 mm ($f_y = 623$ MPa) and 4 mm ($f_y = 302$ MPa) diameters are used for reinforcement of deep beams at the transfer plate (see Figure 3.11), and steel wires of 2 mm diameter ($f_y = 240$ MPa) are used as the main reinforcements of beams in the upper typical stories (see Figure 3.10). As shown in the top close-up attached in Figure 3.10, the stirrups for beams in the typical floors are fabricated utilizing grids cut from steel meshes of appropriate size (of 1.2 mm wire diameter and 12.7 mm spacing, $f_y = 121$ MPa). This new method of fabricating the reinforcement not only accelerates construction greatly, but also makes the resulting beams firmer and more suitable for fixing into the model.

The wall reinforcement consists of two layers of steel mesh of 1.2 mm wire diameter ($f_y = 121$ MPa) and 12.7 mm spacing [see Figure 3.11(b)], whereas the floor slabs (typical of 5 mm thick) are reinforced using one layer of the same steel wire mesh [see Figure 3.12(a)] except for the 2/F slab (of 8 mm thick) at the transfer floor, which consists of two layers of the same steel mesh [see Figure 3.11(b)].

Note that the strengths of concrete and steel of the actual building are not scaled down exactly by proportions in the model. Actually both reinforcement strength and the concrete strength of the model differ from that of the actual building. In addition, it is impossible that the micro-concrete used in the model have completely similar stress-strain characteristics with that of the actual building. Although we cannot accurately scale down the strength of concrete and steel in the model, keeping the reinforcement ratio appears to be a wise choice, and this strategy has been adopted by other researchers as well, for example, adopted in the ASCE paper by Li et al. (2006)

for modeling a 40-story RC building. The structural features of elements will be further compared in details between the model and the prototype in Section 6.3.

3.4 Fabrication of Model

The model fabrication includes the following main steps: a base slab was first fabricated, then the upper structure was built on it story by story using micro-concrete; after the whole model was completed, the formworks were demoulded and any honeycomb in the concrete was repaired; finally the completed model was hoisted onto the shaking table and the additional mass was mounted. This section will summarize the whole procedure in details step by step.

3.4.1 Fabrication of the base slab

The structure model will be built on a reinforced concrete base slab, which provides a solid base for hoisting the model onto the shaking table without inducing unwanted damage. The reinforcements of the first story are fixed onto the reinforcements in the base slab to provide a sufficient band length. The base slab must be stiff enough to resist any bending deflection during construction and hoisting of the model onto the shaking table.

Constrained by the plan dimension of the first story of the model (1620×1253 mm) and the spacing (400 mm) between bolt holes on the shaking table, the dimension of the base slab was designed to be 2300×1900 mm. Figure 3.7 shows the dimensions of the model and the base slab as well we their relative positions on the shaking table. To fulfill the stiffness requirement, the thickness of the base slab was set to 200 mm. The cube strength of the concrete used is 37 MPa; and steel bars of 20 mm diameter were installed at a spacing of 200 mm at both the top and bottom of the slab [Figure 3.8(a)].

Figure 3.8 shows the construction stages of the base slab. As shown in Figure 3.8(a), the reinforcements of columns and walls of the first story of the model were tied onto the reinforcements embedded in the base slab. To assure the reinforcements were in the right locations, an additional thin timber board with pre-drilled holes was used to fix them and to keep them vertical during concreting [Figure 3.8(a)]. Figure 3.8(b) shows the completed base slab, indicating the reinforcements of the ground floor columns and walls. This photograph also shows the hooks for hoisting the model and the screw holes through which the model will be fixed onto the shaking table.

3.4.2 Fabrication of the upper structure

After the base slab was completed, the upper structure was built on it story by story. Micro-concrete made of cement, water and sand in a mixing proportion of 1: 1.65: 7.95 by weight was used as the main construction material. The concrete mixer in mixing the micro-concrete is shown in Figure 3.9(a).

Figure 3.9(b) shows an electrical micro-vibrator used during our concreting to ensure the filling of columns and walls with micro-concrete. The vibrator was necessary here. Without the vibrator, it is difficult to fill the walls of 8 mm thick. In fact, as we will show later that honeycomb is found on some of the 8 mm-thick walls even the vibrator has been used. On the other hand, however, the micro-vibrator should be used with caution because too much vibration will segregate the sand from the cement paste and reduce the strength of the micro-concrete.

Timber boards of 12.7 mm thick were used to build the external formwork whereas foam plastic or more precisely expanded polystyrene (EPS) was used as the inner formwork to separate structural elements. The EPS was chosen because it can be cut easily into various shapes. Figure 3.9(c) shows a custom-made electrically-heated-wire machine used for cutting the EPS blocks and Figure 3.9(d) displays some shaped EPS blocks with grooves for fixing the beams. The softness of the EPS also facilitates easy removal of the interior formwork after concreting. Even if some of them were difficult to be removed after the construction, such as those in the core walls, their existence will have little effect on both the mass and stiffness of the whole model.

The construction sequence of the first story are as follows: (a) stirrups were attached onto the main reinforcements of columns at a spacing of 40 mm [Figure 3.10(a)]; (b) the EPS blocks were inserted as the inner formwork [Figure 3.10(b)]; (c) reinforcements of beams and slabs were fixed to the grooves and the surface of the EPS blocks respectively; (d) these reinforcements were also tied to those of columns using fine wires [Figure 3.10(b)]; (e) timber boards were attached onto the outer surface of the model to act as the external formwork [Figure 3.10(c)]; (f) finally, micro-concrete was poured and the story was finished [Figure 3.10(d)]. The top photographs attached in Figure 3.10 show the close-up views of beam reinforcements. Note that this construction procedure is very labor intensive. The connection of reinforcements of the beams, slabs and columns is particularly difficult due to the limited working space. In the future, other more efficient methods may be proposed for fixing the reinforcement.

The construction of the upper stories was similar to that of the first story. Note that at the transfer plate beams are much wider and deeper (typically of 60 mm depth) than those used in other floors (typically of 24 mm depth) [Figure 3.11(a)]. An enlarged view of the deep beam was also shown in the figure. Note that only shear walls were used above the transfer plate (refer to the scheming plan shown in Figure 2.2) and the steel meshes of those walls must be attached onto the reinforcements of the transfer beams as shown in Figure 3.11(b).

Above the transfer plate level, all upper floors are of the same floor plan. As shown in Figure 3.12, the construction procedure was similar to those of the first story except that structural walls were used here instead of columns. The main difficulty in the construction lies on the alignment of walls along different stories. The cumulation of errors occurred in the alignment of the walls may result in serious distortion. Therefore, a thin timber board with pre-drilled holes prescribing the location of wall reinforcements has been used to ensure the alignment [e.g. see Figure 3.8(a)].

3.4.3 Actual micro-concrete used

During construction, test cubes and cylinders of micro-concrete were made for various stories to check the consistency of material strength. Normally three cubes of $70.7 \times 70.7 \times 70.7$ mm and three cylinders of $\phi 100 \times 200$ mm were made for one story during concrete casting. The results of average strength of various stories are listed in Table 3.5. The variations of both cube strength and Young's modulus are unexpectedly high. The average ratio of Young's modulus ($\lambda_E = 0.236$) was about 34% larger than the design value ($\lambda_E = 0.176$, as discussed in Section 3.3.2). The average cube strength (f_{cu}) was 5.31 MPa, which was about 39% larger than the expected value ($f_{cu} = 3.83$ MPa, i.e. the strength of specimen set No.4 in Table 3.4).

The large variation in the material strength at different stories was partly due to the difficulties in controlling the water-cement ratio used during the construction. The water content of sand was affected by the daily humidity fluctuation and, therefore, may affect our water-cement ratio. The strength of concrete is by large governed by the water-cement ratio (MacGregor and Wight, 2006). In addition, our model is completed in almost 16 months, and thus the daily humidity and temperature during curing of specimens of various stories may fluctuate significantly. The development of concrete compressive strength is also strongly affected by the moisture and temperature conditions during curing (MacGregor and Wight, 2006). The large variations of the micro-concrete strength may also be partly due to the size effect (Neville, 1995), since the higher scatter of results tends to be resulted for the smaller specimens (test cubes of 70.7×70.7×70.7 mm and cylinders of ϕ100×200 mm are used in this study).

For the micro-concrete material, relatively large portions of water and sand are used in the present design to fulfill the relatively low strength requirement (recalling the design mixing proportion of cement, water and sand is 1: 1.65: 7.95 by weight as discussed in Section 3.3.2). Thus, sand is easy to segregate from the cement paste during concreting, and this will also result in variations of the micro-concrete strength. Actually, relatively large variations of strength for the micro-concrete material have also been found in other shaking table tests, such as those by Lu et al. (1999) and Lam et al. (2002). For example, in the 8-story building model tested by Lu et al. (1999), the cube strength of one story may be as large as 2.7 times of that of another story whereas the two stories have the same design strength.

Besides the cube strength and Young's modulus, the splitting tensile strength and the Poisson's ratio of the micro-concrete used were also measured. The splitting tensile strength was estimated from the split tests of three cylinders (ϕ100×200 mm) (i.e. by placing the test cylinder on its side and loading in compression along a diameter). The average splitting tensile strength was 0.44 MPa, which was about 1/12 of the average cube strength. The Poisson's ratio was estimated from the ratio between the transversal strain and the longitudinal strain in compression test of three cylinder specimens, and the resulting Poisson's ratio of the micro-concrete used was 0.16. This value falls in the usual range (0.15-0.20) of the Poisson's ratios for concrete (MacGregor and Wight, 2006).

3.4.4 Demoulding and repairing

After the final set of the micro-concrete at the roof floor, the external timber formworks were detached and the internal EPS blocks were removed [Figure 3.13(a)]. This procedure should be carried out carefully to assure structural elements embedded in the EPS were not damaged. After demoulding, some EPS remains on the inner surface of structural members as shown in Figure 3.13(b). As indicated before, these remains were considered to have little influence on the overall structural response due to their much smaller density and Young's modulus.

Defects and honeycombs on structural elements were inevitable in the model due to the small size of the present model. So, after the demoulding of each story, the surface of the structure was checked to identify the locations of defects. The defects found were then repaired immediately using the same micro-concrete.

Figure 3.14 shows four different types of defects found in the model. Type I defect was the most critical to the overall structural stability, since reinforcements of structural elements were exposed and micro-concrete was missing for a large portion of the structural elements. Fortunately, this kind of defect was found only at five structural walls between 18/F and 19/F, one wall between 2/F and 3/F, and one wall between G/F and 1/F. The second and third kinds (II and III) of defects, corresponding to small cavities and the exposure of reinforcement meshes respectively, were much more common, because concrete was found hard to fill the formworks completely.

Type IV defect was induced during the removal of the internal EPS formworks.

All defects were repaired carefully using the same micro-concrete as used in the model fabrication. After that, the model was hoisted by the crane in the laboratory and installed onto the shaking table. Then additional mass was installed onto the model.

3.4.5 Installation of additional mass

After the model was installed on the shaking table, additional mass was mounted onto it to better fulfill the requirement of similarity law as discussed in Section 3.2.1. But since the actual strength of micro-concrete used in the model construction was larger than the design value as given in Table 3.5, more additional mass was needed according to similarity law. From Table 3.5, the average Young's modulus ratio (λ_E) of the actual micro-concrete was 0.236. So according to Equation (3.18), the required additional mass should be $m_a = \lambda_E \lambda_l^2 m_p - m_m = 5.11$ ton, where $\lambda_l = 0.04$, $m_p = 16285.56$ ton and $m_m = 1.04$ ton. This value was much larger than the design value ($m_a = 3.55$ ton, as discussed in Section 3.3.2).

However, the total mass which can be installed onto the model was constrained by the limited internal space available in the model. In the present study, cast-iron plates of 200×160×35 mm and 200×70×70 mm were used to serve as additional mass as shown in Figure 3.15. The average weights of them were about 8.3 kg and 7.6 kg respectively. The locations of the additional mass on various floors are shown in Figures 3.16-3.18. The total mass of cast-iron plates installed on the model was eventually 4.43 tons, and is about 87% of the required value. Although the additional mass is not sufficient, 13% difference is still considered acceptable in engineering applications.

The distribution of additional mass at different stories was designated proportional to the distribution of structural weights in the prototype. Within each story, the additional mass was distributed evenly over the floor slab as far as possible (refer to Figures 3.16-3.18). The installation of additional mass was carried out from the lower stories to the upper ones. Either micro-concrete or glass cement was used to glue or fix the iron plates onto the slabs. Figure 3.15(b) showed the model with all additional mass mounted. After that, transducers were installed onto the model.

3.5 Instrumentation Strategy

Before the shaking table tests were carried out, various transducers were installed. However, limited by the availability of data acquisition channels (a total of 53), the location for instrumentation needs special consideration.

In our shaking table test, acceleration and displacement responses of the structure under various earthquake inputs were measured, and they were used to estimate other parameters, such as structural modal characteristic, inter-story drift ratio, ductility and Park and Ang damage index. Strain gauges were installed on some selected elements to identify localized stresses and damages. In short, 53 channels were used to record data from 15 accelerometers, 6 displacement transducers and 32 strain gauges. The detailed layout of the instrument is given below.

3.5.1 Accelerometers and displacement transducers

Higher mode vibrations are expected to be important for the 21-story model. Guided by preliminary finite element analysis (see Section 2.3.2), accelerometers were installed on the 1/F, 2/F, 3/F, 9/F, 15/F and 21/F as shown in Figure 3.19. We expect that variations of higher modes can be captured at these levels. It is also obvious that the present asymmetric model is conducive to torsional vibrations even under unidirectional excitation of our shaking table. To capture the torsional responses, at least two accelerometers were installed along the *y*-direction on the 1/F, 2/F, 3/F, 9/F, 15/F and 21/F (see Figure 3.19).

Another two accelerometers were installed in the *y*-direction on the 21/F and 2/F respectively (Figure 3.19) to measure the responses caused by torsion in the direction perpendicular to the ground shaking. In addition, one accelerometer was installed on the surface of the shaking table in the direction of shaking to record the actual input earthquake waves generated by the shaking table.

The accelerometers used in this study are Brüel & Kjær high sensitivity products, including three types: 4370, 4371 and 4382. Accelerometer type 4370 has a maximum operational peak value of 2000g and a residual noise level of 0.02mg. Its working frequency ranges from 0.1 Hz to 4800 Hz. The maximum operational peak values and residual noise levels of types 4371 and 4382 are 6000g, 2000g and 0.24mg, 0.06mg respectively. Their working frequency ranges are 0.1-12600 Hz and 0.1-8400 Hz.

Both Brüel & Kjær amplifier type 2635 (single-channel) and NEXUS conditioning amplifiers (4-channel) were used to amplifier acceleration signals. The signals after amplification were connected to the 24-channel shielded connector block BNC-2115 from National Instruments before they were recorded in the computer. The accelerometers, amplifiers, laser and LED displacement transducers are all shown in Figure 3.20.

The displacement transducers used include four ultra-accurate CCD laser displacement sensors of type KEYENCE LK 503, which has a measuring range of ±100 mm and a resolution of $10\,\mu m$, and two LED (Light-Emitting Diode) sensors of type SUNX LH-512, which has a measuring range of ±30 mm and a resolution of $20\,\mu m$. However, it was found when the vibration level was small, noise level will be comparable with the signal for the LED measurements. For such cases, frequencies above a cutoff frequency of 15 Hz will be filtered out to identify the real signal, which will be explained again in Section 4.3.4.

Due to the limitation of available transducers, displacements were not measured at every story. As shown in Figure 3.19, two laser sensors were installed on the roof level, one laser sensor on the surface of the shaking table, and one on the transfer plate at 2/F. In addition to the laser sensors, one LED transducer was installed on the transfer plate and one on the 3/F (see Figure 3.19).

Before used in experiment, all these transducers were calibrated to assure they were in good working conditions. In experiment, data were collected at a sampling rate of 500 Hz. The computer program LabVIEW v7.0 from National Instruments was used for signal acquisition and data presentation.

3.5.2 Strain gauges

Strain gauges of 5 mm length were attached to some selected structural elements of the model. As shown in Figure 3.21(b), strain data were collected by SCXI modules 1000 with 4-slot SCXI-1314 terminal blocks from National Instruments and a maximum of 32 channels were available.

Since it is impossible to measure strains for all of the structural elements of the model, only those elements which were assumed to be critical and susceptible to damages in earthquake were selected. In this study, the results of FEM analyses as discussed in Chapter 2 were taken as a reference for selecting the locations of strain gauges. According to FEM predictions, the largest stresses are likely to concentrate at the lower three stories (see Section 2.3.3.3), so 27 out of 32 strain gauges were attached on columns or walls in these three stories.

But due to uncertainty involved in FEM analyses, the placements of strain gauges in this study were not totally relying on the FEM results. Within each story, the strain gauges were distributed as evenly as possible, as sketched in Figures 3.22-3.24. The other five strain gauges installed at the upper stories (i.e. at the 4th, 5th and 10th

stories) were shown in Figure 3.24.

Among all of the 32 strain gauges, the strain gauges of No. 19, 20, 27 and 28 were placed horizontally (refer to Figure 3.24) for the purpose of measuring the tension and compression caused by torsional deformation. All other strain gauges were attached vertically to record strains caused by flexural vibrations.

3.6 Summary of the Model Design

In this chapter, preparations for the shaking table test are described, including model design, fabrication and instrumentation. Constrained by similarity law, the model design was carried out, including determinations of the length scale, material strength and reinforcements. Then the 21-story model was fabricated story by story using micro-concrete, steel wires and steel meshes. After the model was completed and installed on the shaking table, cast-iron plates were installed onto the model to serve as the additional mass. Finally various transducers, including accelerometers, displacement transducers and strain gauges, were installed to make preparations for the shaking table test. The detailed procedure and results of the shaking table test will be introduced and discussed in the next chapter.

Table 3.1 Additional mass similarity law for shaking table tests derived from both the Buckingham Pi Theorem and governing equations.

Item	From the Buckingham Pi Theorem	From governing equations
Length	λ_l	λ_l
Density	λ_ρ	$\lambda_\rho = \lambda_m \lambda_l^{-3}$
Elastic modulus	λ_E	$\lambda_E = \lambda_m \lambda_l^{-2}$
Stress	$\lambda_\sigma = \lambda_E$	$\lambda_\sigma = \lambda_E$
Time	$\lambda_t = \lambda_l^{0.5}$	$\lambda_t = \lambda_l^{0.5}$
Displacement	$\lambda_x = \lambda_l$	$\lambda_x = \lambda_l$
Velocity	$\lambda_v = \lambda_l^{0.5}$	$\lambda_v = \lambda_l^{0.5}$
Acceleration	$\lambda_a = 1$	$\lambda_a = 1$
Gravity	$\lambda_g = 1$	$\lambda_g = 1$
Frequency	$\lambda_\omega = \lambda_l^{-0.5}$	$\lambda_\omega = \lambda_l^{-0.5}$
Damping ratio	$\lambda_\xi = 1$	$\lambda_\xi = 1$
Mass	$\lambda_m = \lambda_E \lambda_l^2$	$\lambda_m = \lambda_E \lambda_l^2$
Additional mass	$m_a = \lambda_E \lambda_l^2 m_p - m_m$	$m_a = \lambda_E \lambda_l^2 m_p - m_m$

Table 3.2 Typical dimensions of the model and the prototype (length scale $\lambda_l = 1/25$).

Item	Prototype	Model
Height (m)	69.65	2.786
Width along the *x* direction (m)	35.75	1.43
Width along the *y* direction (m)	31.675	1.267
Story height (m)	3	0.12
200 mm shear wall (mm)	200	8
300 mm shear wall (mm)	300	12
Column diameter (mm)	1200	48
Slab thickness (mm)	125	5

Remark:

x-*y* directions are given in Figure 3.2.

Table 3.3 Two extreme cases of additional mass added for purpose of estimating the target strength of micro-concrete used.

Item	None additional mass	Maximum additional mass
Length scale λ_l	0.04	0.04
Density ratio λ_ρ	1.0	4.975
Young's modulus ratio λ_E	0.04	0.199
Young's modulus E_c (GPa)	1.2	5.97
Mass ratio λ_m	0.64×10^{-4}	3.18×10^{-4}
Model mass m_m (ton)	1.04	1.04
Prototype mass m_p (ton)	16285.56	16285.56
Additional mass m_a (ton)	0	4.14

Table 3.4 Test results of micro-concrete specimens. The mix proportion of cement, sand and water is measured by weight and λ_E denotes the Young's modulus ratio between the specimen and the prototype.

Specimen set	Cement	Water	Sand	Density (kg/m^3)	Cube strength (MPa)	Young's modulus (GPa)	λ_E
1	1	1.34	5.44	1806	6.18	7.851	0.262
2	1	1.36	5.87	1780	6.66	7.333	0.244
3	1	1.82	7.27	1766	3.51	3.159	0.105
4	1	1.65	7.95	1718	3.83	5.294	0.176
5	1	1.59	8.71	1776	3.21	3.943	0.131
6	1	1.82	9.60	1747	2.67	3.622	0.121

Table 3.5 Strength of the micro-concrete used in construction of various stories.

Story	Density (kg/m^3)	Cube strength (MPa)	Young's modulus (GPa)	λ_E
1	1966.53	4.40	6.979	0.233
2	1976.90	4.05	5.085	0.169
3	1869.10	3.86	7.260	0.242
4	1860.53	3.14	5.608	0.187
5	1785.49	3.22	4.795	0.160
6	1775.52	2.72	–	–
7	1896.30	3.45	5.399	0.180
8	2049.89	8.53	11.631	0.388
9	2067.37	8.77	9.196	0.307
10	2002.03	8.42	9.166	0.306
11	2031.95	7.42	10.776	0.359
14	1946.63	6.06	–	–
15	1930.75	5.43	7.802	0.260
16	1917.35	5.48	8.045	0.268
17	1906.32	7.76	8.751	0.292
18	1926.17	4.02	5.285	0.176
19	1893.56	4.90	4.650	0.155
20	1891.52	4.56	4.600	0.153
21	1902.68	4.77	5.561	0.185
Average	1926.14	5.31	7.093	0.236
Standard deviation	78.55	1.96	2.226	0.074

Remark:

"–" denotes no cylinder specimen (used for measuring Young's modulus) is made for that story.

Figure 3.1 Photograph of the completed 1:20 scaled model of a 42-story reinforced concrete residential building in Hong Kong (Lam et al., 2002).

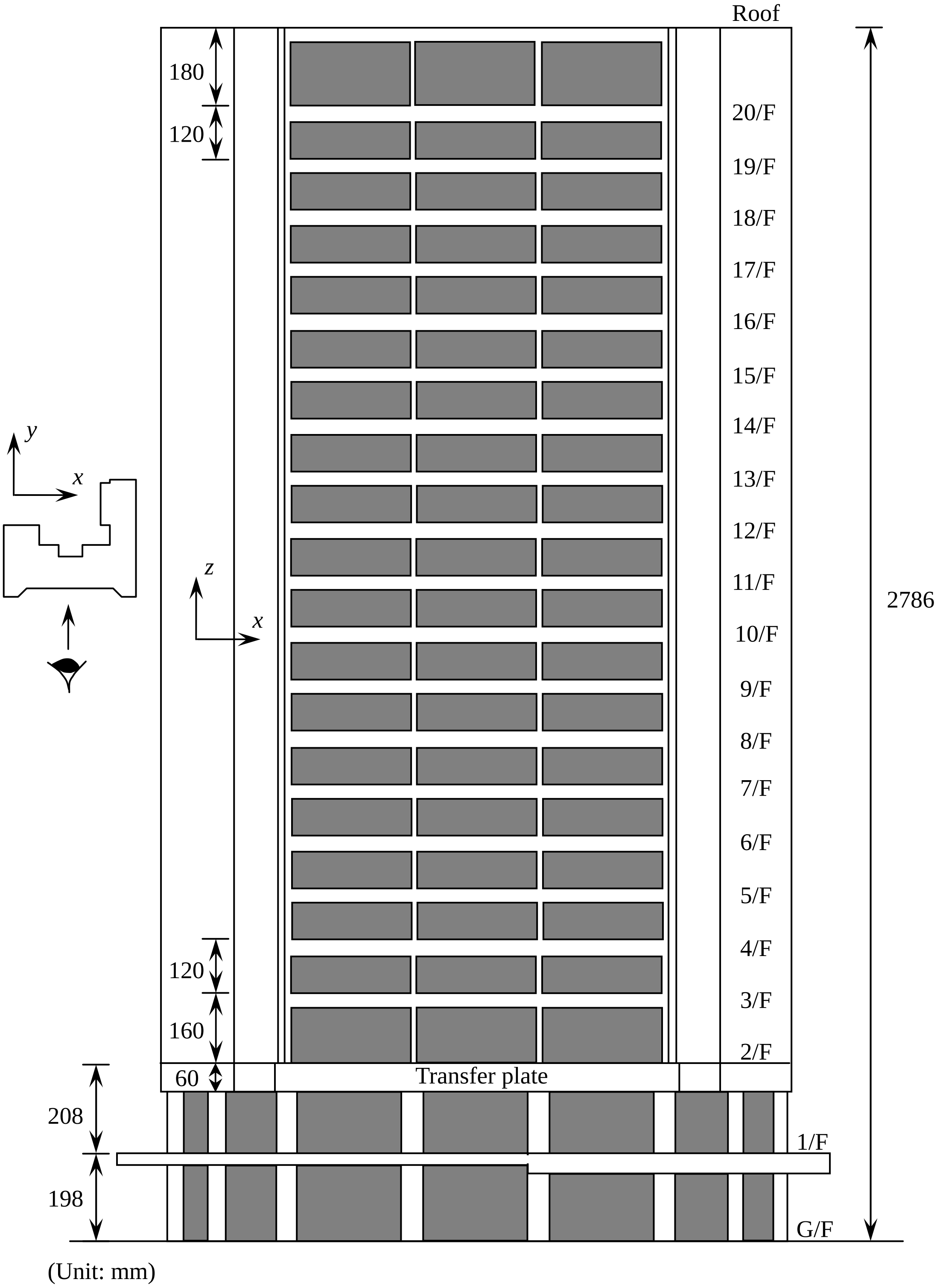

Figure 3.2 Elevation view and story height of the model. Those typical floors which are not specified in the figure are all 120 mm height.

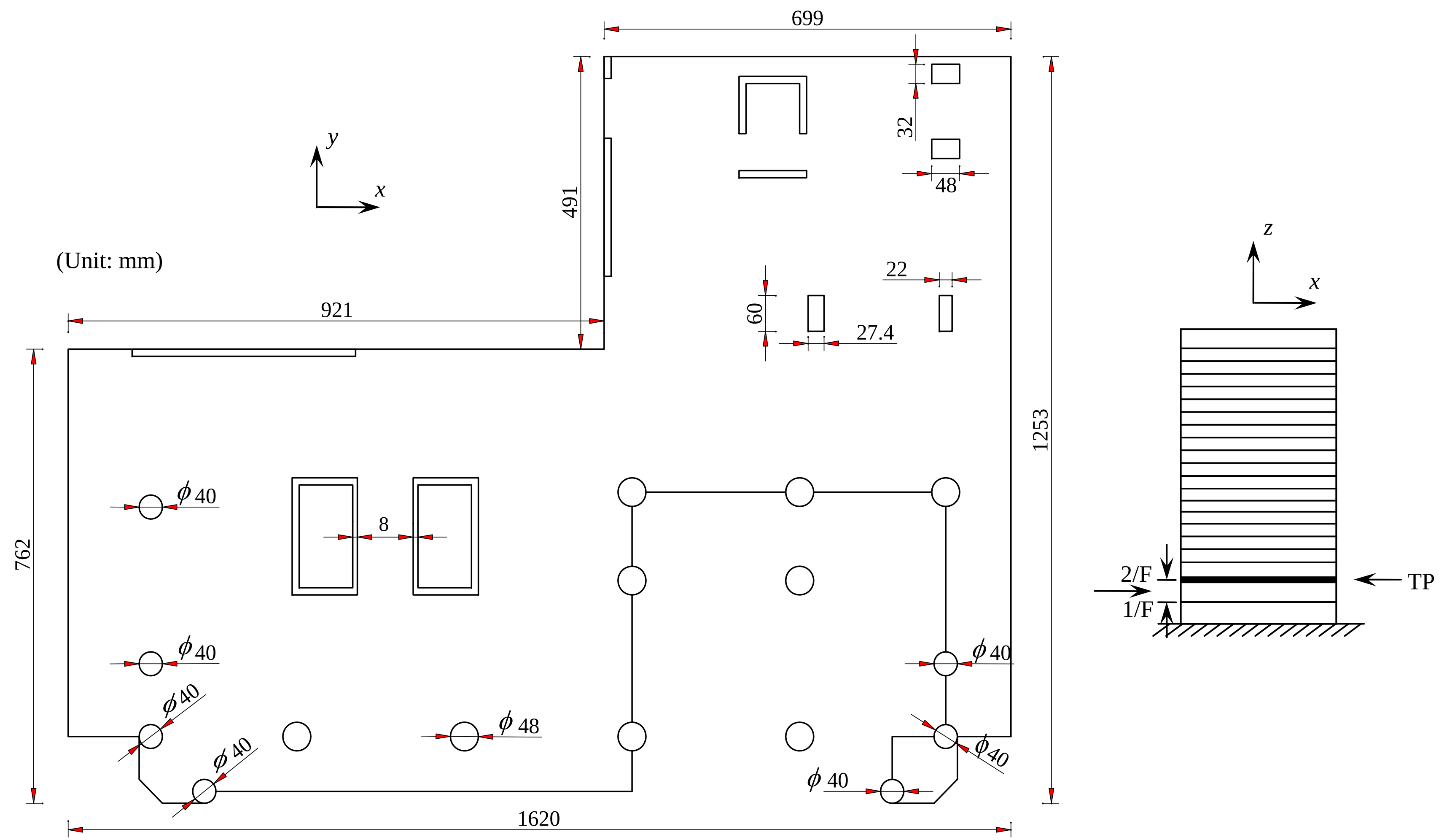

Figure 3.3 Cross section of the model between 1/F and 2/F. Circular columns not specified are all of 48 mm diameter and walls not specified are all of 12 mm thick. The small sketch shows the elevation view of the model, where TP means the transfer plate.

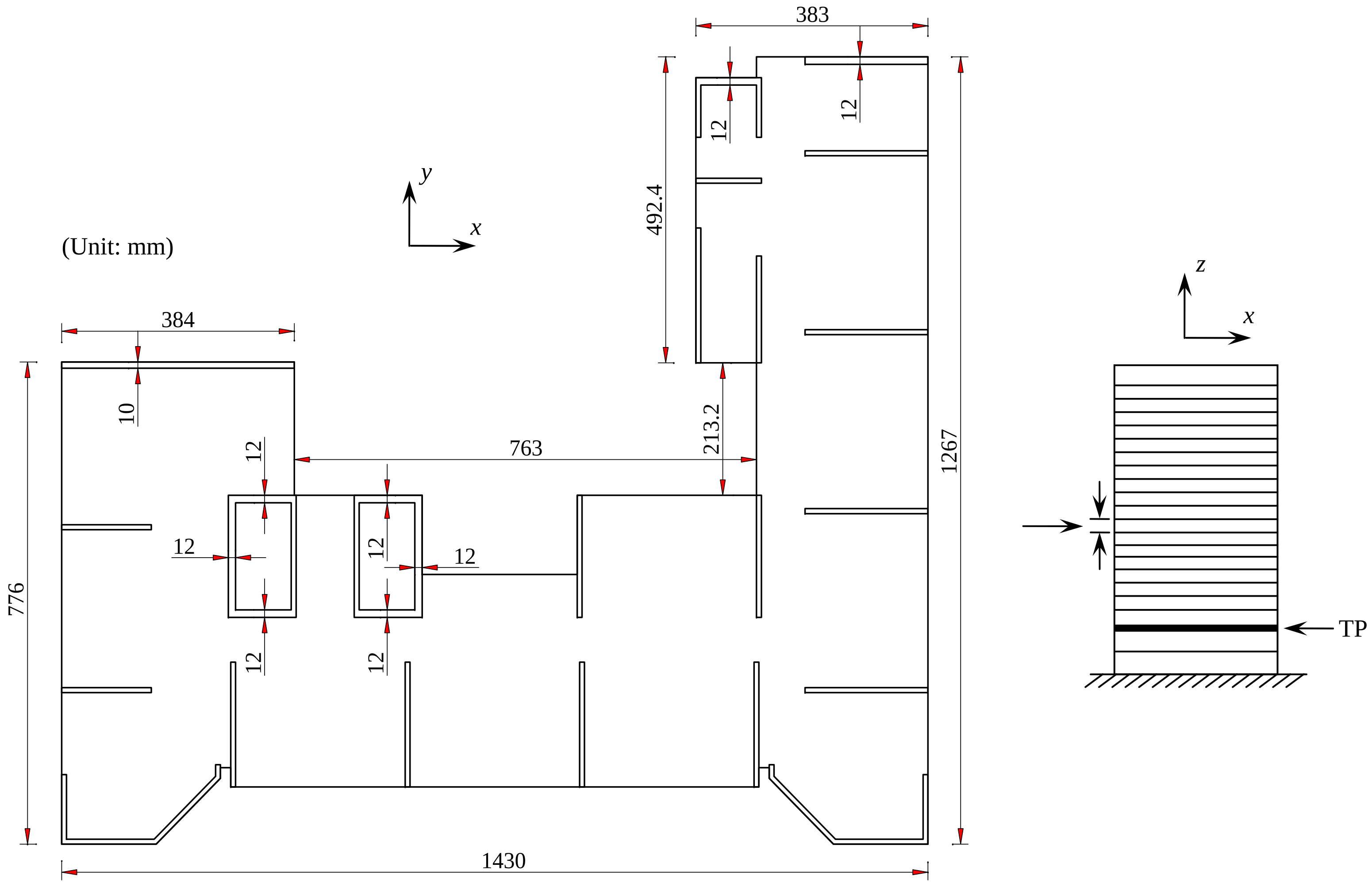

Figure 3.4 Cross section of the model at a typical floor. Walls not specified are all of 8 mm thick. The small sketch shows the elevation view of the model, where TP means the transfer plate.

Figure 3.5 Photographs of finished micro-concrete specimens: (a) cubes of 70.7×70.7×70.7mm; (b) cylinders of ϕ100×200 mm (ϕ means diameter) with strain gauges attached on their surface.

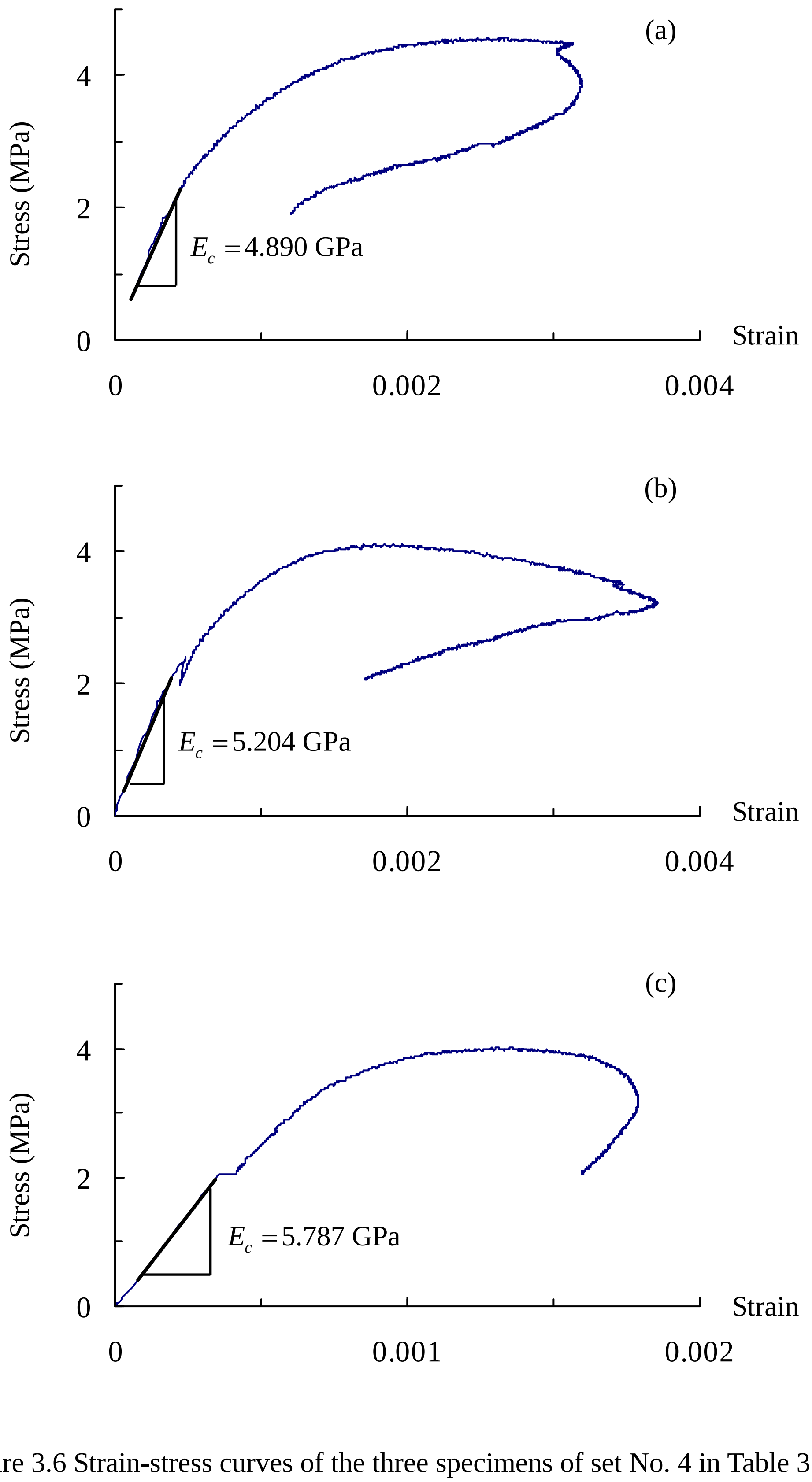

Figure 3.6 Strain-stress curves of the three specimens of set No. 4 in Table 3.4 and their corresponding Young's modulus values (E_c).

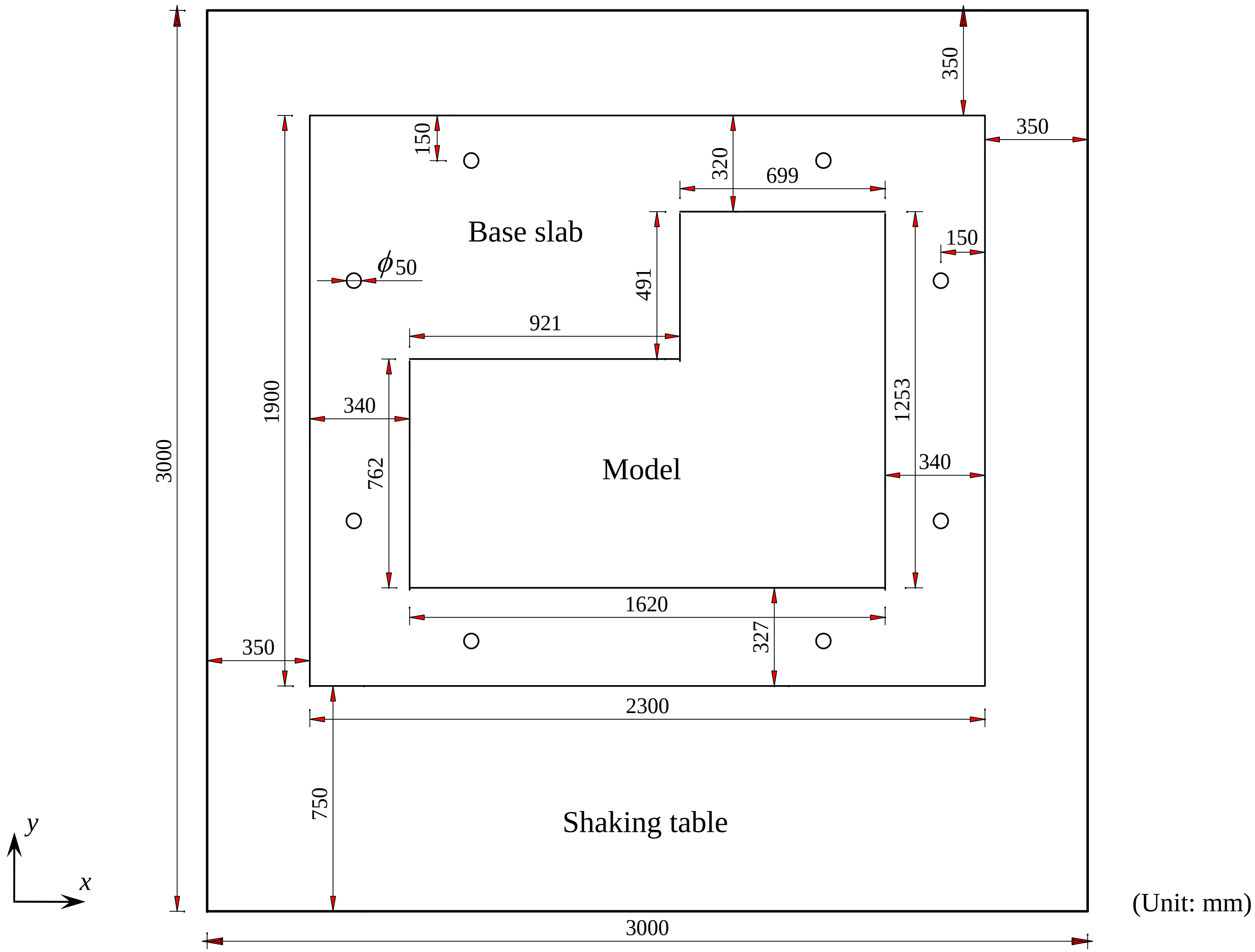

Figure 3.7 Sketch showing the positions of the model and the base slab on the 3m×3m shaking table. The six circles on the base slab denote screw holes which are used to fix it onto the shaking table.

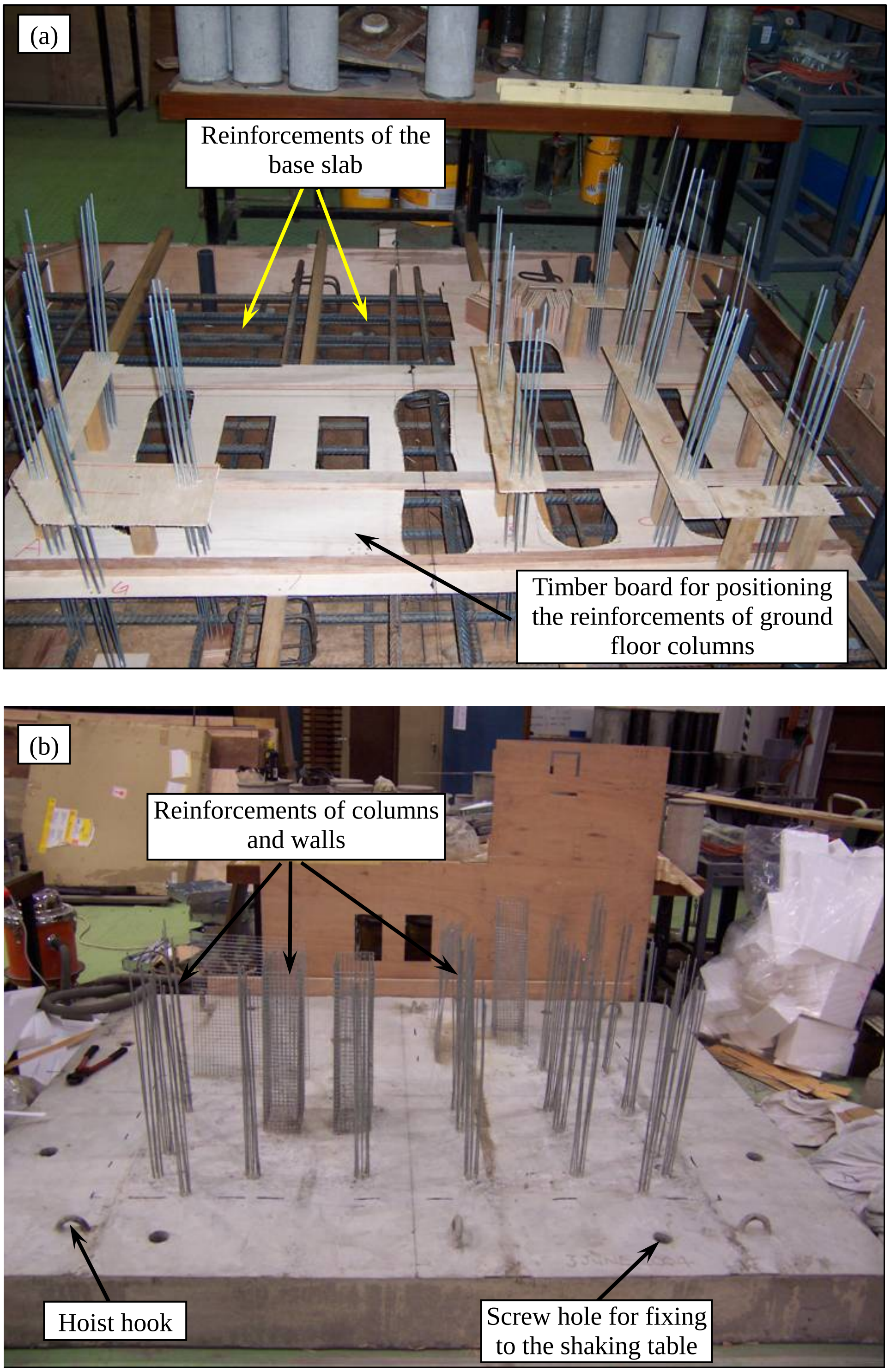

Figure 3.8 Construction of the base slab: (a) connection of reinforcements; (b) the base slab after concreting.

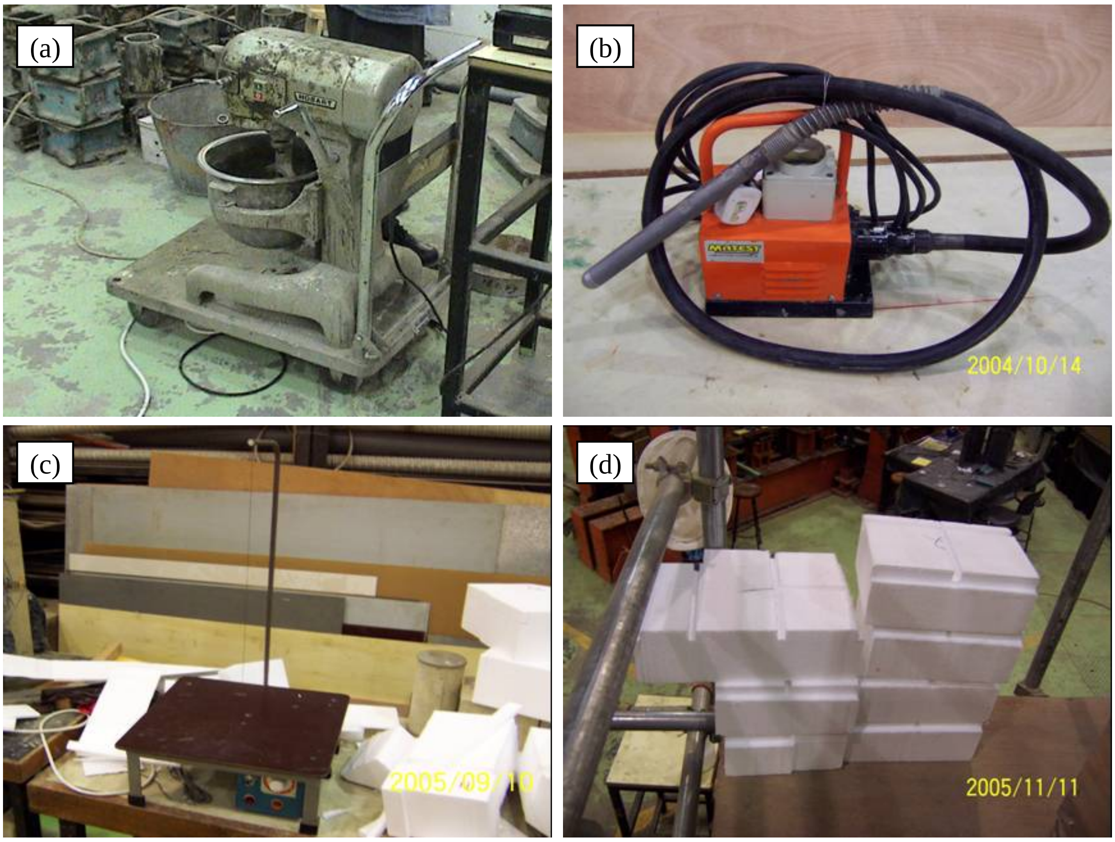

Figure 3.9 Various instruments used in the model construction: (a) concrete mixer; (b) micro-vibrator; (c) electrically-heated-wire cutter for cutting EPS; (d) EPS blocks used to build the inner formwork.

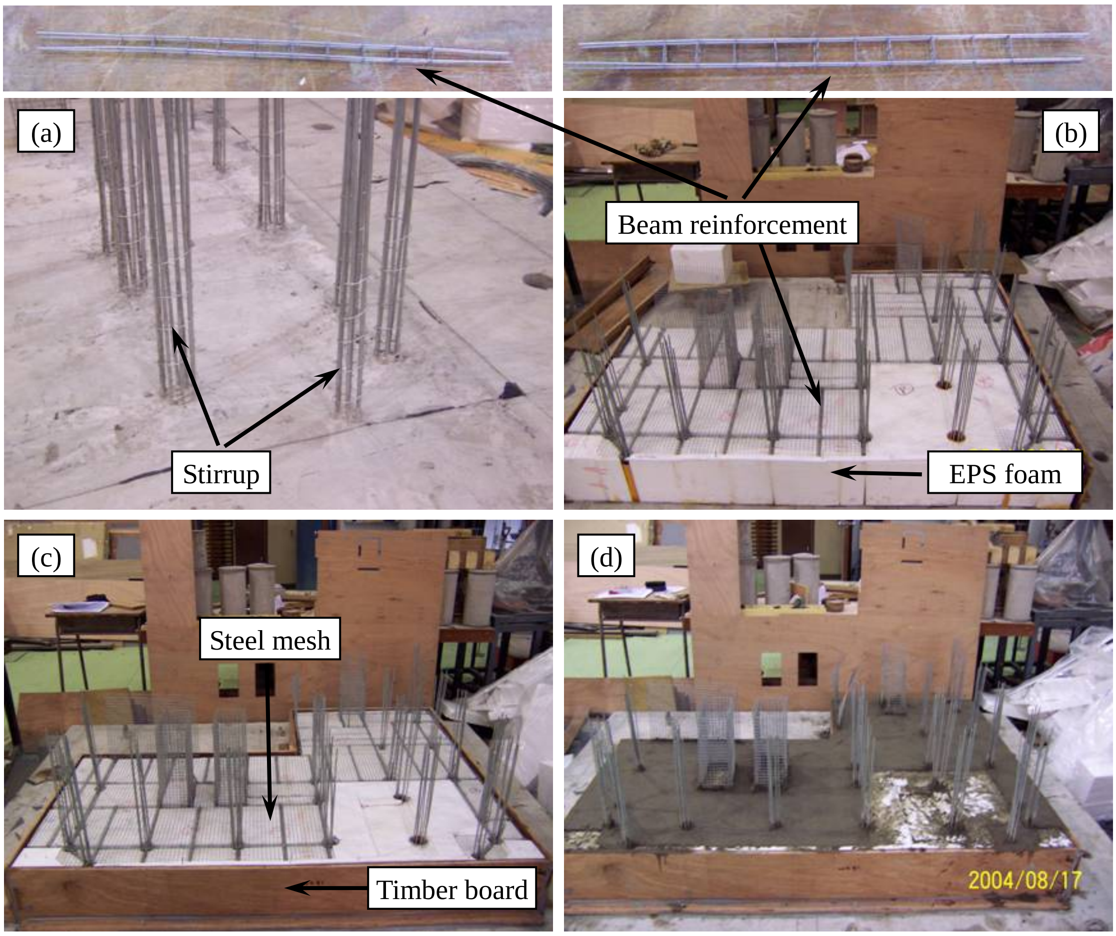

Figure 3.10 Construction procedure of the first story: (a) installation of stirrups; (b) installation of EPS blocks and beam reinforcements; (c) attachment of slab reinforcements and outer formwork; (d) casting of micro-concrete.

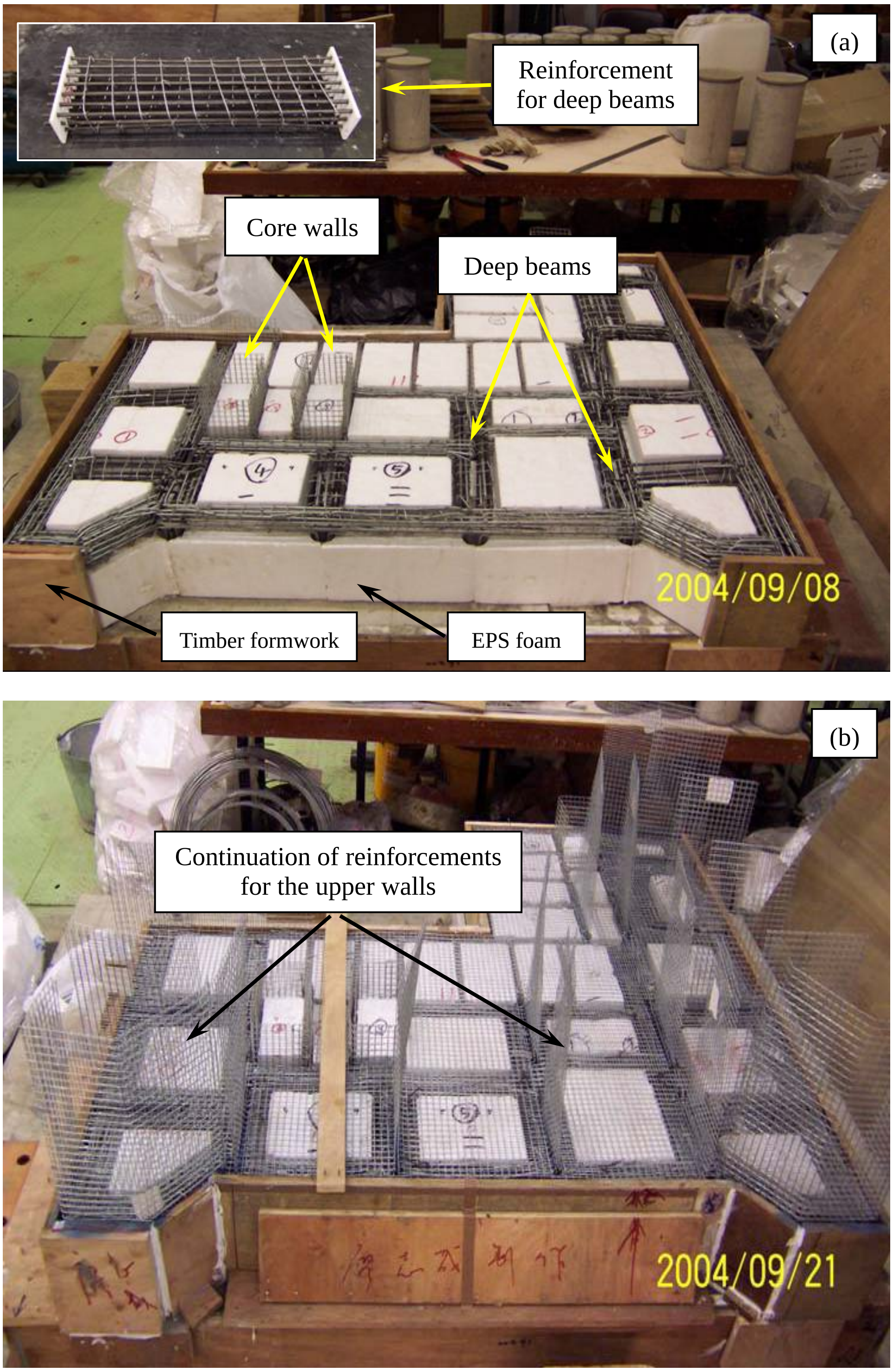

Figure 3.11 Construction of the transfer plate: (a) reinforcements of core walls and transfer beams as well as the timber and EPS foam formwork; (b) continuation of reinforcements of the upper walls above the transfer plate.

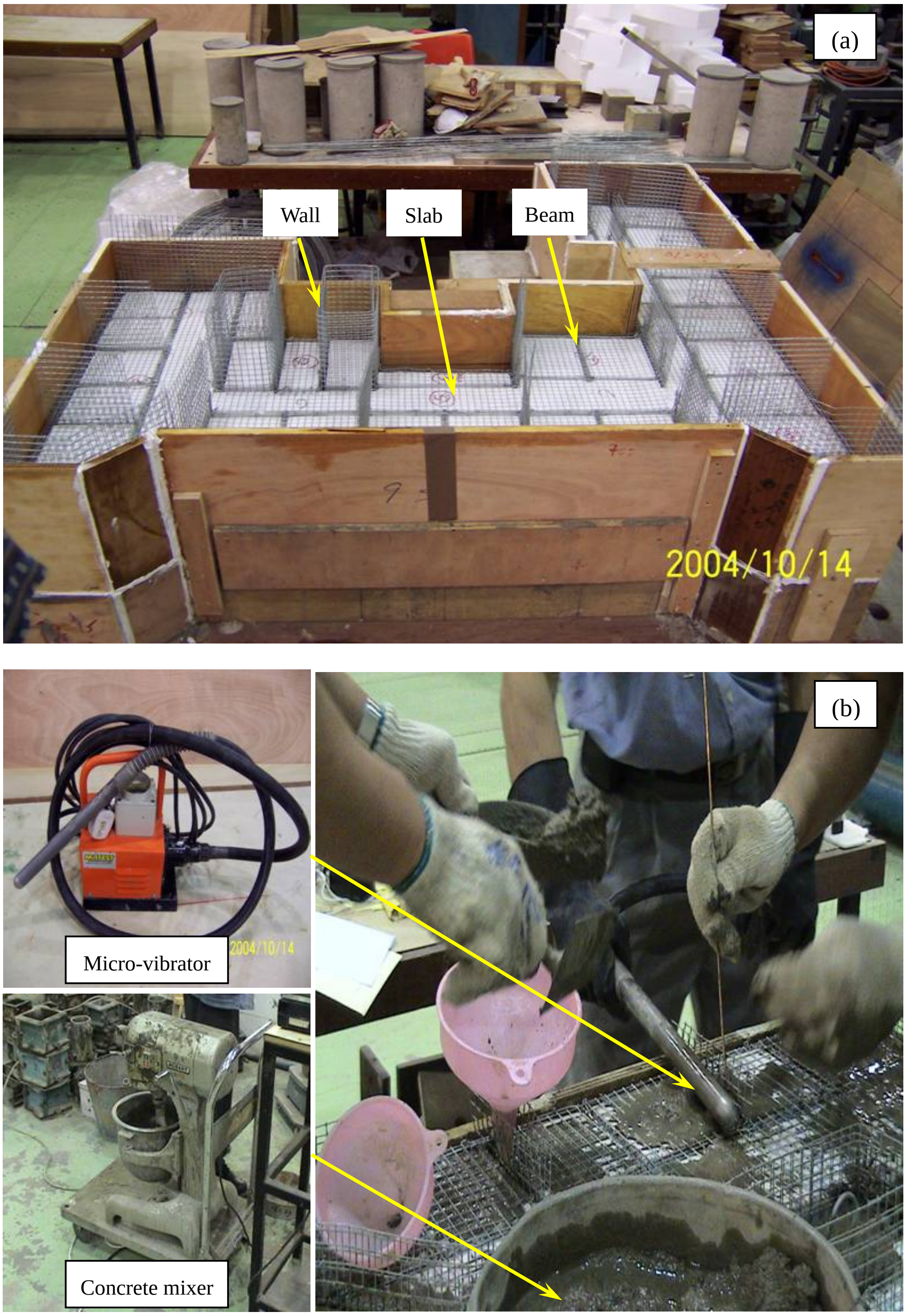

Figure 3.12 Construction of typical stories: (a) reinforcements of beams, walls and slab; (b) casting of concrete, and the two small photographs on the left show the micro-vibrator and concrete mixer used.

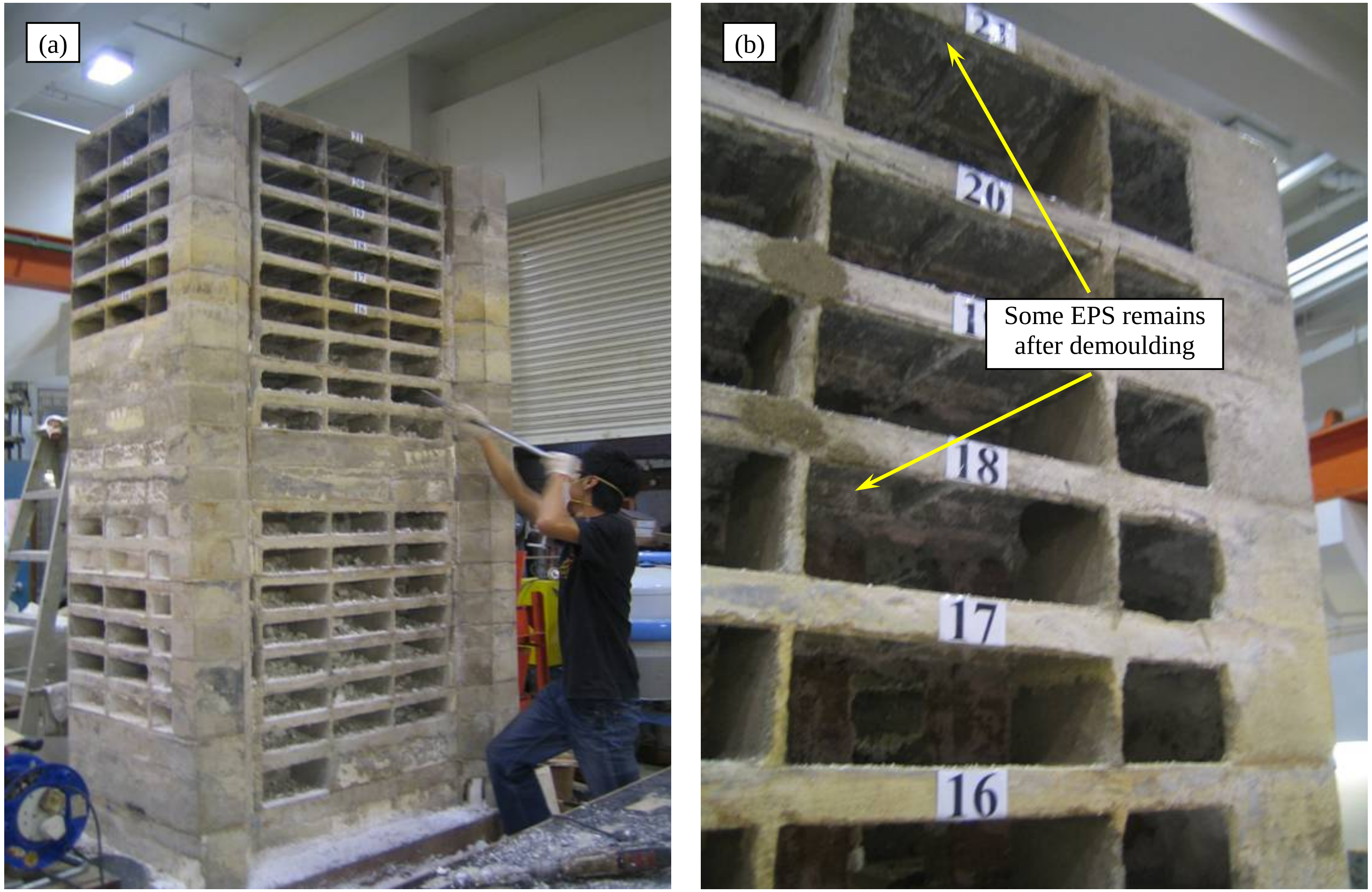

Figure 3.13 Demoulding of EPS formwork after the completion of concreting.

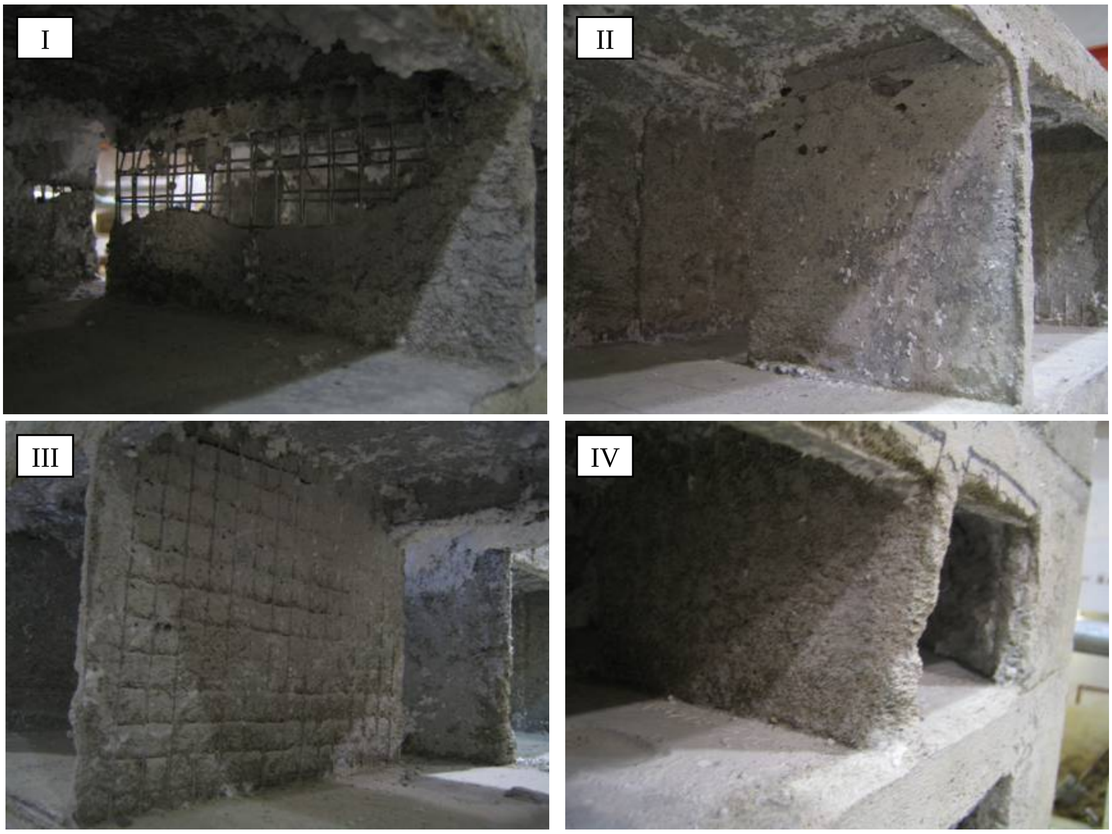

Figure 3.14 Different types of defects found in the model after demoulding.

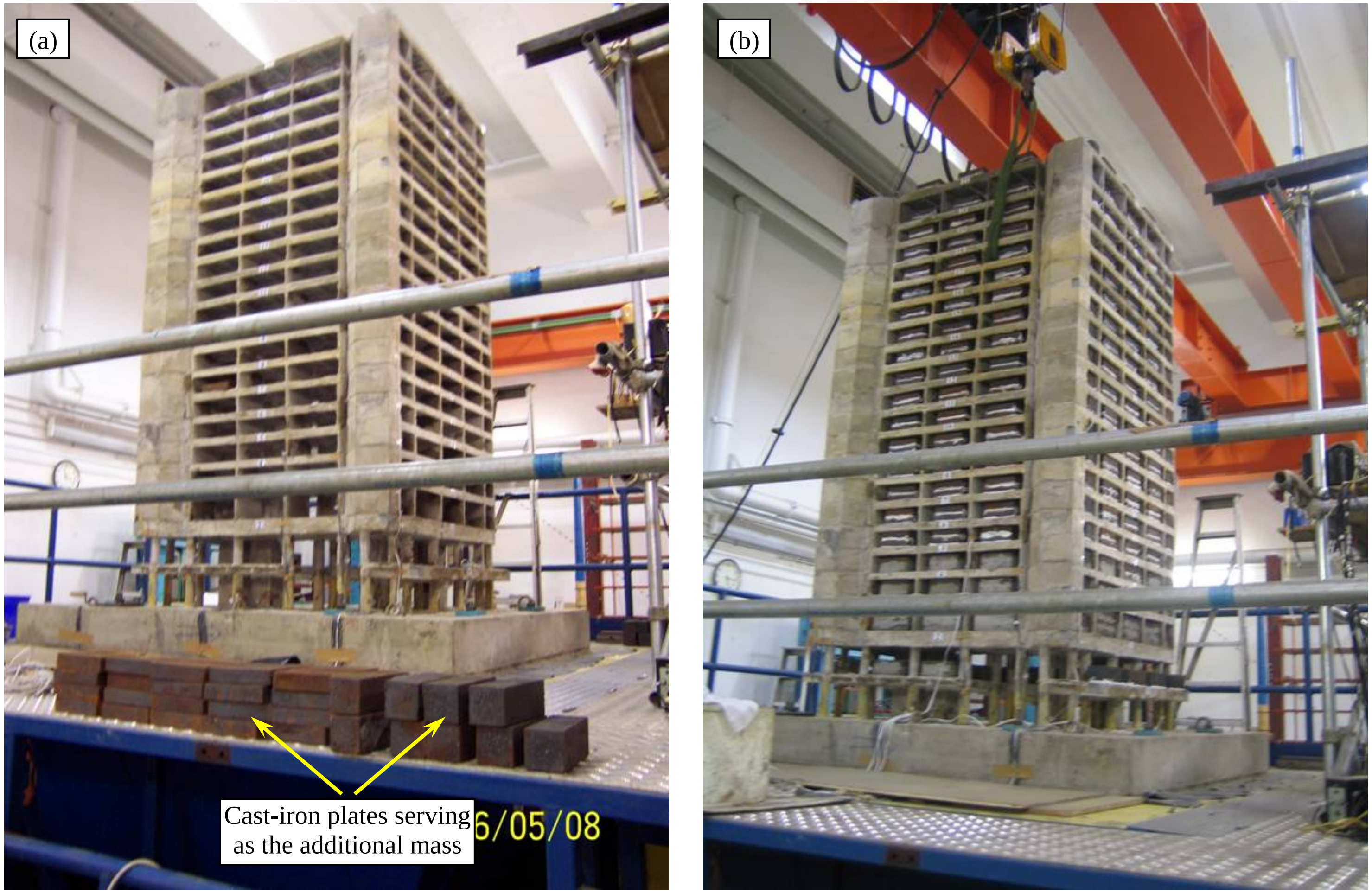

Figure 3.15 Photographs of the completed model: (a) without additional mass; (b) with additional mass installed.

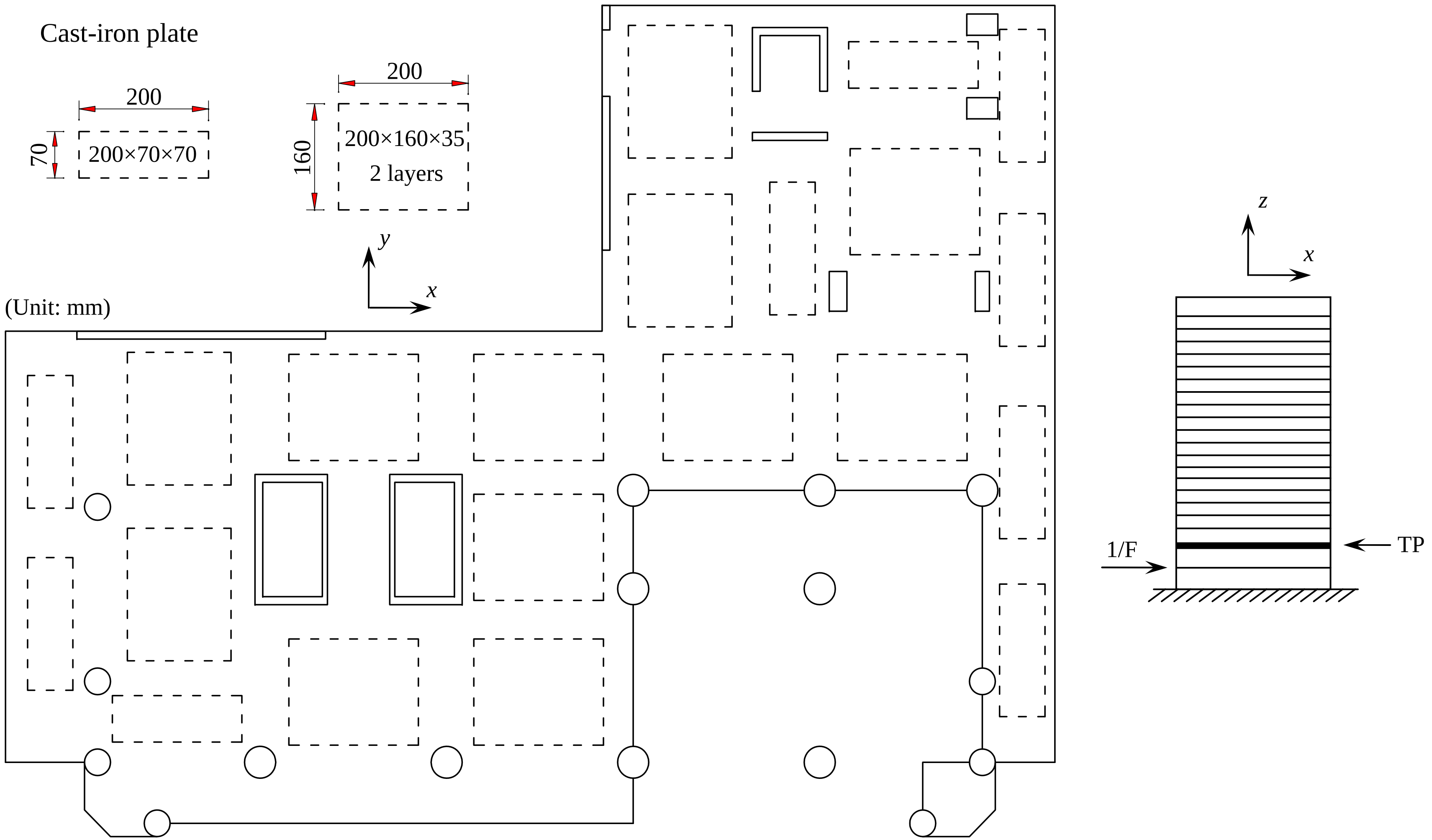

Figure 3.16 Plan view showing the locations of the additional mass (dashed rectangles) placed on 1/F. The small sketch shows the elevation view of the model, where TP means the transfer plate.

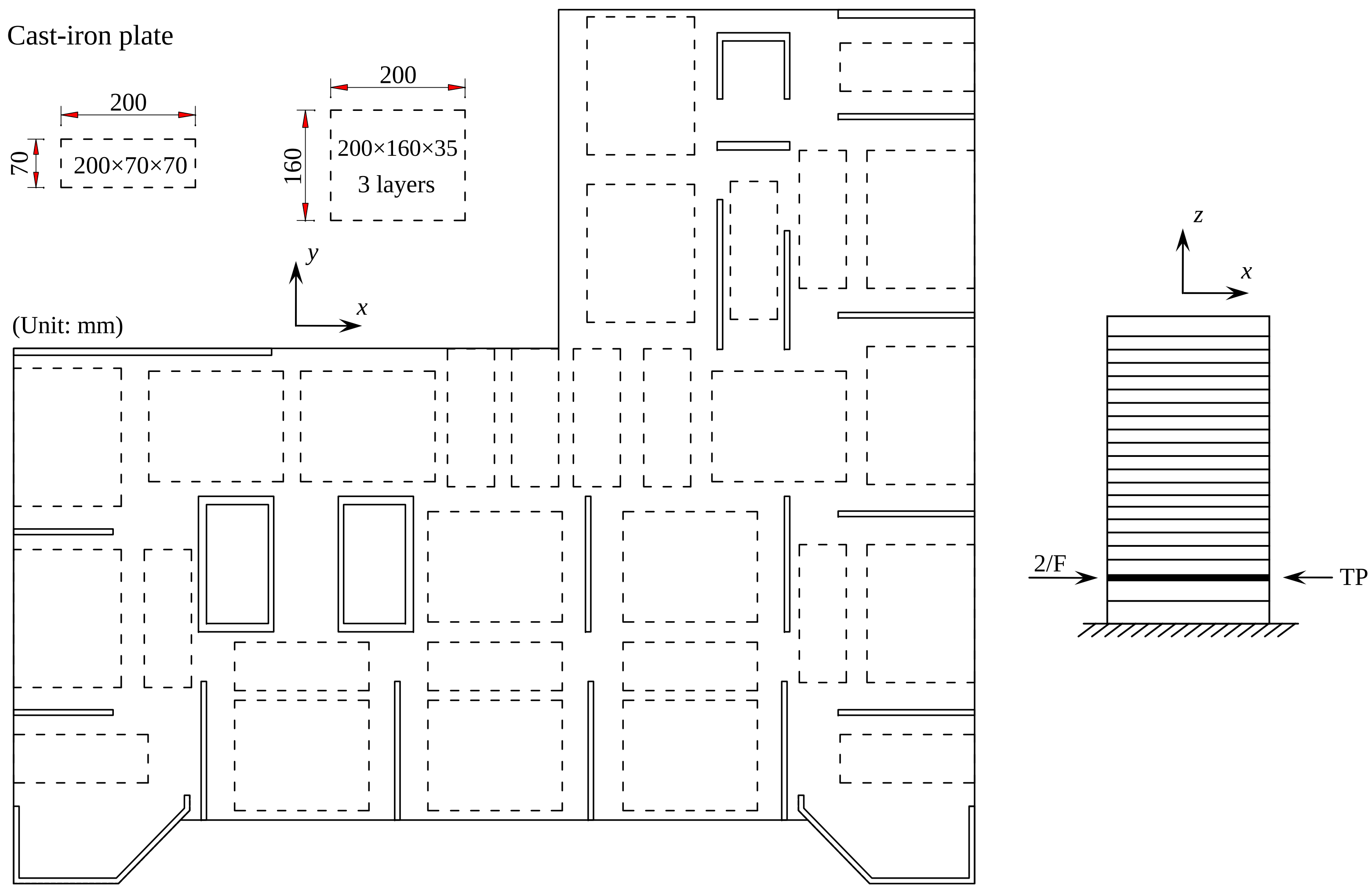

Figure 3.17 Plan view showing the locations of the additional mass (dashed rectangles) placed on 2/F. The small sketch shows the elevation view of the model, where TP means the transfer plate.

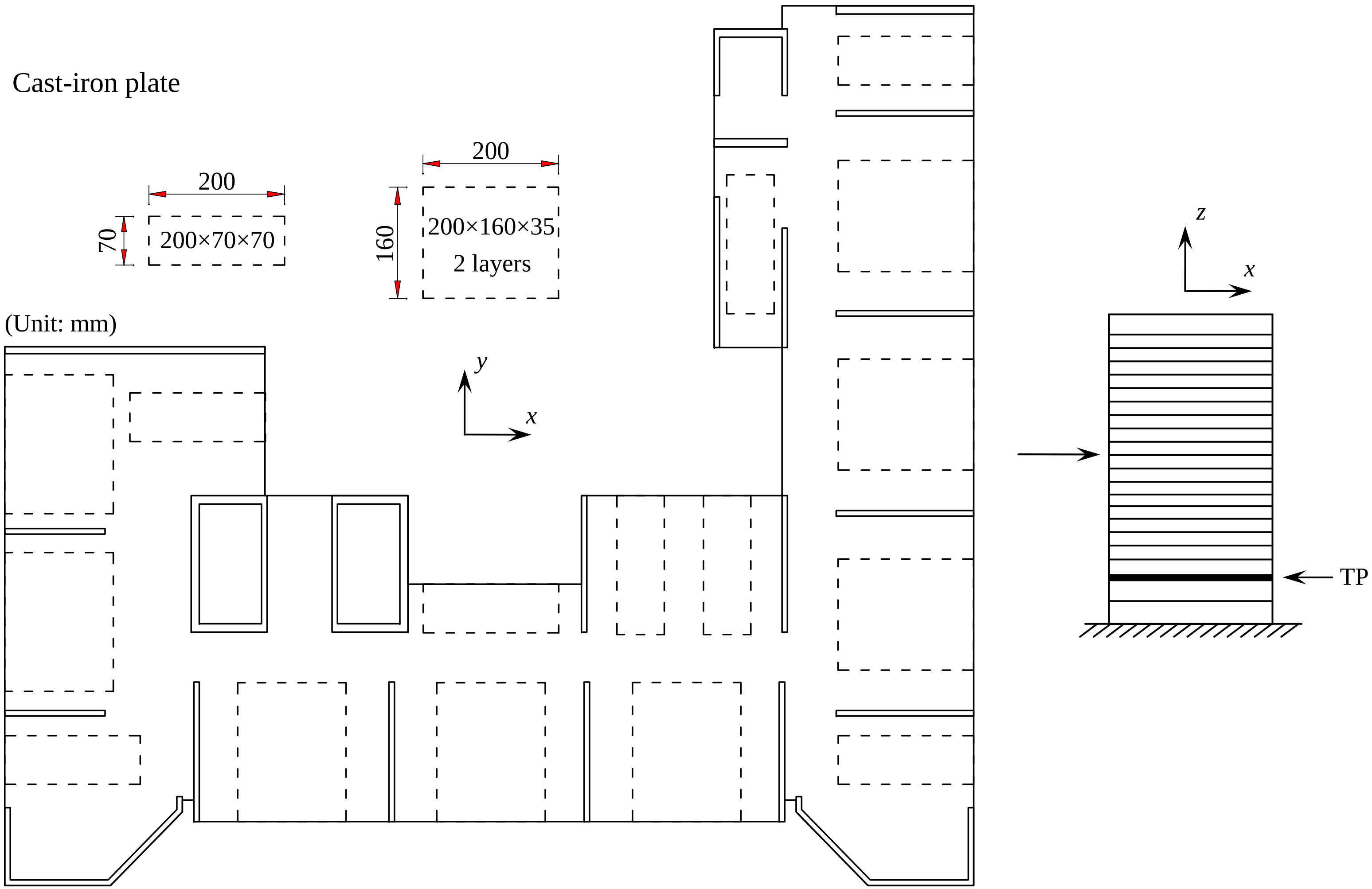

Figure 3.18 Plan view showing the locations of the additional mass (dashed rectangles) placed on a typical floor. The small sketch shows the elevation view of the model, where TP means the transfer plate.

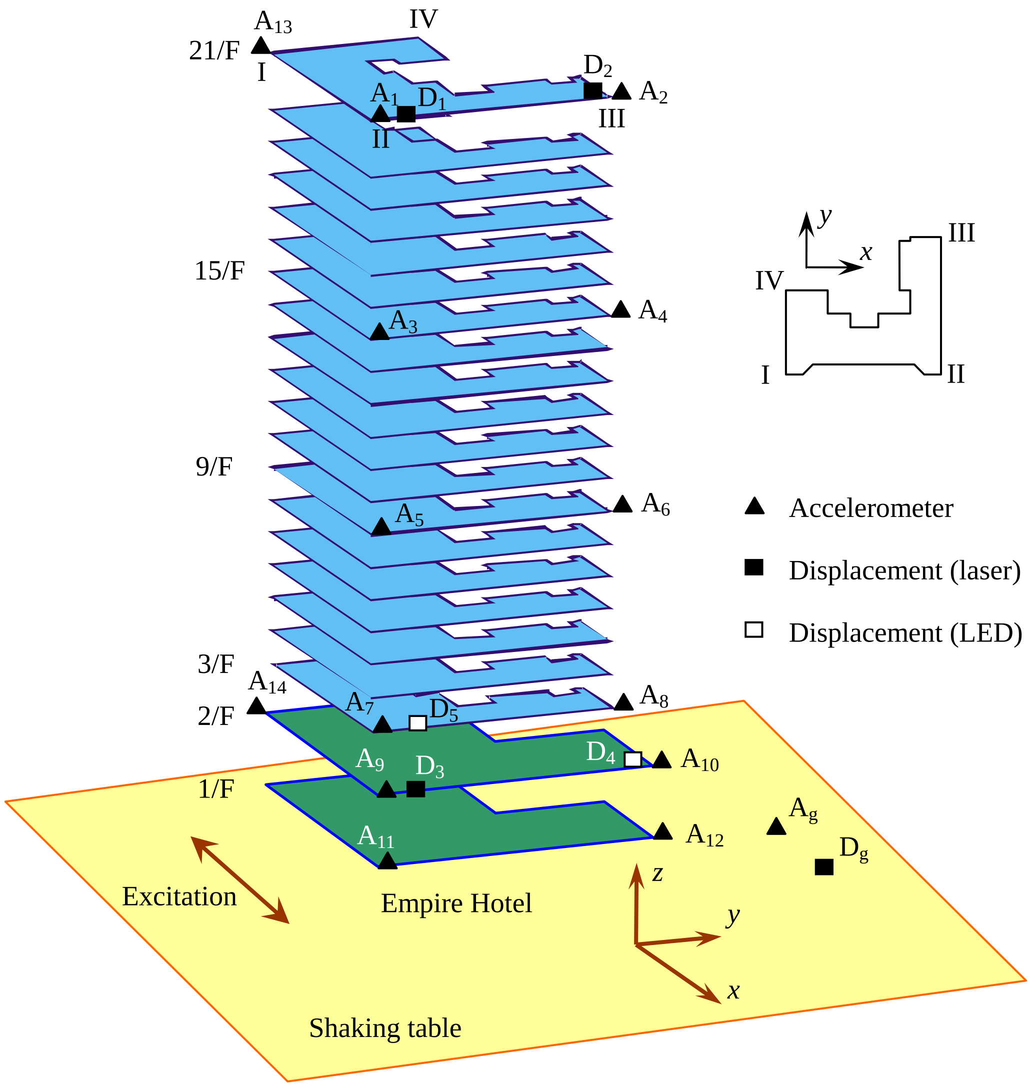

Figure 3.19 Sketch of the model and locations of accelerometers and displacement transducers, where “A” denotes accelerometers and “D” denotes displacement transducers.

Figure 3.20 Accelerometer, amplifiers and displacement transducers and their locations on the model.

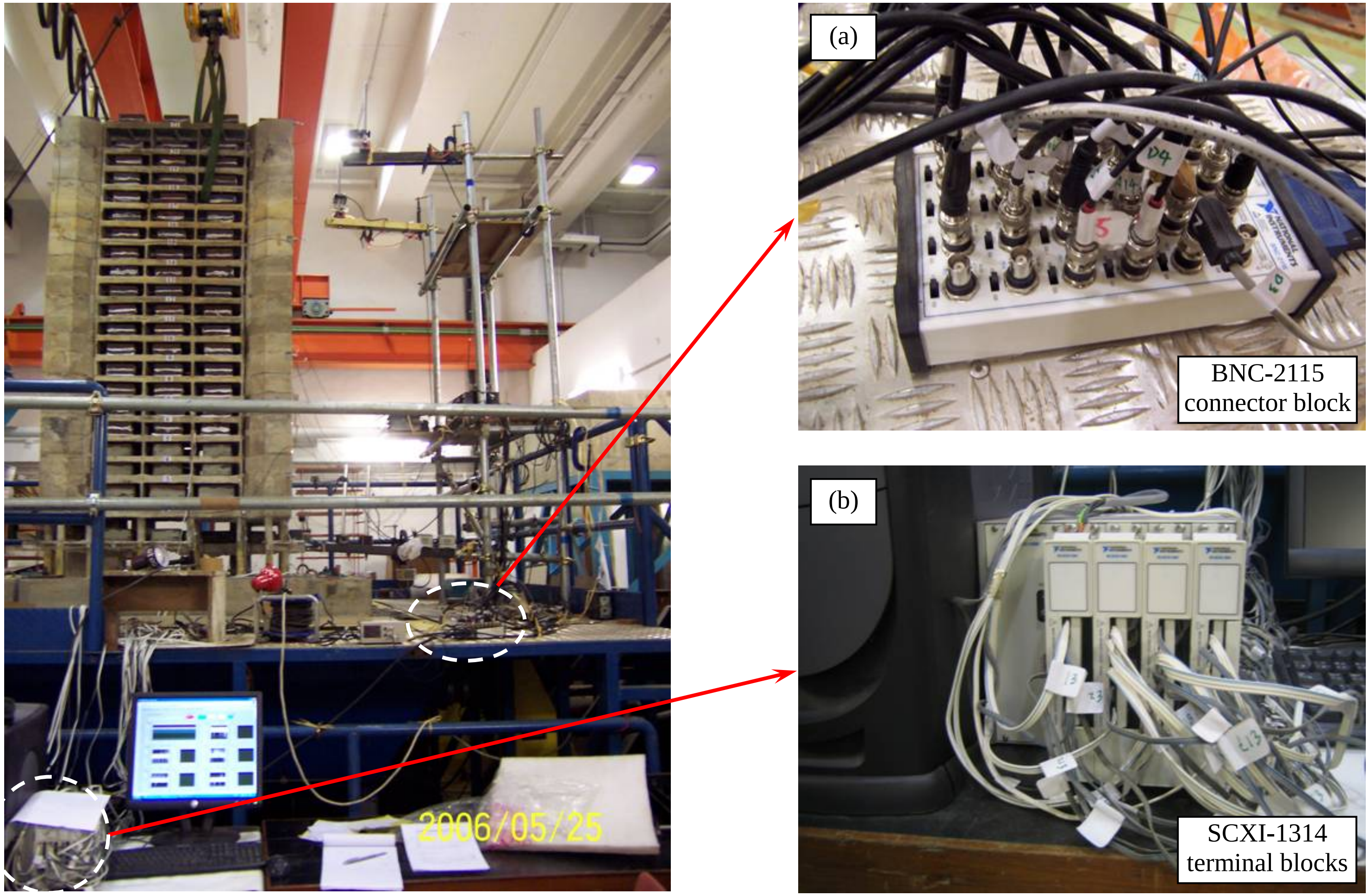

Figure 3.21 Experimental set-ups and data loggers of (a) accelerometers and displacement transducers; (b) strain gauges.

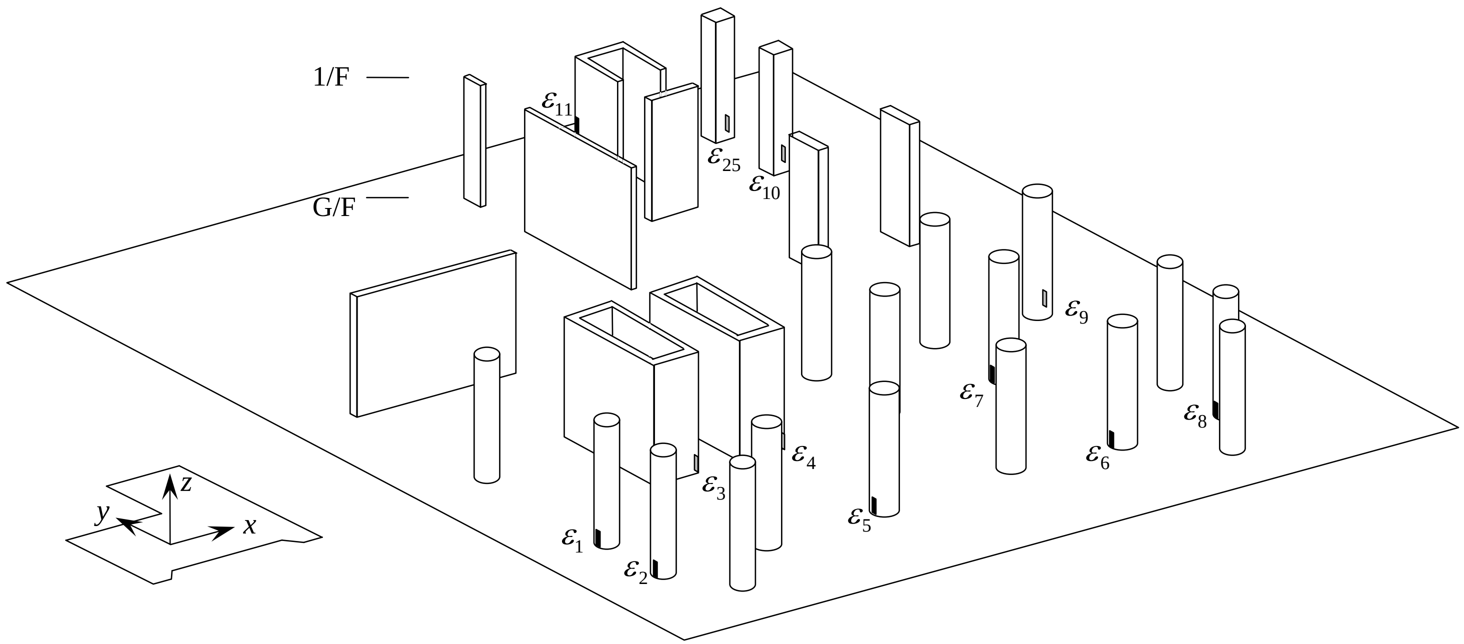

Figure 3.22 Sketch showing the distribution of strain gauges between G/F and 1/F. The strain gauges were denoted by the black rectangles attached on the surfaces of walls or columns. The gray filled rectangles denoted the strain gauges located on the opposite sides.

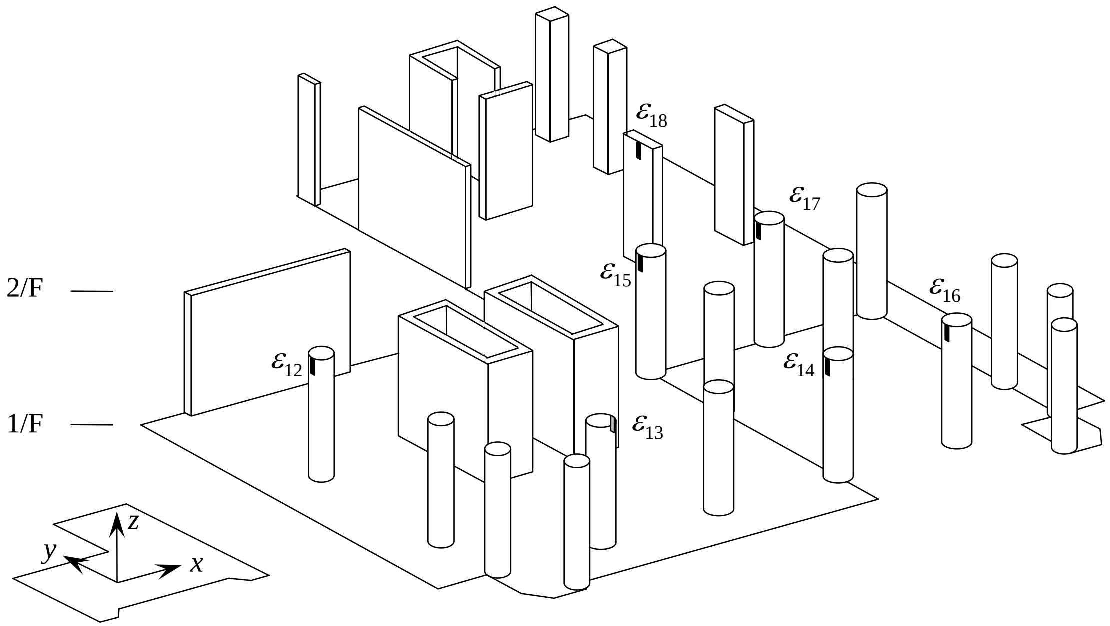

Figure 3.23 Sketch showing the distribution of strain gauges between 1/F and 2/F. The strain gauges were denoted by the black rectangles attached on the surfaces of walls or columns. The gray filled rectangles denoted the strain gauges located on the opposite sides.

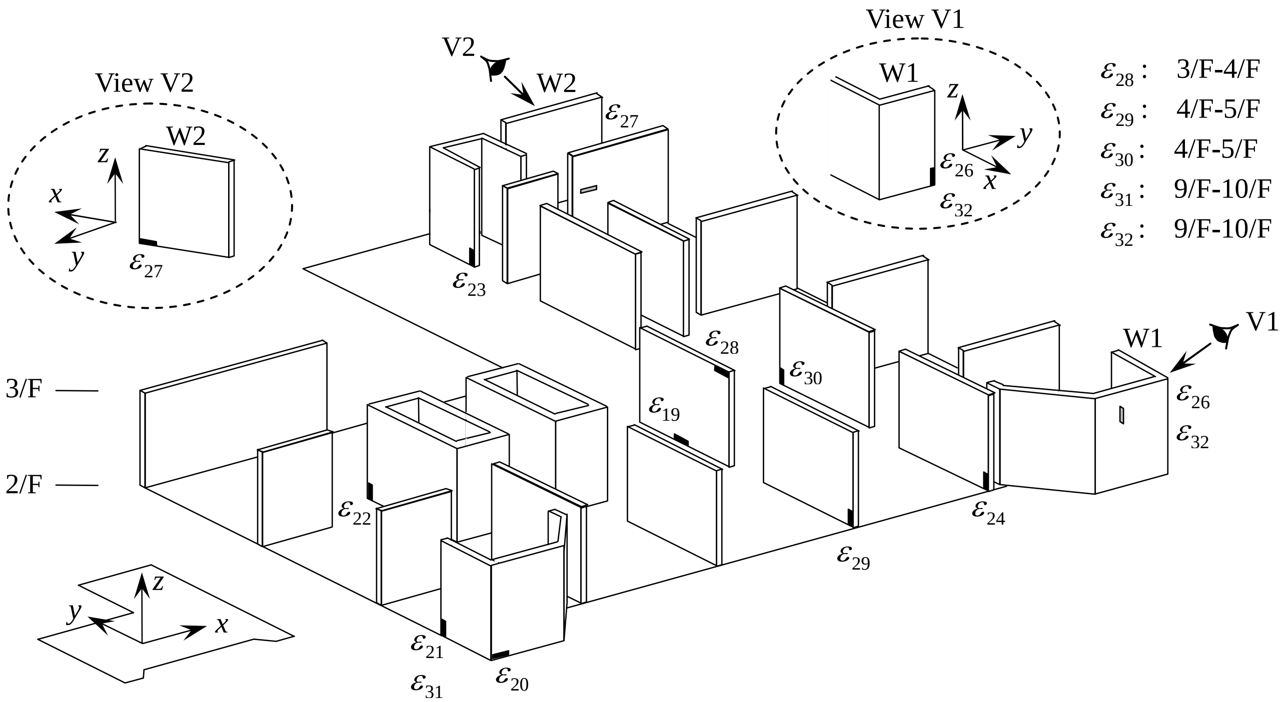

Figure 3.24 Sketch showing the distribution of strain gauges between 2/F and 3/F. The strain gauges were denoted by the black rectangles attached on the surfaces of walls or columns. The gray filled rectangles denoted the strain gauges located on the opposite sides. Those listed in the upper right-hand corner were five strain gauges located at the same locations of upper stories.

CHAPTER 4 SHAKING TABLE TESTS I: DAMAGE OBSERVATIONS

4.1 Input Earthquake Waves

4.1.1 Earthquake waves selection

In the present study, the time history records of five major earthquakes were selected as the inputs in our shaking table tests, including (i) El Centro earthquake, Imperial Valley, California, May 19, 1940; (ii) Kobe earthquake, Jan. 16, 1995; (iii) Northridge earthquake, Jan. 17, 1994; (iv) Loma Prieta earthquake, Oct. 18, 1989; and (v) Chi-Chi earthquake, Sept. 20, 1999. These five earthquake records have been widely used in other shaking table studies in the past. Their moment magnitudes (M_w) and peak ground accelerations (PGA) are compiled in Table 4.1. The digital wave data used here are obtained either from PEER (Pacific Earthquake Engineering Research Center) Strong Motion Database (http://peer.berkeley.edu/smcat/index.html) or from COSMOS (The Consortium of Organizations for Strong-Motion Observation Systems) Virtual Data Center (http://db.cosmos-eq.org/scripts/default.plx).

Before used as the inputs of the shaking table, the time histories of the five earthquake records should be compressed with respect to time according to a time ratio λ_t to fulfill the requirement of similarity law, as discussed in Section 3.2.1. The time ratio between the model and the prototype and is equal to $\lambda_t = \sqrt{\lambda_l} = 1/5$ for the present model (refer to Table 3.1). That is to say, the durations of these seismic records should be compressed by five times. The upper two diagrams in Figure 4.1 show the time history and Fourier spectrum of El Centro earthquake record after time compression. Note that in this figure the peak acceleration of the record has been scaled down to 0.1g for convenience of future manipulation. Similarly, the scaled time histories and Fourier spectra of the other four earthquakes after time compression are shown in Figures 4.2-4.4 respectively.

From the frequency corresponding to the maximum amplitude of Fourier spectrum shown in Figures 4.2-4.4, we can get the predominant frequency of each earthquake record. The results are listed in the fifth column of Table 4.1. Note that the predominant frequencies after time compression increased by five times compared to the original values,

The predominant frequencies of all of the earthquakes except Northridge earthquake are close to the first natural frequency of the model before damage (6.348 Hz, as will be shown in Section 4.2.1). Thus, relatively large responses and damages may be expected under the excitations of these earthquakes. And this is why they were selected as the inputs here. Another reason why Chi-Chi earthquake was selected is that Taiwan is not far away from Hong Kong in the southeast of China and Hong Kong may be affected by similar earthquakes occurred in her neighboring regions. Northridge earthquake wave has a relatively higher predominant frequency (14.486 Hz, see Table 4.1), and it was selected mainly for comparison purposes.

The peak accelerations of the five earthquake records were adjusted based on Chinese code for seismic design of buildings (GB 50011-2001, 2001), which adopts a three-level design philosophy as followings. When a building is subjected to frequently occurring earthquakes (with a return period of 50 years), it should not suffer or only slightly suffer damages, and remain elastic. When subjected to earthquakes of basic design intensity (with a return period of 475 years), the building may suffer damages, but they should be repairable. Under the attack of rare earthquakes (with a return period of about 2000 years), the building may suffer severe and irreparable damage, but collapse and loss of human lives should not occur.

According to Appendix A in Chinese code for seismic design of buildings (pp. 158, GB 50011-2001, 2001), Hong Kong has a basic design intensity of VII and a maximum ground shaking of 0.15g at rock site is expected at least once in every 475 years. In this study the peak accelerations of frequent and rare earthquakes were set as 0.05g and 0.30g respectively. Since there is no unique relation between seismic intensity and peak ground acceleration, in order to study seismic responses of the model under earthquakes of different peak accelerations, earthquakes of 0.10g and 0.20g PGA were also used as inputs.

Therefore, totally five levels of the five earthquakes mentioned previously were used as inputs in the shaking table tests in the present study, with increasing PGAs from 0.05g, 0.10g, 0.15g, 0.20g to 0.30g. For each PGA level, the five earthquakes were input one by one. Note that tests were not carried out for the 0.3g Northridge and Loma Prieta earthquakes (see Table 5.5), since after the shaking of 0.3g El Centro, Kobe and Chi-Chi earthquakes, the model suffered very severe damages and was not suitable for further tests for safety reasons (refer to Section 4.4.4 for details).

4.1.2 Earthquake waves after soil amplification

Soil layers beneath building structures may have significant effects on both intensity and response spectrum of earthquake. For example, on September 16, 1994, an earthquake of magnitude 7.3 occurred 470 km east of Hong Kong, which caused notable vibrations of buildings in reclamation areas in Hong Kong, such as Central, Wanchai, Tsim Sha Tsui, corresponding to an intensity of V; whereas for most of buildings founded on rock site, the shaking was much smaller and the intensity was probably only comparable to those of ambient vibrations caused by wind and traffic (Chau, 2000). This case suggests that the soil amplification effects may be extremely severe in Hong Kong where many buildings are built on reclamation sites. In fact, similar phenomena are well known, and were also observed in the 1985 Mexico City earthquakes (Chau, 2000).

The building studied here is situated at one of reclamation areas in Hong Kong, so the soil amplification effects are also taken into account in this study. The soil condition under the site of the selected building was collected from the Buildings Department of Hong Kong SAR Government. As shown by the soil profile in Figure 4.6, there are nine different layers of soil beneath the building with a total depth of 50 meters. The soil changes from fill materials at the top to marine deposits in the middle, and to completely decomposed granite at the bottom.

The computer program SHAKE91 (Schnabel et al., 1972) was used in this study to estimate the soil amplification effects, which considers the problem of vertical propagation of shear waves through a system of multiple horizontal soil layers from underlying bed rock. Each layer is assumed to be homogeneous, visco-elastic and extending to infinity in the horizontal direction. The vertical propagation of shear waves through such a system will cause only horizontal displacements $u(x,t)$, which satisfy the following wave equation:

$$\rho \frac{\partial^2 u}{\partial t^2} = G^* \frac{\partial^2 u}{\partial x^2} \tag{4.1}$$

where $G^* = G(1+i2\eta)$, G is the shear modulus, η is the damping ratio, ρ is the density of each soil layer, and $i=\sqrt{-1}$. A harmonic solution can be found and the unknown constants of the solution are determined through the compatibility boundary conditions at the interfaces between neighboring soil layers plus the free boundary condition at the ground surface. The detailed solution procedure can be referred to Schnabel et al. (1972) and Chau (2000).

In the above analysis, the dynamic shear modulus of soil, or equivalently the shear wave speed in soil, has to be known. Since there is no systematic field or experimental effort in establishing a data base for Hong Kong soils, two approximate formulae from other regions of the world were used to estimate the shear wave speeds of soil in this study. The first one is the empirical formula suggested by State Seismological Bureau (SSB) of China, which estimates the shear wave speed of a soil layer at a depth of *h* below the ground as (Chau, 2000):

$$v_s = ah^b \tag{4.2}$$

where h is measured in meter and is the depth between the ground surface and the centre line of the soil layer as shown in Figure 4.6. The parameters a and b are empirical constants depending on types of soils and their values can be determined according to Table 1 in Appendices. The second empirical formula is proposed by Ohta and Goto of Japan in 1978 (Chau, 2000):

$$v_s = 78.98kh^{0.312}, \qquad k = \begin{pmatrix} 1.000 - clay \\ 1.260 - \ fine\ sand \\ 1.282 - medium\ sand \\ 4.422 - coarse\ sand \\ 1.641 - sand\ and\ gravel \\ 1.255 - gravel \end{pmatrix} \tag{4.3}$$

where h is the depth of soil layer in meter and k is a constant depending on soil types.

For the whole multi-layered soil system, an equivalent shear wave speed V_{se} can be estimated as:

$$V_{se} = \frac{\sum_{i=1}^{N} H_i}{\sum_{i=1}^{N} H_i / V_{s,i}} \tag{4.4}$$

where H_i and $V_{s,i}$ are the thickness and shear wave speed of the i^{th} soil layer respectively, and N is the total number of soil layers above the bed rock.

Both of these two formulae were applied to estimate the shear wave speed of the soil profile given in Figure 4.6. The values of parameters a, b and k used as well as the resulting shear wave speeds of each soil layer obtained are summarized in Table 4.2. As shown in the table, the equivalent shear wave speeds estimated through the two approaches are close to each other (236.99 m/s from SSB's formula and 248.43 m/s from Ohta and Goto's formula). According to Chinese code for seismic design of buildings

(GB 50011-2001, 2001), the current soil profile belongs to Soil Type II (soil of 3-50 m thick with an equivalent shear wave speed between 140 and 250 m/s). In this study, the shear wave speeds estimated from SSB's formula were used, since Hong Kong is a part of China and it is assumed that the formula proposed by SSB of China is more appropriate for Hong Kong.

With the shear wave speeds estimated in Table 4.2, the five earthquake records described in Section 4.1.1 can be used as input to calculate the soil site response at the ground level using SHAKE91. The resulting time histories and their Fourier spectra are shown in the lower two diagrams in Figures 4.1-4.5. Again the peak accelerations of these time histories have been scaled to 0.10g. Compared to the rock site time histories and Fourier spectra (the upper two diagrams in Figures 4.1-4.5), the time durations of these soil site responses increase whereas the predominant frequencies reduce significantly.

For simplicity, earthquake records before and after soil amplifications sometimes are referred as earthquakes at rock and soil sites respectively in this thesis. The predominant frequencies and soil amplification factors of PGA of the five earthquakes after soil amplification are summarized in the sixth and seventh columns of Table 4.1 respectively. The soil amplification factors range from 1.016 for El Centro earthquake to 1.368 for Kobe earthquake.

The soil amplification factors obtained here are comparable to results from other studies at similar regions in Hong Kong. For example, Chau (2000) analyzed the soil amplification at twelve locations in Hong Kong, among them the Central and

Causeway Bay site are close to the current site. The soil profile at Central is of 33.1 m depth and has an equivalent shear wave speed of 247.48 m/s. The resulting soil amplification factor for rare (with a return period of 2000 years) near and far field earthquakes are 1.47 and 1.85 respectively. The soil profile at Causeway Bay is of 36.75 m thick with an equivalent shear wave speed of 270.72 m/s, and the soil amplification factor for rare near and far field earthquakes are 1.34 and 1.58 respectively. The soil amplification factors obtained in this study are slightly smaller and this may be due to the firmer soil beneath the current site. As shown in the soil profile in Figure 4.6, there is only one layer of sandy clay of 2 m thick within the whole soil profile and all of the other layers consist of either sand or gravel.

To summarize, our shaking table tests were conducted in the following schedule. Totally 28 sets of tests were carried out, with the input peak accelerations increasing from 0.05g, 0.10g, 0.15g, 0.20g to 0.30g (refer to Table 5.5). For each set of tests, the time histories of one earthquake before and after soil amplifications were input in sequence. After the input of each set of tests, a modal test was performed to monitor the change of natural frequencies due to potential damages (refer to Section 4.2.1).

Note that in Table 5.5 the 0.3g PGA El Centro and Kobe earthquakes at both rock and soil sites were all input twice (i.e. test sets No. 21, 22, 26 and 27). This is because during the first time inputs of these earthquakes, strain overflow occurred. After enlarging the amplification factors of strain gauges, these earthquake inputs were repeated. The test sets No. 23-25 were conducted for recalibration of strain signals.

4.2 Dynamic Characteristics of the Model

4.2.1 Natural frequencies

Measurements of structural characteristics during experiments provide a unique way to monitor structural damages (Williams and Sexsmith, 1995; Ndambi et al., 2000). During our shaking table tests, modal testing was used after each shaking table experiment to evaluate the potential damage in the model.

Excitation signals used to determine the modal properties can be input as periodic, random and transient (Ewins, 2000). Among them, sine wave sweep testing, white noise testing and hammer blow testing are three widely used methods in practice (Ndambi et al., 2000; Reynolds and Pavic, 2000). Relatively longer time is needed for the former two test methods (Ewins, 2000). In addition, resonant responses during these tests may cause undesirable damage to the model. Compared to the first two methods, the hammer blow testing is relatively simple and quick, and damages are less likely to be induced (Ewins, 2000; Reynolds and Pavic, 2000). Therefore, the hammer blow testing was adopted for modal tests in this study.

As shown in Figure 4.7(a), hammer blow tests were applied at three different points (*a*, *b* and *c*) at the roof of the model to measure both the translational natural frequencies in the *x*- and *y*- directions and the torsional frequency. The points *a* and *b* were approximately aligned to the center of mass of the floor slab, and the point *c* was selected in order to induce larger torsional vibrations. After each pair of earthquake shakings (including inputs of one earthquake on rock and soil sites), three hammer blow tests were applied at points *a*, *b* and *c*.

Figure 4.7(b) shows an example photograph of hammer blow at point *a* along the *x* direction. To increase the frequency resolution, responses were recorded for about 60 seconds when hammer blows were applied every 2-3 seconds. Data was collected at a sampling rate of 500 Hz and the frequency resolution was about 0.015 Hz.

The three accelerometers installed at the roof [refer to Figure 3.19 and 4.7(a)] provide data for modal analysis. Among them, the accelerometers A_1 and A_2 are in the shaking direction whereas A_{13} is installed perpendicular to the shaking direction. Similar to the method adopted by Li et al. (2006), the Fourier spectra of recorded data are utilized to determine the first six natural frequencies of the model. More specifically, the first peak in the Fourier spectrum of A_1 [Figure 4.8(a)] when hammer impacts at point *a* was deemed as the first natural frequency in the *x* direction (f_1). Similarly, the first peak in the spectrum of A_{13} [Figure 4.8(b)] when hammer impacts at point *b* was taken as the second natural frequency in the *y* direction (f_2). The first peak in the spectrum of A_1−A_2 [Figure 4.8(c)] when hammer impacts at point *c* was taken as the third natural frequency which has vibrations in the θ direction (i.e. torsional frequency, f_3). Note that here the spectrum of A_1 minus A_2 instead of a single acceleration was used in order to detect torsional vibrations. The second peaks in Figures 4.8(a-c) correspond to the 4^{th}-6^{th} mode frequencies of the model (f_4 - f_6) which are all between 20 and 30 Hz.

4.2.2 Damping ratios

Damping ratio was also measured for the model in this study. But since the basic energy-loss mechanisms in most systems are seldom fully understood and structural damping is very sensitive and difficult to be measured (Clough and Penzien, 1993; Ndambi et al., 2000), only the damping ratio of the first mode in the *x* direction were estimated in the present study. More specifically, free vibration test was performed by first pushing the model in the *x* direction by hand and then releasing it. The damping ratio can be estimated from the logarithmic decrement of the free vibrations (Clough and Penzien, 1993).

Figure 4.9 shows two examples of free vibration tests before and after all the shaking tests. From this figure, it is seen that the free decay vibration before damage [Figure 4.9(a)] is much smoother and more regular than the curve after repeated shaking experiments [Figure 4.9(b)]. This may be due to the fact that the model had suffered severe damages and nonlinear behaviors become more dominant.

Exponential curves were fitted to the free decay vibrations as shown in Figure 4.9. Assume the curve has a equation of $y = ae^{-bt}$, where *y* and *t* are the displacement and time, and *a* and *b* are two constants, and we have (Clough and Penzien, 1993)

$$\xi\omega_D = b \tag{4.5}$$

where $\omega_D \equiv \omega_1\sqrt{1-\xi^2}$ is nearly equal to the first circular frequency ω_1 of the structure for low damping values ($\xi < 20\%$), which are typical for most practical structures (Clough and Penzien, 1993). Thus the damping ratio can be estimated as:

$$\xi \approx \frac{b}{\omega_1} = \frac{b}{2\pi f_1} \tag{4.6}$$

where f_1 is the first natural frequency of the model.

As shown in Figure 4.9, the damping ratios before and after all the shaking tests are estimated to be 1.63% and 4.91% respectively. This was consistent with the fact that damping is expected to increase with damages (Williams and Sexsmith, 1995). Similar results have also been observed in previous shaking table tests, such as that by Lee and Woo (2002).

4.3 Maximum Dynamic Responses

4.3.1 Actual inputs generated by the shaking table

As described in Section 4.1, the target input waves include five earthquake records of five different levels of peak accelerations (i.e. 0.05g, 0.1g, 0.15g, 0.2g and 0.3g). However, the response of the model (of about 7.5 tons) can interfere with target motion of the shaking table, so that the excitation generated (i.e. the actual input to the model) may not be exactly the same as the target input, especially when the input PGA was small. Therefore, an accelerometer has been installed on the shaking table in the shaking direction to record the actual shaking generated (refer to Figure 3.19).

For example, the first three diagrams in Figure 4.10 shows the Fourier spectra of actual inputs recorded on the shaking table for Chi-Chi earthquake at rock site. The recorded peak accelerations were actually 0.035g, 0.1g and 0.22g instead of the target PGAs of 0.05g, 0.15g and 0.3g. One probable reason may be that the feedback loop for short-duration-shaking with high frequency (i.e. rapid reversal of shaking direction in short time) is not easy to control.

In the frequency domain, the Fourier spectrum of the 0.05g PGA input shown in Figure 4.10(a) is completely different from the target spectrum [Figure 4.10(d)]. For the 0.05g PGA input, high-frequency noises appear to be dominant. But as the input PGA increased, the control of the shaking table becomes better and the high frequency noises become less dominant. For example, the Fourier spectrum of the 0.3g PGA input shown in Figure 4.10(c) resembles the target spectrum quite well.

Similarly, Figure 4.11 shows the actual Fourier spectra as well as the target one for 0.05g, 0.15g and 0.3g Chi-Chi earthquake after soil amplification. It can be seen the Fourier spectra of achieved signals are much close to the target spectrum. And the actual recorded peak accelerations were 0.067g, 0.16g and 0.32g respectively, equivalent to 134%, 107% and 107% of the target ones. This result reveals that the generated signals by the shaking table for earthquakes after soil amplification were closer to the target signals than those without soil amplification. Again it may be due to the fact that higher frequency contents were filtered out by the soil layers (refer to Figures 4.1-4.5).

In the following analyses, all of the tests of 0.05g target PGA will not be included, as the generated signals were distorted significantly from the target inputs.

In fact, the 0.05g PGA inputs do not induce any measurable or observable damages to the model. For example, a typical overall drift ratio of the model is about 1/2311. The model, therefore, can be regarded as elastic and undamaged.

4.3.2 Maximum strains

The maximum values of the 32 strain gauge records are summarized in Table 5.5 for various inputs. The maximum strains always occurred at columns (ε_2 and ε_{25}) or walls (ε_{11}) at the first story (see Figure 3.22). Numerically the maximum strains recorded for 0.1g, 0.15g, 0.2g and 0.3g PGA inputs are 452, 1147, 2743 and 5152 $\mu\varepsilon$ respectively (note that $\mu\varepsilon$ means 10^{-6} strain). As an example of typical test record, the time histories of all the 32 strain gauges as well as all the displacements and accelerations recorded during the soil site input of 0.2g Kobe earthquake (see the test set No. 17 in Table 5.5) are shown in Figures A-1 to A-7 in the Appendices. In this section, the maximum responses of the model are investigated.

To compare the strain levels caused by different earthquakes, the maximum strains listed in Table 5.5 are plotted with the actual input PGAs in Figure 4.12. Each curve in the figure represents an earthquake, and rock and soil site records are plotted separately in Figures 4.12(a) and (b). It is clear that the maximum strain increases with the input PGA, but the increase rate is not a constant. More specifically, the slopes of strain increment of the curves of El Centro, Kobe and Chi-Chi earthquakes at rock site decrease for PGA>0.15g [Figure 4.12(a)]. This is due to the fact that the natural frequency of the model decreases significantly after the 0.2g Chi-Chi earthquake experiment (see Table 5.2) and becomes farther from the predominant frequencies of these three input earthquakes at rock site (refer to the Fourier spectra shown in Figures 4.1, 4.2 and 4.5).

On the contrary, the slopes of strain increment for El Centro, Kobe and Chi-Chi earthquakes after soil amplification increase with the input PGA, as shown in Figure 4.12(b). This is also due to the reduction of natural frequency of the model, which becomes closer to the predominant frequencies of soil site input of these three earthquakes (refer to Figures 4.1, 4.2 and 4.5).

For Northridge and Loma Prieta earthquakes, since the natural frequency of the model did not change significantly after the 0.2g PGA earthquake inputs and experiments for 0.3g PGA inputs were not conducted (see Table 5.5), the rate of strain increment of these two earthquakes on either rock or soil site remains almost constant [Figures 4.12(a) and (b)].

The predominant frequency of both soil and rock site shaking of Northridge earthquake is far away from the first natural frequency of the model, and thus, as shown in Figure 4.12, the strain value is relatively small. However, Loma Prieta earthquake after soil amplification causes the largest strains among all the earthquakes of similar PGAs [Figure 4.12(b)] because of the rich spectrum contents around the natural frequency of the model (see Figure 4.3).

4.3.3 Maximum accelerations at the roof

As described in Section 3.5.1, fourteen accelerometers were installed at different stories of the model to measure the acceleration responses. The test results show that the roof experiences the maximum accelerations for all earthquake inputs. Figure 4.13 shows that plots of maximum roof acceleration are similar to those for maximum strain shown in Figure 4.12. Therefore, there is a good correlation between the strain and acceleration data.

An acceleration amplification factor β_A is introduced to quantify the response of the model relative to the ground motion as:

$$\beta_A = \left| \frac{A_r}{A_g} \right| \tag{4.7}$$

where A_r and A_g are the peak values of the roof acceleration and the input acceleration respectively. This amplification factor for each experiment is summarized in Table 5.5 and is also plotted in Figure 4.14.

The amplification factors of El Centro, Kobe and Chi-Chi earthquakes decrease significantly for PGA>0.15g for rock site inputs [Figure 4.14(a)], but increase with the input PGA for soil site inputs [Figure 4.14(b)]. Similar to plots of maximum strain shown in Figure 4.12, this is probably because of the deterioration of the natural frequency (i.e. yielding) of the model, which becomes farther from the predominant frequencies of rock site inputs but closer to the frequencies of soil site inputs of these three earthquakes.

4.3.4 Maximum rotations at the roof

To measure rotation, two displacement transducers were installed at the 2/F (the transfer plate level) and 21/F (the roof level) respectively (see Figure 3.19). If we assume the floor slab is rigid within its plan, the rotation angle of the floor slab can be easily computed as the displacement difference between the two transducers divided by the distance between them (equal to 1145 mm).

We find that the rotation at the roof level can easily be identified from data recorded by the two laser transducers, whereas the rotation at the transfer plate level can hardly be recognized from data recorded by one laser and one LED transducers installed at 2/F. This may be due to two reasons. First, the torsional response at 2/F is much smaller than that at the roof, which makes it harder to be measured; and second, the accuracy of the LED transducer installed at 2/F is lower than that of the laser transducer as described in Section 3.5.1. Thus, only the recognized rotations at the roof level are discussed below.

The maximum rotations (θ) at the roof for various earthquake inputs are summarized in Table 5.5 and plotted in Figure 4.15. From the table, the maximum rotation angle occurred during all the tests is 0.1°, which corresponds to a maximum difference of about 2 mm between displacements at the points A_1 and A_2 in Figure 4.7(a). Figure 4.15 shows that the roof rotation angle increases with the input PGA. This is because the reduction of the torsional natural frequency of the model (f_3 in Table 5.2) makes it closer to the predominant frequencies of input earthquakes. Again, Northridge earthquake at rock site induces the minimum rotation, because of the difference between its predominant frequency and that of the model.

To summarize, the maximum responses (including strain, acceleration and rotation) of the model increase as the input PGA increases, but the rate of increase is not linear. The nonlinear rate of increases reflects the amount of damage the model suffered. The responses of the model are clearly controlled by the proximity of the natural frequency of the model to that of the input earthquake.

As shown by Wen et al. (2002), site effect can be detrimental to seismic vulnerability of high-rise buildings. Our experimental results also show that the model responses differ significantly for shaking without and with soil amplification. In general, soil both amplifies the magnitude and changes the frequency content of an earthquake shaking. For the present soil condition, the largest amplification is observed for the Loma Prieta earthquake input. Similar amplifications have also been observed in past earthquakes, such as the 1906 San Francisco, the 1985 Mexico City, the 1967 Caracas, the 1976 Tangshan, the 1989 Loma Prieta, the 1994 Northridge and the 1995 Kobe earthquakes (Wen et al., 2002). A local example in Hong Kong is the earthquake occurred on Sept. 16, 1994 in the South China Sea, which caused notable vibrations to buildings in reclamation areas of Hong Kong, but buildings founded on rock stratum suffered almost no vibrations (Chau, 2000).

In this section, it has been shown that the responses of the model are influenced by its damaged state, since damage may change the modal characteristics of the model. In the next section, the damages of the model will be assessed through visual inspections. Quantitative damage analysis using seismic damage indices will be given in the next chapter.

4.4 Crack Patterns

After the model is subjected to the input of each earthquake shaking (including both rock and soil sites), visual inspection was conducted to identify observable cracks on surfaces of structural elements. Lamps and magnifying glasses were used to identify those fine cracks. Note that only cracks on external surfaces of structural elements can be observed in the tests, because most of internal spaces in the model were filled with cast-iron plates (the additional mass) [see Figure 3.15(b)].

In our tests, no visible crack was observed on the external surface of the model before the input of the second time 0.3g El Centro earthquake. However, modal tests did reveal that the first natural frequency of the model had already dropped to 74% of its original value before the input of that earthquake (refer to Table 5.2). Although no visible crack was observed, stiffness degradation of the model is evident. The value of recorded strain also provides additional evidence of cracking in micro-concrete.

4.4.1 Internal cracking interpreted from strain signals

The strain gauges installed on surfaces of structural elements experienced tension and compression during vibrations, and abnormal change of strain signals can be used as an indicator of local damage. For example, abnormal small tension was observed at some locations during the tests. Figure 4.16 shows the variations of the strain gauge ε_{13} during the inputs of 0.05g, 0.2g and 0.3g PGA El Centro earthquake at soil site. In the figure, positive strains correspond to tension and negative strains correspond to compression. As sketched in Figure 4.16, ε_{13} was located at the upper end of a column situated between 1/F and 2/F (i.e. beneath the transfer plate).

For PGA=0.05g, the strain gauge experienced both tension and compression [Figure 4.16(a)]. However, compared to the compression signals, much smaller tension was observed during the 0.2g and 0.3g inputs [Figures 4.16(b) and (c)]. This implies that cracks might have already appeared above the column or the local reinforcements have begun to loss the force transfer, which reduced the tension of the strain gauge drastically but had little influence on the compression. These damages may either be too small to be visible or exist in the interior of the model. In fact, cracks as sketched in the lower photo of Figure 4.16 did occur at the transfer plate above the column after the excitation of 0.3g Kobe earthquake at soil site.

This phenomenon of abnormal small tension was also observed for strain gauges at other locations, including ε_1 at a column between G/F and 1/F and ε_{22} at a core wall just above the transfer plate (see Figures 3.22 and 3.24). All these phenomena suggest the existence of local damages.

Out-of-phase vibrations between two neighboring strain gauges also suggest local cracking. For example, ε_{21} and ε_{22} are two neighboring strain gauges as shown in Figures 4.17 and 3.24, and their vibrations during the inputs of 0.05g, 0.2g and 0.3g PGA El Centro earthquake after soil amplification are plotted in Figure 4.17.

For 0.05g and 0.2g PGA inputs [Figures 4.17(a) and (b)], the two strain gauges are in phase (i.e. compressive and tensile simultaneously). This is expected since both strain gauges are situated on one side to the center of stiffness of the model and the forces they suffered should be always in the same direction due to the constraint of floor slabs. However, during the input of 0.3g El Centro earthquake, the variations of ε_{21} and ε_{22} become out of phase as shown in Figure 4.17(c). That is, one strain gauge was in tension, while the other was in compression. This may imply the existence of cracks between these two strain gauges. Actually, the strain gauge ε_{21} did experience a permanent deformation of about 250 $\mu\varepsilon$ during this test [Figure 4.17(c)].

Figure 4.18 shows that the strain gauges on a same core wall may also be out of phase. As shown, ε_3 and ε_{22} are two strain gauges located on the opposite sides of one core wall at different heights, with ε_3 situated just above the ground level and ε_{22} above the transfer plate. If the floor slabs were infinitely rigid, the two sides of the core wall should suffer tension or compression at the same time (i.e. the two strain gauges should be in phase), since the entire core wall situated on one side to the center of stiffness of the structure. However, the recorded data reveal that they were out of phase for all of the tests conducted. Figures 4.18(a) and (b) show two examples of the out-of-phase variations of the two strain gauges during the 0.05g and 0.3g PGA Chi-Chi earthquake inputs. This suggests that the core wall has undergone local bending and the constraint from floor slabs was not strong enough. In other words, the rigid slab assumption appears to be invalid for the present model. Stress outputs in our SAP2000 analysis show the two strain gauges ε_3 and ε_{22} are in phase at a same time, i.e. they suffered tension and compression at the same time. In the FEM analysis, rigid diaphragm has been assumed.

Therefore, rigid slab assumption, which is commonly adopted in FEM program, may be questionable in the present case. Actually as Garcia and Sozen (2004) discussed, the infinitely rigid diaphragm approach may be reasonable only for those reinforced concrete structures with floor plans approximately square or rectangular of long to short side ratio less than 3 and with no large openings. For the present L-shaped model, it seems that the rigid slab assumption can not accurately describe, at least, part of its actual behaviors.

The small value tensile ε_{22} shown in Figure 4.18(b) again suggests that horizontal crack might have occurred above the strain gauge. As sketched in the figure, horizontal cracks were actually found on the core wall and tension from the upper structure can not be transferred to the lower part. The details of these cracks will be described in the following sections.

4.4.2 Cracks caused by 0.3g El Centro earthquake

Although both modal properties and strain signals suggest the model suffered damage, visible cracks were actually observed for the first time after the input of 0.30g PGA El Centro earthquake at soil site. In fact, similar problem about visual inspection of damage has also been found in shaking table tests by others. For example, Lee and Woo (2002) tested a 1:5 scale model of a 3-story non-seismic-designed reinforced concrete frame. The model did not show severe damage even after the test of 0.4g PGA input, although the increases of natural period and damping of the model were apparent (Lee and Woo, 2002). Skjaerbaek et al. (1998) conducted shaking table tests on three 1:5 scale models of a 6-story reinforced concrete frame. For one of the models, the visual inspection only indicated light damage even though the structure was considered to be in a moderate damage state through other damage estimation methods. The authors argued that this shows the limited reliability of visual inspection methods even under laboratory conditions (Skjaerbaek et al., 1998).

As shown in Figures 4.19-4.20, cracks induced by the 0.3g El Centro earthquake at soil site (denoted by "E0.3g" in the photographs) mainly concentrate at the two diagonal corners (i.e. Corners I and III) of the transfer plate. Most of the cracks are close to the upper edge of the transfer plate and were apparently caused by the pull from the upper structure. In addition to these horizontal cracks, two fine vertical cracks were also found near Corner I [Figure 4.21(b)].

The other two corners of the transfer plate suffered much less damage. The crack found at Corner II as shown in Figure 4.21(a) is finer than those at Corners I and III, and no crack was observed at Corner IV. This diagonal distribution of cracks on the transfer plate is clearly related to the asymmetric plan of the model, and more even distribution of damage would be expected if the model was symmetric. In fact, a diagonal rocking of the upper model above transfer level was observed during our tests, which is responsible for the severe cracking at Corners I and III and will be discussed in details later.

Besides the cracks on the transfer plate, two fine horizontal cracks were also found at the 10/F and 11/F as showed in Figures 4.22(a) and (b). This kind of crack may be induced by higher mode vibrations of the model. Figure 4.23(a) sketches the second mode deformation shape of the model observed for experiments with PGA greater than 0.2g and the location of 10/F. Note that the two stories below the transfer plate experience much smaller vibrations than the upper stories [see Figure 4.23(a)]. This phenomenon has also been found in the FEM analyses discussed in Section 2.3.3.2 (refer to Figure 2.7).

4.4.3 Cracks caused by 0.3g Kobe earthquake

Figure 4.24 shows the cracks caused by the 0.3g Kobe earthquake (represented by “K0.3g” in the photographs) can be divided into two categories. The first category of crack is the development of existing cracks, that is, lengthening and widening of the cracks caused by the previous 0.3g El Centro earthquake. As shown in Figure 4.24(a), the cracks at Corner I of the transfer plate became longer and wider and spalling of concrete was also found near the corner. Figures 4.25(a) and (b) shows the lengths of cracks at Corner III also increase and the cracks on the two sides become connected throughout the corner.

The second category of crack involves several newly developed cracks. Figure

4.24(b) shows a new horizontal crack occurred at Corner II. New cracks were also found at the ends of lintel beams connecting the two core walls at the 10/F and 11/F, as shown in Figure 4.26. From the two enlarged photographs in the figure, fine vertical cracks occurred at the ends of beams and almost cut through the beam depth.

This kind of crack on the lintel beams between core walls has also been reported in the shaking table test conducted by Lam et al. (2002). Actually, the two core walls in our model are more like a coupled shear wall system in the direction of shaking. As sketched in Figure 4.23(b), when the two walls deflect under earthquake excitation, the ends of the lintel beams are forced to rotate and deform vertically. This bending in double curvature of these beams helps to resist the free bending of the walls (Smith and Coull, 1991). This kind of bending of beams was observed in our tests when the input PGA was larger than 0.3g. The resulting shear forces, which reach the largest value at the ends of beams, induced the cracks on the lintel beams shown in Figure 4.26. A large number of similar cracks were found during the shaking of the following 0.3g Chi-Chi earthquake which will be summarized next

4.4.4 Cracks caused by 0.3g Chi-Chi earthquake

The 0.3g Chi-Chi earthquake at soil site is the last experiment being conducted (see Table 5.5), which caused the severest damages to the model. In this test, Corner I of the transfer plate was torn open by the uplift of the upper structure above the transfer plate and the whole process was captured by a video camera. From the captured video, the opening reached a maximum width of about 2.9 mm as shown in Figure 4.27(a). After the uplift, the upper structure crashed down [Figure 4.27(b)] producing a thundering sound and caused concrete spalling and severe damages to the transfer plate as well as walls above. The rocking motion of the upper structure is apparent. Figure 4.28 shows the photographs and sketches of three severe damaged walls, two of them situated above the transfer plate and one situated between 3/F and 4/F. In these walls, concrete spalled and reinforcements were exposed and buckled. Interestingly, the cracks in these three walls were almost aligned on a tilted straight line at an angle of about 18° with the horizontal direction as shown in Figure 4.28.

Besides the severe damage at Corner I, cracks developed almost throughout the two lateral sides (perpendicular to the direction of shaking) of the transfer plate as shown in Figure 4.29. Horizontal cracks spread close to the upper edge of both the A-A′ and B-B′ sides, and vertical and diagonal cracks also appeared on the B-B′ side. In the tests, the transfer plate suffered large tension due to the rocking of the upper stories. The cracks on the transfer plate may be due to its inadequate detailing for seismic load. Transfer systems normally introduce abrupt changes of stiffness to structures, which is not recommended from the aspect of seismic design. But traditionally seismic load is not considered in the design of buildings in Hong Kong.

As a whole, the story just above the transfer plate suffered the severest damages. Besides the two broken walls shown in Figure 4.28, the core walls at this story were also damaged. As sketched in Figure 4.30, cracks occurred almost throughout the two rectangular core walls (C1 and C2) and exposed reinforcements were also observed.

The severe damages of these core walls may be related to the two broken walls at this story (as shown in Figure 4.28) as well as the damaged transfer plate on this side of the model (Figure 4.29). All of these made the two core walls suffered very large tensile and compressive forces from the upper structure due to rocking motions. The damage of the other core wall C3 was also shown in Figure 4.30. Different from the cracks on C1 and C2, here cracks only concentrated at one corner. All of the cracks at the story above the transfer plate are summarized by the sketches given in Figure 4.31. Three horizontal cracks (①-③) were found on the floor slab of 2/F, and these cracks may be caused by the pull from the upper walls.

Summarizing the above observations, most of the severe cracks concentrated at the two diagonal corners (i.e. Corners I and III) of the model. This can be explained by a diagonal rocking of the upper structure above the transfer plate. In fact, this asymmetric rocking can be seen visually from a distance in our tests and is sketched in Figure 4.32. Probably due to the asymmetric layout of the present model, rocking developed at an angle to the shaking direction, resulting in the uneven distribution of cracks. This asymmetric failure pattern and rocking are observed for the first time in this study. To the best of our knowledge, this rocking mechanism has never been reported in other shaking table tests as well as in field investigations after earthquake.

Besides the cracks on walls, a large amount of cracks were also observed at the ends of lintel beams at the upper stories. Figure 4.33 displays two different patterns of these cracks. The first kind is a single crack cutting through the beam depth, such as those observed at the 12/F, and the second kind involves several separate cracks which are not connected with each other, such as those observed at the 11/F. The cause of these cracks on the lintel beams is the same as that discussed in Section 4.4.3, but the amount of cracks caused by the 0.3g Chi-Chi earthquake was much more than that by the 0.3g Kobe earthquake. As shown by sketches in Figures 4.34-4.37, this kind of cracks were found at beams almost from 3/F to 20/F on both the front (Figure 4.34) and rear (Figure 4.36) sides of the model.

To summarize, all of the cracks on the external surfaces of the model occurred during the inputs of the 0.3g El Centro, Kobe and Chi-Chi earthquakes are sketched using different colors in side views in Figures 4.34-4.37. As a whole, cracks induced by the 0.3g El Centro and Kobe earthquakes concentrated mainly on the transfer plate, whereas the 0.3g Chi-Chi earthquake not only caused severe damages to the transfer plate and the two stories above, but also induced cracks almost all over the model. After the shaking of 0.3g Chi-Chi earthquake, the damage of the model was considered to be irrepairable, and the model is close to the verge of total collapse and is therefore judged not suitable for any further test.

According to the observations in our tests, transfer plate and stories above are most vulnerable and susceptible to severe seismic damage under the attack of earthquakes. Transfer system normally introduces an abrupt change of stiffness in the transfer zone. Asymmetric building layout may induce asymmetric rocking, which may cause especially severe damage to corner elements. Therefore, both abrupt change of stiffness and asymmetric building plan should be avoided as far as possible.

This chapter described the damage observations for the model during various shaking table tests. However, it is still unknown how severe these damages are. To quantitatively evaluate the damages of the model, various seismic damage indices will be used. The detailed damage evaluations will be discussed in the next chapter.

Table 4.1 Earthquake records used in the shaking table tests.

Earthquake	Date	M_w	PGA (g)	Predominant frequency		Soil amplification factor
				Before soil amplification	After soil amplification	
El Centro	1940-05-19	6.9	0.357	7.305	1.374	1.016
Kobe	1995-01-16	6.9	0.821	7.243	2.997	1.368
Northridge	1994-01-17	6.7	1.779	14.486	5.682	1.170
Loma Prieta	1989-10-18	6.9	0.644	6.993	3.497	1.242
Chi-Chi	1999-09-20	7.6	0.968	6.057	2.997	1.314

Remark: soil profile is given in Table 4.2.

Table 4.2 Soil profiles and estimated shear wave speeds using two empirical formulae.

Depth (m)			Soil type	SSB's formula			Ohta and Goto's formula	
From	To	h		a	b	v_s (m/s)	k	v_s (m/s)
0	2.7	1.35	Medium dense fine to coarse sand with gravel	120	0.28	130.52	1.282	111.19
2.7	3.4	3.05	Boulder	140	0.243	183.57	1.255	140.37
3.4	3.95	3.675	Loose fine to coarse sand	80	0.28	115.18	1.282	151.97
3.95	4.7	4.325	Cobbles	140	0.243	199.84	1.255	156.53
4.7	9	6.85	Medium dense fine to coarse sand	120	0.28	205.67	1.282	184.56
9	12	10.5	Loose clayey coarse sand with shell fragment	80	0.28	154.53	4.422	727.36
12	14	13	Loose sandy clay	70	0.3	151.11	1.000	175.82
14	32	23	Medium dense silty fine sand with fine gravel	120	0.243	257.09	1.260	264.70
32	50	41	Dense to very dense slightly silty fine to coarse sand with fine gravel	331	0	331.00	1.260	317.01
Equivalent shear wave speed (m/s)						236.99		248.43

Remark:

Two formulae for estimating the shear wave speed of soil [adopted from Chau (2000)]:

SSB's formula: $v_s = ah^b$

Ohta and Goto's formula: $v_s = 78.98kh^{0.312}$

where h is the depth between the ground level and the centre line of a soil layer measured in meter.

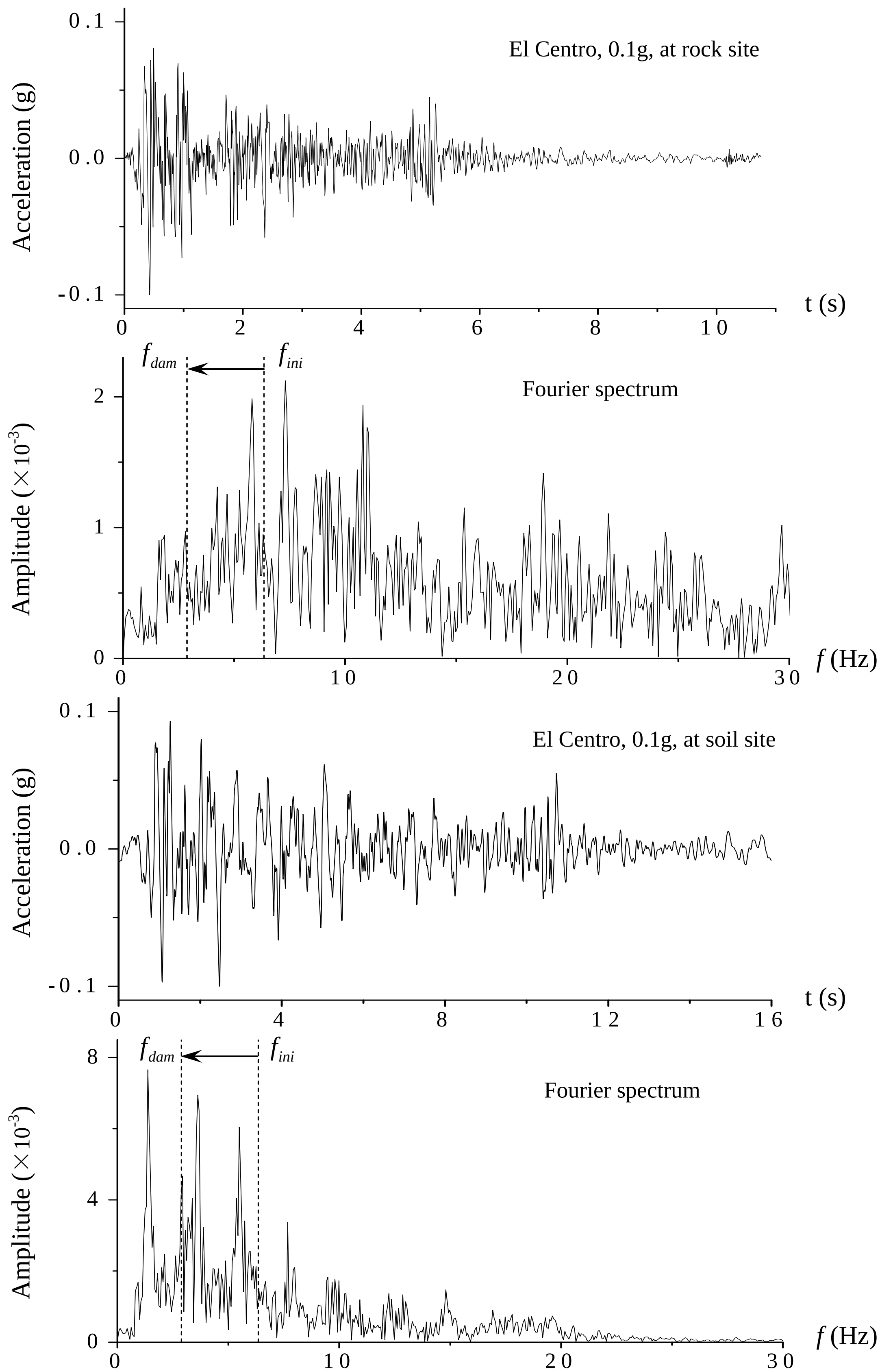

Figure 4.1 The input waves of El Centro earthquake before and after soil amplification and their corresponding Fourier spectra, where f_{ini} and f_{dam} denote the initial and final natural frequencies of the model respectively.

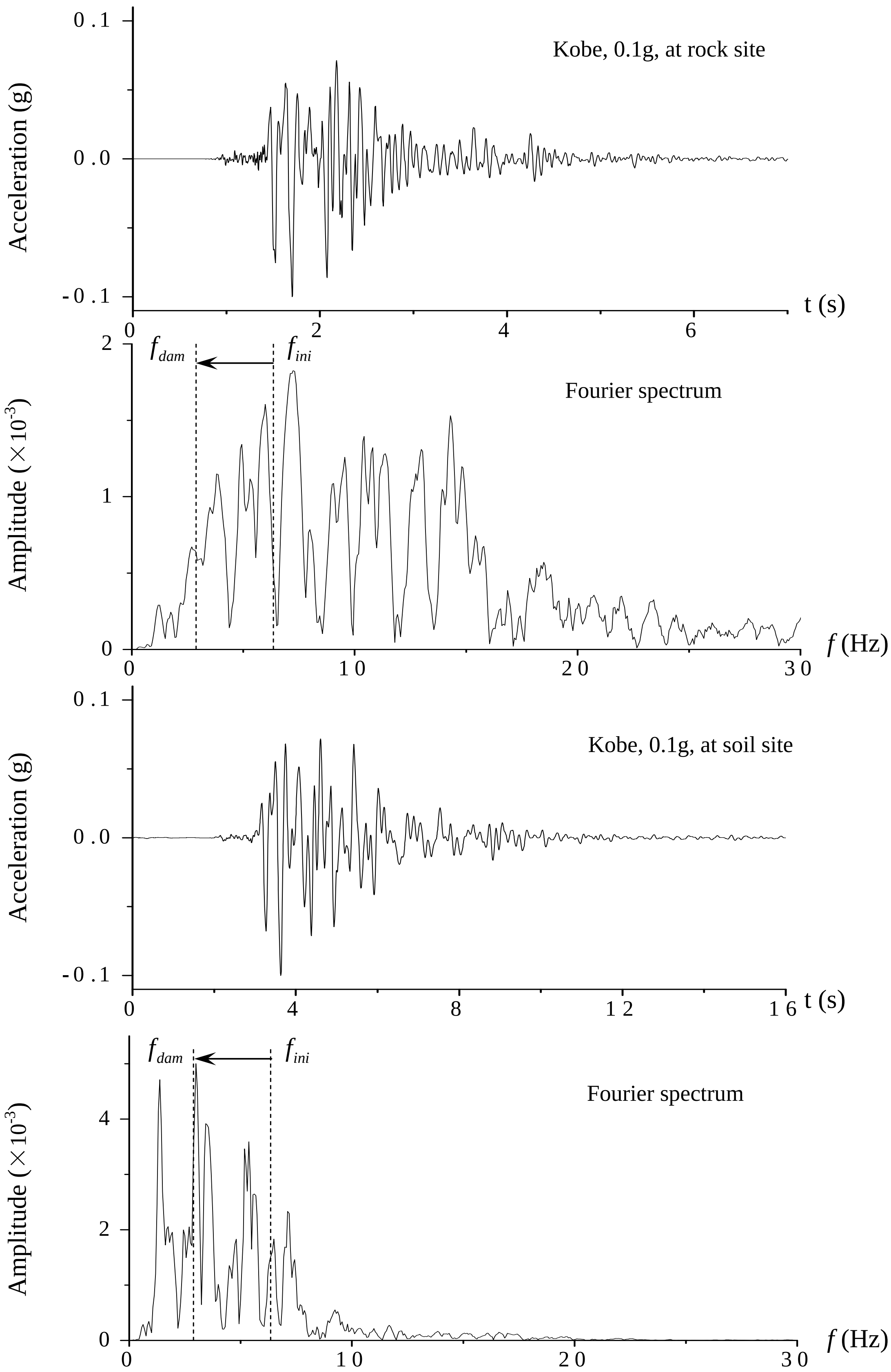

Figure 4.2 The input waves of Kobe earthquake before and after soil amplification and their corresponding Fourier spectra, where f_{ini} and f_{dam} denote the initial and final natural frequencies of the model respectively.

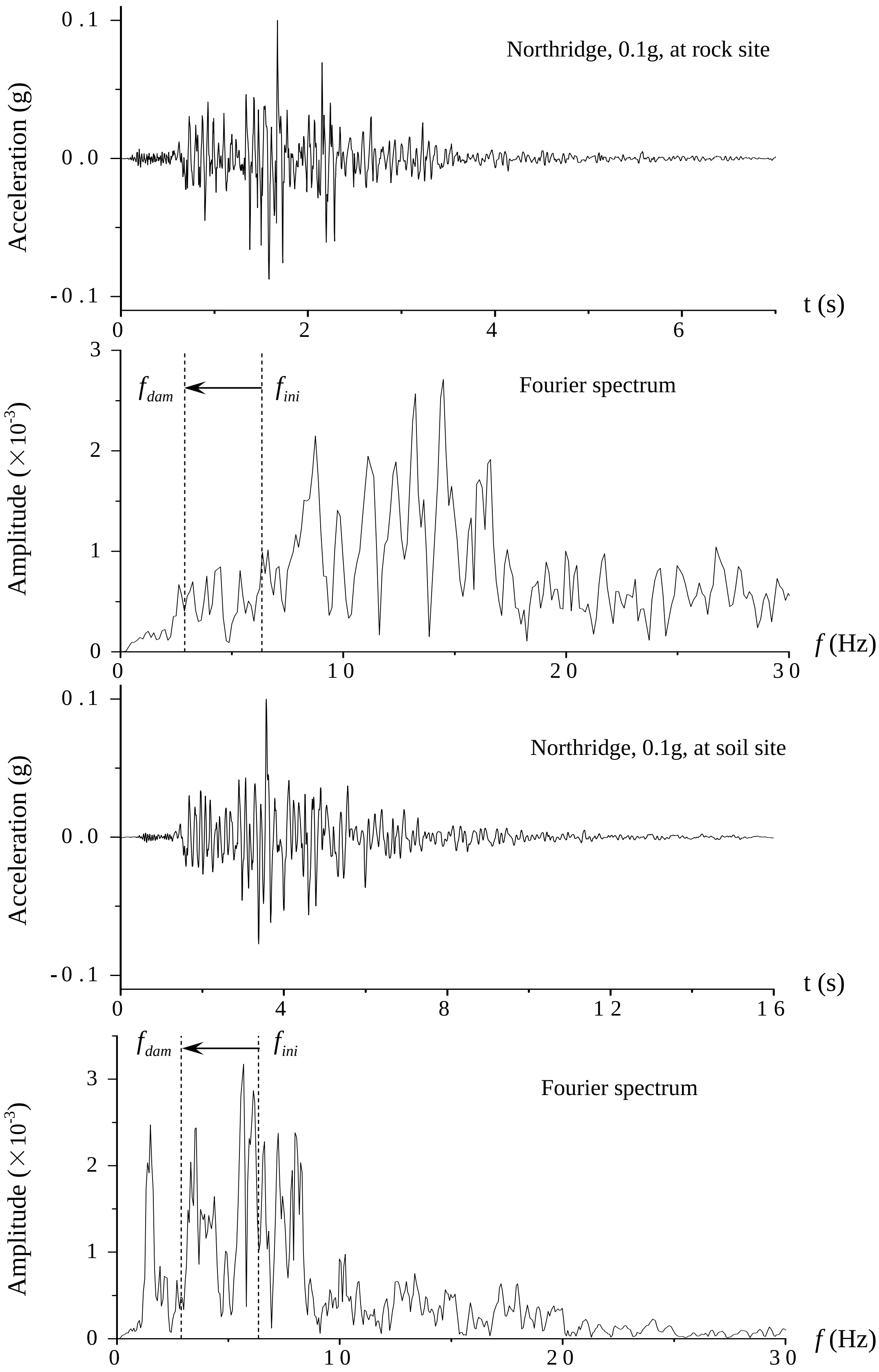

Figure 4.3 The input waves of Northridge earthquake before and after soil amplification and their corresponding Fourier spectra, where f_{ini} and f_{dam} denote the initial and final natural frequencies of the model respectively.

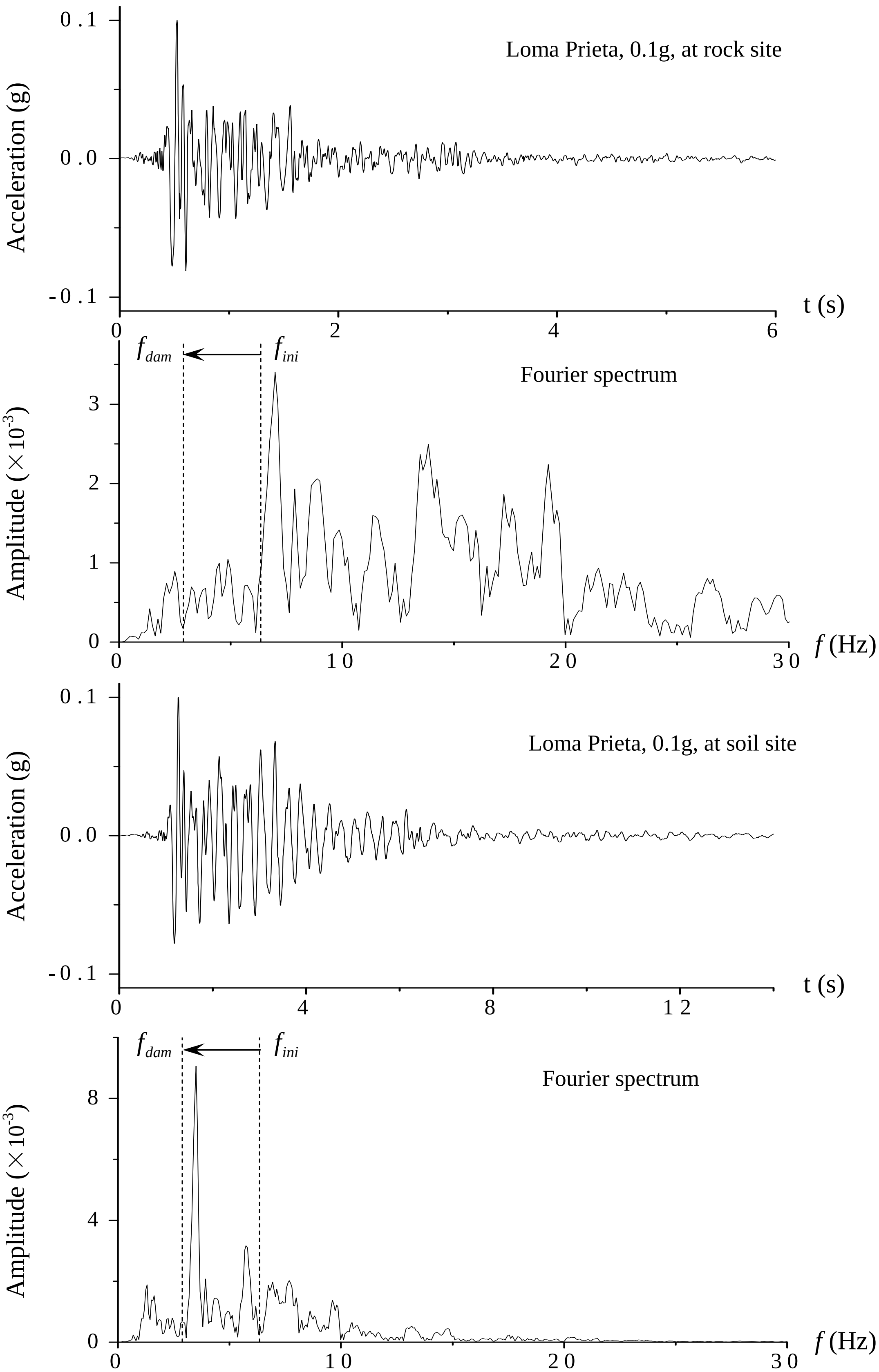

Figure 4.4 The input waves of Loma Prieta earthquake before and after soil amplification and their corresponding Fourier spectra, where f_{ini} and f_{dam} denote the initial and final natural frequencies of the model respectively.

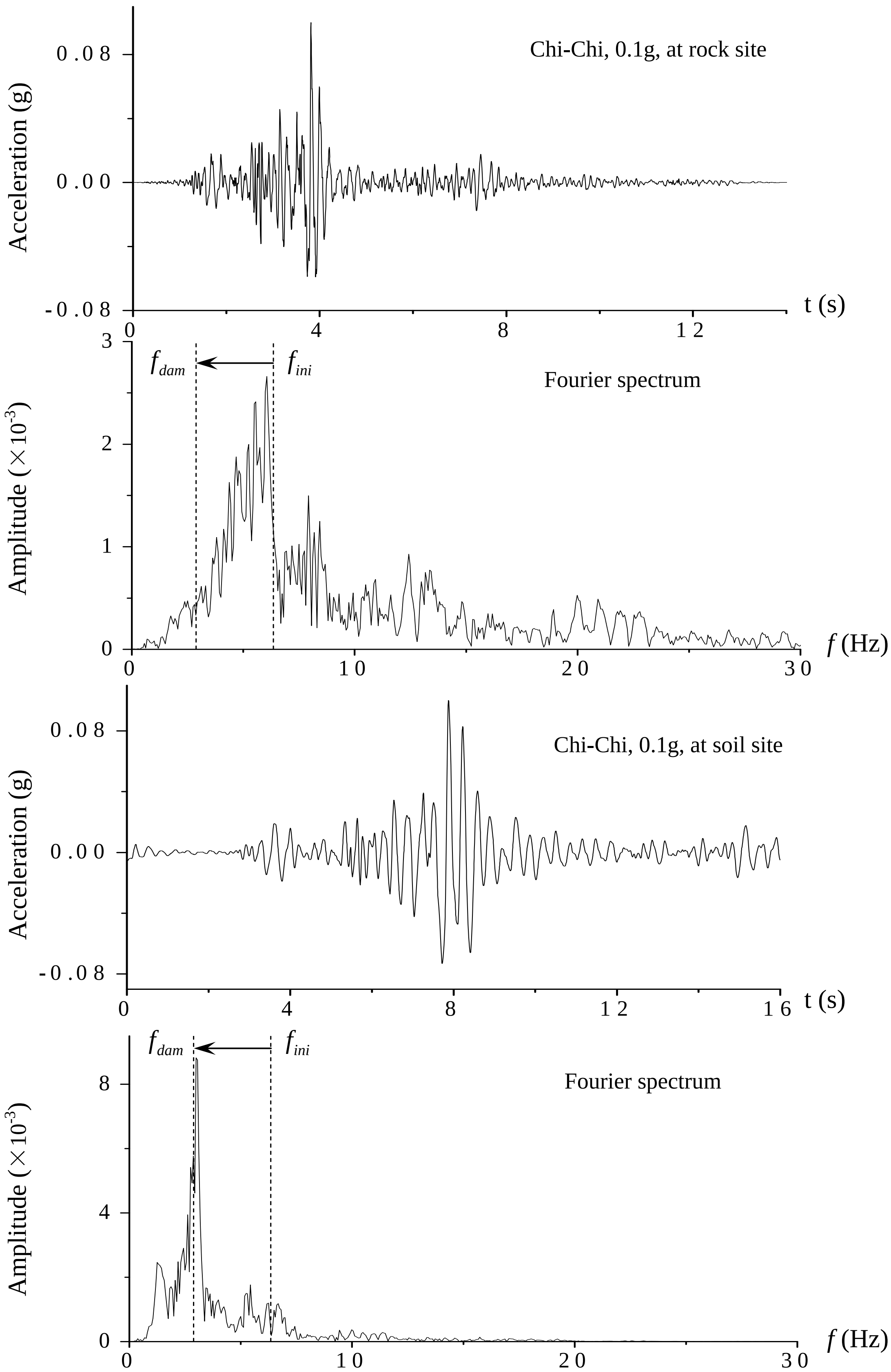

Figure 4.5 The input waves of Chi-Chi earthquake before and after soil amplification and their corresponding Fourier spectra, where f_{ini} and f_{dam} denote the initial and final natural frequencies of the model respectively.

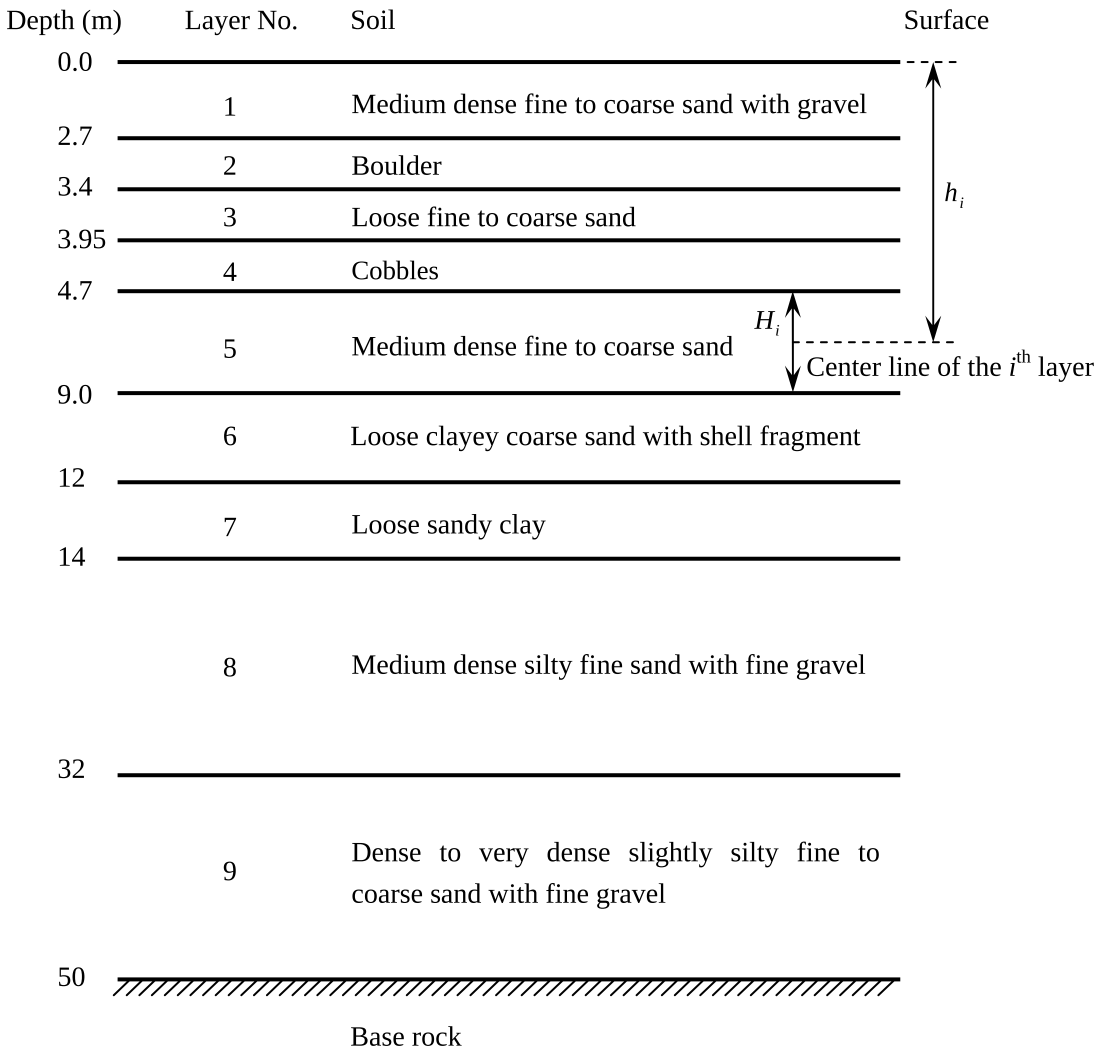

Figure 4.6 Soil profiles beneath the site of the prototype structure.

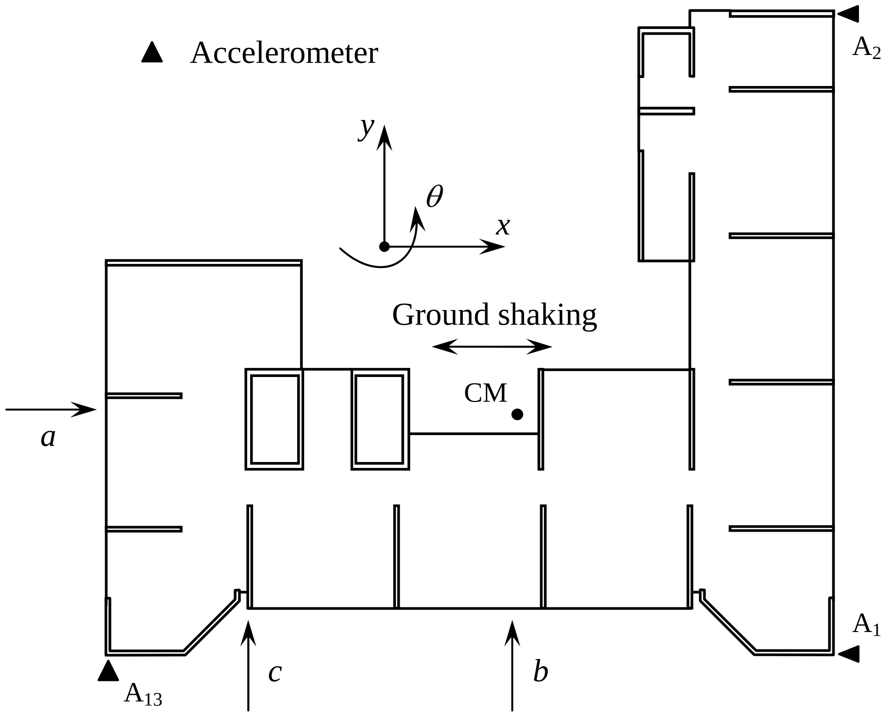

(a)

(b)

Figure 4.7 Set-up of modal test: (a) sketch of the three hammer impact points (*a*, *b* and *c*) and accelerometers at the top floor, where CM means the center of mass; (b) photograph showing hammer impact at the point *a*.

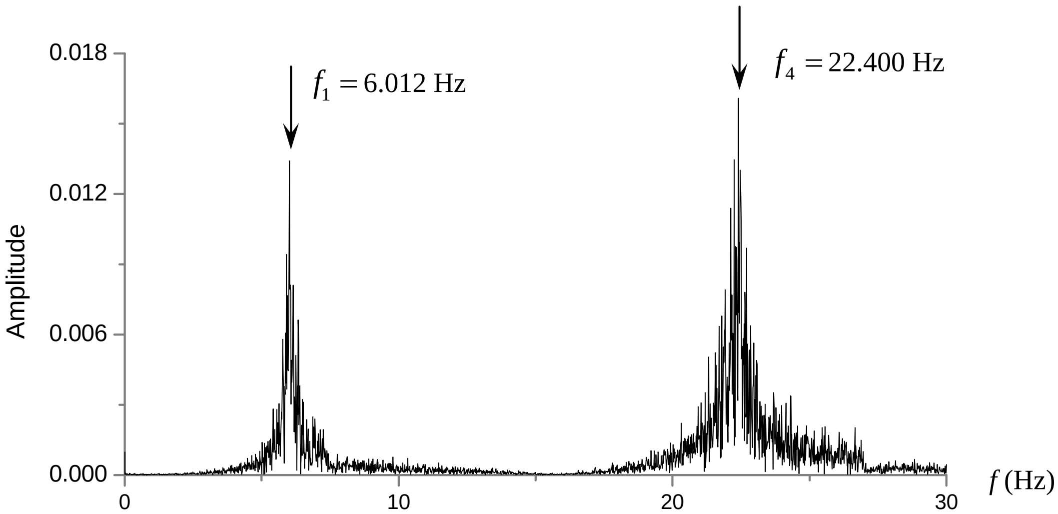

(a) Fourier spectrum of A_1 when the hammer hits at the point *a*;

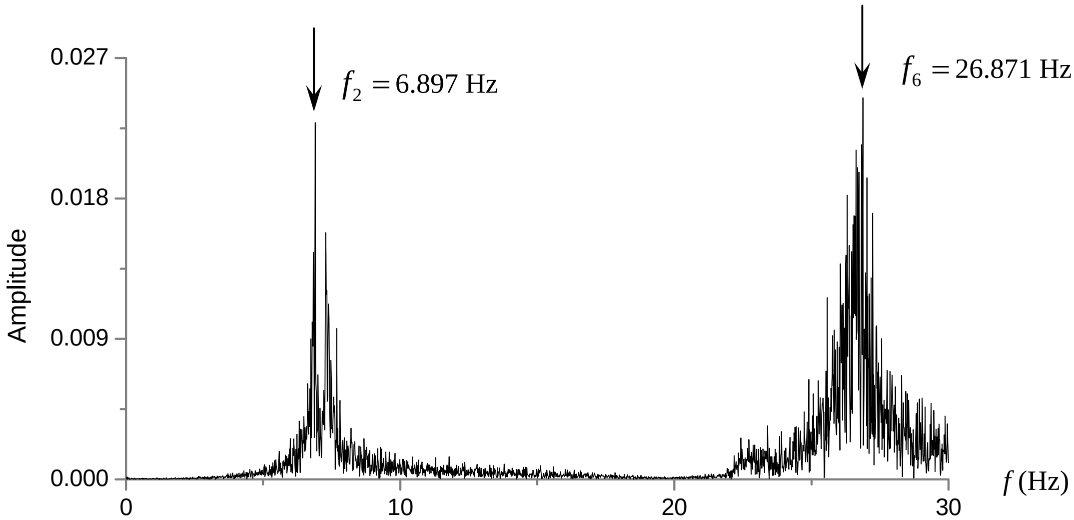

(b) Fourier spectrum of A_{13} when the hammer hits at the point *b*;

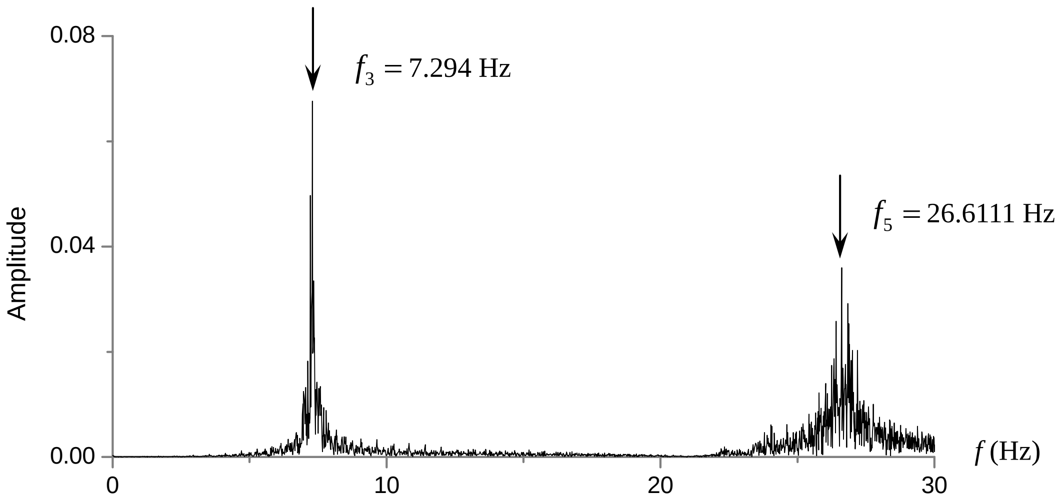

(c) Fourier spectrum of A_1−A_2 when the hammer hits at the point *c*.

Figure 4.8 Fourier spectra of the accelerations at the roof for determining the natural frequencies of the model.

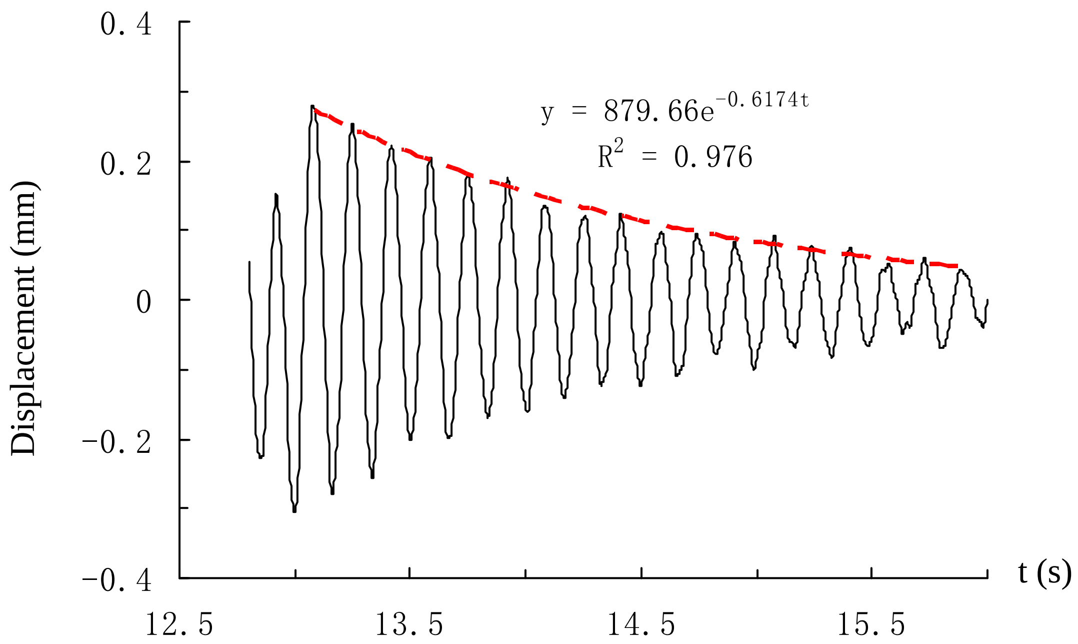

(a) before all shaking tests, $\xi = 1.63\%$;

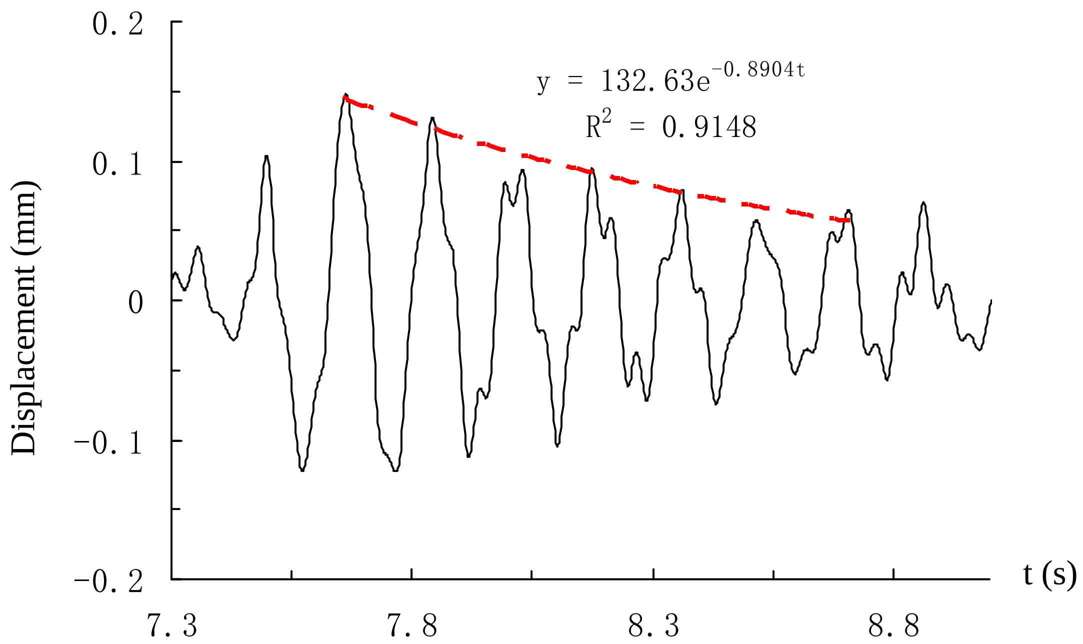

(b) after all shaking tests, $\xi = 4.91\%$.

Figure 4.9 Damping ratios of the first mode of the model: (a) before all shaking tests; (b) after all shaking tests.

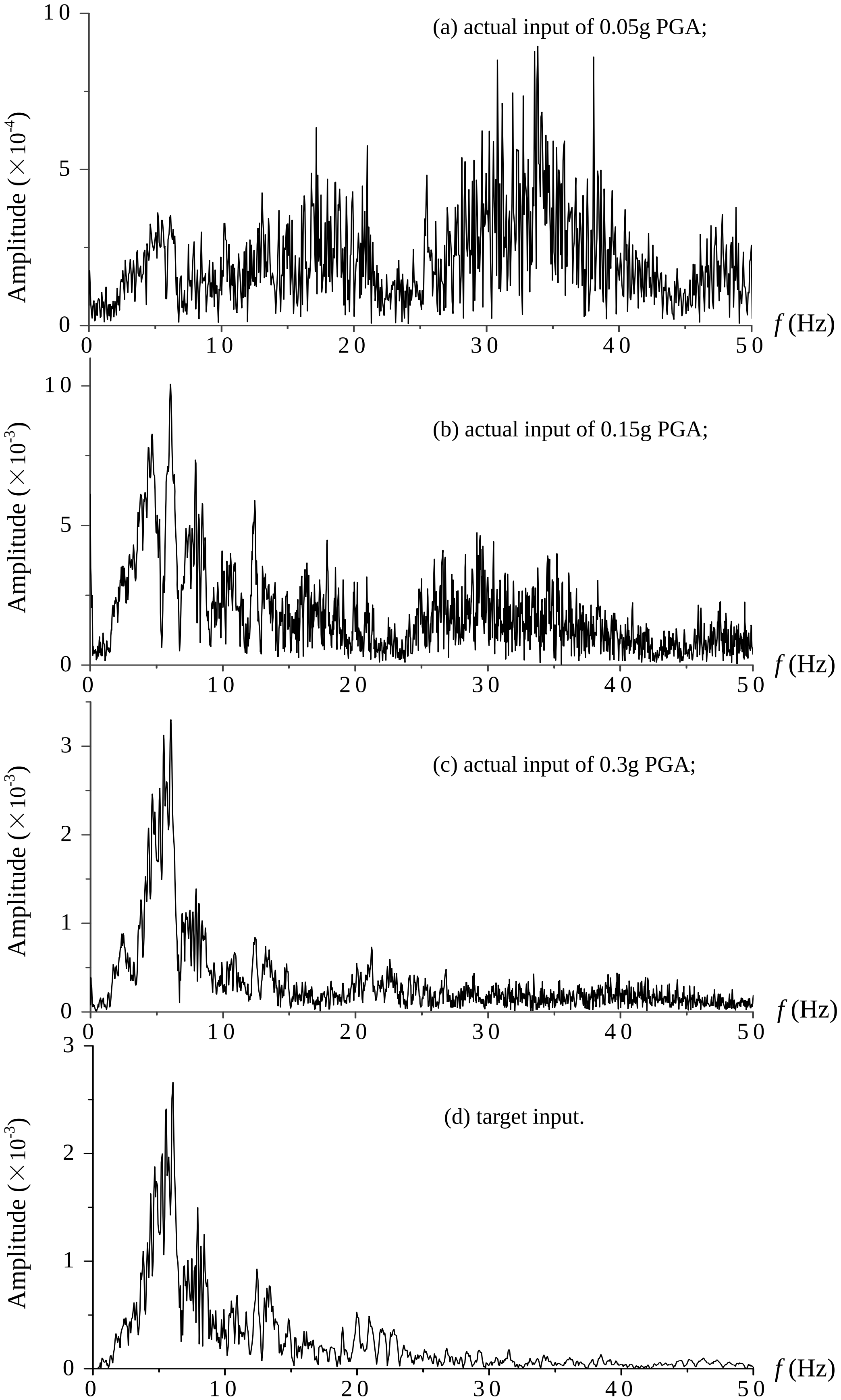

Figure 4.10 Comparison of Fourier spectra of actual inputs generated by the shaking table and the target input for Chi-Chi earthquake without soil amplification.

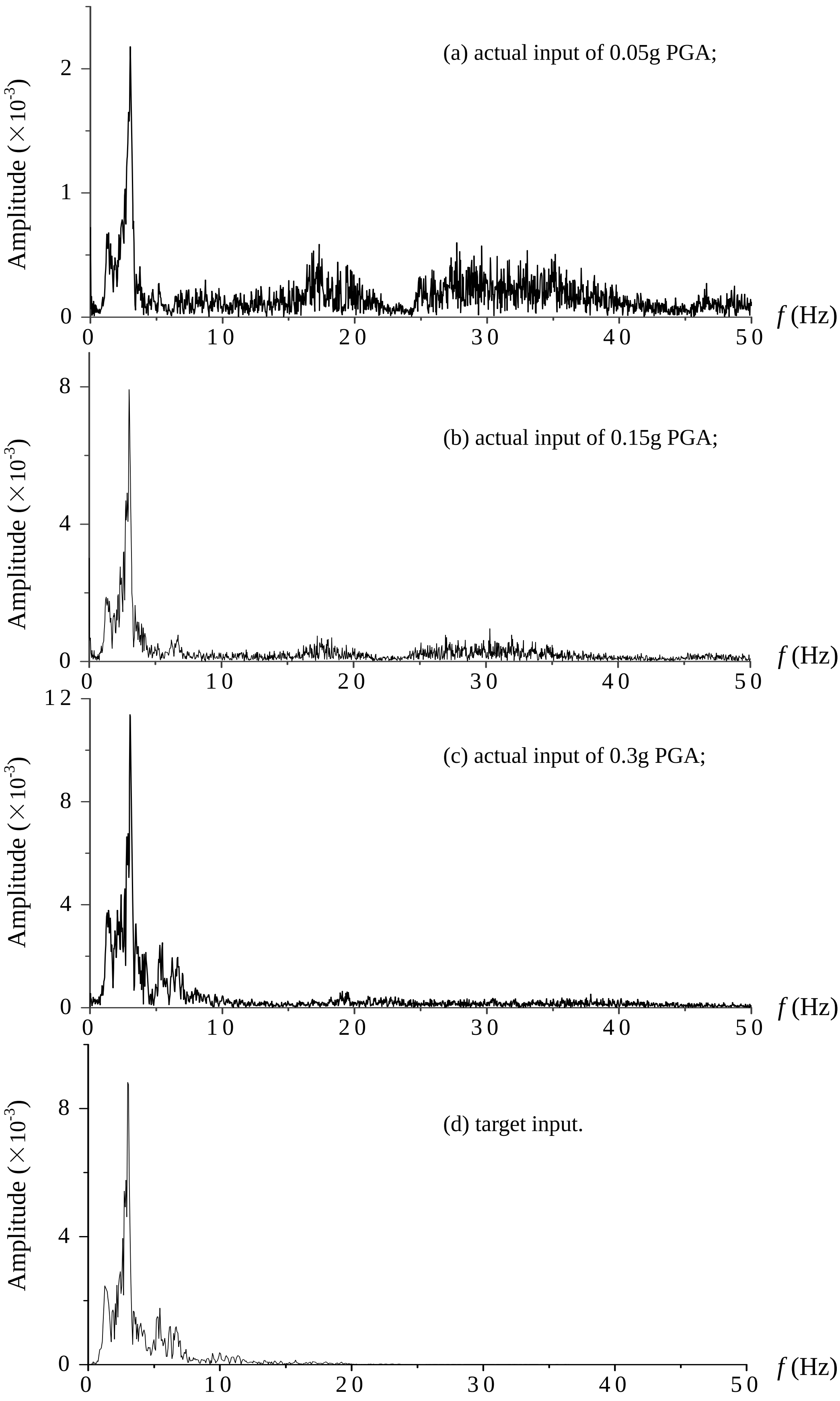

Figure 4.11 Comparison of Fourier spectra of actual inputs generated by the shaking table and target input for Chi-Chi earthquake after soil amplification.

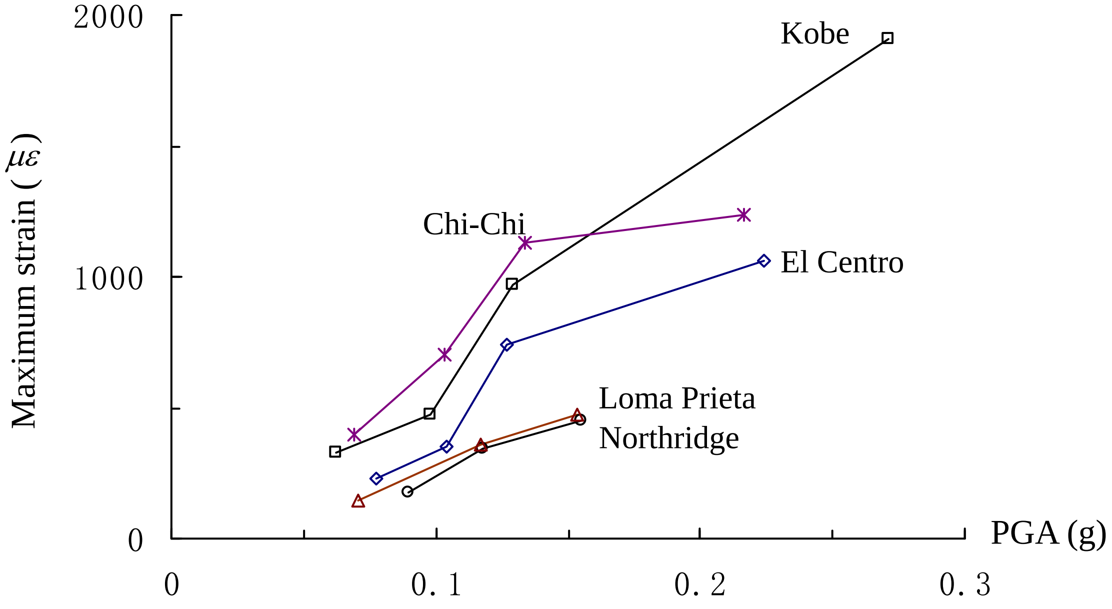

(a) before soil amplification;

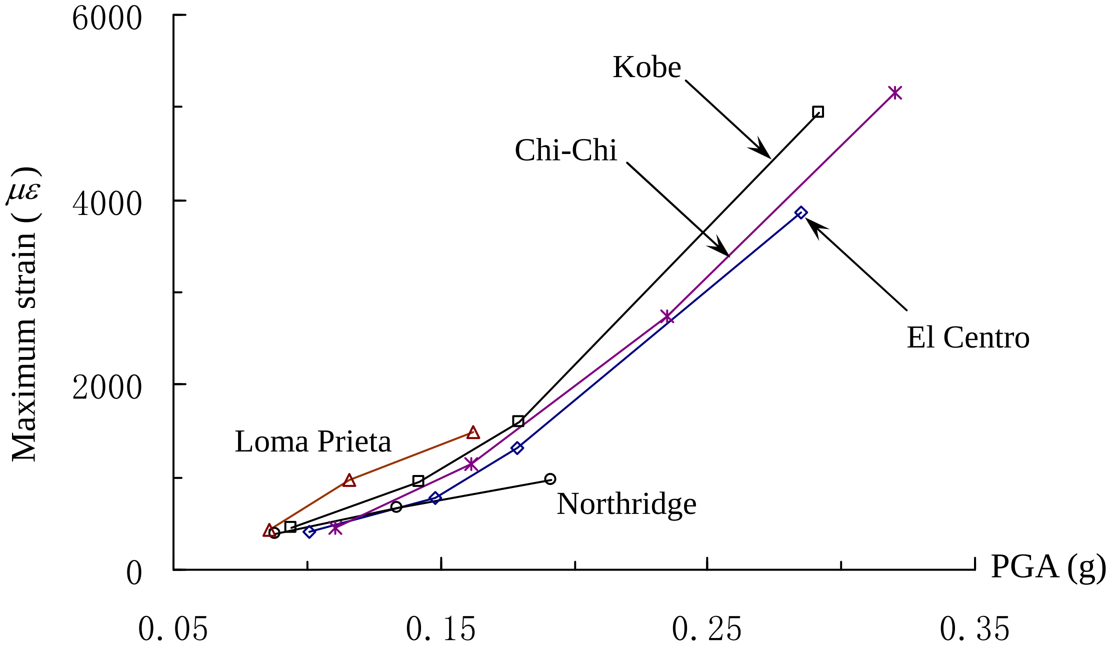

(b) after soil amplification.

Figure 4.12 Maximum strains vs. input PGAs for various earthquakes before and after soil amplification respectively.

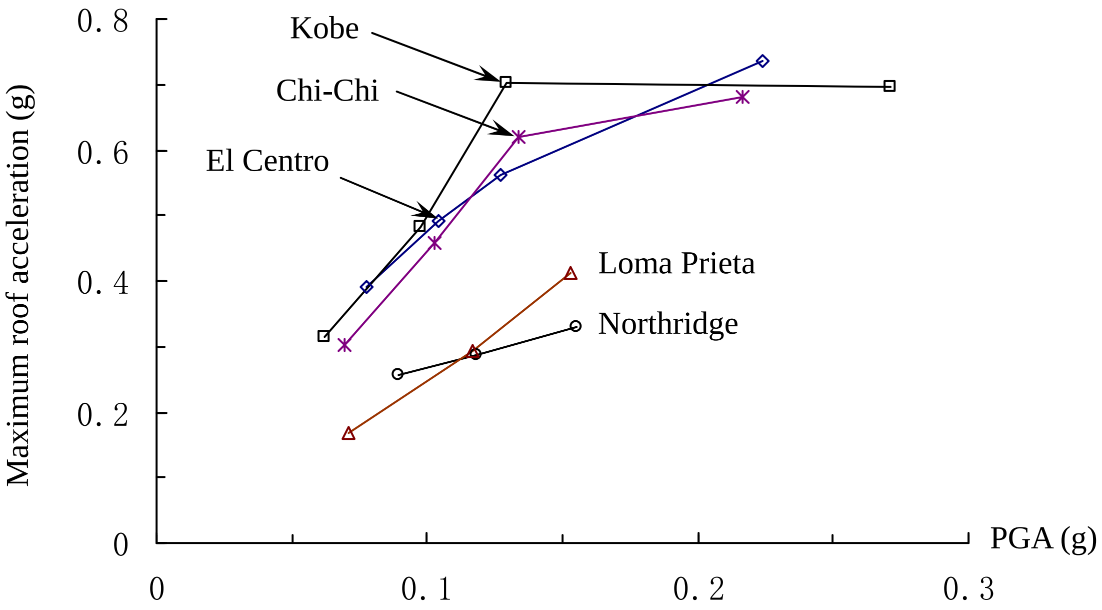

(a) before soil amplification;

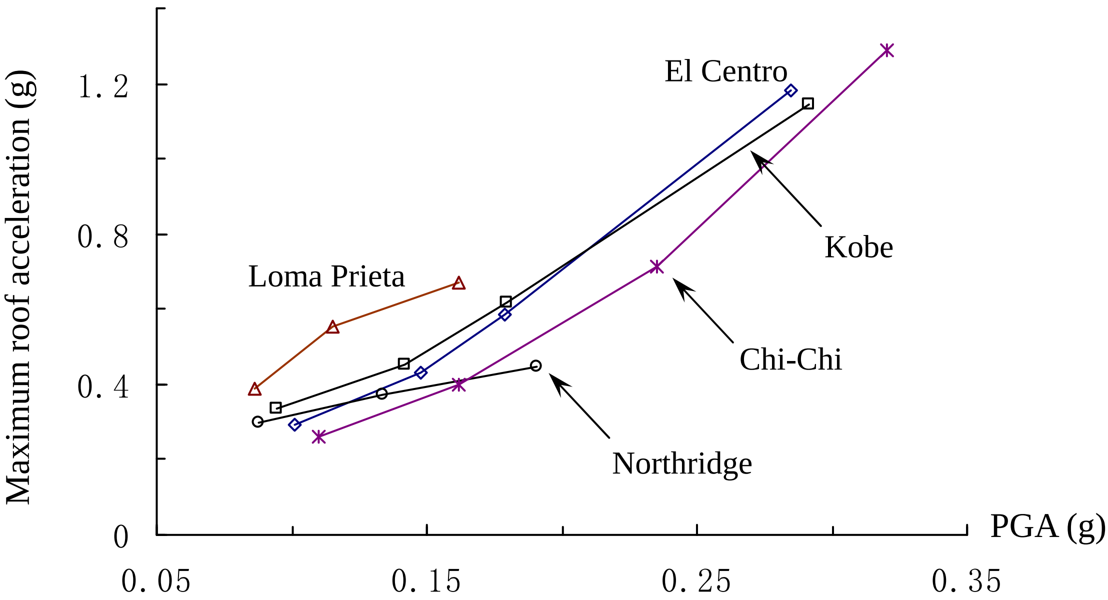

(b) after soil amplification.

Figure 4.13 Maximum accelerations at the roof vs. input PGAs for various earthquakes before and after soil amplification respectively.

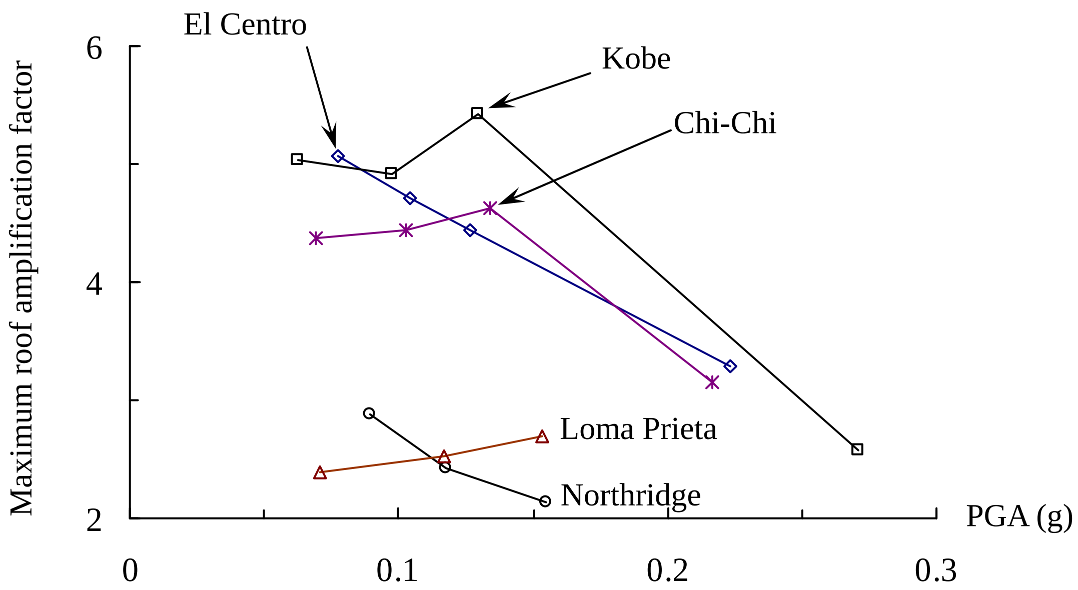

(a) before soil amplification;

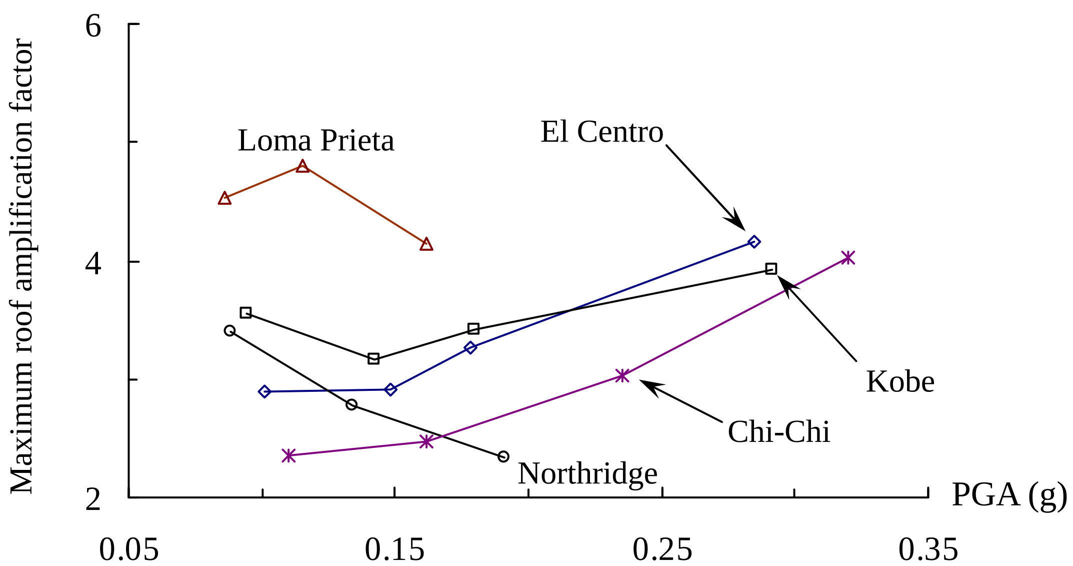

(b) after soil amplification.

Figure 4.14 Maximum acceleration amplification factors at the roof vs. input PGAs for various earthquakes before and after soil amplification respectively.

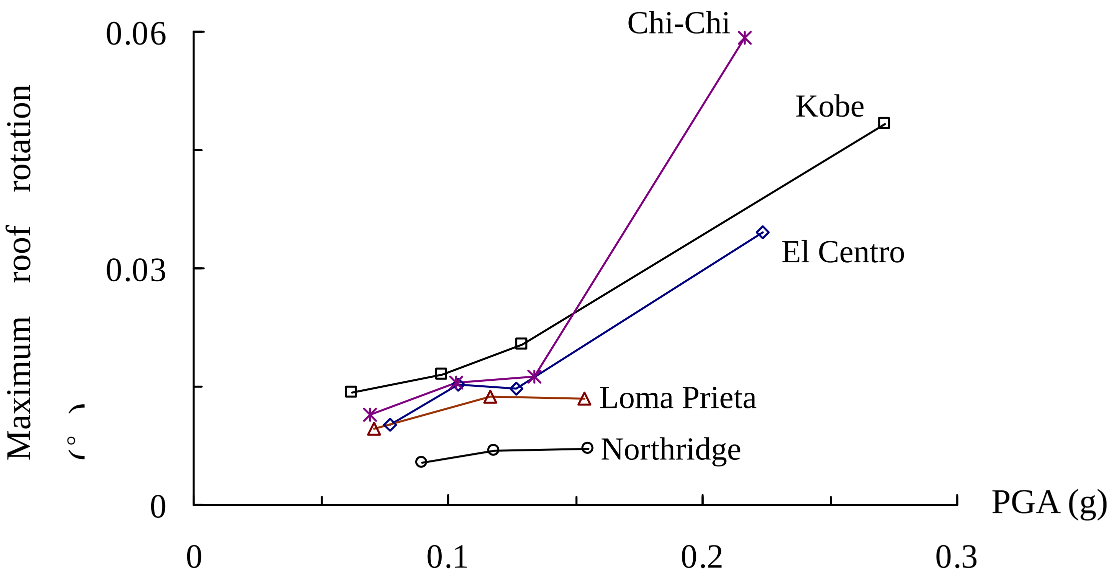

(a) before soil amplification;

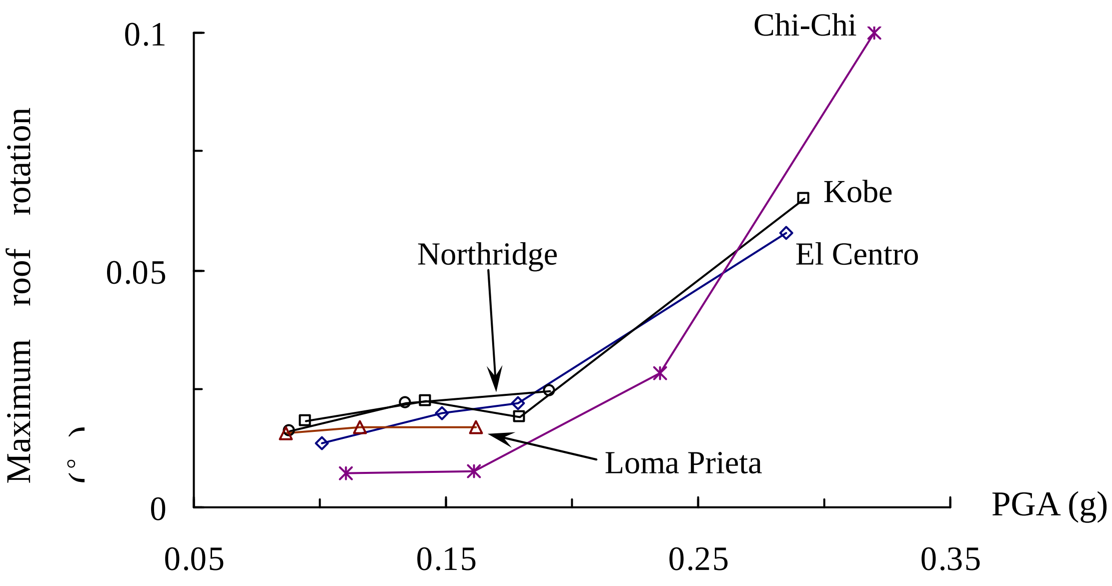

(b) after soil amplification.

Figure 4.15 Maximum rotation angles at the roof vs. input PGAs for various earthquakes before and after soil amplification respectively.

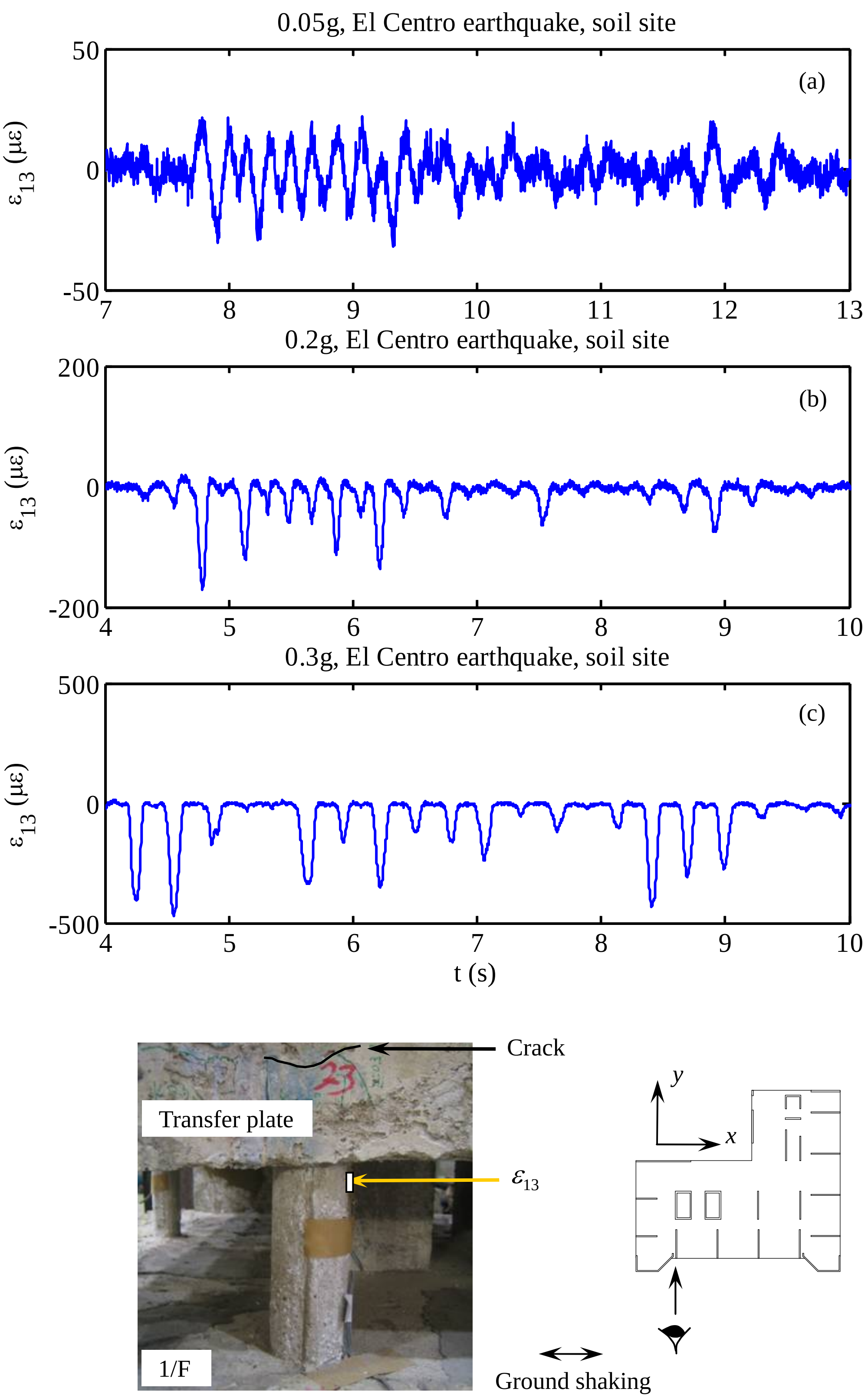

Figure 4.16 Strain time histories of ε_{13} during 0.05, 0.2g and 0.3g PGA El Centro earthquakes after soil amplification. Small tension for ε_{13} occurred during 0.2g El Centro earthquake after soil amplification and implies the existence of local damages.

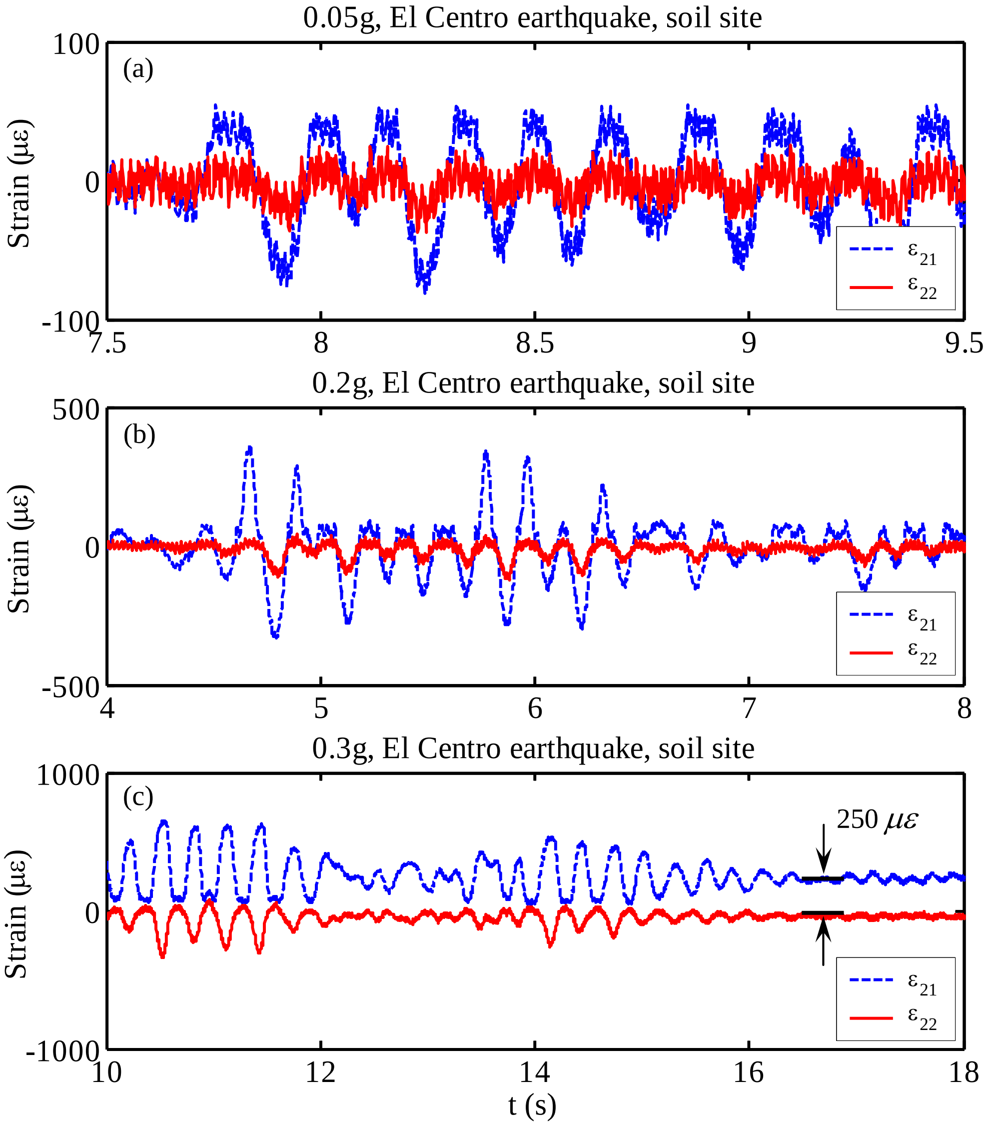

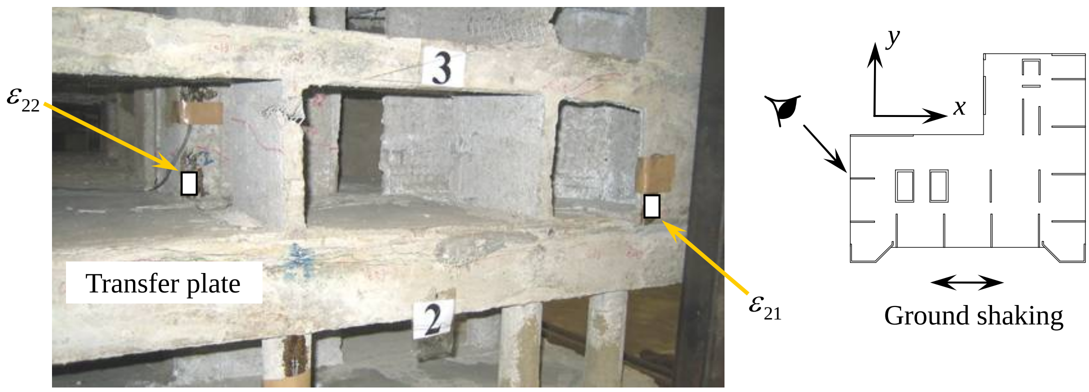

Figure 4.17 Strain time histories of ε_{21} and ε_{22} during 0.05, 0.2g and 0.3g PGA El Centro earthquakes after soil amplification. The variations of the two strain gauges changed from in-phase to out-of-phase. The photo below shows their locations.

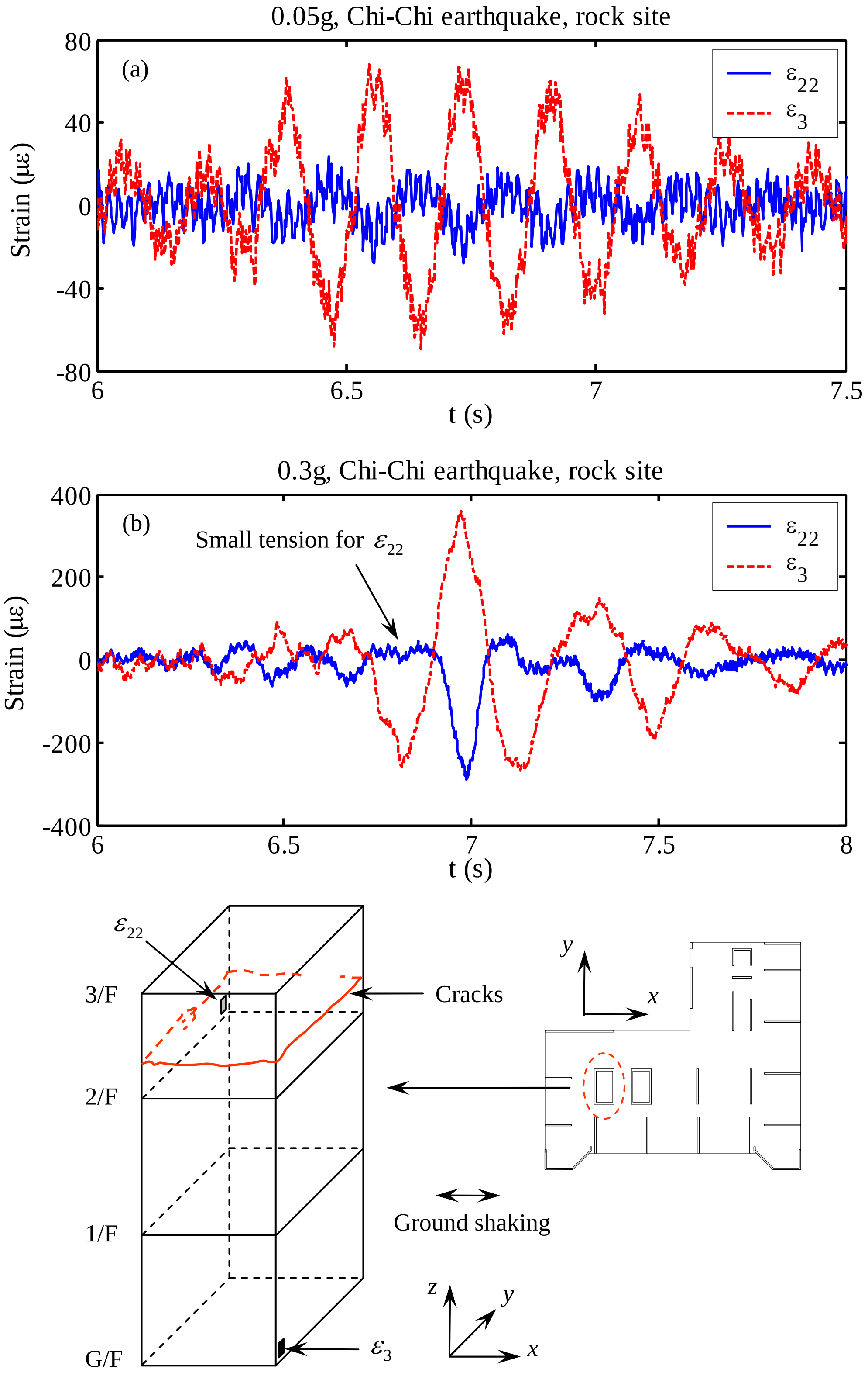

Figure 4.18 The out-of-phase strains of two strain gauges on the opposite sides of a core wall during 0.05g and 0.3g Chi-Chi earthquakes. This phenomenon was found for all other tests, impling the floors slabs were not absolutely rigid. The small tension for ε_{22} in 0.3g Chi-Chi earthquake was probably due to the cracks occurred.

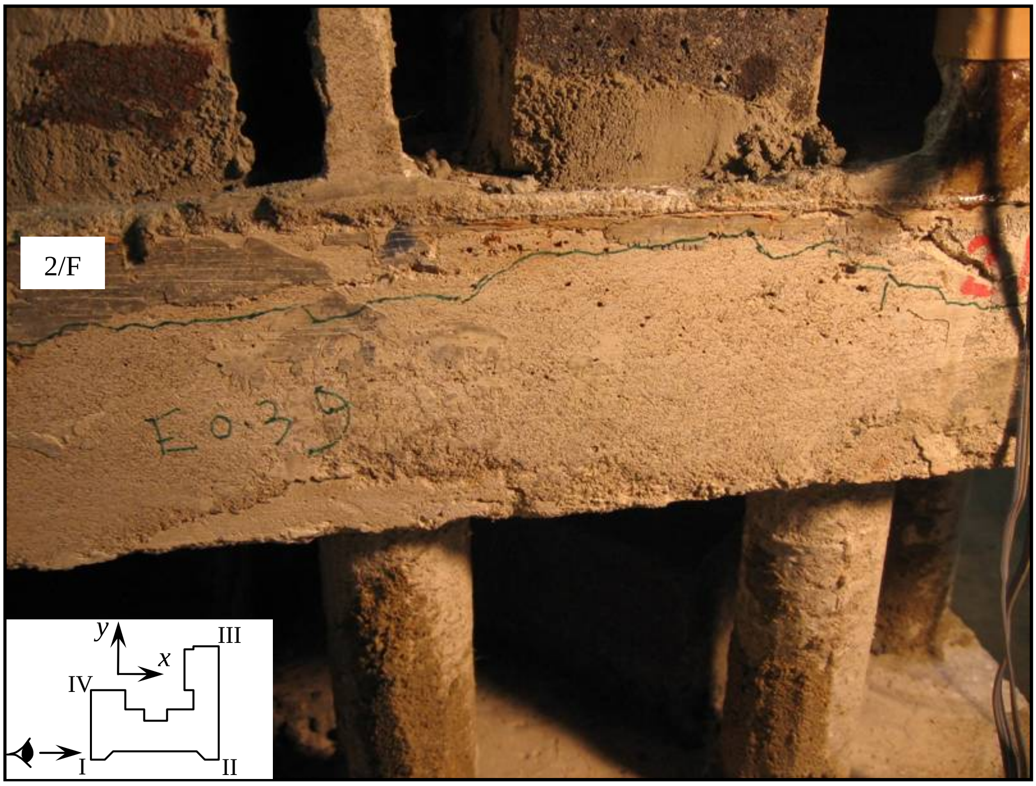

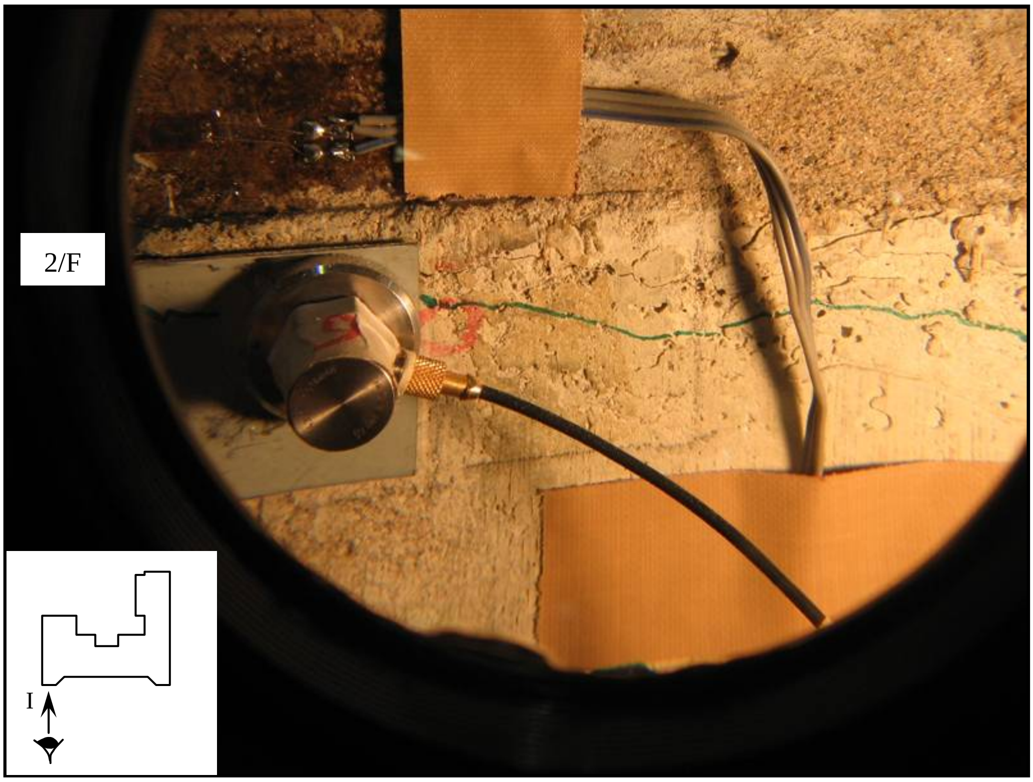

Figure 4.19 Cracks at Corner I of the transfer plate caused by the 0.3g El Centro earthquake at soil site.

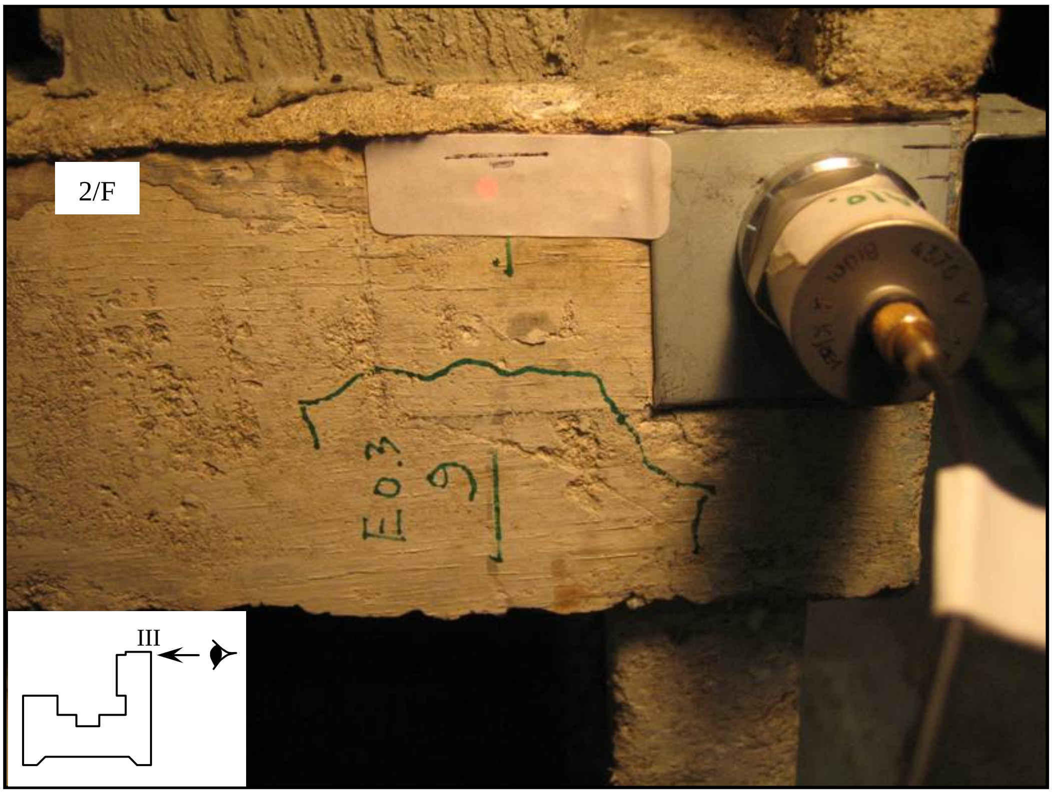

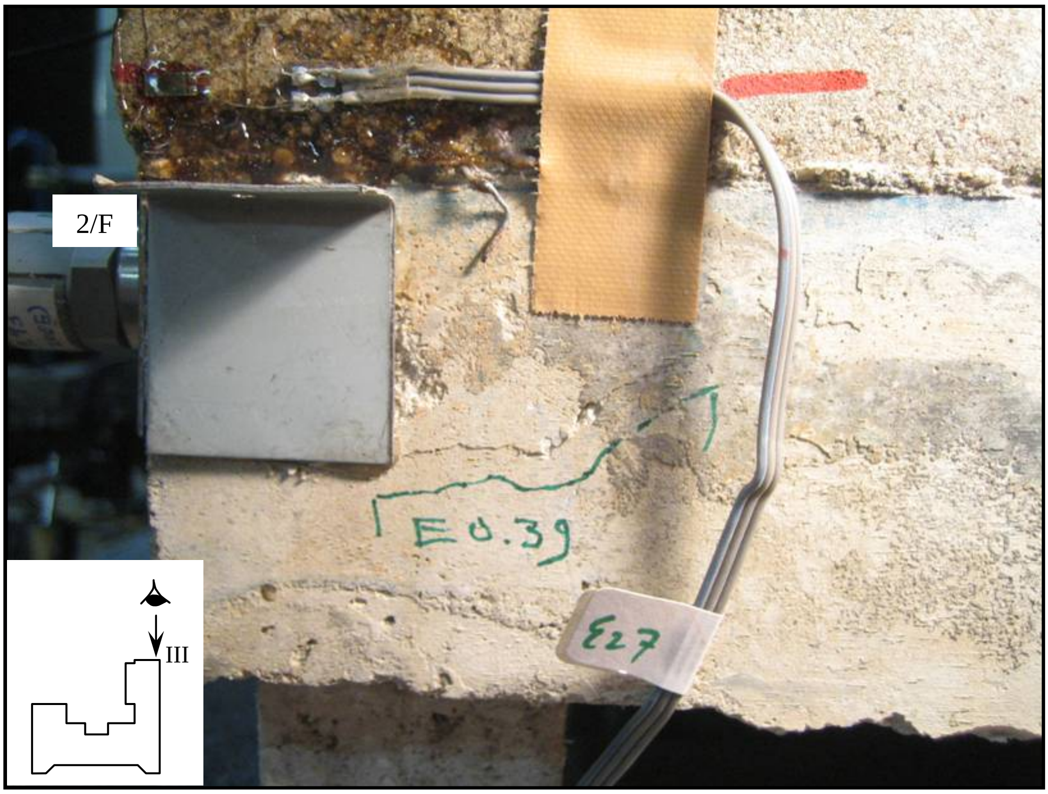

Figure 4.20 Cracks at Corner III of the transfer plate caused by the 0.3g El Centro earthquake at soil site.

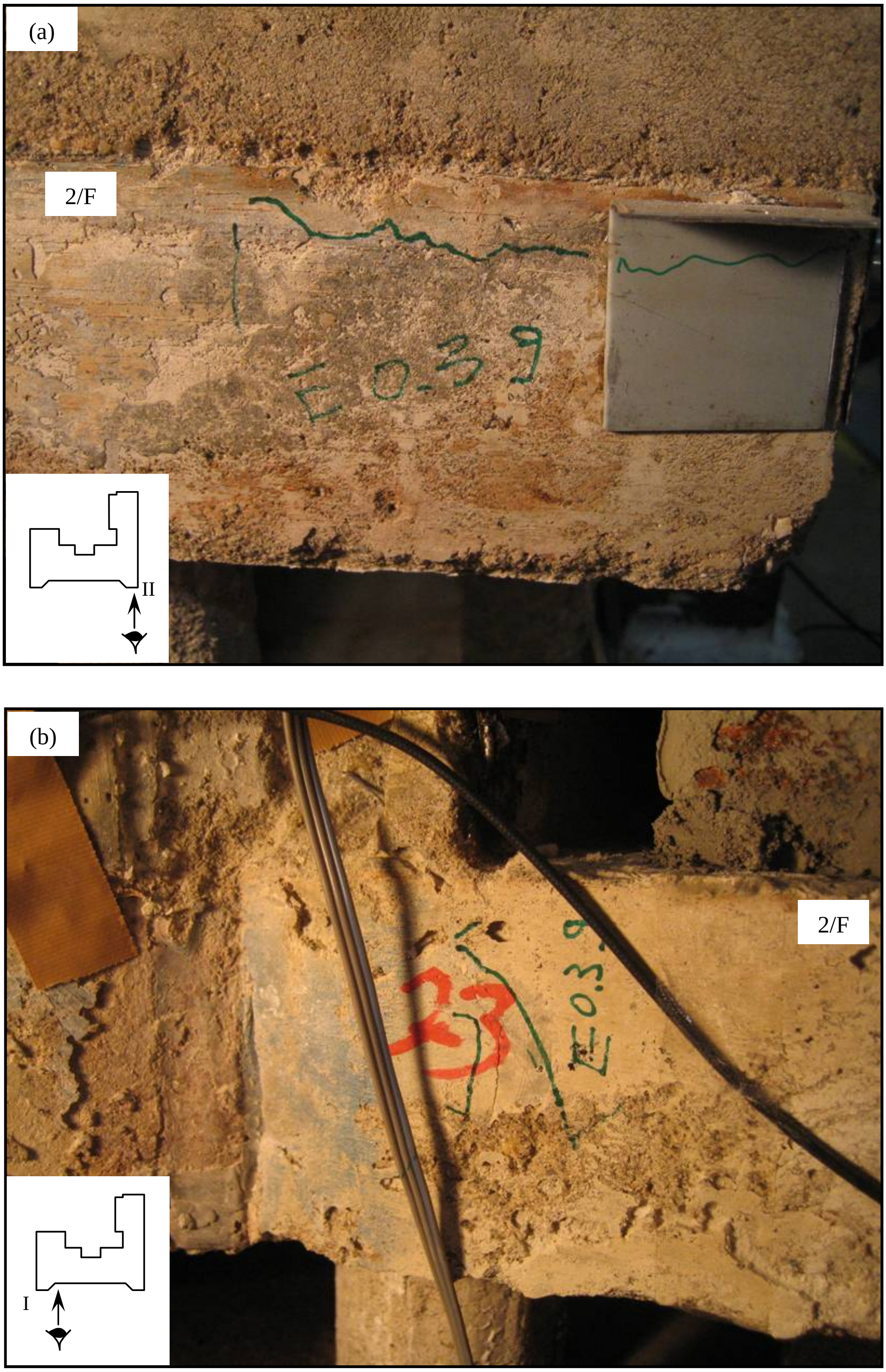

Figure 4.21 Cracks at the transfer plate caused by the 0.3g El Centro earthquake at soil site: (a) crack at Corner II; (b) diagonal cracks.

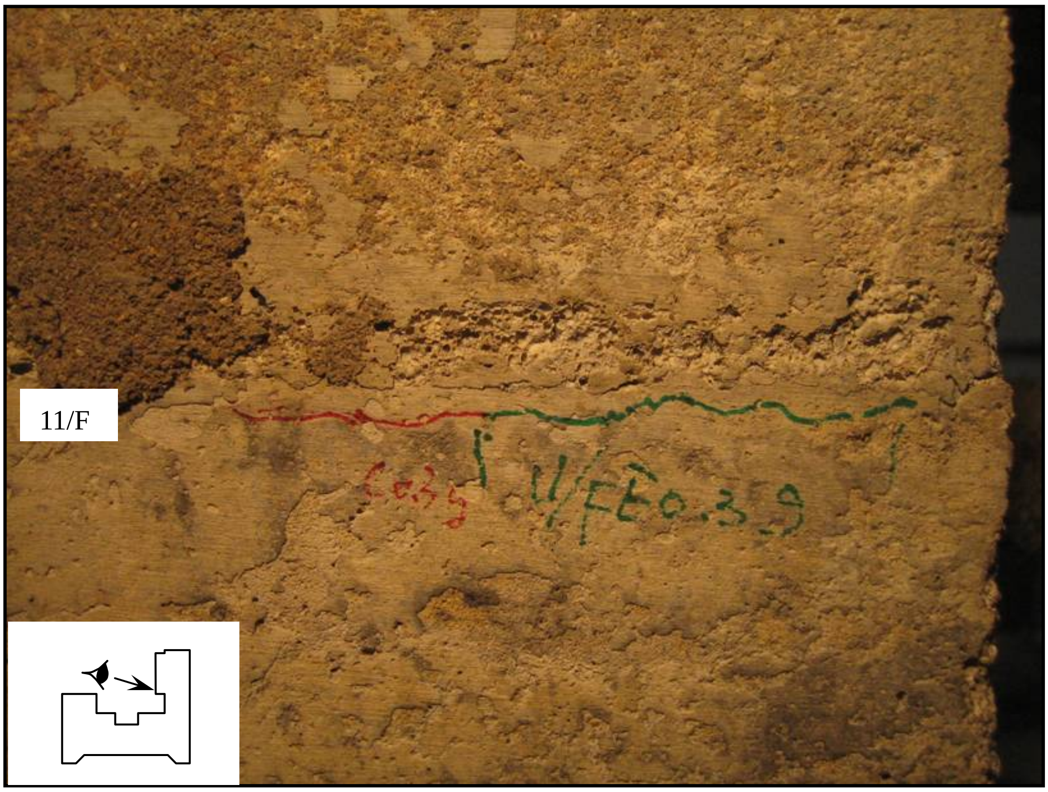

Figure 4.22 Horizontal cracks at the upper stories caused by the 0.3g El Centro earthquake at soil site.

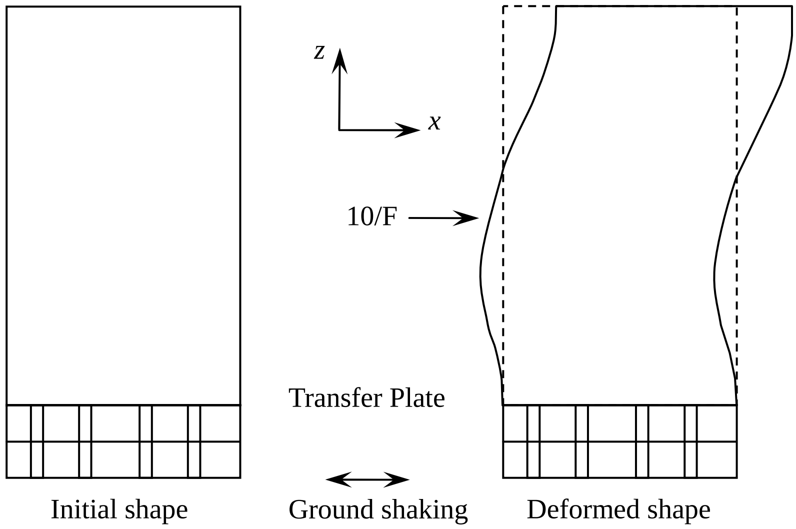

(a)

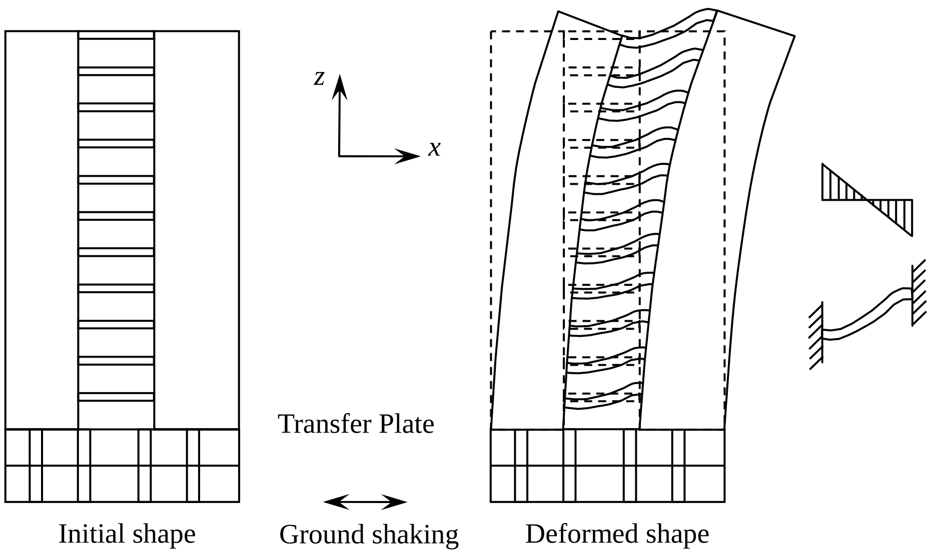

(b)

Figure 4.23 Sketches of two deform patterns observed in the tests: (a) higher mode deformed shape observed when the input PGA was greater than 0.2g. The two stories below the transfer plate have much smaller deformation compared to the upper stories; (b) the shear forces occurred in the lintel beams between core walls induced a number of cracks at the ends of these beams. These phenomena were observed when the input PGA was greater than 0.3g.

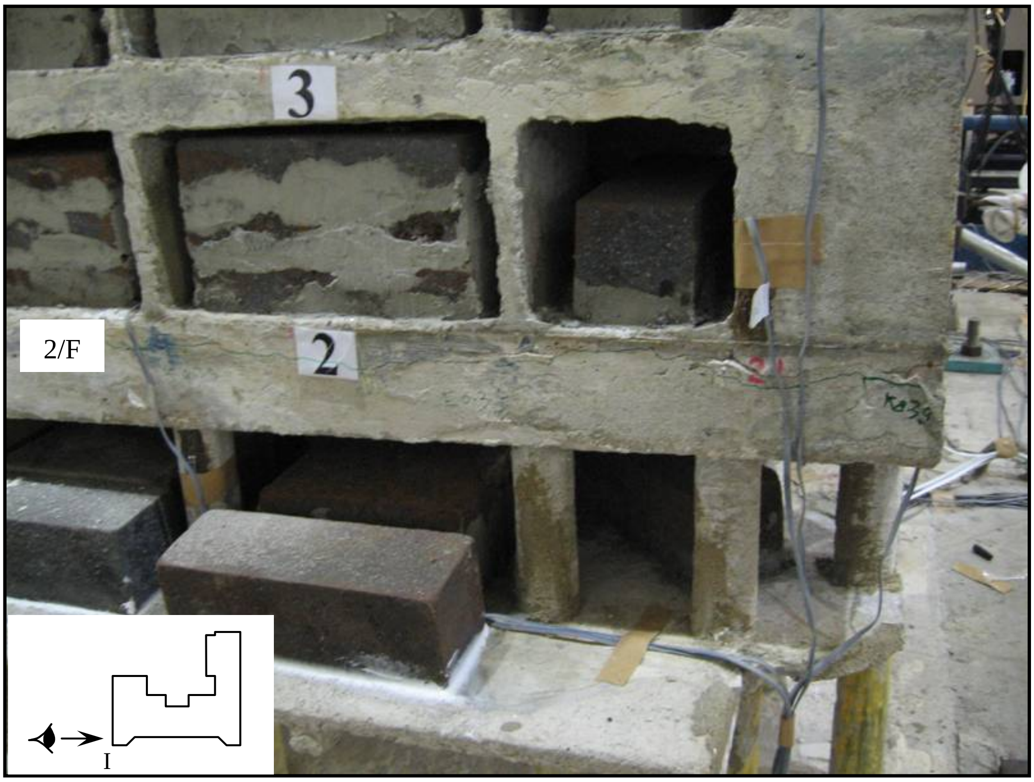

(a) widening and lengthening of existing cracks;

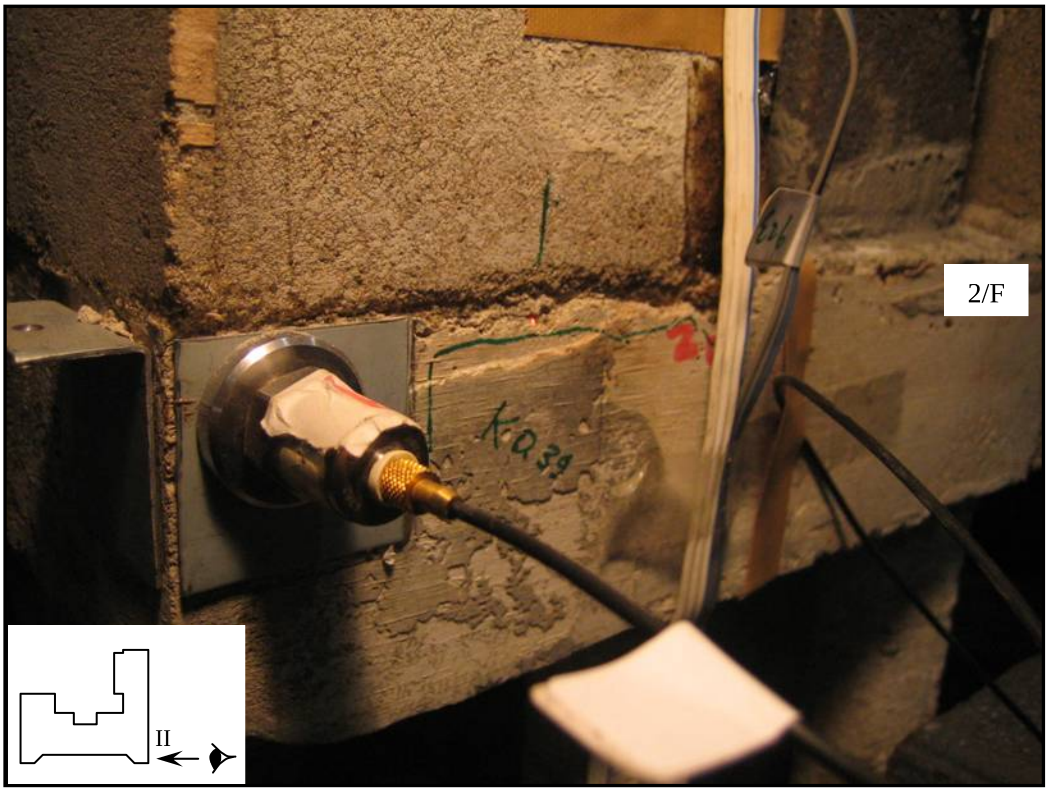

(b) new cracks occurred at Corner II.

Figure 4.24 Cracks at the transfer plate during the 0.3g Kobe earthquake at soil site.

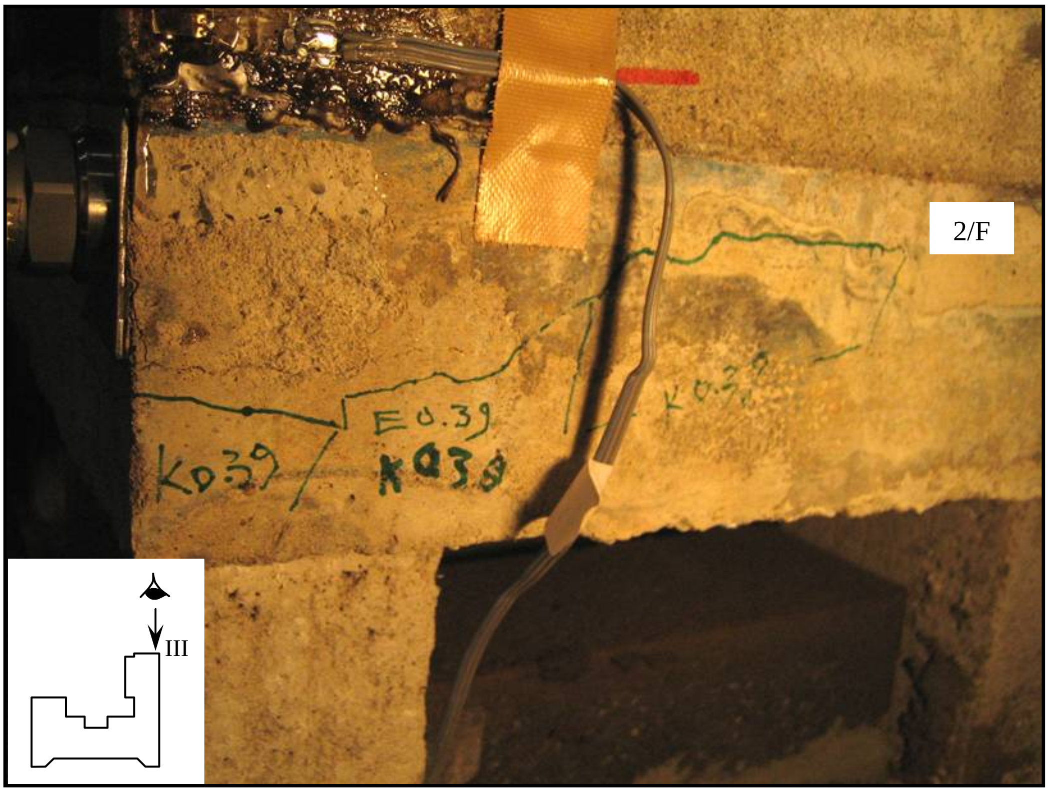

Figure 4.25 Widening and lengthening of existing cracks at Corner III of the transfer plate caused by the 0.3g Kobe earthquake at soil site.

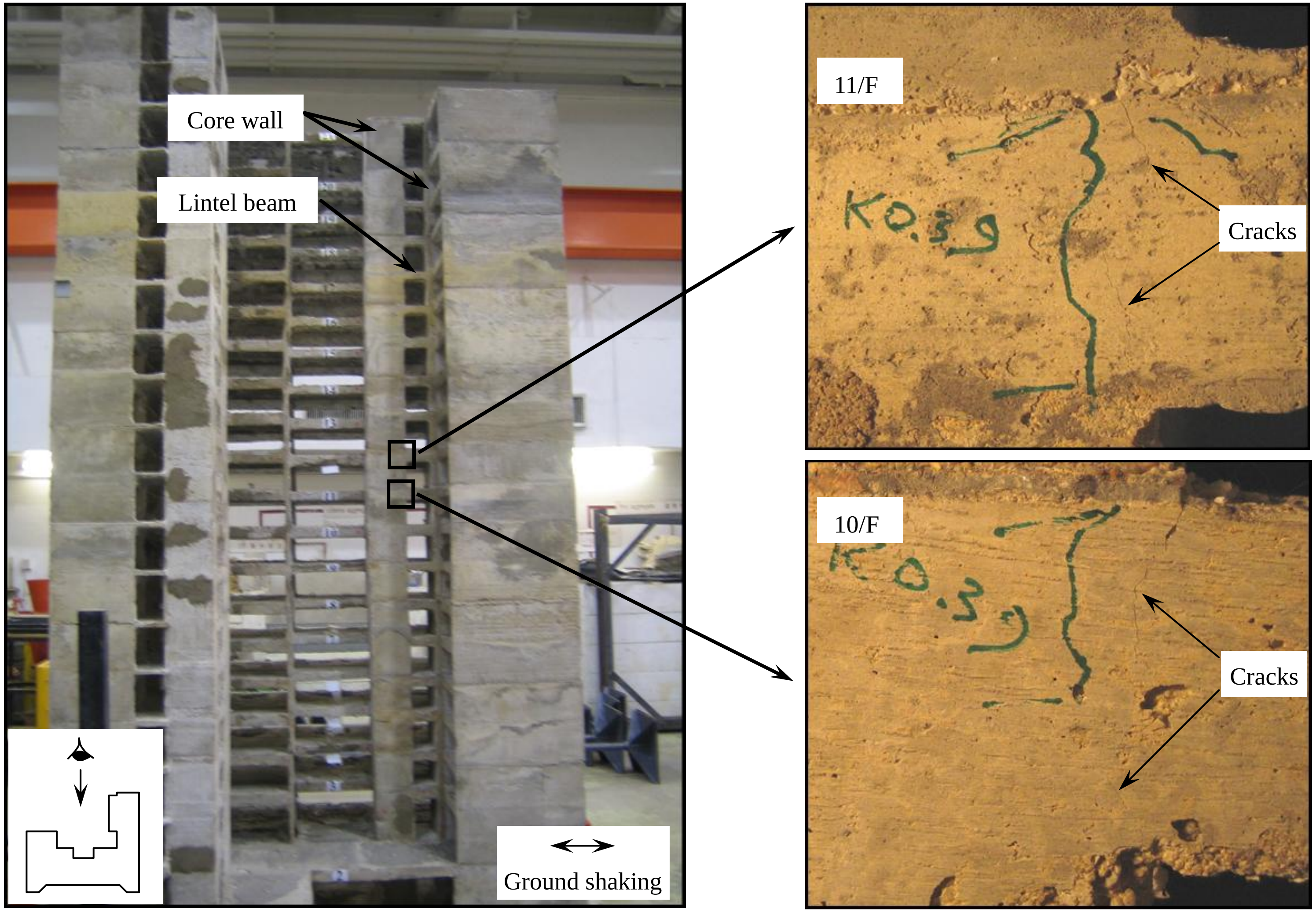

Figure 4.26 Cracks at the ends of lintel beams at the upper floors caused by the 0.3g Kobe earthquake at soil site.

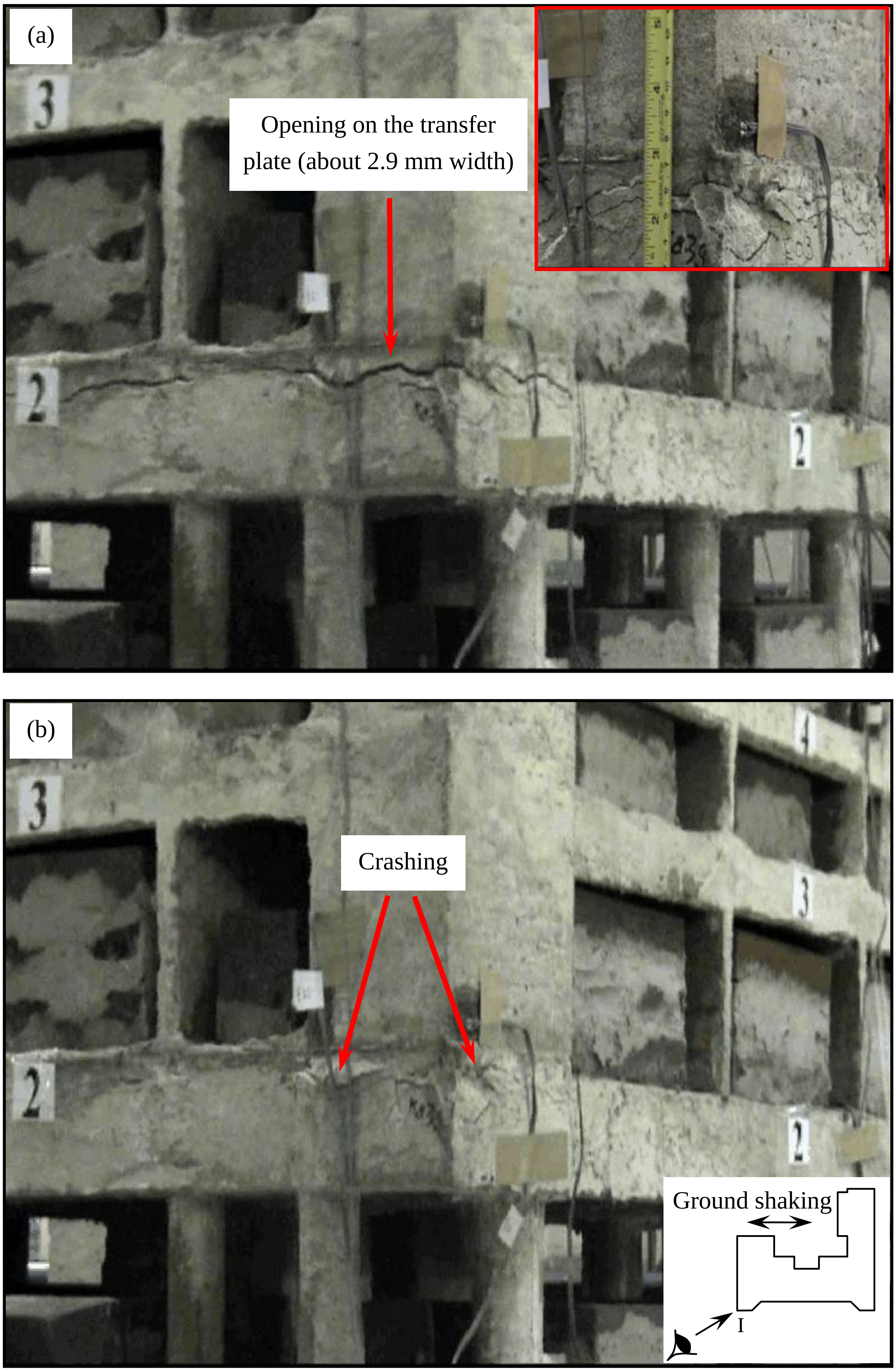

Figure 4.27 Severe damages caused by the 0.3g Chi-Chi earthquake at soil site: (a) the opening due to uplift of the transfer plate as wide as 2.9 mm; (b) the crashing down following the uplift.

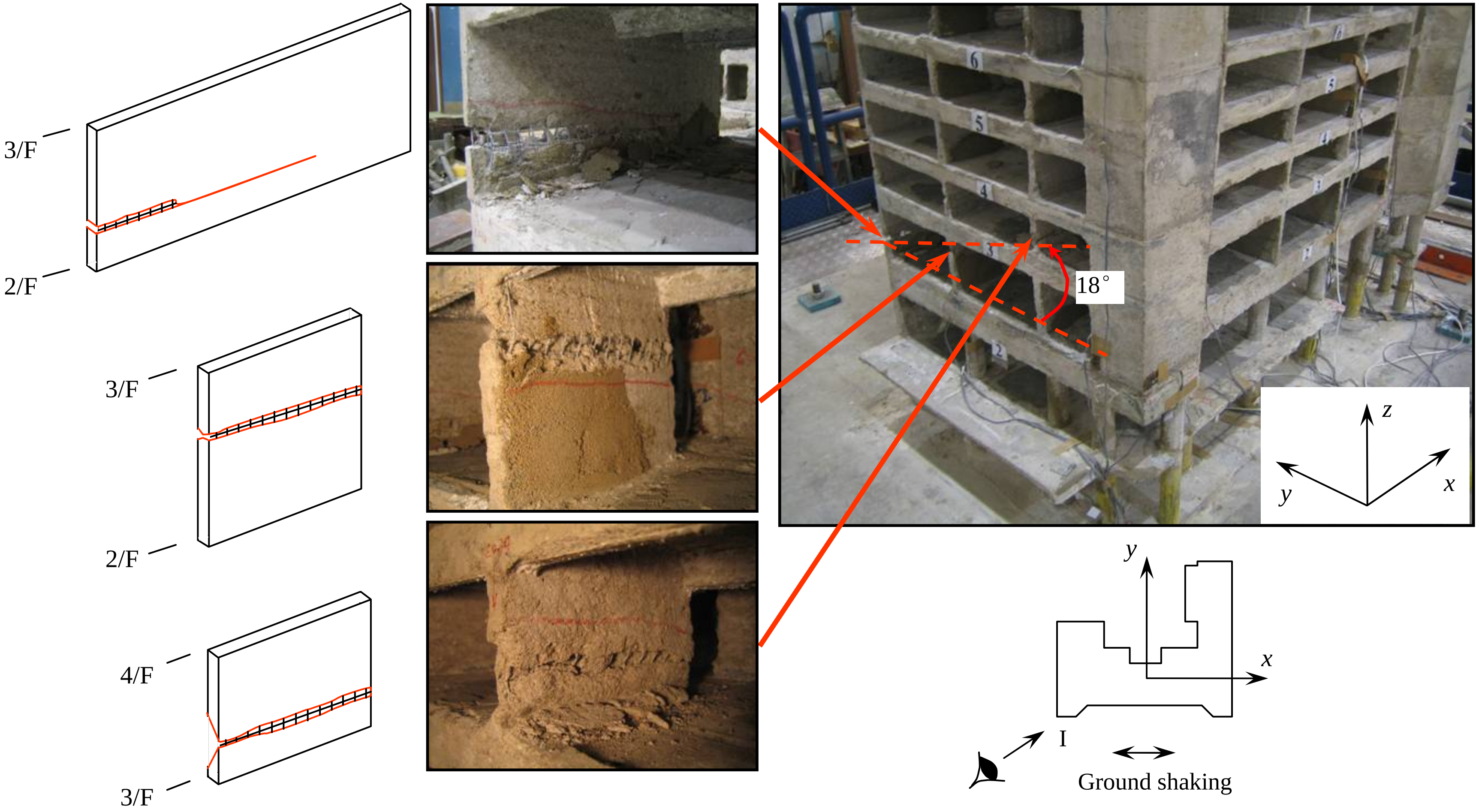

Figure 4.28 3D sketches and photographs of three severely damaged walls between 2/F and 4/F.

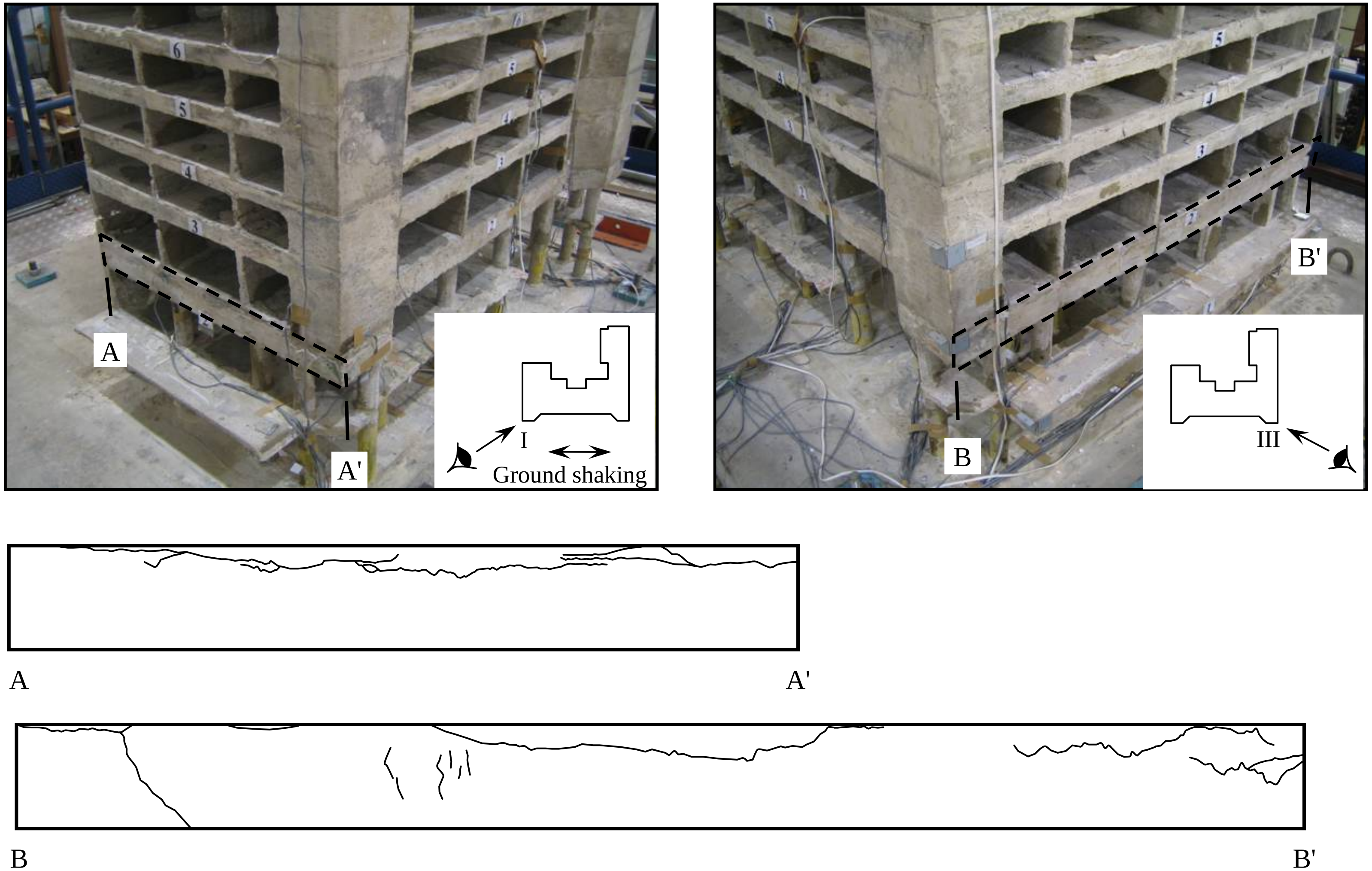

Figure 4.29 Sketches of cracks on the beams of the transfer plate which suffered severe damages during the 0.3g Chi-Chi earthquake input.

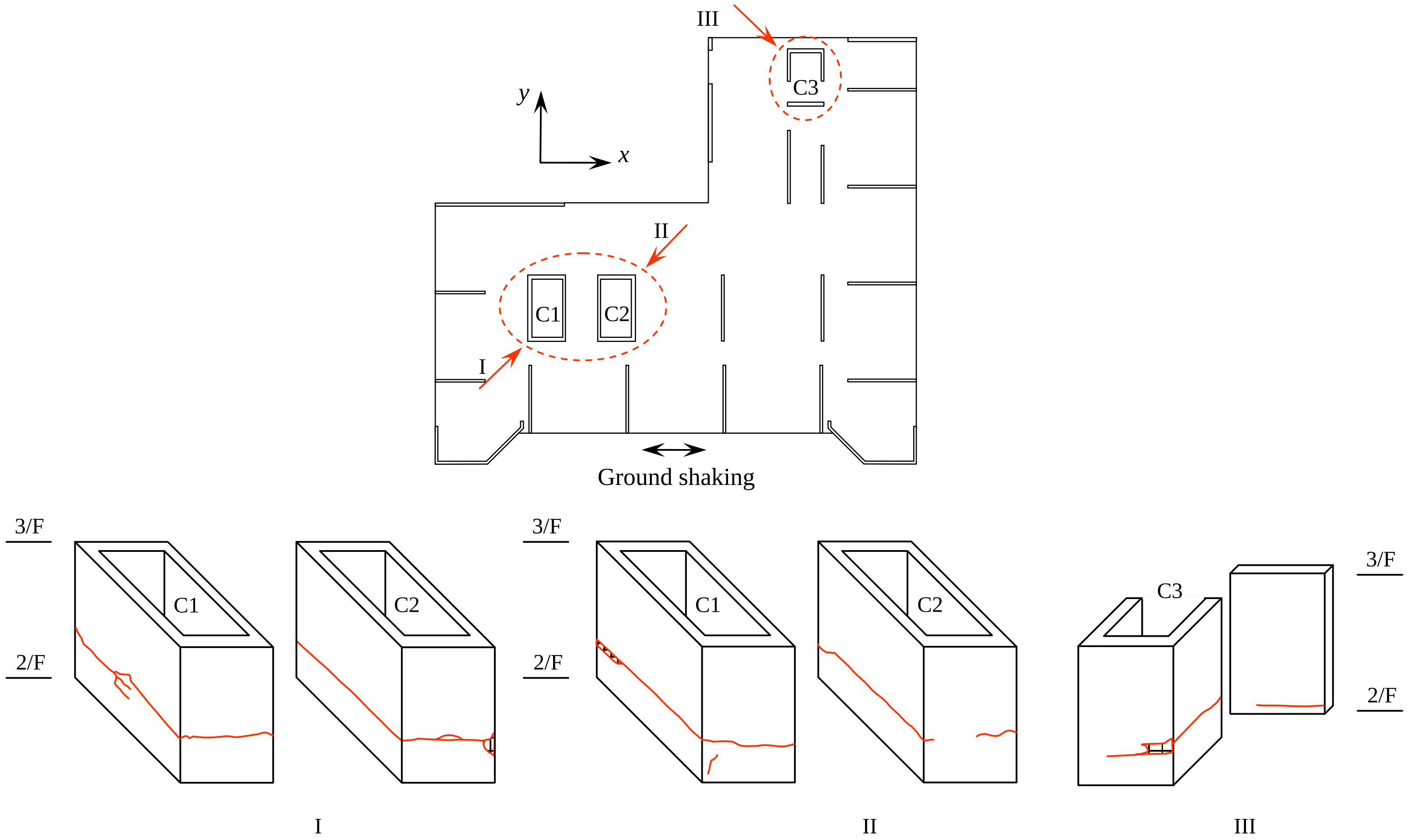

Figure 4.30 3D sketches of cracks on the core walls above the transfer plate caused by the 0.3g Chi-Chi earthquake at soil site.

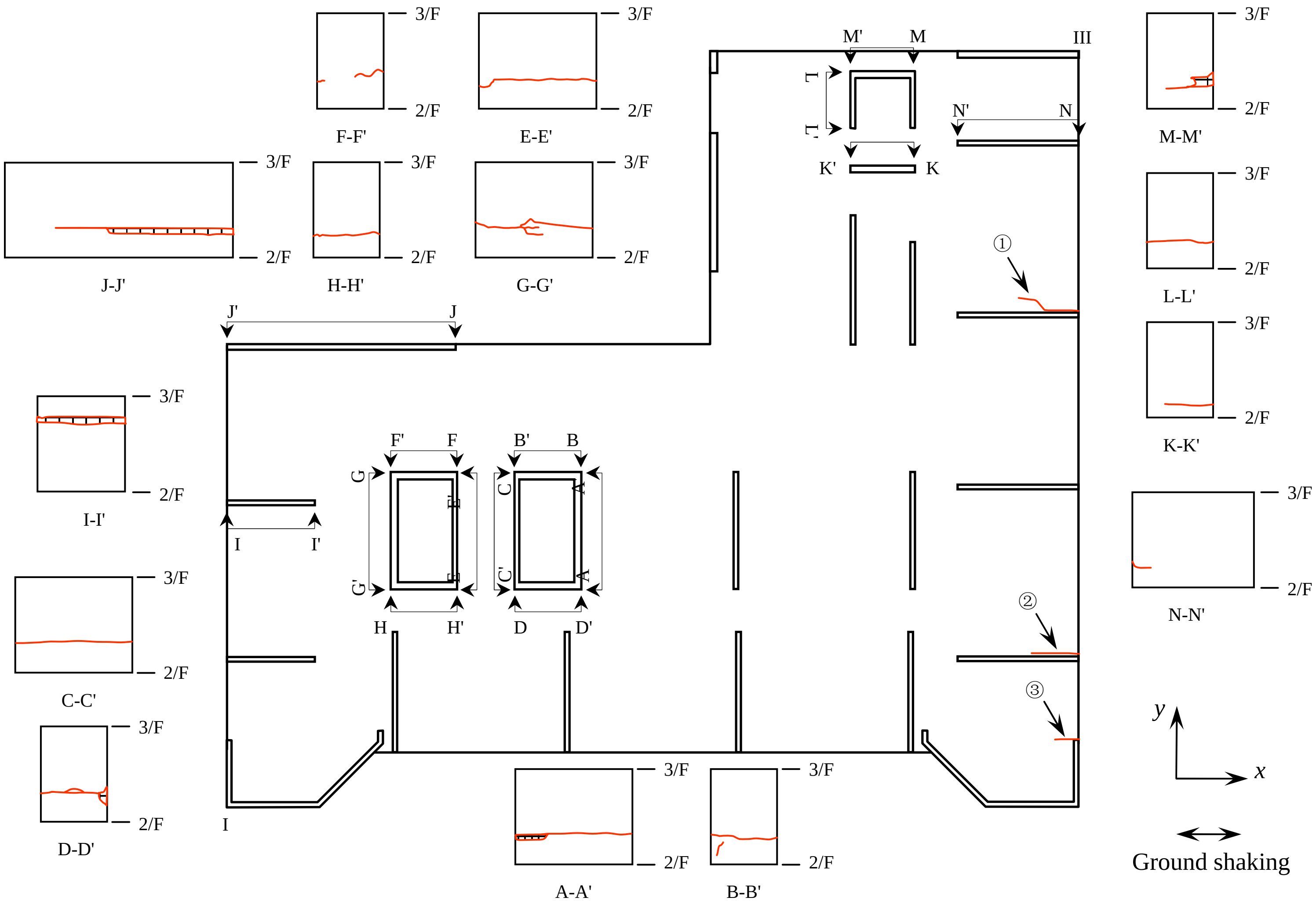

Figure 4.31 Sketches of cracks occurred at the story above the transfer plate caused by the 0.3g Chi-Chi earthquake at soil site.

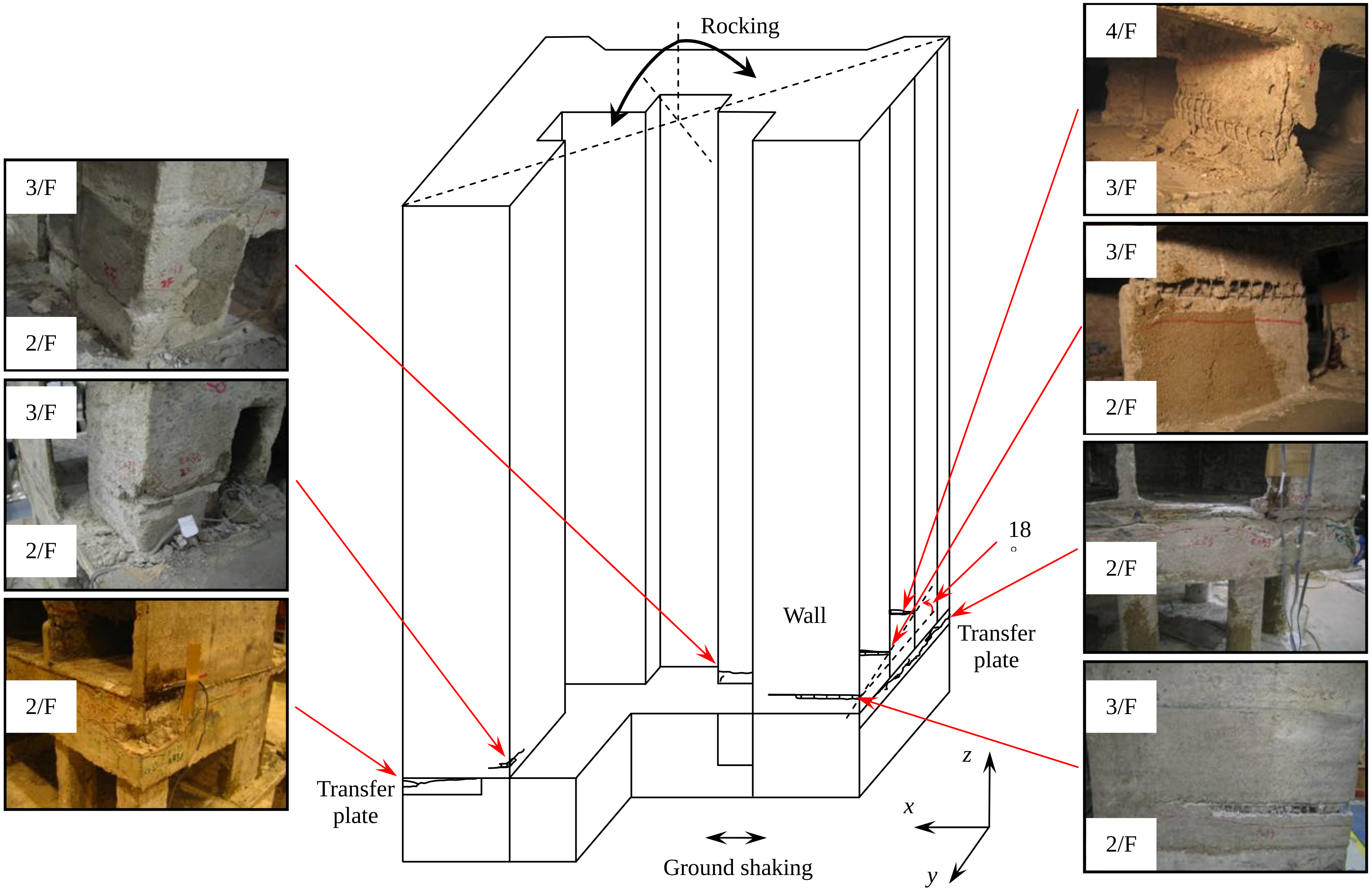

Figure 4.32 Sketch showing the diagonal rocking of the whole structure, which induced severe damage to the transfer plate as well as several walls above it (see attached photos) during the input of 0.3g Chi-Chi earthquake at soil site.

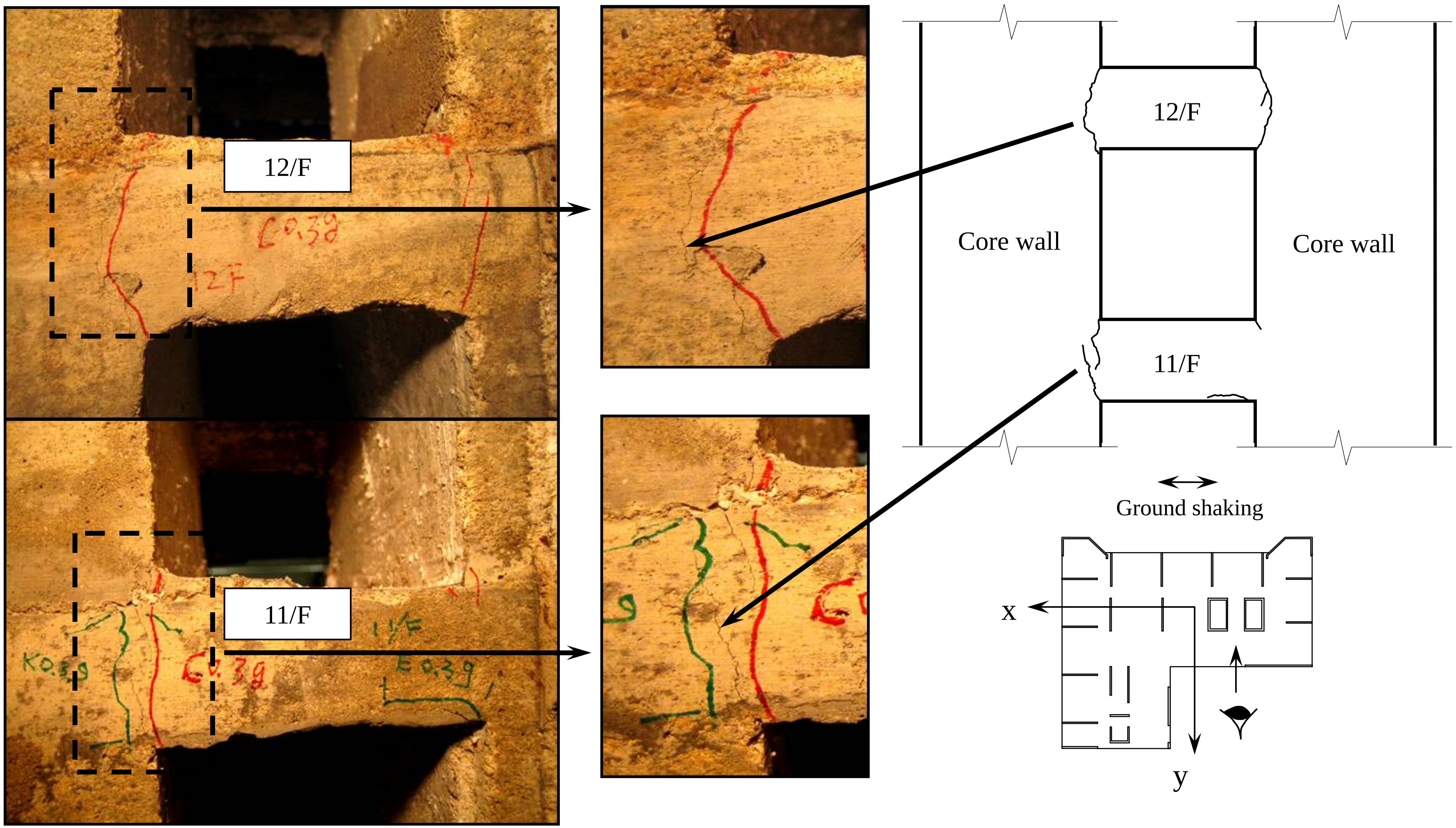

Figure 4.33 Photos and sketches of different crack patterns on the lintel beams between the two core walls. Some cracks were connected with each other, such as those at 12/F, whereas some were separated, such as those at 11/F. Similar phenomena were also found at other stories.

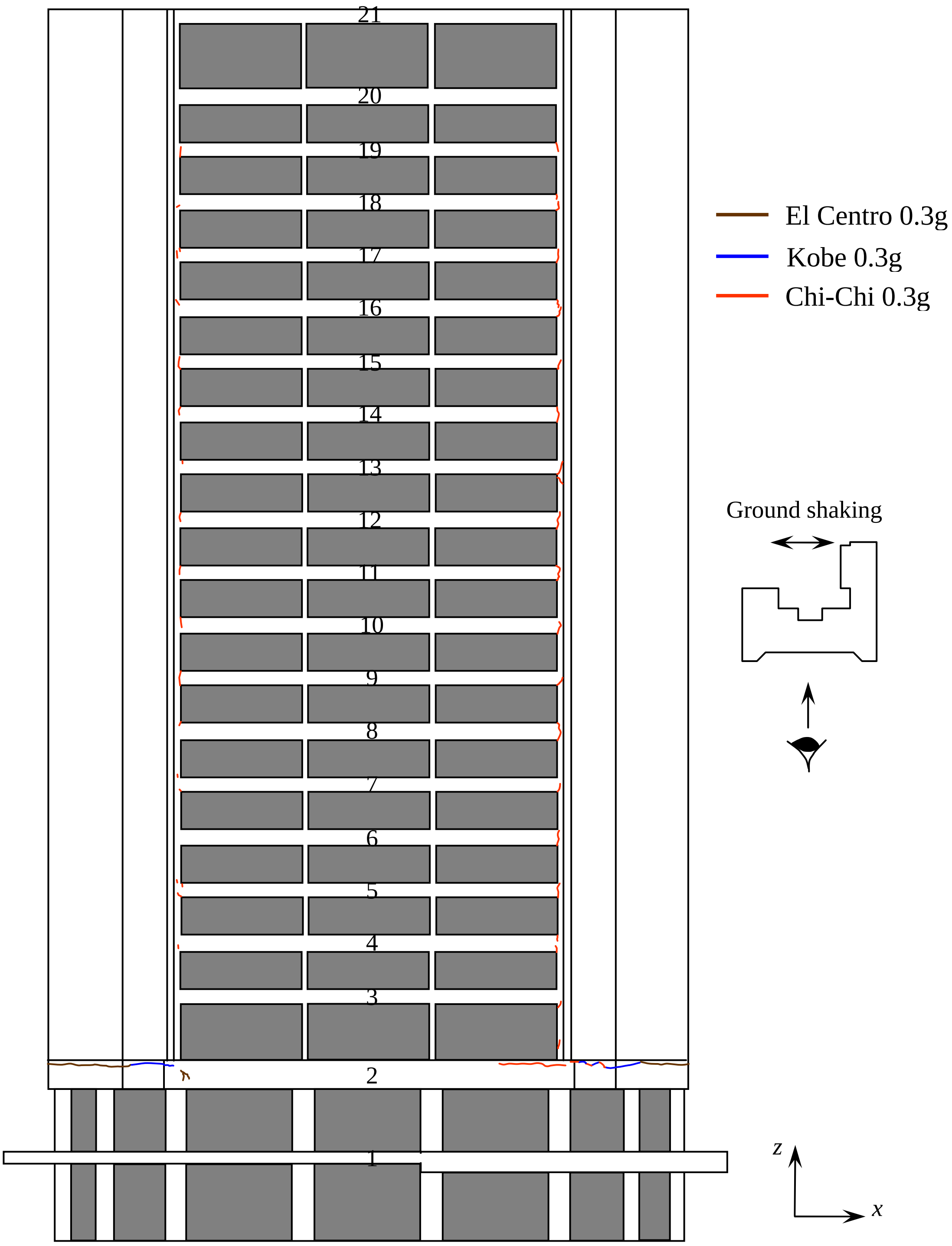

Figure 4.34 Sketches of all the cracks on the front surfaces of the model.

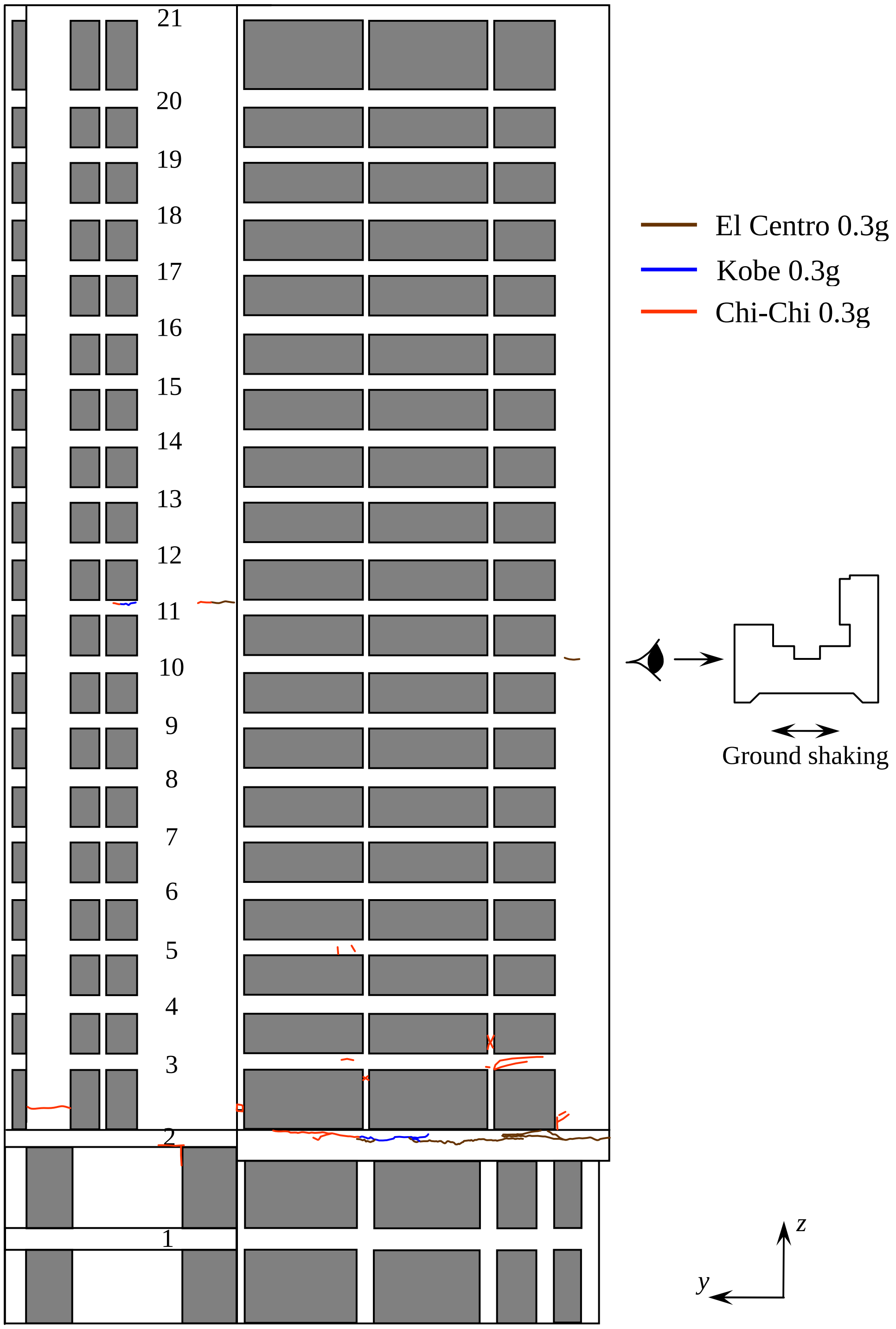

Figure 4.35 Sketches of all the cracks on the right surfaces of the model.

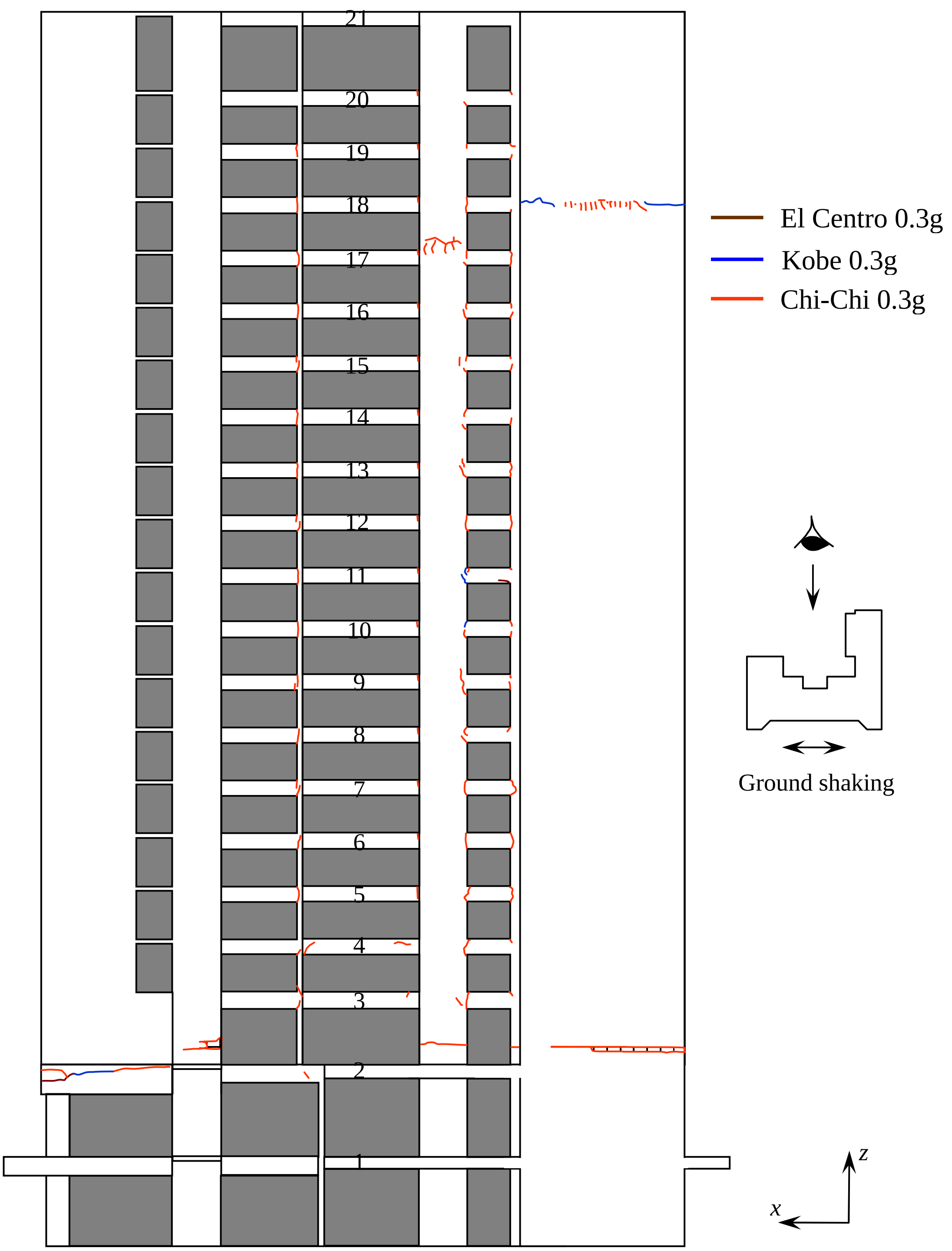

Figure 4.36 Sketches of all the cracks on the rear surfaces of the model.

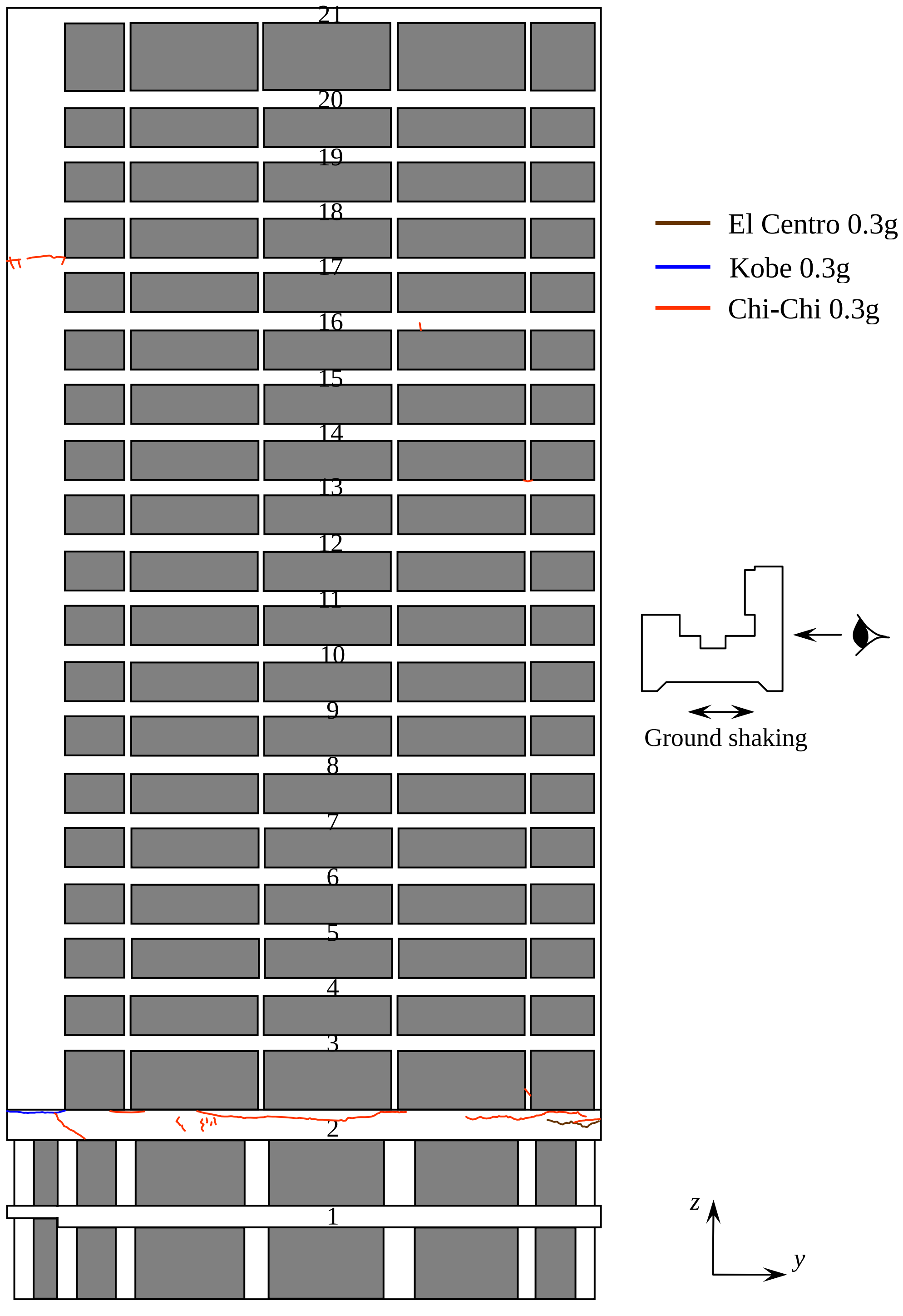

Figure 4.37 Sketches of all the cracks on the left surfaces of the model.

CHAPTER 5 SHAKING TABLE TESTS II: DAMAGE EVALUATIONS

In addition to visual inspections of cracks described in the last chapter, the damages of the model should better be quantitatively evaluated through seismic damage indices, as will be done in this chapter. Various damage indices proposed in the past will be first briefly reviewed.

5.1 Literature Review of Seismic Damage Indices

5.1.1 Classification of seismic damage states

There is little published information on methods to classify seismic damage states available to use by engineers (Williams and Sexsmith, 1995). The guidance given by ATC (Applied Technology Council) in ATC-20 (1989) essentially assesses structures as safe or unsafe based on a wide range of structural criteria, such as crack size, extent of spalling and number of leaning columns.

In assessing the damages of nine reinforced concrete buildings damaged in the 1971 San Fernando earthquake and 1978 Miyagiken-Oki earthquake, Park et al. (1985) adopted a 5-degree damage state classification based on physical appearance as:

- Slight – Sporadic occurrence of cracking.
- Minor – Minor cracks throughout building. Partial crashing of concrete in columns.
- Moderate – Extensive large cracks. Spalling of concrete in weaker elements.
- Severe – Extensive crashing of concrete. Disclosure of buckled reinforcements.
- Collapse – Total or partial collapse of building.

The representative photographs showing the damages of the nine buildings corresponding to the 5 degrees of damage states are shown in Figure 5.1 (after Park et al., 1985). According to the authors, the first three degrees of damages are considered to be repairable whereas the latter two degrees correspond to damages beyond repairing.

Okada and Takai (2004) summarized several damage scales and visualized them in graphical format as shown in Figure 5.2. From the figure, both EMS-98 (European Macroseismic Scale 1998) and AIJ-1980 (Architectural Institute of Japan) ranked damage into 5 degrees according to visual distresses of buildings after earthquakes, whereas Okada and Takai (2000) classified damage into 3 ranks only (i.e. moderate, heavy and major damages).

Some other methods try to relate damage to repairability of buildings. For example, Bracci et al. (1989) and Stone and Taylor (1993) used the following classifications: undamaged or minor damage, repairable, irrepairable, and collapsed. These classifications may be more helpful in retrofit decision-making.

Most of classification methods mentioned above concentrate on damages of structural elements in buildings. However, although protection of structural element is obviously crucial to structural behavior and life safety, non-structural components represent a rather large proportion of building investment and should also be given some considerations in seismic damage assessments. For example, EERI (Earthquake Engineering Research Institute) (1994) adopts a damage scale which includes consideration of non-structural damages (Williams and Sexsmith, 1995).

Since only structural members are modeled in our shaking table tests, the damage classification used by Park et al. (1985) was adopted to rank the damage states of the model in this study. This classification method is relatively simple and directly defined. More important is that Park and Ang (1985) damage index, which is widely used (Williams and Sexsmith, 1995), has been well calibrated to this 5-degree damage state classification.

5.1.2 Seismic damage indices

Seismic damage indices provide a quantitative way to assess damages of structures caused by earthquake in terms of numerical values. They play an important role in post-earthquake assessment. For example, they can help people to decide whether a building is safe to enter immediately for rescue after an earthquake and whether it is safe to be used in the future or what kind of retrofit is needed. In addition, damage indices help in disaster planning before earthquakes — they can help us to estimate the likely damages of buildings when subjected to certain levels of earthquake shaking.

Different damage indices have been proposed in the past several decades and generally they can be categorized into two main classes: local indices and global indices. Local indices assess damage of any individual element or joint whereas global indices assess damage states of the whole structures. Various damage indices proposed in the past will be briefly reviewed below.

Park and Ang (1985) suggested that damages in reinforced concrete elements may be induced by: (i) excessive deformations under monotonic loading; and (ii) accumulated damages caused by repeated cyclic loading. Therefore, to evaluate the damage state of an element or structure, a damage index should include the effects of both the maximum deformation and repeated cyclic loading.

Two primitive and simple forms of damage indices are ductility and inter-story drift. Ductility is defined as the ratio of the maximum deformation of an element during earthquake to the deformation value when the element first yields. Inter-story drift (*ID*) is the displacement of one story relative to the story below whereas inter-story drift ratio (*IDR*) is the ratio of the inter-story drift to the story height. Despite both of them fail to include the cumulative damage caused by repeated cyclic loading, ductility and inter-story drift remains widely used for their simplicity and ease of interpretation (Williams and Sexsmith, 1995).

Other damage indices which consider only the maximum deformation effects include the Damage Ratio (Lybas and Sozen, 1977), and the Flexural Damage Ratio (Banon et al., 1981), and the damage index proposed by Khashaee (2005). These indices not only fail to include the cumulative damages caused by cyclic loading, but also need to be well calibrated against observed damage levels.

A number of cumulative damage indices have also been proposed to include cyclic loading effects. The cumulative damage is measured as a function of either accumulated plastic deformation or hysteretic energy absorbed during cyclic loading (Williams and Sexsmith, 1995). This kind of damage index includes the normalized cumulative rotation (NCR) (Banon et al., 1981) and the indices proposed by Gosain et al. (1977), Krawinkler and Zohrei (1983), Stephens and Yao (1987), Wang and Shah (1987), Chung et al. (1987), Kratzig et al. (1989), and Hindi and Sexsmith (2001), etc.

Park and Ang (1985) proposed a damage index which combined the normalized maximum deformation and energy absorption in cyclic loading through a linear summation. This damage index has been widely used for its simplicity and its well calibration against a large amount of observed seismic damages (Williams and Sexsmith, 1995), and will be introduced in detail in Section 5.1.3.

Global damage index measures the overall damage state of a structure, which depends on the severity as well as the distribution of local damages of its constituting members (Williams and Sexsmith, 1995). Thus, naturally the global damage index can be derived by taking the weighted average of the local indices. The most widely used approach is to take an average of the local indices weighted by the local energy absorptions as (Park et al., 1985; Chung et al., 1989; Kunnath et al., 1992):

$$D = \frac{\sum D_i E_i}{\sum E_i} \tag{5.1}$$

where D_i and E_i are the local damage index and energy absorbed at the i^{th} element, and D is the global index of the structure.

Another method for evaluating global damage is to compare overall dynamic characteristics of a structure before and after damage, such as natural period and damping. This kind of damage assessment method originates from a basic idea that damage normally causes stiffness degradation and energy dissipation to structures, which results in change of structural dynamic characteristics, such as increase of natural period and damping. Usually change of natural period is used to estimate overall damage state of a structure whereas change of mode shape is used to locate the position of damage (Williams and Sexsmith, 1995).

DiPasquale and Cakmak (1987) proposed a series of softening indices based on change of structural fundamental period. First, the time-varying fundamental period of a structure was estimated from the response time history. Then, the change in the fundamental period was used to calculate different softening indices, including the maximum softening

$$D_m = 1 - \frac{T_{und}}{T_m}, \tag{5.2}$$

the plastic softening

$$D_{pl} = 1 - \frac{T_{dam}^2}{T_m^2}, \tag{5.3}$$

and the final softening

$$D_F = 1 - \frac{T_{und}^2}{T_{dam}^2}, \tag{5.4}$$

where T_{und} and T_{dam} are the fundamental periods of the structure before and after damage respectively, and T_m is the maximum period during the whole time history.

From the definitions, the response time history of a structure during earthquake is needed to determine the maximum and the plastic softening indices. However, the final softening can be computed directly from the results of post-earthquake testing, if the initial natural period is known. In this sense, the final softening index is especially useful when no detailed response data is available.

According to Rodriguez-Gomez and Cakmak (1990), the final softening is related to the global stiffness degradation. Actually, for a SDOF system, utilizing the relation $T = 2\pi\sqrt{m/k}$ (where m, k and T are the mass, stiffness and natural period respectively), the final softening given in Equation (5.4) becomes

$$D_F = 1 - \frac{k_{dam}}{k_{und}} \tag{5.5}$$

where k_{und} and k_{dam} are the stiffness of the system before and after damage. It is easy to know that the final softening D_F has a zero value at the initial state and a unity value at failure. However, little information is available to correlate the final softening to intermediate damage levels between elastic state and failure.

The main limitation of the softening indices is that they can provide only an assessment of global damage state of a structure but little information about the distribution of damage within the structure is available. The location of damages can be determined using detailed mode shape information. This is a large and rapidly developing subject currently (Williams and Sexsmith, 1995), but beyond the scope of the present study.

5.1.3 Park and Ang damage index

5.1.3.1 Definition

The most widely used damage index may be the one proposed by Park and Ang (1985). Its popularity partly is due to its simplicity – it consists of a simple linear combination of normalized maximum deformation and energy absorption in cyclic loading as:

$$D = \frac{\delta_m}{\delta_u} + \frac{\beta}{Q_y \delta_u} \int dE \tag{5.6}$$

where δ_u is the ultimate deformation of a member under monotonic loading, δ_m is the maximum deformation under earthquake, Q_y is the calculated yield force, dE is the incremental absorbed hysteretic energy, and β is a non-negative constant coefficient for cyclic loading effect determined from experiments. In this definition, δ_m and $\int dE$ depend on the applied loading history, whereas the other three parameters δ_u, Q_y and β are structural parameters.

Through trial and error analyses of a large set (261) of cyclic test data of beams and columns, Park and Ang (1985) gave regression equations for the optimal values of β, which depends on shear span ratio, axial stress, longitudinal steel ratio and confinement ratio of the element. A large scatter was observed between the calculated values of β through the regression equations and experimental results. Park et al. (1987) performed a regression analysis based on test data of 402 reinforced concrete components of rectangular cross-sections and 132 steel specimens of H-shaped sections and proposed a new minimum-variance solution for β. They suggested

$\beta = 0.05$ for reinforced concrete components and $\beta = 0.025$ for steel components. Therefore, $\beta = 0.05$ was adopted in the present study.

5.1.3.2 Advantages

The advantages of Park and Ang damage index are based on its simplicity and that it takes into account of both the maximum deformation effect and the cumulative damage caused by cyclic loading. In addition, compared to other seismic damage indices, Park and Ang index has been well calibrated against a large amount of observed damages in both experiments and real earthquakes.

The earliest calibration work was carried out by Park et al. (1985), who carried out thorough analyses for nine reinforced concrete buildings damaged during the 1971 San Fernando earthquake in USA and the 1978 Miyagiken-Oki earthquake in Japan. Based on the observed damages from post-earthquake investigations, the damages states of the nine buildings were ranked into five degrees (i.e. slight, minor, moderate, severe damages and collapse) as described in Section 5.1.1.

In order to calculate Park and Ang damage indices for these buildings, Park et al. (1985) used a hybrid model to idealize reinforced concrete buildings by extending the conventional shear-beam model. Elastic bending columns were added between floors, connected by inelastic rotational springs. The overall damage index was estimated as the weighted average of the local damage indices of its constituting members. The resulting Park and Ang damage indices were then compared to the designated damage states from post-earthquake investigations as shown in Figure 5.3, where the symbols A-I represented the nine buildings studied.

Using this calibration results, Park et al. (1985) concluded that an overall damage index of $D \le 0.4$ corresponds to repairable damage, $D > 0.4$ represents damage beyond repair, and $D \ge 1.0$ corresponds to collapse. More recently, Ang et al. (1993) recommended that a global damage index of 0.8 may be considered as the value to cause collapse. Based on these two calibration work as well as Figure 5.3, we drew the following conclusions between the values of Park and Ang damage indices and damage degrees as well as building repairabilities:

$D < 0.12$	None or slight damage (repairable)
$0.12 \le D < 0.25$	Minor damage (repairable)
$0.25 \le D < 0.4$	Moderate damage (repairable)
$0.4 \le D < 0.8$	Severe damage (irrepairable)
$D \ge 0.8$	Collapse (irrepairable)

These correlations are similar to conclusions drawn by other authors (e.g. Williams and Sexsmith, 1995; Ghobarah et al., 1999; Vacareanu et al., 2004), except for the borderline value between none and minor damages, which was set to 0.1 by previous studies (e.g. Williams and Sexsmith, 1995) but was set to 0.12 here (the middle value between the overall damage indices of H and D buildings in Figure 5.3).

5.1.3.3 Limitations

Although Park and Ang damage index has been widely used since it was proposed in 1985, several limitations still exist. A major problem is the determination of the ultimate deformations δ_u and the constant coefficient β (Williams and Sexsmith, 1995). The estimations of β given by different researchers (Park et al., 1987; Kunnath et al., 1992; Cozenza et al., 1993) seem to be scattered. Park and Ang (1985) gave regression expressions for the optimal values of β as function of shear span ratio, axial stress, longitudinal steel ratio and confinement ratio. Park et al. (1987) suggested β=0.05 for reinforced concrete components and β=0.025 for steel components. Kunnath et al. (1992) used a default value of 0.1 and suggested that it should normally not exceed 0.5 in the computer program IDARC (Inelastic Damage Analysis of Reinforced Concrete Structures). Cozenza et al. (1993) suggested the value β have a median of 0.15 and with this value Park and Ang damage index correlated well with the results of other damage models proposed by Banon and Veneziano (1982) and Krawinkler and Zohrei (1983).

The second drawback is that according to the definition in Equation (5.6), the value of Park and Ang damage index may be greater than zero for elastic response and greater than unity when the structure reaches its maximum deformation capacity under monotonic loading (Bozorgnia and Bertero, 2003). Several modifications have been proposed to overcome this drawback. For example, Park and Ang index can be slightly modified by removing the recoverable deformation from the first term in its definition as following:

$$D = \frac{\delta_m - \delta_y}{\delta_u - \delta_y} + \frac{\beta}{Q_y \delta_u} \int dE \qquad (5.7)$$

Kunnath et al. (1992) used a similar expression in IDARC by replacing force and displacement with moment and curvature. More recently, Bozorgnia and Bertero (2003) proposed two improved damage indices which overcome the drawback of Park and Ang index. Both the two indices will be zero for elastic response and be unity at failure. However, two constant coefficients are involved in their definitions, which are not straightforward to be determined.

Finally, the definition of Park and Ang damage index is directly applicable only for a single structural element and the global damage index of a building can only be obtained from the weighted average of local indices. This weighted average method is acceptable in numerical simulations, but is difficult to be applied to structures in experiments or real earthquakes. Even in laboratory environments, it is very difficult, if not impossible, to directly measure the force and response of each element. Normally structural responses (accelerations and/or displacements) are measured at every one or several floors rather than for each element. Therefore, how to estimate Park and Ang damage index for a building structure from recorded data in experiments or earthquakes remains an unsettled issue. To solve this problem, a simple approach was proposed in this study, and will be discussed in Section 5.2.4.

5.1.4 Damage indices adopted in the present study

All of the seismic damage indices discussed above are summarized in Table 5.1, where the term "Member level" means the damage index can be applied to individual members, and the term “Structural level” means the damage index can be applied directly to structures. Among them, some indices, such as the normalized cumulative rotation (Banon et al., 1981) and the indices proposed by Krawinkler and Zohrei (1983), Chung et al. (1987), Kratzig et al. (1987), and Hindi and Sexsmith (2001), are too demanding to be applied in our tests where the structural responses are measured only at some selected floors. Some indices are not well calibrated with observed damages, such as the damage ratio, the flexural damage ratio, and the indices proposed by Gosain et al. (1977), Krawinkler and Zohrei (1983), Kratzig et al. (1989), and Khashaee (2005). Some indices involve extra parameters which are not straightforward to be determined, such as those proposed by Krawinkler and Zohrei (1983), Stephens and Yao (1987), Wang and Shah (1987), and Khashaee (2005).

With all these considerations, four indices were selected to analyze damages for our shaking table tests, including the ductility, inter-story drift ratio, final softening index and Park and Ang damage index. Ductility and inter-story drift ratio were selected for their simplicity, wide adoption and ease of interpretation. The final softening index was selected since it is easy to be obtained, and it was used to assess the change of natural frequency of the model. In this study, the variation of natural frequency will also be expressed directly by the frequency ratio of the model after and before damage.

Park and Ang damage index was selected for their wide adoption and its well calibration against observed damages. In this study, a simple algorithm is proposed to estimate the overall Park and Ang damage index for our model from recorded acceleration and displacement data in the tests. The damage states of the model will be determined based on the resulting Park and Ang indices. This damage information will be used to establish correlations between damage states and other damage indices, including the ductility, inter-story drift ratio, final softening index, and frequency ratio. The details will be discussed further in Section 5.3.

5.2 Damage Quantifications

In this section, the damages of the model during various earthquake inputs will be quantitatively assessed in terms of the selected damage indices as discussed in Section 5.1.4. These damage indices include the inter-story drift ratio, ductility, final softening, natural frequency ratio, and Park and Ang damage index. The results of these indices will be discussed one by one in this section.

5.2.1 Inter-story drift ratio

Both the inter-story drift ratio and overall drift ratio at the roof are studied in our tests. The inter-story drift ratio (*IDR*) is the relative drift between two neighboring stories divided by the story height, whereas the overall drift ratio ($IDR_{overall}$) is the total drift at the roof relative to the ground divided by the total height of the building. Note that before calculation, all the displacement data with frequency higher than 15

Hz were filtered out to eliminate high frequency noises. The noise may come from the vibration of the shaking table or the noise of the displacement transducers, especially those LED transducers as described in Section 3.5.1.

Due to the limited number of transducers available in our laboratory, the displacement responses are available only at the ground, 2/F, 3/F and 21/F as shown in Figure 3.19. To compute the inter-story drift ratios at other stories, linear interpolation method was used to estimate the displacement responses at other floors. More specifically, the displacement on 1/F was estimated from the linear interpolation between the ground motion and the displacement on 2/F. The displacements at the floors above 2/F were estimated from the interpolation between the recorded displacements on 21/F and 2/F. Note that the displacement data on 2/F instead of 3/F was used because the laser transducer on 2/F has a higher accuracy than the LED transducer on 3/F (refer to Section 3.5.1). Since there is no abrupt change of structural form and stiffness for those typical floors above the transfer plate (2/F) and the first mode dominates in the vibrations, the linear interpolation method is considered to be appropriate for most of our experiments, if not all.

To check the validity of the linear interpolation method, comparisons were made between measured data and interpolation results. Figure 5.4 shows the displacement responses at 15/F, 9/F and 3/F respectively during the input of 0.2g Kobe earthquake at rock site. The dashed lines are the estimated displacements from the linear interpolation of recorded displacement data, whereas the solid lines denote either the displacements obtained from the double integration of recorded acceleration data at

15/F and 9/F [Figures 5.4(a) and (b)], or the displacements directly measured by the LED transducer at 3/F [Figures 5.4(c)]. It is seen that these results agree quite well except for some minor discrepancies, suggesting the interpolation method is adequate to be used for most of our tests, if not all.

Based on the estimated displacement data, the inter-story drift ratios can be easily computed. The resulted overall and maximum story drift ratios for various earthquake inputs are summarized in Table 5.5 and plotted with the input PGAs in Figures 5.5 and 5.6 respectively. From the two figures, it is seen that both the overall drift ratio and inter-story drift ratio increases almost linearly with the increase of input PGA for all the earthquakes at rock site, except for the maximum *IDR* curve of El Centro earthquake. The curves for Northridge and Loma Prieta earthquakes almost coincide with each other, and their drift ratios are the smallest compared to the results of the other three earthquakes. As discussed in Section 4.3.2, it is because their dominant frequencies do not coincide with that of the model (see Figures 4.3 and 4.4).

For earthquakes after soil amplification, Figures 5.5(b) and 5.6(b) show that the drift ratio increases with the input PGA, and the increase rate becomes larger for PGA>0.2g. Again it is due to the deteriorated natural frequency becomes closer to the predominant frequencies of the soil site shaking inputs (see Figures 4.1-4.5).

5.2.2 Estimated ductility

By definition, ductility is the ratio of the maximum deformation of a structure during earthquake (δ_m) to the deformation when it first yields (δ_y). The maximum deformation of the model can be readily obtained from displacement time history records. However, the yield deformation can not be measured directly from experiments and need to be estimated through other methods.

As suggested by the Structural Engineers Association of California (SEAOC, 1999), buildings with a transient drift ratio not greater than 0.2% (i.e. 1/500) can be considered to be fully operational (i.e. negligible damage). The wind code of Hong Kong also requires that the maximum top floor drift to height ratio must be limited to within 1/500 in the wind design (Koo et al., 2003). Therefore, in this study the yield drift ratio was set to 1/500. That is to say, the yield deformation (δ_y) at the roof was 1/500 of the total height, which was equal to 5.57 mm.

However, since the present model had a transfer plate at 2/F and the stories below and above the transfer plate adopted totally different structural forms (refer to Section 2.2), a uniform yield drift ratio of 1/500 seems inappropriate for all the stories. Thus, as sketched in Figure 5.7(b) the structure was further divided into two segments: one above and one below the transfer plate (with heights of $H_1 = 406$ mm and $H_2 = 2380$ mm respectively). The ratio between the yield drifts of the two segments were estimated from the displacement records in the hammer blow tests conducted at the beginning of tests. During the hammer tests, the average ratio of the maximum deformations of the two segments at a same time [$d_2 / d_1 = 7.62$ as shown in Figure 5.7(b)] can be obtained. The model was far from yielding under hammer blow excitation. But since up to yielding elastic responses should hold, this ratio is taken as the ratio between the yield drifts of the two segments. Thus, while the total yield drift at the roof remains to be 1/500 of the total height, the yield drifts of the two segments can be determined proportionally according to this ratio (see the equations in Figure 5.7). As a result, a 1/628 yield drift ratio was assumed for the two stories below the transfer plate and a 1/483 yield drift ratio for the upper typical stories. After the yield drift ratios of the two segments were determined, the yield deformation of each story (δ_{yi}) can be easily obtained by multiplying the yield drift ratio with the story height.

Therefore, ductility can be estimated for each story provided that the displacements at those stories were estimated through linear interpolation of available data (as described in Section 5.2.1). Once the displacement at each story was obtained, the relative deformation of each story with respect to the story below can be easily computed. Then, the maximum deformation (δ_m) within the time history record was used to calculate the ductility at that story. Finally, a maximum ductility was selected among all the stories with the most severe damage.

The maximum ductility values caused by various earthquakes are listed in Table 5.6. Ductility was found larger than 1.0 for the first time during the shaking of 0.2g Kobe earthquake at soil site, which means the structure began to yield at that time. The maximum ductility 8.519 occurred in the last test (i.e. the input of 0.3g Chi-Chi earthquake at soil site) and the model was considered nearly collapse. The ductility values during various earthquake inputs are also plotted with the input PGAs in Figure 5.8. It can be seen that the curves of ductility are very similar to those of overall drift ratios shown in Figure 5.5 and can be explained in a similar way.

5.2.3 Deterioration of natural frequency

As described in Section 4.2.1, modal test was carried out after each set of earthquake excitations to check the change of natural frequency of the model. The natural frequencies of the first three modes after various earthquake excitations are summarized in Table 5.2. Also shown in the table are the ratios of the damaged natural frequency f_{dam} to the initial value f_{ini}. The frequency ratios and the final softening indices (D_F) of the first natural frequency are also listed in Table 5.6.

From the two tables, the frequency ratio decreases from 100% to 45.5% with increasing PGA and the final softening increases from zero to 0.794. The natural frequency drops more drastically during the shaking of 0.3g PGA inputs. For example, the 0.3g Chi-Chi earthquake alone induces over 19% reduction of the first natural frequency. As described in Section 4.4.4, this earthquake caused the most severe damage to the structure. Note also that during some tests the frequency shows small increase instead of decrease, such as those in the 0.1g Northridge earthquake and 0.15g El Centro earthquake. But this kind of abnormal increase is all very small (less than 1.7%) and may be caused by the uncertainty in the modal testing.

From Table 5.2, it is also seen that the first natural frequency reduced to 45.4% of the initial value, whereas the second and third natural frequencies remained to be about 75% of the initial values. For the present model, the first vibration mode is in the *x* direction (i.e. the shaking direction), and the second and third modes are in the *y* and θ directions respectively (refer to Section 4.2.1). Thus, the large frequency reduction in the x direction implies that the model was most damaged in the excitation direction.

The reduction of natural frequency observed in this study is consistent with the fact that damage usually causes decrease in frequency due to the stiffness degradation (DiPasquale and Cakmak, 1987; Williams and Sexsmith, 1995). The frequency deterioration has been widely observed in other shaking table tests, for example, those of Lee and Woo (2002) and Li et al. (2006).

However, little information is available on what damage states those frequency reductions represent. In the shaking table test of a 42-story building model by Li et al. (2006), it was concluded that a 40% reduction of frequency will occur for severe damage and a 60% reduction of frequency occur for collapse. This conclusion is close to the finding in the present experiments (33% for severe damage and 55% for collapse respectively, as shown in Table 5.6). However, the damage states in Li et al. (2006) were determined through the visual observations in the tests, whereas the reliability of visual inspections is still arguable (Skjaerbaek et al., 1998). In this study, the damage states of the model are determined through the well calibrated Park and Ang damage index, and through this approach the frequency change can also be related to damage states. The details of this analysis will be discussed in Section 5.3.

5.2.4 Method of estimating Park and Ang damage index

In order to use the well calibrated Park and Ang damage index, a simple algorithm was developed in this study to estimate it from the measured acceleration and displacement data in our experiments. First a *N*-story building is modeled as a lumped mass system and each story is idealized as one equivalent element. Each story has a lumped mass m_j and recorded absolute acceleration $\ddot{x}_i(t)$ and displacement $x_i(t)$, *i=1, 2, …, N*. The inter-story relative deformations $\delta_i(t)$ can be obtained from the displacement of each story with respect to the story below:

$$\delta_i(t) = x_i(t) - x_{i-1}(t) \qquad i=1,\ 2,\ \ldots,\ N \tag{5.8}$$

where $x_0(t)$ is the recorded ground motion. The total resisting force for all the structural elements between the i^{th} and $i-1^{th}$ floors can be computed as the summation of the inertial forces of the i^{th} story and all the stories above it.

$$F_i(t) = -\sum_{k=i}^{N} m_k \ddot{x}_k(t) \qquad i=1,\ 2,\ \ldots,\ N \tag{5.9}$$

Then this resisting force F_i and the inter-story deformation δ_i constitute the hysteretic load-deformation relation of each story, from which the dissipated hysteretic energy can be computed through integration. For the discrete data measured in our tests, the integration is replaced by direct summation. For example, the dissipated energy (E_i) by the i^{th} story is calculated as:

$$E_i = \int F_i d\delta_i = \sum_j F_i(t_j)[\delta_i(t_j) - \delta_i(t_{j-1})] \tag{5.10}$$

where t_j denotes the j^{th} time step. As sketched in Figure 5.9(f), the above integration in one cycle equals the closed area in the load-deformation curve and represents the energy dissipated. Finally the story-wise as well as building-wise Park and Ang damage indices can be calculated according to Equations (5.6) and (5.1).

The resisting force estimating from Equation (5.9) include both the spring force and damping force. Thus, at least a part of the dissipated hysteretic energy calculated using the above method is dissipated by damping, which should not be included in estimating structural damages. However, as Toussi and Yao (1983) demonstrated, damping does not have significant effects on responses of structures when subjected to earthquake excitations. In fact, most actual structures have a rather low damping value, typically lower than 20% (Clough and Penzien, 1993), and the present model has a damping lower than 5% (see Section 4.2.2). In addition, for the small value of the constant β [$\beta = 0.05$ for reinforced concrete components according to Park et al. (1987)], the second term in the definition of Park and Ang damage index, which takes account of hysteretic energy effects, is much smaller than and negligible comparing to the first term (Rodriguez-Gomez and Cakmak, 1990). Therefore, we asserted that the estimation of Park and Ang damage index using Equations (5.9-5.10) is accurate for practical applications.

According to the definition in Equation (5.6), the ultimate deformation δ_u and the yield force Q_y need to be determined for each story to calculate the story-wise Park and Ang damage index. In this study, the two parameters were estimated from experimental results and FEM analyses respectively.

There appears to be no reliable method for determining the ultimate deformation of reinforced concrete components (Park and Ang, 1985). Stephens and Yao (1987) assumed the ultimate deformation of a story to be 10% of the story height for cast-in-place concrete frames, but it was also pointed out that this value required further verification. In this study, the maximum deformation at the roof during the last shaking table test (i.e. the 0.3g Chi-Chi earthquake input at soil site) was assumed to be the ultimate deformation of the model, which was 42.87 mm and equal to about 1/65 of the total height. During this test, the model was severely damaged and was close to the state of nearly collapse (refer to Section 4.4.4 for details). This will underestimate the model stiffness, since the model did not collapse during this test. But since there is no available reliable method for determining the ultimate deformations, it is believed that this value provides an acceptable approximation to the ultimate deformation of the model. This ultimate deformation at the top floor was then distributed to each story to estimate the story ultimate deformation in the same way of distributing the story yield drift as discussed in Section 5.2.2.

The story yield force Q_{yi} was computed through FEM analyses based on the yield inter-story drift δ_{yi} estimated in Section 5.2.2. Using the FEM model built in SAP2000 (refer to Section 2.3.1 for details), the yield strength Q_{yi} of the i^{th} story was estimated in the following way: (a) all translational and rotational degrees of freedom of all the vertical elements of that story are fixed at the bottom (i.e. above the $i-1^{\text{th}}$ floor slab); (b) a horizontal force F_i was applied at the center of mass of the i^{th} floor slab; (c) recording the lateral displacement of the center of mass δ_i; and (d) the story yield strength Q_{yi} is estimated by:

$$Q_{yi} = \frac{\delta_{yi}}{\delta_i} F_i \tag{5.11}$$

The present simple algorithm for estimating Park and Ang damage index for structures from limited experimental data was developed independently in this study.

When our calculations were finished, we found similar idea of finding story-wise Park and Ang index has been proposed by Toussi and Yao (1983) and adopted by Stephens and Yao (1987). They utilized recorded acceleration data to calculate Park and Ang damage index for two 10-story reinforced concrete models. In their approach, first the recorded acceleration was integrated once and twice respectively to get the velocity and displacement. The spring and damping force were assumed to depend solely on the relative displacement and velocity respectively. The whole time history was divided into a set of time intervals so that the displacement and velocity changed monotonically within each interval. Then the spring and damping forces were recognized from the total resisting force within each interval by expressing them in forms of polynomials of the relative velocity and displacement. Finally the obtained spring force was used to estimate the dissipated energy and thus Park and Ang damage index.

There exist some problems with this algorithm. We found that the recognized spring force from this method may be discontinuous between two consecutive time intervals, since there was no measure to ensure the continuity of both the spring and damping forces. In addition, the single and double integrations of acceleration data to obtain the velocity and displacement may also introduce additional errors. In comparison, our algorithm appears to be simpler to use in estimating Park and Ang damage index from experimental data.

5.2.5 Damages caused by energy dissipation

Before we discuss the results of Park and Ang damage indices, the energy dissipation during various earthquake inputs is first studied. Figures 5.9(a)-(e) show typical hysteretic load-deformation behavior of the story between 2/F and 3/F (i.e. the story above the transfer plate) during the inputs of Chi-Chi earthquake at rock site, with PGA increasing from (a) to (e). This story suffered the severest damages in our tests. It is seen that the slopes of these load-deformation curves generally decrease with the input PGA, especially during the 0.216g PGA input [Figure 5.9(e)]. This reflects stiffness degradation and softening of the structure after the shaking of various earthquakes. In addition, the hysteretic curves of the 0.216g PGA input shown in Figure 5.9(e) appear to be more nonlinear and irregular than others.

As sketched in Figure 5.9(f), the dissipated energy was calculated as the closed area in the load-deformation curve, and the resulting energy dissipation *E* during each input is also marked in the figure. It is seen that the dissipated energy increase with the input PGA from (a) to (d), but decrease when the input PGA increase from 0.134g to 0.216g. This final drop is probably again caused by stiffness degradation of the model such that the resisting force *F* drops drastically.

Similarly, Figures 5.10(a)-(e) plot the load-deformation curves of the same story during the inputs of Chi-Chi earthquake with soil amplification of different input PGAs. In addition to the general softening of the structure found with the increase of input PGA, a “soft-to-stiff” type of behavior was observed during the 0.32g PGA input [Figure 5.10(e)]. Similar phenomenon has also been reported by Toussi and Yao

(1983).

In contrast to the results given in Figure 5.9, Figure 5.10 shows that the dissipated energy increase monotonically with the input PGA. This is because the degraded natural frequency of the model becomes closer to the predominant frequency (2.997 Hz) of Chi-Chi earthquake with soil amplification. Thus, larger response and energy dissipation were resulted.

5.2.6 Damage quantification using Park and Ang index

In this section, the damage states of the present model will be assessed using Park and Ang damage index estimated through the proposed simple approach. As an illustration, Table 5.3 shows the energy dissipation and Park and Ang damage index of each story during the shaking of 0.3g Chi-Chi earthquake after soil amplification. The overall Park and Ang damage index of the model in the table was calculated from the weighted average of all the story indices. Recalling the calibration result for Park and Ang damage index, the model was considered close to collapse state after the shaking of this earthquake.

From Table 5.3, the first two stories below the transfer plate had smaller Park and Ang indices than the upper stories. This is consistent with the observations in the tests that almost no visible cracks were found at the first two stories and most of cracks occurred at the upper stories (refer to Section 4.4.4). Similar failure pattern was also reported by Li et al. (2006) in the shaking table test of a 42-story building model with transfer system. Table 5.3 also reveals that the 3^{rd} story which was just above the transfer plate dissipated the largest energy. This agrees well with the experimental observations that the severest damage occurred at this story (refer to Section 4.4.4).

The fourth column p_2/p_1 in Table 5.3 is the ratio between the second term and the first term in the definition of Park and Ang damage index shown in Equation (5.6) [i.e. $p_1=\delta_m/\delta_u$ and $p_2=\beta\int dE/(Q_y\delta_u)$]. It is found that the maximum damage caused by the hysteretic dissipated energy is only 2.1% of that caused by the maximum deformation effect. This suggests that here the value of Park and Ang damage index is largely determined by the maximum deformation in stead of the hysteretic energy. This will be further discussed later.

The overall Park and Ang damage indices of the structure during various earthquake inputs are summarized in Table 5.6. The peak ground acceleration (PGA), maximum response at the roof (Δ_m), energy dissipation (E), natural frequency ratio (f_{dam}/f_{ini}), the final softening index (D_F), and ductility (μ) are also listed. In the table, the damage states of the model are determined based on the overall Park and Ang damage indices according to the calibration results described in Section 5.1.3.

It is seen that the structure began to have minor and moderate damages from the inputs of 0.2g and the first time 0.3g Kobe earthquake at soil site respectively. Severe and irrepairable damage began to occur under the shaking of the second time 0.3g El Centro earthquake at soil site. The last input earthquake (i.e. 0.3g Chi-Chi earthquake at soil site) induced the largest Park and Ang damage index of 1.102, indicating the structure was in the state of nearly collapsed.

Note that in Table 5.6 the 0.3g El Centro and Kobe earthquakes were input twice, due to strain overflow occurred during the first time input of these earthquakes (refer to Section 4.1.2). The second time input of an earthquake of similar PGA may induce quite larger damages to the model because the damages are cumulative. For example, the first and second times 0.3g soil site Kobe earthquake inputs have similar PGA values (0.30g and 0.29g respectively), but the ductility and Park and Ang damage index caused by the second time 0.3g Kobe earthquake (3.983 and 0.519) are much larger than that by the first time input (2.438 and 0.315).

In addition, several other earthquakes were input (including the 0.25g and 0.2g Kobe earthquake at soil site and the second time 0.3g El Centro earthquake), which have induced considerable damages to the model. The cumulative damages reduce both the stiffness and natural frequency of the model. The damaged natural frequency actually becomes closer to the predominant frequencies of the 0.3g soil site Kobe earthquake. And this tends to result in even larger responses and damages.

The overall Park and Ang damage indices during various earthquake inputs are plotted with the input PGAs in Figure 5.11. The variations of these curves are very similar to that of the overall drift ratio curves shown in Figure 5.5, and thus can be explained in a similar way. This suggests that here Park and Ang damage indices are largely determined by the maximum deformation in stead of the hysteretic dissipated energy, similar to the finding given in Table 5.3.

5.3 Correlations between Different Damage Indices

Several damage indices have been discussed above, including the inter-story drift ratio, ductility, natural frequency ratio, final softening index, and Park and Ang damage index. The results of all these damage indices for various earthquake inputs are summarized in Tables 5.5 and 5.6. Each of these indices provides an estimation of the damage state of the structure. In this section, the results from different damage indices are compared and discussed.

First the maximum overall drift ratios (*IDR*) are plotted versus Park and Ang damage indices for various earthquake inputs in Figure 5.12. It is clearly seen that for each site condition they are highly linearly correlated and almost fall onto a straight line with $R^2 \geqslant 0.998$ (R is the correlation coefficient). As discussed in Section 5.2.6, this linear relation implies that here the hysteretic dissipated energy term in the definition of Park and Ang damage index [Equation (5.6)] plays a less significant role compared to the first term of the maximum deformation.

Fitting a straight line in Figures 5.12(a) and (b) respectively, two linear equations are obtained between the overall drift ratio and Park and Ang damage index as:

$$D_{PA} = 0.6535 IDR_{overall} - 0.0003,\ R^2 = 0.9993 \quad \text{(for earthquakes at rock sites)} \quad (5.12)$$

$$D_{PA} = 0.7018 IDR_{overall} - 0.0062,\ R^2 = 0.9989 \quad \text{(for earthquakes at soil sites)} \quad (5.13)$$

where $IDR_{overall}$ denotes the overall drift ratio and D_{PA} denotes Park and Ang damage index. The line slopes are slightly different for earthquakes at rock and soil sites.

Since Park and Ang damage index has been well calibrated to observed seismic damages, the above two regression equations can be used to predict the values of overall drift ratio corresponding to different damage states of structures. The results are shown in Table 5.4. It is estimated that an overall drift ratio larger than 1/543-1/556 indicates the initiation of minor damage (slightly smaller than the assumed 1/500 yield drift ratio), *IDR* larger than 1/261-1/274 corresponds to moderate damage, *IDR* larger than 1/163-1/173 corresponds to severe and irrepairable damage, and *IDR* greater than 1/82-1/87 represents collapse of structures.

The Structural Engineers Association of California (SEAOC) suggests that the transient drift ratios corresponding to the onset of light, moderate, severe damages and collapse are 1/500, 1/200, 1/67 and 1/40 respectively (pp.326 in SEAOC, 1999). The threshold drift ratios estimated in this study (Table 5.4) suggests that moderate damage, severe damage and collapse states may appear earlier than that recommended by SEAOC. In particular, relatively large differences are found for the criteria corresponding to severe damage and collapse. This implies that the behaviors of severely damaged structures tend to be highly dependent on the types of building. Therefore, indiscriminate use of recommendation from SEAOC should be avoided.

Li et al. (2006) concluded from a shaking table test on a 42-story building model that the drift ratios corresponding to slight, moderate and severe damages are 1/1000, 1/300-1/700 and 1/80-1/200 respectively. The drift ratios corresponding to slight and moderate damages are smaller than our results, whereas the ranges of drift ratios for other damage states are far too large for practical interpretations. Note that the damage states of the model in Li et al. (2006) were determined through visual observations as mentioned previously. Thus, it would not be surprising there are some discrepancies between the two studies. We believe that our values of IDR for various damage states are much more reliable.

Finally, utilizing the damage states determined from Park and Ang damage indices, the values of other indices (including the ductility, overall and inter-story drift ratios, frequency ratio and final softening index) corresponding to the onset of various damage states can be established as shown in Table 5.7. To date little work has been done to provide clear relations between these damage indices and damage states, therefore, the present study provides the first correlation of this kind. These threshold values provide a useful reference for similar studies in the future. Strictly speaking, this correlation is, of course, limited to the studied building, however, it is speculated that the results are also applicable to other similar buildings in Hong Kong and is extremely useful for practical purposes in rapid damage assessment.

The ductility values corresponding to various damage states obtained in this study show a good agreement with the empirical conclusion drawn by Yin (1995). For frame structures with shear walls, Yin (1995) proposed the threshold ductility factors for the onset of slightly, moderately, extensively, and completely damaged states are 1.0, 1.5, 3.0, and 5.0 respectively, based on statistic studies on a great number of building structures. Comparing these values with the ductility thresholds of 1.11, 1.97, 3.09 and 8.52 given in Table 5.7, we conclude that different threshold ductility factors should be established for different kinds of structures. The present result should provide the first data set for asymmetric buildings with transfer system.

Table 5.1 Comparison of various seismic damage indices (To be continued).

Damage index	Definition	Member level	Structural level	Reference
Ductility	$\mu = \dfrac{\delta_m}{\delta_y}$	√	√	Park, 1986
Inter-story drift (*ID*)	$ID = \Delta_i - \Delta_{i-1}$	√	√	Mayes, 1995
Damage ratio (*DR*)	$DR = \dfrac{k_0}{k_m}$	√	×	Lybas and Sozen, 1977
Flexural damage ratio (*FDR*)	$FDR = \dfrac{k_f}{k_m}$	√	×	Banon et al, 1981
Khashaee index	$D = \dfrac{1-\mu^{-1}}{1-\mu_u^{-1}}$	√	√	Khashaee, 2005
Normalized cumulative rotation (*NCR*)	$NCR = \dfrac{\sum \lvert \theta_m - \theta_y \rvert}{\theta_y}$	√	×	Banon et al, 1981
Stephens and Yao index	$D = \sum \left(\dfrac{\Delta\delta^+}{\Delta\delta_f} \right)^{1-br}$	√	×	Stephens and Yao, 1987
Wang and Shah index	$D = \dfrac{\exp(sb)-1}{\exp(s)-1} \quad b = c\sum_i \dfrac{\delta_{m,i}}{\delta_f}$	√	×	Wang and Shah, 1987
Chung et al. index	$D = \sum_i \left(w_i^+ \dfrac{n_i^+}{n_{f,i}^+} + w_i^- \dfrac{n_i^-}{n_{f,i}^-} \right)$	√	×	Chung et al, 1987

Table 5.1 Comparison of various seismic damage indices (Continued).

Damage index	Definition	Member level	Structural level	Reference
Krawinkler and Zohrei index	$D = C\sum_{i=1}^{n}(\Delta\delta_{pi})^c$	√	×	Krawinkler and Zohrei, 1983
Gosain et al. index	$D_e = \sum_i \frac{F_i\delta_i}{F_y\delta_y}$	√	×	Gosain et al, 1977
Kratzig et al. index	$D^+ = \frac{\sum E_{p,i}^+ + \sum E_i^+}{E_f^+ + \sum E_i^+}$ $D = D^+ + D^- - D^+D^-$	√	×	Kratzig et al, 1989
Hindi and Sexsmith index	$D_n = \frac{A_0 - A_n}{A_0}$	√	×	Hindi and Sexsmith, 2001
Park and Ang index	$D = \frac{\delta_m}{\delta_u} + \frac{\beta}{Q_y\delta_u}\int dE$	√	×	Park and Ang, 1985
Softening indices	$D_m = 1 - \frac{T_{und}}{T_m}$ $D_{pl} = 1 - \frac{T_{dam}^2}{T_m^2}$ $D_F = 1 - \frac{T_{und}^2}{T_{dam}^2}$	×	√	DiPasquale and Cakmak, 1987

Remark: the term “Member level” in the table means the damage index can be applied to individual members, and the term “Structural level” denotes the damage index can be applied directly to whole structures

Table 5.2 Change of the first three natural frequencies of the model after various earthquake inputs, where f_{ini} and f_{dam} denote the initial and changed frequencies after damage respectively.

Target (g)	Earthquake	$f_1\ (Hz)$	$\frac{f_{dam}}{f_{ini}}$ (%)	$f_2\ (Hz)$	$\frac{f_{dam}}{f_{ini}}$ (%)	$f_3\ (Hz)$	$\frac{f_{dam}}{f_{ini}}$ (%)
Initial		6.348	100.0	7.141	100.0	7.599	100.0
0.05	El Centro	6.287	99.0	7.080	99.1	7.507	98.8
	Loma Prieta	6.012	94.7	6.989	97.9	7.324	96.4
	Kobe	6.012	94.7	6.805	95.3	7.294	96.0
	Northridge	5.997	94.5	6.897	96.6	7.278	95.8
	Chi-Chi	5.981	94.2	6.821	95.5	7.263	95.6
0.10	El Centro	5.936	93.5	6.790	95.1	7.248	95.4
	Kobe	5.920	93.3	6.760	94.7	7.217	95.0
	Northridge	6.027	95.0	6.882	96.4	7.278	95.8
	Loma Prieta	5.875	92.5	6.805	95.3	7.233	95.2
	Chi-Chi	5.844	92.1	6.775	94.9	7.202	94.8
0.15	El Centro	5.920	93.3	6.790	95.1	7.248	95.4
	Kobe	5.859	92.3	6.775	94.9	7.233	95.2
	Northridge	5.890	92.8	6.805	95.3	7.202	94.8
	Loma Prieta	5.936	93.5	6.805	95.3	7.141	94.0
	Chi-Chi	5.920	93.3	6.867	96.2	7.156	94.2
0.20	El Centro	5.814	91.6	6.744	94.4	7.065	93.0
	Kobe	5.631	88.7	6.622	92.7	7.034	92.6
	Northridge	5.585	88.0	6.668	93.4	7.019	92.4
	Loma Prieta	5.753	90.6	6.638	92.9	7.065	93.0
	Chi-Chi	5.615	88.5	6.622	92.7	6.989	92.0
0.30	El Centro	5.127	80.8	6.424	90.0	6.729	88.6
	Kobe	4.807	75.7	6.180	86.5	6.470	85.1
0.25	Kobe						
0.2	Kobe						
0.2	Chi-Chi	4.684	73.8	6.149	86.1	6.363	83.7
0.30	El Centro	4.234	66.7	5.898	82.6	6.274	82.6
	Kobe	4.114	64.8	5.716	80.0	5.760	75.8
	Chi-Chi	2.884	45.4	5.356	75.0	5.722	75.3

Table 5.3 The maximum deformation (δ_m), dissipated energy (E) and estimated Park and Ang index (D_{PA}) of each story under the shaking of 0.3g Chi-Chi earthquake after soil amplification.

Story	δ_m (mm)	E (N.m)	p_2 / p_1 (%)	D_{PA}
1	1.21	36.45	1.65	0.507
2	1.27	34.20	1.41	0.506
3	2.82	217.84	1.54	1.125
4	2.12	157.88	2.10	1.131
5	2.12	152.08	2.02	1.130
6	2.12	145.97	1.94	1.129
7	2.12	139.56	1.86	1.128
8	2.12	132.85	1.77	1.127
9	2.12	125.83	1.68	1.126
10	2.12	118.50	1.58	1.125
11	2.12	110.77	1.47	1.124
12	2.12	102.64	1.37	1.123
13	2.12	94.11	1.25	1.122
14	2.12	85.18	1.13	1.120
15	2.12	75.84	1.01	1.119
16	2.12	66.10	0.88	1.117
17	2.12	56.01	0.75	1.116
18	2.12	45.56	0.61	1.114
19	2.12	34.75	0.46	1.113
20	2.12	23.58	0.31	1.111
21	3.17	18.09	0.17	1.109
Overall Park and Ang damage index				1.102

Remark:

The term p_2/p_1 in the fourth column denotes the ratio between the second term and the first term in the definition of Park and Ang damage index shown in Equation (4.13) [i.e. $p_1=\delta_m/\delta_u$ and $p_2=\beta\int dE/(Q_y\delta_u)$].

Table 5.4 Park and Ang damage indices and overall drift ratios corresponding to the onset of various damage states.

Damage	Park and Ang damage index	Overall drift ratio	
		Before soil amplification	After soil amplification
Minor	0.12	1/543	1/556
Moderate	0.25	1/261	1/274
Severe	0.4	1/163	1/173
Collapse	0.8	1/82	1/87

Table 5.5 Maximum strain, rotation, drift ratio and amplification factor for various earthquake inputs.

No.	Target (g)	Earthquake	Site	PGA (g)	Strain	$\theta(^\circ)$	$IDR_{overall}$	IDR_{max}	β_A	Damage
1	0.05	El Centro	Rock	0.040	131*	0.007	1/3693	1/3524	4.66	None
			Soil	0.055	217*	0.007	1/2692	1/1745	3.02	
2		Loma Prieta	Rock	0.043	55*	0.004	1/13303	1/8463	2.38	
			Soil	0.046	183*	0.008	1/2621	1/2407	3.52	
3		Kobe	Rock	0.037	132*	0.006	1/4194	1/3425	3.12	
			Soil	0.053	253*	0.008	1/2262	1/2038	3.61	
4		Northridge	Rock	0.030	53*	0.004	1/10270	1/9027	2.68	
			Soil	0.049	212*	0.010	1/2783	1/2618	3.25	
5		Chi-Chi	Rock	0.035	172*	0.005	1/3104	1/2836	4.17	
			Soil	0.067	212	0.004	1/2311	1/2280	2.67	
6	0.10	El Centro	Rock	0.08	229*	0.010	1/1914	1/887	5.06	
			Soil	0.10	411*	0.013	1/1294	1/501	2.89	
7		Kobe	Rock	0.06	327*	0.014	1/1561	1/1455	5.04	
			Soil	0.09	443*	0.018	1/1066	1/750	3.55	
8		Northridge	Rock	0.09	179	0.005	1/3755	1/3190	2.88	
			Soil	0.09	381*	0.016	1/1381	1/1282	3.40	
9		Loma Prieta	Rock	0.07	143	0.010	1/4467	1/3362	2.39	
			Soil	0.09	435	0.016	1/1058	1/989	4.53	
10		Chi-Chi	Rock	0.07	398*	0.011	1/1257	1/1171	4.37	
			Soil	0.11	452	0.007	1/1127	1/639	2.35	
11	0.15	El Centro	Rock	0.10	351	0.015	1/1315	1/637	4.72	
			Soil	0.15	774	0.020	1/824	1/370	2.90	
12		Kobe	Rock	0.1	472	0.017	1/972	1/902	4.92	
			Soil	0.14	944	0.022	1/686	1/498	3.17	
13		Northridge	Rock	0.12	340	0.007	1/2438	1/2261	2.43	
			Soil	0.13	671	0.022	1/930	1/866	2.78	
14		Loma Prieta	Rock	0.12	359	0.014	1/2650	1/2312	2.52	
			Soil	0.12	970	0.017	1/695	1/648	4.81	
15		Chi-Chi	Rock	0.10	702	0.016	1/796	1/743	4.44	
			Soil	0.16	1147	0.007	1/708	1/414	2.47	
16	0.20	El Centro	Rock	0.13	742	0.015	1/1011	1/429	4.44	
			Soil	0.18	1309$^\#$	0.022	1/593	1/305	3.27	
17		Kobe	Rock	0.13	971$^\#$	0.020	1/663	1/611	5.43	
			Soil	0.18	1591	0.019	1/447	1/369	3.42	Minor
18		Northridge	Rock	0.16	447	0.007	1/1768	1/1569	2.14	None
			Soil	0.19	982$^\#$	0.024	1/732	1/360	2.34	
19		Loma Prieta	Rock	0.15	476	0.013	1/1696	1/1456	2.70	
			Soil	0.16	1483	0.017	1/462	1/444	4.14	Minor
20		Chi-Chi	Rock	0.13	1132$^\#$	0.016	1/546	1/507	4.63	None
			Soil	0.22	1670	0.012	1/444	1/371	2.48	Minor
21	0.30	El Centro	Rock	0.22	1223	0.021	1/624	1/313	3.17	None
			Soil	0.32	1817	0.030	1/270	1/145	3.21	Minor
22		Kobe	Rock	0.25	1301	0.031	1/478	1/440	2.38	
			Soil	0.30	1825	0.030	1/208	1/166	2.91	Moderate
23	0.25	Kobe	Soil	0.24	3234	0.027	1/207	1/178	3.44	
24	0.20	Kobe	Soil	0.19	2894	0.028	1/225	1/210	3.93	
25	0.20	Chi-Chi	Soil	0.24	2743	0.028	1/254	1/207	3.03	
26	0.30	El Centro	Rock	0.22	1064	0.035	1/579	1/321	3.28	None
			Soil	0.28	3868	0.058	1/169	1/121	4.16	Severe
27		Kobe	Rock	0.27	1908	0.048	1/315	1/295	2.57	Minor
			Soil	0.29	4947	0.065	1/128	1/101	3.93	Severe
28		Chi-Chi	Rock	0.22	1234$^\#$	0.059	1/276	1/247	3.15	Minor
			Soil	0.32	5152	0.100	1/64	1/56	4.03	Collapse

Remarks: for the maximum strain values, the symbol * means the maximum strain occurred at the strain gauge ε_2, $^\#$ means at ε_{25}, and those not specified means at ε_{11}.

Table 5.6 The natural frequency ratio (f_{dam}/f_{ini}), final softening index (D_F), ductility (μ), and Park and Ang damage index (D_{PA}) caused by various earthquake inputs.

No.	Target (g)	Earthquake	Site	PGA (g)	$\Delta_m(mm)$	$E(Nm)$	$\frac{f_{dam}}{f_{ini}}(\%)$	D_F	μ	D_{PA}	Damage
1	0.05	El Centro	Rock	0.040	0.75	2.57			0.137	0.017	None
			Soil	0.055	1.06	12.78	99	0.019	0.282	0.025	
2		Loma Prieta	Rock	0.043	0.19	0.26			0.035	0.004	
			Soil	0.046	1.07	4.16	95	0.103	0.192	0.025	
3		Kobe	Rock	0.037	0.64	1.59			0.125	0.015	
			Soil	0.053	1.22	9.10	95	0.103	0.221	0.028	
4		Northridge	Rock	0.030	0.27	0.21			0.049	0.006	
			Soil	0.049	0.99	7.59	94	0.108	0.181	0.023	
5		Chi-Chi	Rock	0.035	0.89	5.35			0.162	0.021	
			Soil	0.067	1.15	3.44	94	0.112	0.208	0.027	
6	0.10	El Centro	Rock	0.08	1.44	11.01			0.259	0.034	
			Soil	0.1	2.19	60.24	94	0.126	0.483	0.052	
7		Kobe	Rock	0.06	1.77	9.01			0.327	0.041	
			Soil	0.09	2.58	35.12	93	0.130	0.465	0.061	
8		Northridge	Rock	0.09	0.72	1.19			0.134	0.017	
			Soil	0.09	2.00	29.98	95	0.098	0.367	0.047	
9		Loma Prieta	Rock	0.07	0.62	2.14			0.115	0.014	
			Soil	0.09	2.60	28.56	93	0.144	0.481	0.061	
10		Chi-Chi	Rock	0.07	2.21	23.56			0.406	0.052	
			Soil	0.11	2.46	15.26	92	0.152	0.456	0.058	
11	0.15	El Centro	Rock	0.1	2.11	21.86			0.382	0.049	
			Soil	0.15	3.35	135.96	93	0.130	0.725	0.080	
12		Kobe	Rock	0.1	2.83	20.65			0.527	0.066	
			Soil	0.14	4.03	77.99	92	0.148	0.735	0.094	
13		Northridge	Rock	0.12	1.13	2.40			0.208	0.026	
			Soil	0.13	2.97	62.62	93	0.139	0.549	0.070	
14		Loma Prieta	Rock	0.12	1.00	3.72			0.185	0.024	
			Soil	0.12	3.96	65.86	94	0.126	0.720	0.093	
15		Chi-Chi	Rock	0.1	3.46	51.31			0.639	0.081	
			Soil	0.16	3.89	36.90	93	0.130	0.790	0.092	
16	0.20	El Centro	Rock	0.13	2.72	41.11			0.497	0.064	
			Soil	0.18	4.79	275.20	92	0.161	0.992	0.115	
17		Kobe	Rock	0.13	4.16	39.17			0.777	0.097	
			Soil	0.18	6.16	144.18	89	0.213	1.111	0.145	Minor
18		Northridge	Rock	0.16	1.83	3.85			0.563	0.041	None
			Soil	0.19	4.31	83.00	88	0.226	1.252	0.098	
19		Loma Prieta	Rock	0.15	1.58	6.18			0.306	0.037	
			Soil	0.16	6.01	132.85	91	0.179	1.094	0.140	Minor
20		Chi-Chi	Rock	0.13	5.04	93.89			0.937	0.118	None
			Soil	0.22	6.13	89.62	88	0.217	1.103	0.144	Minor
21	0.30	El Centro	Rock	0.22	4.46	77.52			0.804	0.105	None
			Soil	0.32	10.46	737.01	81	0.348	1.911	0.249	Minor
22		Kobe	Rock	0.25	5.96	86.50			1.093	0.140	
			Soil	0.3	13.32	521.06	76	0.427	2.438	0.315	Moderate
23	0.25	Kobe	Soil	0.24	13.31	443.79			2.436	0.315	
24	0.20	Kobe	Soil	0.19	12.28	353.00			2.263	0.289	
25	0.20	Chi-Chi	Soil	0.24	10.83	310.77	74	0.455	1.972	0.255	
26	0.30	El Centro	Rock	0.22	4.94	65.79			0.895	0.116	None
			Soil	0.28	16.84	1465.11	67	0.555	3.085	0.405	Severe
27		Kobe	Rock	0.27	8.74	86.33			1.611	0.204	Minor
			Soil	0.29	21.70	1038.94	65	0.580	3.983	0.519	Severe
28		Chi-Chi	Rock	0.22	10.00	48.52			1.930	0.239	Minor
			Soil	0.32	44.46	1973.79	45	0.794	8.519	1.102	Collapse

Table 5.7 Threshold values for various damage indices corresponding to the onset of various damage states.

Damage	D_{PA}	μ	$IDR_{overall}$	$IDR_{\max}$	$\frac{f_{dam}}{f_{ini}}$ (%)	D_F
Minor	0.145	1.111	1/447	1/369	89	0.213
Moderate	0.255	1.972	1/254	1/207	74	0.455
Severe	0.405	3.085	1/169	1/121	67	0.555
Collapse	1.102	8.519	1/64	1/56	45	0.794

Degree of damage	Photograph	Description
Slight	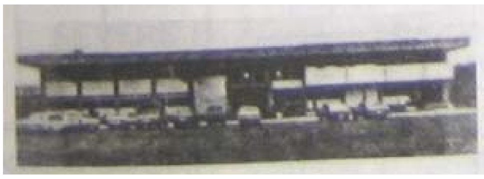	Sporadic occurrence of cracking
Minor		Minor cracks throughout building. Partial crashing of concrete in columns.
Moderate	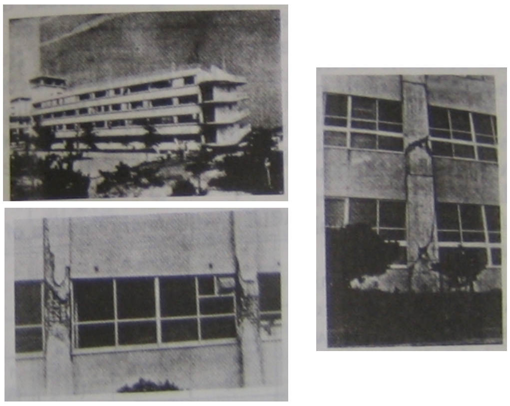	Extensive large cracks. Spalling of concrete in weaker elements.
Severe		Extensive crashing of concrete. Disclosure of buckled reinforcements.
Collapse	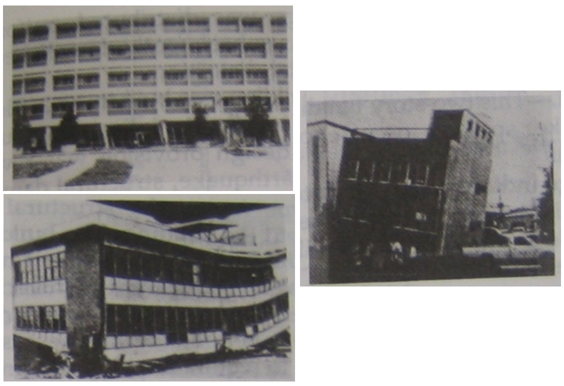	Total or partial collapse of building.

Figure 5.1 Damage degrees classified by Park et al. (1985) and their corresponding descriptions and representative photographs.

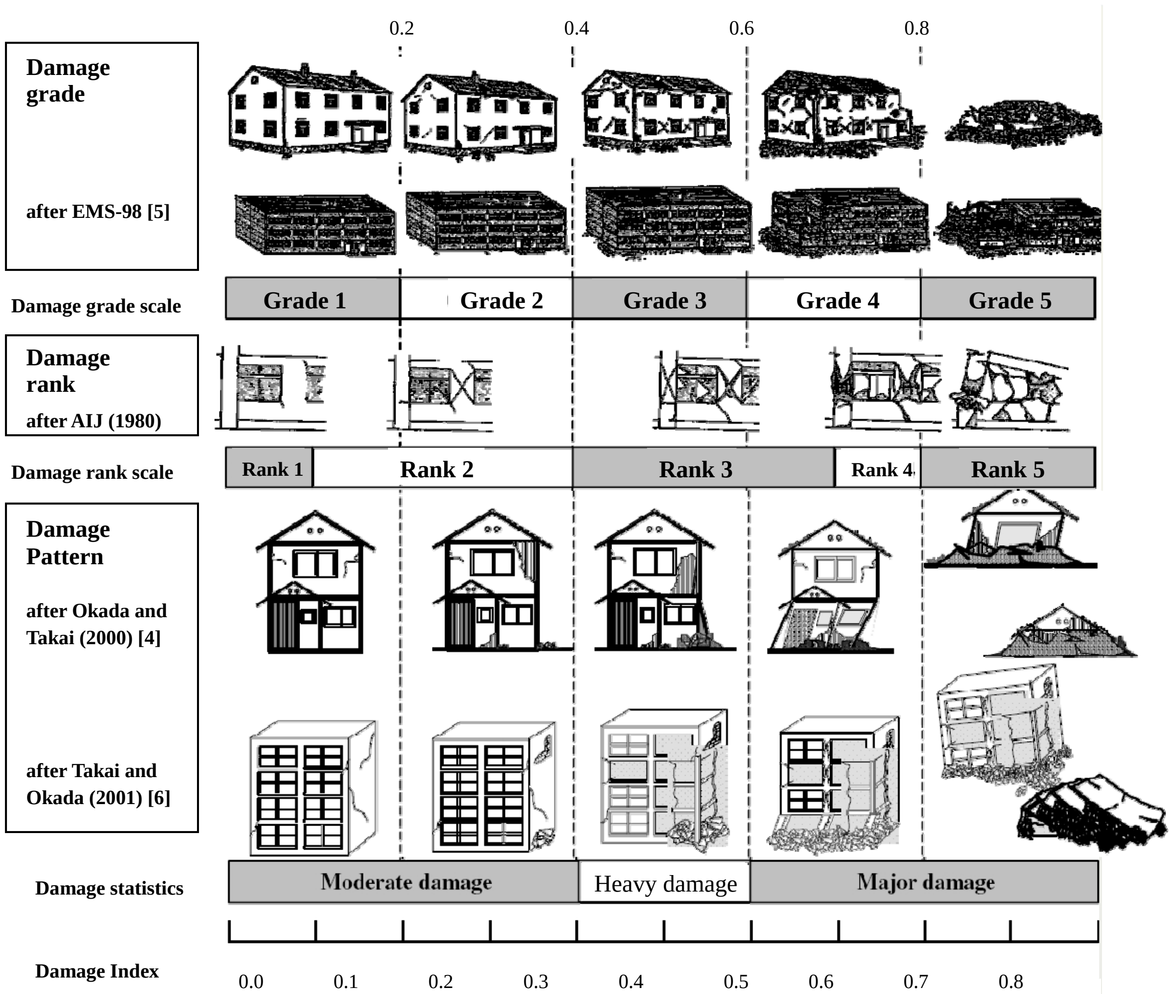

Figure 5.2 Comparison of various damage classifications (Okada and Takai, 2004).

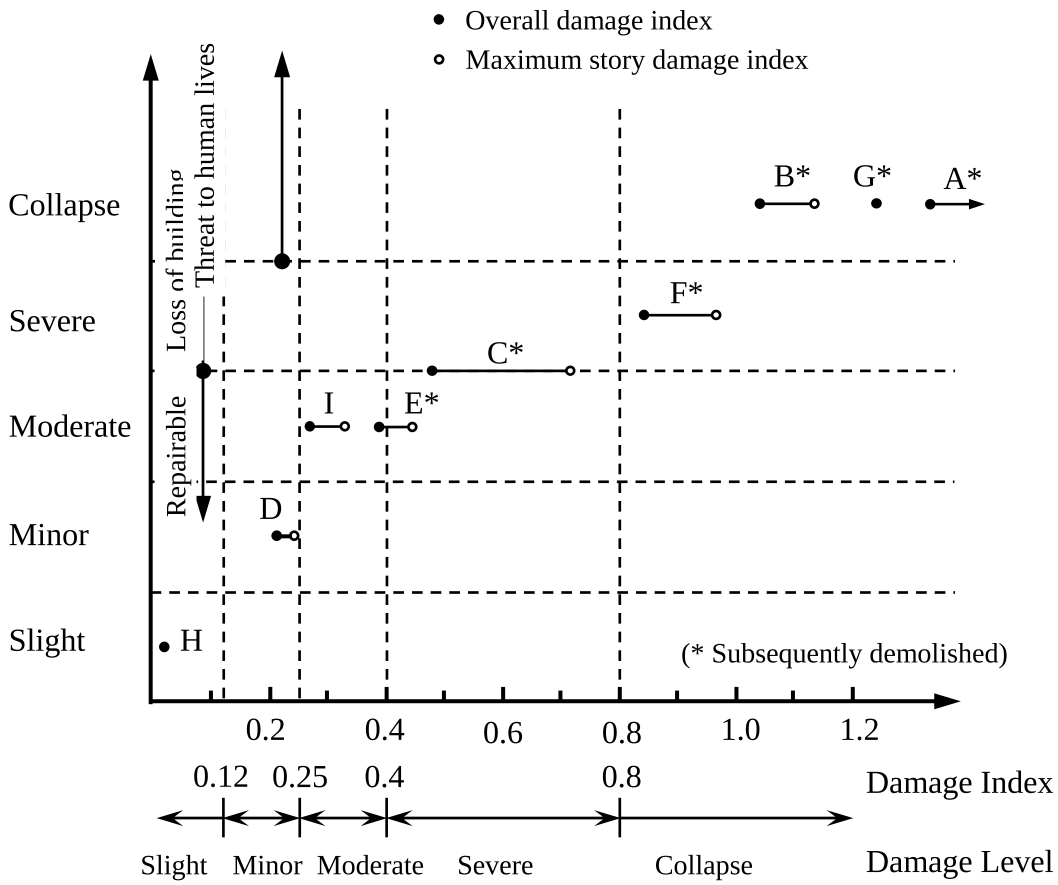

Figure 5.3 Calibration of Park and Ang damage indices with observed damage levels (adapted from Park et al., 1985).

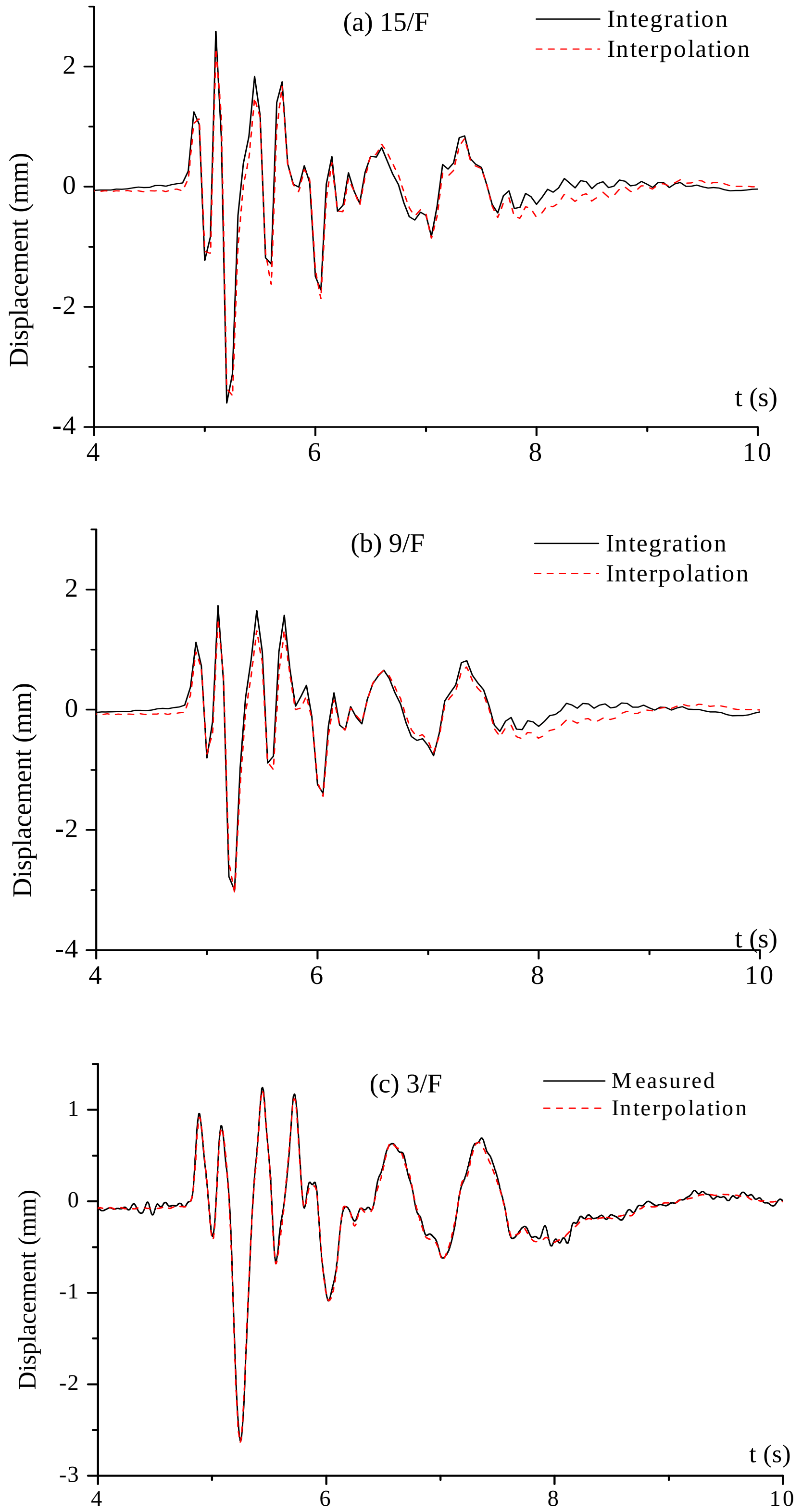

Figure 5.4 Comparison of displacements obtained from interpolation of recorded displacements (dashed line) and that from integration of recorded accelerations (solid line) at 15/F and 9/F as well as the displacements recorded by the LED transducer at 3/F under the 0.2g Kobe earthquake input at rock site.

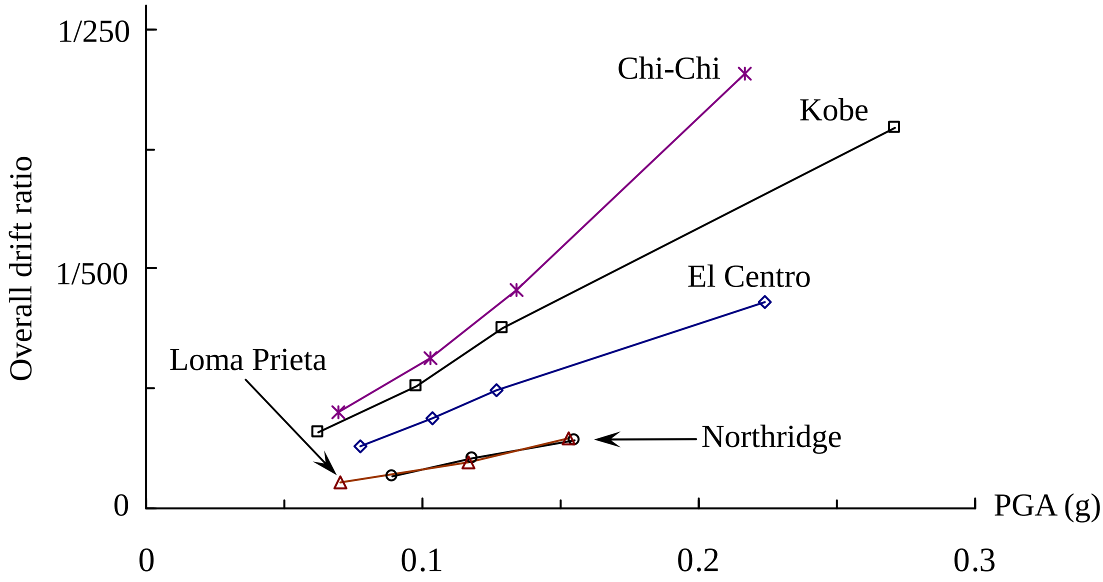

(a) before soil amplification;

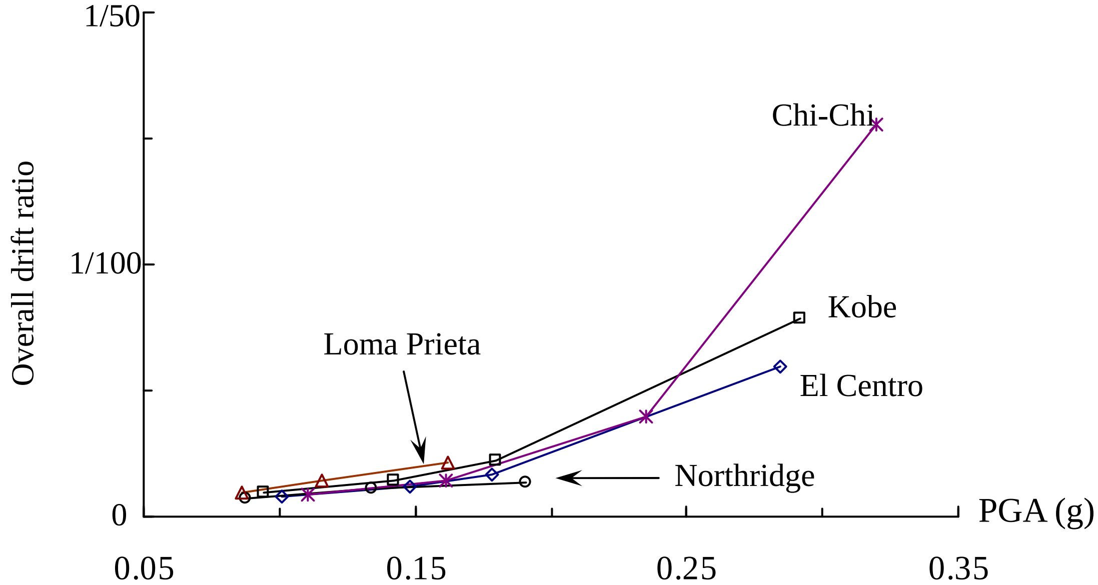

(b) after soil amplification.

Figure 5.5 Maximum overall drift ratios vs. input PGAs for various earthquakes before and after soil amplification respectively.

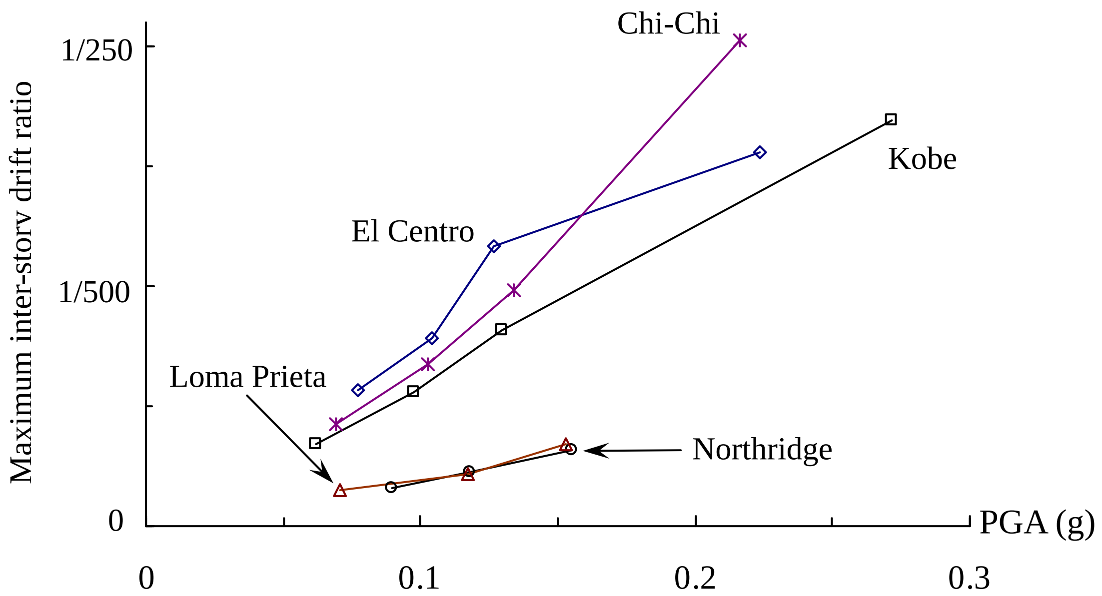

(a) before soil amplification;

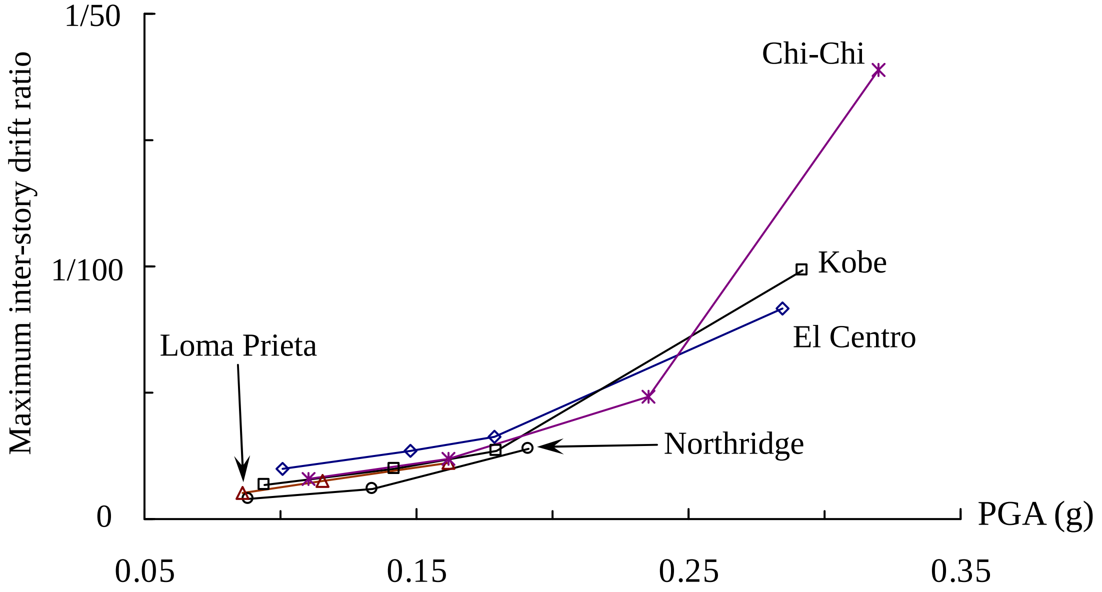

(b) after soil amplification.

Figure 5.6 Maximum inter-story drift ratios vs. input PGAs for various earthquakes before and after soil amplification respectively.

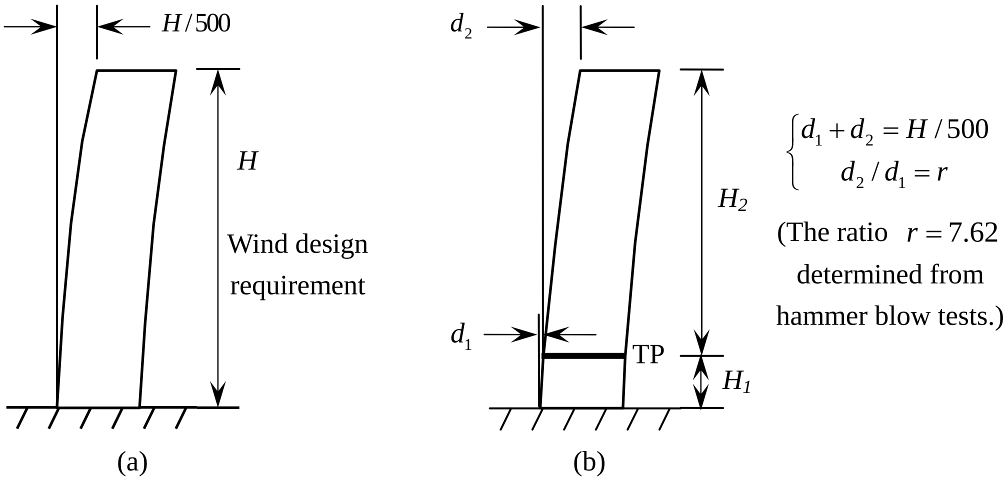

Figure 5.7 Estimation of the yield deformation when: (a) the model is taken as a uniform structure; (b) the model is divided into two segments at the transfer plate ('TP') level.

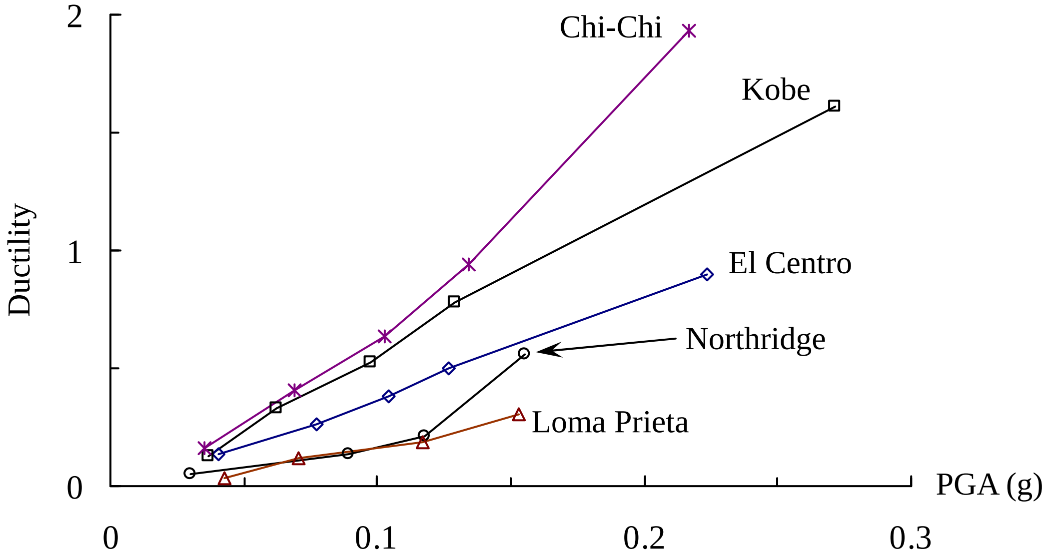

(a) before soil amplification;

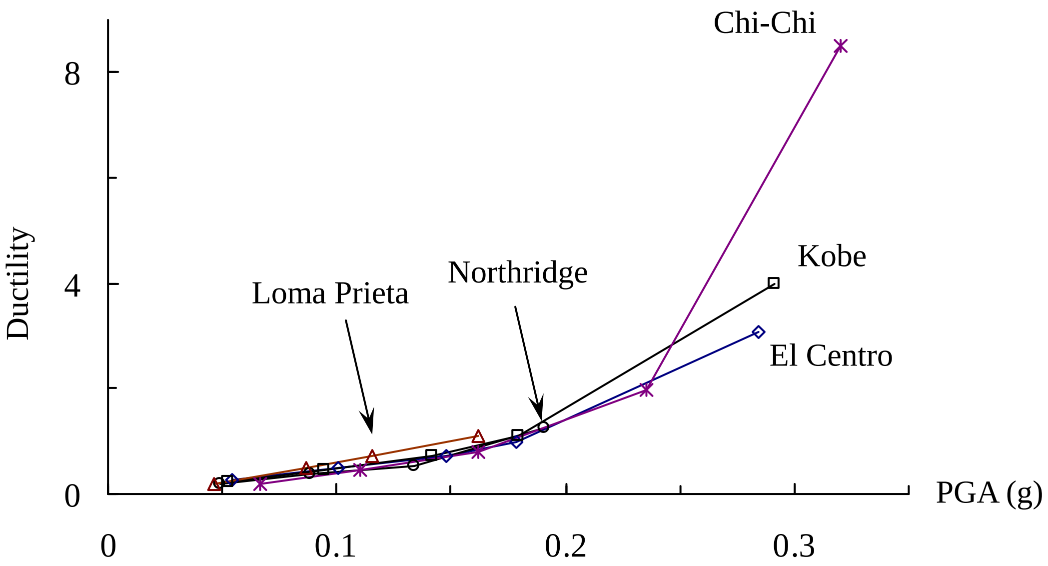

(b) after soil amplification.

Figure 5.8 Maximum ductility vs. input PGA for various earthquakes before and after soil amplification respectively.

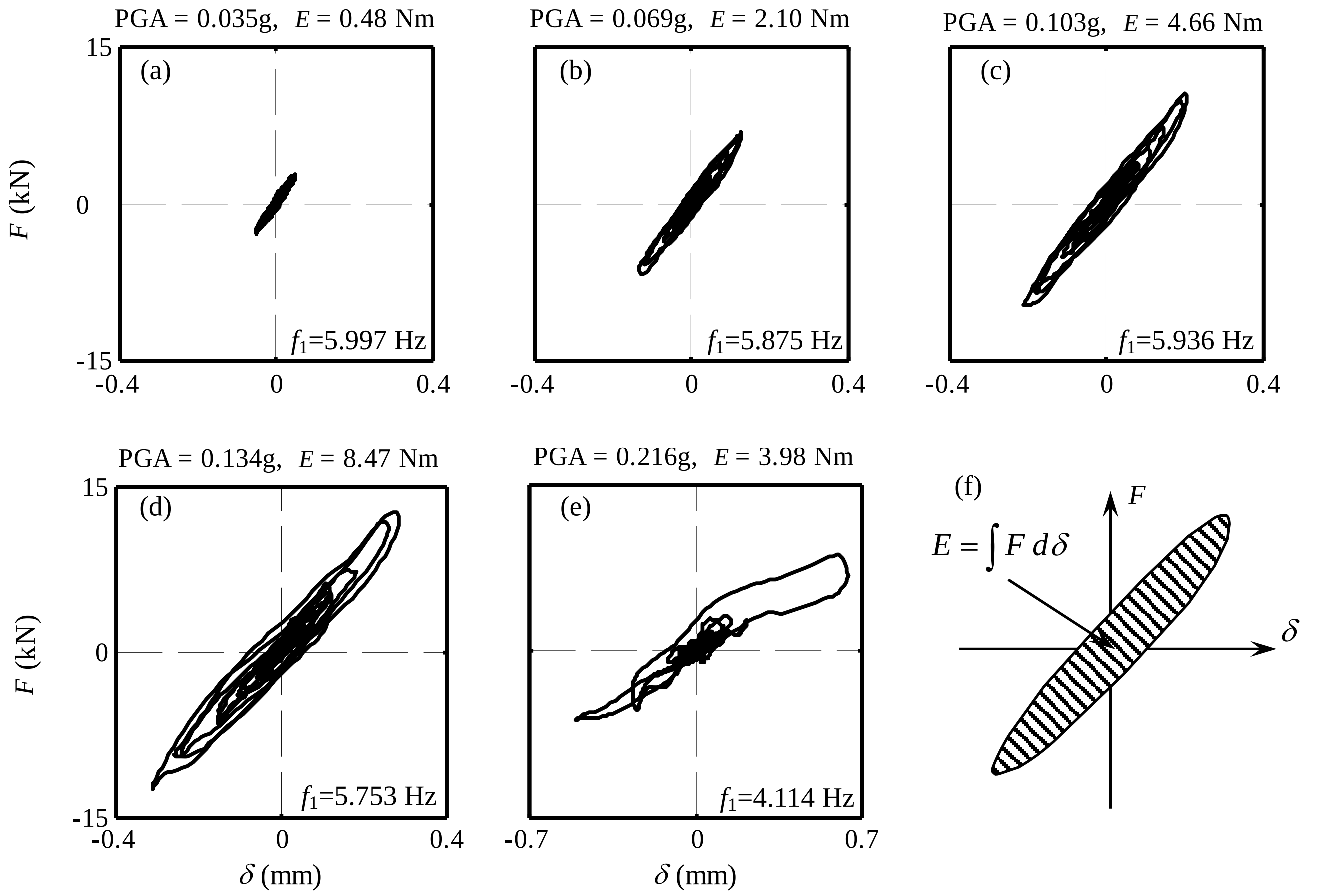

Figure 5.9 (a)-(e) Load-deformation curves of the story between 2/F and 3/F during the inputs of Chi-Chi earthquake without soil amplification of different PGAs, where E denotes the energy dissipated by the story and f_1 is the first natural frequency of the structure; (f) sketch of the load-deformation curve within one cycle, with the shaded area representing the dissipated energy.

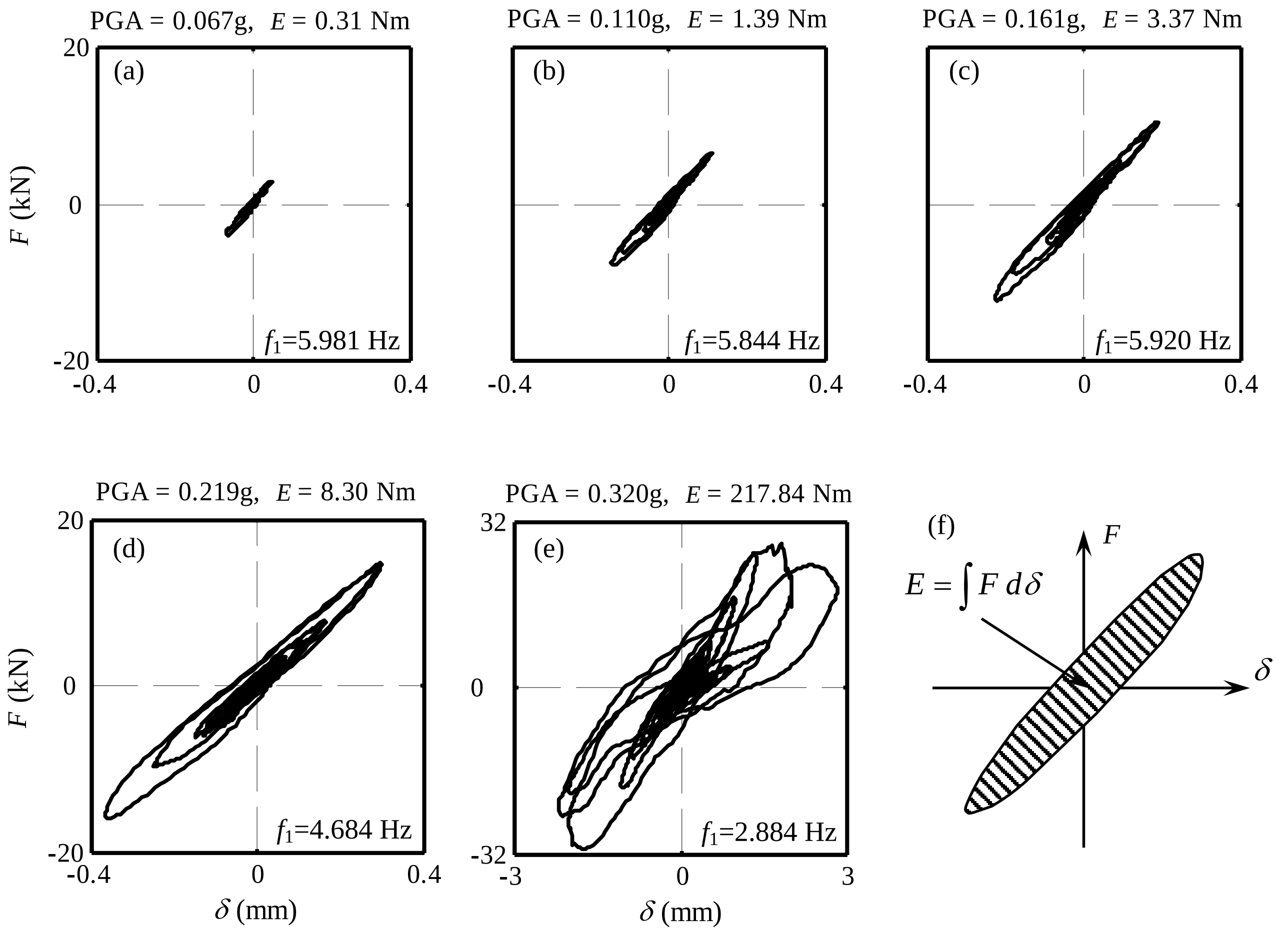

Figure 5.10 (a)-(e) Load-deformation curves of the story between 2/F and 3/F during the inputs of Chi-Chi earthquake after soil amplification of different PGAs, where E denotes the energy dissipated by the story and f_1 is the first natural frequency of the structure; (f) sketch of the load-deformation curve within one cycle, with the shaded area representing the dissipated energy.

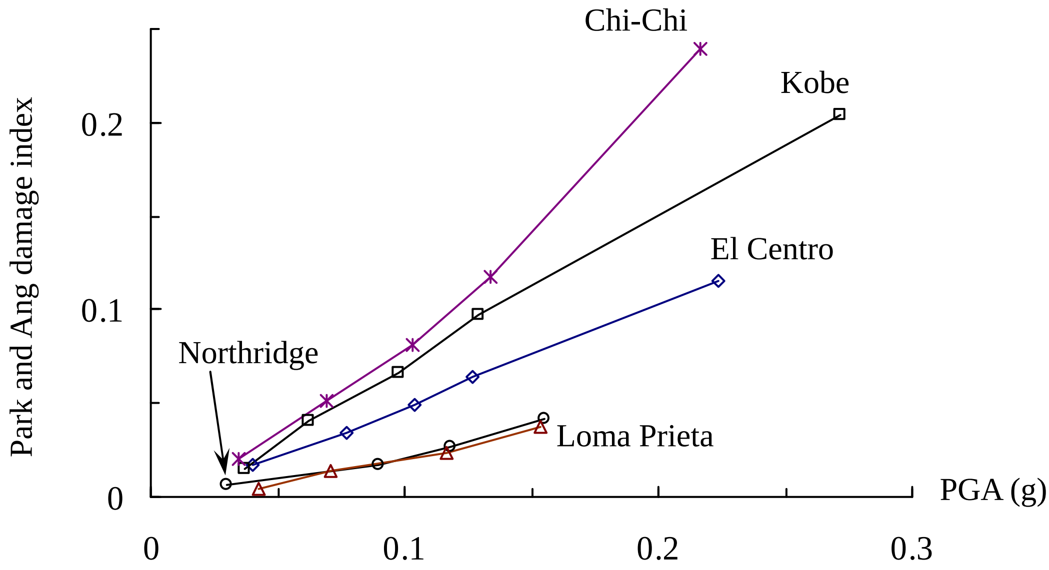

(a) before soil amplification

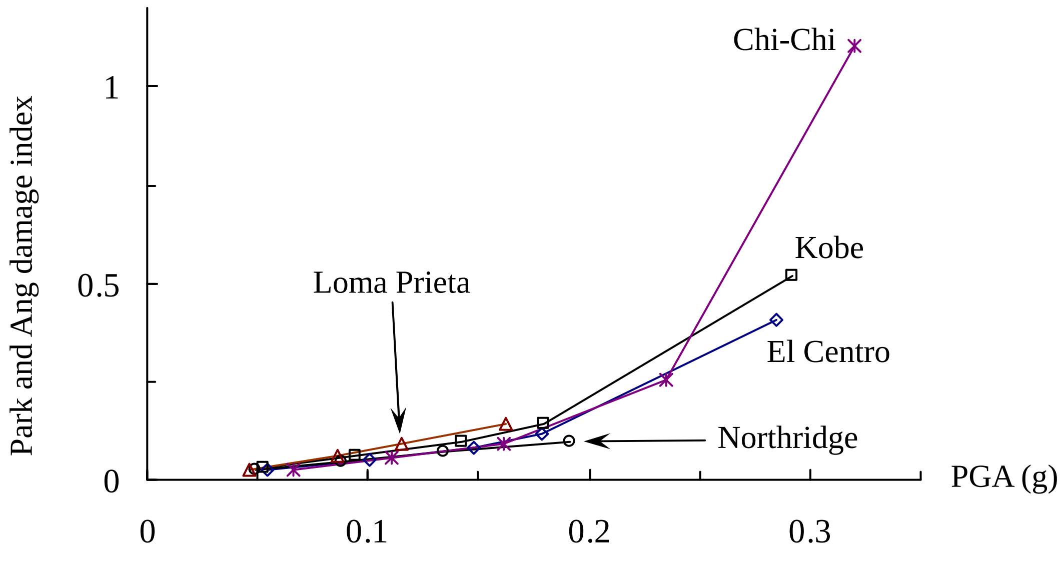

(b) after soil amplification

Figure 5.11 Park and Ang damage indices vs. input PGAs for various earthquakes before and after soil amplification respectively.

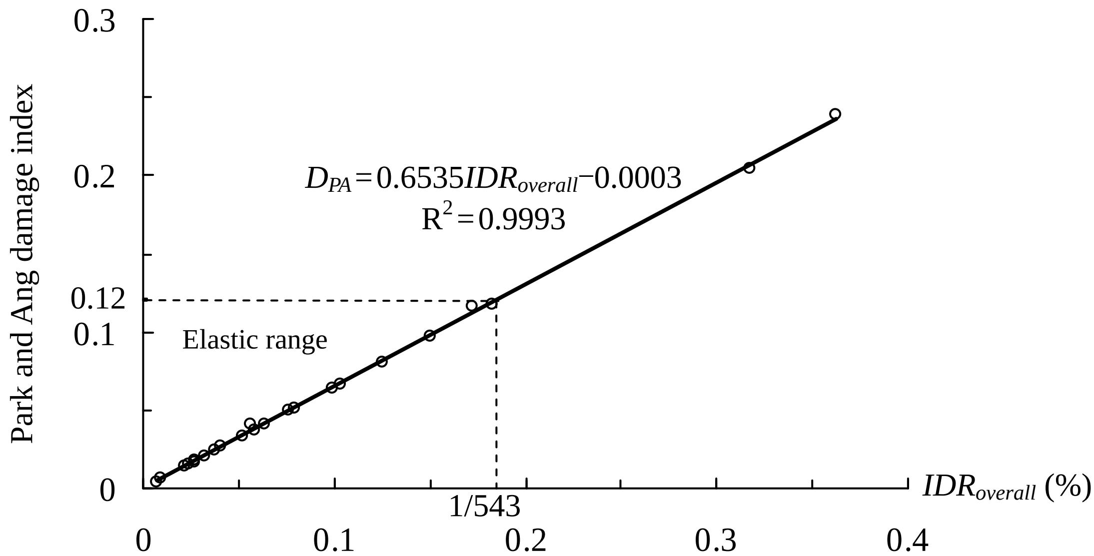

(a) at rock site

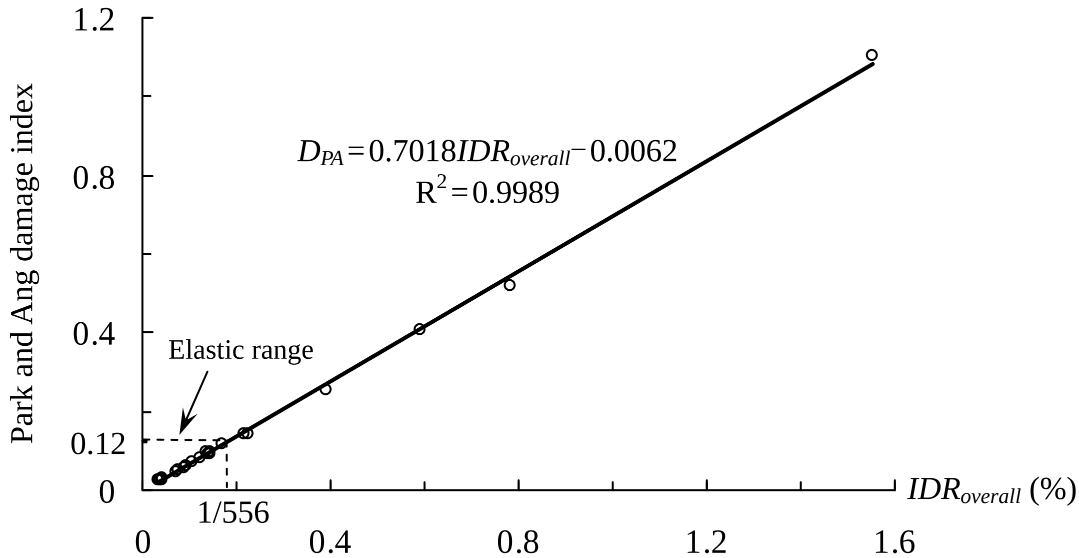

(b) at soil site

Figure 5.12 Park and Ang damage indices (D_{PA}) vs. overall drift ratios ($IDR_{overall}$) for various earthquakes before and after soil amplification respectively.

CHAPTER 6 DISCUSSIONS ON MODEL TESTING

6.1 Summary of Model Tests

In the first part of this thesis, the entire procedure of a reduced-scale model test was introduced, including the design and fabrication of the model, the shaking table tests and the interpretation of experimental results. In addition to visual inspections of cracks, the damages of the model in the tests were quantitatively evaluated using various seismic damage indices.

The 21-story building model suffered none or minor damage when subjected to earthquakes of 0.15g peak acceleration. Under the shaking of earthquakes of 0.3g peak acceleration, the model suffered severe and irrepairable damages, and is close to the verge of total collapse. The performance of this model is considered to satisfy the three-level design philosophy specified in Chinese Code for Seismic Design of Buildings (GB 50011-2001, 2001) as described in Section 4.1.1. From this aspect, the present test results are consistent with the previous shaking table test on a 42-story building model in Hong Kong conducted by Li et al. (2006).

Most of damages occurred at the transfer plate and the upper stories above it. Similar failure pattern has also been observed in the test of Li et al. (2006). Thus, transfer system and the stories above it appear to be the weakest parts for this type of buildings, which are susceptible to severe damage under earthquakes attacks and should be strengthened in design. Abrupt change of stiffness at the transfer zone should be avoided as far as possible.

The asymmetric structural layout induced diagonal rocking in the model, which caused severe damages to corner elements. This rocking failure mechanism was found for the first time in this study and has not been reported in other shaking table tests, including that of Li et al. (2006). Therefore, asymmetric building layout should be used with caution in practice and much attention should be paid to the reinforcement detailings of corner elements.

An approximate but simple algorithm is proposed to estimate Park and Ang damage indices for complex structures from limited measurement of responses in laboratory. Utilizing the well-calibrated Park and Ang damage index as a benchmark, several other damage indices, including the inter-story drift ratio, ductility, frequency ratio and final softening index, are correlated with various damage states. The present results provide a more reliable threshold values for various damage indices for the first time. This correlation is expected to be applicable to other similar buildings in Hong Kong and provides a practical approach to assess seismic damages rapidly. In this sense, the results of this study are of both academic and practical merits.

6.2 Comparison with FEM Analysis Results

In Chapter 2, a FEM model was established in SAP2000 for the same 1:25 building model. Both modal analyses and time history analyses under the shaking of

0.1g Kobe earthquake without soil amplification were conducted. The predictions from the FEM analyses are comparable to the results from the shaking table tests in a number of aspects. For example, in the FEM analyses the maximum inter-story drift ratio occurred at the upper stories above the transfer plate (Figure 2.8), and the first two stories below the transfer plate had much smaller responses compared to the upper stories (Figure 2.7). In the shaking table tests, most of damages occurred at the upper stories and no visible crack was found at the first two stories. However, although the FEM model succeeds in predicting the stress concentration at the story just above the transfer plate, the locations of strain concentration found in the experiments do not agree completely with that of FEM predictions.

The mode shapes of the first six modes at the initial state from both experiments and FEM analyses are compared in Figure 6.1. Note that the mode shape has been normalized with respect to the largest component along the two horizontal directions for each mode. It can be seen that the mode shapes given by the two studies fit fairly good except for some discrepancies for the higher modes.

The acceleration and displacement responses at the roof during the shaking of 0.1g Kobe earthquake are compared in Figure 6.2 for the FEM analyses and shaking table tests. Figure 6.2(a) shows the input generated by the shaking table is quite close to the FEM input. From Figure 6.2(b), the acceleration responses at the roof given by the two studies are quite similar except for one abnormally large negative peak occurring in the tests. Although the displacement responses at the roof from the FEM analyses are different from the recorded responses in the test, the maximum displacements from the two studies are comparable [Figure 6.2(c)].

However, discrepancies also exist between the FEM predictions and the test results. For example, compared to the initial natural frequencies measured in the tests (see Table 5.2), the FEM predictions (see Table 2.2) are much smaller. Both the maximum inter-story drift ratios (1/680, see Figure 2.8) and rotation angle at the roof (0.054°, see Figure 2.9) given by the FEM analyses are larger than the test results (1/902 and 0.017° respectively) for the same earthquake input (the 0.1 PGA Kobe earthquake at rock site in Table 5.5).

These discrepancies may be due to the uncertainties in the FEM analysis. As emphasized in Chapter 2, FEM analysis is for idealized model (such as line element concept for beam and column and rigid floor assumption). Inappropriate assumptions adopted may result in large deviations between FEM predictions and test results. Actually, as found in our tests, the rigid floor assumption may not be appropriate for the present structure (refer to Section 4.3.1). The discrepancies of the FEM analysis may also come from the deviations of material strength and element dimension in the FEM model with respect to the actual physical model. As discussed in Section 3.4.3, substantial amount of variations exists for the strength of micro-concrete at different stories in the physical model, whereas a uniform material was used in the FEM model.

All these factors led to the discrepancies between the FEM predictions and the test results. To eliminate these discrepancies, proper adjustment and refinement of the FEM model, or called model updating, should be carried out by utilizing data acquired from the tests (Mottershead and Friswell, 1993). Model updating has been a rapidly developing subject, but it is out of the scope of the present study.

6.3 Interpretation on Prototype Seismic Performance

Both the shaking table tests and FEM analysis described previously concentrate on the reduced-scale building model. It is important to know how the test results can be interpreted onto the seismic performance of the actual building, or in other words, to what extend the seismic behavior of the model can reflect that of the prototype. For this purpose, the structural features of elements between the model and the actual building are compared in this section. The analytical methods used in this section are mainly suggested by Prof. K. Kasai from Tokyo Institute of Technology.

6.3.1 Beam

Theoretical moment-curvature curves for reinforced concrete sections with flexural and axial load can be derived based on the plane section assumption (Park and Paulay, 1975). Figure 6.3 sketches the procedure of the determination of moment-curvature curve for a rectangular section with axial force and flexure. The stress-strain curves for steel and concrete are shown in Figures 6.3(a) and 6.3(b), where f_y is the yield strength of steel and $f_c^{''}$ is the strength of concrete. For a given concrete strain in the extreme compression fiber ε_{cm} and neutral axis depth kd, the steel strains ε_{si} of bar i at depth d_i can be determined from the strain diagram shown in Figure 6.3(c) as following (Park and Paulay, 1975):

$$\varepsilon_{si} = \varepsilon_{cm} \frac{kd - d_i}{kd} \tag{6.1}$$

Then, the steel stresses f_{si} can be determined from the steel stress-strain curve as shown in Figure 6.3(a), and the steel forces S_i can be found based on the stresses and the areas of bars as:

$$S_i = f_{si} A_{si} \tag{6.2}$$

The concrete strain over the compressed part of the section can be determined similarly from the strain diagram and then the corresponding concrete stress can be determined from the concrete stress-strain curve [Figure 6.3(b)]. As shown in Figure 6.3(c), the concrete compressive force C_c acting at position γkd can be defined as (Park and Paulay, 1975):

$$C_c = \alpha f_c^{''} bkd \tag{6.3}$$

where α and γ are two parameters determined from the stress-strain relationship of the concrete. For rectangular sections, they can be written in the following forms:

$$\alpha = \frac{\int_0^{\varepsilon_{cm}} f_c d\varepsilon_c}{f_c^{''} \varepsilon_{cm}} \tag{6.4}$$

$$\gamma = 1 - \frac{\int_0^{\varepsilon_{cm}} \varepsilon_c f_c d\varepsilon_c}{\varepsilon_{cm} \int_0^{\varepsilon_{cm}} f_c d\varepsilon_c} \tag{6.5}$$

where f_c and ε_c denote the stress and strain of the concrete [Figure 6.3(b)].

Then the force equilibrium equations can be written as (Park and Paulay, 1975):

$$P = \alpha f_c^{''} bkd + \sum_{i=1}^{n} f_{si} A_{si} \tag{6.6}$$

$$M = \alpha f_c^{''} bkd \left(\frac{h}{2} - \gamma kd\right) + \sum_{i=1}^{n} f_{si} A_{si} \left(\frac{h}{2} - d_i\right) \tag{6.7}$$

And the curvature of the element is given as (Park and Paulay, 1975):

$$\varphi = \frac{\varepsilon_{cm}}{kd} \tag{6.8}$$

Thus the theoretical moment-curvature relation for a rectangular section can be determined by incrementing the concrete strain at the extreme compression fiber ε_{cm}. For each value of ε_{cm}, the neutral axis depth *kd* is found by adjusting *kd* until the force equilibrium in Equation (6.6) is satisfied.

Figure 6.4 shows the obtained moment-curvature curve of a beam (of 12×22mm) at 1/F of the model (the solid line), where the dashed line is the moment-curvature curve of the corresponding beam in the prototype after scaled down according to the similarity law ($\lambda_M = \lambda_\sigma \lambda_l^3$). The sections of the model and prototype beams are also shown in the figure (refer to Section 3.3.3 for steel strength). Note that the moment and curvature values in the figure have been normalized by bd^2 and d respectively. It is seen that the moment capacity of the model beam is about 2.5 times of the desired value. The same calculation has been done for several other typical beams and the ratios range from 2.5 to 6 times. On the other hand, the model beams have a smaller ductility compared to the prototype elements, suggesting that they are over-reinforced.

Although the beams of the model are over-designed from the aspect of bending, most of their damages occurring in our shaking table test are shear failures (see Figures 4.26, 4.33, 4.34 and 4.36). The shear capacities of beams have also been estimated using the formula from Chinese Code for Design of Concrete Structures (GB50010-2002, 2002) as following:

$$V_u = 0.7 f_t b h_0 + 1.25 f_{yv} \frac{A_{sv}}{s} h_0 \tag{6.9}$$

where f_t is the tensile strength, b and h_0 are the width and effective depth of the section, f_{yv} is the yield strength of the hoop, A_{sv} and s are the cross-sectional area and spacing of the hoop respectively. The results are listed in Table 6.1. It is seen that although deviations exist between the model and the prototype, their shear capacities are comparable. Thus from the aspect of shear resistance, the design of beams should be reasonable.

6.3.2 Column

Using the same method, the theoretical moment-curvature curves were obtained for rectangular columns in the model and prototype. Figure 6.5 shows an example, where the solid line is the moment-curvature curve of a column (of 27.4×60mm) at 1/F of the model and the dashed line is the desired curve determined from the prototype. Similarly the column has an over 2 times larger moment capacity.

The theoretical moment-curvature curves have also been obtained for circular columns in the model using a similar method as that of Park and Paulay (1975). As sketched in Figure 6.6, the determination procedure is similar as that described in Section 6.3.1 except for the determination of the concrete compressive force C_c and its acting position γkd. Using the coordinate system shown in Figure 6.6(c), the concrete compressive force C_c can be obtained as:

$$C_c = \iint f_c(y)dxdy = \int_0^{kd} dy \int_{-l(y)}^{l(y)} f_c(y)dx = 2\int_0^{kd} l(y)\, f_c(y)dy \qquad (6.10)$$

where $f_c(y)$ is the concrete stress and $l(y) = \sqrt{(h/2)^2 - (h/2 - kd + y)^2}$. Since from the strain diagram we have $y = \dfrac{kd}{\varepsilon_{cm}}\varepsilon_c$, the concrete force C_c can be further written as:

$$C_c = \frac{2kd}{\varepsilon_{cm}} \int_0^{\varepsilon_{cm}} l(\varepsilon_c) f_c(\varepsilon_c) d\varepsilon_c \tag{6.11}$$

In a similar way, the moment of the compressed part of concrete about the neutral axis M_{cn} can be obtained as:

$$M_{cn} = 2\left(\frac{kd}{\varepsilon_{cm}}\right)^2 \int_0^{\varepsilon_{cm}} l(\varepsilon_c) f_c(\varepsilon_c) \varepsilon_c d\varepsilon_c \tag{6.12}$$

Thus the acting position γkd of the concrete compressive force C_c can be determined through $(1-\gamma)kdC_c = M_{cn}$ as:

$$\gamma = 1 - \frac{\int_0^{\varepsilon_{cm}} l(\varepsilon_c) f_c(\varepsilon_c) \varepsilon_c d\varepsilon_c}{\varepsilon_{cm} \int_0^{\varepsilon_{cm}} l(\varepsilon_c) f_c(\varepsilon_c) d\varepsilon_c} \tag{6.13}$$

Similar as Equations (6.6) and (6.7), the force equilibrium equations can be written as:

$$P = C_c + \sum_{i=1}^{n} f_{si} A_{si} \tag{6.14}$$

$$M = C_c\left(\frac{h}{2} - \gamma kd\right) + \sum_{i=1}^{n} f_{si} A_{si}\left(\frac{h}{2} - d_i\right) \tag{6.15}$$

Thus, with the curvature given by Equation (6.8), the theoretical moment-curvature relation for the circular section can be determined by incrementing the concrete strain at the extreme compression fiber ε_{cm}.

The shear strength of circular columns has been estimated using the ATC-40 shear assessment equations as following (Kowalsky and Priestley, 2000):

$$V_u = 0.29\left[k_1 + \frac{P_e}{13.8A_g}\right]\sqrt{f_c^{'}}\left(0.8A_g\right) + \frac{A_v f_{yh}}{0.6s} D' \tag{6.16}$$

where $f_c^{'}$ is the compressive strength of concrete, f_{yh} is the yield strength of the hoop, A_v and s are the cross-sectional area and spacing of the hoop, A_g is the column gross section area, D' is the core diameter measured to the centerline of the hoop, P_e is the axial load, and the variable k_1 equals 1 for a displacement ductility of 2 or less and equals 0 for a displacement ductility greater than 2. The results for two types of circular columns are also listed in Table 6.1. Note that here $P_e = 0$ and $k_1 = 1$ have been assumed to compare the element features of the model and the actual building.

Figure 6.7 shows an example of the obtained moment-curvature curves of a circular column of 48mm diameter. It is seen that the moment capacity of the model column is over 6 times of the desired value. However, although the bending capacity of the prototype is over-estimated, the shear capacities of the columns (rectangular or circular) between the model and prototype are more comparable (see Table 6.1). Since frame structures normally tend to deflect in a shear mode (Smith and Coull, 1991), the model appears to be more reasonable in reflecting the shear behavior of the prototype.

6.3.3 Wall

The ultimate strength of walls in compression and bending was determined using the idealized stress block method (Irwin, 1984). As shown in Figure 6.8, collapse occurs when the sketched plastic stress blocks are reached. The compressive resistance of the concrete is $N_c = 0.4 f_{cu} tL$ and that of the total steel area (A_s) is $N_s^{'} = 0.72 f_y A_s$, where f_{cu} and f_y are the strength of the concrete and steel, t and L are the depth and length of the wall section respectively, and the tensile strength of the steel is $N_s = 0.87 f_y A_s$ (Irwin, 1984). In the presence of an axial load N, the neutral axis depth x_p is given by equilibrium of concrete and steel stress blocks as:

$$x_p / L = (N_s + N)/(N_u + N_s) \tag{6.17}$$

where $N_u = N_c + N_s^{'}$ is the ultimate compressive strength of the wall in the absence of moment (Irwin, 1984). The ultimate moment that the wall can transfer is (Irwin, 1984)

$$M_u = \frac{L}{2} \frac{(N_s + N)(N_u - N)}{N_u + N_s} \tag{6.18}$$

Figure 6.8 shows a normalized ultimate moment-axial load diagram of a wall above the transfer plate in the model and prototype. The wall in the model (t=14 mm, L=168 mm) uses 2 layers of steel mesh of 1.2 mm diameter wire at 12.7 mm spacing as reinforcements, whereas the prototype wall (t=350 mm, L=4200 mm) has the reinforcements of 2 layers of 20 mm diameter bars at 150 mm spacing. It is seen that the bending behaviors of the walls are comparable between the model and the prototype. There is an about 12% deviation on the ultimate bending moment capacity between the model and prototype. Since walls tend to deflect in a flexural configuration (Smith and Coull, 1991), the simulation of walls in the model is deemed to be reasonable. Actually no shear failure of walls has been observed in the test. Therefore the failure pattern of walls in the model may also happen to the actual building, for example, the crashing of walls above the transfer plate (see Figure 4.28), provided similar horizontal cracks occur at the transfer plate.

6.3.4 Discussion and recommendation

It is difficult to exactly satisfy the similarity law in reduced-scale modeling of reinforced concrete structures, especially in small-scale modeling. Due to technique constraints, a small length scale ($\lambda_l = 1/25$) was used in the present study. It remains a major challenge on how to satisfy the similarity law as much as possible using existing techniques and commercially available materials.

Figure 6.9 shows such an example. In the figure the solid line is the desired moment-curvature curve for the 12×22mm beam (the beam shown in Figure 6.4) scaled from the prototype following the similarity law and the dashed lines are the moment-curvature curves of beams with different reinforcements, where the symbol $m\phi n$ means *m* units of bars of *n*mm diameter. It is seen that the design of $4\phi 1$ reinforcement has a lower bending capacity than the desired value. Although the other two designs with $1\phi 2$ and $2\phi 2$ reinforcements have more comparable bending capacities to the desired curve, it is questionable the behaviors of these sections with only 1 or 2 reinforcements can reflect the behavior of the actual element. Therefore, how to achieve an optimal design should be the primary task and paid much more attention to in the future reduced-scale modeling of reinforced concrete structures.

Table 6.1 Estimated shear capacity (V_u) of several columns and beams of the model and prototype, where ϕ means diameter, the subscript '*p*' means the prototype, '*m*' means the model and '*md*' means the desired value for the model.

Item	b (mm)	h (mm)	$V_{u,p}$ (kN)	$V_{u,md}$ (kN)	$V_{u,m}$ (kN)	Deviation (%)
Beam	12	22	482.22	0.18	0.22	−20.8
Beam	12	20	319.06	0.12	0.19	−57.7
Column	22	60	1793.14	0.68	0.81	−19.6
Column	27.4	60	2154.05	0.81	0.90	−10.7
Column	32	48	1947.03	0.74	0.76	−3.4
Column	ϕ40		1318.24	0.50	0.88	−76.8
Column	ϕ48		1826.43	0.69	1.24	−79.8

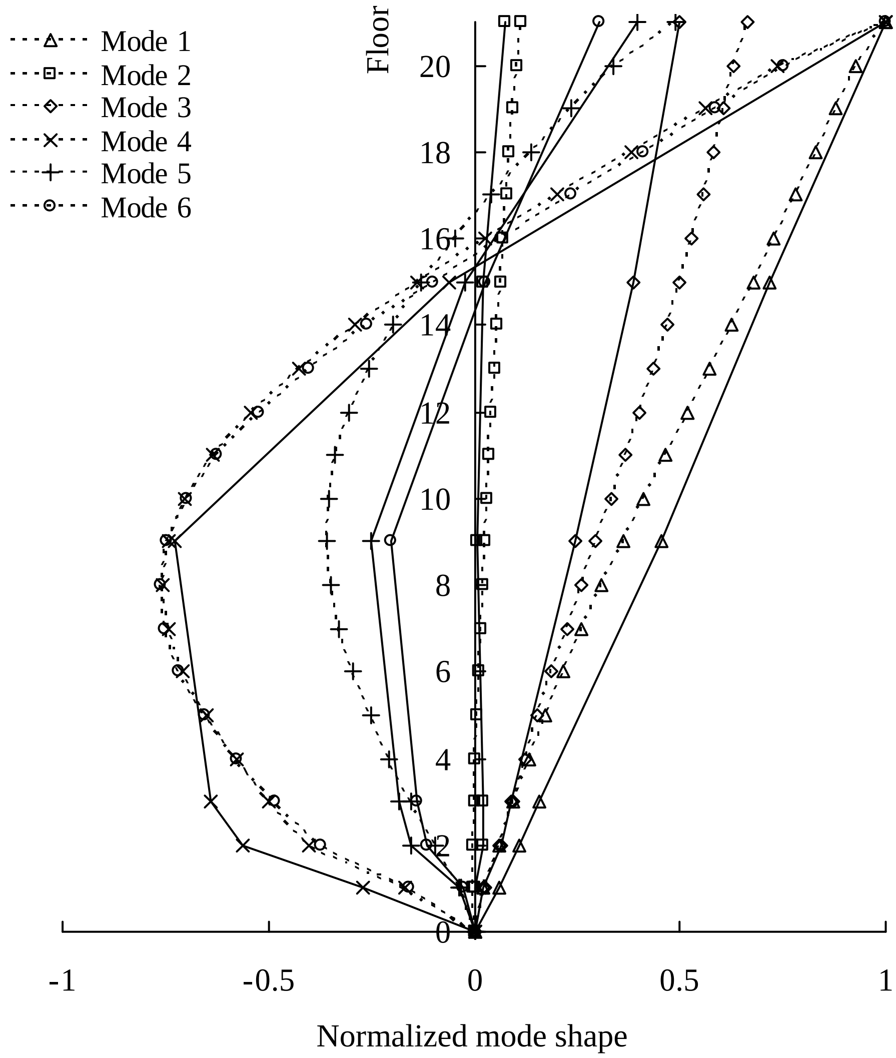

Figure 6.1 Comparison of the mode shapes of the first six modes at the initial state from both experimental measurements (solid lines) and FEM analyses (dashed lines).

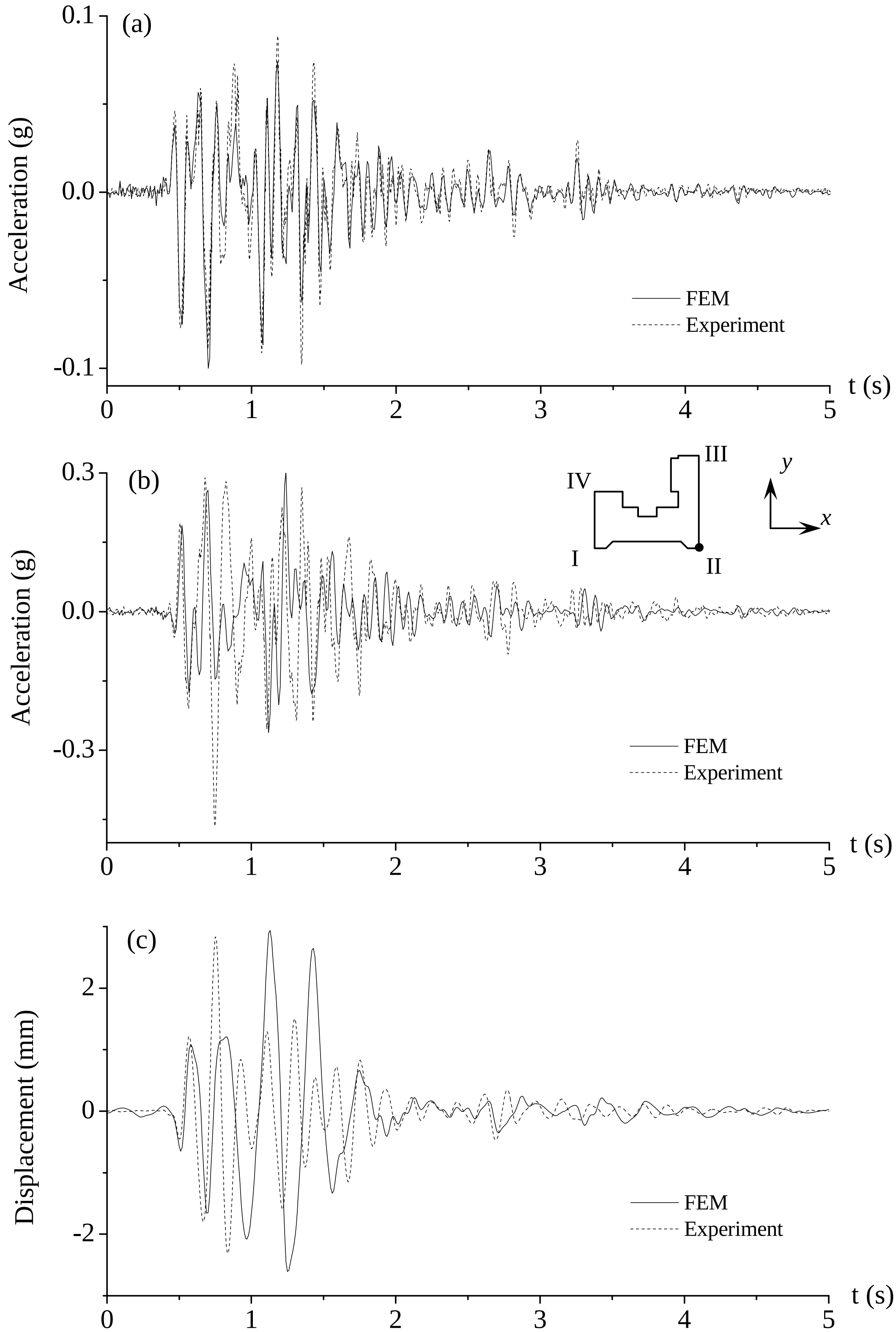

Figure 6.2 Comparison of time histories from FEM analyses and shaking table tests during the input of 0.1g Kobe earthquake at rock site: (a) the inputs; (b) acceleration and (c) displacement responses at Corner II of the roof.

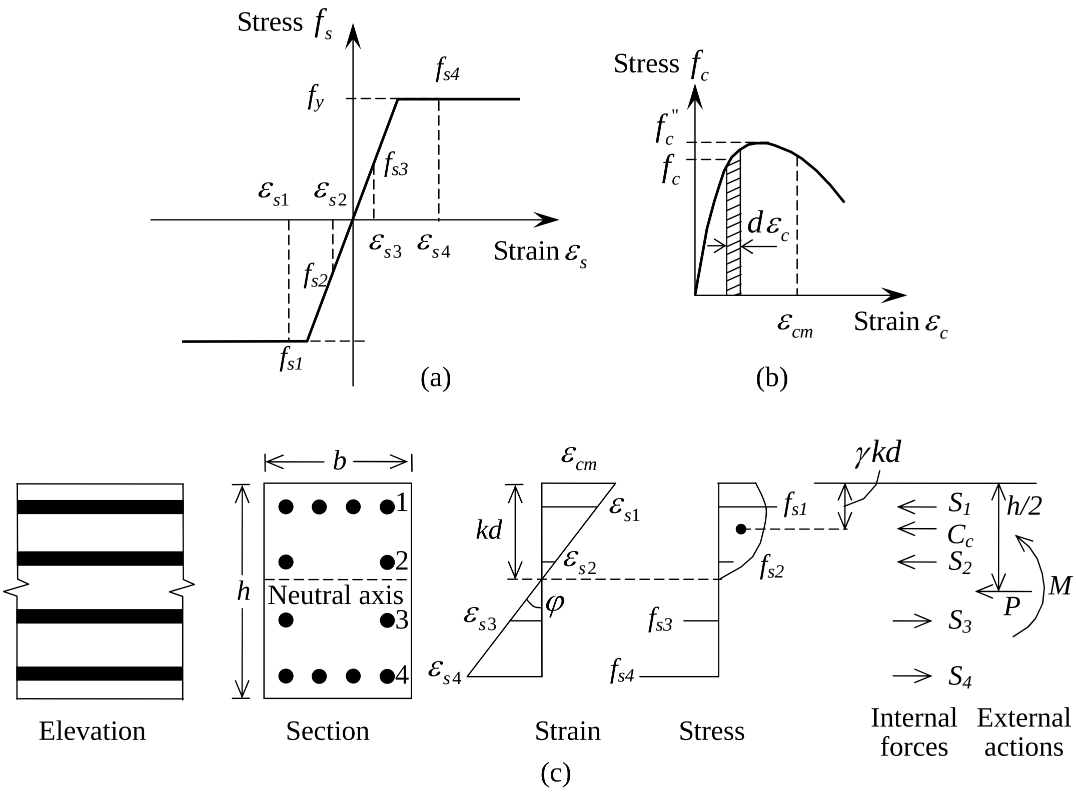

Figure 6.3 Theoretical moment-curvature determination for rectangular sections [modified from Fig. 6.5 of Park and Paulay (1975)].

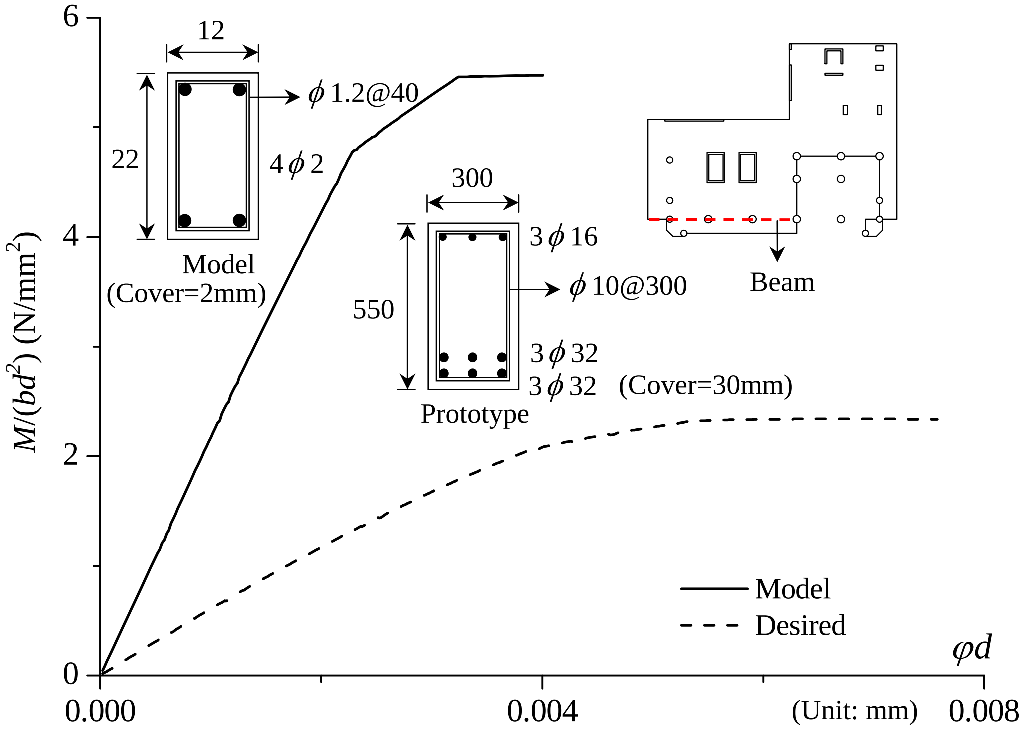

Figure 6.4 Theoretical moment-curvature curves for beams of the model and prototype (where ϕ means diameter and @ means spacing).

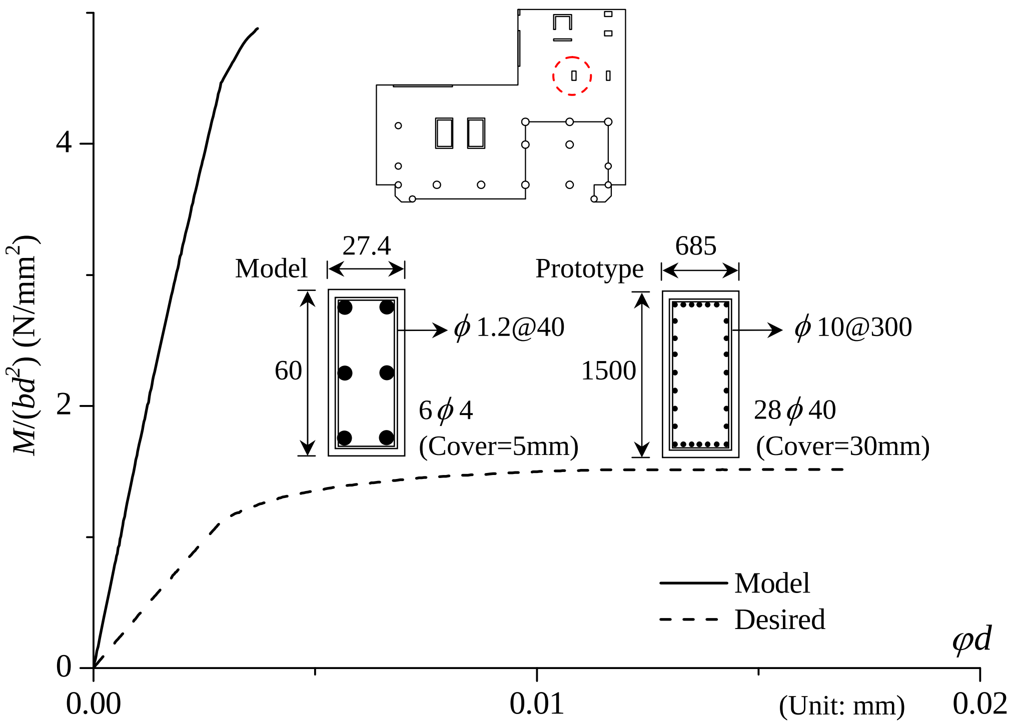

Figure 6.5 Theoretical moment-curvature curves for rectangular columns (in the dashed circle) of the model and prototype (where ϕ means diameter and @ means spacing).

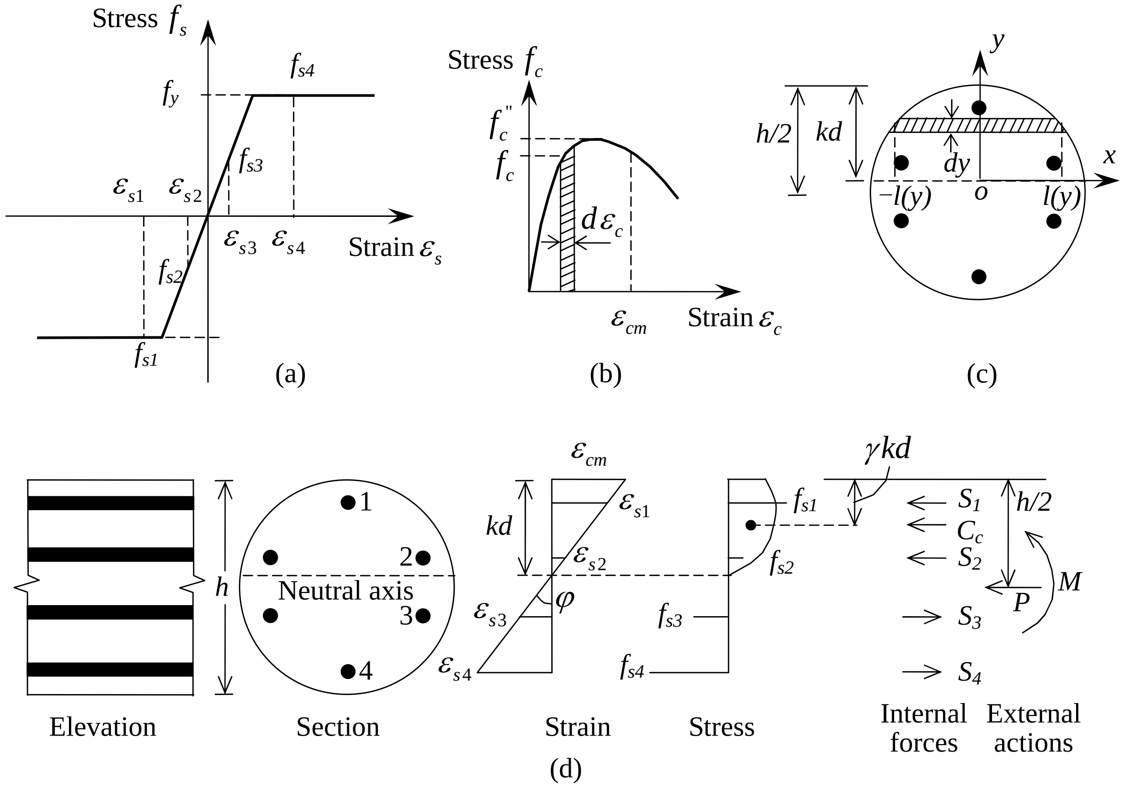

Figure 6.6 Theoretical moment-curvature determination for circular sections [modified from Fig. 6.5 of Park and Paulay (1975)].

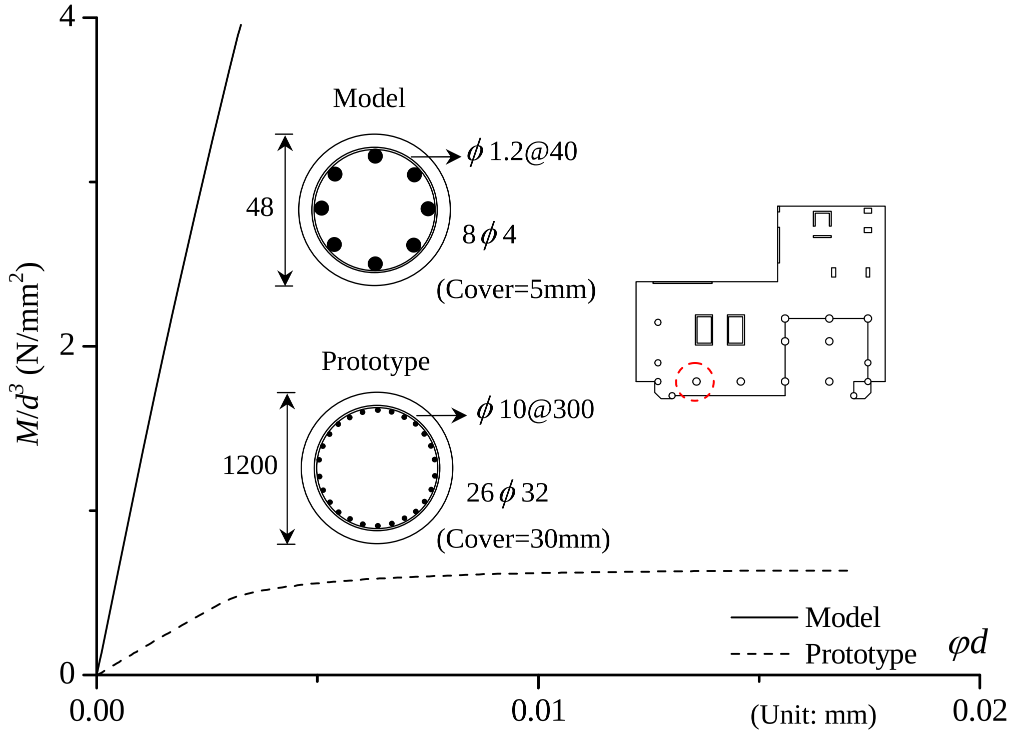

Figure 6.7 Theoretical moment-curvature curves for circular columns (in the dashed circle) of the model and prototype (where ϕ means diameter and @ means spacing).

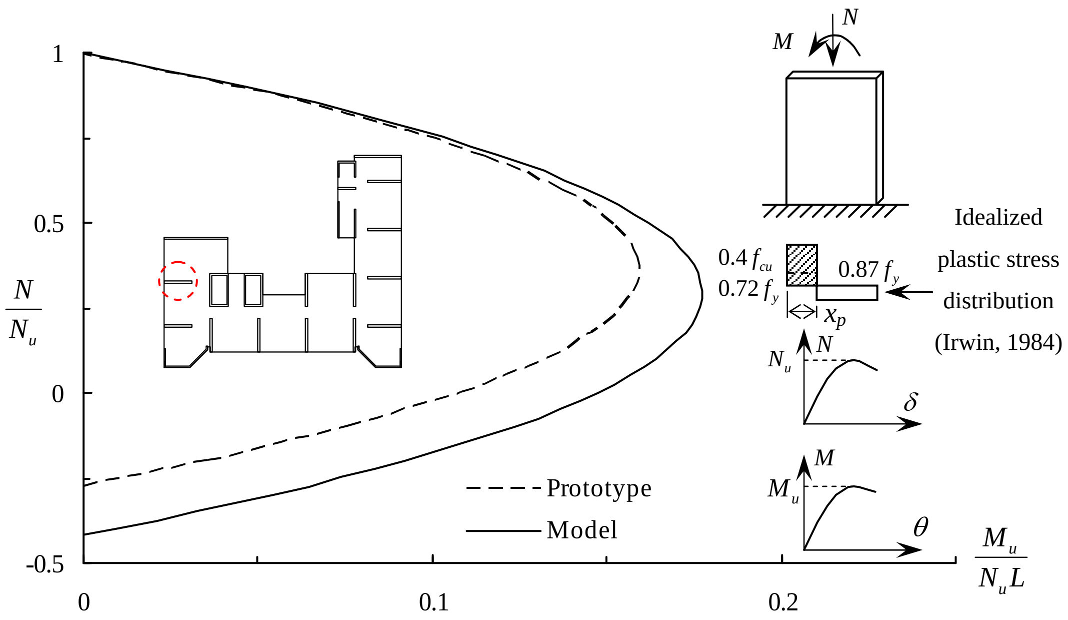

Figure 6.8 Ultimate moment-axial force curves for walls (in the dashed circle) of the model and prototype.

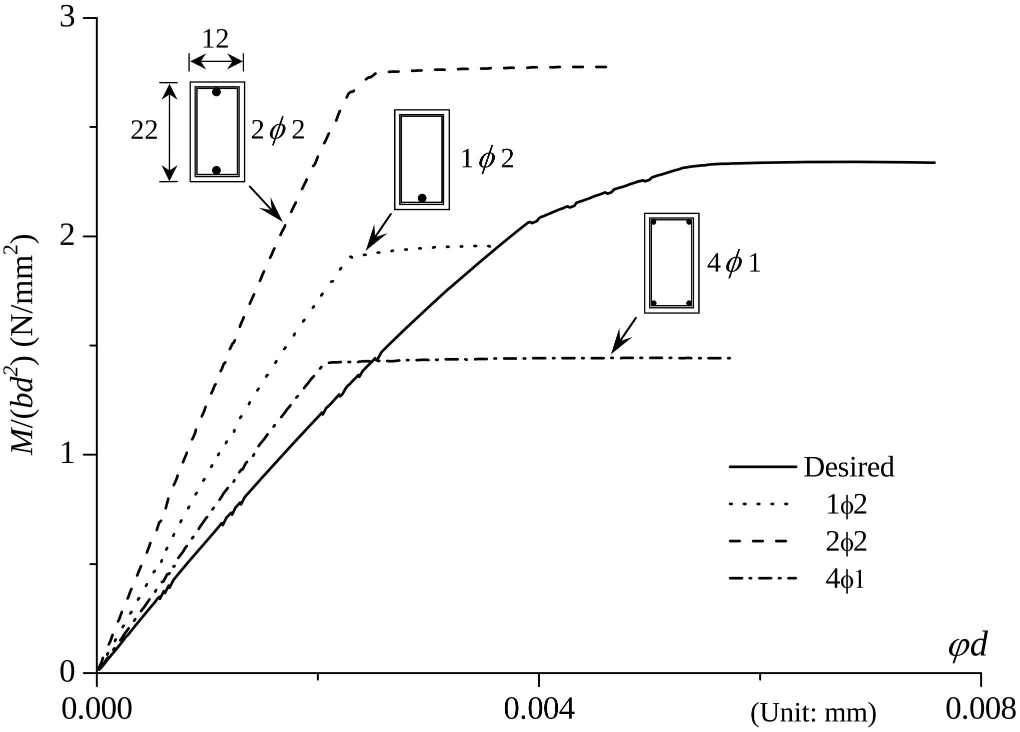

Figure 6.9 Theoretical moment-curvature curves for beams of the model and prototype (where ϕ means diameter).

PART B

SEISMIC TORSIONAL POUNDINGS

CHAPTER 7 NUMERICAL SIMULATION AND ANALYTICAL SOLUTION FOR TORSIONAL POUNDING

7.1 Introduction

Pounding between adjacent structures (such as buildings or bridges) or between different parts of a same structure during major earthquakes has been reported, and identified as one of the main causes of structural damages or complete collapse of structures (Berg and Degenkolb, 1973; Bertero and Collins, 1973; Bertero, 1986, 1987; Davis, 1992; Filiatrault et al., 1994; Anagnostopoulos, 1988, 1994). For example, poundings between structures have been observed in the 1964 Alaska earthquake, the 1971 San Fernando earthquake, the 1985 Mexico City earthquake, the 1989 Loma Prieta earthquake, the 1995 Kobe earthquake and the 1999 Chi-Chi earthquake. Both high-rise and low-rise adjacent structures are susceptible to pounding induced damage if they are not adequately separated. Pounding hazards may be especially severe in highly populated and crowded metropolis areas such as Hong Kong. Therefore, pounding induced hazards should also be considered when assessing the seismic vulnerability of buildings in Hong Kong.

7.1.1 Review of previous studies on seismic poundings

7.1.1.1 Pounding hazard

Seismic pounding means earthquake induced collision between adjacent structures, which have been identified as one of the causes of damages and, in some rare cases as, a primary cause for the initiation of collapse (Anagnostopoulos, 1994). Such collisions could be expected in city blocks, where buildings are in contact to each other, in case of buildings with external stairway towers or between units of interconnected complex structures such as hospitals, schools and industrial facilities (Anagnostopoulos, 1994). In essence, when adjacent structures having different dynamic characteristics are subjected to ground motion excitations, their vibrations will be out-of-phase and pounding will tend to occur when there are inadequate separations between them.

Pounding between adjacent structures have been commonly observed during past earthquakes. Figure 7.1(a) shows an example of pounding induced severe damage during the 1999 Chi-Chi earthquake (Naeim et al., 2000). Previous investigations have revealed poundings may cause both architectural and structural damages. For example, pounding was observed in over 15% of the 330 collapsed or severely damaged structures during the 1985 Mexico City earthquake (Rosenblueth and Meli, 1986; Anagnostopoulos, 1996). During the 1989 Loma Prieta earthquake, there were over 200 pounding occurrences involving more than 500 buildings in San Francisco, Oakland, Santa Cruz, and Watsonville (Kasai and Maison, 1997).

Surveying nine earthquakes occurring from 1964 to 1989, Anagnostopoulos (1994) found that although pounding is frequently observed during strong earthquakes, most of the observed damages are local, non-structural, or minor structural damage. The severest damages occur when the columns of a building are hammered at mid-story by the roof or a floor slab of a stiff and massive building. Such column damages may even cause partial or total failure (Anagnostopoulos, 1994).

At present, buildings in metropolis cities tend to be increasingly taller and closer to each other due to the shortage of land and the ever increasing population. Figure 7.1(b) shows an example of two 21-story buildings in Hong Kong which are almost touching with each other, and this is not uncommon in other places of Hong Kong. Under such circumstance, pounding may be the main cause of seismic damages in buildings.

7.1.1.2 Pounding hazard mitigation

Various remedial measures have been used to mitigate the seismic pounding hazard. The most straightforward method is to provide adequate separation distance between adjacent buildings to completely preclude the occurrence of pounding during strong earthquakes. This requirement has been prescribed in many building codes, such as the Uniform Building Code (UBC) 1993, National Building Code of Canada (NBCC) 1990, Chinese Code for Seismic Design of Buildings (GB50011-2001) 2001, and the National Earthquake Hazards Reduction Program code (NEHRP) 1991 [see the summary by Chau and Wei (2001)].

For instance, Chinese Code for Seismic Design of Buildings (GB50011-2001, 2001) prescribes a gap of 70 mm for frame structures shorter than 15 m and the gap should increase by 20 mm for every 4 m increase of height when the fortification intensity of the region is VII. For frame-shear wall structures and shear wall structures, the gap can be reduced to 70% and 50% respectively of the values prescribed above, but the minimum width should not be less than 70 mm.

However, there is no well-accepted approach for the estimation of adequate separation distance between adjacent structures and much more research remains to be done. For example, UBC 1993 and NEHRP 1991 recommended the use of the "absolute sum" (ABS) method in summing the maximum vibrations of two adjacent buildings to estimate the required separation between them, whereas more refined approaches include the use of the "spectral difference" (SPD) method (Kasai et al., 1996) and the "complete-quadratic-combination" (CQC) method (Hahn and Valenti, 1997; Penzien, 1997).

To determine the separation distance requirement between two structures during earthquakes, other approaches have also been proposed. For example, Stavroulakis and Abdalla (1991) used the pseudo static method, Filiatrault and Cervantes (1995) employed the nonlinear time history analysis, and Lin (1997) proposed a stochastic method of random vibration. Despite all these different methods have been used, there is, however, a consensus that the existing building codes for seismic pounding separations are too conservative (Chau and Wei, 2001).

However, pounding hazard mitigation by providing adequate separation distance sometimes is constrained by the limited land available, especially in crowded cities. Other pounding mitigation techniques proposed include the use of beam linkages between adjacent structures (Westermo, 1989), strong collision walls in structures (Anagnostopoulos, 1996), and rubber bearing between superstructure segments of bridges (Jankowski et al., 1998).

7.1.1.3 Previous studies on seismic poundings

In the last few decades, many investigations have been carried out on modeling seismic poundings between structures (Jing and Young, 1991; Davis, 1992; Maison and Kasai, 1992; Papadrakakis et al., 1996; Pantelides and Ma, 1998; Hao and Zhang, 1999; Chau and Wei, 2001; Jankowski, 2005). In general, these studies can be divided into two main categories: namely, theoretical studies and experimental studies. Review on experimental investigations on this topic will be introduced in the next chapter and this chapter will concentrate on theoretical studies on seismic poundings.

Seismic pounding between adjacent structures is a very complex phenomenon, which may involve plastic deformation, local crushing as well as fracturing at the contact, and these nonlinear deformations are not easy to be incorporated into the modeling of pounding. Therefore, idealizations and simplifications have inevitably been used in previous theoretical models. For example, structures have been idealized as rigid barriers, single-degree-of-freedom (SDOF) oscillators or multi-degree-of-freedom (MDOF) oscillators, and pounding between structures has been modeled by linear dashpot-spring system or nonlinear impact model. Despite these simplifications, theoretical analyses have been valuable in providing insight into the complex pounding mechanisms.

In general, previous theoretical studies can be based on either SDOF systems or MDOF systems as shown in Figure 7.2. The collisions between adjacent buildings are simulated either by means of special contact elements or by applying the impact laws of mechanics, with a coefficient of restitution for plastic impacts (Anagnostopoulos, 1994; Mouzakis and Papadrakakis, 2004).

The problem of pounding between SDOF systems has been studied by Kobrinski (1969), Miller (1980), Jing and Young (1991), and Davis (1992). The case of several buildings standing in a row subjected to pounding has also been studied by Anagnostopoulos (1988). The results revealed that the exterior structures, which are subjected to impacts in a single direction, tend to experience larger response amplifications than the interior structures.

Among those studies, the pounding model by Davis (1992), which incorporates the nonlinear Hertzian impact, deserves more deliberation. In particular, Davis (1992) considered impacts between a SDOF oscillator and a neighboring barrier. The impact forces were described by the Hertz contact law. An analytical solution was obtained for the case of rigid impact. This model is considered to be more realistic because nonlinear contact has been incorporated, which reflects the reality that seismic poundings are seldom linear.

Employing the model of Davis (1992), Pantelides and Ma (1998) examined poundings between a damped SDOF structural system and a stationary rigid structure. The structural behavior may be either elastic or inelastic. The results showed that for moderate damping levels the displacement response is larger in the inelastic structure, however, the peak velocity, acceleration and pounding force as well as the number of pounding occurrences of the inelastic structure are significantly smaller than those of the elastic structure.

Chau and Wei (2001) extended the model of Davis (1992) to consider poundings between two SDOF oscillators (Figure 7.3). An analytical solution is obtained for the case of rigid impact, which agrees qualitatively with their numerical simulations. Parametric studies are conducted to examine the influences of stand-off distance, natural period, damping ratio and contact parameter on poundings.

Jankowski (2005) compared the linear viscoelastic model and nonlinear elastic model used for simulating seismic pounding. A nonlinear viscoelastic model was proposed, which modified the Hertz contact law by introducing a nonlinear damper during the approach period of the collision in order to simulate energy dissipation. Comparisons between the numerical simulations and the results of previous impact experiments [including the shaking table test conducted by Chau et al. (2003)] suggested that the proposed model can provide a reliable simulation of structural pounding during earthquakes.

More recently, Muthukumar and DesRoches (2006) compared various impact models in modeling the seismic pounding response of adjacent structures, including the stereomechanical model, linear spring model, Kelvin model, Hertz model, and Hertz model with a nonlinear damper (referred to as the Hertzdamp model by the authors). The results suggest that the Hertz model provides adequate results at low PGA (0.1-0.3g) levels of ground shaking, and the Hertzdamp model performs better at moderate (0.4-0.6g) and high (0.7-0.9g) PGA levels, for energy loss during impact being more significant at higher levels of PGA.

Most of these studies assume a two-dimensional behavior, and only translational pounding is considered. However, as indicated in Chapter 1, actual structures may undergo torsional vibrations when subjected to earthquake excitations due to structural or non-structural reasons (Sedarat, 1989). Even when the adjacent buildings are nominally symmetric and the vertical plane passing through the centers of stiffness of the two buildings is parallel to the direction of excitation, the impact between them, as indicated by Leibovich et al. (1996), is not likely to be symmetric. This is because the gap between the two colliding floor slabs may be closed or narrowed at arbitrary points by accumulated hard debris [Figure 7.4(a)], and thus is seldom of exact constant width. In addition, as sketched in Figure 7.4(b), the vertical plane through the centers of stiffness of the two buildings is, more often than not, at an angle to the direction of excitation (Leibovich et al., 1996). All these factors may result in eccentric impacts. Therefore, torsional pounding is more common in practice and should be taken into account in modeling.

Maison and Kasai (1990) considered pounding at a single floor level between a multi-story building and a rigid adjacent structure. The contact was modeled using a linear spring. Torsional response was included and eccentric impacts were considered. But the impacts were enforced to occur only at the assumed contact point, whereas in practice floor rotation can lead to pounding at some other points along the interface of the two floor slabs (Leibovich et al., 1996).

Leibovich et al. (1996) studied possible eccentric pounding between two symmetric single-story systems under seismic excitation as sketched in Figure 7.4. Pounding rebounds were modeled using the coefficient of restitution. It was found that eccentric impact results in larger response amplification than symmetric impact, but the amplification does not increase with eccentricity for symmetrically aligned systems due to the mutual constraint of the adjacent slabs.

Papadrakakis et al. (1996) developed a three-dimensional finite element model for the simulations of the pounding response of two or more adjacent buildings during earthquakes. The contact-impact problem was formulated using the Lagrange multiplier method. The structures were modeled as MDOF systems using finite elements and with the possibility of contact between slabs or between slabs and columns. The contact points were located through a searching procedure among the candidate contact surfaces. However, it will be difficult and time-consuming to set up reliable finite element models for actual complex buildings.

More recently, Mouzakis and Papadrakakis (2004) investigated the three-dimensional pounding of two adjacent buildings with linear and nonlinear responses. The formulation took into account three-dimensional dynamic contact conditions for both velocities and accelerations based on the impulse-momentum relationship, using the coefficient of restitution and the ratio of tangential to normal impulses. The proposed formulation is computationally more efficient and easy to be incorporated into commercial computer codes compared to the Lagrange multiplier approach (Papadrakakis et al., 1996).

7.1.2 Motivation of the present study

Although considerable amount of research have been conducted on seismic pounding, the more realistic Hertz contact law has not been used to model torsional pounding between asymmetrical structures. Therefore, this chapter is intended to extend the models of Davis (1992) and Chau and Wei (2001) to consider the seismic torsional pounding between two adjacent asymmetrical single-story towers using the nonlinear Hertz contact law. This proposed problem is the simplest earthquake-induced torsional pounding problem. The result of this problem should provide insights for more complicated torsional poundings between real buildings. The fourth-order Runge-Kutta integration algorithm with an adaptive step size control will be used to numerically solve the differential equations. The details will be introduced in Section 7.2.

An analytical solution will be derived for periodic rigid single pounding between an asymmetrical single-story tower and a neighboring barrier under sinusoidal wave excitations. Parametric studies will be carried out to investigate the influence of various parameters on torsional pounding. The details will be introduced in Section 7.3.

7.2 Numerical Simulation for Pounding between Two Flexible Towers

In this section, torsional pounding between two asymmetrical single-story towers under harmonic ground shaking is considered. The Hertz contact law is used to model the impact force. The equations of motion of the system are first formulated and calculation of impact forces is discussed. Then the governing equations are numerically solved. Finally parametric studies are carried out to investigate the effects of excitation frequency, damping ratio, separation distance and eccentricity on torsional pounding.

7.2.1 Formulation

7.2.1.1 Equations of motion

As shown in Figure 7.5, two adjacent rectangular single-story towers (A and B) of equal height and separated by a distance of a' are considered. Each tower is supported by four identical square columns at its four corners. For simplicity, the dimensions of the two towers are assumed to be equal in this study (i.e. $l'_A = l'_B = l'$ and $w'_A = w'_B = w$). The letters 'CM' and 'CS' in the figure denote the center of mass and center of stiffness of each tower respectively. Since the four supporting columns are identical and symmetrically distributed, CS coincides with the geometric center of each tower. The position of CM, however, is assumed to be a variable. The eccentricities between CM and CS are denoted by e'_{ix}, e'_{iy} $(i = A, B)$ along the x and y directions respectively. Without loss of generality, only eccentricity along the y direction and ground motion along the x direction are considered in the present study (i.e. $e'_{Ax} = e'_{Bx} = 0$). In addition, the tower slabs are assumed to be rigid in their own planes and frictionless contact is assumed.

The motion of each model is described by three degrees of freedom, that is, two translational displacements along the x and y directions, $u_i(\tau)$ and $v_i(\tau)$, and one rotation about CM, $\theta_i(\tau)$ ($i = A, B$), where τ is the time. Then the equations of motion of each tower can be written in matrix form as:

$$\begin{bmatrix} m_i & 0 & 0 \\ 0 & m_i & 0 \\ 0 & 0 & I'_i \end{bmatrix} \begin{Bmatrix} \ddot{u}_i \\ \ddot{v}_i \\ \ddot{\theta}_i \end{Bmatrix} + \begin{bmatrix} c_i & 0 & 0 \\ 0 & c_i & 0 \\ 0 & 0 & c'_i \end{bmatrix} \begin{Bmatrix} \dot{u}_i - \dot{u}_g \\ \dot{v}_i \\ \dot{\theta}_i \end{Bmatrix} + \underset{\sim}{\mathbf{K}}_i \begin{Bmatrix} u_i - u_g + \Delta_i \\ v_i - e_{iy} \\ \theta_i \end{Bmatrix} = \begin{Bmatrix} F'_{ix} \\ F'_{iy} \\ T'_{i\theta} \end{Bmatrix}$$

$$(i = A, B) \qquad (7.1)$$

where m_i is the lumped mass, I'_i is the moment of inertia of each tower about a vertical axis through the center of mass, c_i and c'_i denote the translational and torsional damping respectively, F'_{ix} and F'_{iy} are the pounding forces acting on each tower along the x and y directions respectively, $T'_{i\theta}$ is the torqure caused by pounding, and $u_g(\tau) = A_g \sin \omega\tau$ is the input ground motion, where A_g and ω are the amplitude and the circular frequency of the ground excitation. The matrix $\underset{\sim}{\mathbf{K}}_i$ is the stiffness matrix of each tower. For the model shown in Figure 7.5, it has the form

$$\underset{\sim}{\mathbf{K}}_i = \begin{bmatrix} 4k_i & 0 & 4k_i e'_{iy} \\ 0 & 4k_i & -4k_i e'_{ix} \\ 4k_i e'_{iy} & -4k_i e'_{ix} & [l'^2_i + w'^2_i + 4(e'^2_{iy} + e'^2_{ix})]k_i \end{bmatrix} \qquad (i = A, B) \qquad (7.2)$$

where k_i is the lateral stiffness of each supporting column of the i^{th} tower. For simplicity, all of the columns of the two towers are assumed to be identical (i.e. each column has a lateral stiffness of k). Thus, if we define K_A and K_B are the lateral stiffness of the two towers respectively, we have $K_A = K_B = 4k$. The two parameters $\Delta'_i \ (i = A, B)$ in Equation (7.1) have the following forms:

$$\begin{aligned} \Delta'_{\mathrm{A}} &= \frac{a'}{2} + \left(\frac{w'_A}{2} - e'_{Ax}\right) \\ \Delta'_{\mathrm{B}} &= -\frac{a'}{2} - \left(\frac{w'_B}{2} - e'_{Bx}\right) \end{aligned} \qquad (7.3)$$

Dividing the first two equations in Equation (7.2) by m_i and the third equation by I_i respectively, we get

$$\begin{Bmatrix} \ddot{u}_i \\ \ddot{v}_i \\ \ddot{\theta}_i \end{Bmatrix} + \begin{bmatrix} 2\zeta_{ix}\omega_{ix} & 0 & 0 \\ 0 & 2\zeta_{ix}\omega_{ix} & 0 \\ 0 & 0 & 2\zeta_{i\theta}\omega_{ix} \end{bmatrix} \begin{Bmatrix} \dot{u}_i - \dot{u}_g \\ \dot{v}_i \\ \dot{\theta}_i \end{Bmatrix} + \underset{\sim}{\mathbf{K}}'_i \begin{Bmatrix} u_i - u_g + \Delta'_i \\ v_i - e'_{iy} \\ \theta_i \end{Bmatrix} = \begin{Bmatrix} F'_{ix} / m_i \\ F'_{iy} / m_i \\ T'_{i\theta} / I_i \end{Bmatrix}$$

$$(i = A, B) \qquad (7.4)$$

In the above equations, the following definitions have been used:

$$\omega^2_{ix} = \frac{4k}{m_i}, \quad \omega^2_{i\theta} = \frac{[l'^2_i + w'^2_i + 4(e'^2_{ix} + e'^2_{iy})]k}{I'_i}$$

$$\zeta_{ix} = \frac{c_i}{2m_i\omega_{ix}}, \quad \zeta_{i\theta} = \frac{c'_i}{2I'_i\omega_{ix}} \qquad (i = A, B) \qquad (7.5)$$

where ω_{ix} and $\omega_{i\theta}$ are the circular translational and rotational frequencies, and ζ_{ix} and $\zeta_{i\theta}$ denote the translational and rotational damping ratios of the i^{th} tower. Using these definitions, the stiffness matrix becomes

$$\underset{\sim}{\mathbf{K}}_i' = \begin{bmatrix} \omega_{ix}^2 & 0 & e_{iy}'\omega_{ix}^2 \\ 0 & \omega_{ix}^2 & -e_{ix}'\omega_{ix}^2 \\ e_{iy}'\omega_{ix}^2 m_i / I_i' & -e_{ix}'\omega_{ix}^2 m_i / I_i' & \omega_{i\theta}^2 \end{bmatrix} \qquad (i = A, B) \tag{7.6}$$

If we further normalize the dimensions with the excitation amplitude (A_g) as $x_i = u_i / A_g$, $y_i = v_i / A_g$ $(i = A, B)$ and normalize the time with the translational natural frequency (ω_{Ax}) of Tower A as $t = \tau\omega_{Ax}$, Equation (7.4) can be written in a dimensionless form as:

For Tower A,

$$\begin{Bmatrix} \ddot{x}_A \\ \ddot{y}_A \\ \ddot{\theta}_A \end{Bmatrix} + \begin{bmatrix} 2\zeta_{Ax} & 0 & 0 \\ 0 & 2\zeta_{Ax} & 0 \\ 0 & 0 & 2\zeta_{A\theta} \end{bmatrix} \begin{Bmatrix} \dot{x}_A - \dfrac{1}{p_1}\cos\dfrac{t}{p_1} \\ \dot{y}_A \\ \dot{\theta}_A \end{Bmatrix}$$
$$+ \begin{bmatrix} 1 & 0 & e_{Ay} \\ 0 & 1 & -e_{Ax} \\ e_{Ay}\dfrac{m_A}{I_A} & -e_{Ax}\dfrac{m_A}{I_A} & \left(\dfrac{p_3}{p_1}\right)^2 \end{bmatrix} \begin{Bmatrix} x_A - \sin\dfrac{t}{p_1} + \Delta_A \\ y_A - e_{Ay} \\ \theta_A \end{Bmatrix} = \begin{Bmatrix} F_{Ax} \\ F_{Ay} \\ T_{A\theta} \end{Bmatrix} \tag{7.7}$$

For Tower B,

$$\begin{Bmatrix} \ddot{x}_B \\ \ddot{y}_B \\ \ddot{\theta}_B \end{Bmatrix} + \frac{p_2}{p_1}\begin{bmatrix} 2\zeta_{Bx} & 0 & 0 \\ 0 & 2\zeta_{Bx} & 0 \\ 0 & 0 & 2\zeta_{B\theta} \end{bmatrix} \begin{Bmatrix} \dot{x}_B - \dfrac{1}{p_1}\cos\dfrac{t}{p_1} \\ \dot{y}_B \\ \dot{\theta}_B \end{Bmatrix}$$
$$+ \begin{bmatrix} \left(\dfrac{p_2}{p_1}\right)^2 & & e_{By}\left(\dfrac{p_2}{p_1}\right)^2 \\ & \left(\dfrac{p_2}{p_1}\right)^2 & -e_{Bx}\left(\dfrac{p_2}{p_1}\right)^2 \\ e_{By}\left(\dfrac{p_2}{p_1}\right)^2\dfrac{m_B}{I_B} & -e_{Bx}\left(\dfrac{p_2}{p_1}\right)^2\dfrac{m_B}{I_B} & \left(\dfrac{p_4}{p_1}\right)^2 \end{bmatrix} \begin{Bmatrix} x_B - \sin\dfrac{t}{p_1} + \Delta_B \\ y_B - e_{By} \\ \theta_B \end{Bmatrix} = m\begin{Bmatrix} F_{Bx} \\ F_{By} \\ T_{B\theta} \end{Bmatrix} \tag{7.8}$$

where $e_{ix} = e'_{ix} / A_g$, $e_{iy} = e'_{iy} / A_g$, $\Delta_i = \Delta'_i / A_g$, $I_i = I'_i / A_g^2$ $(i = A, B)$, $a = a' / A_g$, $l = l' / A_g$, $w = w' / A_g$, $p_1 = T / T_{Ax} = \omega_{Ax} / \omega$, $p_2 = T / T_{Bx} = \omega_{Bx} / \omega$, $p_3 = T / T_{A\theta} = \omega_{A\theta} / \omega$, $p_4 = T / T_{B\theta} = \omega_{B\theta} / \omega$, T is the period of the ground motion (i.e. $T = 2\pi / \omega$), and $m = m_A / m_B$ is the mass ratio between the two towers. Since the two towers are assumed to have identical lateral stiffness (i.e. $K_A = K_B = 4k$), recalling $\omega_{ix}^2 = K_i / m_i$, we have $m = (\omega_{Bx} / \omega_{Ax})^2 = (p_2 / p_1)^2$. The impact forces have been normalized as $F_{ix} = F'_{ix} / (A_g k_{Ax})$ and $F_{iy} = F'_{iy} / (A_g k_{Ax})$, and the impact torques have been normalized as $T_{i\theta} = T'_{i\theta} / (k_{Ax} I_i / m_i)$ $(i = A, B)$.

7.2.1.2 Calculation of impact force

Following the models of Davis (1992) and Chau and Wei (2001), the pounding forces are modeled by the Hertz contact law (Goldsmith, 1960) in this study:

$$F' = \begin{cases} \beta' \cdot d'^{\chi} & \text{for } d' > 0 \\ 0 & \text{for } d' \le 0 \end{cases} \tag{7.9}$$

where d' denotes the penetration depth between the two towers at the pounding point, β' is the impact stiffness parameter, which is a function of the elastic properties and geometry of the two contact bodies (Goldsmith, 1960), and χ is the contact force exponent. The value $\chi = 3/2$ corresponds to the Hertz contact law, whereas $\chi = 1$ represents linear contact. After applying normalization as described above, Equation (7.9) becomes

$$F = \begin{cases} \beta \cdot d^{\chi} & \text{for } d > 0 \\ 0 & \text{for } d \le 0 \end{cases} \tag{7.10}$$

where the penetration depth is normalized as $d = d' / A_g$ and the impact stiffness is normalized as $\beta = \beta' /(k_{Ax} A_g^{1-\chi})$.

Note that pounding does not necessarily occur between neighboring corners of the two towers due to the possible torsional responses in this problem. For example, Corner C of Tower A may impact onto an arbitrary point on the edge EF of Tower B [see Figure 7.6(ii)]. In our calculations, the relative locations of the two towers are checked at every step to determine whether pounding occurs or not. If any pounding occurs, the locations of the impact point and consequently the penetration depth d are determined. Then the impact forces and torques on each tower can be calculated using Equation (7.10).

Totally there are thirteen different cases [(i)-(xiii)] for the torsional pounding between the two towers, as sketched in Figure 7.6. In the figure, boxes in bold lines represent towers without any rotation ($\theta = 0$) whereas boxes in thin lines represent towers having rotation ($\theta \neq 0$). The letters A and B denote the centers of mass, and C, D, E and F denote the four corners on the adjacent edges of the two towers (with C, D on Tower A and E, F on Tower B). Since the tower slabs are assumed to be rigid in their own planes, the coordinates of the four corners (x_i, y_i) (i = C, D, E, F) at any time can be calculated from the displacements and rotations of the two towers. For example, the coordinates of Corner C can be determined as

$$\begin{cases} x_C = x_A + (\dfrac{w_A}{2} - e_{Ax}) \cos\theta_A - (\dfrac{l_A}{2} - e_{Ay}) \sin\theta_A \\ y_C = y_A + (\dfrac{l_A}{2} - e_{Ay}) \cos\theta_A + (\dfrac{w_A}{2} - e_{Ax}) \sin\theta_A \end{cases} \tag{7.11}$$

Depending on the rotations of the two towers when impact occurs and the direction of the resultant impact force, the thirteen impact cases shown in Figure 7.6 can be categorized into three types (I-III). For each type, the penetration depths as well as the impacts forces and torques on each tower are sketched in Figure 7.7. Since frictionless contact is assumed in this study, the penetration depth and the resultant impact force are always perpendicular to the edges CD or EF when they are impacted by a corner of the other tower (see Figure 7.7). The checking of pounding condition and the calculation of impact forces will be discussed in details for each type of impact as follows:

Type I: no tower has rotation [i.e. $\theta_A = \theta_B = 0$, Figure 7.7(a)]. That is to say, the edge CD of Tower A is parallel to the edge EF of Tower B when impact occurs. Thus, the problem can be simplified to translational pounding between two SDOF oscillators, the same as the problem studied by Chau and Wei (2001). The pounding condition is $x_C > x_E$ and the penetration depth is $d = x_C - x_E$. The impact forces along the *x* direction on the two towers are $F_{Ax} = -F_{Bx} = -\beta \cdot d^{\chi}$, whereas the impact forces along the *y* direction (F_{Ay}, F_{By}) and the impact torques ($T_{A\theta}, T_{B\theta}$) are all zero.

Type II: only one of the towers rotates and the resultant impact force is along the *x* direction [including the cases (ii)-(v) in Figure 7.6]. For example, when only Tower A rotates (i.e. $\theta_A \neq 0$ and $\theta_B = 0$) and Corner C impacts onto Tower B [see Figure 7.7(b)], the pounding condition is

$$x_C > x_E \quad \text{and} \quad y_E \geq y_C \geq y_F \,. \tag{7.12}$$

The penetration is $d = x_C - x_E$, and the impact forces along the *x* direction on the two towers are $F_{Ax} = -F_{Bx} = -\beta \cdot d^{\chi}$. The impact forces along the *y* direction (F_{Ay}, F_{By}) are still equal to zero, but the torques ($T_{A\theta}, T_{B\theta}$) caused by pounding are not zero.

$$T_{A\theta} = -F_{Ax}(y_C - y_A),\ \ T_{B\theta} = -F_{Bx}(y_C - y_B) \tag{7.13}$$

Note that torque in the anticlockwise direction is defined to be positive in this study. The above procedure illustrates the calculation of pounding forces when Corner C of Tower A impacts onto Tower B. The calculation procedure is similar for the case when Corner D of Tower A impacts onto Tower B or for the case when Tower B rotates and Tower A has no rotation.

Type III: the resultant impact force is not parallel to the *x* direction [including the cases (vi)-(xiii) in Figure 7.6]. Our checking criterion for this type of pounding is that only when one corner of one tower and the center of mass of the other tower are on the same side of the adjacent edge of the latter tower, pounding will occur. For example, for Corner C of Tower A [see Figure 7.7(c)], the pounding condition is the points C and B are on the same side (below or above) of the edge EF, or in mathematic form,

$$y_C > y_E + \frac{y_E - y_F}{x_E - x_F}(x_C - x_E) \ \text{ and } \ y_B > y_E + \frac{y_E - y_F}{x_E - x_F}(x_B - x_E)$$

$$\text{or } \ y_C < y_E + \frac{y_E - y_F}{x_E - x_F}(x_C - x_E) \ \text{ and } \ y_B < y_E + \frac{y_E - y_F}{x_E - x_F}(x_B - x_E) \tag{7.14}$$

When both Equation (7.14) and $y_E \geq y_C \geq y_F$ are satisfied, it is considered that Corner C impacts onto Tower B. Similar checking procedure is also applicable to the other three corners.

When Corner C impacts onto Tower B, the penetration depth d is equal to the perpendicular distance of Corner C to the edge EF, as sketched in Figure 7.7(c). The resultant impact force caused by this penetration is $F = \beta \cdot d^{\chi}$. Decompose this force into the x and y directions, and we get

$$F_{Ax} = -F_{Bx} = -F\cos\alpha\,,\quad F_{Ay} = -F_{By} = -F\sin\alpha \tag{7.15}$$

where α is the angle between the resultant force F and the x direction. Then the torques acting on each tower by pounding can be written as:

$$T_{A\theta} = -F_{Ax}(y_C - y_A) + F_{Ay}(x_C - x_A)\,,\quad T_{B\theta} = -F_{Bx}(y_C - y_B) + F_{By}(x_C - x_B) \tag{7.16}$$

7.2.1.3 Method of solution

After impact forces and torques are determined, the torsional pounding between the two towers can be solved through Equations (7.7) and (7.8), which comprise of six coupled second-order differential equations. Although analytical solutions have been obtained for translational poundings between a SDOF oscillator and a neighboring rigid barrier by Davis (1992) as well as between two SDOF oscillators by Chau and Wei (2001), however, it is very difficult to obtain an analytical solution for the present torsional pounding problem. Therefore, numerical integration is used here to solve the system of differential equations. First we define the following vector:

$$\underset{\sim}{\mathbf{y}} = \left\{ x_A \quad \dot{x}_A \quad y_A \quad \dot{y}_A \quad \theta_A \quad \dot{\theta}_A \quad x_B \quad \dot{x}_B \quad y_B \quad \dot{y}_B \quad \theta_B \quad \dot{\theta}_B \right\}' \tag{7.17}$$

where the symbol $'$ means transpose of vector. Then Equations (7.7) and (7.8) are rewritten as a set of 12 first-order differential equations as:

$$\dot{\underset{\sim}{\mathbf{y}}} = f(t, \underset{\sim}{\mathbf{y}}) \tag{7.18}$$

with a initial value of $\underset{\sim}{\mathbf{y}}(t_0) = \underset{\sim}{\mathbf{y}}_0$ representing the initial displacements and velocities of the two towers. Finally this set of differential equations is numerically solved using the fourth-order Runge-Kutta method with an adaptive step size control (Press et al., 1992). For each time step, the next value ($\underset{\sim}{\mathbf{y}}_{\mathbf{n+1}}$) is determined by the present value ($\underset{\sim}{\mathbf{y}}_{\mathbf{n}}$) plus the product of the size of the time interval (*h*) and an estimated weighted average slope. If the error is larger than a tolerance, a smaller time step will be tried automatically. The allowable error in the iterations was set to 0.1%. The initial time step was set by the program automatically, typically in the order of 0.01, but this change with the current values of the first derivatives of the displacement variables.

In the numerical calculations, we found at some excitation frequencies there are only one or several transient impacts occurring at the beginning of excitation, and no continuous impacts occur. However, our interest in this study will be the cases with continuous impacts. To search for continuous impacts, the approach used by Davis (1992) and Chau and Wei (2001) is adopted here. In particular, the numerical integrations are first performed for 40 excitation cycles and all impacts occurred in the next eight cycles are reported. Through extensive numerical simulations, we found this approach also appears to be reasonable for our problem of torsional pounding. Note that when chaotic impacts occur, there are no steady-state responses and the adopted approach can only record the continuous impacts during the selected eight cycles. Thus, for chaotic impacts the results may be quite different if we choose another eight cycles. This is the intrinsic property of chaotic impacts, and will be shown further in Section 7.2.2.1.

7.2.1.4 Validation of the solving method

Since error control has been followed in the iterations by using the fourth-order Runge-Kutta method with an adaptive step size control, the results obtained using the method are deemed to be reliable. But studies have still been conducted to validate the method before torsional pounding phenomena are discussed.

For translation pounding, the results given by the present method have been compared with the results published by Davis (1992) and Chau and Wei (2001), and they gave nearly the same results. For torsional pounding, the method was further validated through the following way: setting the normalized eccentricity of Tower A (e_{Ay}/l) to be +0.1 and -0.1 respectively while keeping the other parameters all the same (e_{By}/l=0, $T/T_{Ax}=0.7$, $T_{Ax}/T_{Bx}=1.5$, $\zeta_{Ax}=\zeta_{Bx}=0.03$, $\zeta_{A\theta}=\zeta_{B\theta}=0.03$ and a = 1.0), and comparing the resulting steady pounding phase diagrams. As shown in Figure 7.8, when the eccentricity of Tower A is changed from +0.1 and −0.1, the translational phase diagrams at the CMs of the two towers remain unchanged whereas the rotation phase diagrams change to be opposite. The results are considered to be reasonable, suggesting the method used in this study is valid.

7.2.2 Numerical simulations and discussions

7.2.2.1 Comparison of translational and torsional poundings

First, we set Tower A to be asymmetric ($e_{Ay}/l=0.1$) and keep Tower B to be symmetric ($e_{By}/l = 0.0$). The contact force exponent is set as $\chi = 3/2$ representing the Hertz contact, and the impact stiffness is set as $\beta = 1000$ representing a relatively stiff contact (Davis, 1992). In Figure 7.9, we plot the normalized relative impact velocity spectrum $V/(A_g\omega_{Ax})$ versus the normalized excitation period T/T_{Ax} for $T_{Ax}/T_{Bx} = 1.5$, $\zeta_{Ax} = \zeta_{Bx} = 0.03$, $\zeta_{A\theta} = \zeta_{B\theta} = 0.03$, $w/l = 0.55$ and $a = 1.0$. Recalling $m = m_A/m_B$ and $m = (\omega_{Bx}/\omega_{Ax})^2 = (T_{Ax}/T_{Bx})^2$, we get $m_A/m_B = 2.25$, which means Tower A is more massive than Tower B. Each dot in the figure represents an impact. The impact velocity spectrum for translational pounding when $e_{Ay}/l = 0.0$ [i.e. Figure 5 in Chau and Wei (2001)] is also plotted for comparison. It is seen that the impact velocity spectra for translational and torsional poundings have similar patterns. For both cases, the maximum impact velocity occurs at an excitation period between the natural periods of the two towers. Compared to translational pounding, the excitation period corresponding to the maximum impact velocity for torsional pounding shifts slightly towards the natural period of the more massive tower (T_{Ax}).

However, several differences still exist between translational and torsional poundings. First, more chaotic impacts occur for torsional pounding. For translational pounding [Figure 7.9(a)], chaotic impacts only occur at limited excitation periods and most of the impacts are periodic or group periodic [i.e. a group of non-periodic impacts repeating themselves periodically, as discussed in Chau et al. (2003)]. However, for torsional pounding, most of the impacts are chaotic and group periodic impacts only occur at a limited range of the excitation periods. For these chaotic impacts, the recorded impact velocities within eight excitation cycles appear to be quite scattered. In addition, the maximum impact velocity of torsional pounding is almost three times of that of translational pounding. All of these suggest that torsional pounding appears to be more complex and severer than translational pounding.

As shown in Figure 7.9, differing from the translational pounding spectrum, there appears to be a local peak of impact velocity around the torsional period of Tower A ($T_{A\theta}$). Finally, the excitation periods corresponding to the onset of continuous impacts are the same (i.e. $T/T_{Ax} = 0.44$) for both translational and torsional poundings, whereas the longest excitation period at which continuous impacts occur for torsional pounding (i.e. $T/T_{Ax} = 1.39$) is slightly larger than that of translational pounding ($T/T_{Ax} = 1.32$). This suggests that torsional pounding is possible to occur in a wider excitation period range. But the overall difference is not significant.

As discussed in Section 7.2.1.3, the impact velocity spectra shown in Figure 7.9 are obtained by recording all of the impacts during the next eight cycles after forty excitation cycles (i.e. the 40-48th cycles). For comparison, the velocity spectrum during the 80-88th cycles for the same problem ($e_{Ay}/l = 0.1$) is plotted in Figure 7.9(b). It is seen that the overall spectrum pattern remains unchanged, except for some excitation periods at which chaotic impacts evolve. The largest difference occurs at the excitation period of $T/T_{Ax} = 1.1$, where the chaotic impact velocities during the 80-88th cycles may be more than 10 times of that during the 40-48th cycles. This illustrates the unpredictability of chaotic impacts. However, the overall difference can be considered as minor and the approach of reporting impacts within the 40-48th

excitation cycles can be considered as acceptable.

In Figure 7.9, the relative impact velocities are investigated, however, damages induced by pounding may be related more directly to impact forces. For comparison, both the impact force and the impact velocity spectra for the same problem are plotted in Figure 7.10. Compared to the impact velocity spectrum, the impact force spectrum seems to be more scattered [see the small attached diagram in Figure 7.10(b)]. Especially around the excitation period of $T/T_{Ax} = 0.9$, the maximum normalized impact forces reach almost 3000, whereas most of the forces are smaller than 500. Note that for such large impact force, the adopted Hertz impact may become invalid and plastic yielding or crushing must be incorporated into the contact law. However, as a whole the impact force and velocity spectra have a similar pattern, and normally large impact velocities correspond to large impact forces. Therefore, the impact velocities are considered to be able to describe the severity of pounding and will be shown instead of impact forces in the following sections.

Figure 7.9 reveals group periodic impacts (Chau et al., 2003) occur at a few excitation periods (e.g. $T/T_{Ax} = 0.68$-0.77, 0.87, 0.93-0.95 and 1.3-1.39). As an example, Figure 7.11 shows the phase diagrams and impact forces within one excitation cycle for $T/T_{Ax} = 0.70$. From the impact force time history, there are three impacts within one excitation cycle, occurring at the corners C, F and C respectively. These three impacts were represented by three sudden jumps to both translational and torsional velocities as observed in the phase diagrams.

7.2.2.2 Effect of separation distance

All the previous figures are for $a = 1.0$, which means the separation distance between the two towers is equal to the amplitude of the ground motion. Here the Figures 7.12(a) and (b) show the results when the normalized separation (a / A_g) is changed to 0.5 and 4.0. For comparison, the impact velocity spectrum for $a = 1.0$ shown in Figure 7.9 is also plotted as “+” symbols. With the separation distance increasing from 0.5 to 1.0 and further to 4.0, fewer impacts are observed and the excitation period ranges during which impacts can occur become narrower. However, the magnitude of the maximum impact velocity does not necessarily decrease with the increasing separation. For example, in Figure 7.12 the maximum velocity occurs when $a = 1.0$ instead of $a = 0.5$. In general, the overall patterns of these velocity spectra are similar.

This suggests that the impact velocity spectra seem to be insensitive to the variation of separation distance between adjacent structures as long as pounding is developed. This finding for torsional pounding is consistent with the conclusion on translational pounding drawn by Chau and Wei (2001). But if we keep increasing the separation distance to a critical value, no pounding will occur. And this critical separation is called the maximum stand-off distance, which means the minimum distance needed to preclude the occurrence of pounding between adjacent structures. The maximum stand-off distance will be investigated in Section 7.2.2.5.

7.2.2.3 Effect of damping ratio

In all the previous figures, both the translational and the rotational damping ratios (ζ_{ix} and $\zeta_{i\theta}$, $i = A, B$) have been set as 0.03. In Figure 7.13, we increase the translational damping ratios of the two towers to $\zeta_{Ax} = \zeta_{Bx} = 0.10$ and remain the rotational damping ratios at $\zeta_{A\theta} = \zeta_{B\theta} = 0.03$. The results for $\zeta_{Ax} = \zeta_{Bx} = 0.03$ shown in Figure 7.9 have also been plotted as "+" symbols for comparison.

With the increased translational damping ratios, the impact velocities normally decrease and the maximum velocity decreases to only 20% of the original value. The excitation period (T / T_{Ax}) corresponding to the onset of continuous impact increases from 0.44 to 0.47. In addition, with the higher damping, more group periodic impacts instead of chaotic impacts occur. All these findings suggest that the translational damping ratios may influence the impact velocity significantly. Higher damping tends to result in a lower impact velocity and a simpler pounding pattern.

In Figure 7.14, the rotational damping ratios of the two towers are increased to $\zeta_{A\theta} = \zeta_{B\theta} = 0.10$ and the translational damping ratios are kept at $\zeta_{Ax} = \zeta_{Bx} = 0.03$. When ζ_{θ} increases from 0.03 to 0.10, the shape of the velocity spectrum remains almost unchanged and the maximum impact velocity drops to about 63%. However, at some excitation periods (for example, two particular periods near the rotational period $T_{A\theta}$ of Tower A), even larger chaotic impact velocities are observed for larger rotational damping. This illustrates the complexity of chaotic torsional pounding. But on the whole, the rotational damping seems to have a less significant effect on pounding than the translational damping.

7.2.2.4 Effect of eccentricity

In all of the above investigations on torsional pounding, an eccentricity of 0.1 has been assumed for Tower A ($e_{Ay}/l = 0.1$) whereas Tower B has been assumed to be symmetric ($e_{By}/l = 0.0$). To investigate the effect of eccentricity, we first double the eccentricity of Tower A (i.e. $e_{Ay}/l = 0.2$) and keep all the other parameters the same as those used in Figure 7.9. The results are shown in Figure 7.15.

Compared to the spectrum of $e_{Ay}/l = 0.1$, the shape of the impact velocity spectrum of $e_{Ay}/l = 0.2$ remains almost unchanged, and the maximum velocity is about 20% smaller. But at some excitation periods (such as those periods near $T_{A\theta}$ and T_{Bx}), the maximum impact velocities of $e_{Ay}/l = 0.2$ are larger than that of $e_{Ay}/l = 0.1$. For $e_{Ay}/l = 0.2$, the excitation period range during which impact is developed extends to about $T/T_{Ax} = 1.5$, suggesting pounding is possible to occur at longer excitation periods for large eccentricity. However, on the whole the impact velocity spectrum is not affected significantly by the doubling of eccentricity. This may be due to the mutual rotational constraint of the two towers. Similar phenomenon has also been observed by Leibovich et al. (1996).

In Figure 7.16, we keep the eccentricity of Tower A to be 0.1 and change Tower B to be asymmetric. In particular, the impact velocity spectra for $e_{By}/l = 0.1$ and $e_{By}/l = -0.1$ are plotted in Figures 7.16(a) and (b) respectively. Both of them are compared with the spectrum of $e_{By}/l = 0$ given earlier in Figure 7.9. It is seen that when Tower B is also asymmetric, the excitation period (T/T_{Ax}) corresponding to the onset of continuous impacts decreases to near 0.3 and impacts are developed around the torsional period of Tower B ($T_{B\theta}$). However, on the whole the shapes of velocity spectra are similar to that of $e_{By}/l = 0$. But the pounding between two asymmetric structures seems to be more complex and almost all the impacts are chaotic.

For the maximum impact velocity among the three cases ($e_{By}/l = 0.1, 0, -0.1$), the largest impact velocity is found for the case $e_{Ay}/l = 0.1$ and $e_{By}/l = 0.1$, whereas the smallest velocity is found for the case $e_{Ay}/l = 0.1$ and $e_{By}/l = -0.1$. Thus, it seems that larger impact velocity may be resulted when the two structures have eccentricities in a same direction, and medium impact velocity may be resulted when one structure is asymmetric and the other is symmetric.

7.2.2.5 Maximum stand-off distance

Figure 7.17 shows the maximum stand-off distances versus the normalized excitation period T/T_{Ax} for three different eccentricities of Tower A (i.e. $e_{Ay}/l = 0.0$, 0.1 and 0.2). Tower B is still set to be symmetric ($e_{By}/l = 0$). All the other parameters are the same as those in Figure 7.9. These curves are obtained in the following manner: the numerical calculations are done for all T/T_{Ax} from 0.01 to 2.0 in steps of 0.05 and for all a from 0 to 20 in steps of 0.25; for each T/T_{Ax}, the maximum value of a on which continuous pounding is developed is recorded. The physical meaning of these curves is that the separation distance between the two towers must be larger than those critical values of a to preclude the occurrence of pounding.

The curves of the maximum stand-off distances for the three eccentricities have similar shapes. The maximum stand-off distances of all cases occur near the natural period of the more massive tower (T_{Ax}) and the secondary peaks occur near the natural period of the other tower (T_{Bx}). It is easy to understand since structures tend to have larger responses when the excitation period is close to their natural periods, and thus larger distance is needed to avoid pounding. For the large eccentricity ($e_{Ay}/l = 0.2$), the excitation period corresponding to the maximum stand-off distance has a small shift towards a value larger than T_{Ax} (Figure 7.17). In addition, there is a local peak near the torsional period of Tower A ($T_{A\theta}$), although it is not very clear from the plots.

7.3 Analytical Solution for a Special Case: Torsional Pounding on Rigid Barrier

In the previous section, the torsional pounding between two asymmetric single-story towers is modeled using the nonlinear Hertz contact law. The resulting governing equations are numerically solved. It is very difficult to obtain any analytical solution for such a coupled system [see Equations (7.7) and (7.8)]. However, the analytical solution is possible for a less complicated system, that is, the periodic rigid pounding between an asymmetric single-story tower and a neighboring rigid barrier. In this section, the equations of motion of such a system are first formulated and then the method of solution is proposed. Finally parametric studies are carried out to investigate the effects of input frequency, damping ratio, separation distance and eccentricity on torsional poundings. The analytical solution will also be compared with numerical simulations. Although the method of solution proposed here is modified from that of Davis (1992) and Chau and Wei (2001), the mathematical problem here becomes more challenging with the inclusion of θ variable.

7.3.1 Formulation of rigid barrier pounding and method of solution

7.3.1.1 Equations of motion

As shown in Figure 7.18, the torsional pounding between an asymmetric single-story tower (Tower A) and a neighboring barrier is considered. Tower A is supported by four identical square columns at its four corners. The center of mass (CM) of Tower A is offset from the center of stiffness (CS), which is also the geometric center of the tower. For simplicity, only eccentricity along the y direction (e'_y) is considered here. The ground motion is perpendicular to the direction of eccentricity so that torsional response can be triggered. The translation $u(\tau)$ and rotation $\theta(\tau)$ of CM are defined in Figure 7.18(b), where τ is the time.

In this study, two different cases of the neighboring rigid barrier are considered following Davis (1992), that is,

Case 1: the barrier is stationary, representing a very flexible and long period neighboring structure. The input excitation is characterized by a constant displacement amplitude as $u_g = A_g \sin \omega\tau$;

Case 2: the barrier is locked to the ground motion, representing a very stiff and short period neighboring structure. The input excitation is characterized by a constant acceleration amplitude as $\ddot{u}_g = A_g \sin \omega\tau$.

In these excitations, A_g and ω are the amplitude and circular frequency of the input respectively. These two cases represent limits of response which are possible in the actual neighboring structure (Davis, 1992). For both cases, the equations of motion of Tower A can be expressed as:

$$\begin{cases} m\ddot{u} + c\dot{u} + 4ku + 4ke'_y\theta = F'_x + G[u_g(\tau)] \\ I'\ddot{\theta} + c'\dot{\theta} + 4ke'_y u + (l'^2 + w'^2 + 4e'^2_y)k\theta = T'_\theta \end{cases} \tag{7.19}$$

where m and I' are the mass and moment of inertia of Tower A, c and c' are the translational and rotational damping coefficients respectively, k denotes the lateral stiffness of each column of the tower, l' and w' are the dimensions of the tower along the y and x directions respectively, e'_y is the eccentricity, F'_x and T'_θ are the force and torque on Tower A caused by pounding, and $G[u_g(\tau)]$ denotes the forcing function which takes different forms for the two cases,

$$\text{Case 1:} \quad G[u_g(\tau)] = 4ku_g(\tau) + c\dot{u}_g(\tau) \tag{7.20}$$

$$\text{Case 2:} \quad G[u_g(\tau)] = -m\ddot{u}_g(\tau) \tag{7.21}$$

Note that in the above three equations, the displacement $u(\tau)$ is the absolute displacement of the tower for Case 1 condition, and is the relative displacement of the tower to the ground motion for Case 2 condition. Following Davis (1992), the same symbol $u(\tau)$ is used for both Case 1 and Case 2 for their mathematical similarity.

For both cases, the impact force between Tower A and the barrier can be represented as:

$$F_x' = \begin{cases} -\beta'[u_i - (a' + \frac{w'}{2})]^\chi & for \quad u_i > (a' + \frac{w'}{2}) \quad (i = C, D) \\ 0 & for \quad u_i \le (a' + \frac{w'}{2}) \quad (i = C, D) \end{cases} \tag{7.22}$$

where u_i $(i = C, D)$ is the displacement of either Corner C or Corner D on the tower, a' is the separation distance, β' is the impact stiffness, and χ is the impact force component, which is equal to $\chi = 3/2$ when the Hertz contact is assumed.

If we normalize the displacement as $x = u / A_g$ and the time as $t = \tau\omega_x$, where $\omega_x = \sqrt{4k/m}$ is the translational natural frequency of Tower A along the *x* direction, Equation (7.19) can be rewritten in a dimensionless form as:

$$\begin{cases} \ddot{x} + 2\zeta_x \dot{x} + x + \eta_\theta \theta = F_x + G[x_g(t)] \\ \ddot{\theta} + 2\zeta_\theta \dot{\theta} + \lambda_x x + \gamma_\theta \theta = T_\theta \end{cases} \tag{7.23}$$

Note that the superimposed dots in the above equations denote the derivatives with respect to the normalized time t. In addition, the following definitions have been used:

$$\zeta_x = c/(2m\omega_x), \zeta_\theta = c'/(2I'\omega_x), \eta_\theta = e_y'/A_g, \gamma_\theta = \omega_\theta^2/\omega_x^2, \omega_\theta^2 = (l'^2 + w'^2 + 4e_y'^2)k/I',$$

$$\lambda_x = me_y' A_g / I', \quad F_x = F_x'/(mA_g\omega_x^2), \quad T_\theta = T_\theta'/(I'\omega_x^2), \quad p = \omega_x/\omega = T/T_x$$

$$e_y = e_y'/A_g, \quad a = a'/A_g, \quad l = l'/A_g, w = w'/A_g, \quad I = I'/A_g^2 \tag{7.24}$$

where T and T_x denote the periods of the input and of the tower respectively, and p is the ratio between them. Note that all the displacement or length variables have been normalized with respect to the amplitude of the excitation A_g. The impact stiffness is normalized as $\beta = \beta'/(k_{Ax}A_g^{1-\chi})$. After the normalization, the forcing function $G[x_g(t)]$ becomes

$$G[x_g(t)] = E_1 \sin(t/p) + E_2 \cos(t/p) \tag{7.25}$$

where $E_1 = 1$ and $E_2 = 2\zeta_x / p$ for Case 1 condition, and $E_1 = 1$ and $E_2 = 0$ for Case 2 condition.

The torsional pounding between the tower and the barrier is fully described by Equations (7.22)-(7.25). Similar to the procedure described in Section 7.2.1, this system of equations can be numerically solved. However, analytic solution is possible for this problem when the impact is rigid [i.e. $\beta' \to \infty$ in Equation (7.22)]. For rigid impact, the contact time can be assumed to be zero and the rebound velocity is exactly equal to the negative of the impact velocity. For this special case, a closed-form solution will be obtained for periodic pounding between the tower and the barrier following the solution procedure by Davis (1992) and Chau and Wei (2001). In particular, they have obtained analytic solutions for translational pounding between a SDOF oscillator and a rigid barrier as well as between two SDOF oscillators. Their solution method will be further extended to torsional pounding in this section.

7.3.1.2 Boundary conditions for periodic impact

First of all, we assume a periodic pounding exists between the tower and the barrier. The rigid impact between them is governed by the law of conservation of translational momentum as well as the law of conservation of angular momentum. Between two consecutive impacts, the tower is in free flight, and thus the impact force and the impact torque in Equation (7.23) are all zero. When periodic pounding occurs, we can assume $t = t_0$ is the time right after an impact (i.e. the beginning of the free flight motion) and $t = t_0 + 2n\pi p$ is the time just before the next impact to occur, where $2n\pi p$ represents the normalized time duration of the free flight and n is a positive integer. Recalling that p denotes the excitation period measured in units of the natural period of the tower ($p = T/T_x$), the term $2n\pi p$ represents there are n ground excitation cycles between two neighboring impacts.

First, we assume the periodic impacts occur at Corner C of Tower A [Figure 7.18(b)]. The boundary conditions for the free flight motion can be expressed as:

$$x_C(t_0) = a + w/2 \tag{7.26}$$

$$x_C(t_0 + 2n\pi p) = a + w/2 \tag{7.27}$$

$$\theta(t_0) = \theta(t_0 + 2n\pi p) \tag{7.28}$$

$$\dot{x}(t_0) = -\dot{x}(t_0 + 2n\pi p) \tag{7.29}$$

$$\dot{\theta}(t_0) = -\dot{\theta}(t_0 + 2n\pi p) \tag{7.30}$$

where x and θ are the normalized translation and rotation of the center of mass respectively, and x_C is the translation of Corner C, which can be expressed in the form of x and θ based on the following geometric relation:

$$x_C = x + w/2 - (l/2 - e_y)\theta \tag{7.31}$$

And the boundary condition (7.26) and (7.27) means Corner C will touch on the neighboring barrier when impacts occur. If we define $h = l/2 - e_y$ and substitute Equation (7.31) into Equations (7.26) and (7.27), we can express all the boundary conditions in terms of the motion of the center of mass (i.e. x and θ):

$$x(t_0) - h\theta(t_0) = a \tag{7.32}$$

$$x(t_0 + 2n\pi p) - h\theta(t_0 + 2n\pi p) = a \tag{7.33}$$

Now Equations (7.28)-(7.30) and (7.32)-(7.33) constitute five independent boundary conditions for the free flight of the torsional pounding problem.

7.3.1.3 General solution for free flight motion between impacts

By simply letting the impact force F_x and the torque T_θ to be zero in Equation (7.23), we can get the equations of motion for the free flight of the tower. From the first equation in Equation (7.23), we have

$$\theta = \left\{ G[x_g(t)] - \ddot{x} - 2\zeta_x \dot{x} - x \right\} / \eta_\theta . \tag{7.34}$$

Substituting it into the second formula in Equation (7.23), we can get

$$\begin{aligned} &\ddot{\ddot{x}} + 2(\zeta_x + \zeta_\theta)\dddot{x} + (1 + 4\zeta_x\zeta_\theta + \gamma_\theta)\ddot{x} + 2(\zeta_\theta + \gamma_\theta\zeta_x)\dot{x} + (\gamma_\theta - \lambda_x\eta_\theta)x \\ &= H_1 \sin(t/p) + H_2 \cos(t/p) \end{aligned} \tag{7.35}$$

where the two parameters H_1 and H_2 are equal to

$$H_1 = -\frac{E_1}{p^2} - 2\zeta_\theta \frac{E_2}{p} + \gamma_\theta E_1, \quad H_2 = -\frac{E_2}{p^2} + 2\zeta_\theta \frac{E_1}{p} + \gamma_\theta E_2 . \tag{7.36}$$

To get the particular solution for Equation (7.35), first we assume the following solution form:

$$x = D_1 \sin(t/p) + D_2 \cos(t/p) . \tag{7.37}$$

After substituting it into Equation (7.35) and letting the right and left sides to be equal, finally we can get the expressions for D_1 and D_2 as:

$$D_1 = \frac{H_1H_3 - H_2H_4}{H_3^2 + H_4^2}, \quad D_2 = \frac{H_1H_4 + H_2H_3}{H_3^2 + H_4^2} \tag{7.38}$$

where

$$H_3 = \frac{1}{p^4} - \frac{1 + 4\zeta_x\zeta_\theta + \gamma_\theta}{p^2} + \gamma_\theta - \lambda_x\eta_\theta, \quad H_4 = \frac{2(\zeta_x + \zeta_\theta)}{p^3} - \frac{2(\zeta_\theta + \gamma_\theta\zeta_x)}{p} \tag{7.39}$$

To get the homogeneous solution, we have to solve the following characteristic equation:

$$s^4 + 2(\zeta_x + \zeta_\theta)s^3 + (1 + 4\zeta_x\zeta_\theta + \gamma_\theta)s^2 + 2(\zeta_\theta + \gamma_\theta\zeta_x)s + (\gamma_\theta - \lambda_x\eta_\theta) = 0 \tag{7.40}$$

Assuming the roots of the above equation in the forms $s = \alpha_j \pm i\beta_j$ (j=1, 2 and $i = \sqrt{-1}$), we can get the following general solution for Equation (7.35):

$$\begin{aligned} x &= e^{\alpha_1(t-t_0)}\left[c_1 \sin\beta_1(t-t_0) + c_2\cos\beta_1(t-t_0)\right] \\ &+ e^{\alpha_2(t-t_0)}\left[c_3 \sin\beta_1(t-t_0) + c_4\cos\beta_1(t-t_0)\right] + D_1\sin(t/p) + D_2\cos(t/p) \end{aligned} \tag{7.41}$$

where c_i (i=1, 2, 3, 4) are four unknown constants to be determined by boundary conditions. Substituting Equation (7.41) into Equation (7.34), we can get the following expression for the rotation (θ) of the center of mass:

$$\begin{aligned} \theta &= e^{\alpha_1(t-t_0)}\left[(\gamma_1 c_1 + \gamma_2 c_2)\sin\beta_1(t-t_0) + (-\gamma_2 c_1 + \gamma_1 c_2)\cos\beta_1(t-t_0)\right] \\ &+ e^{\alpha_2(t-t_0)}\left[(\gamma_3 c_3 + \gamma_4 c_4)\sin\beta_1(t-t_0) + (-\gamma_4 c_3 + \gamma_3 c_4)\cos\beta_1(t-t_0)\right] \\ &+ \gamma_5\sin(t/p) + \gamma_6\cos(t/p) \end{aligned} \tag{7.42}$$

where

$$\begin{aligned} &\gamma_1 = -\left[\alpha_1^2 - \beta_1^2 + 2\zeta_x\alpha_1 + 1\right]/\eta_\theta, \quad \gamma_2 = 2\beta_1(\alpha_1 + \zeta_x)/\eta_\theta \\ &\gamma_3 = -\left[\alpha_2^2 - \beta_2^2 + 2\zeta_x\alpha_2 + 1\right]/\eta_\theta, \quad \gamma_4 = 2\beta_2(\alpha_2 + \zeta_x)/\eta_\theta \\ &\gamma_5 = \left[E_1 + D_1/p^2 + 2\zeta_x D_2/p - D_1\right]/\eta_\theta \\ &\gamma_6 = \left[E_2 + D_2/p^2 - 2\zeta_x D_1/p - D_2\right]/\eta_\theta \end{aligned} \tag{7.43}$$

7.3.1.4 Determination of unknown parameters

Totally we have five unknowns to be determined, including c_i (i=1, 2, 3, 4) and t_0 (the onset time of the periodic impacts). These five unknowns will be determined uniquely using the five independent boundary conditions in Equations (7.28)-(7.30) and (7.32)-(7.33).

Substituting Equations (7.41) and (7.42) into Equation (7.32) and letting $t = t_0$, we get

$$\begin{aligned}&c_2 + c_4 + D_1 \sin(t_0/p) + D_2 \cos(t_0/p) - h(\gamma_1 c_2 - \gamma_2 c_1) - h(\gamma_3 c_4 - \gamma_4 c_3) \\ &-h\gamma_5 \sin(t_0/p) - h\gamma_6 \cos(t_0/p) = a\end{aligned} \tag{7.44}$$

Substitution of Equations (7.41) and (7.42) into Equation (7.33) plus some simple transformations leads to

$$q_1 c_1 + q_2 c_2 + q_3 c_3 + q_4 c_4 = (h\gamma_5 - D_1)\sin(t_0/p) + (h\gamma_6 - D_2)\cos(t_0/p) + a \tag{7.45}$$

where q_i (i=1, 2, 3, 4) are defined as follows:

$$q_1 = \left[(1-h\gamma_1)\sin(2n\pi p\beta_1) + h\gamma_2 \cos(2n\pi p\beta_1)\right]e^{2n\pi p\alpha_1}$$

$$q_2 = \left[(1-h\gamma_1)\cos(2n\pi p\beta_1) - h\gamma_2 \sin(2n\pi p\beta_1)\right]e^{2n\pi p\alpha_1}$$

$$q_3 = \left[(1-h\gamma_3)\sin(2n\pi p\beta_2) + h\gamma_4 \cos(2n\pi p\beta_2)\right]e^{2n\pi p\alpha_2}$$

$$q_4 = \left[(1-h\gamma_3)\cos(2n\pi p\beta_2) - h\gamma_4 \sin(2n\pi p\beta_2)\right]e^{2n\pi p\alpha_2} \tag{7.46}$$

Similarly substitution of Equation (7.42) into Equation (7.28) leads to

$$q_5 c_1 + q_6 c_2 + q_7 c_3 + q_8 c_4 = 0 \tag{7.47}$$

where

$$q_5 = \gamma_2 + \left[\gamma_1 \sin(2n\pi p\beta_1) - \gamma_2 \cos(2n\pi p\beta_1)\right]e^{2n\pi p\alpha_1}$$

$$q_6 = -\gamma_1 + \left[\gamma_2 \sin(2n\pi p\beta_1) + \gamma_1 \cos(2n\pi p\beta_1)\right]e^{2n\pi p\alpha_1}$$

$$q_7 = \gamma_4 + \left[\gamma_3 \sin(2n\pi p\beta_2) - \gamma_4 \cos(2n\pi p\beta_2)\right]e^{2n\pi p\alpha_2}$$

$$q_8 = -\gamma_3 + \left[\gamma_4 \sin(2n\pi p\beta_2) + \gamma_3 \cos(2n\pi p\beta_2)\right]e^{2n\pi p\alpha_2} \tag{7.48}$$

Then, by differentiating Equation (7.41) and substituting it into Equation (7.29), we obtain

$$q_9 c_1 + q_{10} c_2 + q_{11} c_3 + q_{12} c_4 = -2D_1 \cos(t_0/p)/p + 2D_2 \sin(t_0/p)/p \tag{7.49}$$

where

$$q_9 = \beta_1 + \left[\alpha_1 \sin(2n\pi p\beta_1) + \beta_1 \cos(2n\pi p\beta_1)\right]e^{2n\pi p\alpha_1}$$

$$q_{10} = \alpha_1 + \left[-\beta_1 \sin(2n\pi p\beta_1) + \alpha_1 \cos(2n\pi p\beta_1)\right] e^{2n\pi p\alpha_1}$$

$$q_{11} = \beta_2 + \left[\alpha_2 \sin(2n\pi p\beta_2) + \beta_2 \cos(2n\pi p\beta_2)\right] e^{2n\pi p\alpha_2}$$

$$q_{12} = \alpha_2 + \left[-\beta_2 \sin(2n\pi p\beta_2) + \alpha_2 \cos(2n\pi p\beta_2)\right] e^{2n\pi p\alpha_2} \qquad (7.50)$$

Similarly differentiating Equation (7.42) and substituting it into Equation (7.30), we have

$$q_{13}c_1 + q_{14}c_2 + q_{15}c_3 + q_{16}c_4 = -2\gamma_5 \cos(t_0 / p)/p + 2\gamma_6 \sin(t_0 / p)/p \qquad (7.51)$$

where

$$q_{13} = -\alpha_1\gamma_2 + \beta_1\gamma_1 + \left[(\alpha_1\gamma_1 + \beta_1\gamma_2)\sin(2n\pi p\beta_1) + (-\alpha_1\gamma_2 + \beta_1\gamma_1)\cos(2n\pi p\beta_1)\right] e^{2n\pi p\alpha_1}$$

$$q_{14} = \alpha_1\gamma_1 + \beta_1\gamma_2 + \left[(\alpha_1\gamma_2 - \beta_1\gamma_1)\sin(2n\pi p\beta_1) + (\alpha_1\gamma_1 + \beta_1\gamma_2)\cos(2n\pi p\beta_1)\right] e^{2n\pi p\alpha_1}$$

$$q_{15} = -\alpha_2\gamma_4 + \beta_2\gamma_3 + \left[(\alpha_2\gamma_3 + \beta_2\gamma_4)\sin(2n\pi p\beta_2) + (-\alpha_2\gamma_4 + \beta_2\gamma_3)\cos(2n\pi p\beta_2)\right] e^{2n\pi p\alpha_2}$$

$$q_{16} = \alpha_2\gamma_3 + \beta_2\gamma_4 + \left[(\alpha_2\gamma_4 - \beta_2\gamma_3)\sin(2n\pi p\beta_2) + (\alpha_2\gamma_3 + \beta_2\gamma_4)\cos(2n\pi p\beta_2)\right] e^{2n\pi p\alpha_2}$$

(7.52)

Rearranging Equation (7.44), the following equation is obtained:

$$q_{17}c_1 + q_{18}c_2 + q_{19}c_3 + q_{20}c_4 = (h\gamma_5 - D_1)\sin(t_0 / p) + (h\gamma_6 - D_2)\cos(t_0 / p) + a \qquad (7.53)$$

where

$$q_{17} = h\gamma_2\,, \quad q_{18} = 1 - h\gamma_1\,, \quad q_{19} = h\gamma_4\,, \quad q_{20} = 1 - h\gamma_3 \qquad (7.54)$$

Subtracting Equation (7.45) from Equation (7.53) leads to

$$(q_{17} - q_1)c_1 + (q_{18} - q_2)c_2 + (q_{19} - q_3)c_3 + (q_{20} - q_4)c_4 = 0 \qquad (7.55)$$

Finally, Equations (7.55), (7.47), (7.49) and (7.51) constitute a system of linear equations for c_i (i=1, 2, 3, 4), and these four equations can be expressed in a matrix form as:

$$\underset{\sim}{\mathbf{Q}}\underset{\sim}{\mathbf{c}} = \underset{\sim}{\mathbf{b}} \qquad (7.56)$$

where

$$\underset{\sim}{\mathbf{Q}} = \begin{bmatrix} q_{17}-q_1 & q_{18}-q_2 & q_{19}-q_3 & q_{20}-q_4 \\ q_5 & q_6 & q_7 & q_8 \\ q_9 & q_{10} & q_{11} & q_{12} \\ q_{13} & q_{14} & q_{15} & q_{16} \end{bmatrix}$$

$$\underset{\sim}{\mathbf{c}} = \begin{Bmatrix} c_1 \\ c_2 \\ c_3 \\ c_4 \end{Bmatrix} \qquad \underset{\sim}{\mathbf{b}} = \begin{Bmatrix} 0 \\ 0 \\ -2\dfrac{D_1}{p}\cos\left(\dfrac{t_0}{p}\right)+2\dfrac{D_2}{p}\sin\left(\dfrac{t_0}{p}\right) \\ -2\dfrac{\gamma_5}{p}\cos\left(\dfrac{t_0}{p}\right)+2\dfrac{\gamma_6}{p}\sin\left(\dfrac{t_0}{p}\right) \end{Bmatrix} \tag{7.57}$$

Let Δ to be the determinant of the matrix $\underset{\sim}{\mathbf{Q}}$. Then, according to Cramer's rule, if $\Delta \neq 0$, Equation (7.56) has an unique solution with the following form:

$$c_i = \frac{\Delta_i}{\Delta} \qquad \text{(i=1, 2, 3, 4)} \tag{7.58}$$

where Δ_i is the corresponding determinant obtained by replacing the i^{th} column of Δ by the vector $\underset{\sim}{\mathbf{b}}$. Since the first two elements of vector $\underset{\sim}{\mathbf{b}}$ are zeros, we can further rewrite Δ_i as:

$$\Delta_i = \Delta_{3i}\left[-\frac{2D_1}{p}\cos\left(\frac{t_0}{p}\right)+\frac{2D_2}{p}\sin\left(\frac{t_0}{p}\right)\right]+\Delta_{4i}\left[-\frac{2\gamma_5}{p}\cos\left(\frac{t_0}{p}\right)+\frac{2\gamma_6}{p}\sin\left(\frac{t_0}{p}\right)\right] \tag{7.59}$$

where Δ_{3i} and Δ_{4i} are the cofactors of the entries (3, *i*) and (4, *i*) in the determinant Δ_i respectively (Strang, 2003). For example, Δ_1, Δ_{31} and Δ_{41} have the following forms:

$$\Delta_1 = \begin{vmatrix} 0 & q_{18}-q_2 & q_{19}-q_3 & q_{20}-q_4 \\ 0 & q_6 & q_7 & q_8 \\ -\dfrac{2D_1}{p}\cos\left(\dfrac{t_0}{p}\right)+\dfrac{2D_2}{p}\sin\left(\dfrac{t_0}{p}\right) & q_{10} & q_{11} & q_{12} \\ -\dfrac{2\gamma_5}{p}\cos\left(\dfrac{t_0}{p}\right)+\dfrac{2\gamma_6}{p}\sin\left(\dfrac{t_0}{p}\right) & q_{14} & q_{15} & q_{16} \end{vmatrix}$$

$$\Delta_{31}=(-1)^{3+1}\begin{vmatrix} q_{18}-q_2 & q_{19}-q_3 & q_{20}-q_4 \\ q_6 & q_7 & q_8 \\ q_{14} & q_{15} & q_{16} \end{vmatrix}$$

$$\Delta_{41}=(-1)^{4+1}\begin{vmatrix} q_{18}-q_2 & q_{19}-q_3 & q_{20}-q_4 \\ q_6 & q_7 & q_8 \\ q_{10} & q_{11} & q_{12} \end{vmatrix} \tag{7.60}$$

Using this notation, Equation (7.58) can be rewritten as:

$$c_i=\frac{\Delta_{3i}}{\Delta}\left[-\frac{2D_1}{p}\cos\left(\frac{t_0}{p}\right)+\frac{2D_2}{p}\sin\left(\frac{t_0}{p}\right)\right]+\frac{\Delta_{4i}}{\Delta}\left[-\frac{2\gamma_5}{p}\cos\left(\frac{t_0}{p}\right)+\frac{2\gamma_6}{p}\sin\left(\frac{t_0}{p}\right)\right] \tag{7.61}$$

Substituting the above formula into Equation (7.45), we obtain an equation for t_0:

$$W_1\sin\left(\frac{t_0}{p}\right)+W_2\cos\left(\frac{t_0}{p}\right)=a \tag{7.62}$$

where

$$W_1=D_1-h\gamma_5+\frac{2}{p\Delta}\sum_{i=1}^{4}q_i(D_2\Delta_{3i}+\gamma_6\Delta_{4i})$$

$$W_2=D_2-h\gamma_6-\frac{2}{p\Delta}\sum_{i=1}^{4}q_i(D_1\Delta_{3i}+\gamma_5\Delta_{4i}) \tag{7.63}$$

Finally, the unknown t_0 can be solved from Equation (7.62) as:

$$\frac{t_0}{p}=\sin^{-1}\left(\frac{a}{\sqrt{W_1^2+W_2^2}}\right)-\tan^{-1}\left(\frac{W_2}{W_1}\right) \tag{7.64}$$

From this equation, the first condition that is required to ensure the existence of valid solution is $a\le\sqrt{W_1^2+W_2^2}$, which implies the normalized separation distance must be equal or smaller than a certain value if pounding are to occur. Since multiple branches exist for both the $\sin^{-1}$ and $\tan^{-1}$ functions, attention should be paid to the selection of appropriate solutions. Only those solutions for which t_0/p lies between 0 and $2n\pi$ and for which the velocity of the impact point is positive should be accepted.

The obtained value of t_0 then can be used to calculate the other four unknown constants c_i through Equation (7.61), and further to find the translation (x) and rotation (θ) of the center of mass from Equations (7.41) and (7.42). The translational and rotational velocities can be obtained from the differentials of the corresponding displacements. Thus the problem is completely solved.

Note that the above solution procedure is for the case when Corner C impacts onto the neighboring barrier. Similar procedure is also applicable for the other case when Corner D impacts periodically onto the barrier and the details will not be shown here due to mathematical similarity. In this study, impacts at both Corner C and Corner D will be tried for any specified input parameters and the corner which bring out valid solutions will be deemed as the actual impact point.

Note that the proposed analytical solution only provides a possible solution for pounding which occurs periodically at one single corner of the tower. The actual torsional pounding between the asymmetric tower and the neighboring barrier may be much more complicated. As already shown in our numerical simulations in Section 7.2.2.1, the pounding may be group periodic or chaotic, and may happen at the two corners consecutively. To capture these phenomena, more sophisticated mathematical models are needed, but these are out of the scope of the present analytical study. Strictly speaking, the present analytical solution and the numerical simulation can not be compared. But comparisons are still made in the following sections for qualitative comparisons to show that this quite simple analytical model does provide some valuable insights into the complex torsional pounding phenomena.

7.3.2 Results and discussions

7.3.2.1 Comparison of translational and torsional poundings

Based on the analytical solution obtained above, parametric studies have been conducted to investigate effects of input parameters, structural characteristics and separation distances on torsional pounding between the asymmetric tower and the barrier. Numerical simulations will also be carried out using the fourth-order Runge-Kutta method as described in Section 7.2.1 and the numerical results will be compared with the analytical solution. Without loss of generality, only positive eccentricities (i.e. the center of mass of the tower is situated closer to Corner C than to Corner D as shown in Figure 7.18) are considered in all of the following studies.

Figure 7.19 shows the normalized impact velocity spectra $V/(A_g\omega_x)$ versus the excitation periods T/T_x for both translational ($e_y/l=0$) and torsional ($e_y/l=0.1$) poundings under Case 1 condition. The other parameters are $\zeta_x=0.10$, $\zeta_\theta=0.10$, $w/l=0.55$, $a=1.0$ and $n=1$ (i.e. one impact per cycle). The curves of translational pounding (the solid lines) are modified from Figure 11 of Davis (1992). The difference is that all the invalid solutions are eliminated from these curves. Actually Davis (1992) has pointed out that at some excitation periods, multiple impacts occur and the trajectories given by the analytical solution exceed the position of the neighboring barrier at least once in mid-flight (i.e. impacts happen during the free flight period). Since there can not be any impact during the free flight period in the analytical solution, obviously those solutions are invalid and should be removed.

Note that the impact velocity of torsional pounding shown in Figure 7.19 (the dashed lines) is the velocity of the impact point, which may be either Corner C or Corner D. Compared to the spectrum of translation pounding, there is an abrupt jump in the impact velocity spectrum of torsional pounding. This abrupt jump is caused by the transition of the impact point from Corner D to Corner C as sketched in the figure. This unique characteristic suggests that torsional pounding tend to be more complex than translational pounding. Small changes of excitation periods may induce very different impact patterns, especially near the jump.

Except for the abrupt jump, the impact velocity spectra of translational and torsional poundings have similar patterns and similar impact-occurring excitation period ranges around $T/T_x = 1.0$. The impact-occurring excitation period range means the range of excitation period during which impact is developed, which is $T/T_x = 0.53\text{-}1.43$ for torsional pounding and $T/T_x = 0.57\text{-}1.45$ for translational pounding. However, for longer excitation periods ($T/T_x > 1.5$), solutions exist for translational pounidng whereas no valid solution exists for torsional pounding.

The analytical solutions for both translational and torsional poundings shown in Figure 7.19 are compared to the numerical simulations (with $\beta = 1000$ and $\chi = 3/2$) in Figures 7.20(a) and (b) respectively. The numerical results are denoted by solid dots and each dot denotes one impact occurring within the 40-48$^{\text{th}}$ excitation cycles as discussed in Section 7.2.1.3. Figure 7.20(a) is modified from Figure 11 of Davis (1992). The three small diagrams I, II and III show the enlarged views of three selected period ranges. Comparing the numerical results in Figures 7.20(a) and (b), torsional pounding appears to be much more complex than translational pounding. Almost all the torsional impacts are either multiple impacts (i.e. group periodic pounding) or chaotic impacts (for example, those around $T/T_x = 1.5$). The diagram III shows an example of the transition between periodic impacts and chaotic impacts.

The analytical solutions agree well with the numerical results for translational pounding [Figure 7.20(a)], whereas the fit is not so good for torsional pounding [Figure 7.20(b)]. This shows the insufficiency of the simple analytical solution for the complex torsional pounding phenomenon. Most of the torsional poundings are multiple impacts (either group periodic or chaotic), whereas single periodic impact is assumed in our analytical solution.

However, although large differences exist between the analytical solution and numerical simulation for torsional pounding, they have similar overall patterns within the excitation range of $T/T_x =$ 0.53-1.43. What is more important is that the analytical solution succeeds in predicting the abrupt jump in the numerical results as shown in the diagram II. As discussed previously, this abrupt jump is caused by the transition of the impact points from one corner to the other. Therefore, although this simple analytical solution can not predict the exact impact velocities of torsional pounding, it does provide some useful insights into this complicated problem.

7.3.2.2 Effect of separation distance

In Figures 7.19 and 7.20, $a = 1.0$ is assumed, that is, the separation distance between the tower and the neighboring barrier is equal to the amplitude of the ground excitation. In Figure 7.21, the separation distance is increased to be 1.5 and all of the other parameters are the same as those in Figure 7.20. With the increased separation, the impact-occurring excitation period ranges decrease drastically for both translational and torsional poundings, implying fewer impacts occur. However, the maximum impact velocities only decrease slightly comparing to that of $a = 1.0$. Similar as that in Figure 7.20(b), although the analytical solution can not predict the exact impact velocities of multiple torsional pounding, the overall patterns of the analytical solution and numerical results are similar.

The impact velocity spectra of both translational and torsional poundings for $a = 0.5$ are plotted in Figure 7.22. Compared to that of $a = 1.0$, the spectra tend to be more complex and more chaotic impacts occur, especially at longer excitation periods. But the maximum torsional impact velocity remains close to that of $a = 1.0$. The analytical solutions only exist within the excitation period (T / T_x) range of 0.53-1.26 for translational pounding and 0.49-1.26 for torsional poundings.

To summarize, with the increasing separation distances, fewer impacts are observed and the impact-occurring excitation period ranges become narrower. In addition, the impact velocity spectra tend to be less complex, implying the interaction between the two structures becomes weaker. However, the maximum impact velocity appears to be not too sensitive to the variation of the separation distance as long as pounding occurs. Similar phenomena have been found for translational pounding between two SDOF oscillators (Chau and Wei, 2001) as well as torsional pounding between two flexible structures as discussed in Section 7.2.2.2.

7.3.2.3 Effect of contact stiffness and force exponent

In the previous figures, the normalized contact stiffness (β) have been set to be 1000, which represents a relatively stiff contact (Davis, 1992). In Figure 7.23, the contact stiffness is reduced to 100 and the other parameters are the same as those used in Figure 7.22. Note that the analytical solutions shown in Figure 7.23 are exactly the same as shown in Figure 7.22. Comparing the numerical results in the two figures, it is seen that reducing the contact stiffness by an order of magnitude has little effect on the spectrum of translational pounding, whereas the maximum chaotic impact velocity of torsional pounding increases by as large as 74% for the softer contact ($\beta = 100$).

We further reduce the contact stiffness to 1.0 in Figure 7.24 and all of the other parameters remain unchanged. Comparing to the spectra shown in Figures 7.22 and 7.23 for stiffer contact, the maximum velocities occur at the excitation periods closer to $T/T_x = 1.0$ for both translational and torsional pounding. In addition, both spectra become much less complex. This implies that for very soft contact the effect of the barrier diminishes and the impact velocity spectrum becomes similar to that of a non-impacting structure (for which the maximum response occurs at $T/T_x = 1.0$). Similar phenomenon has been found by Davis (1992). For this soft contact, the analytical solutions are quite different from the numerical results. This is expected since rigid impact is assumed in the analytical solution.

The Hertz contact ($\chi = 3/2$) is assumed in all of the previous figures. In Figure

7.25, this force component is increased to 5.0 and all of the other parameters are the same as those in Figure 7.24. It is seen that the spectrum of translational pounding is similar to that of $\chi = 3/2$, except for an abrupt discontinuity occurred [Figure 7.25(a)], which is probably caused by the highly nonlinear nature of the contact law (Davis, 1992). The overall pattern of torsional pounding spectrum [Figure 7.25(b)] does not change significantly, but the maximum velocity resulted from chaotic impacts is larger than that of the Hertz contact.

To summarize, the change of the contact stiffness and force component (i.e. the details of the contact law) appears to have little effect on the maximum impact velocity of translational pounding. This is consistent with the conclusions by Davis (1992) and Chau and Wei (2001). However, the maximum impact velocity of chaotic torsional pounding [see Figures 7.23(b) and 7.25(b)] may change significantly for different contact stiffness and force component. Thus, chaotic torsional pounding appears to be more sensitive to the details of the contact law. For soft contact, the effect of the neighboring barrier diminishes and the impact velocity spectrum appears to be less complex and more closely resembles that of a non-impacting structure.

7.3.2.4 Effect of damping ratio

In all the previous figures, both the translational and rotational damping ratios (ζ_x and ζ_θ) of Tower A have been set to be 0.10. In Figure 7.26, the translational damping ratio is reduced to 0.05 and all the other parameters are the same as those in Figure 7.20. For smaller translational damping, the maximum impact velocities increase as expected for both translational and torsional pounding. In addition, the velocity spectra at longer excitation periods are more complex and more chaotic impacts occur. However, the overall patterns of those spectra remain similar to that given in Figure 7.20. The analytical solution provides a better prediction for those single translational pounding than for those multiple torsional pounding.

In Figure 7.27, we reduce the rotational damping ratio (ζ_θ) to 0.05 and remain the translational damping at 0.10. Note that Figure 7.27(a) is exactly the same as Figure 7.20(a). Comparing Figure 7.27(b) with Figure 7.20(b), it is seen that again more complex responses are found, however, reducing the rotational damping ratio by half only results in a slight increase of the maximum velocity. Therefore, the rotational damping appears to have a less significant effect on pounding than the translational damping, similar to the conclusion on torsional pounding between two flexible structures as discussed in Section 7.2.2.3.

7.3.2.5 Case 2 conditions

All previous figures are for Case 1 condition, that is, the neighboring barrier is stationary and absolute displacement is used in analysis. As discussed in Section 7.3.1, Case 2 condition can also be considered in this study, which means the barrier is locked to the ground motion and relative displacement is used in analysis. For translational pounding, Davis (1992) has shown that the results for Case 1 condition remain almost the same as those for Case 2 condition, as long as the relative motion rather than the absolute motion of the structure is used to interpret the results.

Actually as Davis (1992) discussed, the only difference of Case 1 and Case 2 conditions in the governing equations is the forcing function $G[x_g(t)]$, in which $E_2 = 2\zeta_x / p$ for Case 1 condition and $E_2 = 1$ for Case 2 [see Equation (7.25)]. Thus, the forcing function changes very slightly for the two cases as long as the damping ζ_x is small and the excitation period $p = T / T_x$ is not small (Davis, 1992).

In Figure 7.28(a), the impact velocity spectra of torsional pounding ($e_y / l = 0.1$) are compared for Case 1 and Case 2 conditions. The input parameters are the same as those used in Figure 7.20. Figure 7.28(b) shows an enlarged view within the range of $T / T_x = 0.6$-1.5. Note that in this figure the impact velocity should be interpreted as the absolute velocity for Case 1 condition and as the relative velocity for Case 2 condition. It can be seen that the velocity spectra are very similar for these two cases. The only bigger differences occur for several chaotic impacts within the excitation period range of $T / T_x = 1.0$-1.1.

Figures 7.29 and 7.30 show two additional examples of both translational and torsional pounding of Case 2 condition for $a = 0.2$ and 0.0 respectively. The other parameters are the same as those in Figure 7.20. Note that the impact velocity is plotted versus the normalized excitation frequency ω / ω_x rather than the excitation period T / T_x in order to make the short-period response more visible. As discussed above, the difference of the forcing functions for Case 1 and Case 2 conditions can become relatively large for short frequency excitations. The analytical solutions for $n = 1$, 2 and 3 are also plotted in the figures. The number n represents there are n ground excitation cycles between two neighboring impacts.

Comparing the numerical results in Figures 7.29 and 7.30, the maximum impact velocity of chaotic torsional pounding is almost double that of translation pounding. In addition, torsional pounding appears to be much more complex and chaotic. The analytical solutions provide close estimations to the numerical results in those ranges where single impacts occur. The discrepancy becomes large when group periodic or chaotic impacts occur, especially for torsional pounding.

7.3.2.6 Effect of eccentricity

In all the previous figures on torsional pounding, an eccentricity of 0.1 has been assumed for Tower A (i.e. $e_y / l = 0.1$). In Figure 7.31(a), we change the eccentricity to $e_y / l = 0.2$ and keep all the other parameters the same as those used in Figure 7.20(b). It is seen the analytical solution provides a fairly good estimation to the maximum impact velocities in those ranges where single or group periodic impacts occur. In addition, the analytical solution succeeds in predicting the abrupt jump of impact velocity at the short excitation periods in the numerical results.

In Figure 7.31(b), the impact velocity spectrum of $e_y / l = 0.2$ is compared to that of $e_y / l = 0.1$. The two spectra have similar overall patterns. But the chaotic impacts within the excitation period range of $T / T_x = 1.0$-2.0 yield much larger impact velocities for $e_y / l = 0.2$. Except for these chaotic impacts, the doubled eccentricity does not change the impact velocity spectrum significantly. This is consistent with the conclusion on torsional pounding between two flexible structures (refer to Section 7.2.2.4). As discussed previously, this may be due to the rotational constraint from the neighboring barrier.

7.3.2.7 Maximum stand-off distance

As shown in Section 7.3.1, the $\sin^{-1}$ function has been used to calculate the unknown t_0 (the onset time of the periodic impacts) in the analytical solution [see Equation (7.64)]. To make the argument of the $\sin^{-1}$ function lie between −1.0 and +1.0, we have to constrain the separation distance *a* as:

$$a \leq \sqrt{W_1^2 + W_2^2} \tag{7.65}$$

where a is the normalized separation distance, and W_1 and W_2 are defined in Equation (7.63). The above equation is the first condition required to ensure the existence of valid analytical solution. Note that this is a necessary but not sufficient condition. In other words, Equation (7.65) provides an upper bound on the value of *a*, only under which impact is possible. The upper bounds obtained in this way are plotted versus the excitation frequencies ω / ω_x for both translational ($e_y / l = 0.0$) and torsional ($e_y / l = 0.1$) pounding of Case 2 condition in Figure 7.32. All the other parameters are the same as those used in Figure 7.20.

The numerical results for the maximum stand-off distances between the tower and the barrier are also plotted as solid dots in Figure 7.32. The numerical calculations are done for all ω / ω_x from 0.01 to 3.0 in steps of 0.05 and for all a from 0 to 10 in steps of 0.25. If continuous impacts occur at a particular frequency ω / ω_x and stand-off distance a, a dot is plotted in the figure. Note that Figure 7.32(a) is modified from Figure 13 in Davis (1992).

For frequencies lower than 2.0, the analytical bound provides a close upper limit to the numerical results for both translational and torsional pounding. But large discrepancies exist for frequencies close to and higher than 2.0, implying the insufficiency of the condition in Equation (7.65) at higher excitation frequency. Comparing the numerical results for translational [Figure 7.32(a)] and torsional pounding [Figure 7.32(b)], the maximum stand-off distance both occurs at the natural frequency of the structure (ω_x), but a local peak occurs at the torsional natural frequency (ω_θ) of the structure for torsional pounding. This is a unique characteristic of torsional pounding and has also been found in the torsional pounding between two flexible structures (refer to Section 7.2.2.5). This local peak can not be predicted by the analytical solution [Figure 7.32(b)]. To summarize, the upper bound from the analytical solution estimate provides a conservative estimation to the maximum stand-off distance, except for those frequencies near the torsional frequency of the structure.

7.4 Conclusions and Discussions

In this chapter, the torsional pounding between two flexible asymmetric single-story structures as well as pounding between an asymmetric single-story structure and a neighboring barrier were investigated through numerical simulations. The impacts were modeled using the nonlinear Hertz contact law. The resulting governing equations were integrated numerically using the fourth-order Runge-Kutta method with error control. An analytical solution was obtained for periodic rigid impacts between an asymmetric single-story tower and a neighboring barrier under sinusoidal wave excitations. The following main conclusions are reached.

Generally, torsional pounding tends to be much more complex than translational pounding and chaotic poundings become more common than periodic poundings, which are the dominant impact mode in translational poundings (e.g. see Fig. 5 of Chau and Wei 2001). The maximum relative impact velocity of torsional pounding can be up to three times of that of translational pounding. An important feature of the present model is that periodic group pounding observed in shaking table tests by Chau et al. (2003) was simulated and replicated numerically for the first time by incorporating torsional responses (e.g. see the phase diagrams of a periodic group of three impacts per excitation cycle shown in Figure 7.11), which cannot be explained through numerical simulations for translational poundings alone.

For pounding between an asymmetric structure and a neighboring barrier, the maximum impact velocity occurs at excitation period near half the natural period of the structure, except for cases of very soft contact. This is similar to the conclusion on translational pounding by Davis (1992). For pounding between two flexible towers, the maximum impact velocity occurs at excitation period between the natural periods of the two structures. As argued by Chau and Wei (2001), this is not unexpected since pounding on a flexible neighboring structure is similar to the case of soft contact.

However, different from translational pounding, the maximum impact velocity between the asymmetric structure and the barrier may also occur at other periods where chaotic impacts occur (e.g. when e_y/l = 0.2 in Figure 7.31). For translational pounding, Davis (1992) found that the velocity in the chaotic regions appears to be bounded, and thus it is believed that the chaotic response is of limited interest from an earthquake engineering standpoint. However, this conclusion does not always hold for torsional pounding, for which the chaotic impacts seem not to be bounded and in some cases may yield the maximum impact velocity in the velocity spectrum. Therefore, torsional pounding seems to be more unpredictable for its possible chaotic responses.

The maximum torsional impact velocity appears to be insensitive to the change of the separation distance as long as impact is developed, consistent with the conclusions on translation pounding by Davis (1992) and Chau and Wei (2001). More group periodic impacts and less chaotic impacts were observed when damping ratio increases. Therefore, increasing of damping ratio appears to be an effective way to alleviate torsional pounding problems. The translational damping has a more significant effect on torsional pounding than the rotational damping. In addition, torsional pounding appears not to be significantly influenced by the change of eccentricity, and larger impact velocity may be resulted when the two structures have eccentricities on the same side of their centers of stiffness. The maximum stand-off distance envelopes do not strongly depend on whether torsional responses are included in the analysis.

Although the present model is highly idealized comparing to actual asymmetric multi-story structures, we believe that the present results can capture the essence of nonlinear seismic torsional pounding phenomenon with the minimum number of parameters involved. The results of this semi-analytical study do provide valuable insights into this unknown domain of seismic torsional pounding, and can serve as a benchmark for future more complicated models. Therefore, this study should provide the first order approximation to this highly nonlinear phenomenon. More importantly, group periodic poundings have been numerically simulated for the first time using this simplified model, although their existence in real structures has been demonstrated experimentally by Chau et al. (2003) in shaking table tests.

The proposed analytical solution provides a possible solution for periodic single impacts between the asymmetric tower and the neighboring barrier. Although it fails to accurately predict impact velocity of periodic group torsional pounding, this simple solution does provide an accurate and useful upper bound for the maximum stand-off distance that can preclude pounding occurrence between adjacent structures. In addition, although the present analytical solution is only for rigid impacts, the results obtained here can provide a useful mean to validate and guide future numerical simulations especially for seismic torsional pounding, because it is a highly nonlinear phenomenon and the determination of contact stiffness between adjacent structures is also not straightforward.

(a) (b)

Figure 7.1 Pounding hazard: (a) serious structural damages caused by pounding during the 1999 Chi-Chi earthquake (Naeim et al., 2000); (b) closely spaced buildings in Hong Kong (potential pounding problem).

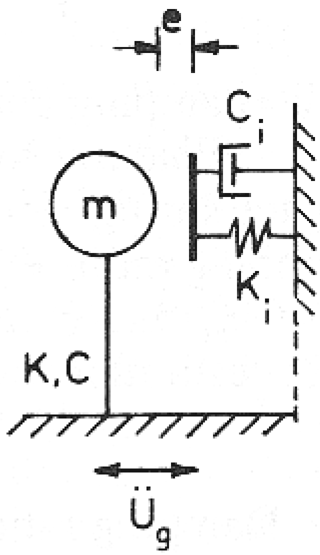

(a) SDOF system

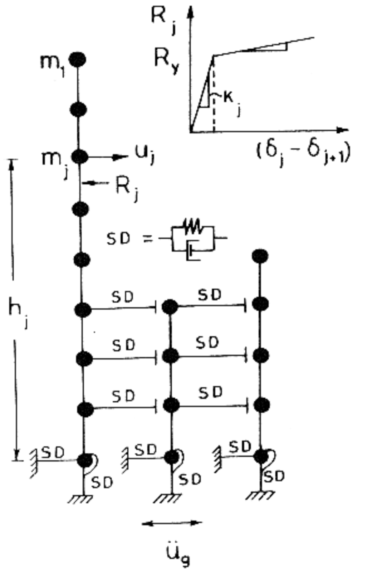

(b) MDOF system

Figure 7.2 Sketches of single-degree-of-freedom (SDOF) and multi-degree-of-freedom (MDOF) systems used to model seismic poundings (Anagnostopoulos, 1994).

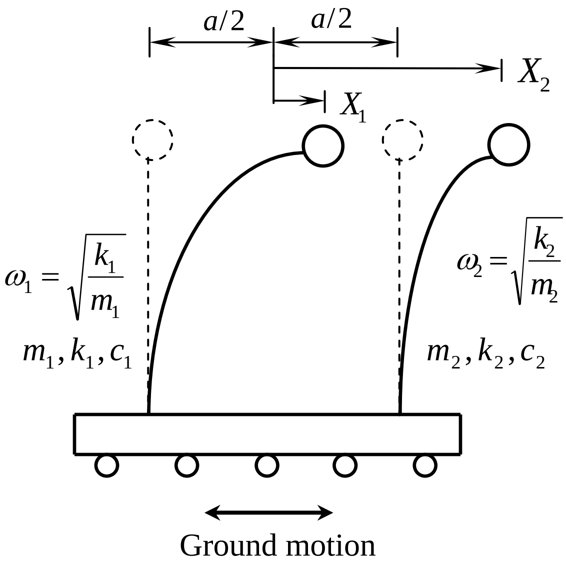

Figure 7.3 Pounding of two adjacent buildings modeled as Hertzian impact of two SDOF oscillators (Chau and Wei, 2001).

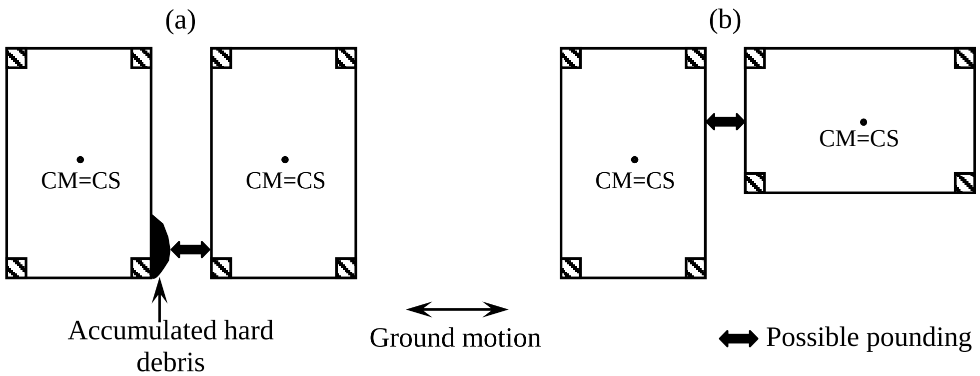

Figure 7.4 Sketches of possible eccentric poundings between structures with symmetric floor slabs [i.e. the center of mass (CM) coincides with the center of stiffness (CS)]: (a) accumulated hard debris may induce torsional pounding between symmetrically aligned floor slabs; (b) possible torsional pounding between asymmetrically aligned floor slabs (after Leibovich et al., 1996).

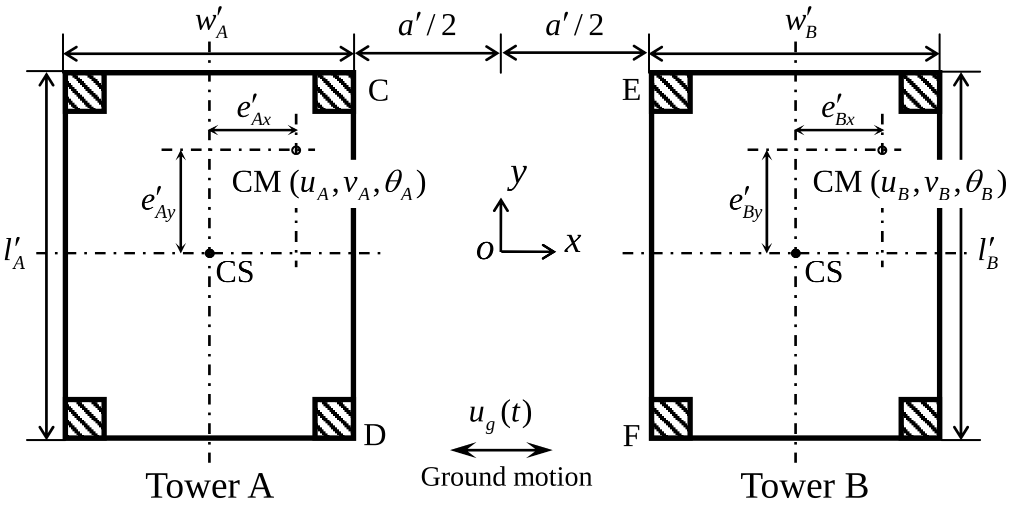

Figure 7.5 Sketch of two asymmetric rectangular towers separated by a distance a'. Both towers are supported by four identical square columns (with a lateral stiffness of k) at their four corners. The eccentricities between the center of stiffness (CS) and the center of mass (CM) are denoted by e'_{ix} and e'_{iy} (i=A, B) respectively.

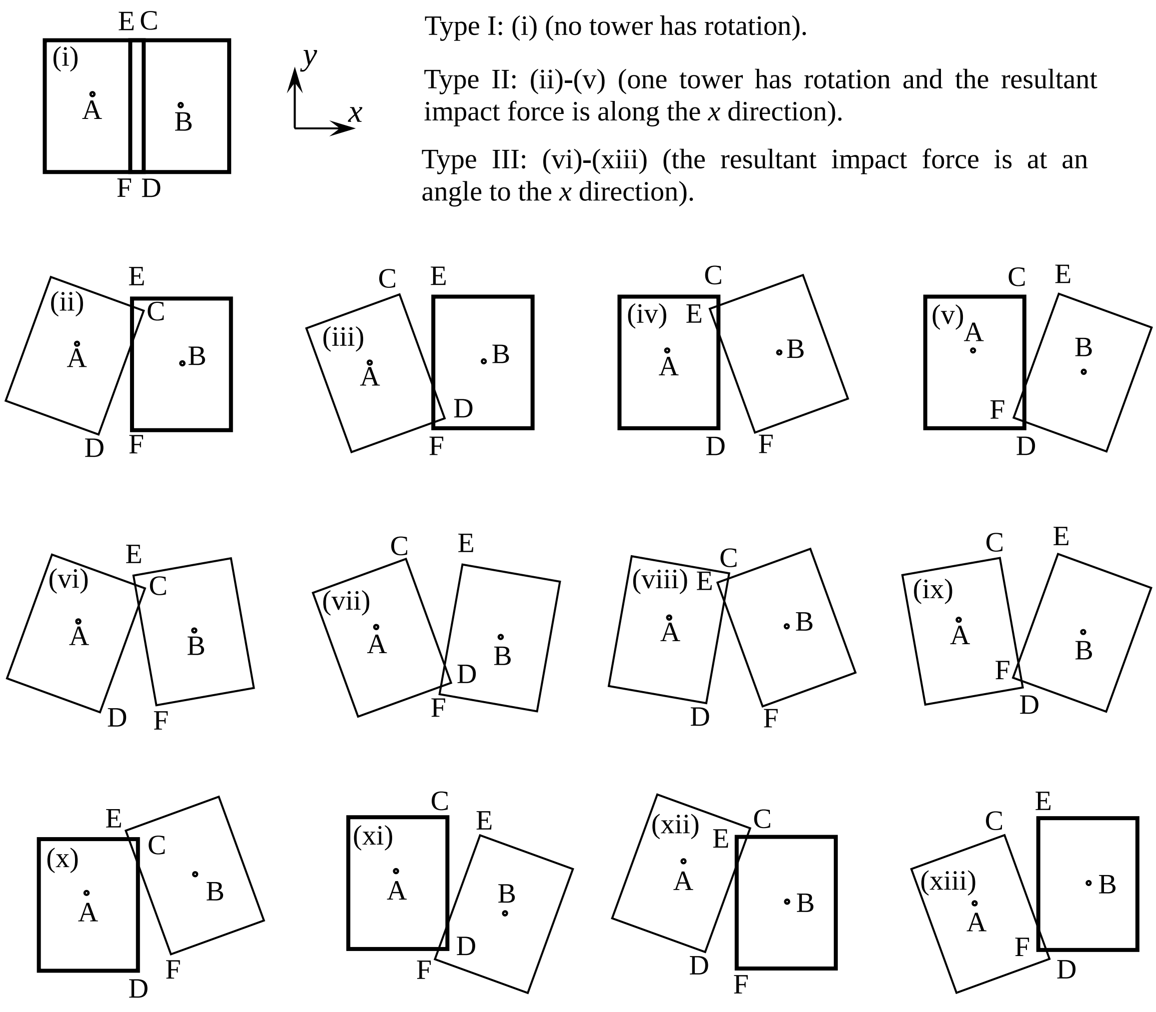

Figure 7.6 Sketch of thirteen different cases [(i)-(xiii)] of pounding between Tower A and Tower B, where A and B are the centers of mass of the two towers, and C, D, E and F are four corners along the adjacent edges. Boxes in bold lines represent towers without any rotation ($\theta = 0$) whereas boxes in thin lines represent towers having rotation ($\theta \neq 0$).

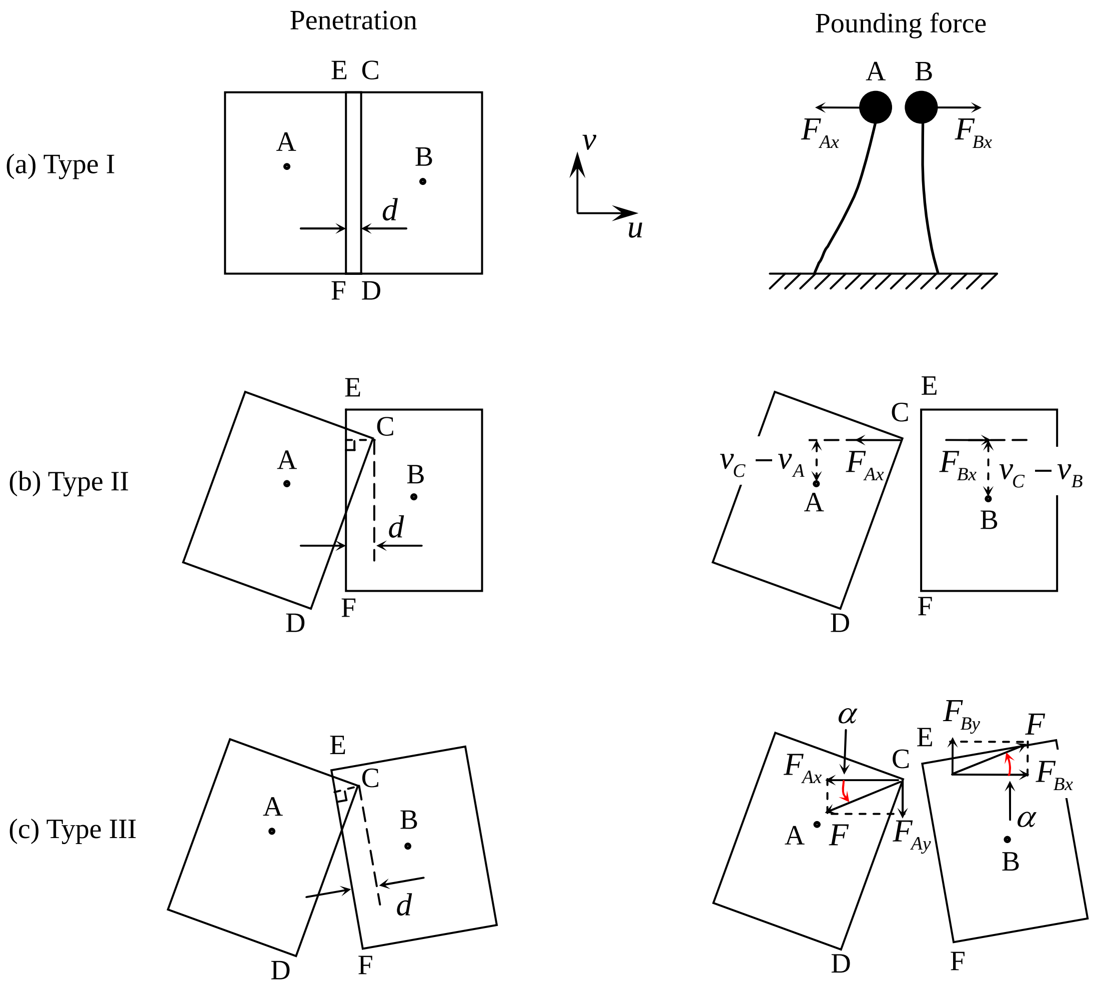

Figure 7.7 Sketch of three different cases of pounding between Tower A and Tower B, where A and B are the centers of mass of the two towers, and C, D, E and F are four corners along the adjacent edges. The right three sketches show the forces on each tower caused by pounding.

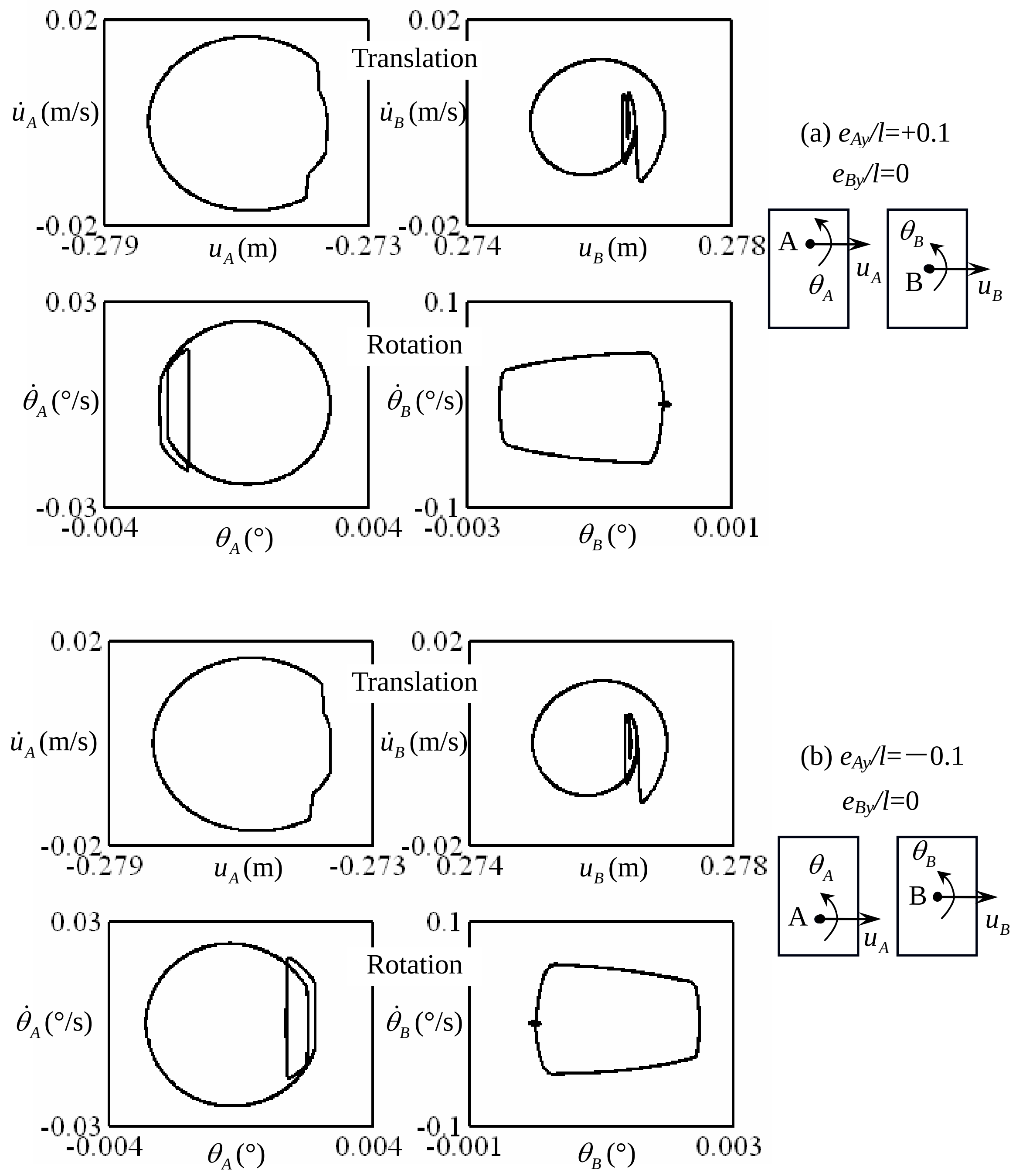

Figure 7.8 Validation of the solving method by comparing the steady pounding phase diagrams when the Tower A has opposite eccentricities: (a) e_{Ay}/l = +0.1; (b) e_{Ay}/l = −0.1. Other parameters are e_{By}/l = 0, $T/T_{Ax} = 0.7$, $T_{Ax}/T_{Bx} = 1.5$, $\zeta_{Ax} = \zeta_{Bx} = 0.03$, $\zeta_{A\theta} = \zeta_{B\theta} = 0.03$ and a = 1.0.

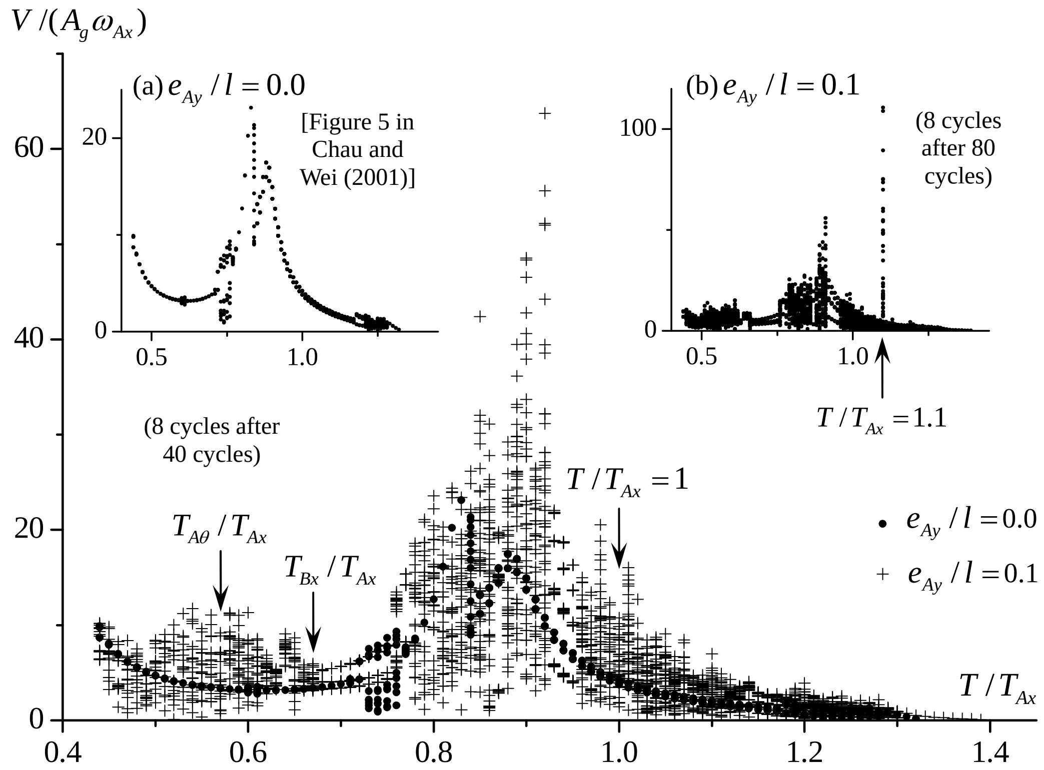

Figure 7.9 Comparison of relative impact velocity spectra versus T/T_{Ax} for torsional (e_{Ay}/l = 0.1) and translation (e_{Ay}/l = 0.0) pounding ($T_{Ax}/T_{Bx} = 1.5$, $\zeta_{Ax} = \zeta_{Bx} = 0.03$, $\zeta_{A\theta} = \zeta_{B\theta} = 0.03$ and a = 1.0). The two attached diagrams are: (a) impact velocity spectra for translational pounding when e_{Ay}/l = 0 [i.e. Figure 5 in Chau and Wei (2001)]; (b) impact velocity spectra during the 80-88th excitation cycles for the same torsional pounding problem (e_{Ay}/l = 0.1), whereas for the other two diagrams the impact velocities during the 40-48th excitation are plotted. The phase diagrams for one of the group pounding ($T/T_{Ax} = 0.7$) are shown in Figure 7.11.

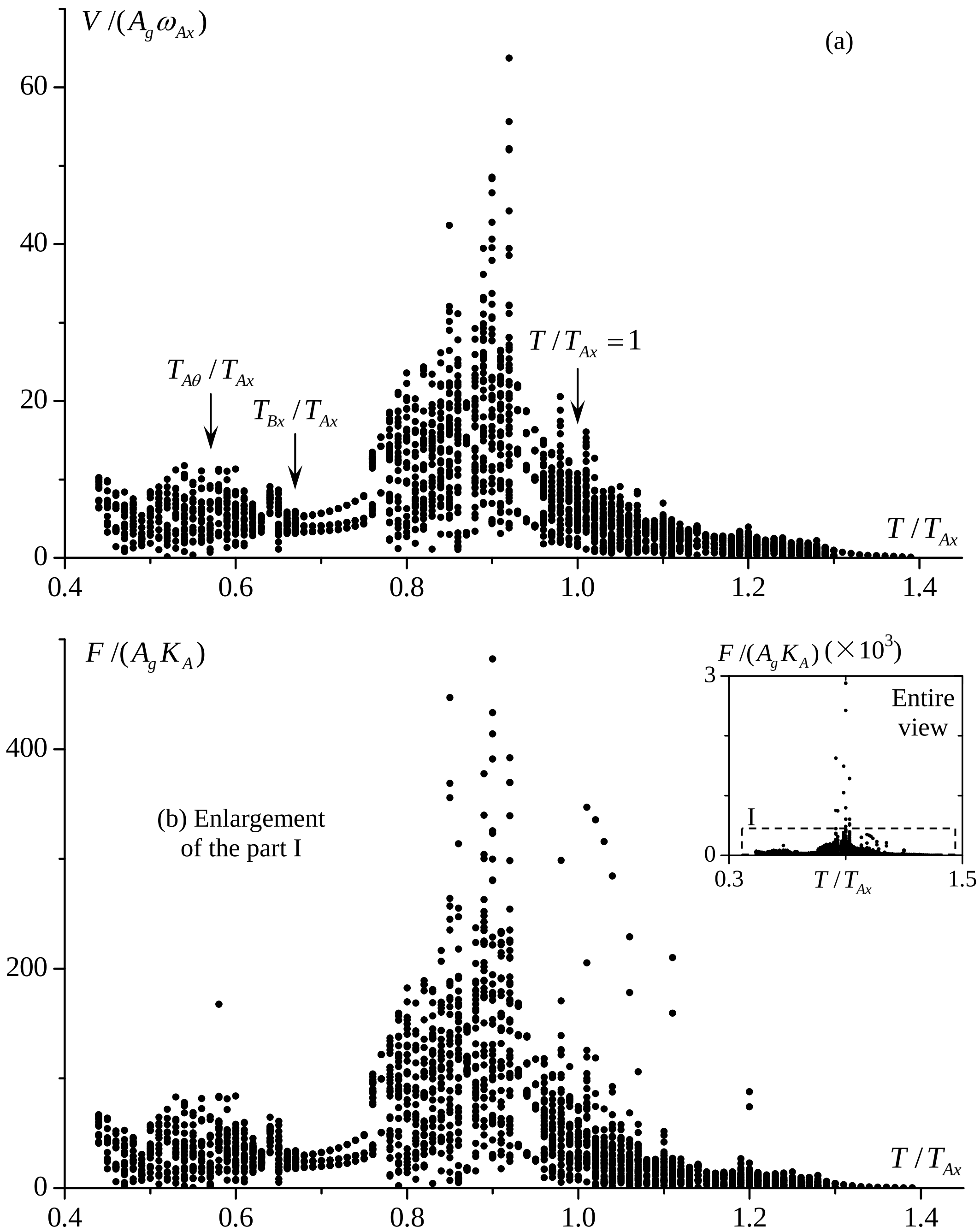

Figure 7.10 Comparison of (a) relative impact velocity spectrum (same as Figure 7.9); (b) impact force spectrum for torsional pounding when a = 1.0 and e_{Ay}/l = 0.1 ($T_{Ax}/T_{Bx}=1.5$, $\zeta_{Ax}=\zeta_{Bx}=0.03$ and $\zeta_{A\theta}=\zeta_{B\theta}=0.03$). The small diagram shows the entire force spectrum, whereas the diagram (b) is the enlargement of the part I.

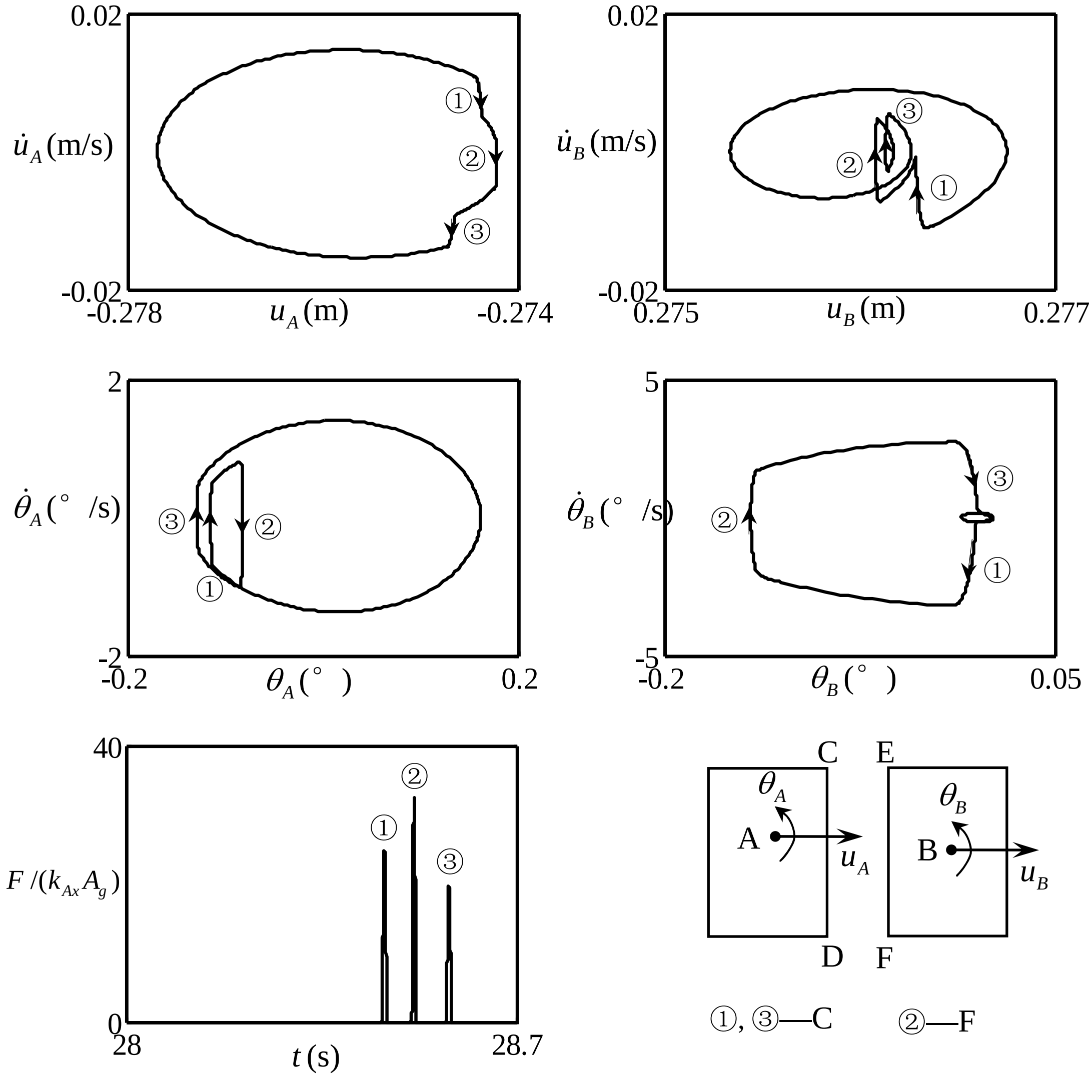

Figure 7.11 Phase diagrams and relative impact velocity time history within one cycle (28-28.7 s) after 40 excitation cycles when the input period is $T/T_{Ax} = 0.7$. The three impacts (①-③) shown in the figure repeat themselves every excitation cycle and demonstrate a kind of group pounding. Other parameters are e_{Ay}/l = 0.1, $T_{Ax}/T_{Bx} = 1.5$, $\zeta_{Ax} = \zeta_{Bx} = 0.03$, $\zeta_{A\theta} = \zeta_{B\theta} = 0.03$ and a = 1.0.

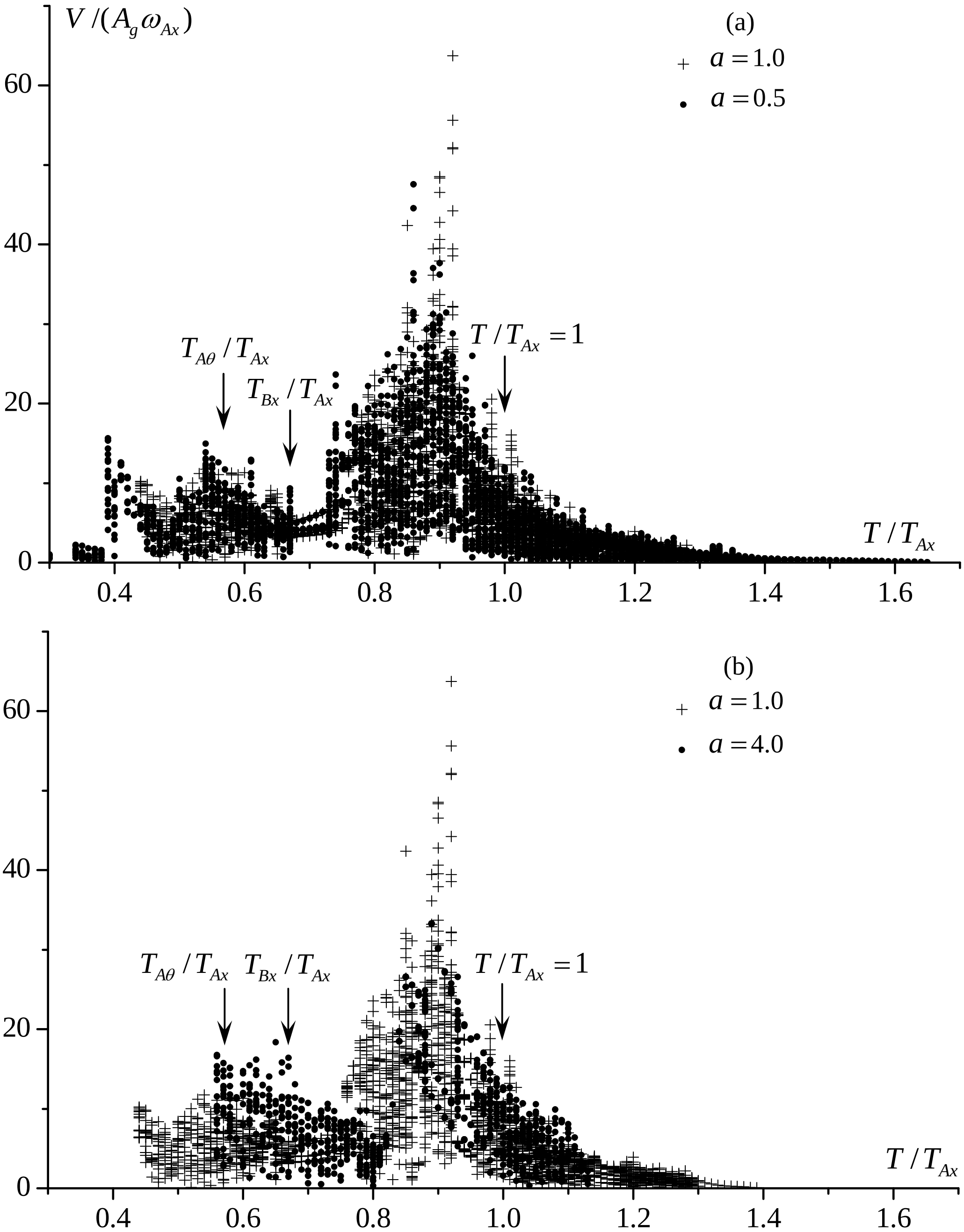

Figure 7.12 Relative impact velocity spectra versus T/T_{Ax} for torsional pounding when a = 0.5 and 4.0 respectively (e_{Ay}/l = 0.1, $T_{Ax}/T_{Bx} = 1.5$, $\zeta_{Ax} = \zeta_{Bx} = 0.03$ and $\zeta_{A\theta} = \zeta_{B\theta} = 0.03$). The impact velocity spectra for torsional pounding when a = 1.0 shown in Figure 7.9 are also plotted for comparison.

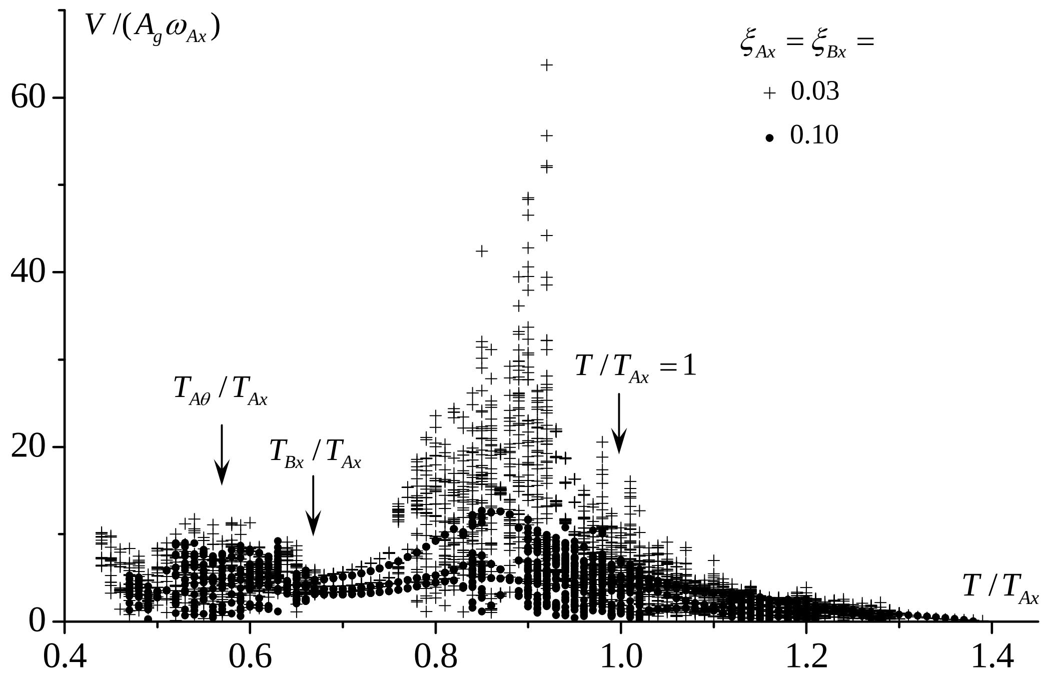

Figure 7.13 Relative impact velocity spectra versus T/T_{Ax} for torsional pounding when e_{Ay}/l = 0.1 and $\zeta_{Ax} = \zeta_{Bx} = 0.10$ ($T_{Ax}/T_{Bx} = 1.5$, $\zeta_{A\theta} = \zeta_{B\theta} = 0.03$ and a = 1.0). The impact velocity spectrum for torsional pounding when $\zeta_{Ax} = \zeta_{Bx} = 0.03$ shown in Figure 7.9 is also plotted for comparison.

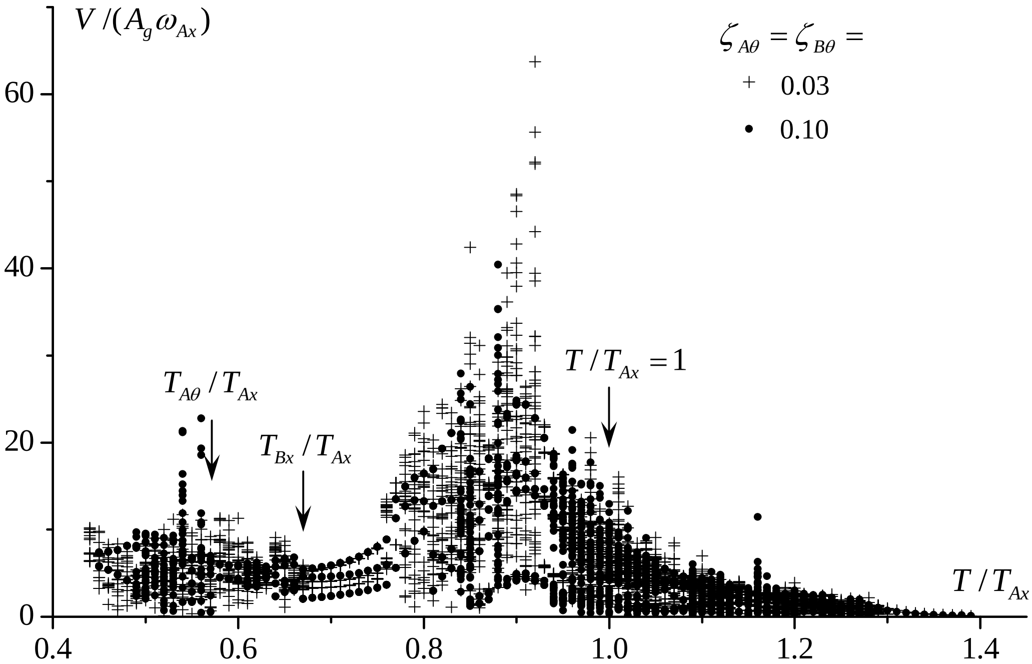

Figure 7.14 Relative impact velocity spectra versus T/T_{Ax} for torsional pounding when e_{Ay}/l = 0.1 m and $\zeta_{A\theta}=\zeta_{B\theta}=0.10$ ($T_{Ax}/T_{Bx}=1.5$, $\zeta_{Ax}=\zeta_{Bx}=0.03$ and a = 1.0). The impact velocity spectrum for torsional pounding when $\zeta_{A\theta}=\zeta_{B\theta}=0.03$ shown in Figure 7.9 is also plotted for comparison.

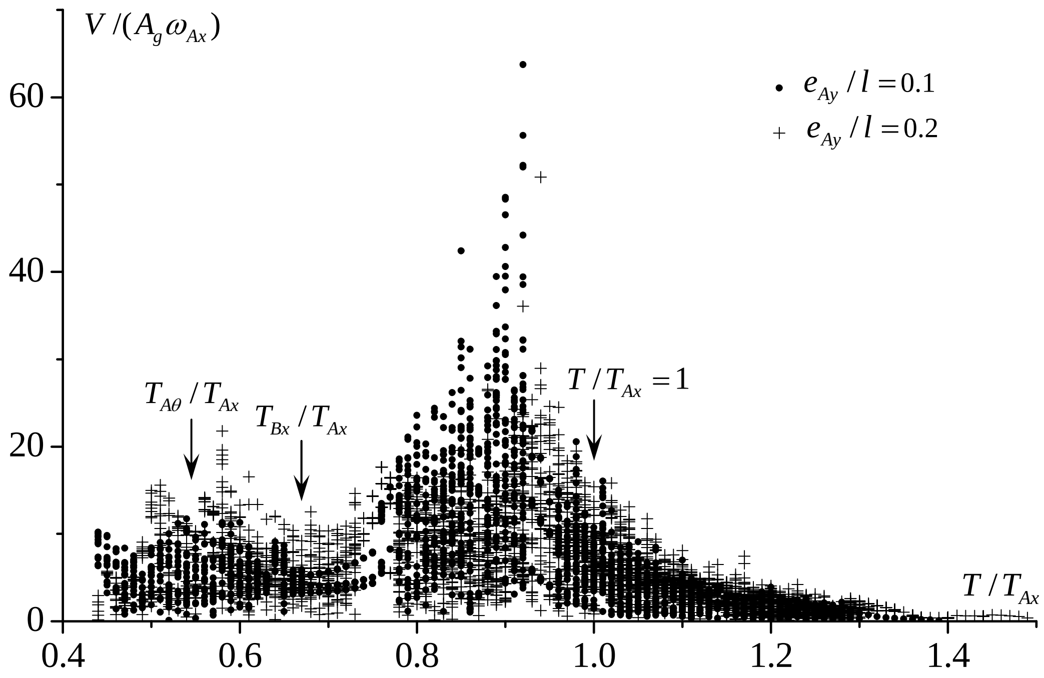

Figure 7.15 Comparison of relative impact velocity spectra for e_{Ay}/l = 0.1 and 0.2 ($T_{Ax}/T_{Bx} = 1.5$, $\zeta_{Ax} = \zeta_{Bx} = 0.03$, $\zeta_{A\theta} = \zeta_{B\theta} = 0.03$ and a = 1.0).

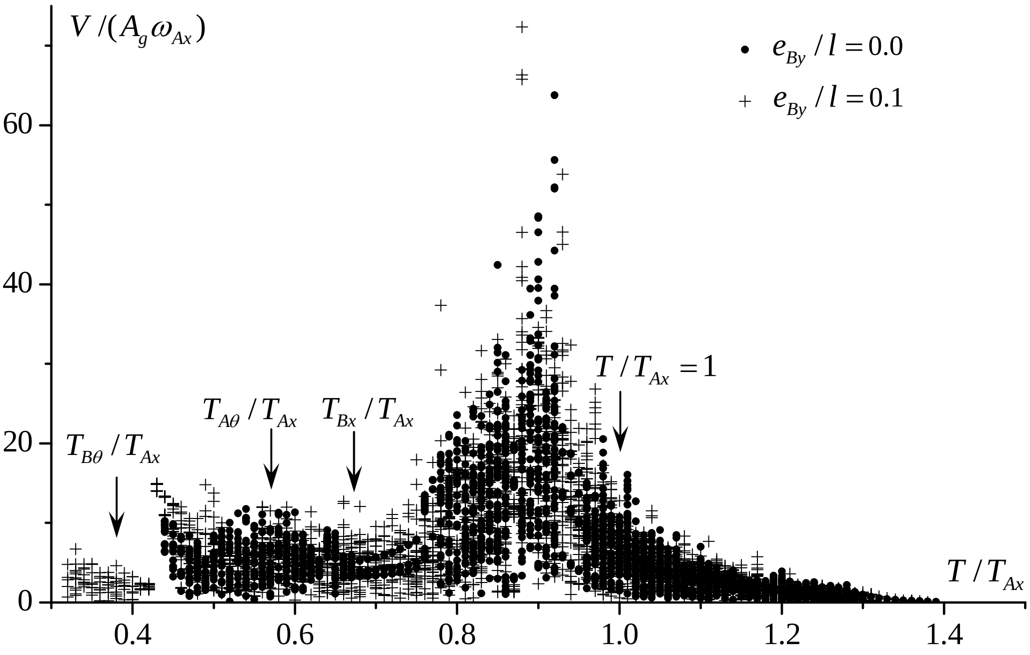

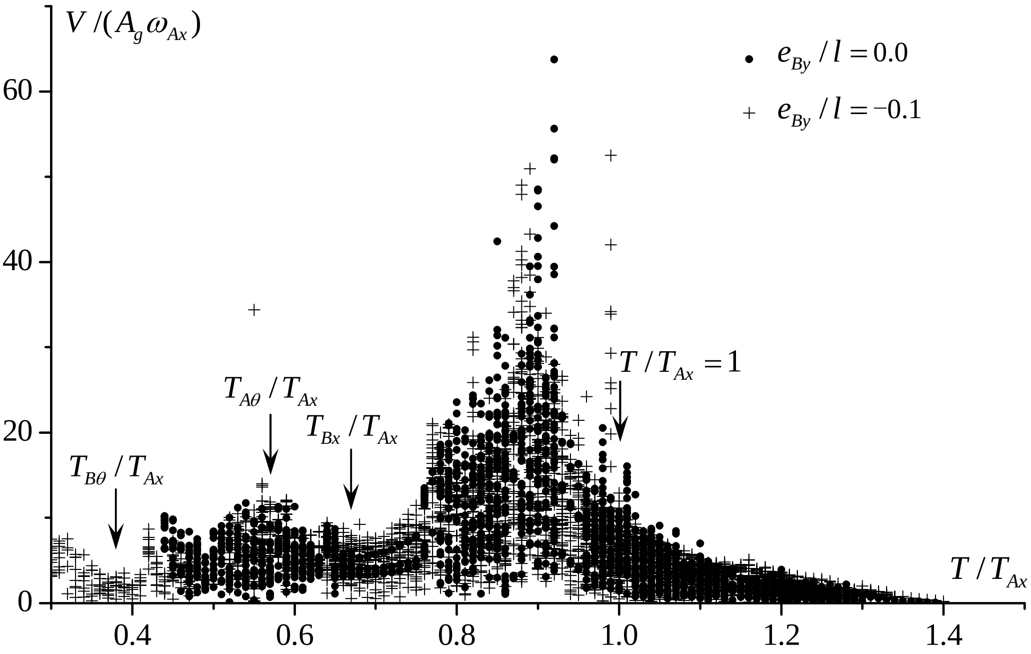

Figure 7.16 Relative impact velocity spectra versus T/T_{Ax} for torsional pounding when Tower B has different eccentricities (e_{By}/l = +0.1, 0, −0.1). The case when e_{By}/l = 0.0 has been shown in Figure 7.9. Other parameters are e_{Ay}/l = 0.1, $T_{Ax}/T_{Bx} = 1.5$, $\zeta_{Ax} = \zeta_{Bx} = 0.03$, $\zeta_{A\theta} = \zeta_{B\theta} = 0.03$ and a = 1.0.

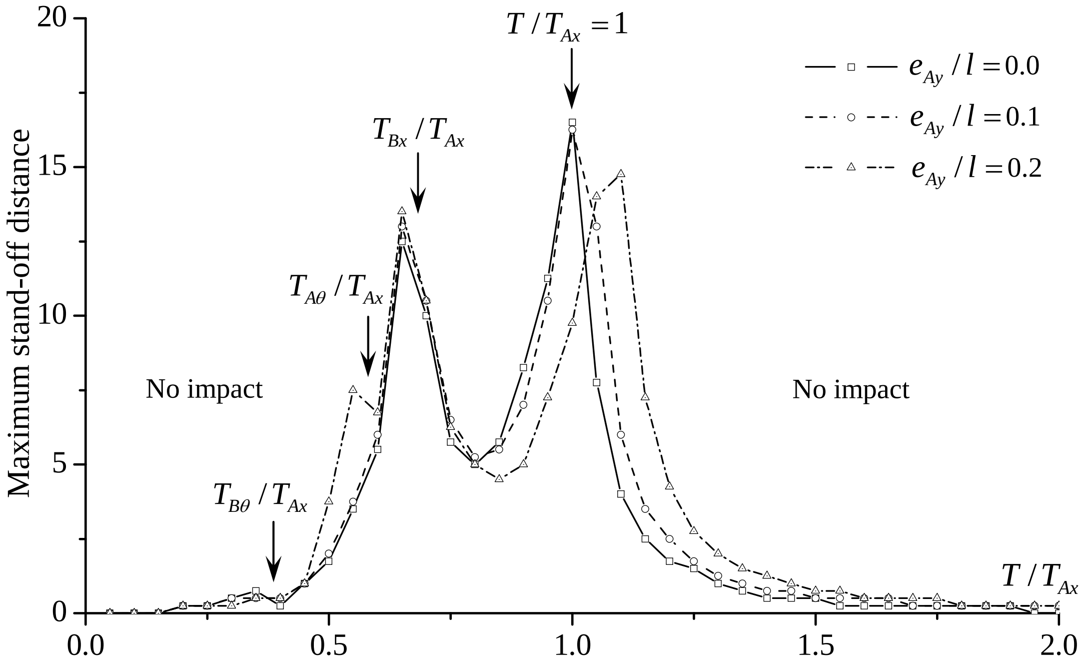

Figure 7.17 Comparison of normalized maximum stand-off distances for different eccentricities of Tower A (e_{Ay}/l = 0.0, 0.1 and 0.2). Other parameters are e_{By}/l = 0.0, $T_{Ax} / T_{Bx} = 1.5$, $\zeta_{Ax} = \zeta_{Bx} = 0.03$ and $\zeta_{A\theta} = \zeta_{B\theta} = 0.03$.

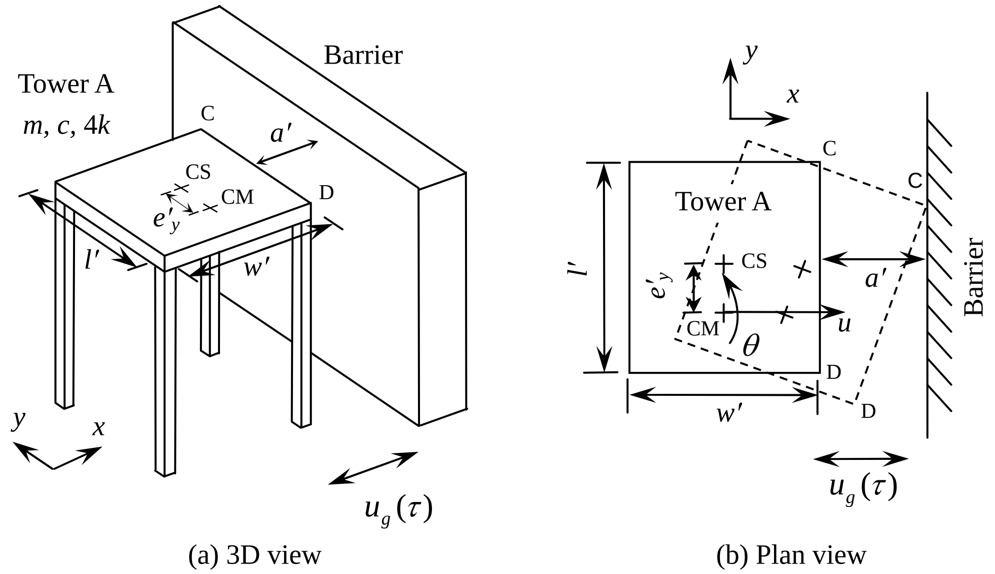

Figure 7.18 Sketch of an asymmetric tower and a neighboring barrier. With an eccentricity e'_y between its center of stiffness (CS) and center of mass (CM), Tower A is supported by four identical columns (each with a lateral stiffness of k) at its four corners. As shown by the dashed line in the plan view, torsional impact may occur at either Corner C or Corner D when the separation distance is not adequate even under unidirectional ground excitations.

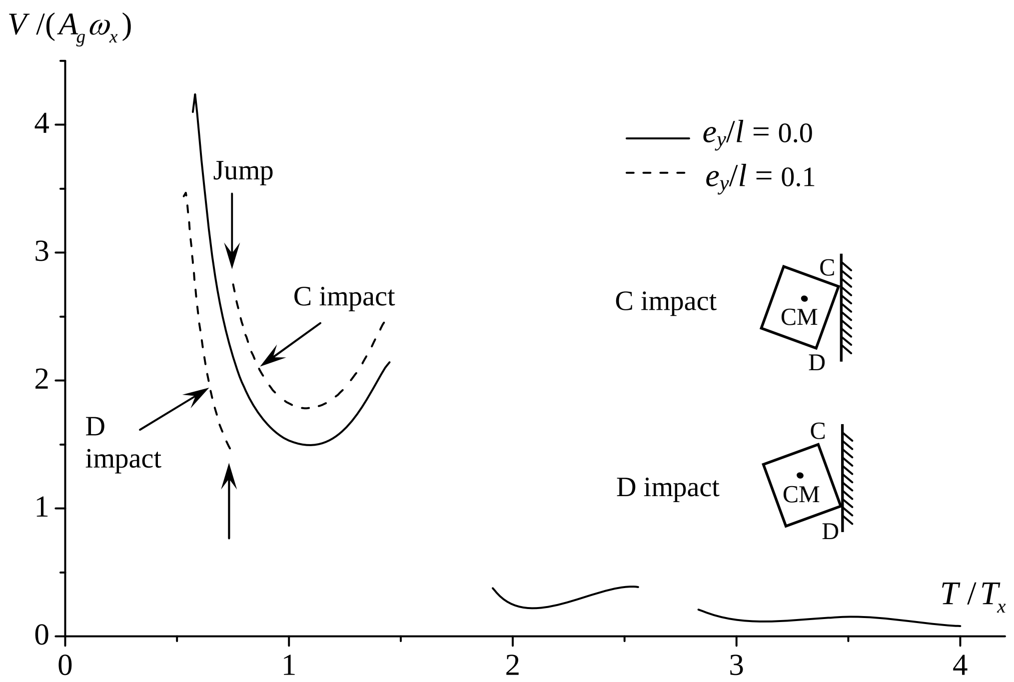

Figure 7.19 Comparison of normalized impact velocity for torsional (e_y/l = 0.1) and translational (e_y/l = 0.0) pounding. The results are both analytical solutions and the solid lines are modified based on Figure 11 of Davis (1992). Other parameters are $\zeta_x = 0.10$, $\zeta_\theta = 0.10$, a = 1.0, $\beta = 1000$ and n=1 (Case 1). Note that for torsional pounding there is a sudden jump between $T/T_x = 0.74$ and 0.75, which is caused by the impact point changing from Corner D to Corner C as sketched in the figure.

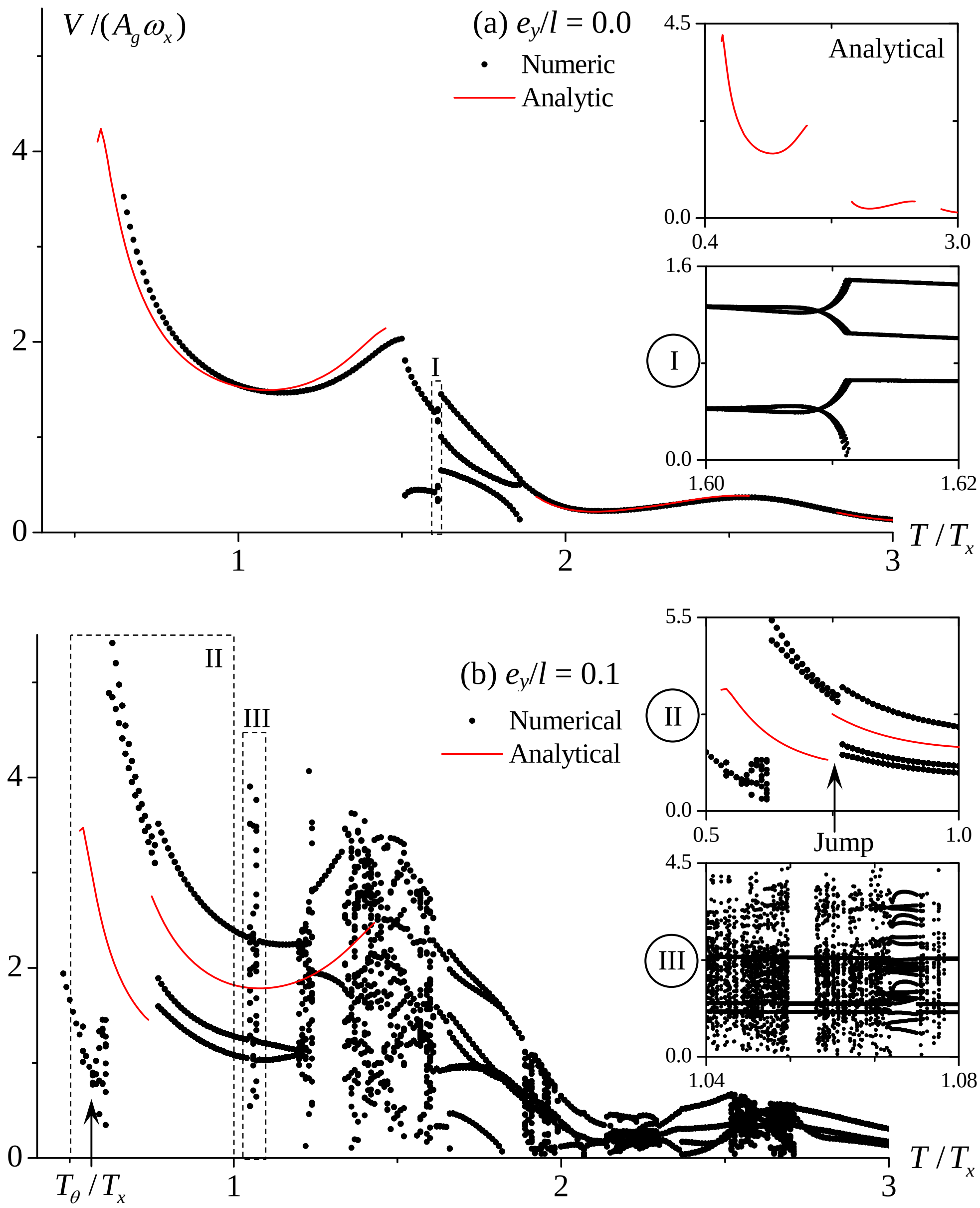

Figure 7.20 Comparison of analytical and numerical solutions of relative impact velocity spectra for translational and torsional pounding ($\zeta_x = 0.10$, $\zeta_\theta = 0.10$, a = 1.0, $\beta = 1000$, n=1 and Case 1 condition): (a) translational pounding when e_y/l = 0.0 [modified from Figure 11 of Davis (1992)]; (b) torsional pounding when e_y/l = 0.1. The four small diagrams show the translational analytical solution and the enlarged views of the parts I, II and III.

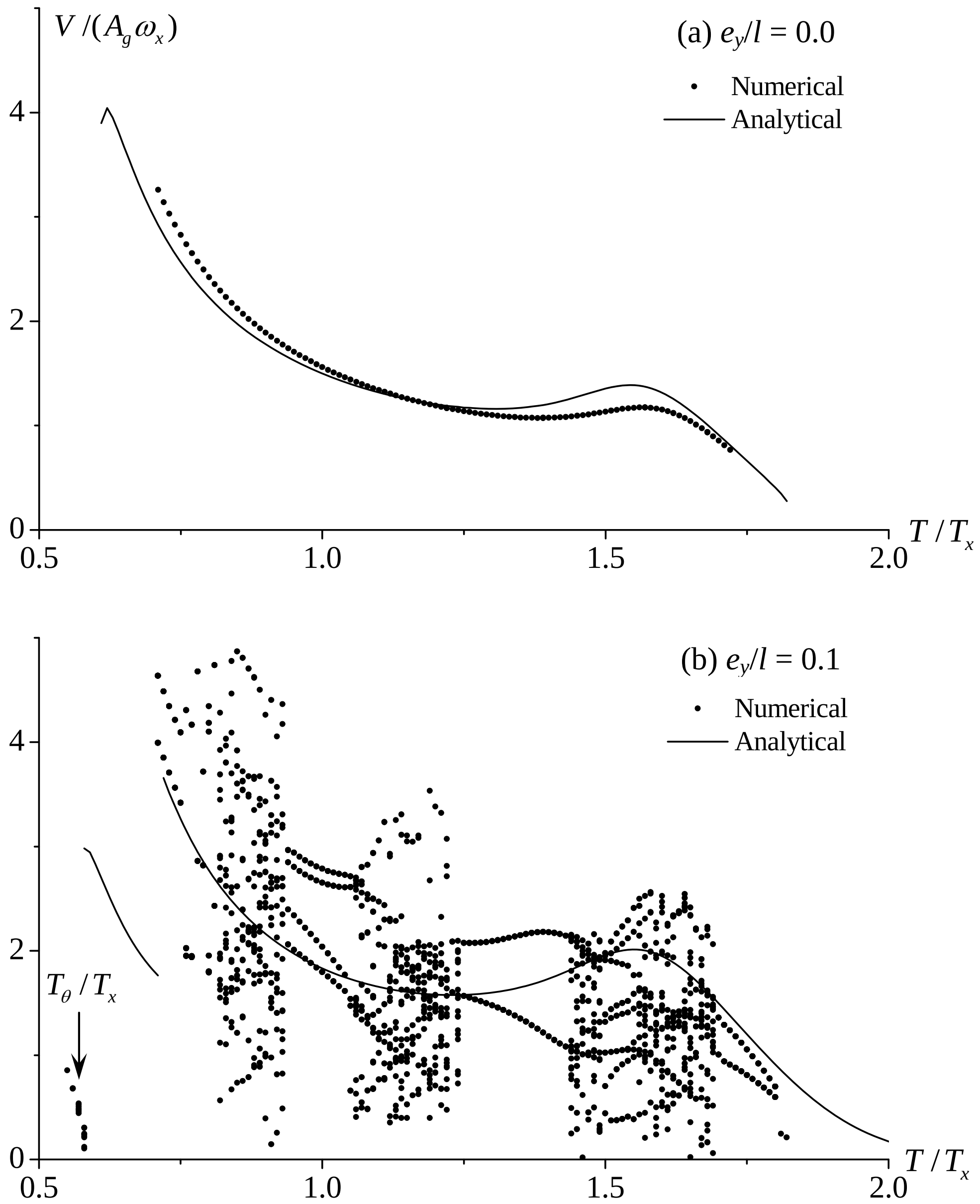

Figure 7.21 Comparison of analytical and numerical solutions of relative impact velocity spectra for translational and torsional pounding when a = 1.5 ($\zeta_x = 0.10$, $\zeta_\theta = 0.10$, $\beta = 1000$, n=1 and Case 1 condition): (a) translational pounding when e_y/l = 0.0; (b) torsional pounding when e_y/l = 0.1.

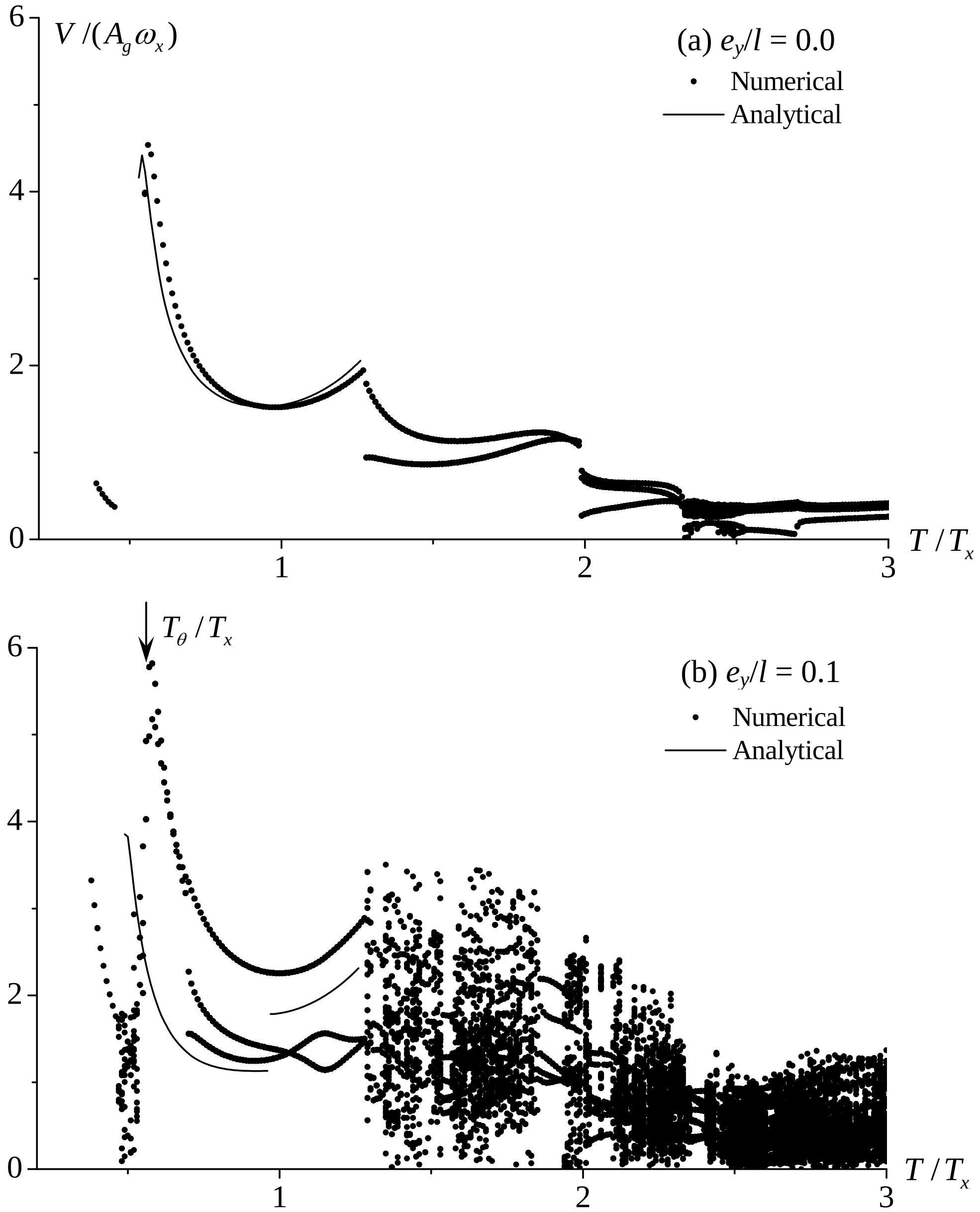

Figure 7.22 Comparison of analytical and numerical solutions of relative impact velocity spectra for translational and torsional pounding when a = 0.5 ($\zeta_x = 0.10$, $\zeta_\theta = 0.10$, $\beta = 1000$, n=1 and Case 1 condition): (a) translational pounding when e_y/l = 0.0 [modified from Figure 7(c) of Davis (1992)]; (b) torsional pounding when e_y/l = 0.1.

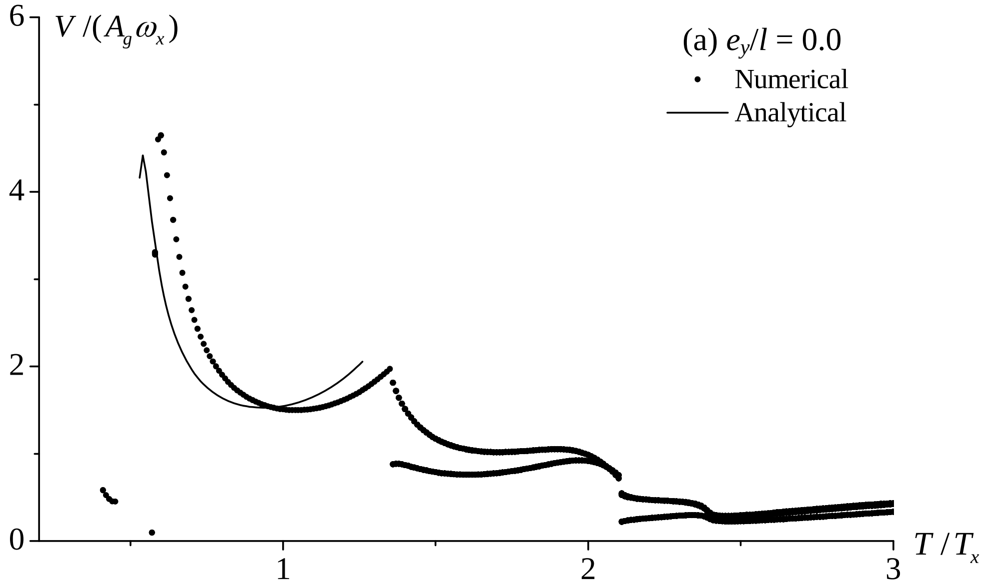

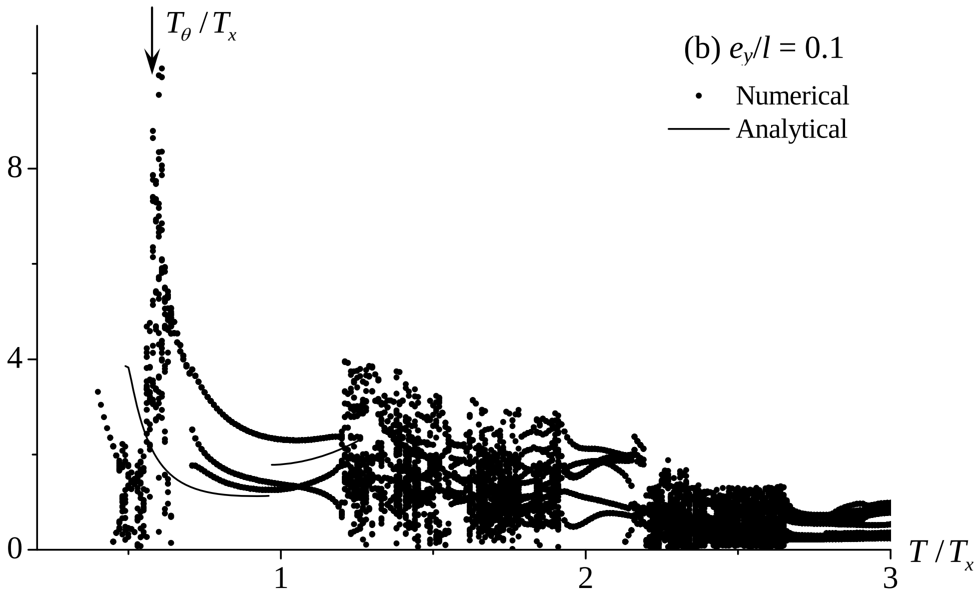

Figure 7.23 Comparison of analytical and numerical solutions of relative impact velocity spectra for translational and torsional pounding when a = 0.5 and $\beta = 100$ ($\zeta_x = 0.10$, $\zeta_\theta = 0.10$, n=1 and Case 1 condition): (a) translational pounding when e_y/l = 0; (b) torsional pounding when e_y/l = 0.1.

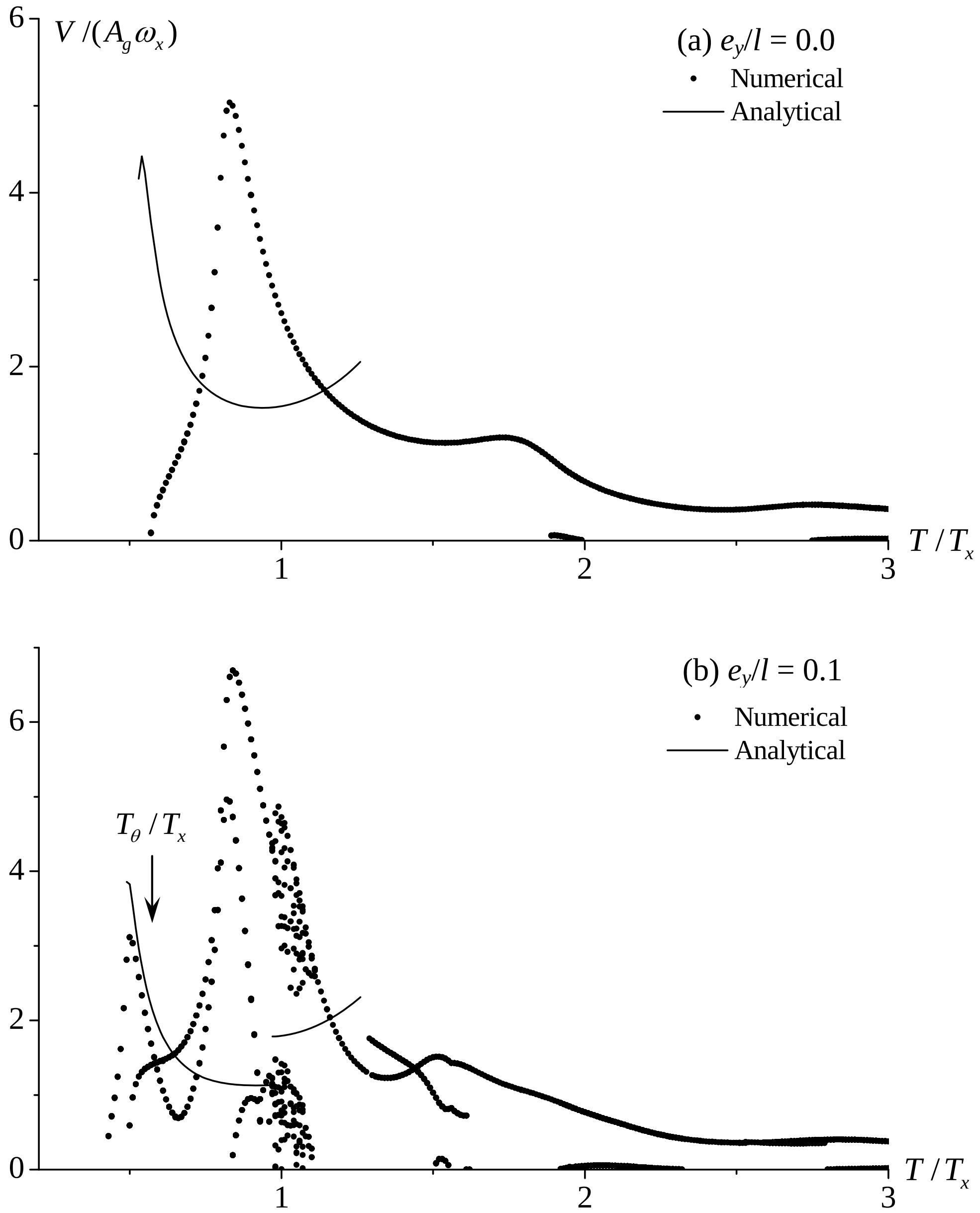

Figure 7.24 Comparison of analytical and numerical solutions of relative impact velocity spectra for translational and torsional pounding when a = 0.5 and $\beta = 1$ ($\zeta_x = 0.10$, $\zeta_\theta = 0.10$, n=1 and Case 1 condition): (a) translational pounding when e_y/l = 0.0; (b) torsional pounding when e_y/l = 0.1.

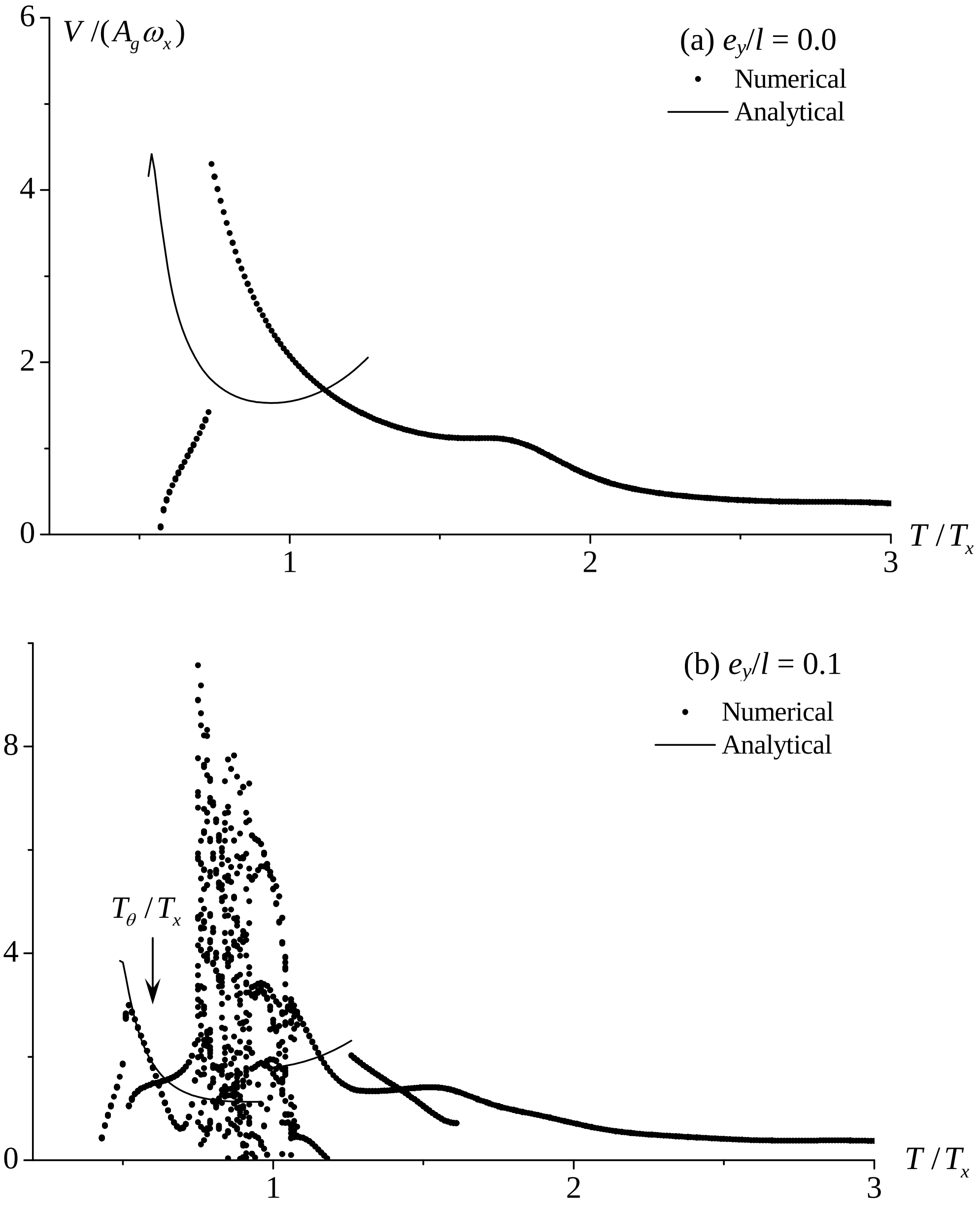

Figure 7.25 Comparison of analytical and numerical solutions of relative impact velocity spectra for translational and torsional pounding when $\beta = 1$ and $\chi = 5.0$ (a = 0.5, $\zeta_x = 0.10$, $\zeta_\theta = 0.10$, n=1 and Case 1 condition): (a) translational pounding when e_y/l = 0.0; (b) torsional pounding when e_y/l = 0.1.

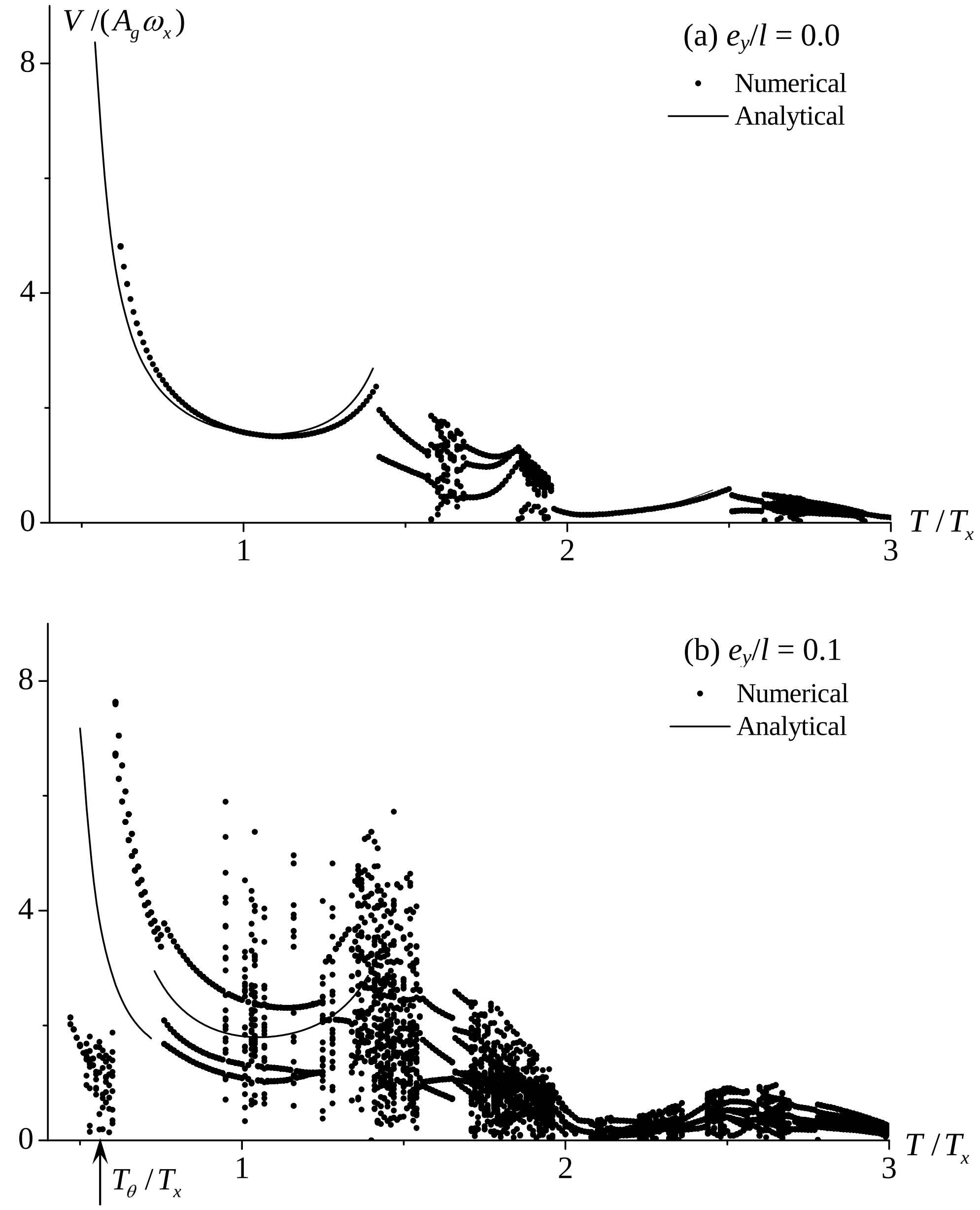

Figure 7.26 Comparison of analytical and numerical solution of relative impact velocity spectra for translational and torsional pounding when a = 1.0 and $\zeta_x = 0.05$ ($\zeta_\theta = 0.10$, $\beta = 1000$, n=1 and Case 1 condition): (a) translational pounding when e_y/l = 0.0 [modified from Figure 10 of Davis (1992)]; (b) torsional pounding when e_y/l = 0.1.

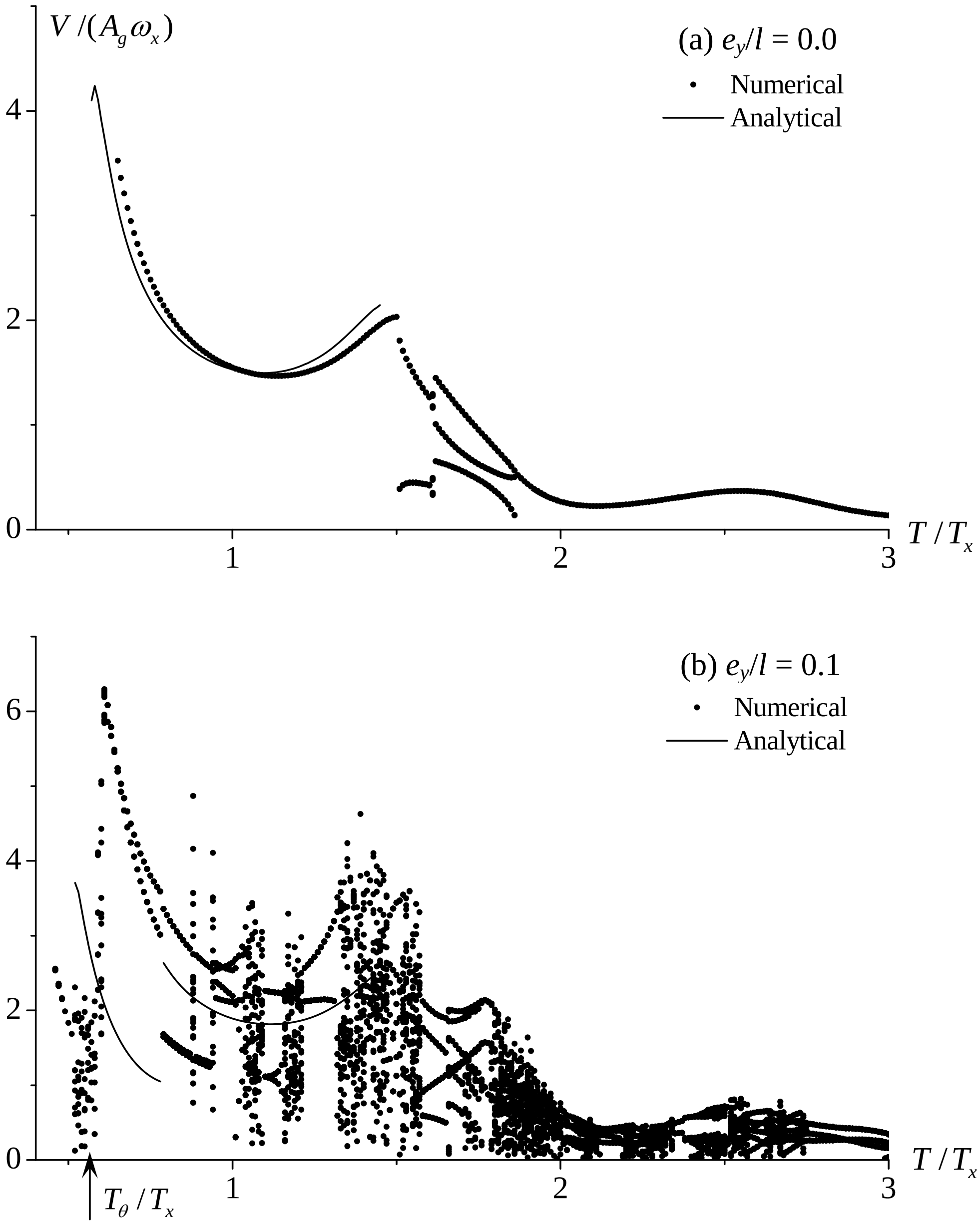

Figure 7.27 Comparison of analytical and numerical solution of relative impact velocity spectra for translational and torsional pounding when a = 1.0 and $\zeta_\theta = 0.05$ ($\zeta_x = 0.10$, $\beta = 1000$, n=1 and Case 1 condition): (a) translational pounding when e_y/l = 0.0 [modified from Figure 11 of Davis (1992)]; (b) torsional pounding when e_y/l = 0.1.

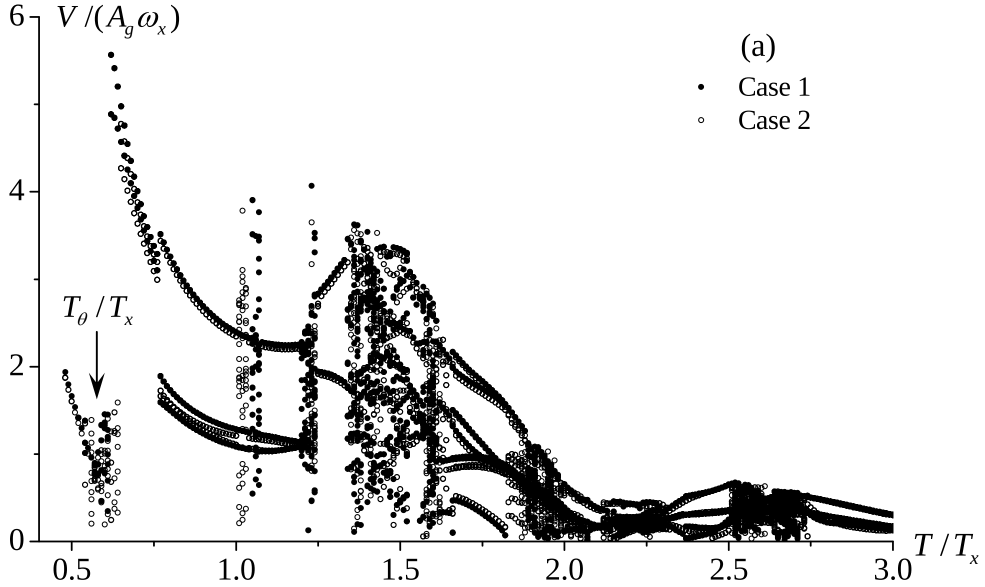

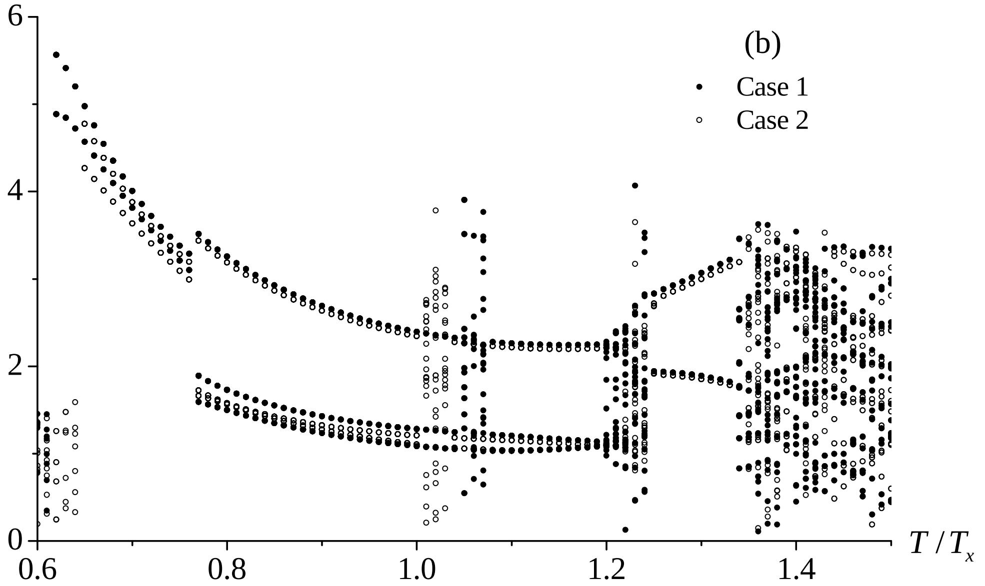

Figure 7.28 Comparison of relative impact velocity spectra for torsional (e_y/l = 0.1) pounding when a = 1.0 ($\xi_x = 0.10$, $\xi_\theta = 0.10$, $\beta = 1000$ and n=1): (a) Case 1 vs. Case 2 conditions; (b) an enlarged view.

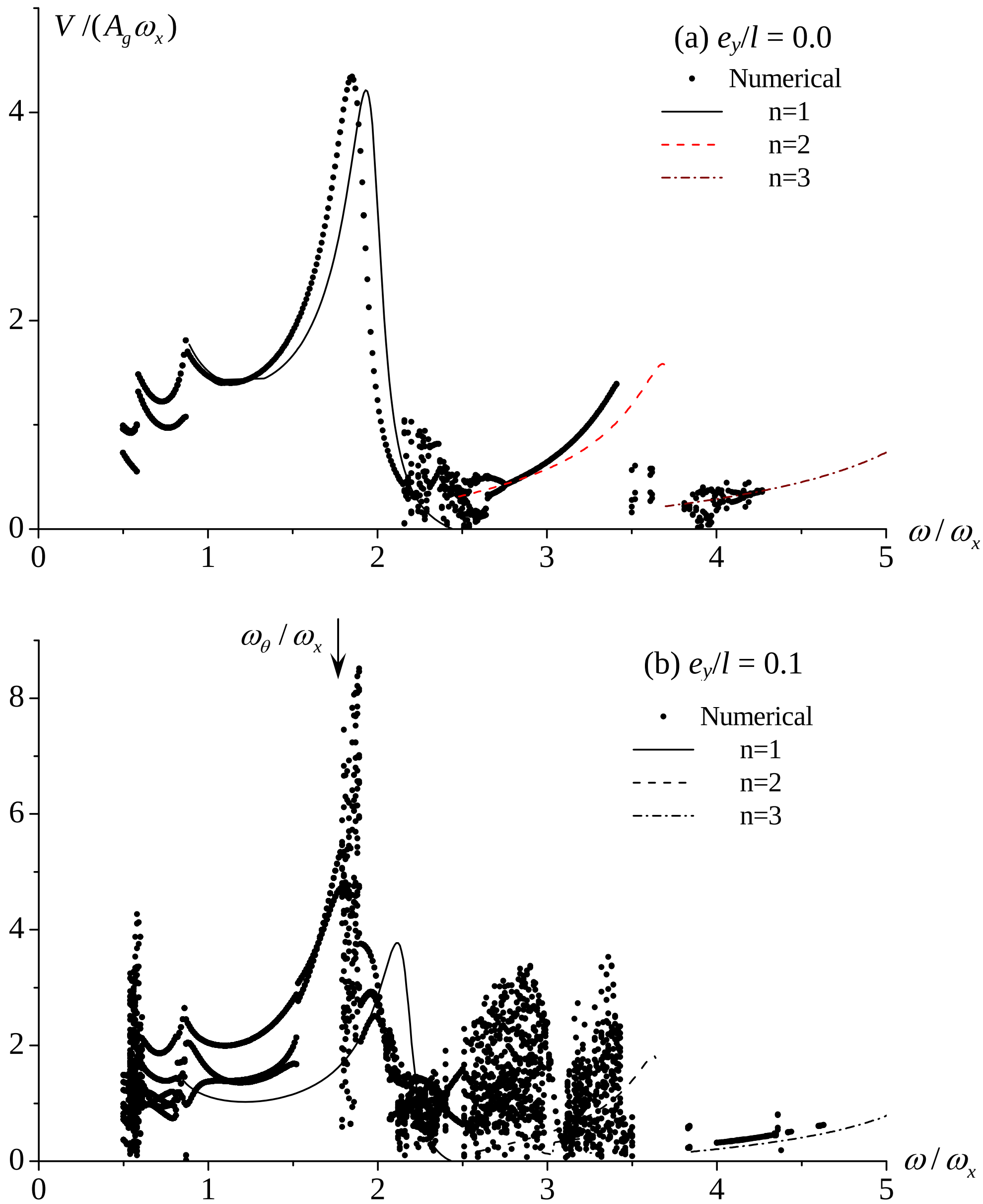

Figure 7.29 Comparison of analytical and numerical solutions of relative impact velocity spectra for translational and torsional pounding when a = 0.2 ($\xi_x = 0.10$, $\xi_\theta = 0.10$, $\beta = 1000$, n=1 and Case 2 condition): (a) translational pounding when e_y/l = 0.0 [modified from Figure 12(a) of Davis (1992)]; (b) torsional pounding when e_y/l = 0.1.

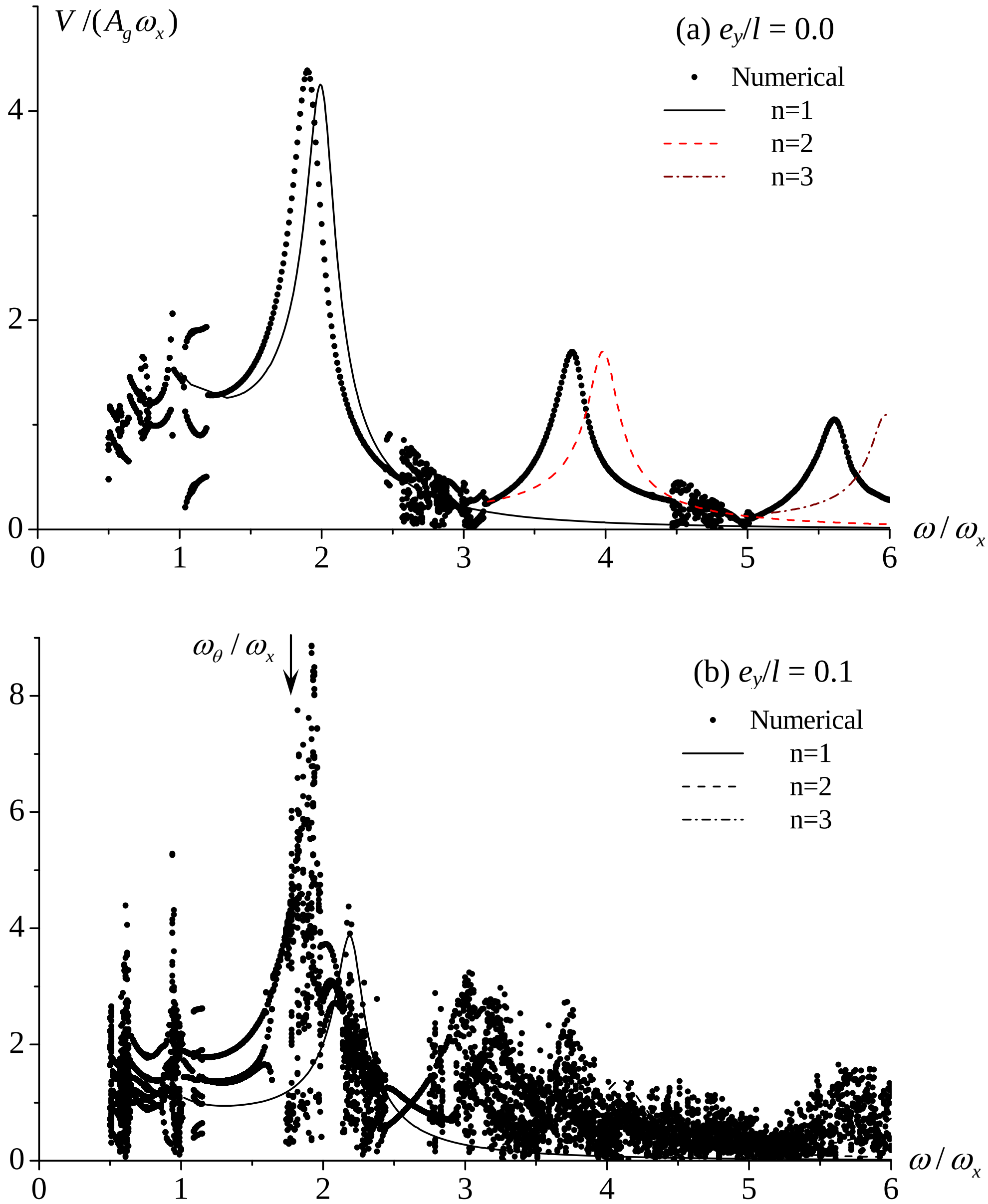

Figure 7.30 Comparison of analytical and numerical solutions of relative impact velocity spectra for translational and torsional pounding when a = 0.0 ($\xi_x = 0.10$, $\xi_\theta = 0.10$, $\beta = 1000$, n=1 and Case 2 condition): (a) translational pounding when e_y/l = 0.0 [modified from Figure 12(b) of Davis (1992)]; (b) torsional pounding when e_y/l = 0.1.

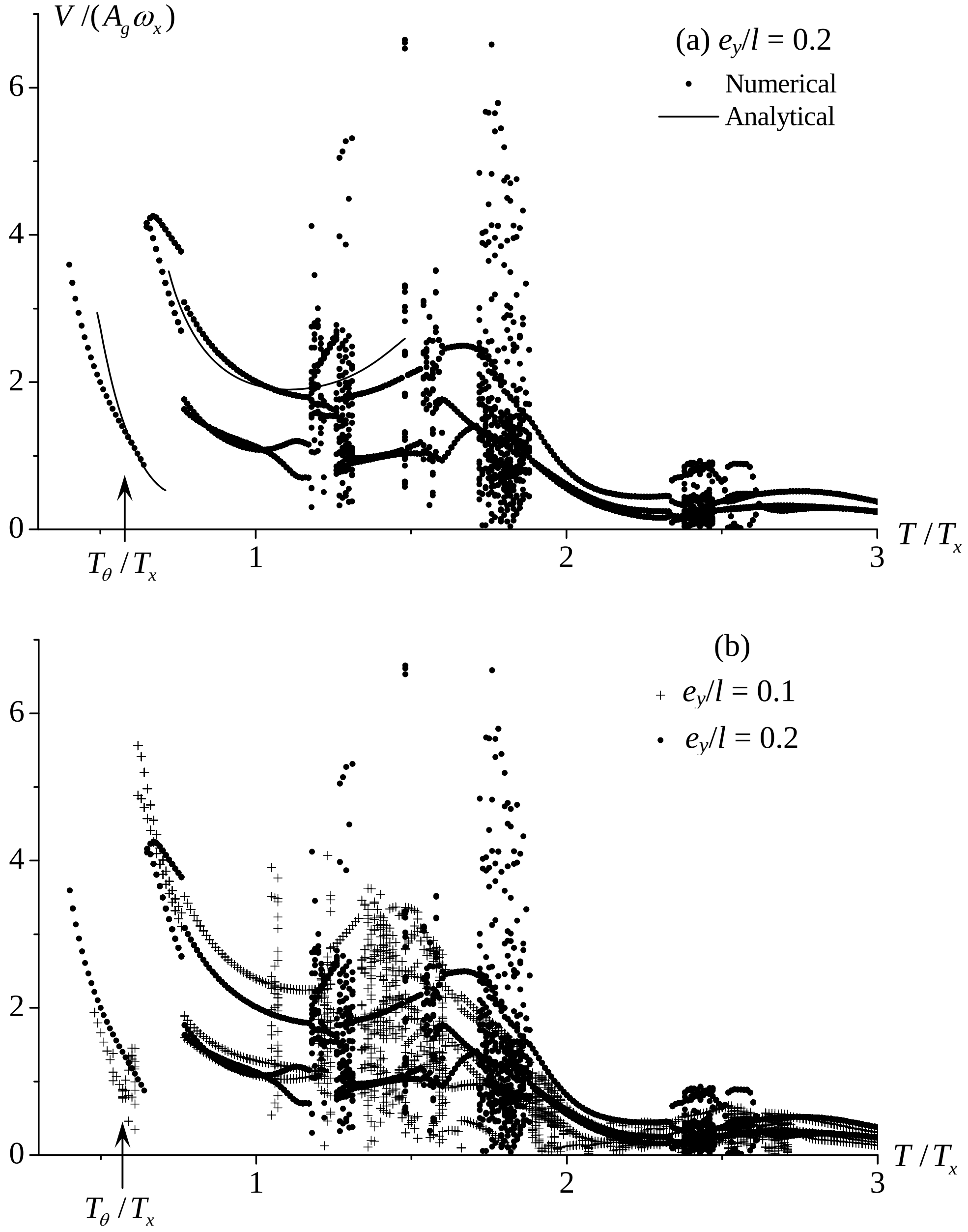

Figure 7.31 Comparison of (a) analytical and numerical solutions of impact velocity spectra for torsional pounding when e_y/l = 0.2; (b) numerical results of impact velocity spectra when e_y/l = 0.1 [same as Figure 7.20(b)] and 0.2 respectively. Other parameters are a = 1.0, $\zeta_x = 0.10$, $\zeta_\theta = 0.10$, $\beta = 1000$, n=1 and Case 1 condition.

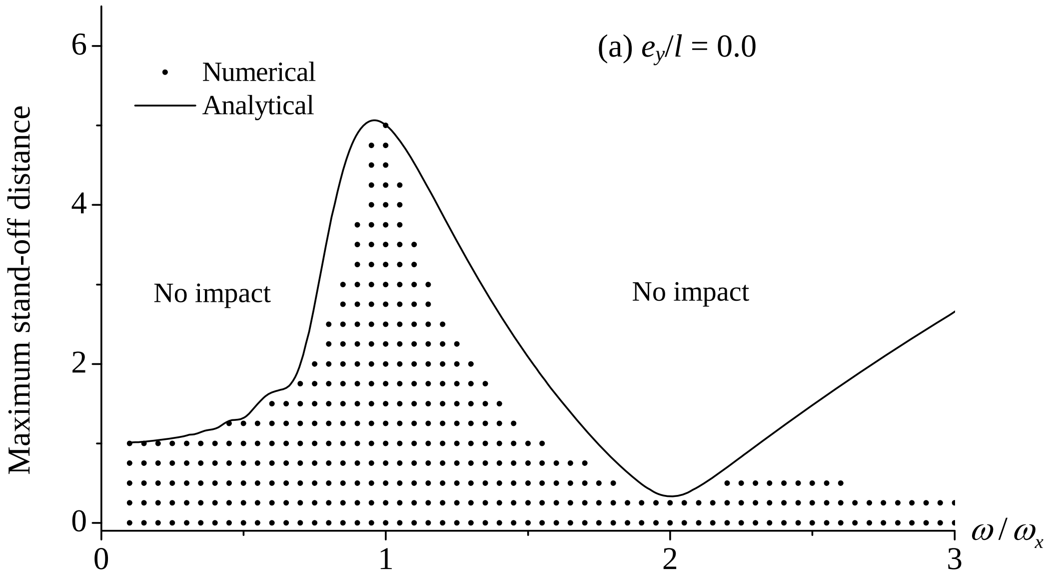

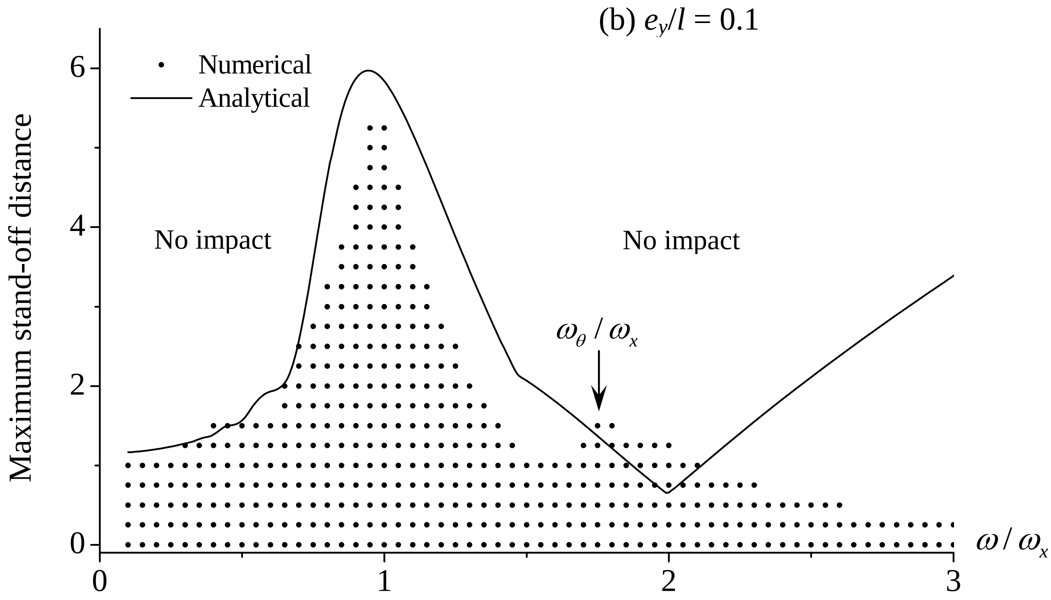

Figure 7.32 Comparison of analytical and numerical predictions of maximum stand-off distance for translational and torsional pounding: (a) translational pounding when e_y/l = 0.0 [modified from Figure 13 of Davis (1992)]; (b) torsional pounding when e_y/l = 0.1. Other parameters are $\xi_x = 0.10$, $\xi_\theta = 0.10$, n=1 and Case 2 condition. Each dot in the numerical solutions represents an impact occurring at a particular frequency ω / ω_x and a stand-off distance a.

CHAPTER 8 SHAKING TABLE TESTS FOR TORSIONAL POUNDING

8.1 Introduction

As introduced in Section 7.1.1, extensive theoretical studies have been carried out on seismic pounding in the past few decades. However, only few experiments have been performed to check the validity of those theoretical models. Inevitably, theoretical models are always formulated with various assumptions and simplifications. Therefore, it is essential to conduct experiments in verifying or disapproving their validity.

Among the several shaking table tests done on this topic, Papadrakakis and Mouzakis (1995) performed shaking table experiments on pounding between two two-story reinforced concrete frames with zero separation, subject to sinusoidal and random motions, and their experimental results were compared to the analytical predictions by using the Lagrange multiplier method.

Filiatrault et al. (1995) conducted another shaking table test for poundings between two adjacent building of three- and eight-story steel frames subject to the time history of the 1940 El Centro earthquake, and the experimental results were compared to the predictions from results of pounding analysis by two programs SLAM-2 and PC-ANSR. The results showed that when elastic gap elements were used in these two programs, accurate displacement and impact force were obtained, but the displacement and force for the case of short acceleration pulses were not well predicted. Relative rotations between adjacent floors were observed and these rotations induce grinding contacts that cannot be captured by uniaxial gap elements in numerical modeling.

The experiments by Papadrakakis and Mouzakis (1995) are for zero separation, whereas those by Filiatrault et al. (1995) are for either zero or 15 mm separation. Thus, none of these tests provide the estimation of maximum stand-off distance between adjacent structures that precludes the occurrence of pounding. In addition, torsional vibrations are not significant in both of these two experimental studies. However, as discussed in Section 7.1.1.1, torsional pounding may be more commonly observed than unidirectional pounding during real earthquakes.

Chau et al. (2003) conducted shaking table tests to investigate the pounding between two single-story steel towers of different natural frequencies and damping ratios, subject to different excitations. The experimental observations were compared with both analytical and numerical predictions of the pounding model proposed by Chau and Wei (2001). For most of the cases, the theoretical predictions are found comparable with the experimental results. A type of group periodic poundings (i.e. a group of non-periodic poundings repeating themselves periodically) was observed for the first time in their tests, which have not been considered by theoretical models.

To further study the torsional pounding, Chau et al. (2004) conducted pounding tests between two asymmetric single-story steel towers. As shown in Figure 8.1, additional masses can be moved along railing systems at the top of the two towers so that their eccentricities can be changed. Similar to the shaking table tests for translational pounding (Chau et al., 2003), the torsional pounding can be periodic, group periodic, or chaotic.

However, it remains questionable whether these idealized models can accurately simulate the seismic pounding between real multi-story asymmetric buildings, for which higher modes may play a more important role. In addition, as remarked in Chapter 1, transfer systems are widely used for both residential and commercial buildings in Hong Kong. But to date none experiments have been conducted to study the effects of transfer system on seismic pounding between real multi-story buildings.

Therefore, in this study shaking table tests will be conducted to investigate torsional poundings between two adjacent asymmetrical multi-storey building models with transfer systems. More specifically, two 1:45 scale steel models were designed and fabricated first to simulate two selected adjacent buildings in Hong Kong. Then, a number of shaking table tests with different excitations and separation distances were conducted between the two flexible models as well as between a flexible model and a nearly rigid wall. The maximum stand-off distances, dynamic responses and pounding forces were investigated. The experimental results will be compared to the theoretical studies proposed in Chapter 7. The detailed experimental setups, pounding tests and results will be summarized in this chapter.

8.2 Model Design and Construction

In this study, the torsional pounding between two asymmetric adjacent multi-story buildings in Hong Kong is investigated through conducting shaking table tests on scaled models. The model design and fabrication will be introduced in this section. First the two selected buildings are described and analyzed using FEM models. Then the model design philosophy is presented. The members of these two steel models are joined by applying welding. Finally, the dynamic properties of the models are measured.

8.2.1 Two selected adjacent buildings in Hong Kong

8.2.1.1 Prototypes

As discussed in Section 7.1, this study will concentrate on seismic torsional pounding between asymmetric buildings with transfer system in Hong Kong. Through extensive field investigations, two adjacent 21-story reinforced concrete buildings in Wanchai on the Hong Kong Island, which is one of the most crowded areas in Hong Kong, were selected for the present study. As shown in Figure 8.2, the L-shaped building is a hotel (called Empire Hotel which will be referred as EH hereafter), which is highly asymmetric; and the other smaller one is a residential building (called Gold Star which will be referred as GS hereafter), which is more regular in shape. The two buildings are built nearly touching each other (see the photograph in the upper right-hand corner of Figure 8.2), probably with a nominal separation of 25 mm (i.e. the thickness of a typical wooden formwork used in Hong Kong). Actually due to the limited land and dense population, this situation is very common in Hong Kong. Note that the seismic vulnerability of the EH building has been studied through shaking table tests in the first part of this thesis.

The two buildings are of similar heights, but they adopt quite different structural forms. The EH building is a frame-shear wall structure, with the upper 19 typical stories supported by a transfer plate through which vertical loads were transferred to the two lower stories. A typical stories consists of shear walls (typically of 200 mm thick), whereas for the two stories below the transfer plate, 20 columns (typically of 1200 mm diameter) are used to support the upper structure. A typical story has a height of 3.0 m whereas the first two stories and the top story have heights varying from 3.7 m to 4.95 m. The more detailed information of this building can be referred to Section 2.2.

The GS building is a 21-story frame structure. A transfer plate is situated on the 4th floor. For the four stories below the transfer plate, the floor plan consists of 20 rectangular columns of five different sizes (ranging from 460×380 mm to 838×610 mm); whereas for the upper stories, the floor plan consists of 12 rectangular columns of sizes from 533×330 mm to 686×457 mm. The first story has a height of 5.6 m and the other stories have a height of 3.0 m. The concrete of grade C30 (corresponding to a cubic compressive strength of 30 MPa) is used in both buildings.

The different structural forms of the two buildings result in their different dynamic characteristics, such as natural frequencies and damping ratios. Thus, under earthquake excitations, their vibrations will be out of phase and pounding is likely to occur since there is no adequate separation between them. In addition, due to the asymmetric distribution of mass and stiffness, especially for the EH structure, it is expected that even under unidirectional ground shaking, torsional responses will be induced and, in turn, torsional pounding will.

8.2.1.2 FEM analyses of the prototypes

After the two buildings were selected, their detailed design diagrams were obtained from the Buildings Department of the Hong Kong SAR Government. Based on the detailed technical drawings, FEM models were set up using the commercial package SAP2000 Nonlinear version 8.1.2. Frame elements were used to model columns and beams whereas shell elements were used to model walls and floor slabs. All the floor slabs were assumed to be rigid in their planes.

Figure 8.3(a) shows the 3D view of the FEM model for EH and the other three diagrams show the mode shapes of the first three modes at the top floor. It is clear that torsional motions are highly coupled with translational vibrations. These torsional motions are induced by the asymmetric arrangement of the structural elements. Similarly, the FEM model and mode shapes of the first three modes of the GS building are given in Figure 8.4. The first mode shape is mainly translational, but torsional responses are coupled with translational motions for the second and third modes. The natural frequencies of the first six modes of the two buildings are summarized in the second column of Table 8.1. Note that the natural frequencies of GS are much lower than that of EH.

8.2.2 Model design and construction

8.2.2.1 Design of two steel models

Similar with the model design discussed in Chapter 3, the design of the two pounding models here was also carried out according to the similarity law. The main difference is that steel is used here to build the models although the actual buildings are built of reinforced concrete. The main reason of using steel material is to allow us to repeat pounding tests on the two models at various shaking magnitudes, input frequencies and separation distances, without suffering substantial damages. The other reason is that the structural elements have rather small dimensions in the scaled model and it is hard to control the quality of micro-concrete used for constructing the models.

The size and weight of our models are constrained by the 3.3 m headroom of the laboratory, shaking table size of 3 m×3 m, and the 10 ton load capacity of the MTS shaking table at the Hong Kong Polytechnic University. Therefore, a length scale of 1:45 was adopted in the present study (i.e. $\lambda_l = 1/45$). The plan dimensions and story heights of the models were all scaled down using the same λ_l, so that the shape of the buildings is preserved.

To guide our design, similarity law will be considered next. In our shaking table tests, the equations of motion of the model and the prototype under earthquake excitations can be written as:

$$m_m \ddot{x}_m + c_m \dot{x}_m + k_m x_m = -m_m \ddot{x}_{gm} \quad (8.1)$$

$$m_p \ddot{x}_p + c_p \dot{x}_p + k_p x_p = -m_p \ddot{x}_{gp} \quad (8.2)$$

where m, c and k represent the mass, damping and stiffness matrices respectively, the subscripts m and p correspond to the model and the prototype respectively, x is the displacement response, and x_g is the input ground motion.

Since in our tests pounding occurs when the model is still undergoing elastic deformation, to simplify the problem the damping effect was ignored in the model design. Actually as will be shown later, the damping ratios of the two steel models are both less than 1% and are considered negligible. Thus, the above two equations can be simplified as:

$$m_m \ddot{x}_m + k_m x_m = -m_m \ddot{x}_{gm} \quad (8.3)$$

$$m_p \ddot{x}_p + k_p x_p = -m_p \ddot{x}_{gp} \quad (8.4)$$

Dividing the above two equations with m_m and m_p respectively and using $\omega^2 = k/m$, we have

$$\ddot{x}_m + \omega_m^2 x_m = -\ddot{x}_{gm} \quad (8.5)$$

$$\ddot{x}_p + \omega_p^2 x_p = -\ddot{x}_{gp} \quad (8.6)$$

where ω_m and ω_p are the circular natural frequencies of the model and prototype respectively. Note that the ratio of displacement is equal to the length scale (i.e. $x_m / x_p = \lambda_l$). For the present 1-g environment of shaking table test, we have

$\ddot{x}_m / \ddot{x}_p = \ddot{x}_{gm} / \ddot{x}_{gp} = 1$. It is straightforward to show from Equations (8.5) and (8.6) that the following equation must be satisfied:

$$\frac{\omega_m}{\omega_p} = \frac{1}{\sqrt{\lambda_l}} \tag{8.7}$$

Since Equations (8.5) and (8.6) are similar mathematically and so do their solutions.

Since steel (with a Young's modulus of 210 GPa) was used to build the present models and the ratio of Young's modulus between the model and the prototype equals 7 (i.e. $\lambda_E = 7$), the required model mass (m_m) plus additional mass (m_a) will be 57.6 and 18.5 ton for EH and GS models respectively according to the additional mass similarity law [using Equation (3.18), we have $m_m + m_a = \lambda_E \lambda_l^2 m_p$, where $\lambda_l = 1/45$ and the total masses m_p of the prototypes EH and GS are 16656.2 and 5343.4 tons respectively]. These two weights are much heavier than the load capacity of out shaking table of 10 tons. Therefore, the additional mass similarity law can not be used here and thus further simplification is needed. To simplify the problem, we will only consider the similarity of the natural frequencies between the model and prototype. That is, we will only enforce Equation (8.7). Despite this simplification, we expect that the seismic responses of the model and prototype should remain similar.

Since the natural frequencies of the two prototypes have been given by FEM analysis in Section 8.2.1, the natural frequencies of target models can be determined as $f_m / f_p = 1/\sqrt{\lambda_l} \approx 6.7$. The results of the first six modes for both models are listed in the third columns of Table 8.1. The target frequencies of the first six modes of the models are all within the working frequency range (1-50 Hz) of the shaking table.

Then, FEM analysis was used to determine the locations of the structural members of the two models such that the target natural frequencies can be achieved. The mass distributions among different floors of each model are designed according to that of actual buildings. As far as possible, the locations of walls and columns in the models are the same as those of the real buildings, except for some minor tuning of the target frequencies. For easiness of construction, circular columns were mainly used in the model, although nearby all columns and walls in the real buildings are rectangular.

After a number of trial and error in choosing the column locations, the detailed structural forms of the two steel models were fixed as shown in Figures 8.5 and 8.6. For EH model, the structural plans for floors below and above the transfer plate are given in Figures 8.5(a) and 8.5(b) respectively. All columns are either circular (8 and 10 mm in diameter) or rectangular (typical of 20×6.5 mm and 12.5×6.5 mm) steel bars, and the detailed dimension of these vertical elements are listed in Table 8.2. Steel plates of 30 mm thick were used as the floor slabs. Rectangular holes were cut from the slabs to simulate the stair cases in the EH prototype (see Figure 8.5). The story heights, floor areas and weights of the model are summarized in Table 8.3. The first two floors and the upper typical floors have weights of 104.09 kg and 76.58 kg respectively. The total weight of the model is about 1.66 ton.

For GS model, the structural plans for floors below and above the transfer plate are given in Figures 8.6(a) and (b) respectively. The first four stories below the transfer plate take a rectangular shape whereas the typical floors above transfer plate have a more irregular form [Figure 8.6(b)]. Four rectangular steel bars of dimension

12.5×6.5 mm were welded at the corners of 1^{st}-4^{th} story and all other columns are circular bars of 6 mm diameter (see also Table 8.2). Table 8.3 also lists the story heights, floor areas and weights of the GS model. The weights of the first four floors, the typical floors and the whole model are 36.82, 22.43 and 528.51 kg respectively. Therefore, the GS model was much lighter than the EH model.

The natural frequencies and mode shapes of these two modes were estimated from FEM analysis and are shown in fourth column of Table 8.1 and Figures 8.7-8.8 respectively. The natural frequencies of the first six modes predicted by FEM are fairly close to that of the target models given in the third column. From Figures 8.7-8.8, the mode shapes of the designed models resembled closely that of the prototypes given in Figures 8.3-8.4. Similar to the prototype buildings, the translational responses were also coupled with torsional vibrations. Therefore, the current design is considered acceptable.

8.2.2.2 Model construction

Circular holes were drilled in advance on the 30 mm-thick steel plate slabs at the locations of columns as shown in Figures 8.5-8.6; continuous circular steel bars were installed through the drilled holes and welding was used to fix the columns to the slabs [Figures 8.9(a) and (b)]; and additional rectangular bars were added to the edges of lower floors.

Figures 8.9(a) and (b) show the completed models of EH and GS respectively. Note that the steel columns were continuous from the roof to the ground. Figure 8.9(c) was a photograph of the two models putting together on the shaking table. Note that the floor slabs below and above the transfer plates were painted with different colors for easy identification. As shown in Figure 8.9(d), the EH model was fixed to the base slab whereas the GS model was bolted down into slots at the base slab such that fine adjust separation distance can be made.

The elevation views of the two models were illustrated in Figure 8.10. Note that steel webs of 60 mm long (refer to the close-up photograph) were welded at the base of each vertical column between 1/F and 2/F of the EH model to adjust the heights of the upper floors, so that the neighboring floor slabs of the two models are nearly situated at the same heights to avoid pounding between floor slabs and columns.

8.2.3 Dynamic characteristics of the two models

To verify the target natural frequencies of our models, modal tests were conducted using hammer blow excitations. Fourier spectra of measured data were then utilized to determine their natural frequencies, mode shapes and damping ratios. For this purpose, seven accelerometers were installed on 21/F, 18/F, 15/F, 12/F, 9/F, 7/F, 5/F and 4/F of the GS model, and 21/F, 18/F, 15/F, 12/F, 9/F, 7/F, 5/F and 2/F of the EH model respectively. The measured natural frequencies of both EH and GS are listed in the last columns of Table 8.1. The actual frequencies are found smaller than the predictions by FEM analysis. Subsequently, additional rectangular steel bars had been added for the EH model (indicated by the open rectangles in Figure 8.5) to tune the natural frequencies.

The obtained mode shapes are plotted in Figure 8.11. More specifically, the shapes of the first two translational motion along the *x* direction as well as the first two torsional modes of the two models are shown in Figure 8.11. For all four modes, the roofs of both models possess the largest responses are at the roof level. However, te higher modes are evident from the modes of f_2^{GS}, f_{T2}^{GS}, f_2^{EH} and f_{T2}^{EH}.

In the following study, only the first several modes of each model were measured, including the first translational (f_1^{EH}) and torsional (f_T^{EH}) modes of EH, the first and second translational modes (f_1^{GS} and f_2^{GS}) and the first torsional mode (f_T^{GS}) of GS. To visualize the mode shape, the five modes considered are illustrated by 3D sketches in Figure 8.12, where the solid lines represent the original forms of the models and the dashed lines show the deformed shapes. And the main direction of motion for each mode was also marked on the sketches.

The damping ratio of each modes was estimated using the half-power method based on the Fourier spectra of recorded displacement data at the roof of each model during the hammer blow testing. Figure 8.13 illustrates the estimation procedure of the half-power method for the damping ratios of the first translation modes of the two models (f_1^{GS} and f_1^{EH}) and the results are 0.36% and 0.23% for GS and EH respectively. The damping ratios of the torsional mode (f_T^{GS}) and second translation mode (f_2^{GS}) of GS are 0.18% and 0.17%, and the torsional mode of EH (f_T^{EH}) has a damping ratio of 0.19%. The obtained damping values seem to be rather small compared to that of reinforced concrete structures (normally 5%), which is not unexpected for the present steel models fabricated by welding.

8.3 Poundings Tests between Two Flexible Models

In this section, pounding experiments between the two asymmetric steel models are reported. First, the installation of contactors and instrumentation are discussed. The maximum stand-off distances between the two models are investigated as a function of excitation frequency. Pounding phenomena will be studied at different separation distances under the shaking of both sine waves and real earthquake records. Finally, the phase diagrams, maximum responses, and the maximum impact forces are presented for different inputs.

8.3.1 Experimental setups

8.3.1.1 Location of contactors

The locations of contactors where pounding take place are decided according to the mode shapes obtained earlier. Since the roofs of the two models always have the maximum displacements (see Figure 8.11), a pair of contactor was installed between the roof of GS and 20/F of EH, which were almost at the same heights as shown in Figure 8.10. In order to record potential pounding caused by higher mode vibrations, a pairs of contactor was also installed on 9/F of the more flexible GS model. This is because 9/F of GS has the largest 2nd mode response other than for the roof (see Figure 8.11). From the elevation view shown in Figure 8.10, impacts may take place between 9/F of GS and 8/F of EH.

To record torsional pounding, two pairs of contactors were installed on both the roof and the middle (9/F) levels as shown in Figure 8.14. Thus, totally there are four possible contact points in between the two models.

The close-up photograph in Figure 8.14 shows the details of a contactor, which consists of a circular steel bar of 16 mm diameter on the EH model and a rectangular steel plate of 90×90×15 mm on the GS model. The relatively large area steel plate is used to allow for the possibility of torsional impacts. Two strain gauges of 2 mm length were installed at the upper and below surfaces of the circular steel bar. The average strains recorded by the two strain gauges will be used to calculate the impact forces. Also shown in the photo, a rubber pad of 5 mm thick was attached at the end of the steel bar in order to reduce damage to the models induced by pounding, so that repeated tests can be conducted.

8.3.1.2 Instrumentations

In addition to the strain gauges, Figure 8.15 shows the location of displacement transducers, velocity transducers and accelerometers installed on the roofs of both GS and EH. Since the steel floor slabs are relatively rigid, the torsional response of a slab can easily be determined through two off-set measurements on it. Accelerations are measured using Brüel & Kjær accelerometers of types 4370, 4371 and 4382, whereas velocities are obtained through converting the acceleration data using Brüel & Kjær amplifier of type 2635 or NEXUS conditioning amplifiers. The four displacement transducers used are the KEYENCE LK 503 laser displacement sensor. The details of these transducers can be referred to Section 3.5.1. Two accelerometers installed on 8/F of EH and 9/F of GS were designed to capture pounding induced by higher modes. Accelerometers installed on 2/F and 3/F of EH and on 4/F and 5/F of GS can capture the sudden change of responses across the transfer plates. Finally, one accelerometer and one LED sensor (SUNX LH-512) were installed on the surface of the shaking table to record the actual shaking generated.

All these transducers were calibrated to assure they were in good working conditions. LabVIEW v7.0 from National Instruments was used for signal acquisition and data presentation. The data were collected at a sampling rate of 2000 Hz.

8.3.2 Maximum stand-off distances

Shaking table tests were conducted to estimate the maximum stand-off distance between the two models under sine wave excitations. In these experiments, the two models were set apart for about 40 mm to assure that no impact will occur. Then, sine waves of different frequencies were input. Finally, the maximum responses of two models were added to yield the maximum stand-off distance.

Figure 8.16 shows the maximum stand-off distances versus the input frequencies. The natural frequencies of the two models are indicated by arrows. The stand-off distances are at maximum when the excitation frequency coincides with the f_1^{GS} and f_1^{EH}. This result was consistent with the findings in the translational pounding tests by Chau et al. (2003) and the theoretical simulations by Chau and Wei (2001). The maximum stand-off distance is about 9.8 mm, equivalent to a stand-off of 0.441 m for the actual buildings by recalling the 1:45 length scale. According to Chinese Code for Seismic Design of Buildings (GB50011-2001, 2001), the anti-seismic gap between this two buildings is 0.323 m. Therefore, the Chinese Code is not conservative enough for the present models. Note also that there are peaks in Figure 8.16 at frequency equal to f_T^{GS} and f_2^{GS}, but no peak is observed near the torsional frequency of EH. This is probably because torsional response of the more rigid EH model was much smaller compared to that of GS. Note that for the whole range of input frequency (1-12 Hz), the maximum stand-off distances are always larger than 1.2 mm. Therefore, if the separation is smaller than this value, pounding will always occur. The equivalent value for the prototypes is 54 mm, which is larger than the actual separation between the two buildings. Thus, these two buildings may be subject to rather high risk of seismic pounding.

8.3.3 Poundings under harmonic excitations

After the “non-pounding” tests, pounding tests under sine wave excitations were conducted by reducing the separation distance between the two models to 0 and 4 mm respectively. The magnitudes of the sine wave inputs varies from 0.05g to 0.1g and the excitation frequencies changes from 3 Hz to 12 Hz with a step of 0.5 Hz.

8.3.3.1 Phase diagrams and velocity time histories

Different types of phase diagrams of steady state responses at the roof of the more flexible GS model are summarized in Figure 8.17. The separation distance is zero and the input magnitude is 0.07g. The input frequencies are also given in the figure. These phase diagrams are plotted using displacement as the horizontal axis and velocity as the vertical axis. The “Translation 1” and “Translation 2” phase diagrams corresponding to the two independent measurements at the roof of GS (see Figure 8.15). The rotation phase diagrams plots the rotation angles versus the rotation velocities at the top of GS.

When the input frequency is 3 Hz, no pounding occurs. The response is periodic and the rotation is relatively small. When the input frequencies are higher than 4 Hz, impacts occur and the phase diagrams become much more complex. A total of nine classes (PI-PXI) of phase diagrams are categorized in Figure 8.17. The pounding responses can be simply periodic (such as PI and PII), a big cycle of oscillation containing smaller ones (such as PVIII), or group periodic (such as PIX). The group periodic impacts mean a group of non-periodic impacts repeating themselves periodically, and this unique pounding phenomenon has also been found in translational pounding tests by Chau et al. (2003).

As shown in Figure 8.17, the torsional responses are much larger when pounding occurs. They can also be periodic, group periodic or chaotic. In addition, the translation phase diagrams at the two corners of GS (Translations 1 and 2 in Figure 8.17) may be quite different, such as the cases of PVI, PVII, PIX and PX. This reflects strong torsional responses in these cases.

The velocity time histories within two input cycles are plotted in Figure 8.18 for the pounding types PI, PVII, PVIII and PIX. The locations where pounding occurs are marked in the figure. The phase diagram for PI is the simplest, whereas those for PVII and PVIII reflect smaller oscillations within the bigger oscillation cycle. The phase diagram for PIX demonstrates the case of group periodicity.

8.3.3.2 Energy transfer through pounding

Energy transfer from the more rigid and massive structure (EH) to the lighter and more flexible one (GS) through pounding is observed in our shaking table experiments. Figure 8.19 shows such an example, where the pounding and non-pounding responses of the two models in two different tests with similar excitations are plotted and compared. More specifically, at zero separation distance, pounding occurred, whereas no pounding occurred when the separation distance was increased to 4 mm.

As shown in Figures 8.19(g) and (h), the excitations of the two cases are almost identical. However, the responses of GS when impact occurred (the dashed lines) are much larger than that of non-pounding experiments (the solid lines) [refer to Figures 8.19(a), (c) and (e)]. The velocity plots for these two cases demonstrate completely different responses. On the contrary, the changes in responses of EH caused by impacts are much smaller and negligible [refer to Figures 8.19 (b), (d) and (f)] The stiffer and more massive EH model is not very responsive to pounding; whereas, the lighter GS model is very responsive to pounding. Clearly, most of the vibration in GS is gained from energy transferred from the poundings. Thus, the energy transfer induced by pounding may cause severer damages to the lighter and more flexible buildings, but would has little influence on those more massive and rigid structures.

8.3.3.3 Maximum responses

The maximum responses and pounding forces under harmonic sine wave excitations are also investigated. Figure 8.20 plots the maximum velocity and accelerations spectra at the roofs of GS and EH respectively when the separation distance is zero and the input magnitude is 0.05g. The symbols ⊙ represent the pounding cases.

Impacts occurred for all the input frequencies higher than 4.5 Hz. Because of the energy transfer by poundings, the responses of the more flexible GS model are much larger. In addition, the response spectrum for the GS model is not symmetric with respect to the x-axis [Figure 8.20(b)]. That is, the positive responses are much larger than the negative responses. As sketched in the figure, these abnormal large positive responses are caused by impacts whereas the negative responses were constrained by the adjacent rigid EH model.

In Figure 8.20, the maximum responses do not occur at the natural frequencies of the two models, but at a frequency (about 6.5 Hz) between these two first natural frequencies. Similar phenomenon was also observed in translational pounding tests by Chau et al. (2003). This implies that when the separation distance is zero (i.e. the adjacent structures are touching with each other), the two models may vibrate together as a new system, which may have a quite different dynamic property from the individual structures.

To further investigate this phenomenon, the two models were locked together (as shown in the photographs of Figure 8.21) and hammer blow testing was conducted to measure the natural frequency of the new system. From the resulting Fourier spectrum plotted in Figure 8.21, it is found that this system has a first torsional natural frequency of 6.378 Hz and a translational frequency of 8.026 Hz. This finding explains the abnormal large responses at about 6.5 Hz in Figure 8.20. Note that the translational frequency is close to that of the EH model (8.118 Hz), which is expected since EH is much more massive and rigid than GS.

Similarly, the maximum velocities and accelerations of GS and EH are also plotted with the input frequencies in Figure 8.22 when the separation distance is 4 mm and the input magnitude is 0.05g. It can be seen that less impacts occur with the increased separation distance and impacts only occur when the input frequency is near the first translational and torsional frequencies of GS as well as the first translational frequency of EH. In addition, the maximum responses always occur at excitation frequency near the natural frequencies of the two models. This observation is quite different from that of zero separation, implying that the two models respond more individually when separated by a distance. The unsymmetrical responses with respect to *x*-axis of the more flexible GS model are again caused by pounding (similar to that in Figure 8.20).

8.3.3.4 Maximum pounding forces

Figure 8.23 shows the maximum pounding forces recorded for various excitation frequencies when the input magnitude is 0.05g and the separation distances are zero and 4 mm respectively. It is found that for 4 mm separation, the maximum forces occur near the translational frequencies of GS and EH: whereas for zero separation, the maximum force again occurs at about 6.5 Hz which is between the natural frequencies of the two models. As discussed previously, this is because the two models behavior as a new system when touching with each other.

In addition, the maximum force of zero separation distance is much larger than that of 4 mm separation. This is probably due to larger energy transfer when the two structures are touching with each other. This implies severer pounding hazard would be expected in Hong Kong, where many buildings are very closely spaced due to the limited land (such as the two prototype buildings studied here). Note that pounding also occurred at the middle level (9/F of GS) both at zero and 4 mm separation distances, due to higher mode responses. But for all the cases, the forces at the roof are larger than that at the middle level.

8.3.4 Poundings under real earthquake excitations

All the results discussed above are for harmonic sine wave excitations. However, real earthquakes may be much more complicated than sine waves. In this study, pounding tests under the shaking of real earthquakes were also conducted at zero and 3.2 mm separation distances respectively. The time histories of three past earthquakes were used as inputs, including the 1940 El Centro earthquake, the 1989 Loma Prieta earthquake and the 1994 Northridge earthquake. As discussed in Section 4.1, the duration of these time histories were all compressed according to the similarity law ($t_m / t_p = \sqrt{\lambda_l} \approx 0.15$) before used as inputs.

The peak ground accelerations (PGA) of these earthquake inputs, the maximum acceleration and velocity responses at the roof of the GS model are summarized in Table 8.4. The time histories of the inputs, the acceleration responses at the roof of GS as well as the pounding force for the three earthquake inputs at two separation distances are shown in Figures 8.24-8.26. In these figures, extremely large acceleration responses caused by pounding are clearly seen. For example, when the peak acceleration of El Centro earthquake input is only 0.229g, the maximum response of GS can reach 13.37g when pounding occurred.

The duration and numbers of impacts as well as the minimum and maximum pounding forces for different earthquake inputs are also summarized in Table 8.4. It is found that with the separation distance increasing from zero to 3.2 mm, both the number of impacts and the magnitudes of impact forces reduced significantly. For example, for zero separation distance, 35 impacts occurred within 3.6s under the excitation of Northridge earthquake and the maximum pounding force reached 8.27 kN; when the separation distance was increased to 3.2 mm, only 6 impacts occurred and the maximum forces reduce to 2.73 kN. This again suggests that the closely spaced buildings may suffer from much heavier pounding damages under the attack of earthquake. And this is consistent with the conclusion drawn from the sine wave excitation tests (see Figure 8.23).

8.3.5 Comparison with theoretical study

In Section 7.2, torsional pounding between two flexible single-story towers under harmonic excitations has been studied through numerical simulations. Although the theoretical model is much simpler than the present 21-story building models, the results from the two studies are briefly compared here.

The maximum stand-off distance spectra from the theoretical prediction (Figure 7.16) and the experiments (Figure 8.16) are similar. For both cases, the maximum stand-off distances occur when the input frequency is near the translational natural frequencies of the two structures. In addition, a local peak occurs near the torsional frequency of the long-period structure (the GS model in the test and Tower A in the numerical study). This shows that even quite simple theoretical models can provide useful insight into the complex torsional pounding phenomenon.

Comparing the phase diagrams shown in Figure 7.9 and Figure 8.18, it is found that for both cases, impacts always result in sudden change of velocities. The difference is that in the tests, the impact-induced reduction of velocity appears to be much smaller than that in the theoretical study and displacement does not remain constant during impacts (Figure 8.18). This means in the experiment the impact duration may not be short, and within the duration of impact the two structures are locked and vibrate together. In the theoretical study, since relatively stiff contact is assumed, the impact duration is close to zero and thus displacement appears to be constant during impacts (see Figure 7.9).

In addition, both group periodic and chaotic pounding observed in the shaking table tests have also been found in the theoretical study (see Figures 7.8 and 7.9).

For the impact velocity spectra from the numerical study (Figures 7.8 and 7.11), the maximum velocities all occur at excitation frequency between the translational natural frequencies of the two structures. Similar phenomenon is also observed in the tests when the separation distance between the two structures is zero (refer to Figures 8.20 and 8.23). However, when the separation distance increases to 4.0 mm in the experiments, the maximum response (Figure 8.22) and impact forces (Figure 8.23) all occur at excitation frequency near the natural frequencies of the two structures. This observation can not be captured by the theoretical model.

It should be borne in mind that the theoretical simulation models are close to SDOF systems whereas the models in the experiments are MDOF systems. Strictly speaking, the two results can not be compared together. The comparisons were made just to show some common characteristics between the pounding phenomena of the idealized SDOF model and the MDOF systems in the experiments. It is shown that even this quite simple theoretical model can provide valuable insights into the highly nonlinear pounding phenomena between actual multi-story structures. For example, periodic group and chaotic poundings were observed in both theoretical simulations and experiments. In this sense, the present theoretical study is of considerable merits and provides guidance for future researches in this area.

8.4 Pounding Tests between One Flexible Model and a Nearly Rigid Wall

In the previous section, seismic poundings between two asymmetric high-rise steel models were investigated and the results showed that the more flexible GS model was subject to more serious damage due to energy transfer from the more massive and more rigid EH model through pounding. Motivated by this results, it is of fundamental interest and importance to investiagte how the more flexible GS model will response when it impacts with an even more massive and rigid structure. In Chapter 4, an analytical solution has been obtained for torsional pounding between a two degree-of-freedom tower and a rigid barrier. In this section, torsional pounding experiments will be conducted between the high-rise GS structure and a nearly rigid wall, and the observed results will be compared with the analytical solution discussed in Chapter 4.

8.4.1 Experimental setups

8.4.1.1 Details of the nearly rigid wall

In this study, a massive steel wall shown in the photographs of Figure 8.27 was utilized as a nearly rigid wall. The wall was designed and built at the Hong Kong Polytechnic University before the commencement of the present PhD study, but the massive wall has never been used until the present study. As shown in Figure 8.28, the wall has a rectangular front elevation view of 2394 mm high and 1706 mm wide and a triangular side elevation plan (see also Figure 8.27). It mainly consists of five steel H-section columns and a set of support steel bars transferring horizontal loads to the inclined channels, and a rectangular steel plate of 1706×650×30 mm was welded to the top portion of the wall in connecting all five steel columns together (see the front view photo in Figure 8.27). The detailed dimensions and structural forms were given in Figure 8.28. All the connections are made by welding.

Modal tests were carried out through hammer excitation tests in determining the dynamic characteristics of the wall. The Fourier spectrum of the measured acceleration response at the top was shown in the lower plot in Figure 8.27. As can be seen, the natural frequencies of first three modes of the wall were 39.734, 59.937 and 74.768 Hz respectively. Recall that the natural frequencies of the first three modes of GS are all less than 12 Hz. Considering these big differences, the steel wall shown in Figures 8.27 and 8.28 can be reasonably assumed to be nearly rigid and will be referred as RW (short form for Rigid Wall) hereafter.

8.4.1.2 Instrumentations

The instrumentations used in the pounding tests between the GS model and RW were illustrated by a sketch in Figure 8.29, together with some actual photographs of the models. Similar to the previous experimental settings in the tests between GS and EH (refer to Figure 8.8), two set of contactors were installed between the roof of the GS model and RW. To estimate the impact forces between these two structures, two strain gauges were attached onto the surface of each of the steel bars at the contact points. To avoid excess damages to the GS model during parametric studies, a circular rubber pad of about 5 mm was glued to the contact surface of the contact bars. This rubber padding, in effect, also reduces pounding forces between these two steel models. Note that impacts are only allowed at the top level, and consequently mid-level impacts between actual buildings, if there is any, can not be accounted for in this particular experimental set-up. It is equivalent to assuming that the higher mode deformation of the GS model is not significant during impacts.

As shown in Figure 8.29, laser displacement transducers, velocity and acceleration accelerometers were all installed on the far end of the floor slab of the GS model, away from the pounding side next to RW. The velocities data were obtained through converting the acceleration data using amplifiers as discussed earlier. Two accelerometers were installed on the 4/F and 5/F of the GS model to record the probable changes in responses below and above the transfer plate, if there is any. Another four accelerometers were installed on the 9/F to measure the velocities and accelerations, such that any potential second mode deformation of GS can be captured. Finally, two remaining accelerometers were installed on the 15/F, which is about half-way between the accelerometers at the roof and those at 9/F. To ensure the validity of our rigid wall assumption, one accelerometer was installed at the top of RW behind the pounding portion of the wall. One accelerometer and a laser displacement sensor were installed on the surface of the shaking table to record the actual inputs generated. Again LabVIEW v7.0 from National Instruments was used for signal acquisition and the data collection rate was set to 2000 Hz to record the instantaneous responses caused by short-duration impacts.

8.4.2 Poundings under harmonic excitations

Pounding tests between GS and RW were conducted under the excitations of sine wave at two different separation distances: 0 mm and 3 mm. The magnitudes of the sine wave inputs vary from 0.05g to 0.08g and the excitation frequencies range from 2 Hz to 12 Hz. The results of phase diagrams and time history responses of our shaking tabe experiments will be presented separately for the two different separation distances as follows.

8.4.2.1 Zero separation distance

Figure 8.30 plots four different types (PI-PIV) of phase diagrams of responses at the roof of GS when the separation distance is zero and the input magnitude is 0.05g. The first two columns of Figure 8.30 show the phase diagrams of displacement versus velocity and velocity versus acceleration respectively; whereas the third and fourth columns show the phase diagrams corresponding to rotations. As can be seen, because of the higher frequency contents, the phase diagrams between velocity and acceleration are much more complex than that between displacement and velocity.

Similar to the patterns found previously in the tests between GS and EH, here the phase diagrams can be classified as: (i) periodic (PI); (ii) periodic cycle of oscillations with smaller oscillation cycles (PII); (iii) group periodic pounding (PIII); and (iv) chaotic (PIV). To further illustrate these pounding phenomena, the velocity time histories within two input cycles are plotted in Figure 8.31, together with the phase diagrams. The locations of pounding occurrence are marked by arrows in the figure.

Theoretically, pounding can be seen from a sudden change of velocity at the same displacement. However, some of impacts cannot be seen clearly from Figure 8.31. From these plots, the following conclusions can be drawn. For PI, impact occurred once during each input cycle. For PII, two impacts happened within one input cycle but the response was still periodic and impacts occurred at the same two places during each input cycle. For PIII, there were still two impacts in one input cycle, but the tracks of phase diagram did not coincide with that the previous cycle, and the pounding occurred at different locations during two consecutive input cycles. This pattern repeated itself every two cycles and formed a group periodic pounding as found in the tests between GS and EH. Finally, for PIV, the response was chaotic because no periodic tracks can be found from one cycle to the other.

8.4.2.2 Non-zero separation distance

When the separation distance increased from zero to 3 mm, the response of GS differs significantly from that for zero separation. For the cases of no poundings (or called non-pounding tests), Figure 8.32 shows three different patterns of response. The case of NPI showed a highly periodic response, NPII showed a more complex response with smaller oscillations within a bigger cycle of oscillations, and NPIII represented a rather chaotic response. These different patterns depended on the excitation frequencies of sine wave inputs.

When pounding did occur, the phase diagrams are also quite different from that of zero separation distance. As shown in Figure 8.33, a total of eight different patterns of responses were identified. The responses can be periodic, such as PI-PIII and PV-PVII; group periodic, such as PVIII; or completely chaotic, such as PIV. To illustrate different responses, velocity time histories of four distinguished patterns (PI, PIV, PVII and PVIII) are selected and plotted in Figure 8.34.

The case PI showed a highly periodic oscillation; PVII was also roughly periodic but the tracks and the locations of impacts varies from cycle to cycle; PVIII represented a group periodic response repeating itself every two input cycles; whereas PIV was chaotic and no periodic pattern can be found. All these cases are having a impact per excitation cycle.

Comparing the impact patterns showed in Figures 8.31 and 8.34, it can be concluded that more impacts occur within one input cycle for the case of zero separation; whereas there is only one impact during one cycle for 3 mm separation distance. Therefore, more impacts were expected to occur for smaller separations.

To further investigate seriousness of these impacts, and spectrum of maximum responses will be discussed next.

8.4.2.3 Maximum responses

Figure 8.35 plots the maximum velocities at the roof of GS with respect to the input frequencies for separation distances of 0, 3 and 4.7 mm. The responses spectra for 3 and 4.7 mm separations are similar in shape, with the peak responses occur at excitation frequencies very close to the natural frequencies of the first three modes of GS. The spectrum for zero separation distance is completely from the two former cases. Only one maximum response occurred at a frequency between those of the first two translational modes, but is very close that of the first torsional mode of GS. It appears that when the separation distance was zero, the two structures GS and RW respond as a new system, which had a totally different dynamic characteristic from those of individual models.

Figure 8.36 plots the maximum accelerations at the roof of GS with respect to the input frequencies for separation distances of 0, 3 and 4.7 mm. Note that the magnitudes of positive maximum acceleration is much smaller than that of the negative acceleration probably because of the constraint posed by RW in the forward direction, as illustrated by the small sketch in Figure 8.36.

One main difference between Figures 8.35 and 8.36 is that the spectra in Figure 8.35 are roughly symmetric with response to the horizontal axis whereas those in Figure 8.36 do not. This demonstrates that impacts cause much more drastic changes to acceleration in comparison with velocity. This can also be reflected in Figures 8.30 and 8.33 discussed earlier.

8.4.2.4 Maximum pounding forces

Finally, the maximum pounding forces recorded during the inputs of different frequencies are plotted in Figure 8.37 when the input magnitudes are 0.05g and the separation distances are 0, 3 and 4.7 mm respectively. It can be seen that the maximum pounding forces for cases of 3 and 4.7 mm separations are abut the same (about 1.2 kN). This observation agrees with the conclusion by Chau and Wei (2001) on translational pounding that the maximum impact velocity appears to be not too sensitive to the change of separation distance as long as the impact is developed. Note that the maximum pounding forces occurred near the first translational natural frequency of GS. For excitation freqncury close to the second translational natural frequency of GS, pounding occurs only for Δ = 3 mm but not for Δ = 4.7 mm.

However, the force spectrum is quite different for Δ = 0. As discussed earlier for Figure 8.35, the two structures behave as a new system and impacts occur at frequencies between the first and second translational natural frequencies of GS. As a whole, the magnitudes of impact forces are much smaller than that of 3 and 4.7 mm separation distances. This is quite different from the patterns found in the pounding tests between GS and EH in Figure 8.23. The reason may be that the adjacent RW structure was much more rigid than EH and it moves almost together with the ground. Thus, unlike the situation of pounding between GS and EH, little vibration energy is transferred from the barrier to the more flexible GS model when the separation distance was zero, resulting in the smaller impact forces here.

8.4.3 Comparison with theoretical study

Above torsional pounding between an asymmetric 21-story building model and a nearly rigid wall are studied through shaking table tests. In previous Section 7.3, pounding between an asymmetric single-story tower and a rigid barrier was studied theoretically through both analytical solution and numerical simulation. In this section, we attempt to compare the earlier theoretical results with experimental observations.

In earlier numerical simulations, group periodic and chaotic pounding occur at different excitation periods [refer to Figures 7.20(a) and 7.29(b)]. Similar pounding phenomena have also been found in the shaking table tests. For example, the pounding type PIII in Figure 8.30 and the type PVIII in Figure 8.33 belong to group periodic pounding, and the pounding type PIV in these two figures belong to chaotic pounding.

It is found in the theoretical study that change of separation distance will not influence the maximum impact velocity significantly (Figures 7.19, 7.21 and 7.22). The same phenomenon was observed in our experiments reported in this chapter. More specifically, as shown in Figure 8.37, the maximum impact forces at separation distance of 3.0 and 4.7 mm are very close to each other. These findings suggest the severity of pounding seems insensitive to separation distance as long as pounding develops at that distance. This is also consistent with the conclusions on translational pounding by Davis (1992) and Chau and Wei (2001).

However, there are some experimental findings that can not be explained by our simple theoretical model. For example, the observed structural responses and measured impact forces are quite different when the separation distance is zero and when it is larger than zero (see Figures 8.35-8.37). In addition, when the separation distance is 3.0 or 4.7 mm, the maximum responses and impact forces occur at excitation frequency near the natural frequencies of the GS structure (Figures 8.35-8.37), whereas the maximum impact velocity is not found at the excitation period of $T/T_x = 1.0$ in the numerical simulation (Figure 7.20). These facts show that our simple single-story theoretical model using Hertz contact may be not enough in accurately predicting torsional pounding between multi-story buildings (i.e. our steel models) and more sophisticated models are needed.

8.5 Conclusions and Discussions

In this chapter, seismic torsional poundings between two adjacent 21-story building models as well as between a building model and a nearly rigid wall were studied through shaking table tests. Two steel models were designed and fabricated to simulate two adjacent 21-story buildings with transfer systems and asymmetric plans. A great number of tests were conducted on shaking table at different separation distances and subjected to different harmonic inputs and real earthquake inputs. Pounding induced responses and impact forces were investigated. The following main conclusions are obtained.

Torsional pounding phenomena between real multi-story buildings are more complex than the predictions from the simple theoretical models. Experiments show that seismic poundings can manifest as periodic, group periodic or chaotic responses, depending on dynamic characteristics of the model, separation distance between the models, frequency content and magnitude of ground shakings. For adjacent multi-story asymmetric buildings, pounding may occur at both corners of buildings due to torsional responses, and may occur at the middle heights due to higher mode vibrations. This is for the first time those phenomena of torsional and higher-mode poundings are observed and verified in torsional pounding experiments between actual structural models.

Energy may transfer from the more massive and rigid building to the lighter and more flexible building through pounding. And this energy transfer may cause abnormal large responses and damages to the lighter building, which when stand alone would not suffer any damages under similar ground shakings. We expect the same energy transfer will happen between real buildings in earthquakes. This also implies that when two stand-alone structures behave satisfactorily under certain ground excitations, they may behave quite differently when pounding occurs due to the proximity of the two structures. Therefore, special consideration must be made when a new building is proposed to be constructed right next to a pre-existing building, like many cases in Hong Kong.

When separation distance is zero (i.e. adjacent buildings are touching with each other), two adjacent structures may behave as one unit, with their response linked by periodic impacts. The new system can have a totally different dynamic characteristic from that of individual structures. The process is highly nonlinear, involving frequent energy transfer between adjacent structures through impacts, and thus makes pounding phenomena more unpredictable.

When two buildings impacts with each other, larger responses and pounding forces may be resulted for zero separation distance than for non-zero separations due to the energy transfer; whereas the case is opposite for pounding between one flexible building and a rigid wall, where larger impacts occur when they are separated by a distance. But for both cases, impacts appear to be insensitive to change of separation distance as long as pounding is developed. Similar phenomena have been observed in our theoretical simulations and also by Davis (1992) and Chau and Wei (2001).

The analytical simulations described in the last chapter and the pounding experiments described in this chapter are intended to study the seismic torsional pounding from two different aspects. We hope both the two studies will contribute to our knowledge of this highly nonlinear phenomenon. In Sections 8.3.5 and 8.4.3, preliminary comparisons have been made between the idealized single-story analytical models and the multi-story experimental models. As discussed previously, although the theoretical models can provide some valuable insights into the complex pounding phenomenon between actual structures, strictly speaking they are not comparable. Special techniques are needed to extrapolate the results of SDOF systems to the MDOF systems. To simulate the real poundings between actual multi-story structures more accurately, more sophisticated models are needed. All of these may be the aims of future studies.

Table 8.1 Natural frequencies of the first six modes of the prototype, the target model, the model from FEM analysis, and actual fabricated models.

Empire Hotel

Mode	Prototype (FEM, Hz)	Target model (Hz)	Model (FEM, Hz)	Actual model (Hz)
1	1.712	11.471	12.029	8.80
2	2.079	13.929	15.947	9.07
3	2.399	16.074	20.667	10.54
4	4.616	30.930	36.453	27.89
5	5.081	34.040	47.817	28.97
6	5.934	39.760	61.048	33.48

Golden Star

Mode	Prototype (FEM, Hz)	Target model (Hz)	Model (FEM, Hz)	Actual model (Hz)
1	0.633	4.242	5.259	3.45
2	0.783	5.247	5.867	4.00
3	0.822	5.508	7.423	6.05
4	1.736	11.631	14.364	12.11
5	2.209	14.798	17.278	16.34
6	2.261	15.149	21.227	18.13

Table 8.2 Dimensions of columns of the two steel models.

Empire Hotel

Columns	Form	Dimensions (mm)
C1-C4, C9-C10, C17, C21-C22	Circular	ø8
C5-C8, C11-C16, C18-C20	Circular	ø10
W1	Rectangular	20×6.5
W2	Rectangular	25×6.5
W3	Rectangular	30×6.5
W4	Rectangular	12.5×6.5

Golden Star

Columns	Form	Dimensions (mm)
C6-C8, C10-C13, C15, C17-C18	Circular	ø6
C1, C5, C16, C20	Rectangular	12.5×6.5

Remark:

ø8 means 8 mm in diameter.

Table 8.3 Story heights, areas and mass of various stories of the EH and GS models.

Empire Hotel

Floor	Height (mm)	Area (m^2)	Mass (kg)
1	135	0.4420	104.09
2	180	0.4420	104.09
3	130	0.3252	76.58
4-20	102	0.3252	76.58
21	155	0.3252	76.58
Total	2334		1663.29

Golden Star

Floor	Height (mm)	Area (m^2)	Mass (kg)
1	145	0.1563	36.82
2-4	102	0.1563	36.82
4-20	102	0.0952	22.43
21	117	0.0952	22.43
Total	2200		528.51

Table 8.4 Summary of responses during the inputs of three earthquakes when the separation distance between GS and EH is 0 and 3.2 mm respectively. In the table, A_{max} and V_{max} are the maximum acceleration and velocity at the roof of GS, duration and Ni represent the time duration and number of impacts occurred, and F_{min} and F_{max} denote the minimum and maximum impact forces.

Δ (mm)	Earthquake	PGA (g)	A_{max} (g)	V_{max} (m/s)	Duration (s)	Ni	F_{min} (kN)	F_{max} (kN)
0	El Centro	0.229	13.37	34.14	4.62	36	0.49	7.95
	Loma Prieta	0.228	8.16	24.11	2.80	27	0.48	5.04
	Northridge	0.354	11.97	23.79	3.60	35	0.49	8.27
3.2	El Centro	0.229	10.45	26.30	4.45	13	0.51	4.29
	Loma Prieta	0.230	9.46	26.73	2.23	9	0.49	2.62
	Northridge	0.380	9.50	24.71	1.21	6	0.78	2.73

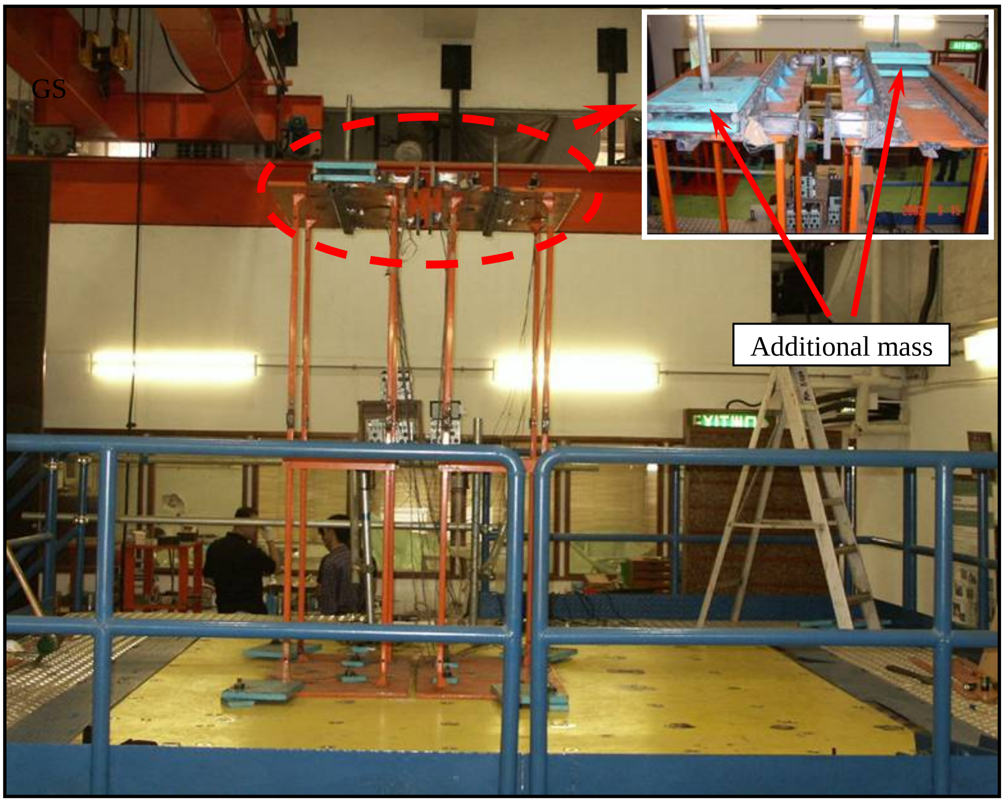

Figure 8.1 Photograph of shaking table tests of seismic torsional pounding between two asymmetric steel towers conducted by Chau et al. (2004). The close-up view showed the additional masses at the top of the towers which can be off-set along railing systems to change the eccentricities of the towers.

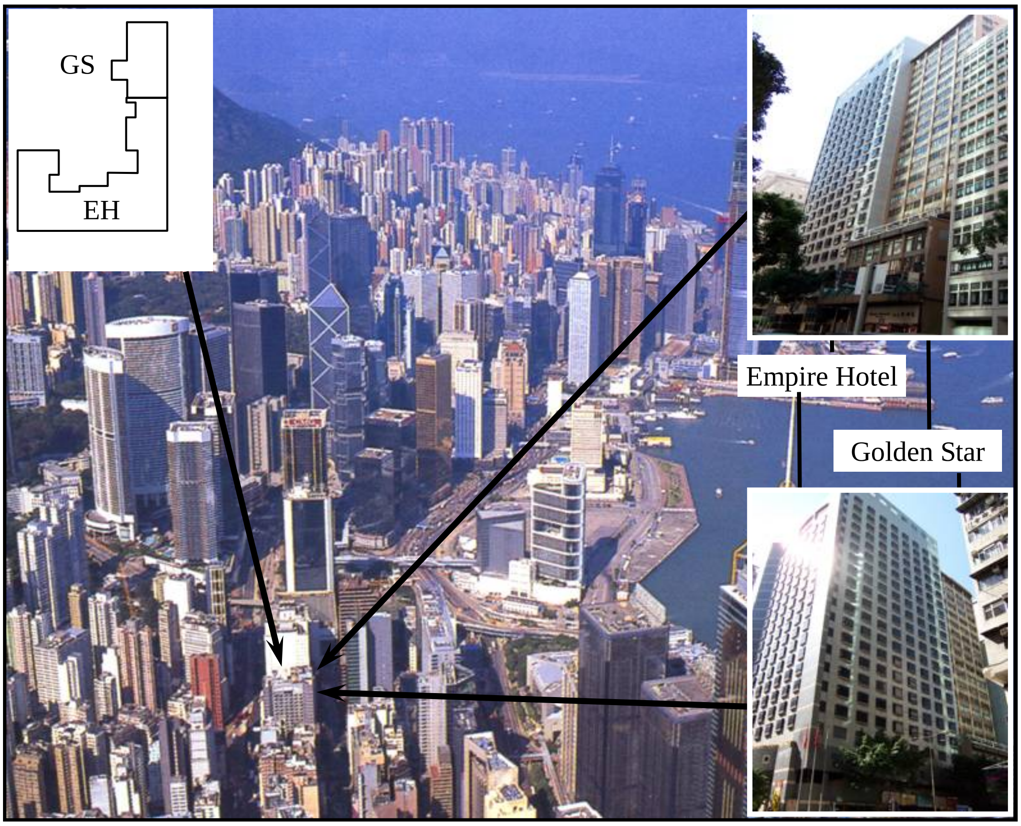

Figure 8.2 The location and photographs of the two selected 21-story adjacent prototype buildings in Wanchai on the Hong Kong Island. The L-shaped building is Empire Hotel (EH) and the other one which is more regular in shape is a residential and commercial building called Golden Star (GS). Transfer systems are used for both the two structures.

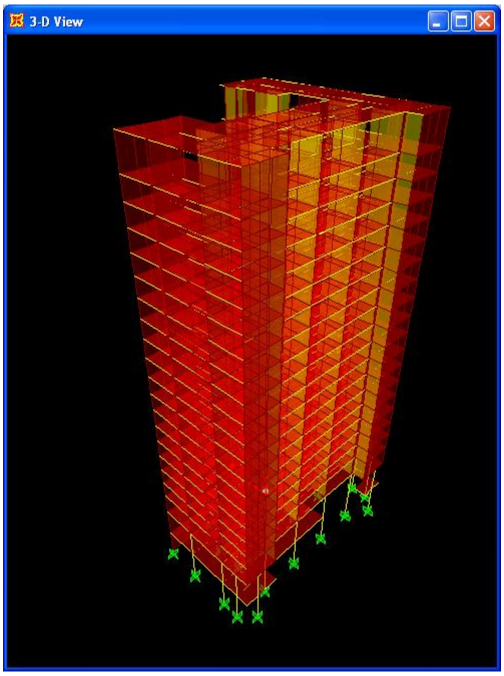

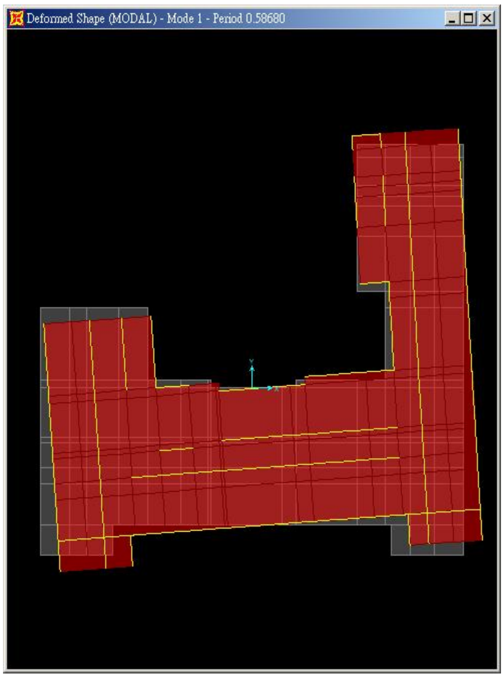

(a) 3D view of FEM model;

(b) 1^{st} mode, f=1.712 Hz;

(c) 2^{nd} mode, f=2.079 Hz;

(d) 3^{rd} mode, f=2.399 Hz.

Figure 8.3 FEM model of the EH building and its first three mode shapes.

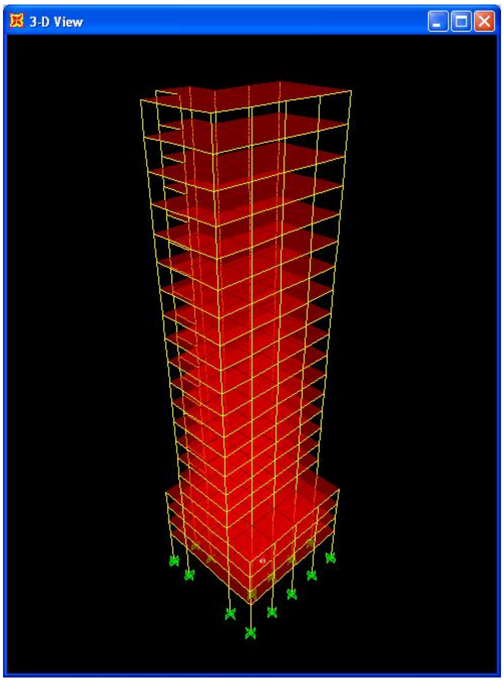

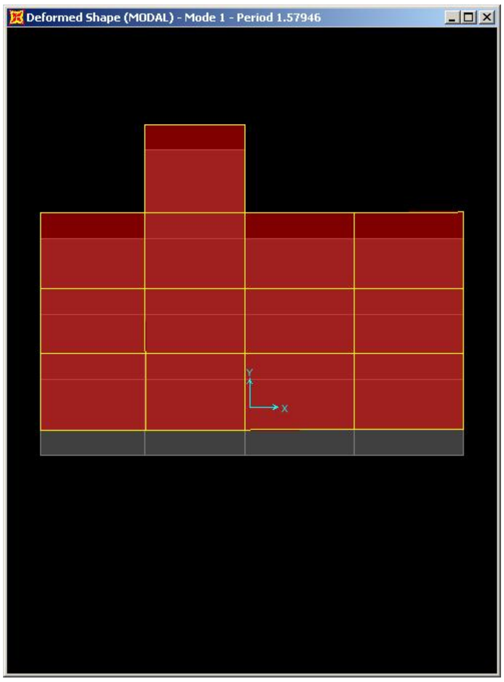

(a) 3D view of FEM model; (b) 1st mode, f=0.633 Hz;

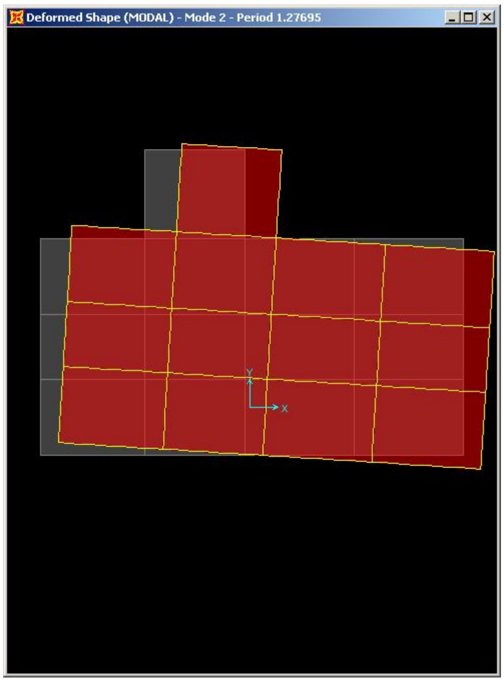

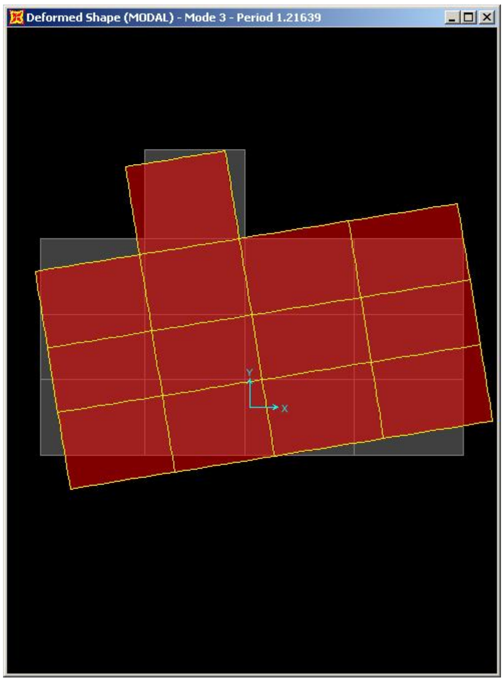

(c) 2nd mode, f=0.783 Hz; (d) 3rd mode, f=0.822 Hz.

Figure 8.4 FEM model of the GS building and its first three mode shapes.

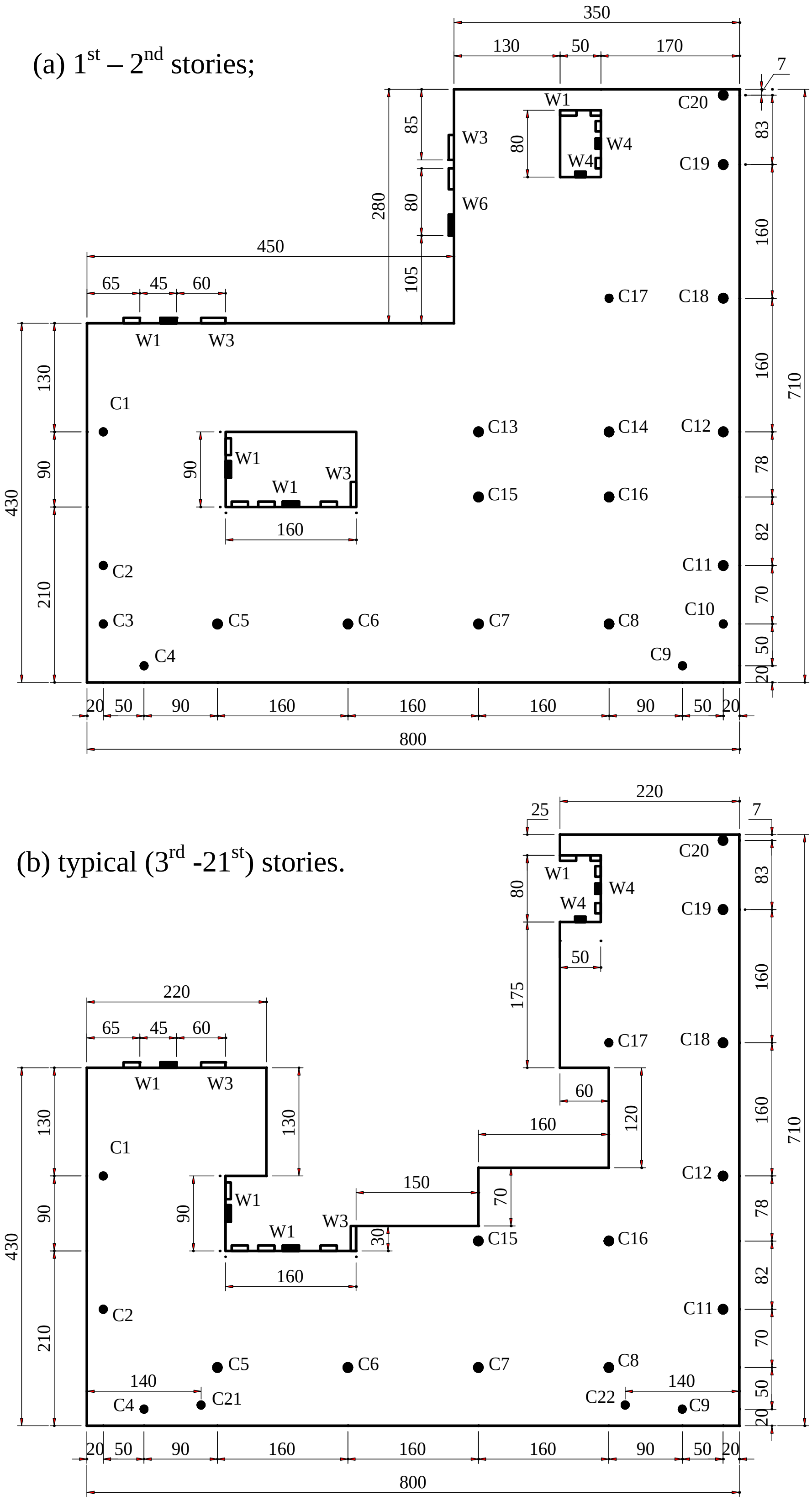

Figure 8.5 Two different floor plans of the EH model. The floor slabs were fabricated using 30 mm-thick steel plates and the dimensions of columns and walls are listed in Table 8.2. The open rectangles represented the columns added for the purpose of adjusting the model frequencies.

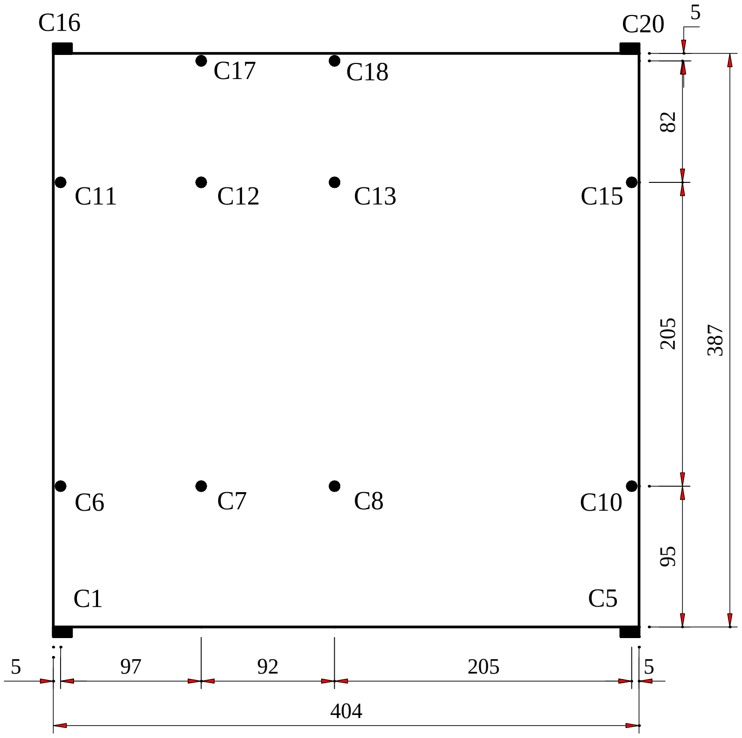

(a) 1st – 4th floors;

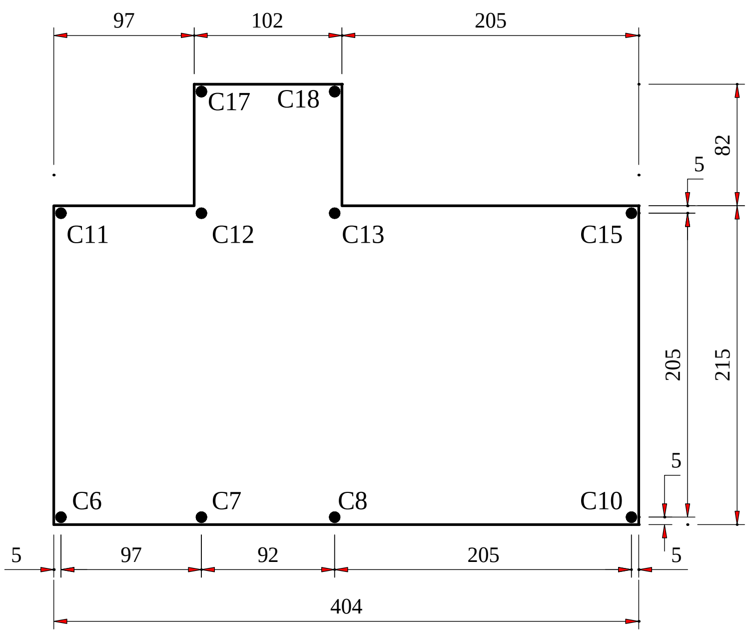

(b) 5th – 21st floors.

Figure 8.6 Two different floor plans of the GS model. The floor slabs were all fabricated using 30 mm-thick steel plates and the dimensions of columns were listed in Table 8.2.

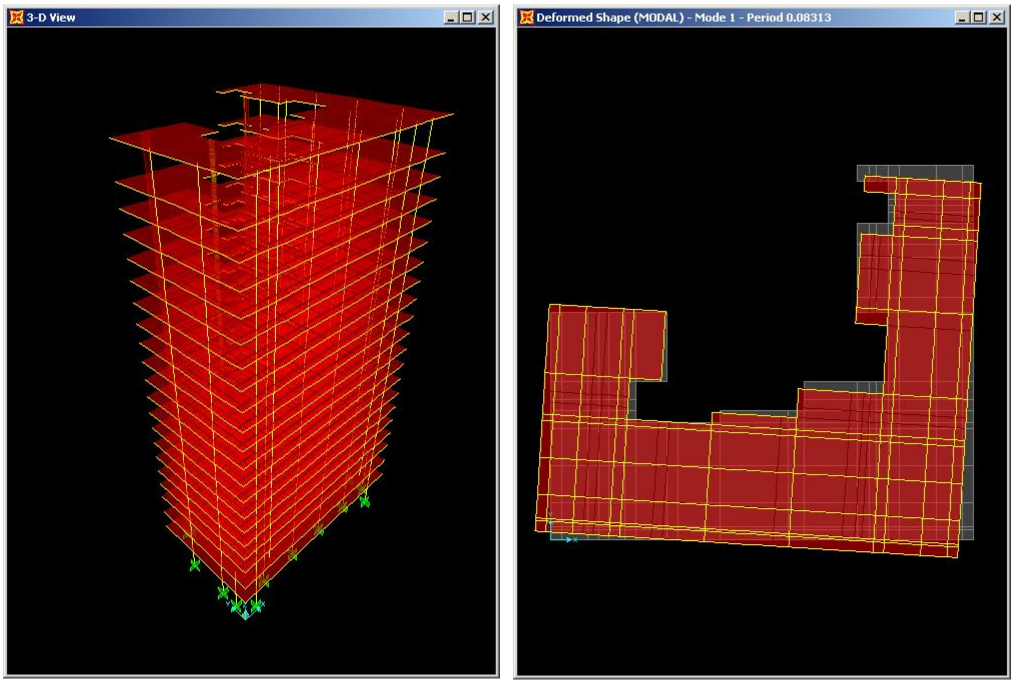

(a) 3D view of FEM model; (b) 1st mode, f=12.029 Hz;

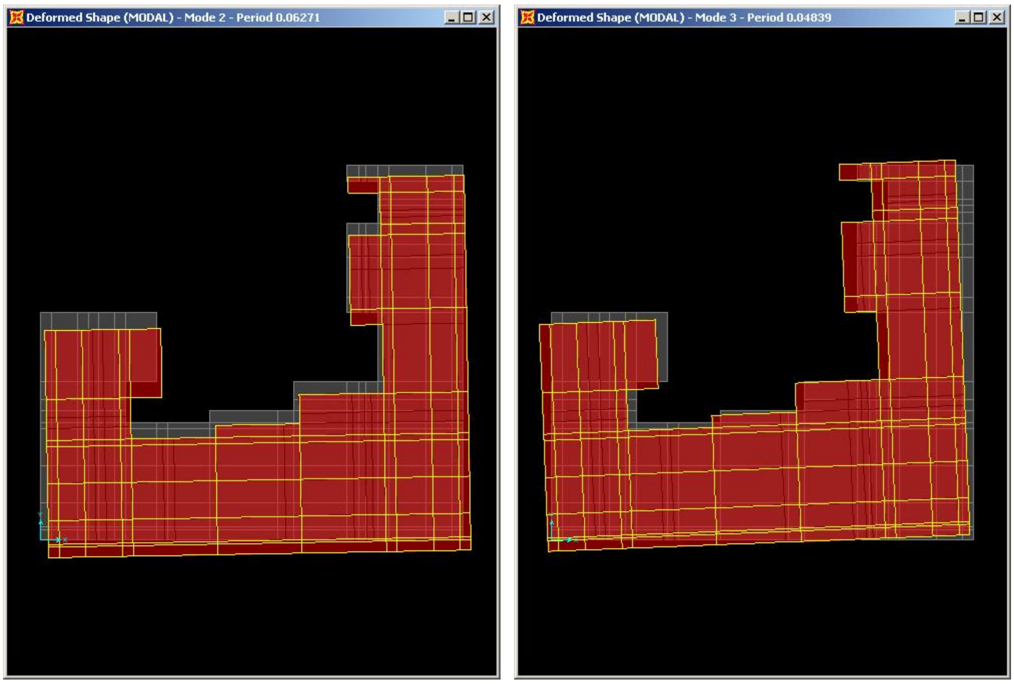

(c) 2nd mode, f=15.947 Hz; (d) 3rd mode, f=20.677 Hz.

Figure 8.7 FEM model of the EH model and its first three mode shapes.

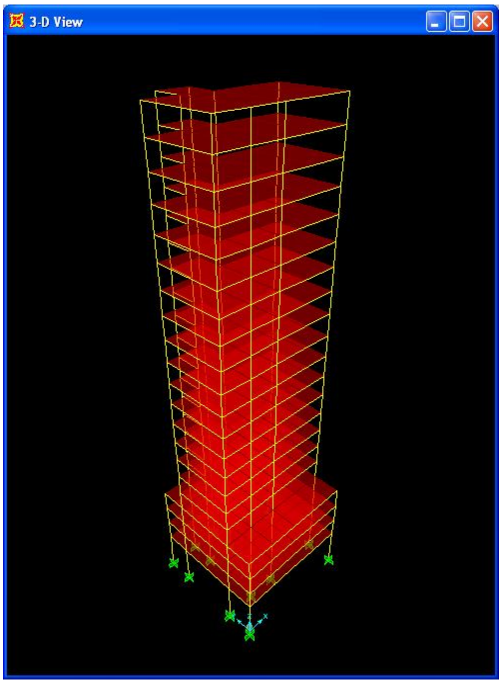

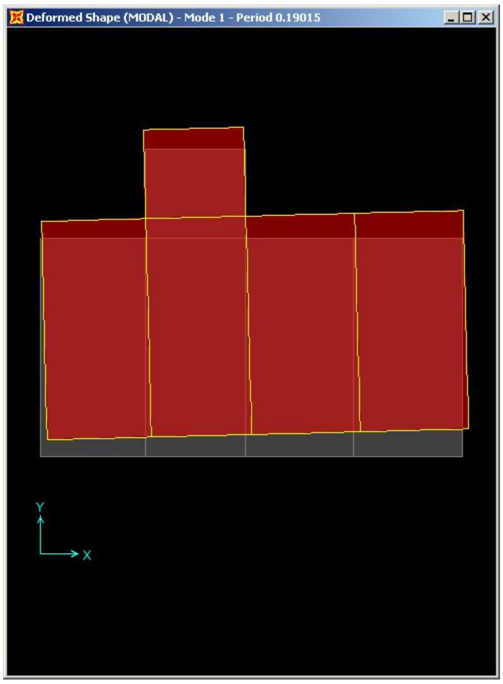

(a) 3D view of FEM model; (b) 1st mode, f=5.259 Hz;

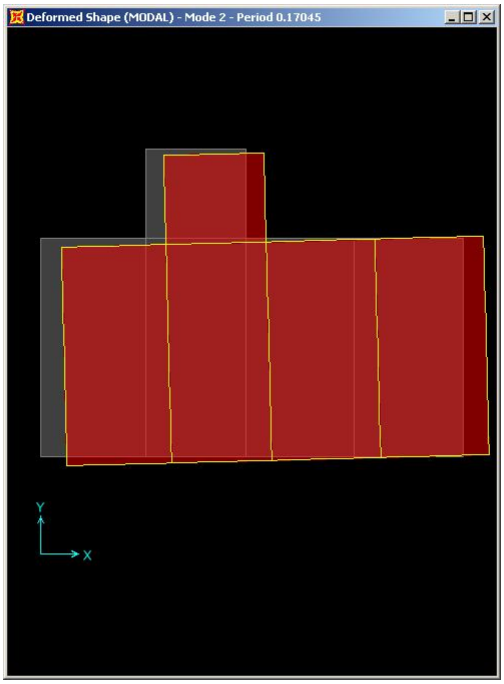

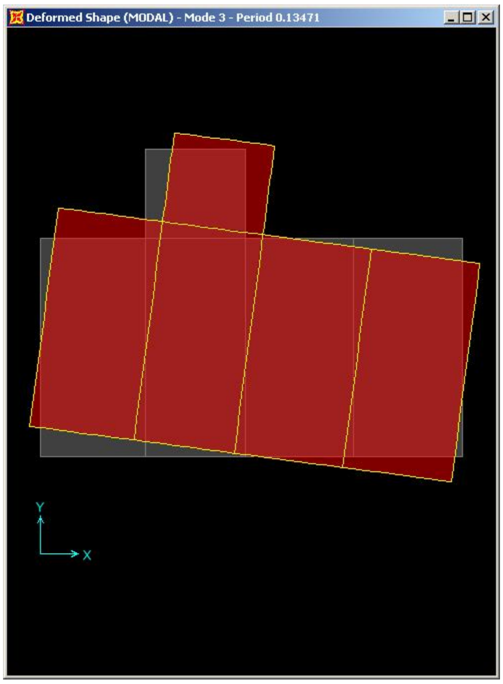

(c) 2nd mode, f=5.867 Hz; (d) 3rd mode, f=7.423 Hz.

Figure 8.8 FEM model of the GS model and its first three mode shapes.

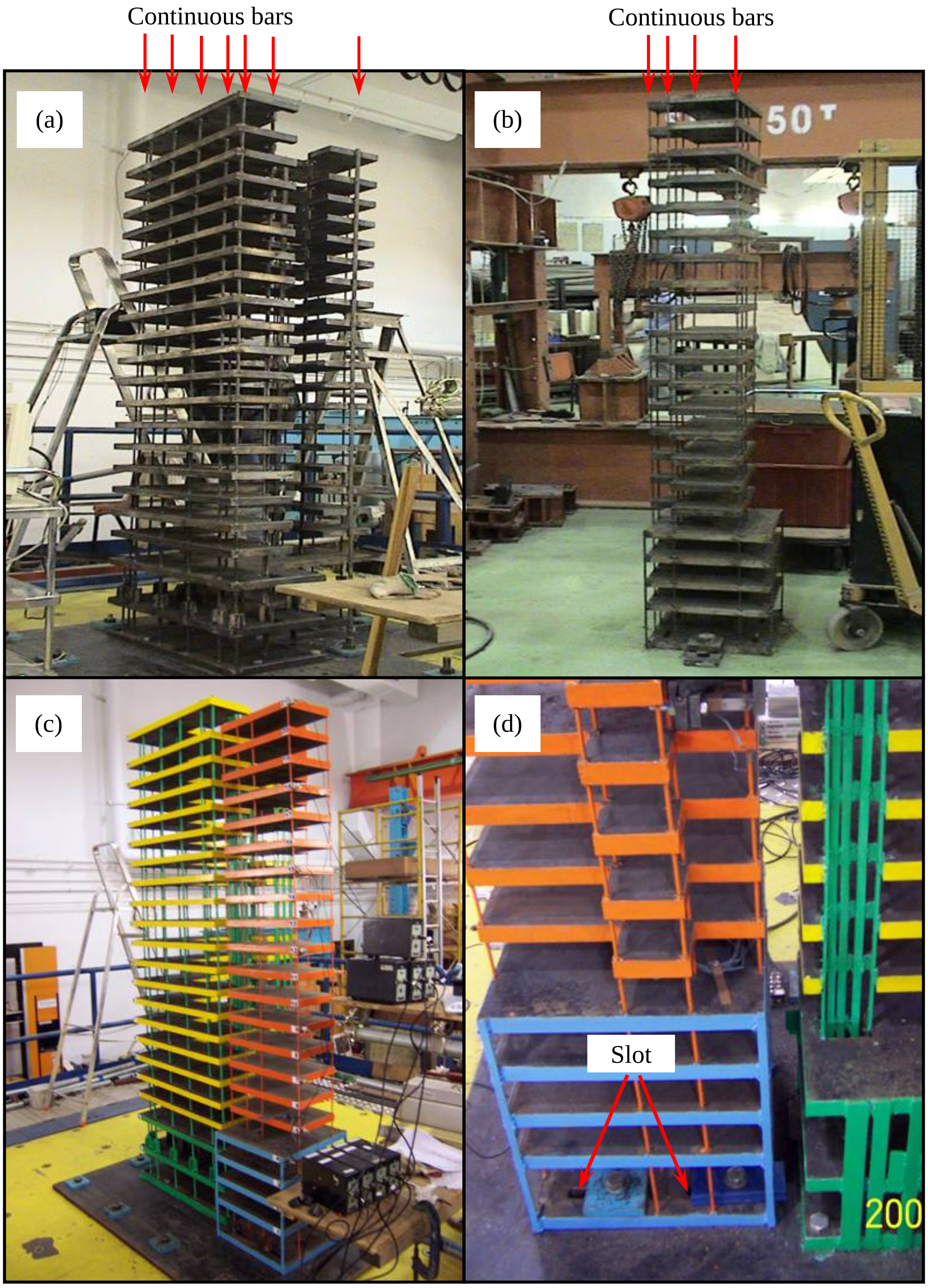

Figure 8.9 Photographs of the completed models for (a) EH and (b) GS, during the construction, the continuous steel bars serving as columns and walls were installed through the specified holes drilled on the steel plate slabs and welding was used to fix them; (c) EH and GS put together with different colors for those floors below and above the transfer plates; (d) slots at the base of GS allowing for change of separation distances between the two models.

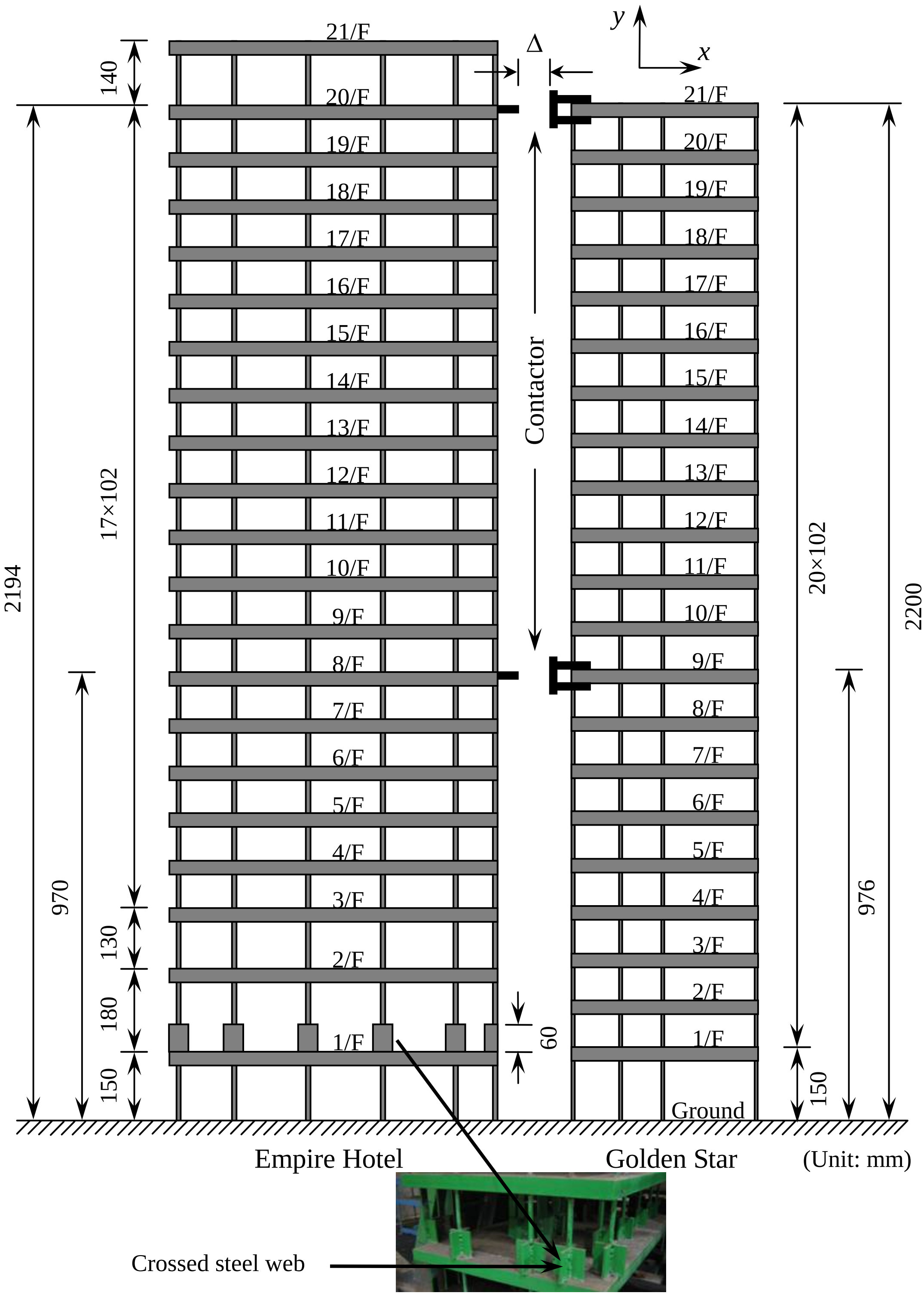

Figure 8.10 Sketch of elevation view of the two building models showing the relative elevations of their different floors and the locations of contactors. The floor slabs were all 30 mm-thick steel plates. The crossed steel bars as shown in the photo above 1/F of EH were used to adjust the story heights.

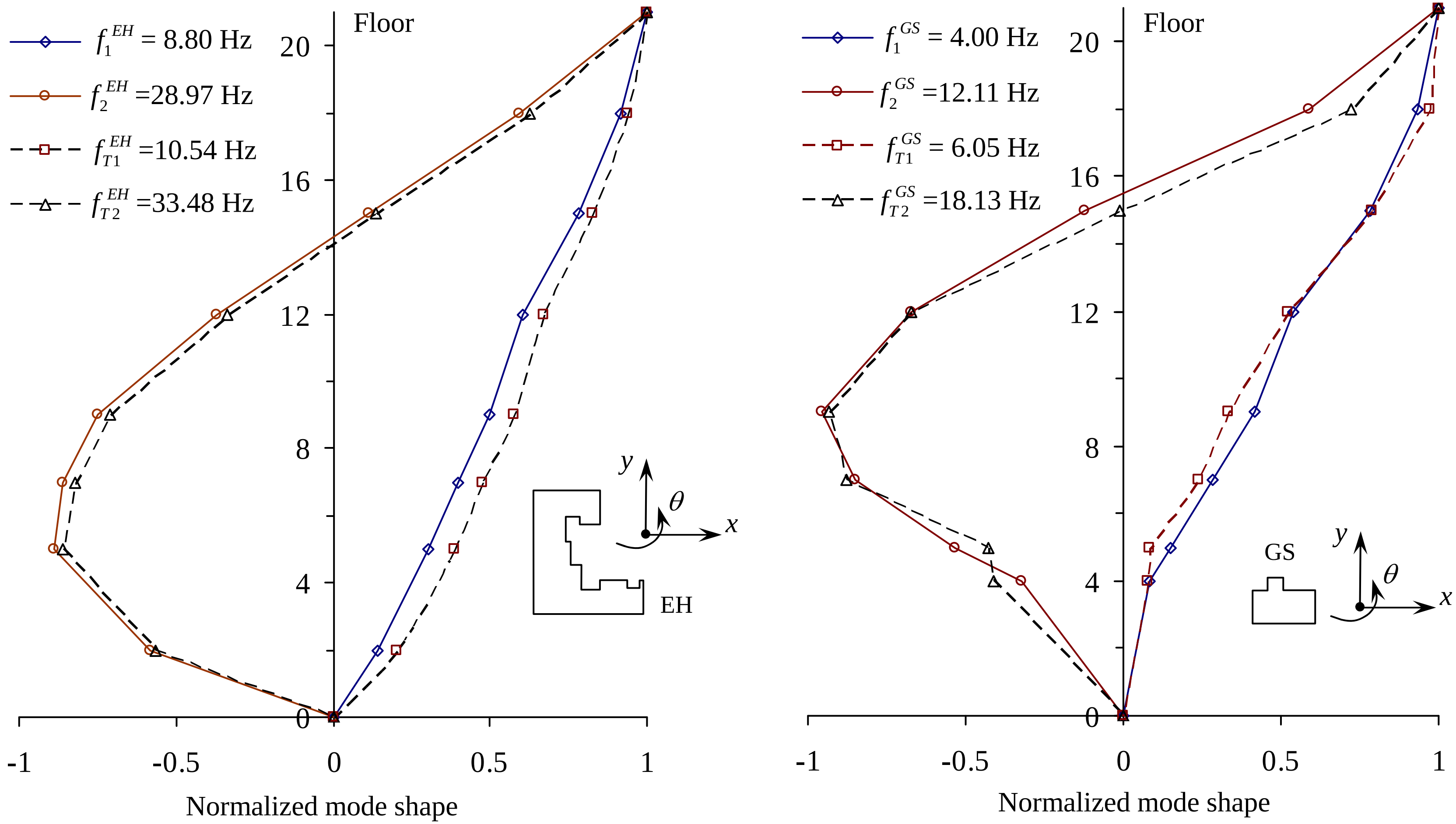

Figure 8.11 The mode shapes and natural frequencies of the first several modes of EH and GS model, where f_1 and f_2 were the first two frequencies in x direction, and f_{T1} and f_{T2} denoted the first two frequencies in θ direction.

GS building

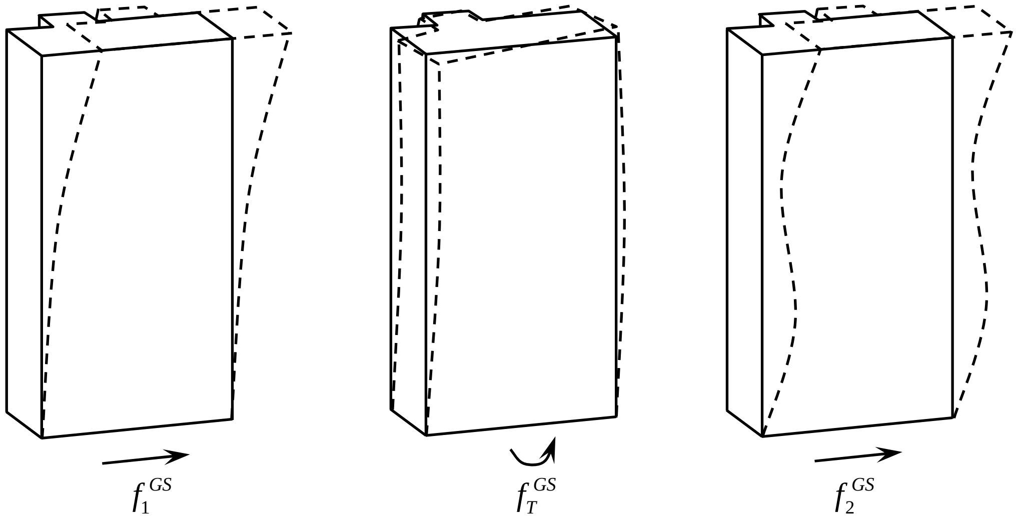

EH building

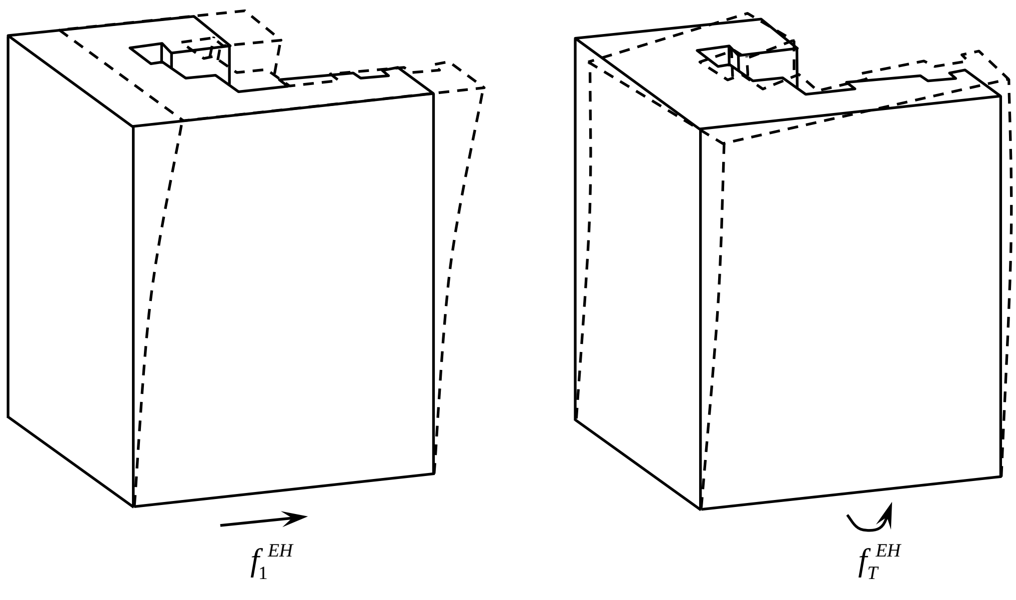

Figure 8.12 Sketches of the first several mode shapes and natural frequencies of the GS and EH models, where f_1^{GS} and f_2^{GS} were the first and second translational natural frequencies of GS respectively, f_T^{GS} was its first torsional frequency; similarly, f_1^{EH} and f_T^{EH} were the first translational and torsional natural frequencies of EH respectively.

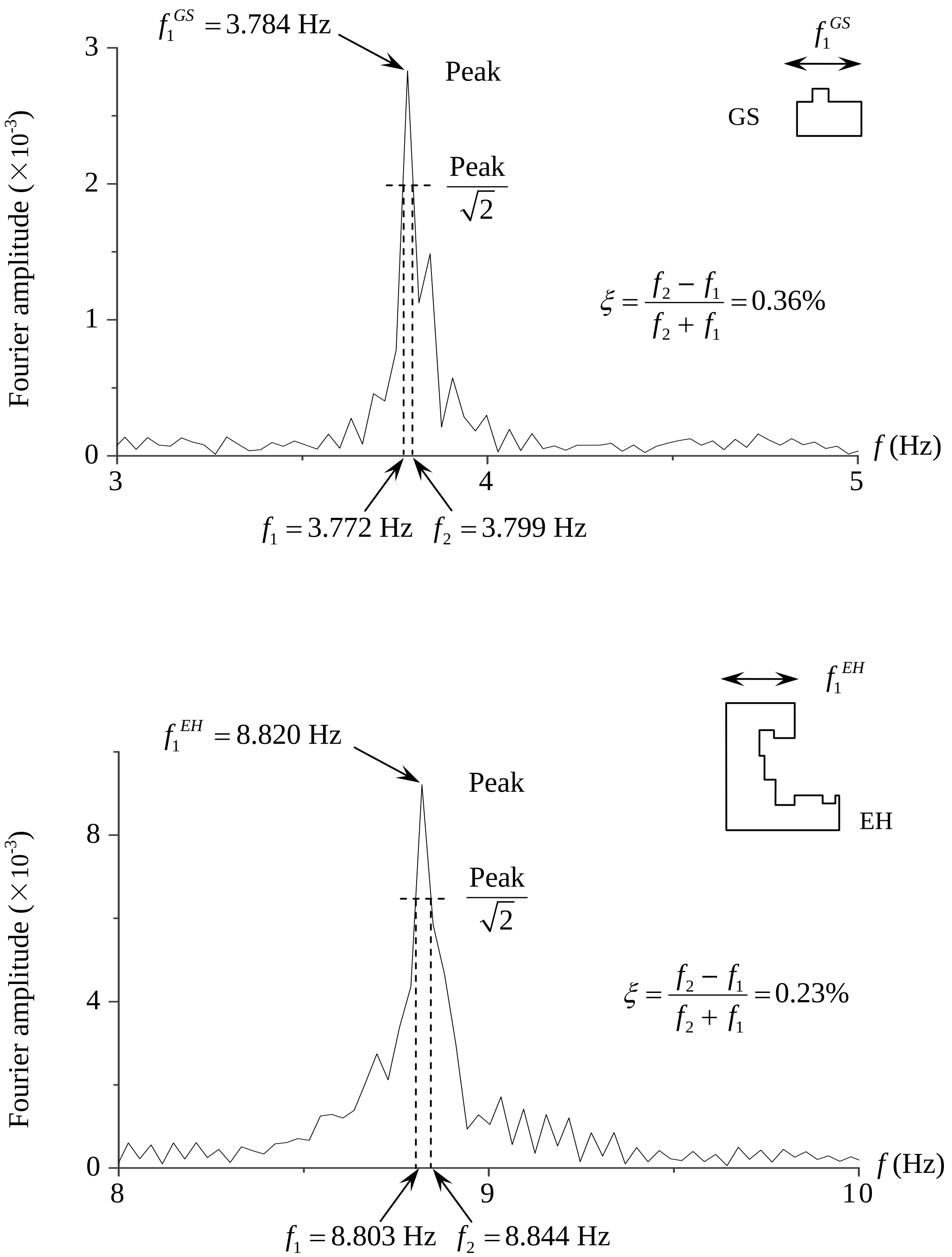

Figure 8.13 Estimation of the damping ratios of the first modes of GS and EH respectively using half-power method. The shown diagrams were the Fourier spectra of displacements at the roofs of the two models.

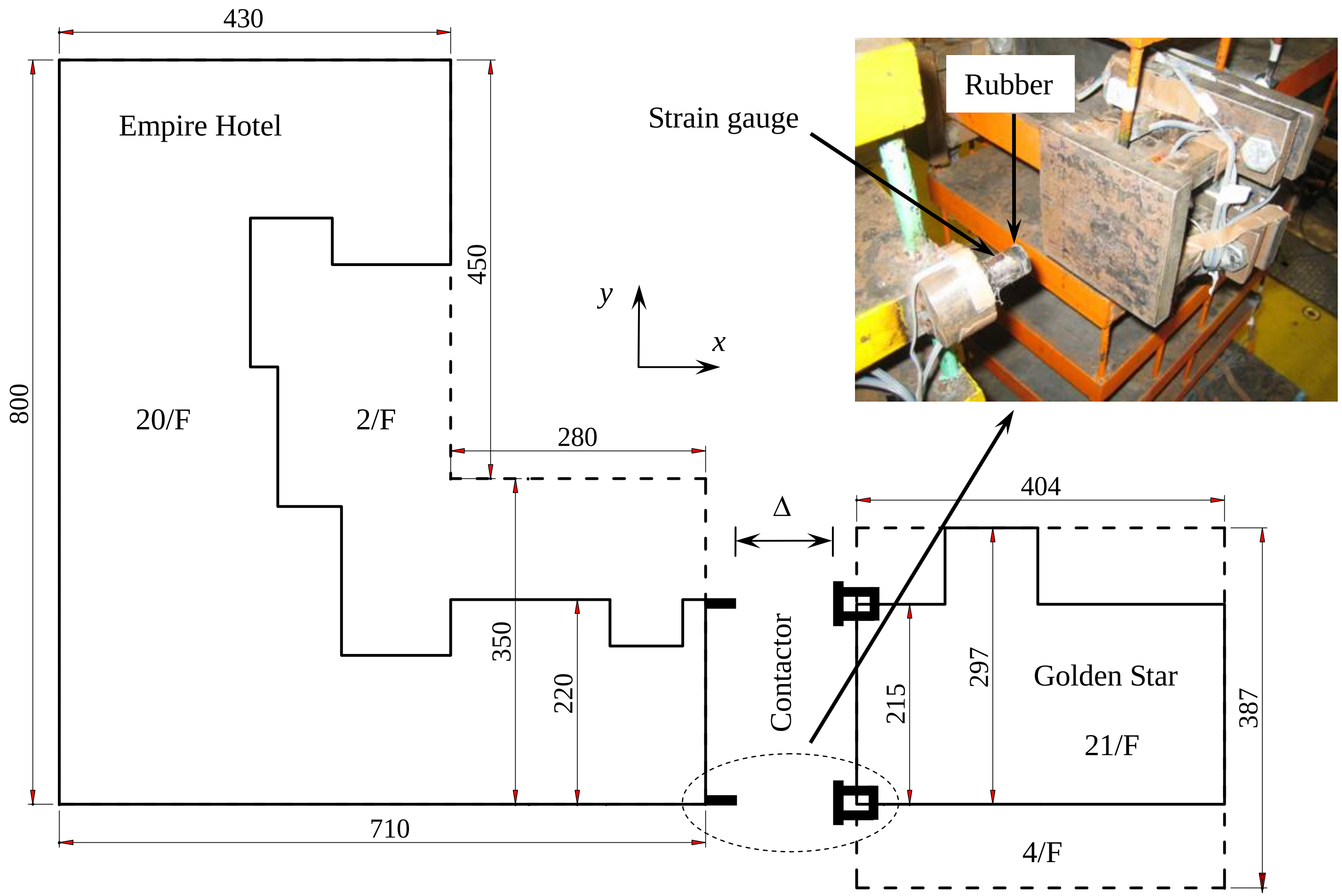

Figure 8.14 Plan view from the top of the two building models showing their relative locations as well as the two pairs of contactors installed between 20/F of EH and 21/F of GS. The attached photo showed the strain gauge attached and the rubber used to reduce the impact forces.

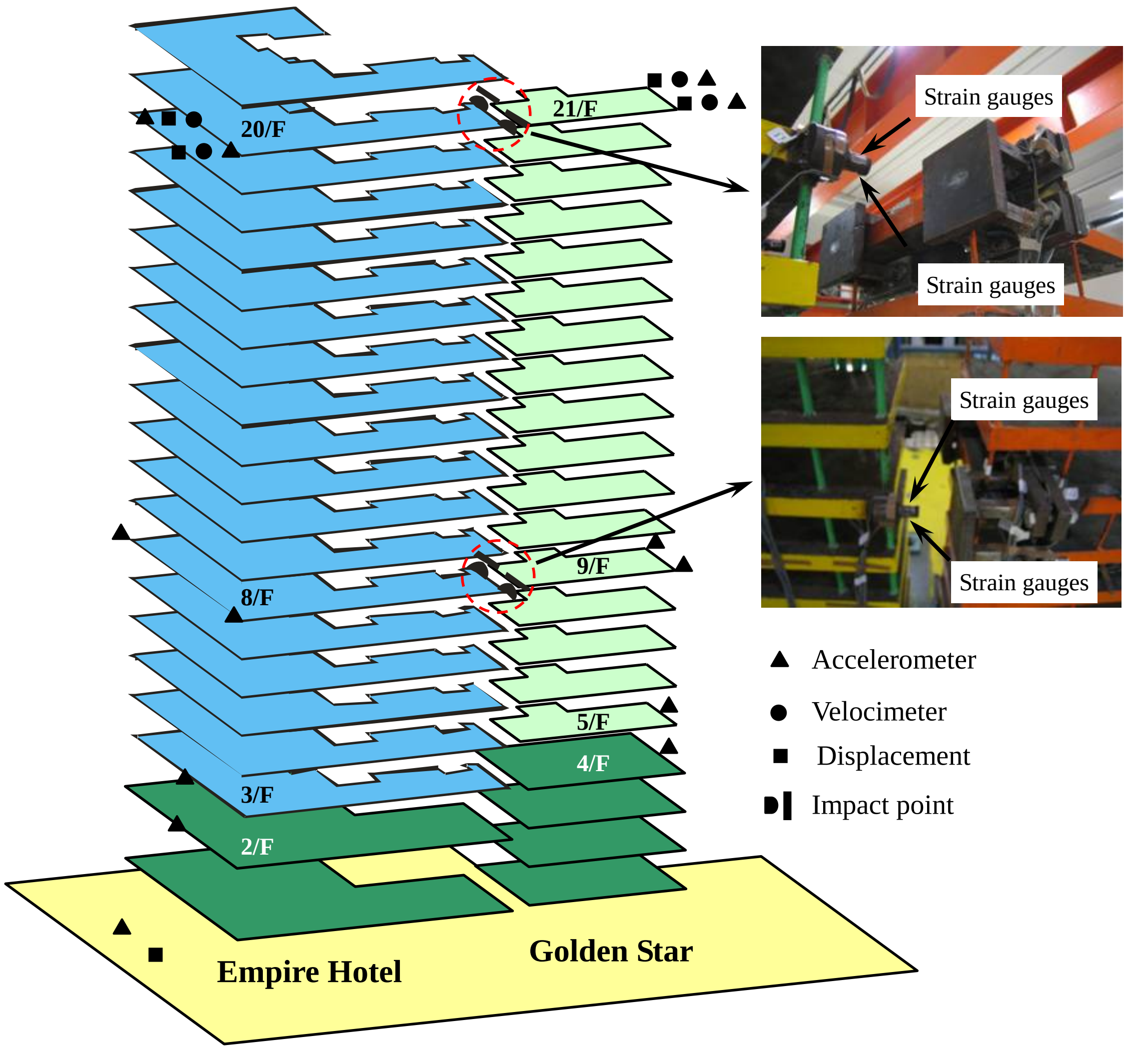

Figure 8.15 3D sketches of the EH and GS models and the locations of contactors and transducers. The two close-up photographs showed the details of the contactors.

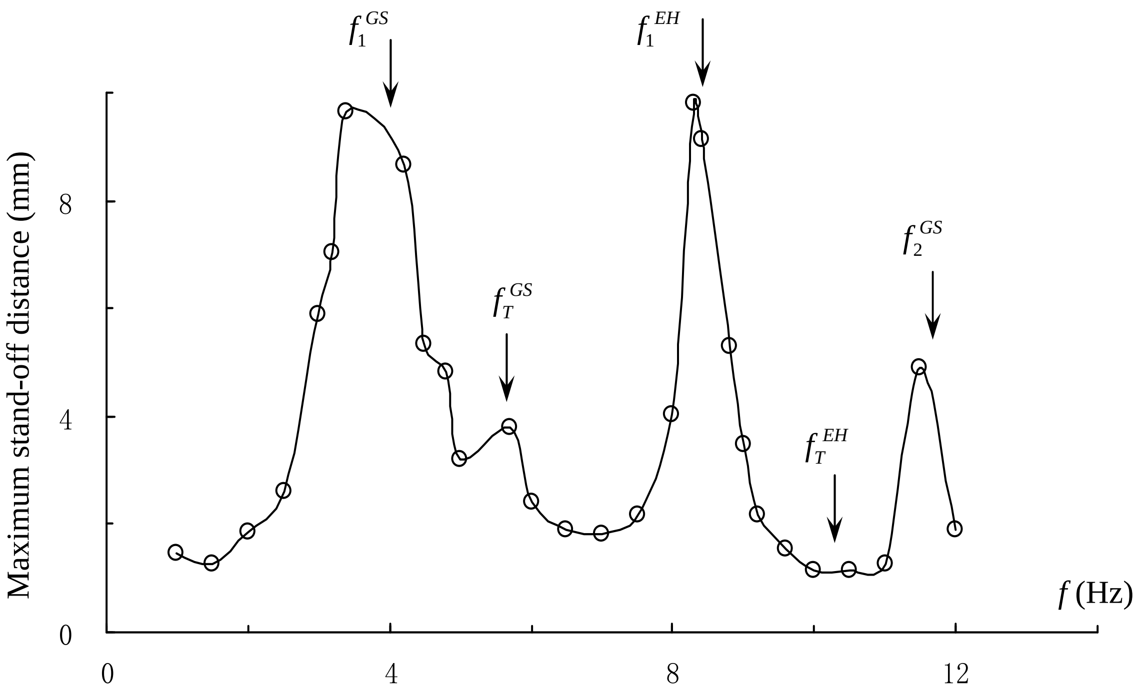

Figure 8.16 Maximum stand-off distances between GS and EH versus input frequencies. The five vertical arrows represented the first several natural frequencies of the two structures; they take the following values respectively $f_1^{GS} = 3.83$ Hz, $f_T^{GS} = 5.615$ Hz, $f_2^{GS} = 11.597$ Hz and $f_1^{EH} = 8.362$ Hz, $f_T^{EH} = 10.315$ Hz.

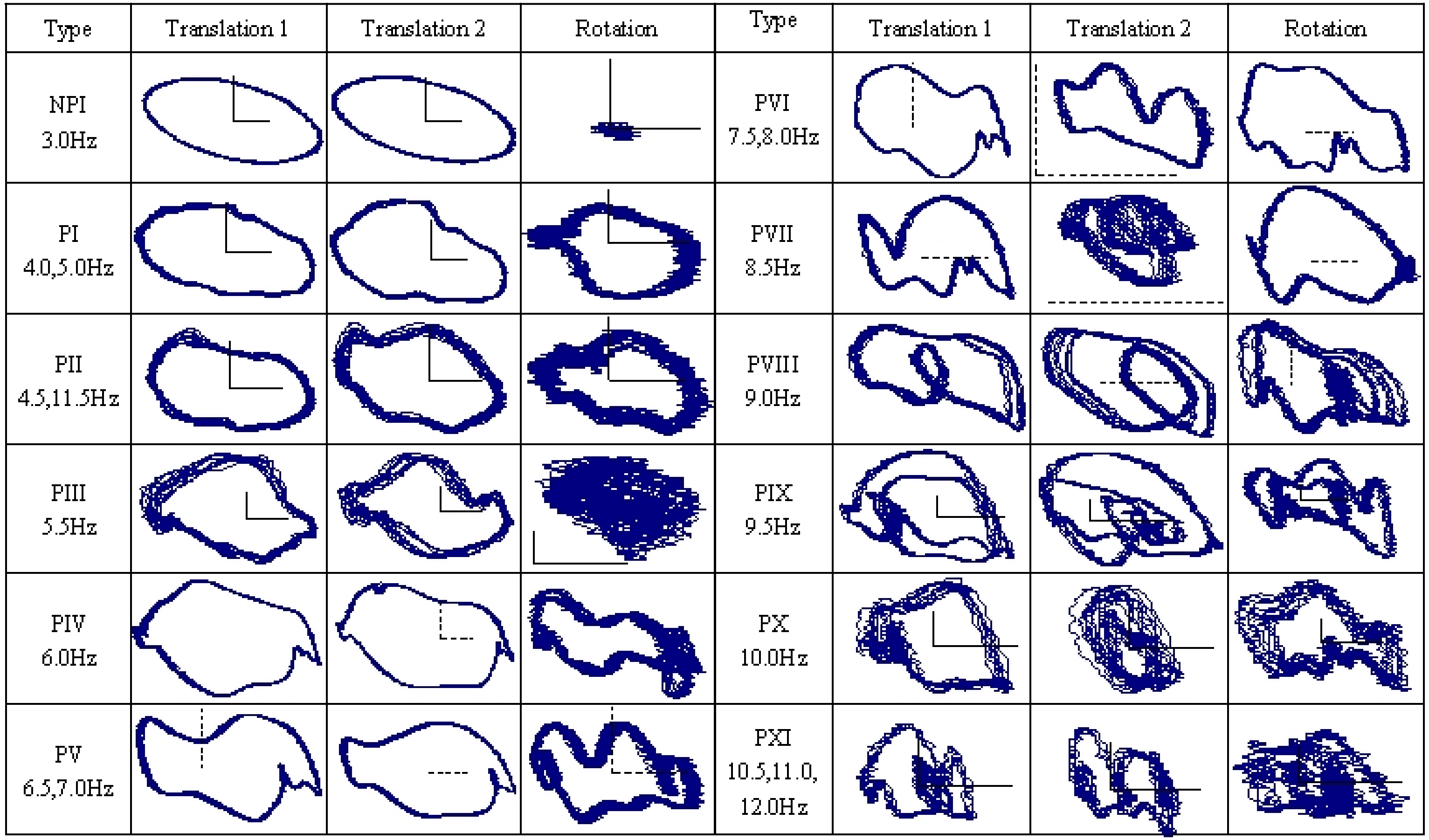

Figure 8.17 Different patterns of phase diagrams at the roof of GS in pounding tests between GS and EH when Δ=0 mm and A_g=0.07g. The graphs listed were in different scales, that is, in the Translation 1 and 2 columns, the solid and dashed horizontal lines denoted 1 and 2 mm and the solid and dashed vertical lines denoted 0.05 and 0.2 m/s respectively. In the Rotation columns, the solid and dashed horizontal lines corresponded to 3.5×10^{-3} and 3.5×10^{-3} rad while the solid and dashed vertical lines corresponded to 0.17 and 0.7 rad/s respectively.

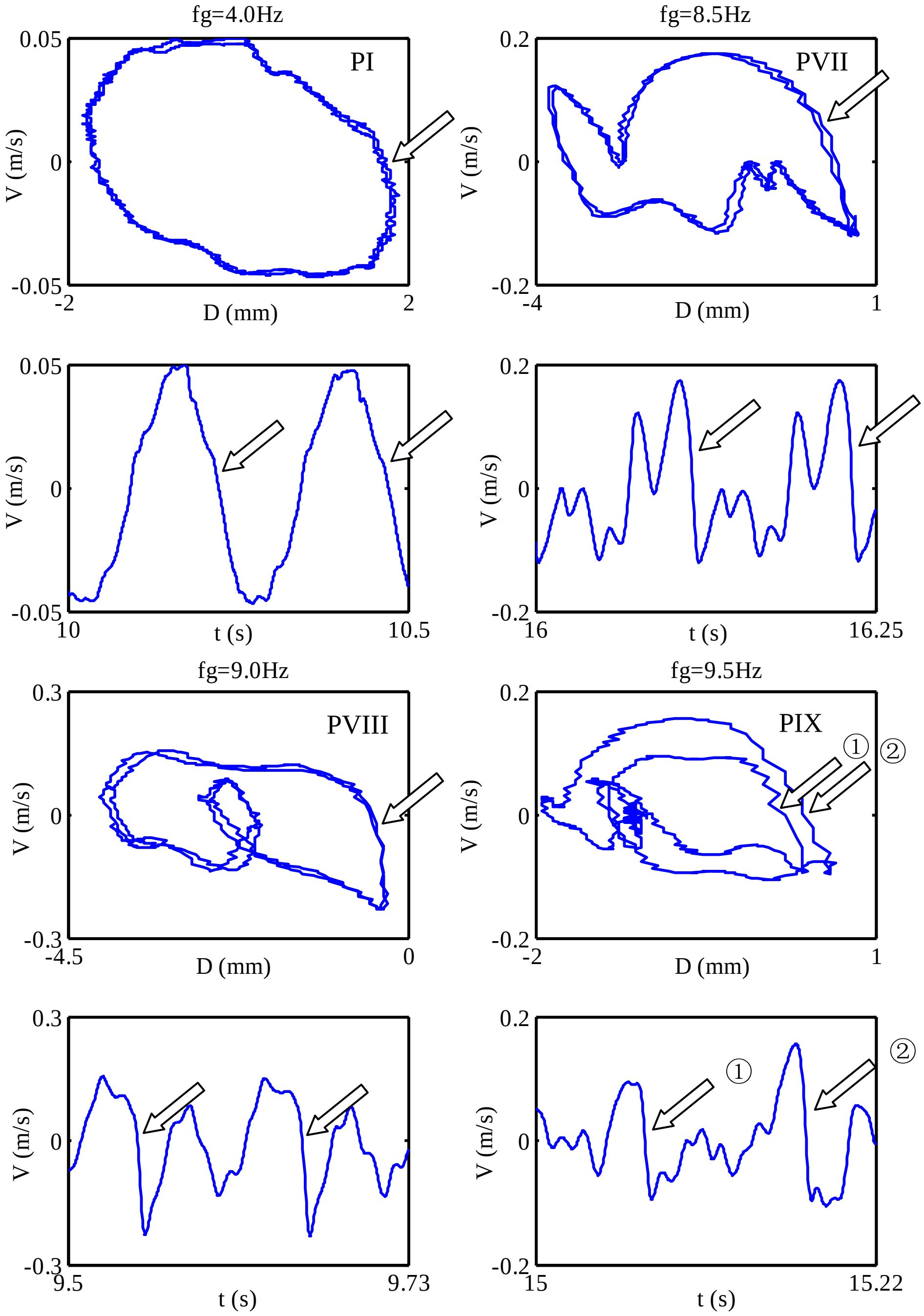

Figure 8.18 Four different phase diagrams selected from Figure 8.17 and time histories of velocity at the roof of GS for different input frequencies during pounding tests between GS and EH when $\Delta = 0$ mm and $A_g = 0.07$g. The arrows attached indicated where pounding occurred.

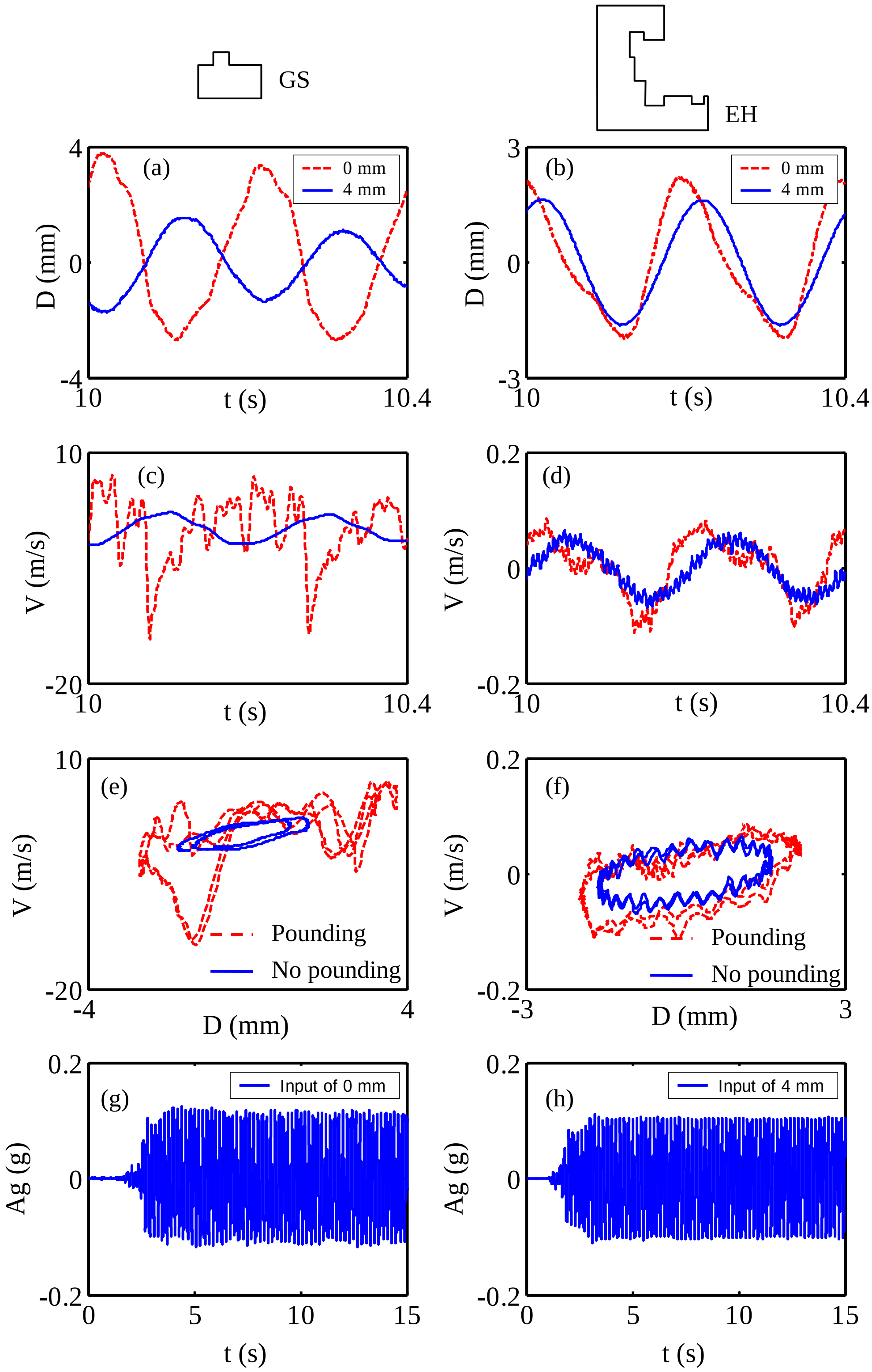

Figure 8.19 Comparison of the responses of GS and EH when the inputs were similar (A_g = 0.1g, f_g = 5.0 Hz) but the separation distances were 0 and 4 mm respectively. Pounding occurred at zero separation distance and no pounding for 4 mm distance. It was clear seen that the responses of GS were much larger when pounding occurred due to the energy transfer from EH.

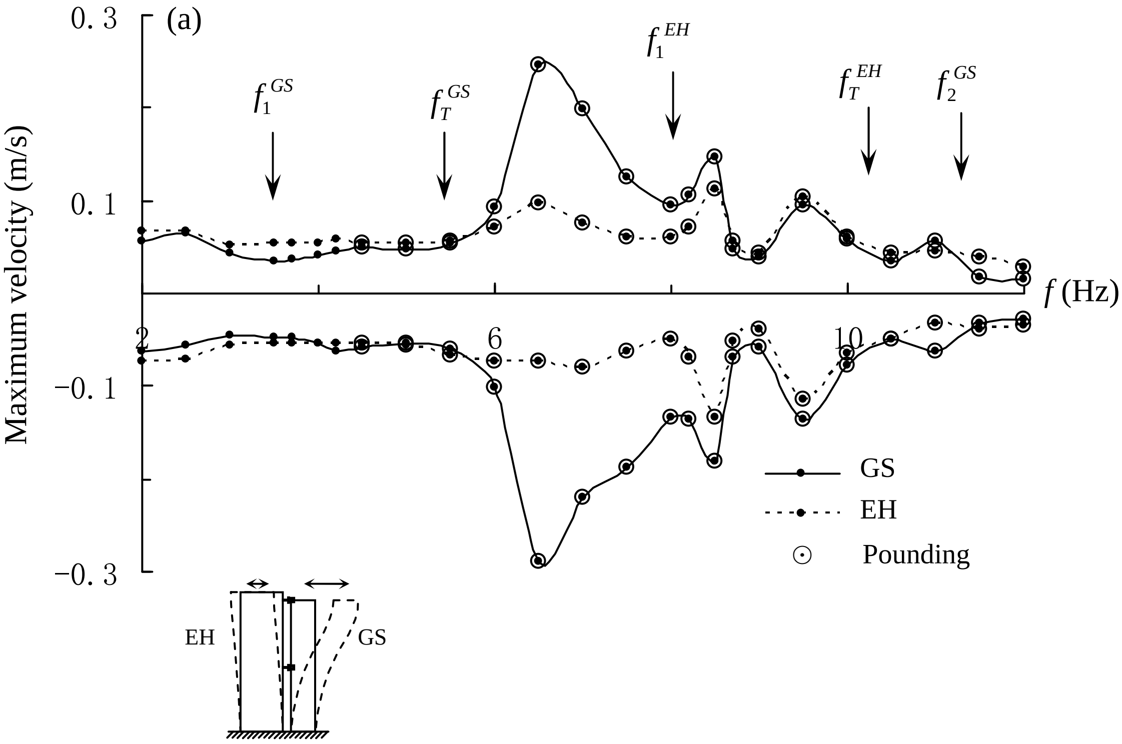

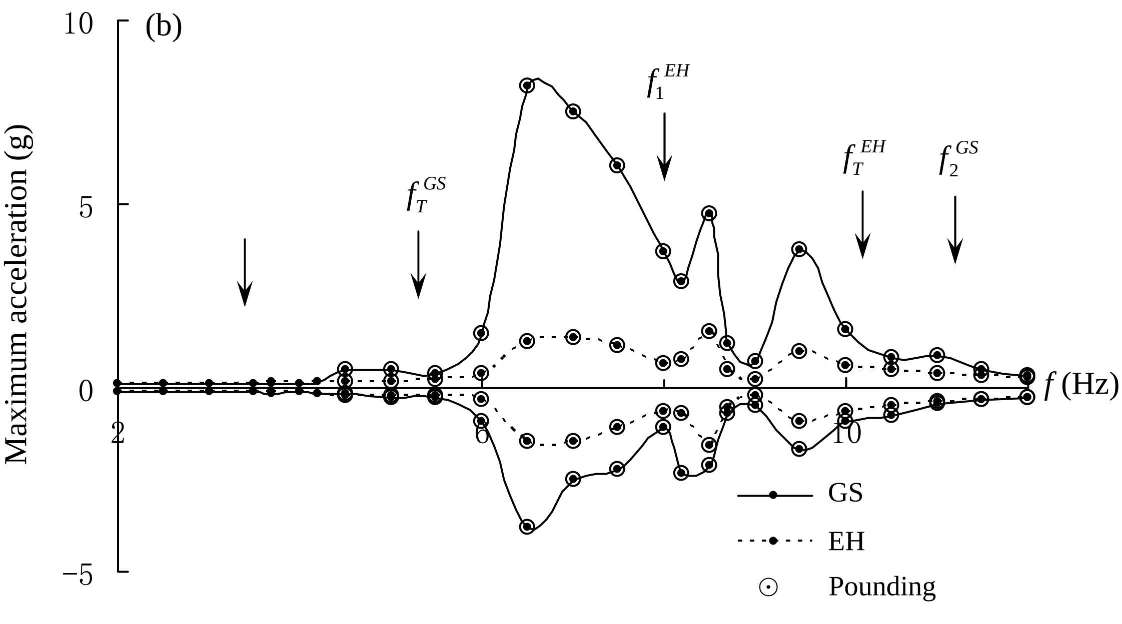

Figure 8.20 The maximum (a) velocities and (b) accelerations spectra at the roof of GS in the pounding tests between GS and EH when the separation distances were 0 mm. The five vertical arrows represented the first several natural frequencies of the two structures; they took the following values respectively $f_1^{GS} = 3.54$ Hz, $f_T^{GS} = 5.493$ Hz, $f_2^{GS} = 11.353$ Hz and $f_1^{EH} = 8.118$ Hz, $f_T^{EH} = 10.315$ Hz.

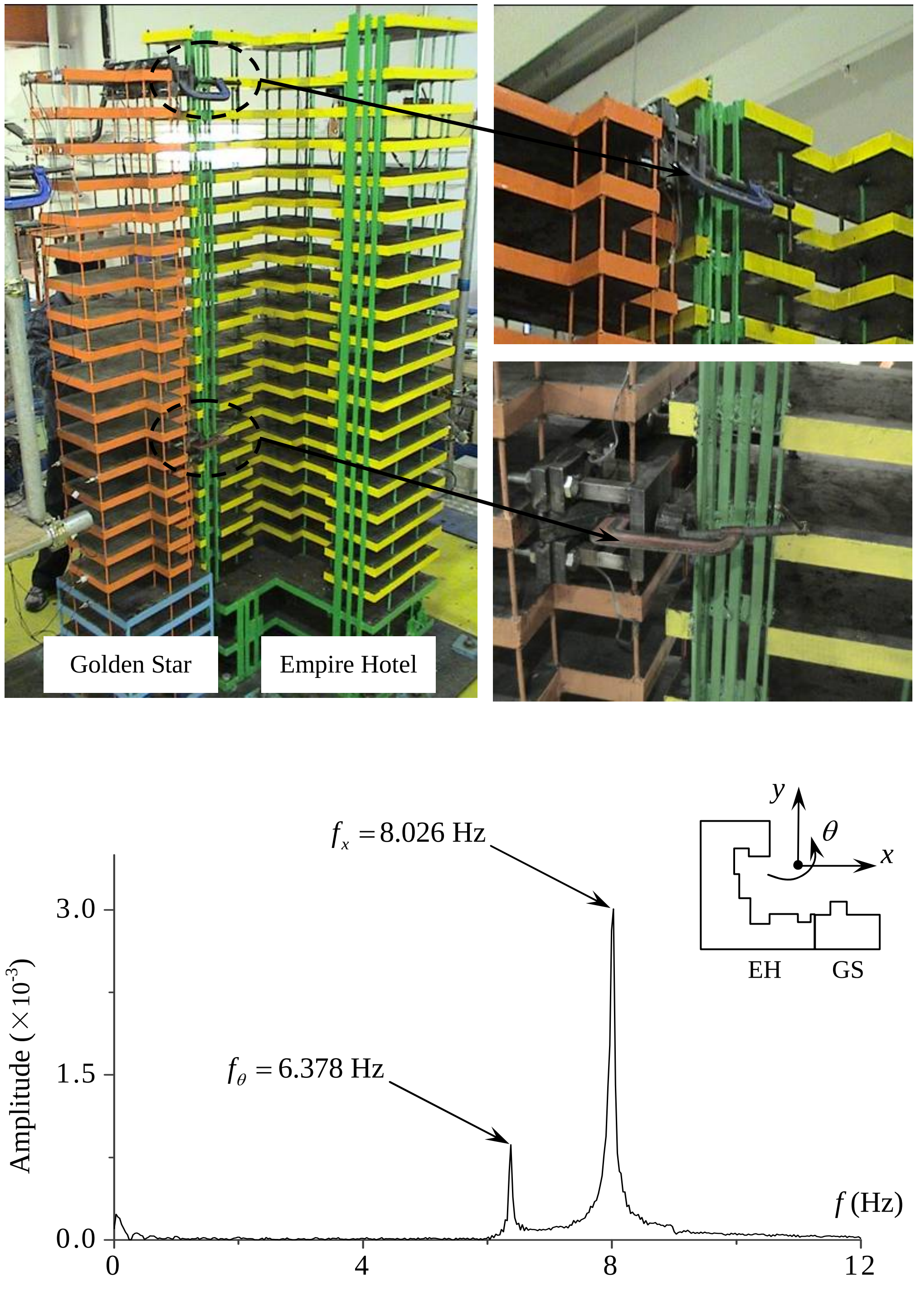

Figure 8.21 Photographs of the two models locked together to measure the natural frequency of the new system as sketched below. Also shown were the Fourier spectrum of the acceleration at the roof and the first two frequencies.

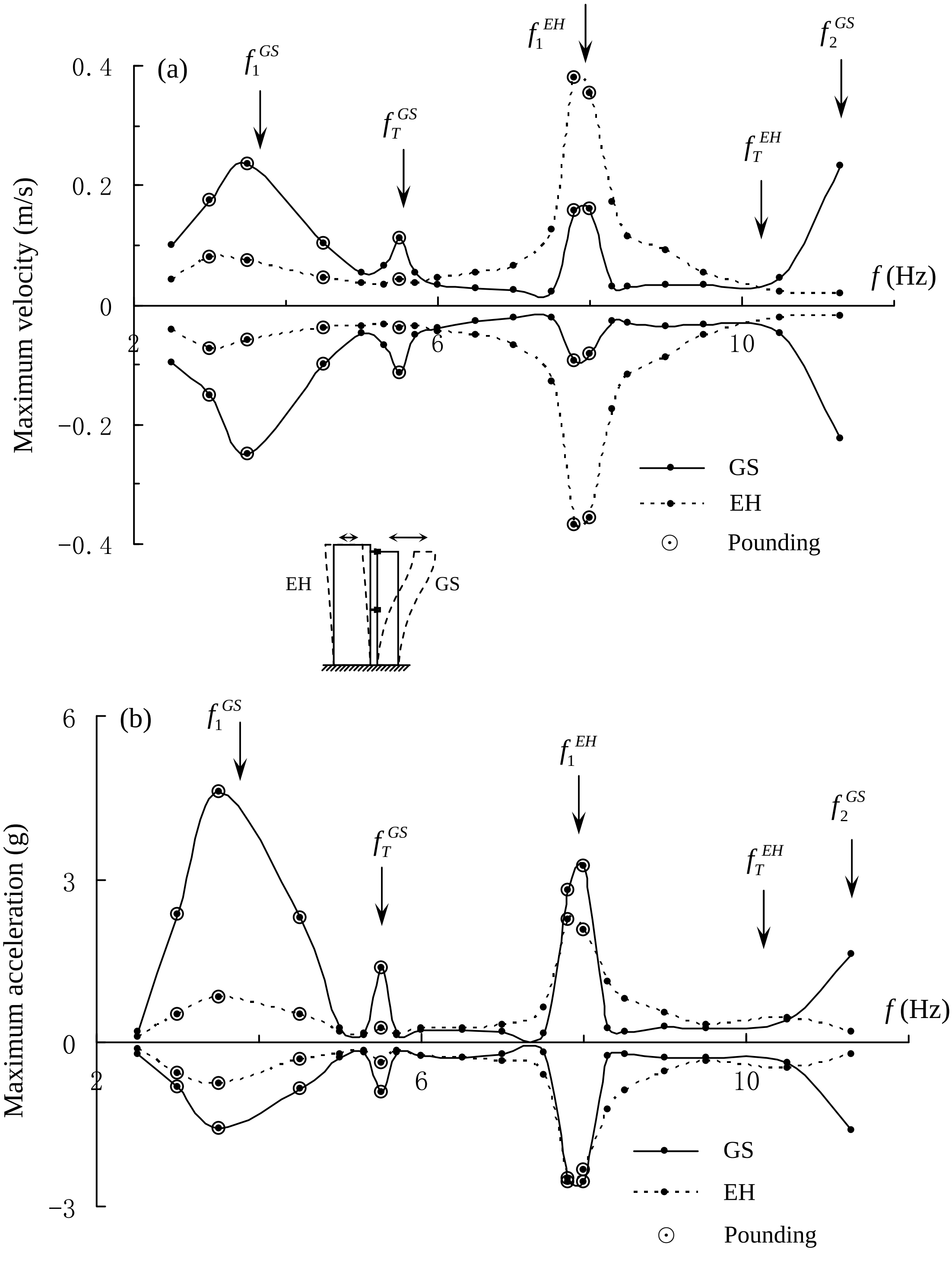

Figure 8.22 The maximum (a) velocities and (b) accelerations spectra at the roof of GS in the pounding tests between GS and EH when the separation distances were 4.0 mm. The five vertical arrows represented the first several natural frequencies of the two structures; they took the following values respectively $f_1^{GS} = 3.601$ Hz, $f_T^{GS} = 5.554$ Hz, $f_2^{GS} = 11.353$ Hz and $f_1^{EH} = 7.996$ Hz, $f_T^{EH} = 10.315$ Hz.

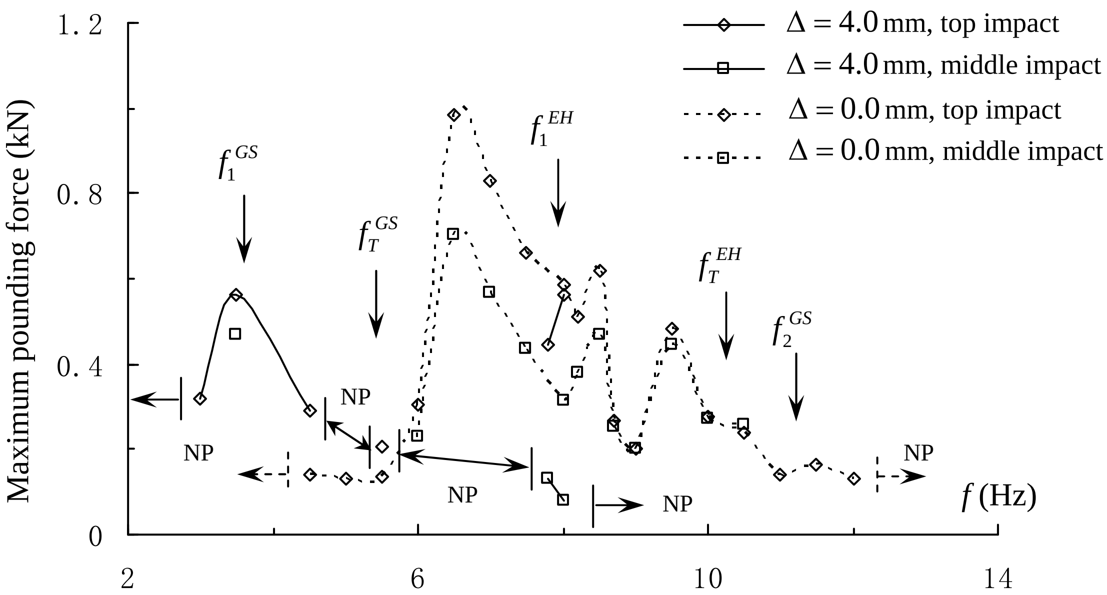

Figure 8.23 Comparisons of the maximum pounding forces in the pounding tests between GS and EH when the separation distances were 0 and 4 mm respectively. The symbol 'NP' meant no pounding occurring. The five vertical arrows represented the first several natural frequencies of the two structures; they take the following values respectively $f_1^{GS} = 3.601$ Hz, $f_T^{GS} = 5.554$ Hz, $f_2^{GS} = 11.353$ Hz and $f_1^{EH} = 7.996$ Hz, $f_T^{EH} = 10.315$ Hz.

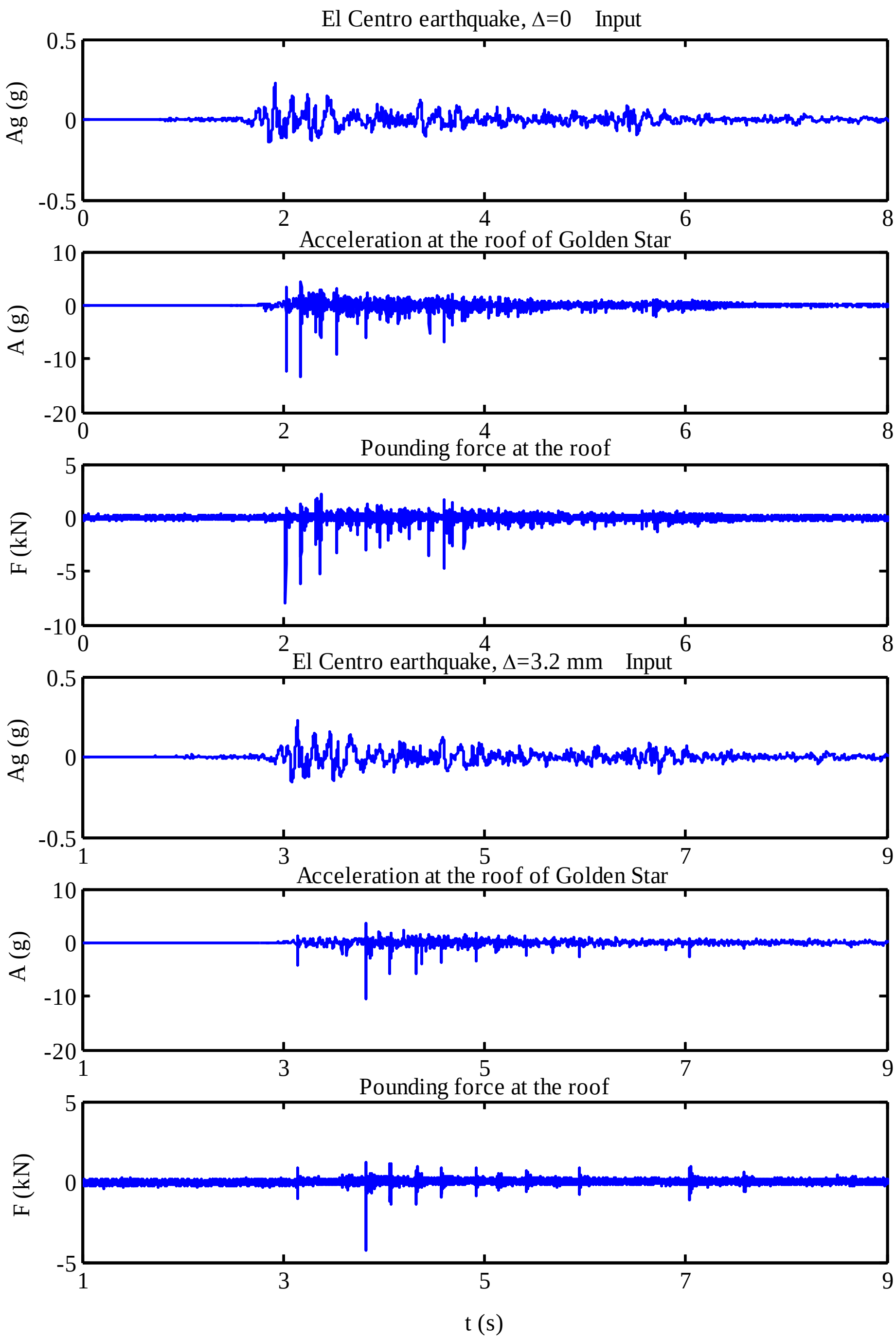

Figure 8.24 Time histories of input, acceleration and pounding force at the roof of GS during the input of El Centro earthquake in pounding tests between GS and EH when $\Delta = 0$ and 3.2 mm respectively.

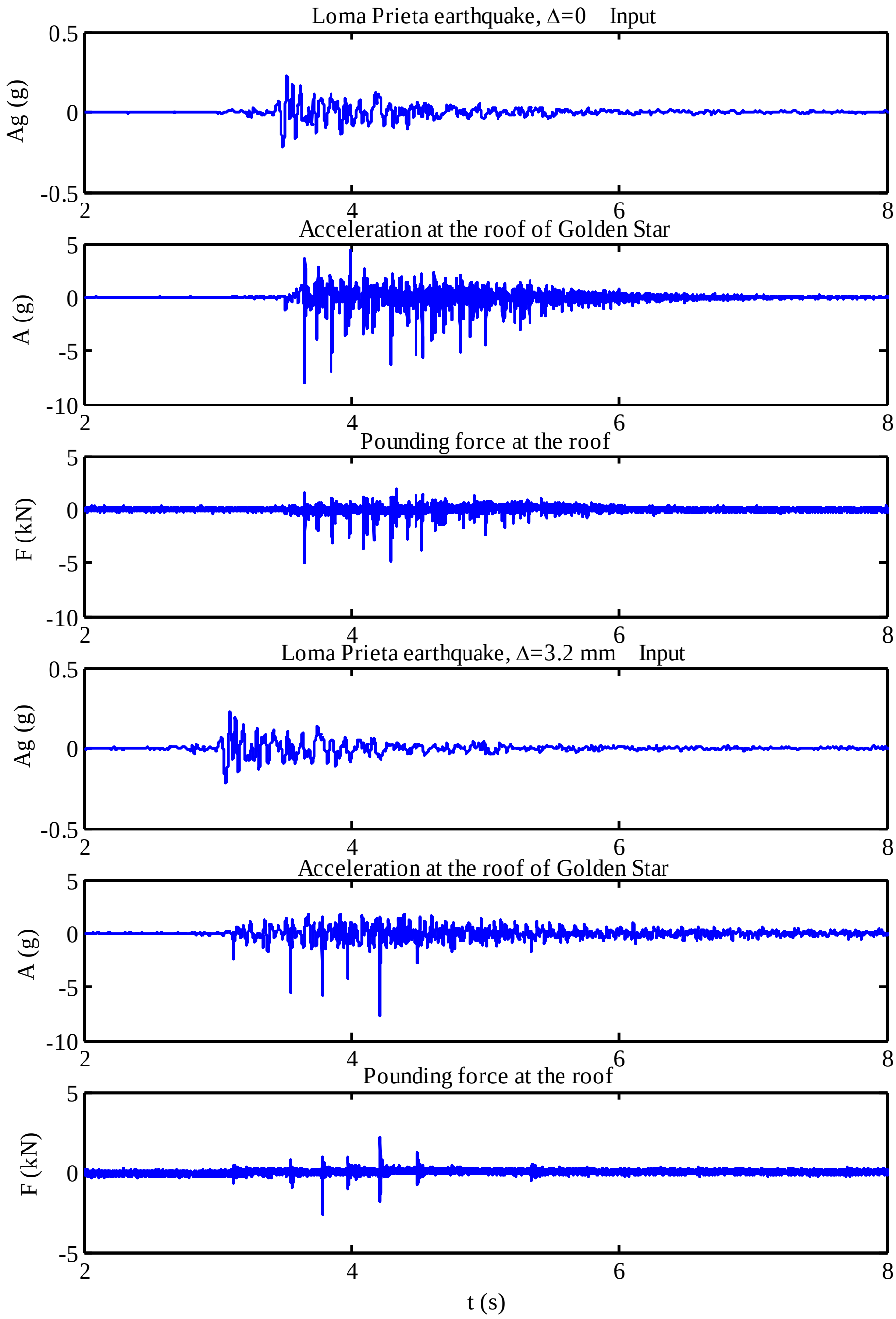

Figure 8.25 Time histories of input, acceleration and pounding force at the roof of GS during the input of Loma Prieta earthquake in pounding tests between GS and EH when $\Delta = 0$ and 3.2 mm respectively.

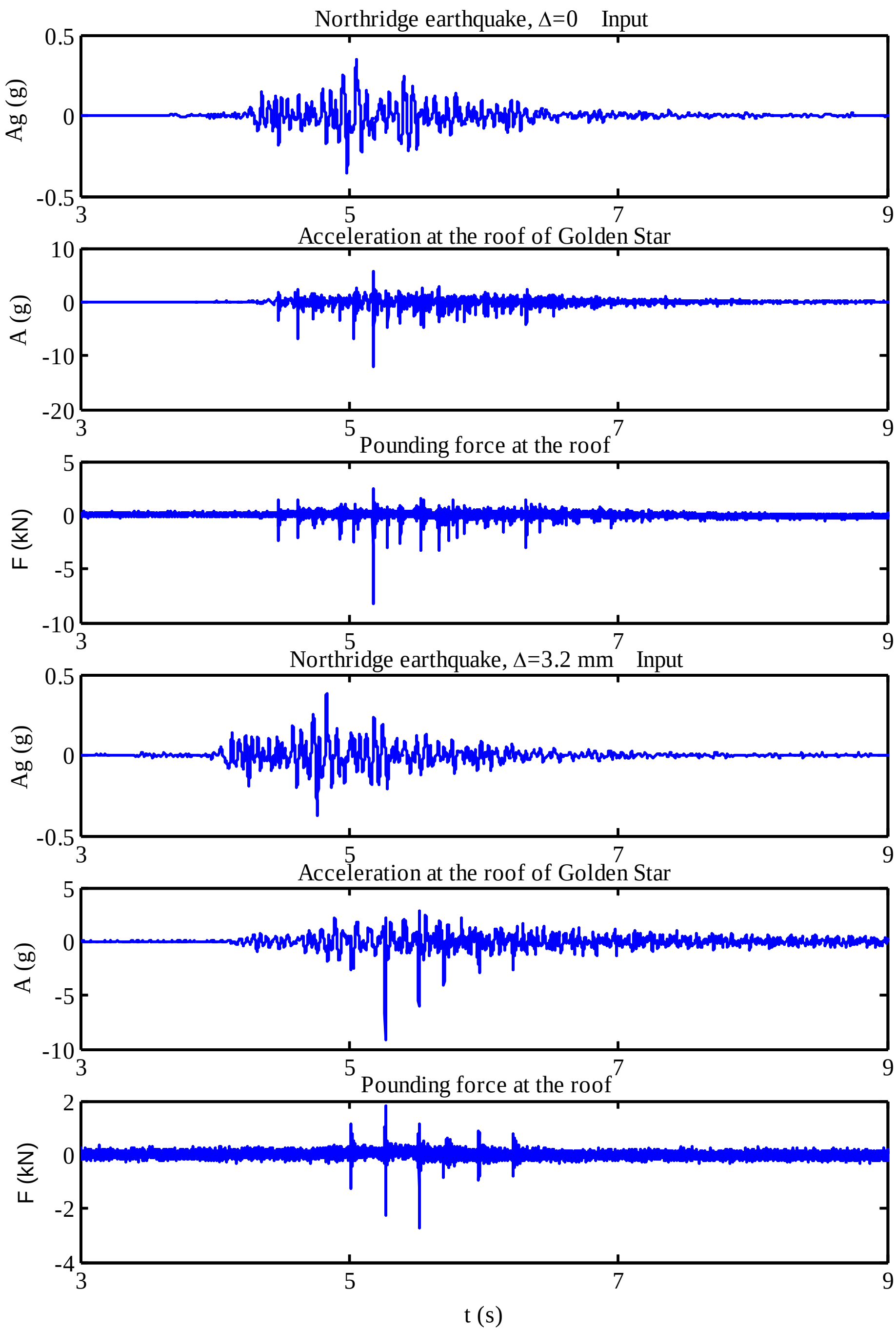

Figure 8.26 Time histories of input, acceleration and pounding force at the roof of GS during the input of Northridge earthquake in pounding tests between GS and EH when $\Delta = 0$ and 3.2 mm respectively.

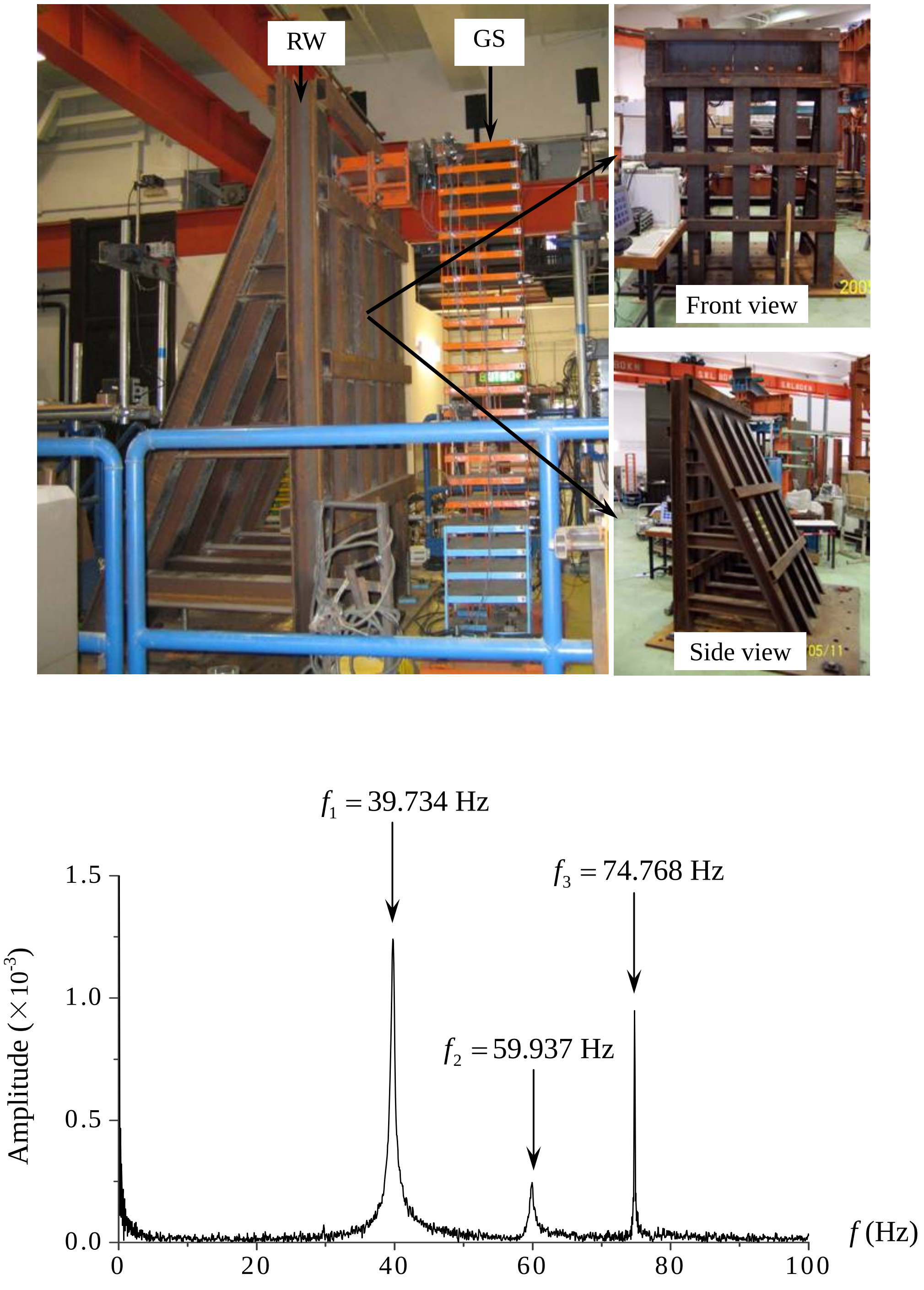

Figure 8.27 Photographs of the nearly rigid wall (RW) and Golden Star (GS) as well as the close-up views of RW. The below Fourier spectrum from hammer tests on RW showed that the first natural frequency of RW was much higher than that of GS, which justified the assumption of rigid wall.

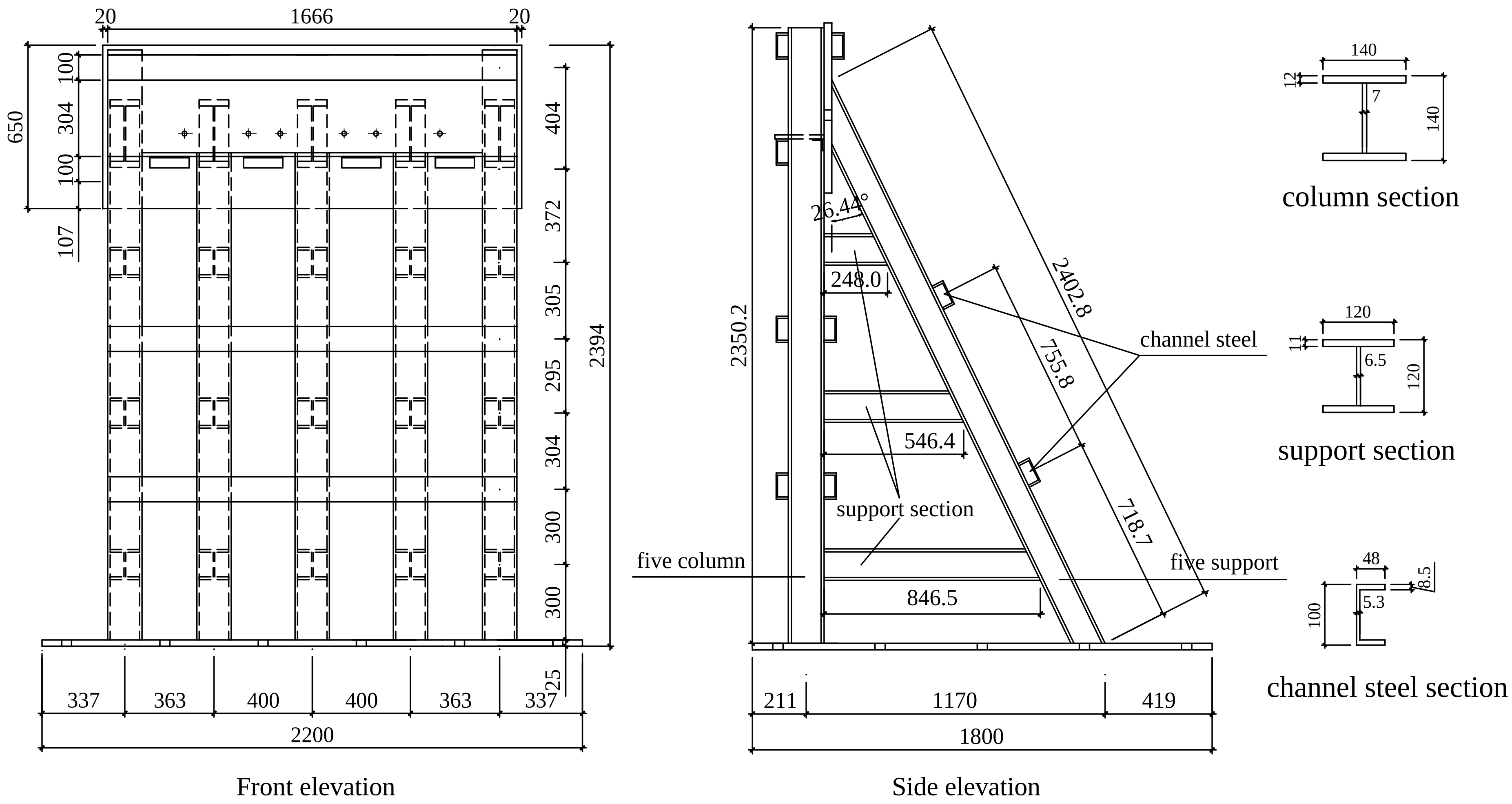

Figure 8.28 Dimensions of the nearly rigid wall (RW).

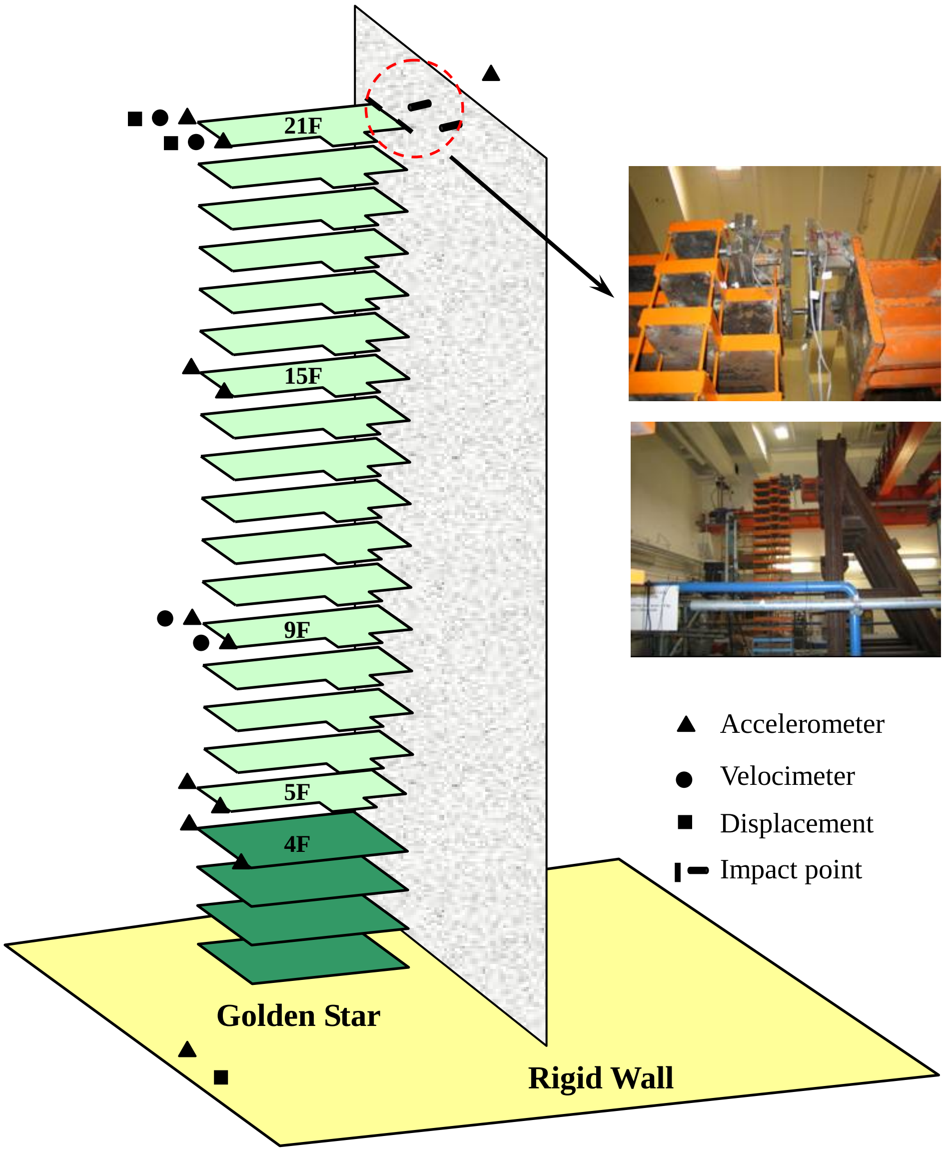

Figure 8.29 3D sketch of the GS and RW structures and the locations of contactors and transducers. The upper photo on the right side showed the details of the impact points and the lower photo showed the overall experiment sets.

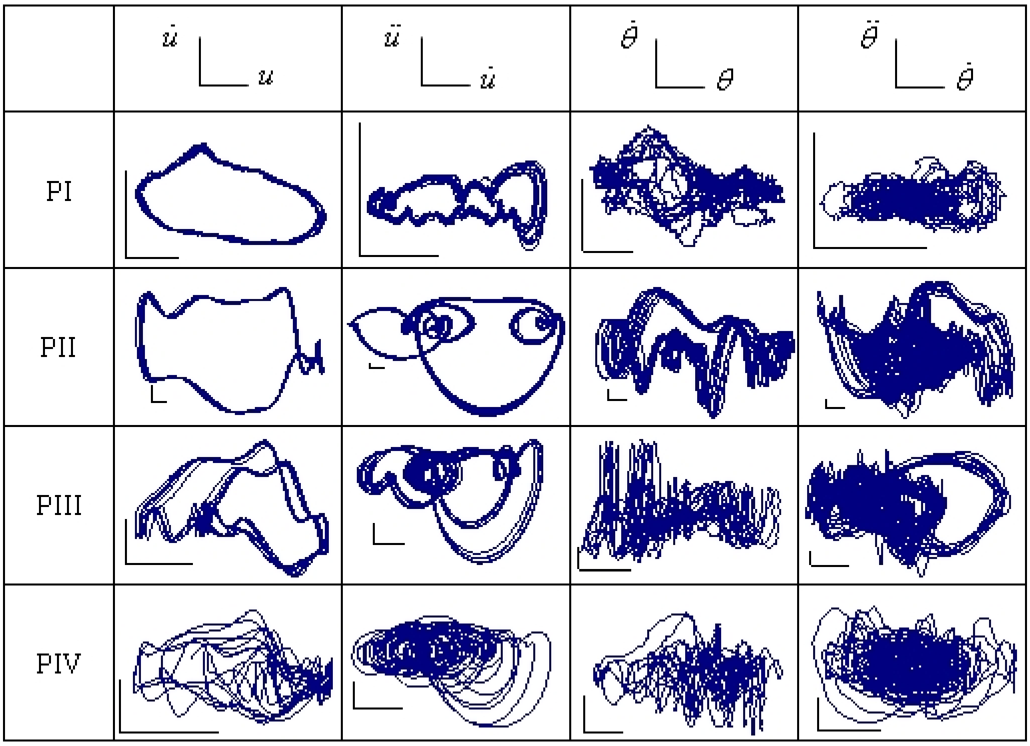

Figure 8.30 Different patterns of phase diagrams at the roof of GS in the pounding tests between GS and RW when Δ=0 mm and A_g=0.05g. The graphs listed were in different scales, that is, the horizontal lines in the 2nd, 3rd, 4th and 5th columns denoted 0.5 mm, 0.025 m/s, 3.5×10^{-4} rad and 0.087 rad/s respectively, while the vertical lines in the four columns represented 0.05 m/s, 0.5g, 0.087 rad/s and 17 rad/s^2 respectively.

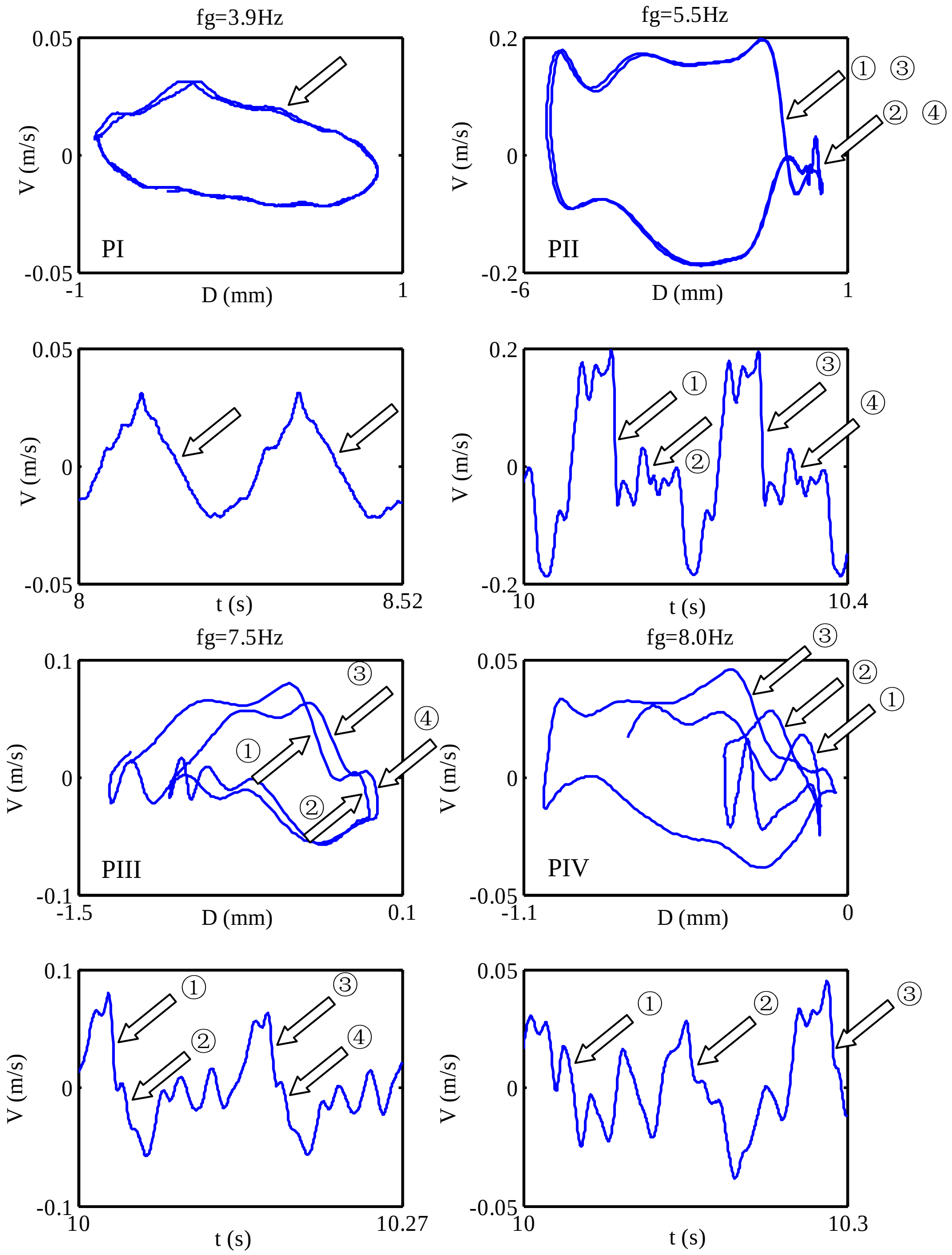

Figure 8.31 Four different phase diagrams shown in Figure 8.30 and time histories of velocity at the roof of GS for different input frequencies during pounding tests between GS and RW when $\Delta = 0.0$ mm and $A_g = 0.05g$. The arrows attached indicated where pounding occurred.

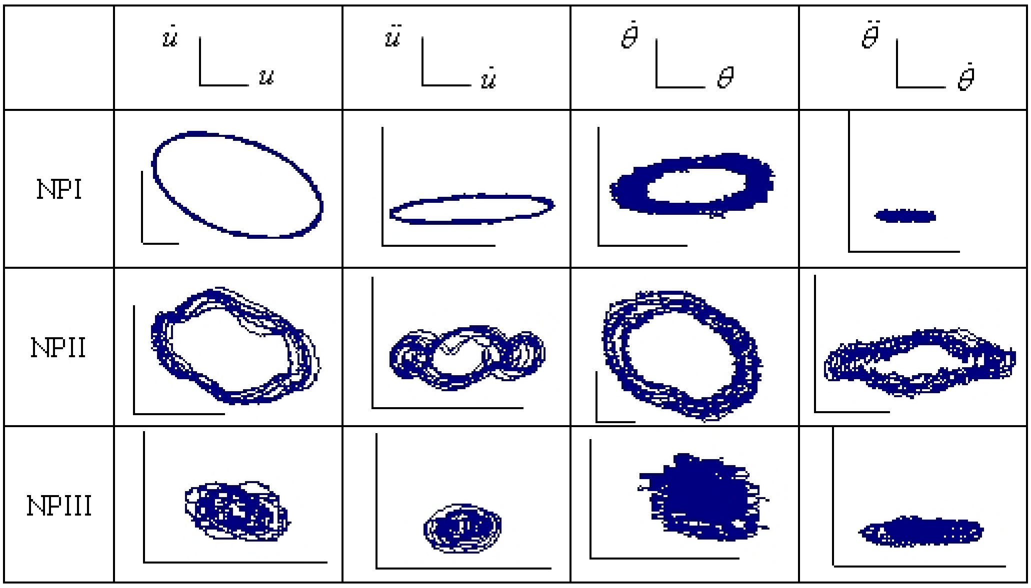

Figure 8.32 Different patterns of phase diagrams at the roof of GS in the non-pounding tests between GS and RW when Δ=3.0 mm and A_g=0.05g. The graphs listed were in different scales, that is, the horizontal lines in the 2nd, 3rd, 4th and 5th columns denoted 2 mm, 0.1 m/s, 3.5×10^{-3} rad and 0.17 rad/s, while the vertical lines in the four columns represented 0.1 m/s, 1g, 0.17 rad/s and 34.9 rad/s^2 respectively.

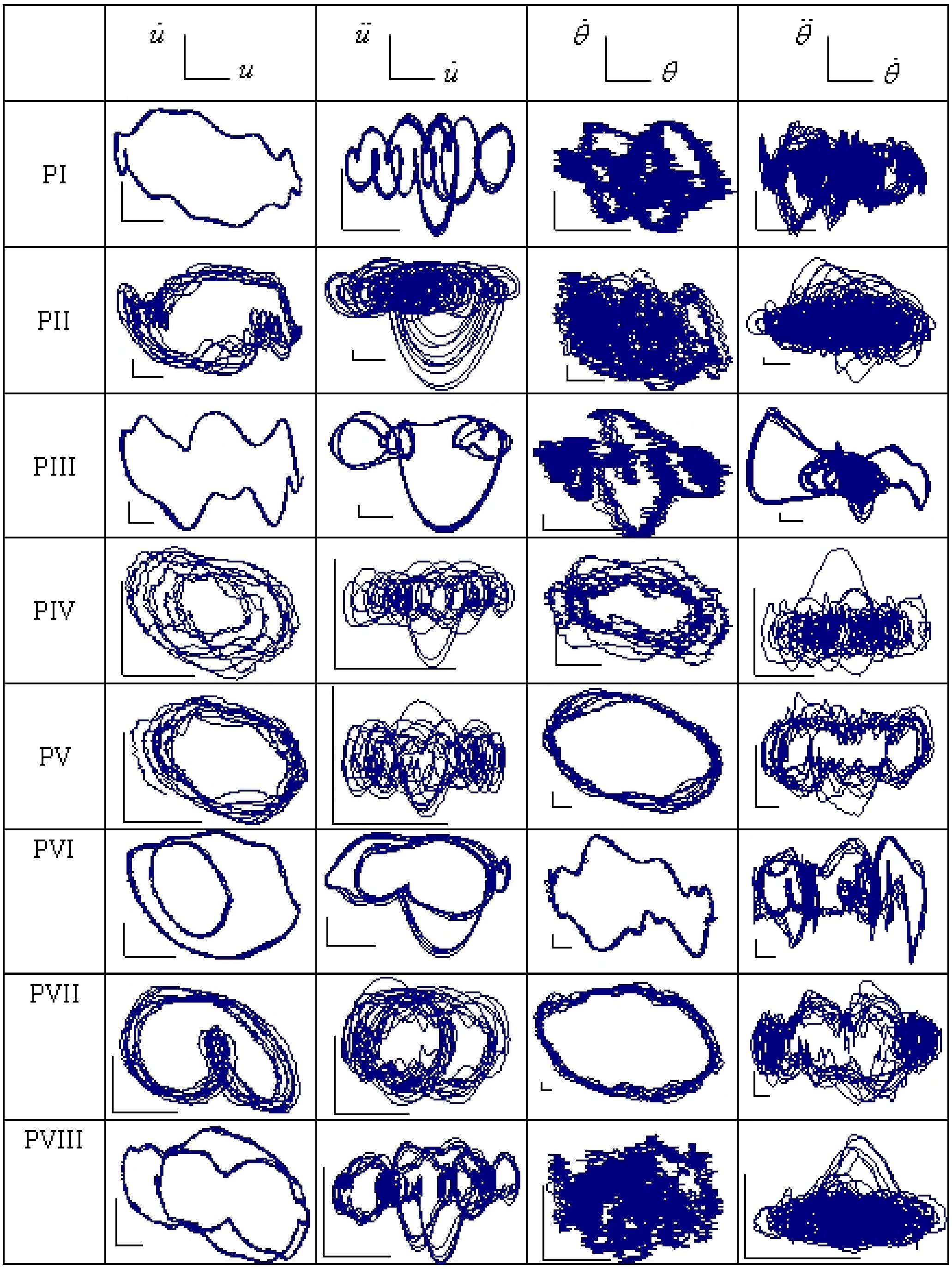

Figure 8.33 Different patterns of phase diagrams of GS in the pounding tests when Δ=3.0 mm. The graphs listed were in different scales, that is, the horizontal lines in the 2nd, 3rd, 4th and 5th columns denoted 2 mm, 0.1 m/s, 3.5×10^{-3} rad and 0.17 rad/s, while the vertical lines in the four columns represented 0.1 m/s, 1g, 0.17 rad/s and 34.9 rad/s^2 respectively.

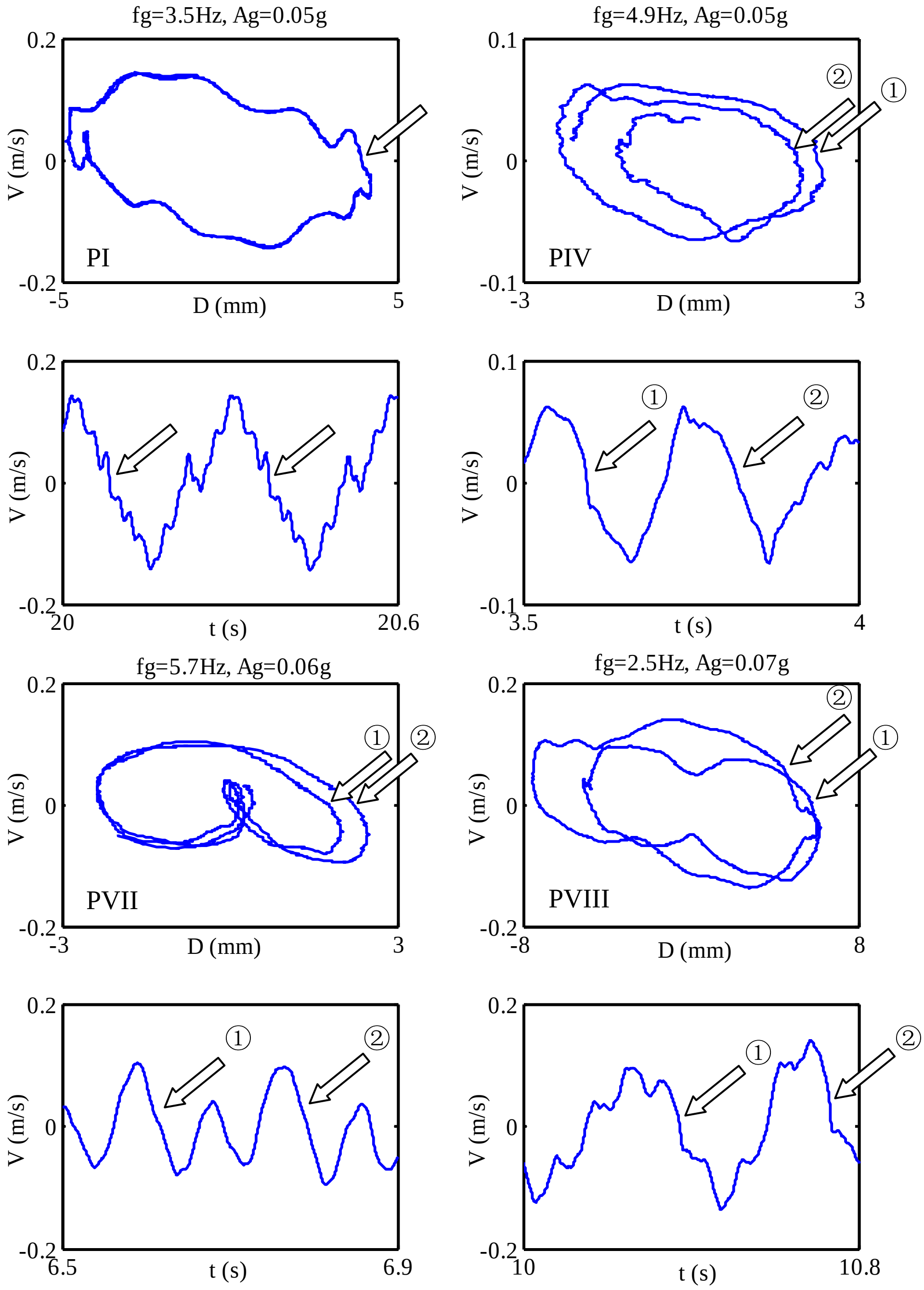

Figure 8.34 Four different phase diagrams selected from Figure 8.33 and time histories of velocity at the roof of GS for different input frequencies during pounding tests between GS and RW when $\Delta = 3.0$ mm. The arrows attached indicated where pounding occurred.

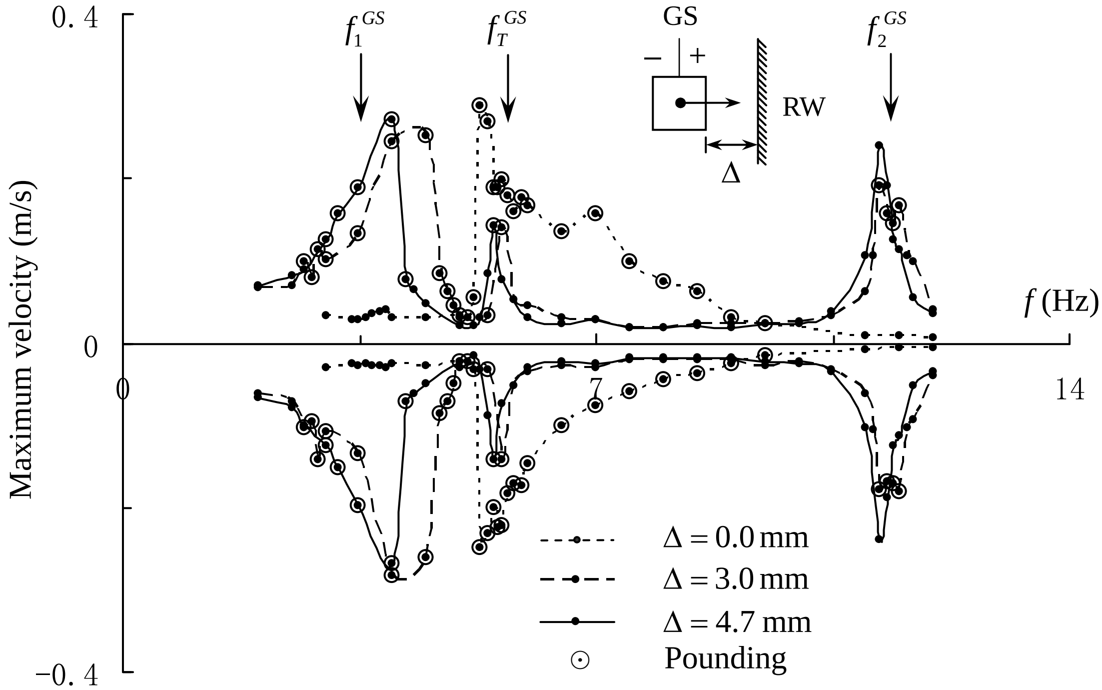

Figure 8.35 Comparisons of the maximum roof velocities of GS in the pounding tests between GS and RW when the separation distances were 0, 3 and 4.7 mm respectively. The horizontal axis was the frequencies of input sine waves and the magnitudes of the inputs were all 0.05g. The three vertical arrows represented the first three natural frequencies of GS, i.e. the first translational natural frequency $f_1^{GS} = 3.693$Hz, the first torsional frequency $f_T^{GS} = 5.615$Hz and the second translational frequency $f_2^{GS} = 11.475$Hz.

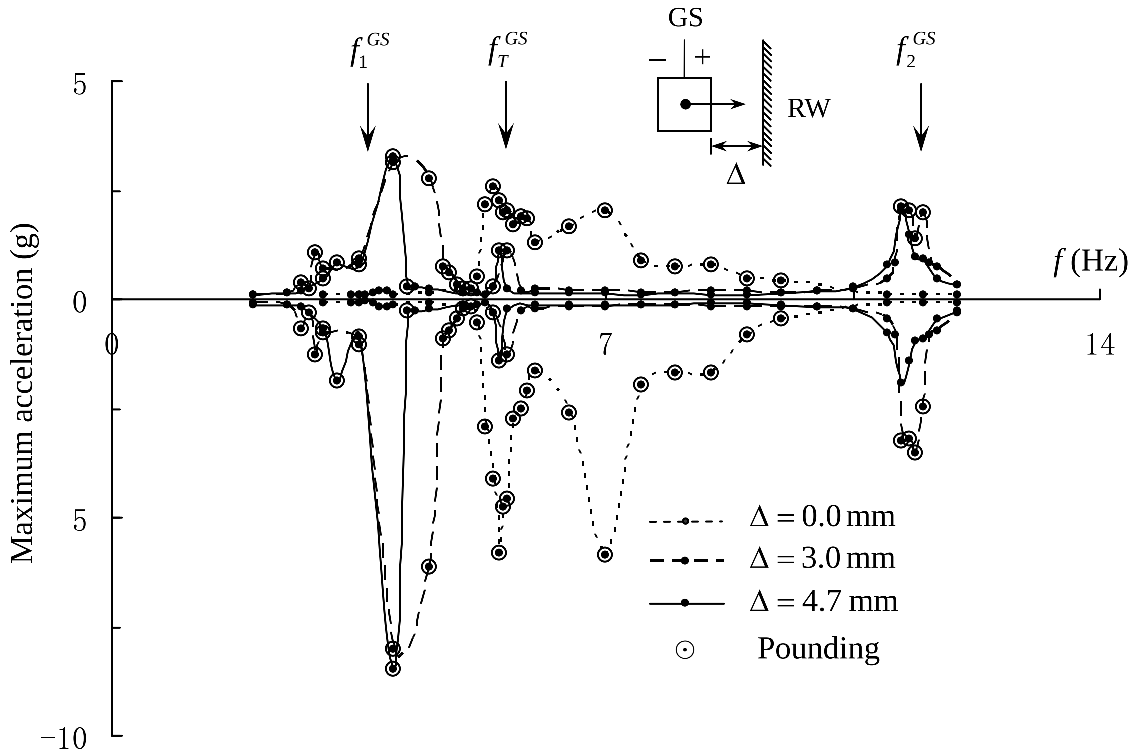

Figure 8.36 Comparisons of the maximum roof accelerations of GS in the pounding tests between GS and RW when the separation distances were 0, 3 and 4.7 mm respectively. The horizontal axis was the frequencies of input sine waves and the magnitudes of the inputs were all 0.05g. The three vertical arrows represented the first three natural frequencies of GS, i.e. the first translational natural frequency $f_1^{GS} = 3.693\text{Hz}$, the first torsional frequency $f_T^{GS} = 5.615\text{Hz}$ and the second translational frequency $f_2^{GS} = 11.475\text{Hz}$.

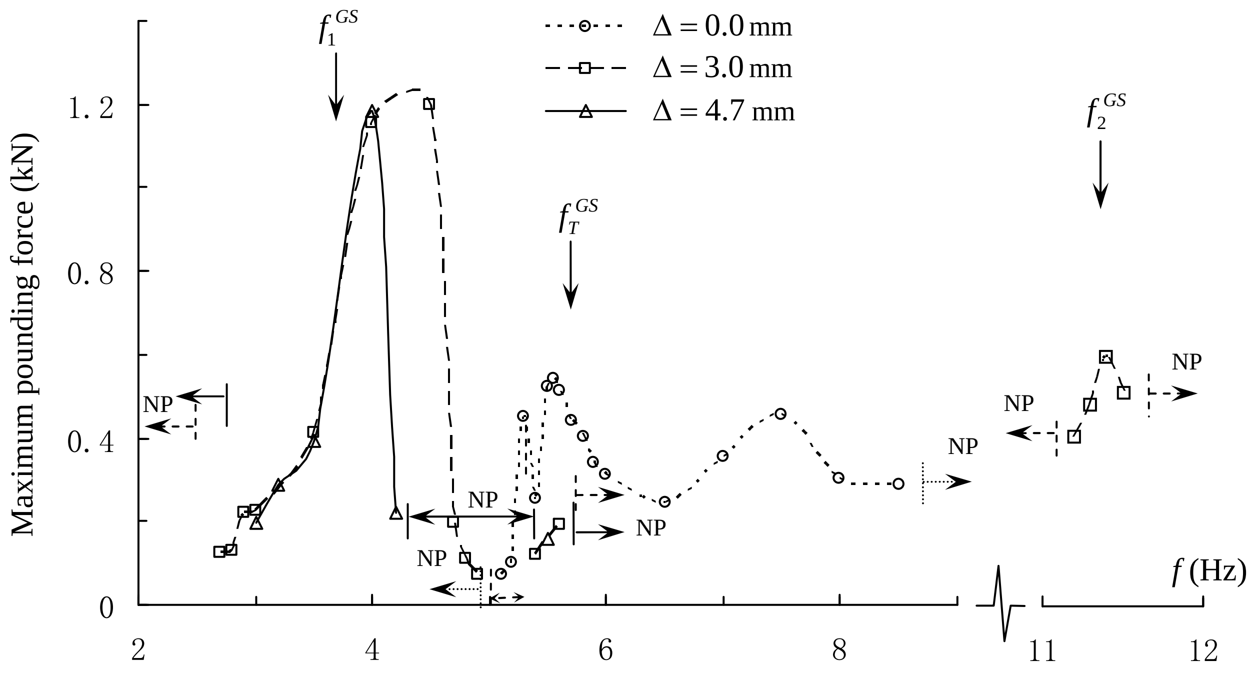

Figure 8.37 Comparisons of the maximum pounding forces in the pounding tests between GS and RW when the separation distances were 0, 3 and 4.7 mm respectively. The symbol 'NP' meant no pounding occurring. The three vertical arrows represented the first three natural frequencies of GS, i.e. the first translational natural frequency $f_1^{GS} = 3.693$Hz, the first torsional frequency $f_T^{GS} = 5.615$Hz and the second translational frequency $f_2^{GS} = 11.475$Hz.

CHAPTER 9 CONCLUSIONS

9.1 Main Conclusions and Implications

This thesis contains two main parts. In the first part (Chapters 2-6), the seismic vulnerability of an asymmetric 21-story building model with transfer system in Hong Kong was studied through conducting shaking table tests. In the second part (Chapters 7 and 8), the seismic torsional pounding between adjacent structures was investigated both theoretically and experimentally. The main conclusions drawn in the preceding chapters are summarized below.

9.1.1 Seismic vulnerability

Guided by the similarity law, a 1:25 scale model was fabricated for an asymmetric 21-story reinforced concrete building with a transfer system found in Hong Kong. Shaking table tests were conducted by inputting the time history of five past earthquakes with various adjusted peak accelerations. The damages of the model were quantitatively evaluated using various seismic damage indices. The following main conclusions are reached.

Both visual observations and damage evaluations suggest the transfer plate and stories above are most vulnerable and susceptible to severe damages under the attack of earthquake. Transfer system normally introduces an abrupt change of stiffness in the transfer zone. Asymmetric building layout may induce asymmetric rocking of the upper structure above transfer system, which may cause especially severe damages to corner elements; and this rocking is likely to cause the total collapse of this kind of buildings. This asymmetric failure pattern and rocking mechanism are observed for the first time in this study. According to our test results, both abrupt change of stiffness in the transfer zone and asymmetric building layout should be avoided as far as possible. However, these two forms of structures are commonly adopted in non-seismic- designed buildings in Hong Kong. Thus, severe damages would be expected for these buildings under the attack of strong earthquakes.

A simple algorithm is proposed to evaluate Park and Ang damage indices for real structures from measured responses in our experiments. The proposed method is also applicable to real structures with limited instrumentations under the attack of earthquakes. The damage states of the model were quantitatively evaluated through the well-calibrated Park and Ang index. Based on the estimated damages, other seismic damage indices, including the inter-story drift ratio, ductility, frequency ratio and final softening index, are correlated with various damage states (i.e. slight damage, minor damage, moderate damage, severe damage and collapse). This correlation will be very valuable to damage assessments of other similar buildings in Hong Kong and provides a practical and efficient approach to assess seismic damages.

9.1.2 Seismic torsional pounding

Besides the damages caused by insufficient seismic resistance of a building, considerable damages may also be induced through pounding between adjacent structures, especially in crowded metropolitan cities such as Hong Kong. In the second part of this thesis, seismic torsional poundings are studied through both theoretical simulations and shaking table tests.

Theoretically, pounding is modeled as the nonlinear Hertz contact. Numerical simulations are conducted to study the torsional pounding between two flexible single story towers as well as between a flexible tower and a neighboring barrier. An analytical solution is obtained for the latter case. The results show torsional pounding is much more complex than translational pounding. Possible chaotic impacts make torsional pounding difficult to be predicted. The proposed analytical solution succeeds in providing us useful insights into the complex torsional pounding phenomenon.

The more complex torsional pounding between adjacent multi-story buildings is studied through conducting shaking table tests. Two steel models were fabricated to simulate two adjacent 21-story buildings found in Hong Kong with transfer plates and asymmetric plans. A number of pounding tests were conducted for various separation distances and inputs. The observed pounding can be periodic, group periodic or chaotic. Through pounding, energy may be transferred from the more massive and rigid structure to the lighter and more flexible one, which causes abnormal large responses and damages to the lighter structure. When the separation distance is zero, the two models respond like a new system, which has a totally different dynamic characteristic from those of the individual structures. In other words, pounding may induce an unplanned period shift to existing structures, which makes their seismic responses more unpredictable than stand alone building.

Although the theoretical models are much simpler than the 21-story building models in the shaking table tests, it succeeds in providing us some useful insights into the highly nonlinear torsional pounding phenomenon. Group periodic and chaotic impacts are observed in both the numerical simulations and experiments. Both studies suggest the torsional pounding seems to be not too sensitive to the change separation distance as long as pounding is developed, consistent with the conclusions on translational pounding by Davis (1992) and Chau and Wei (2001).

9.2 Recommendations for Further Studies

In this thesis, the seismic vulnerability and torsional pounding of asymmetric buildings with transfer system are studied. The selected buildings are situated at one of the reclamation areas in Hong Kong. But soil-pile-structure interaction has not been taken into account in either the shaking table tests or theoretical studies, which may be incorporated in the future studies.

In the pounding experiments, the transfer systems in the prototypes are not well simulated in the designed models due to the small length scale. In addition, only impacts between floor slabs of adjacent structures are considered, whereas impacts between floor slabs and vertical elements (such as walls or columns) may be more dangerous in damaging adjacent structures. All these problems should be taken into consideration in the future research.

Last but not least, the proposed analytical solution in this thesis for torsional pounding between an asymmetric tower and a rigid barrier provides a possible solution for periodic single impacts. But, as shown in both of our numerical simulations and pounding tests, the torsional pounding between real multi-story structures may be far more complex. More sophisticated or MDOF models are needed to better understand this highly nonlinear torsional pounding phenomenon.

APPENDICES

Table A-1 Determination of constant values of *a* and *b* for estimating shear wave speeds in soil layer using SSB's formula (Chau, 2000).

Rock and soil	Constant	Soil types			
		Clay	Silt and fine sand	Medium and coarse sand	Cobble, gravel and detritus
Consolidated plastic or low plastic clay, loose or moderately dense crushed rock fill	*a*	70	90	80	—
	b	0.300	0.243	0.280	—
Low plastic or plastic clay, medium or moderately dense sand, gravel, cobble, fine rock fill	*a*	100	120	120	170
	b	0.300	0.243	0.280	0.243
High plastic clay, dense sand, cobble, fine rock fill	*a*	130	150	150	200
	b	0.300	0.243	0.280	0.243
More dense sand, gravel, cobble, fine rock fill, weathered rock	*a*	300-500			
	b	0.000			

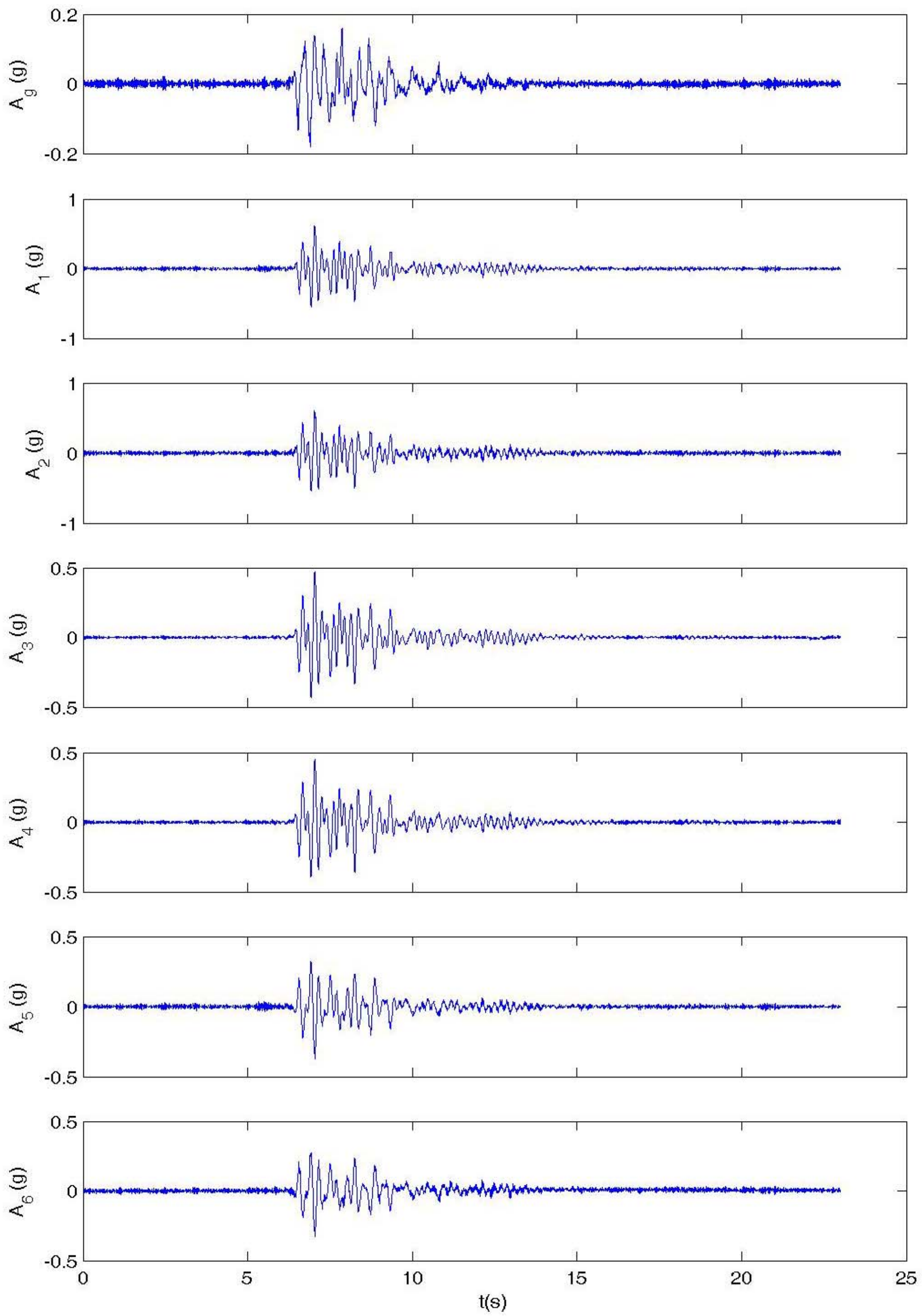

Figure A-1 Acceleration records during the soil site input of 0.2g Kobe earthquake. The locations of these accelerations can be referred to Figure 3.19.

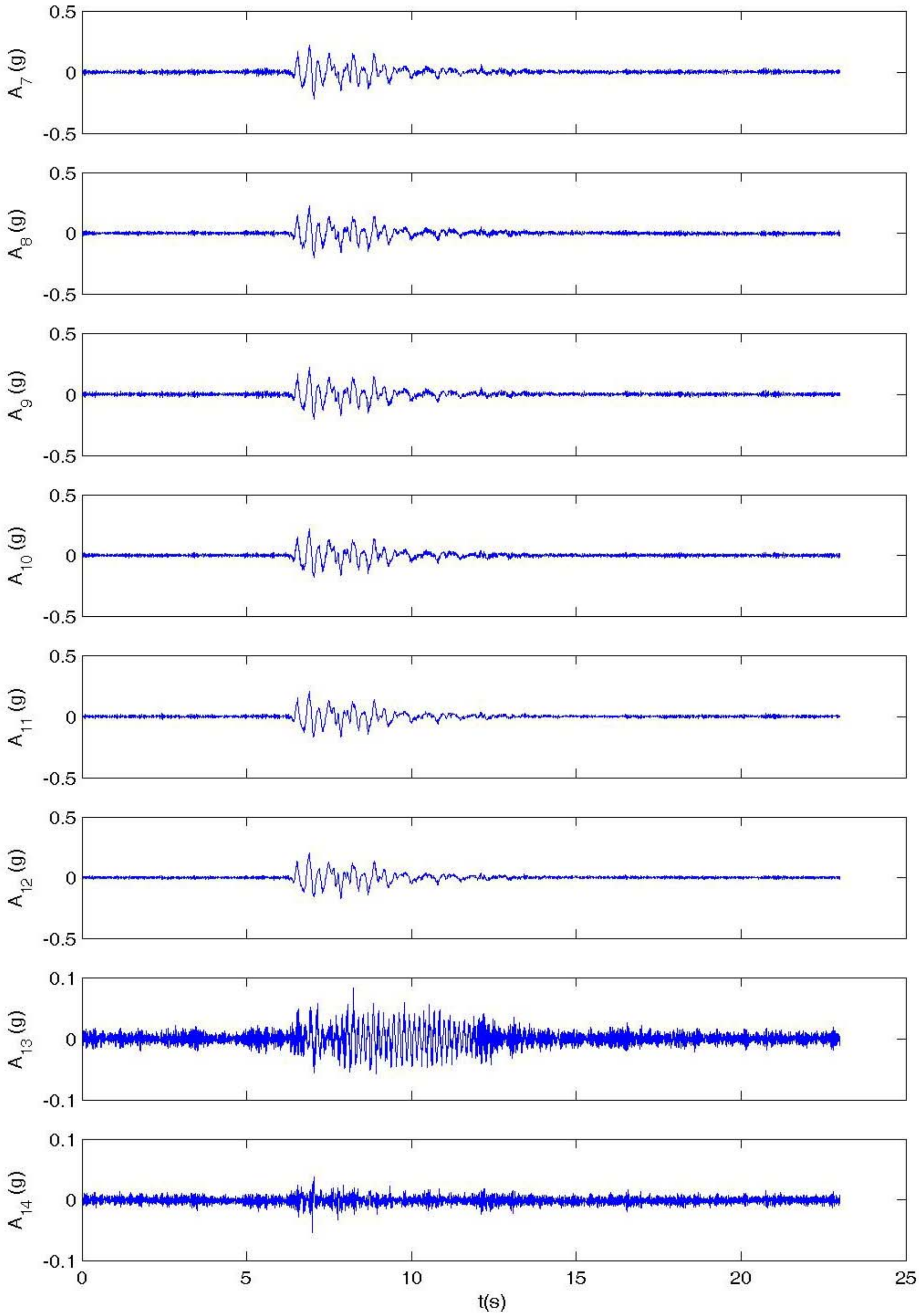

Figure A-2 Acceleration records during the soil site input of 0.2g Kobe earthquake. The locations of these accelerations can be referred to Figure 3.19.

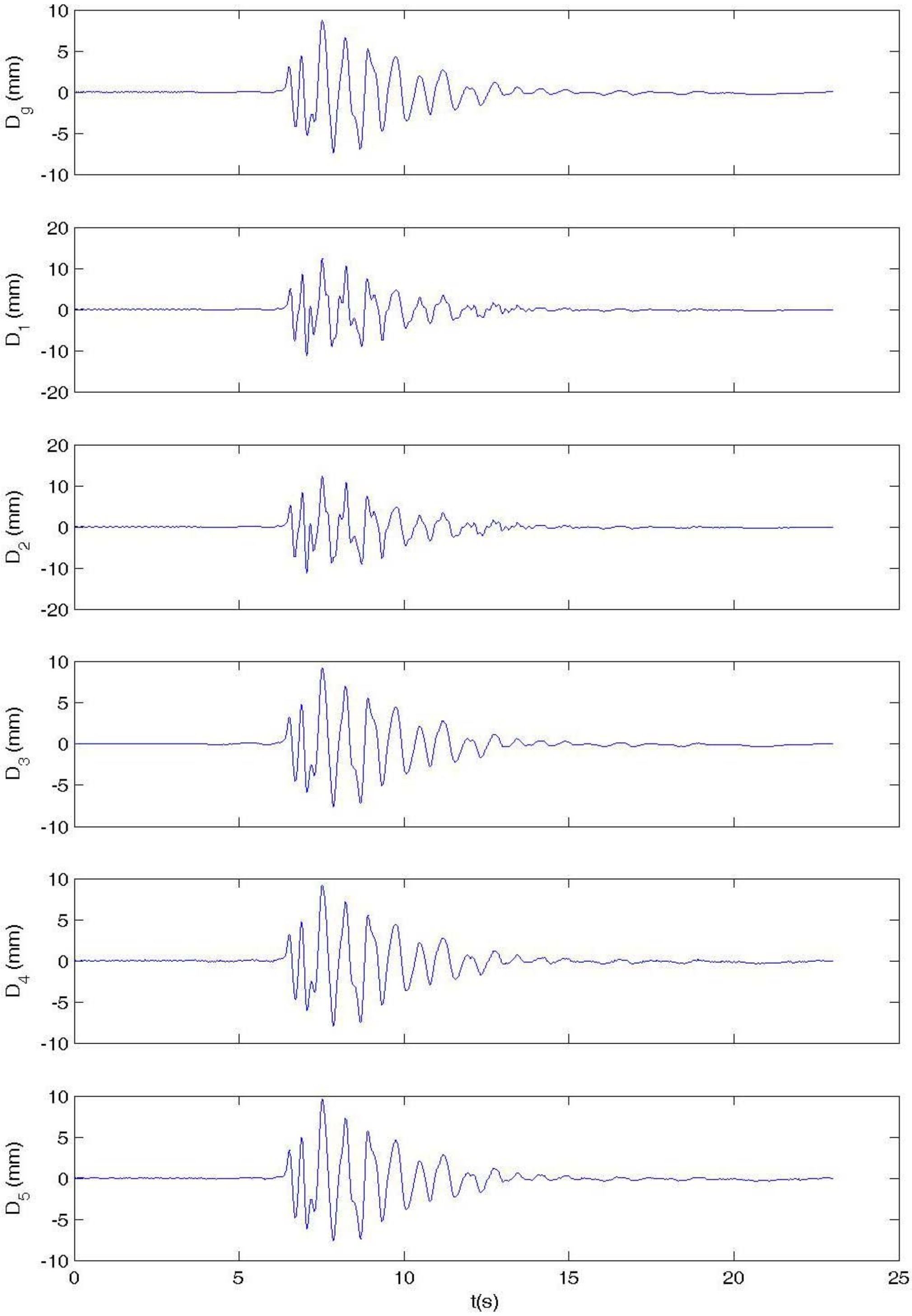

Figure A-3 Displacement records during the soil site input of 0.2g Kobe earthquake. The locations of these accelerations displacement can be referred to Figure 3.19.

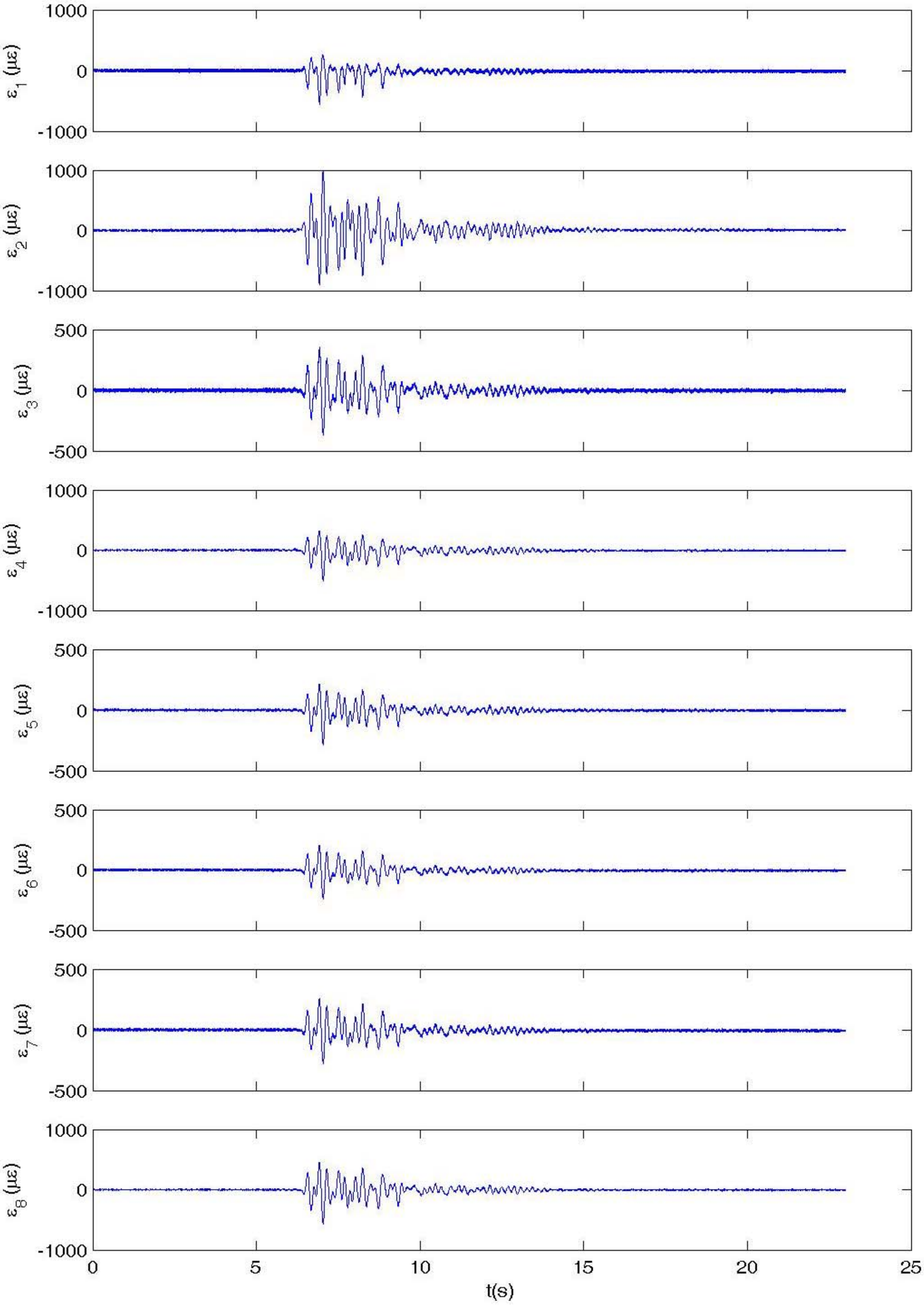

Figure A-4 Strain records during the soil site input of 0.2g Kobe earthquake. The locations of strain gauges can be referred to Figures 3.22-3.24.

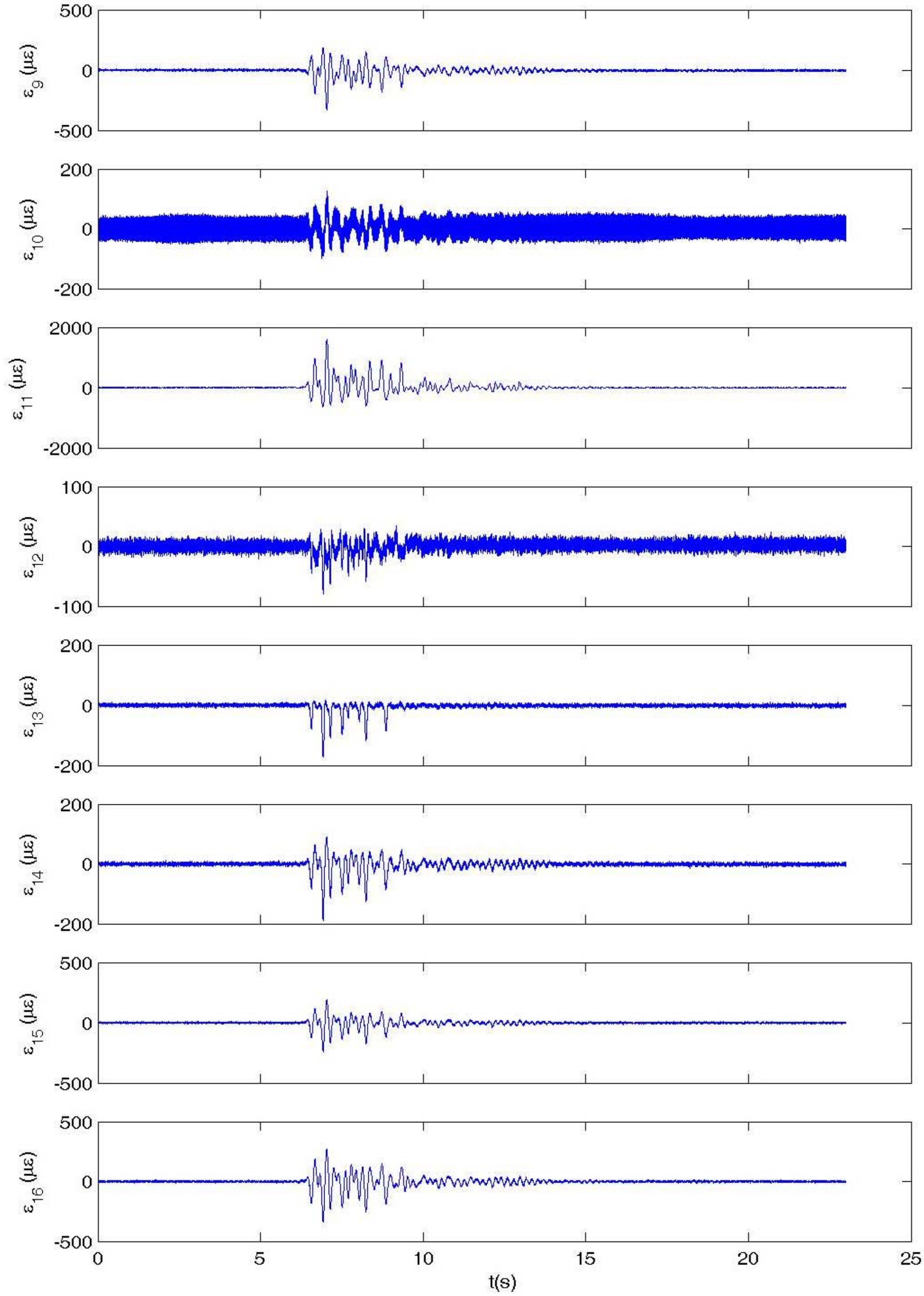

Figure A-5 Strain records during the soil site input of 0.2g Kobe earthquake. The locations of strain gauges can be referred to Figures 3.22-3.24.

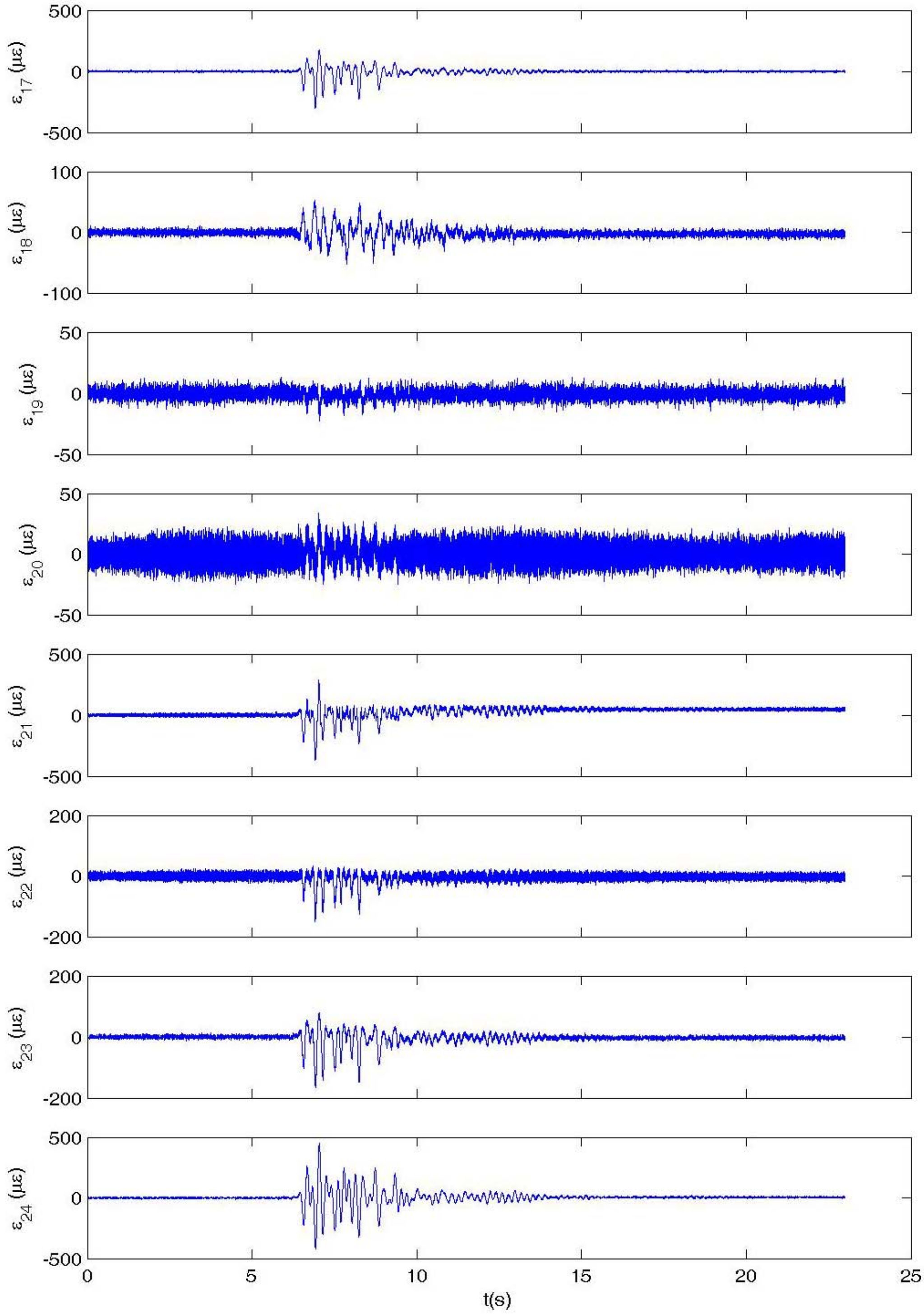

Figure A-6 Strain records during the soil site input of 0.2g Kobe earthquake. The locations of strain gauges can be referred to Figures 3.22-3.24.

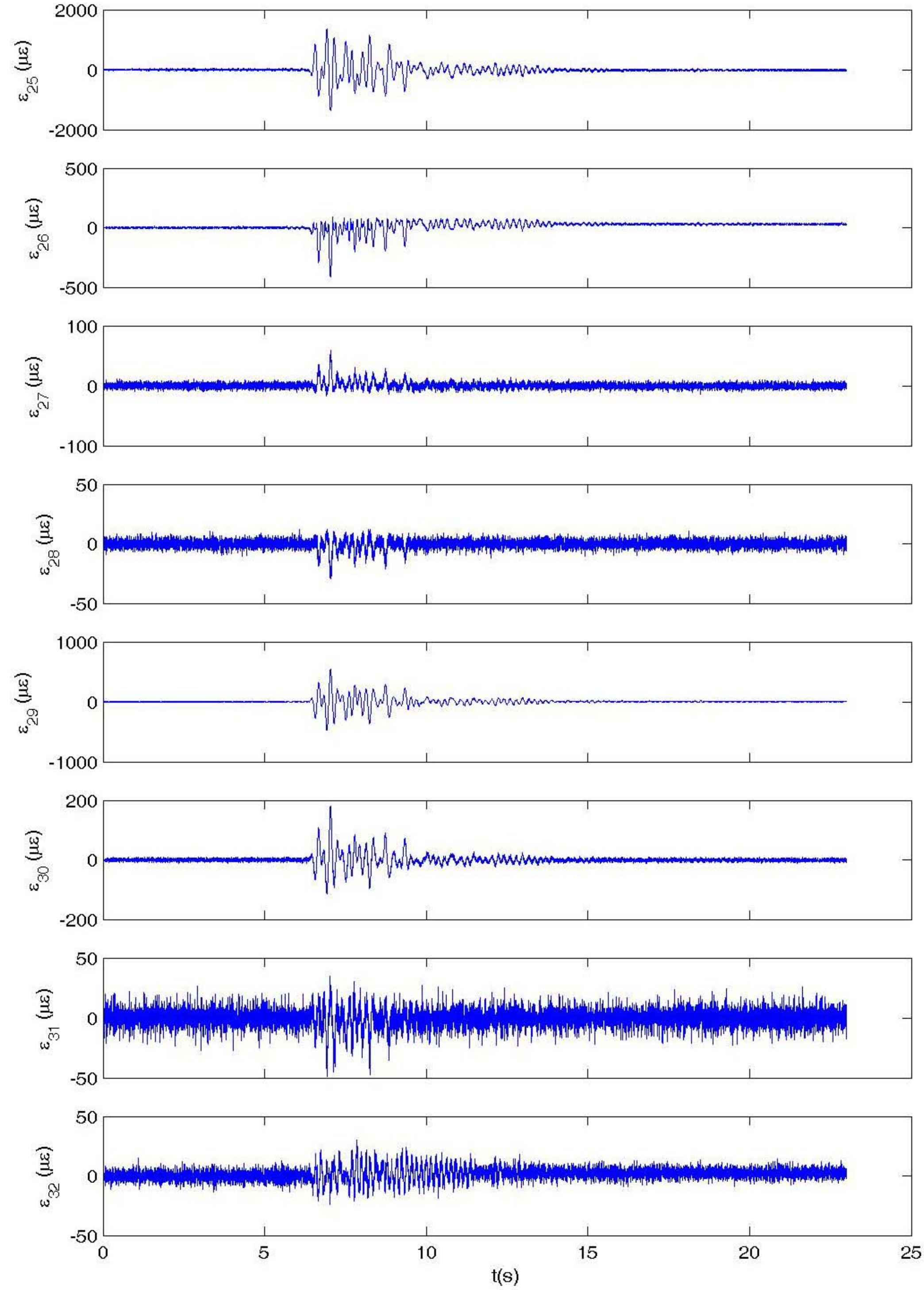

Figure A-7 Strain records during the soil site input of 0.2g Kobe earthquake. The locations of strain gauges can be referred to Figures 3.22-3.24.

REFERENCES

Akiyama, H., 2000. Evaluation of fractural mode of failure in steel structures following Kobe lessons. *Journal of Constructional Steel Research,* **55(1-3)**: 211-227.

Anagnostopoulos, S.A., 1988. Pounding of buildings in series during earthquakes. *Earthquake Engineering and Structural Dynamics,* **16**: 443-456.

Anagnostopoulos, S.A., 1994. Earthquake induced pounding: State of the art. *Proceedings of the 10th European Conference on Earthquake Engineering,* Aug. 28-Sept. 2, Vienna, Austria, **2**: 897-905.

Anagnostopoulos, S.A., 1996. Building pounding reexamined: How serious a problem is it. *Proceedings of the 11th World Conference on Earthquake Engineering,* Paper No. 2108, Acapulco, Mexico.

Anagnostopoulos, S.A. and Spiliopoulos, K.V., 1992. An investigation of earthquake induced pounding between adjacent buildings. *Earthquake Engineering and Structural Dynamics,* **21**: 289-302.

Anderson, J.C., Chen, W. and Yin, P., 1997. Seismic behavior of a high-strength concrete framed tube. *Structural Design of Tall Buildings,* **6**: 333-350.

Ang, A.H-S., Kim, W.J. and Kim, S.B., 1993. Damage estimation of existing bridge structures. *Structural Engineering in Natural Hazards Mitigation: Proc. ASCE Structures Congress 1993,* Irvine, CA, **2**: 1137-1142.

ATC, 1985. *ATC-13: Earthquake Damage Evaluation Data for California.* Applied

Technology Council, Redwood City, CA.

ATC, 1989. *ATC-20: Procedures for post-earthquake safety evaluation of buildings.* Applied Technology Council, Redwood City, CA.

Bairrao, R., Chrzanowski, M., Duque, J. and Latus, P., 2005. Ultrasonic damage measurement in reinforced concrete beams. *Key Engineering Materials,* **293-294**: 695-702.

Baker, W.E., Westine, P.S. and Dodge, F.T., 1991. *Similarity methods in engineering dynamics: Theory and practice of scale modeling.* Revised Edition, Amsterdam; New York: Elsevier, 1991.

Balendra, T., Tan, K.H. and Kong, S.K., 1999. Vulnerability of reinforced concrete frames in low seismic region, when designed according to BS 8110. *Earthquake Engineering and Structural Dynamics,* **28(11)**: 1361-1381.

Banon, H., Biggs, J.M. and Irvine, H.M., 1981. Seismic damage in reinforced concrete frames. *Journal of Structural Engineering, ASCE,* **107(9)**: 1713-1729.

Bao, S.H., 1992. Flexure-torsion coupled vibrations for tall building frame-shear wall-thin walled member cooperating systems. *China Civil Engineering Journal,* **25(1)**: 12-20.

Berg, G.V. and Degenkolb, H.J., 1973. *Engineering lessons from the Managua earthquakes.* American Iron and Steel Institute Report.

Bertero, V.V., 1986. Observations of structural pounding. *The Mexico earthquakes, 1985: factors involved and lessons learned. Proceedings of the International Conference,* Camino Real Hotel, Mexico City, Mexico, September 19-21, 1986.

ASCE, New York, pp. 264-278.

Bertero, V.V., Anderson, J.C., Krawinkler, H. and Miranda, E., 1991. *Design Guidelines for Ductility and Drift Limits.* Report No. EERC 91-15, Earthquake Engineering Research Center, University of California, Berkeley, CA.

Bertero, V.V., Atkan, A.E., Harris, H.G. and Chowdhury, A.A., 1983. *Mechanical Characteristics Used in the 1/5 Scale Model of the 7-story Reinforced Concrete Test Structure.* Report No. EERC 83-21, Earthquake Engineering Research Center, University of California, Berkeley, CA.

Bertero, V.V. and Collins, R.G., 1973. *Investigation of the Failures of the Olive View stairtowers during the San Fernando Earthquake and Implications on Seismic Design.* Report No. EERC 73-26, Earthquake Engineering Research Center, University of California, Berkeley, CA.

Bolt, B.A., 2004. *Earthquakes.* Fifth Edition, W.H. Freeman and Company, New York, NY 10010, 2004.

Bozorgnia, Y. and Bertero, V.V., 2003. Damage spectra: characteristics and applications to seismic risk reduction. *Journal of Structural Engineering, ASCE*, **129(10)**: 1330-1340.

Bracci, J.M., Reinhorn, A.M., Mander, J.B. and Kunnath, S.K., 1989. *Deterministic Model for Seismic Damage Evaluation of Reinforced Concrete Structures,* Technical Report NCEER-89-0033, National Center for Earthquake Engineering Research, State University of New York, Buffalo, NY.

Buckingham, E., 1914. On physically similar systems: illustrations of the use of dimensional equations. *Physical Review D*, **4**: 345-376.

Chang, K.C. and Lin, Y.Y., 2004. Seismic response of full-scale structure with added viscoelastic dampers. *Journal of Structural Engineering, ASCE*, **130(4)**: 600-608.

Chau, K.T., 2000. Attenuation relation and uncertainty analysis, site response, and seismic hazard assessment of Hong Kong. *Lecture Notes for Short Course: Earthquake Mechanics and Seismic Hazard Analysis*. Department of Civil and Structural Engineering, The Hong Kong Polytechnic University, Hong Kong, Jul. 17-19, 2000.

Chau, K.T. and Wei, X.X., 2001. Pounding of structures modeled as nonlinear impacts of two oscillators. *Earthquake Engineering and Structural Dynamics*, **30(5)**: 633-651.

Chau, K.T., Wei, X.X., Guo, X. and Shen, C.Y., 2003. Experimental and theoretical simulations of seismic pounding between adjacent structures. *Earthquake Engineering and Structural Dynamics*, **32(4)**: 537-554.

Chau, K.T., Wei, X.X. and Wang, L.X., 2004. Experimental and theoretical simulations of seismic torsional poundings between two adjacent structures. *Proceedings of the 13th World Conference of Earthquake Engineering*, Paper No. 2176, Vancouver, Canada, Aug. 1-6, 2004.

Chau, K.T., Wong, Y.L., Lam, E.S.S. and Lee, C.M., 1998. *Seismic Risk Assessment for Hong Kong*. CIDARC, The Hong Kong Polytechnic University, Hong Kong.

Chau, K.T., Xu, Y.L., Ko, J.M., Lam, E.S.S., Wong, Y.L., Lee, C.M. and Ni, Y.Q., 2002. Earthquake hazard evaluation and risk mitigation in Hong Kong.

Proceedings of the International Conference on Advances and New Challenges in Earthquake Engineering Research (ICANCEER), Hong Kong Volume, edited by Ko, J.M. and Xu, Y.L., Aug. 15-20, 2002, Harbin and Hong Kong, pp. 17-32.

Chau, K.T. and Yang, X., 2005. Nonlinear interaction of soil-pile in horizontal vibration. *Journal of Engineering Mechanics, ASCE,* **131(8)**: 847-858.

Chen, Y., 2000. Seismic hazard and risk analysis: a simplified approach. *Lecture notes for short course: Earthquake mechanics and seismic hazard analysis.* Department of Civil and Structural Engineering, The Hong Kong Polytechnic University, Hong Kong, Jul. 17-19, 2000.

Chesi, C. and Schnobrich, W.C., 1991. 3-dimensional effects in lateral behavior of frame-wall systems. *Journal of Structural Engineering, ASCE,* **117(2)**: 391-409.

Chung, Y.S., Meyer, C. and Shinozuka, M., 1987. *Seismic damage assessment of RC members.* Technical Report NCEER-87-0022, National Center for Earthquake Engineering Research, State University of New York, Buffalo, NY.

Clough, R.W. and Penzien, J., 1993. *Dynamics of structures.* Second Edition. McGraw-Hill, Inc., 1993.

Cohen, G.L., Klingner, R.E., Hayes, J.R. and Sweeney, S.C., 2004. Seismic evaluation of low-rise reinforced masonry buildings with flexible diaphragms: 1. Seismic and quasi-static testing. *Earthquake Spectra,* **20(3)**: 779-801.

Cosenza, E., Manfredi, G. and Ramasco, R., 1993. The use of damage functionals in earthquake engineering: a comparison between different methods. *Earthquake Engineering and Structural Dynamics,* **22:** 855-868.

Davis, R.O., 1992. Pounding of buildings modeled by an impact oscillator. *Earthquake Engineering and Structural Dynamics,* **21**: 253-274.

DiPasquale, E. and Cakmak, A.S., 1987. *Detection and Assessment of Seismic Structural Damage.* Technical Report NCEER-87-0015, National Center for Earthquake Engineering Research, State University of New York, Buffalo, NY.

DiPasquale, E. and Cakmak, A.S., 1989. *On the Relation between Local and Global Damage Indices.* Technical Report NCEER-89-0034, National Center for Earthquake Engineering Research, State University of New York, Buffalo, NY.

Dumova-Jovanoska, E., 2000. Fragility curves for reinforcement concrete structures in Skopje (Macedonia) region. *Soil Dynamics and Earthquake Engineering*, **19**: 455-466.

EERI, 1994. *Expected seismic performance of buildings.* Publication Number SP-10, Earthquake Engineering Research Institute, Oakland, CA, 1994.

Elenas, A., 2000. Correlation between seismic acceleration parameters and overall structural damage indices of buildings. *Soil Dynamics and Earthquake Engineering,* **20(1-4)**: 93-100.

Ewins, D.J., 2000. *Modal Testing: Theory, Practice and Application.* Second Edition. Research Studies Press Ltd., Hertfordshire, England.

FEMA, 1999. *HAZUS99: Earthquake Loss Estimation Methodology: User's Manual*. The Federal Emergency Management Agency (FEMA), Washington, D.C.

Filiatrault, A. and Cervantes, M., 1995. Separation between buildings to avoid pounding during earthquakes. *Canadian Journal of Civil Engineering,* **25**:

331-341.

Filiatrault, A., Cervantes, M., Folz, B. and Prion, H., 1994. Pounding of buildings during earthquakes: A Canadian perspective. *Canadian Journal of Civil Engineering*, **21**: 251-265.

Filiatrault, A., Lachapelle, E. and Lamontagne, P., 1998. Seismic performance of ductile and nominally ductile reinforced concrete moment resisting frames. I. Experimental study. *Canadian Journal of Civil Engineering,* **22**: 164-179.

Filiatrault, A., Wagner, P. and Cherry, S., 1995. Analytical prediction of experimental building pounding. *Earthquake Engineering and Structural Dynamics,* **24**: 1131-1154.

Garcia, L.E. and Sozen, M.A., 2004. Earthquake-resistant design of reinforced concrete buildings. *Earthquake Engineering: From Engineering Seismology to Performance-Based Engineering*, edited by Bozorgnia, Y. and Bertero, V.V., CRC Press, Florida, 2004.

GB50010-2002, 2002. *Code for Design of Concrete Structures.* Ministry of Construction, The People’s Republic of China, Beijing, China, 2002.

GB50011-2001, 2001. *Code for Seismic Design of Buildings.* Ministry of Construction, The People’s Republic of China, Beijing, China, 2001.

GB/T 50081-2002, 2003. *Standard for Test Method of Mechanical Properties of Ordinary Concrete.* Ministry of Construction, The People’s Republic of China, Beijing, China, 2003.

Ghobarah, A., Abou-Elfath, H. and Biddah, A., 1999. Response-based damage assessment of structures. *Earthquake Engineering and Structural Dynamics*, **28:** 79-104.

Goldsmith, W., 1960. *Impact.* Edward Arnold: London.

Gosain, N.K., Brown, R.H. and Jirsa, J.O., 1977. Shear requirements for load reversals on RC members. *Journal of Structural Engineering ASCE,* **103(7)**: 1461-1476.

Hahn, G.D. and Valenti, M.C., 1997. Correlation of seismic responses of structures. *Journal of Structural Engineering, ASCE,* **123**: 405-413.

Hao, H. and Zhang, S.R., 1999. Spatial ground motion effect on relative displacement of adjacent building structures. *Earthquake Engineering and Structural Dynamics,* **28**: 333-349.

Hindi, R.A. and Sexsmith, R.G., 2001. A proposed damage for RC bridge columns under cyclic loading. *Earthquake Spectra*, **17(2)**: 261-290.

Hirano, S. and Ando, N., 2003. Full-scale shaking table tests of a Japanese post and beam wooden house I. Dynamic performance and damages of a wooden house excited by real and simulated seismic motions. *Mokuzai Gakkaishi*, **49(2)**: 104-116.

Hosoya, H., Abe, I., Kitagawa, Y. and Okada, T., 1995. Shaking table tests of three-dimensional scale models of reinforced concrete high-rise frame structures with wall columns. *ACI Structural Journal*, **92(6)**: 765-780.

Irwin, A.W., 1984. *Design of shear wall buildings.* London: CIRIA, 1984.

Jankowski, R., 2005. Non-linear viscoelastic modeling of earthquake-induced structural pounding. *Earthquake Engineering and Structural Dynamics,* **34**: 595-611.

Jankowski, R., Wilde, K. and Fujino, Y., 1998. Pounding of superstructure segments in isolated elevated bridge during earthquakes. *Earthquake Engineering and Structural Dynamics,* **27**: 487-502.

JGJ 101-96, 1996. *Specification of Testing Methods for Earthquake Resistant Building.* Ministry of Construction, The People's Republic of China, Beijing, China, 1996.

JGJ 3-2002, 2002. *Technical Specification for Concrete Structures of Tall Building.* Ministry of Construction, The People's Republic of China, Beijing, China, 2002.

Jing, H.S. and Young, M.H., 1991. Impact interactions between two vibration systems under random excitation. *Earthquake Engineering and Structural Dynamics,* **20**: 667-681.

Kan, C.L. and Chopra, A.K., 1976. *Coupled Lateral Torsional Response of Buildings to Ground Shaking.* Report No. EERL 76-13, Univ. of California, Berkeley.

Kasai, K., Jagiasi, A.R. and Jeng, V., 1996. Inelastic vibration phase theory for seismic pounding mitigation. *Journal of Structural Engineering, ASCE,* **122**: 1136-1146.

Kasai, K., Jeng, V., Patel, P.C., Munshi, J. A. and Maison, B.F., 1992. Seismic pounding effect - survey and analysis. *Proceedings of the 10th World Conference of Earthquake Engineering*, Madrid, Spain, July 19-24, 1992: 3893-3898.

Kasai, K. and Maison, B.F., 1997. Building pounding damage during the 1989 Loma Prieta Earthquake. *Engineering Structures,* **19**: 195-207.

Khashaee, P., 2005. Damage-based seismic design of structures. *Earthquake Spectra,* **21(2)**: 371-387.

Kim, J.K. and Ryu, H., 2003. Seismic test of a full-scale model of a five-storey stone pagoda. *Earthquake Engineering and Structural Dynamics,* **32(5)**: 731-750.

Kobrinski, A.E., 1969. *Dynamics of Mechanisms with Elastic Connections and Impacts Systems.* English translation: R. Lennox-Napier, London.

Koo, K.K., Chau, K.T., Yang, X., Lam, S.S. and Wong, Y.L., 2003. Soil-pile-structure interaction under SH save excitation. *Earthquake Engineering and Structural Dynamics,* **32:** 395-415.

Kowalsky, M.J. and Priestley, M.J.N., 2000. Improved analytical model for shear strength of circular reinforced concrete columns in seismic regions. *ACI Structural Journal,* **97(3)**: 388-396.

Kratzig, W.B., Meyer, I.F. and Meskouris, K., 1989. Damage evolution in reinforced concrete members under cyclic loading. *Proceedings of the 5th International Conference on Structural Safety and Reliability (ICOSSAR 89),* San Francisco, CA, **II**: 795-802.

Krawinkler, H. and Seneviratna, G.D.P.K., 1998. Pros and cons of pushover analysis of seismic performance evaluation. *Engineering Structures,* **20**: 452-464.

Krawinkler, H. and Zohrei, M., 1983. Cumulative damage in steel structures subjected to earthquake ground motions. *Computers and Structures,* **16(1-4)**: 531-541.

Kunnath, S.K. and Jenne, C., 1994. Seismic damage assessment of inelastic RC structures. *Proceedings of 5th U.S. National Conference on Earthquake Engineering*, EERI, Oakland, CA, **1**: 55-64.

Kunnath, S.K., Reinhorn, A.M. and Lobo, R.F., 1992. *IDARC Version 3.0: A Program for the Inelastic Damage Analysis of RC Structures.* Technical Report NCEER- 92-0022, National Center for Earthquake Engineering Research, State University of New York, Buffalo NY.

Lam, S.S.E., Li, C.S., Zhang, M.Z., Wong, Y.L. and Chau, K.T., 2002. *Seismic Study of Hong Kong: Shaking Table Tests of a Typical High-rise Building in Hong Kong.* CIDARC, Hong Kong.

Lee, C.F., Ding, Y.Z., Huang, R.H., Yu, Y.B., Guo, G.A., Chen, P.L. and Huang, X.H., 1996. *Seismic Hazard Analysis of the Hong Kong Region.* Publication No. 65, Geotechnical Engineering Office of Hong Kong.

Lee, H.S. and Woo, W.S., 2002. Seismic performance of a 3-story RC frame in a low-seismicity region. *Engineering Structures,* **24**: 719-734.

Leibovich, E., Rutenberg, A. and Yankelevsky, D.Z., 1996. On eccentric seismic pounding of symmetric buildings. *Earthquake Engineering and Structural Dynamics,* **25**: 219-233.

Li, C.S., Lam, S.S.E., Zhang, M.Z. and Wong, Y.L., 2006. Shaking table test of a 1:20 scale high-rise building with a transfer plate system. *Journal of Structural Engineering, ASCE,* **132(11)**: 1732-1744.

Lin, J.H., 1997. Separation distance to avoid seismic pounding of adjacent buildings. *Earthquake Engineering and Structural Dynamics*, **26**: 395-403.

Lin, Y.F., Lin, Y.C. and Tsai, B.Y., 2004. Evaluating bond quality at interface between reinforcing bars and concrete using impact-echo method. *ACI Materials Journal*, **101(2)**: 154-161.

Liu, D.H., Yang, C.R. and Zhong, X.G., 1993. *Seismic Design of Tall Buildings*. China Architecture & Building Press, Beijing, China, 1993 (in Chinese).

Lu, X.L., Zhang, H.Y., Hu, Z.L. and Lu, W.S., 1999. Shaking table testing of a U-shaped plan building model. *Canadian Journal of Civil Engineering*, **26**: 746-759.

Lybas, J. and Sozen, M.A., 1977. *Effect of Beam Strength Ratio on Dynamic Behavior of Reinforced Concrete Coupled Walls.* Report SRS No. 444, University of Illinois, Urbana-Champaign.

Ma, G.W., Ha, H. and Lu, Y., 2003. Modeling damage potential of high-frequency ground motions. *Earthquake Engineering and Structural Dynamics,* **32(10)**: 1483-1503.

MacGregor, J.G. and Wight, J.K., 2006. *Reinforced Concrete: Mechanics and Design.* Fourth edition in SI units, Singapore: Pearson/Prentice Hall, 2006.

Maison, B.F. and Kasai, K., 1992. Dynamics of pounding when two buildings collide. *Earthquake Engineering and Structural Dynamics*, **21**: 771-786.

Miller, R.K., 1980. Steady vibroimpact at a seismic joint between adjacent structures. *Proceedings of the 7th World Conference of Earthquake Engineering*, Istanbul, **6**: 57-64.

Ministry of Construction, 2003. *Outlines for Approval of Seismic Design of Tall Building Structures beyond the Code-specification.* Ministry of Construction [2003]46, Beijing, China (http://www.realestate.gov.cn/file.asp?recordno=26331&teamno=103&line=100).

Ministry of Construction, 2006. *Essentials in Approval of Seismic Design of Tall Building Structures beyond the Code-specification.* Ministry of Construction [2006]220, Beijing, China (http://www.cin.gov.cn/indus/file/2006091207.htm).

Moehle, J.P. and Alarcon, L.F., 1986. Seismic analysis methods for irregular building. *Journal of Structural Engineering, ASCE*, **112(1)**: 35-52.

Mottershead, J.E. and Friswell, M.I., 1993. Model updating in structural dynamics: a survey. *Journal of Sound and Vibration*, **167(2)**: 347-375.

Mouzakis, H.P. and Papadrakakis, M., 2004. Three dimensional nonlinear building pounding with friction during earthquakes. *Journal of Earthquake Engineering*, **8(1)**: 107-132.

Muthukumar, S. and DesRoches, R., 2006. A Hertz contact model with non-linear damping for pounding simulation. *Earthquake Engineering and Structural Dynamics*, **35**: 811-828.

Naeim, F., Lew, M., Huang, S.C., Lam, H.K. and Carpenter, L.D., 2000. The performance of tall buildings during the 21 September 1999 Chi-Chi earthquake, Taiwan. *The Structural Design of Tall Buildings*, **9**: 137-160.

Ndambi, J.M., Peeters, B., Maeck, J., Visscher, J.D., Wahab, M.A., Vantomme, J., Roeck, G.D. and Wilde, W.P.D., 2000. Comparison of techniques for modal analysis of concrete structures. *Engineering Structures*, **22**: 1159-1166.

Neville, A.M., 1995. *Properties of concrete*. 4th ed. Harlow: Longman Group, 1995.

Ng, S.C. and Kuang, J.S., 2000. Triply coupled vibration of asymmetric wall-frame structures. *Journal of Structural Engineering, ASCE,* **126(8)**: 982-987.

Noor, F.A., 1991. Recent developments in modeling materials. *Small Scale Modeling of Concrete Structures*, edited by Noor, F.A. and Boswell, L.F., Elsevier Science Publishers LTD, London, 1991, pp.89-118.

Nordenson, G.J.P., 1989. Wind versus seismic designs. *Annals of the New York Academy of Sciences*, **558**: 262-274.

Okada, S. and Takai, N., 2000. Classifications of structural types and damage patterns of buildings for earthquake field investigation. *Proceedings of the 12th World Conference of Earthquake Engineering,* Paper No. 705, Auckland, New Zeeland, 2000.

Okada, S. and Takai, N., 2004. Damage index functions of wooden buildings and reinforced buildings for seismic risk management. *Proceedings of the 13th World Conference of Earthquake Engineering,* Paper No. 727, Vancouver, Canada, Aug. 1-6, 2004.

Pantelides, C.P. and Ma, X., 1998. Linear and nonlinear pounding of structural systems. *Computers and Structures,* **66**: 79-92.

Papadrakakis, M., Apostolopoulou, C., Zacharopoulos, A. and Bitzarakis, S., 1996. Three-dimensional simulation of structural pounding during earthquakes. *Journal of Engineering Mechanics, ASCE,* **122**: 423-431.

Papadrakakis, M. and Mouzakis, H., 1995. Earthquake simulator testing of pounding between adjacent buildings. *Earthquake Engineering and Structural Dynamics,* **24**: 811-834.

Park, Y.J. and Ang, A.H-S., 1985. Mechanistic seismic damage model for reinforced concrete. *Journal of Structural Engineering, ASCE,* **111(ST4)**: 722-739.

Park, Y.J., Ang, A.H-S. and Wen, Y.K., 1985. Seismic damage analysis of reinforced concrete buildings. *Journal of Structural Engineering, ASCE,* **111(ST4)**: 740-757.

Park, Y.J., Ang, A.H-S. and Wen, Y.K., 1987. Damage-limiting aseismic design of buildings. *Earthquake Spectra,* **3(1)**: 1-26.

Park, R. and Paulay, T., 1975. *Reinforced concrete structures.* New York: Wiley, 1975.

Park, S.W., Yen, W.P., Cooper, J.D., Unjoh, S., Terayama, T. and Otsuka, H., 2003. A comparative study of US-Japan seismic design of highway bridges: II. Shake-table model tests. *Earthquake Spectra,* **19(4)**: 933-958.

Penzien, J., 1997. Evaluation of building separation distance required to prevent pounding during strong earthquakes. *Earthquake Engineering and Structural Dynamics,* **26**: 849-858.

Press, W.H., Teukolsky, S.A., Vetterling, W.T. and Flannery, B.P., 1992. *Numerical recipes in FORTRAN: the art of scientific computing* (2nd Ed.). Cambridge University Press, 1992.

Qi, S.Q. and Jiang, K.X., 1999. *Selection of Epigraph and Photos etc. on Earthquakes in China.* Seismological Press, Beijing, China.

Reynolds, P. and Pavic, A., 2000. Impulse hammer versus shaker excitation for the modal testing of building floors. *Experimental Techniques,* **24(3)**: 39-44.

Rodriguez-Gomez, S. and Cakmak, A.S., 1990. *Evaluation of seismic damage indices for RC structures.* Technical Report NCEER-90-0022, National Center for Earthquake Engineering Research, State University of New York, Buffalo, NY.

Rosenblueth, E. and Meli, R., 1986. The 1985 earthquake: causes and effects in Mexico City. *Concrete International*, American Concrete Institute, **8(5)**: 23-34.

Roufaiel, M.S.L. and Meyer, C., 1987a. Analytical modeling of hysteretic behaviour of R/C frames. *Journal of Structural Engineering, ASCE*, **113(3)**: 429-444.

Roufaiel, M.S.L. and Meyer, C., 1987b. Reliability of concrete frames damaged by earthquakes. *Journal of Structural Engineering, ASCE,* **113(3)**: 445-457.

Rutenburg, A. and Heidebrecht, A.C., 1975. Approximate analysis of asymmetric wall-frame structures. *Building Science*, **10**: 27-35.

Saatcioglu, M. and Humar, J., 2003. Dynamic analysis of buildings for earthquake-resistant design. *Canadian Journal of Civil Engineering,* **30(2)**: 338-359.

Schnabel, P.B., Lysmer, J. and Seed, H.B., 1972. *SHAKE: A computer program for* *earthquake response analysis of horizontally layered sites.* Report No. EERC 72-12, Earthquake Engineering Research Center, University of California, Berkeley, CA.

SEAOC, 1999. *Recommended lateral force requirements and commentary.* Seventh Edition, Structural Engineers Association of California (SEAOC), Sacramento, CA.

Sedarat, H., 1989. *Effects of torsion on the seismic response of structures*. Ph.D. thesis, University of California, Berkeley, USA.

Seo, J.M., Choi, I.K. and Lee, J.R., 1999. Experimental study on the aseismic capacity of a wooden house using shaking table. *Earthquake Engineering and Structural Dynamics,* **28(10)**: 1143-1162.

Shinde, A. and Hou, Z.K., 2005. A wavelet packet based sifting process and its application for structural health monitoring. *Structural Health Monitoring - An International Journal,* **4(2)**: 153-170.

Singhal, A. and Kiremidjian, A.S., 1996. Method for probabilistic evaluation of seismic structural damage. *Journal of Structural Engineering, ASCE,* **122(12)**: 1459-1467.

Skjaerbaek, P.S., Nielsen, S.R.K., Kirkegaard, P.H. and Cakmak, A.S., 1998. Damage localization and quantification of earthquake excited RC-frames. *Earthquake Engineering and Structural Dynamics,* **27(9)**: 903-916.

Smith, B.S. and Coull, A., 1991. *Tall Building Structures: Analysis and Design.* John Wiley & Sons, Inc., 1991.

State Seismological Bureau, 1991. *Seismic Intensity Zoning Map of China (1:10m scale).* Seismological Press, Beijing, China.

State Seismological Bureau, 1995. *Catalogue of Chinese Historical Strong Earthquakes (From 23 B.C. to 1911 A.D.)*. Seismological Press, Beijing, China.

Stavroulakis, G.E. and Abdalla, K.M., 1991. Contact between adjacent structures. *Journal of Structural Engineering, ASCE,* **117**: 2838-2850.

Stephens, J.E. and Yao, J.T.P., 1985. Estimation of interstory load deformation relations for damaged structures. *Proceedings of the 4th International Conference on Structural Safety and Reliability (ICOSSAR 85)*, Kobe, Japan, **II**: 61-70.

Stephens, J.E. and Yao, J.T.P., 1987. Damage assessment using response measurement. *Journal of Structural Engineering, ASCE*, **113(4)**: 787-801.

Sternik, M. and Gluck, J., 1993. Decoupling of lateral equilibrium equations for asymmetric multistory structures. *Journal of Structural Engineering, ASCE*, **119(10)**: 2871-2882.

Stone, W.C. and Taylor, A.W., 1993. Seismic performance of circular bridge columns designed in accordance with AASHTO/CALTRANS standards. *NIST Building Science Series 170*, National Institute of Standards and Technology, Gaithersburg MD.

Su, R.K.L., Chandler, A.M., Li, J.H. and Lam, N.T.K., 2002. Seismic assessment of transfer plate high rise buildings. *Structural Engineering and Mechanics*, **14(3)**: 287-306.

Thambiratnam, D.P. and Corderoy, H.J.B., 1994. Effects of asymmetry on the response of multistorey buildings to earthquakes, *Engineering Structures,* **6(3)**, 210-221.

Thambiratnam, D.P. and Thevendran, V., 1992. Simplified analysis of asymmetric buildings subjected to lateral loads. *Computers and Structures*, **43(5)**: 873-880.

Tomazevic, M. and Klemenc, I., 1997. Verification of seismic resistance of confined masonry buildings. *Earthquake Engineering and Structural Dynamics,* **26(10)**: 1073-1088.

Toussi, S. and Yao, J.T.P., 1983. Hysteresis identification of existing structures. *Journal of Engineering Mechanics, ASCE*, **109(5)**: 1189-1203.

Tso, W.K. and Cheung, V.W.T., 1986. Decoupling of equations of equilibrium in lateral load analysis of multistory buildings. *Computers and Structures*, **23(5)**: 679-684.

Tso, W.K. and Meng, V., 1982. Torsional provisions in building codes. *Canadian Journal of Civil Engineering,* **9(1)**: 38-46.

Vacareanu, R., Radoi, R., Negulescu, C. and Aldea, A., 2004. Seismic vulnerability of RC buildings in Bucharest, Romania. *Proceedings of the 13th World Conference of Earthquake Engineering*, Paper No. 1798, Vancouver, Canada, Aug. 1-6, 2004.

Wakabayashi, M., 1986. *Design of Earthquake-Resistant Buildings.* McGraw-Hill, Inc., 1986.

Wang, M.L. and Shah, S.P., 1987. Reinforced concrete hysteresis model based in the damage concept. *Earthquake Engineering and Structural Dynamics,* **15(8)**: 993-1003.

Wang, Q.F., Wang, L.Y. and Liu, Q.S., 1999. Seismic response of stepped frame-shear wall structures by using numerical method. *Computer Methods in Applied Mechanics and Engineering,* **173**: 31-39.

Wen, Z.P., Hu, Y.X. and Chau, K.T., 2002. Site effect on vulnerability of high-rise shear wall buildings under near and far field earthquakes. *Soil Dynamics and Earthquake Engineering*, **22**: 1175–1182.

Westermo, B.D., 1989. The dynamics of interstructural connection to prevent pounding. *Earthquake Engineering and Structural Dynamics,* **18**: 687-699.

Wilkinson, S. and Thambiratnam, D.P., 2001. Simplified procedure for seismic analysis of asymmetric buildings. *Computers and Structures*, **79**: 2833-2845.

Williams, M.S. and Sexsmith, R.G., 1995. Seismic Damage Indices for Concrete Structures: A State-of-the Art Review. *Earthquake Spectra*, **11(2)**: 319-349.

Wong, Y.L., Zhao, J.X., Chau, K.T. and Lee, C.M., 1998a. Assessment of seismicity model for Hong Kong region. *The HKIE Transactions,* **5(1)**: 50-62.

Wong, Y.L., Zhao, J.X., Lam, E.S.S. and Chau, K.T., 1998b. Assessing seismic response of soft soil sites in Hong Kong by using microtremor records. *The HKIE Transactions*, **5(3)**: 70-79.

Xu, Y.L. and Chen, J., 2004. Structural damage detection using empirical mode decomposition: Experimental investigation. *Journal of Engineering Mechanics, ASCE,* **130(11)**: 1279-1288

Yao, G.C.C. and Chang, K.C., 1995. A study of damage diagnosis from earthquake records of a steel gable frame. *Journal of the Chinese Institute of Engineers,* **18(1)**: 115-123.

Yin, Z.Q., 1995. *The Method of Seismic Damage and Loss Prediction*. Seismological Press, Beijing, China, pp. 49–72, in Chinese.

Zhang, M.Z., 1997. Some opinion on the application of similitude law in earthquake simulation test. *Earthquake Engineering and Engineering Vibration,* **17(2)**: 52-58, in Chinese.